Imperial College of Science, Technology & Medicine

University of London

# Exploiting the Laser Scanning Facility for Vibration Measurements

Milena Martarelli

A thesis submitted to the University of London
for the degree of Doctor of Philosophy

# Abstract

The aim of this research was to explore a vibration measurement technique based on the use of a non-contacting response transducer which can be set continuously scanning over the surface of a sinusoidally-excited structure. Specifically in this context, a laser Doppler vibrometer (LDV) was employed as a remote velocity transducer so that the specific testing technique studies was classified as continuous scanning laser Doppler vibrometry (CSLDV).

This technique is a type of “spatial field” measurement (such as is holography) that aims to overtake the essential limitation of conventional vibration tests, i.e. the number of measured points is limited by the set of transducers that can be physically attached to the structure so that the spatial resolution of mode shapes derived from such measurements is limited. By using an optical non-contacting transducer which scans continuously across the area under test, vibration information can be derived at each point of the scanned pattern without any physical restriction.

Basically, the work is divided into two main sections. The first section presents an introduction to laser vibrometry, while the second concentrates on both theoretical and practical aspects of the CSLDV method.

When an LDV is scanned continuously along an arbitrarily line, the LDV output is an amplitude-modulated sine wave according to the structure operational deflection shape (combination of mode shapes). Smooth mode shapes, which can be defined by polynomial functions across the scanned area, may be recovered as a set of polynomial coefficients derived from the LDV output analysed in the frequency domain, which spectrum comprises sidebands centred on the excitation frequency and spaced at multiples of the scan frequency(ies). When the extent of the scanned line reduces until it becomes shorter than the wavelength of the vibration pattern, the number of sidebands decreases to a single pair only, from which angular and translational vibration responses at the point addressed can be recovered.

The methodical approach of the research investigation consisted of a theoretical analysis of the continuous scanning technique, the numerical simulation (virtual testing) and the experimental validation on simple experimental models. Software for control, data-acquisition and post-processing was developed in order to build a user-friendly laboratory tool to apply the CSLDV in all its facets. Finally, the techniques were shown to work successfully in practical test conditions, by applying them to complex structures taken from industrial case studies.

# Acknowledgements

I wish to express my gratitude to my supervisor Professor D. J. Ewins for his interest in this project, his strategic guidance concerning the scientific development of this work and for his philosophical suggestions during the writing up of this thesis.
Special thanks are due to Mr A. B. Stanbridge for his fundamental teaching and useful discussion throughout the duration of this research. I would like to thank also my former colleagues Drs Götz Von Groll and Saeed Ziaei-Rad for their friendship over the years and their scientific and technical assistance in solving practical problems.
I thank the entire Dynamics group for the cooperation and the encouraging support during my stay at Imperial College, especially Ms Liz Savage for her help and friendly advise.

I acknowledge the financial support of the BRITE/EURAM VALSE project which entirely funded this research. I would like to thank all the partners involved in the project and, in particular, Dr Paolo Castellini, Professors E. P. Tomasini and N. Paone from University of Ancona, Dr Karl Bendel from Bosch, Dr David Storer from CRF and Dr Fernando Baldoni from Bridgestone/Firestone.

# Contents

# List of Figures

# List of Tables

# Chapter 1 Introduction

## *1.1. Background*

The experimental approach to structural vibration is a fundamental activity required for use in most engineering problems in order to control the vibration nature and level of mechanical structures. Experimental observations have been applied to structures for which a rigorous knowledge of dynamic characteristics is essential because vibration is related to the structure's performance and cannot be reliably predicted. Unwanted structural vibrations lead to malfunction during excessive motion or they cause disturbance or discomfort, including noise. Then, the major objective of experimental studies is to observe structural vibration behaviour which has not been predicted or, if mathematical model has been produced, to tell how the prediction is accurate.

Structural dynamic measurements are often carried out to identify or to verify a mathematical model of a test structure. Vibration modes deduced from analysis of measured data can be compared with corresponding data generated by a finite element model and the results are used to adjust or to correct the theoretical model (Model Updating) by making it suitable for predictive design.

Vibration measurements for modeling purposes are called “Experimental Modal Analysis” (EMA) or “Modal Testing” [1], which activity is focused on determining a mathematical model of structure’s dynamic behaviour from measured applied inputs and resulting outputs.

Undertaking a modal test requires expert knowledge of techniques of instrumentation, signal processing and modal parameter estimation. Essentially, the aspects of the measurement process which demand particular attention are: experimental test rig preparation, correct transduction to measure force input and vibration response, and signal conditioning and processing. Great care must be taken in these aspects during the experiment in order to acquire high-quality data. The first stage of test preparation involves some mechanical topics such as the structure’s support and excitation conditions. The second stage consists of transducer selection, which is related to the structure characteristics and to environmental conditions. At the third stage, the vibration response measurement takes place and the experimenter must pay particular attention to acquisition accuracy and data quality. The last stage consists of a detailed analysis of measurement data, including digital signal processing, which should be appropriate to the type of test used.

A basic measurement set-up used for modal tests consists of three major items: (i) an excitation device (attached shaker or hammer), (ii) a transduction system, and (iii) an analyser which measures the signals in output from the transducers. There are many different possibilities in the area of transduction mechanisms but for the most part, piezoelectric transducers (such as accelerometers) are widely used. As these devices are attached to the tested structure, they often introduce a non-trivial mass loading, especially in light or small structures. In these cases, non-contact transducers are required. Moreover, some applications need vibration measurements to be made at many points in order to have a high spatial resolution, for instance in detecting small-size structural faults [2]. Conventional transducers are often not suitable to perform this type of test.

## *1.2. Test Requirements for Advanced Applications*

### *1.2.1 Introduction*

As stated above, non-contact techniques can be very useful to measure vibrations; such a kind of technique is the optical device known as Laser Doppler Vibrometer. The traditional way to use the LDV is as a single-point sensor which measures vibrations by discretely stepping the LDV's measurement target through a grid of points marked on the structure. The single-point laser sensor is then used together with a scanning system, made up of two mirrors having orthogonal axes, which rapidly and precisely deflects the laser beam towards the pre-selected measurement points. The assembly of the two systems (laser sensor and scanning device) constitutes the so-called Scanning Laser Doppler Vibrometer (SLDV). This particular capability provides both spatial information and time dependence of the vibration, and constitutes the difference with other competing optical techniques, including Electronic Speckle Pattern Interferometry (ESPI) and double-pulse laser holography, which provide only spatial information and no means to control the time dependence. Nevertheless, in practice, if the structure's geometry is complicated, a very large number of measurement points may be necessary and the discrete point-by-point approach becomes time-consuming. In addition, the response needs to be acquired and post-processed at all these grid points which means that the data storage requirements becomes large. Until now, the SLDV has been used in many applications (i.e. modal analysis, dynamic testing, noise and quality control and damage identification) mainly to replace conventional transducers, and its powerful and innovative capabilities have not been fully explored. The present work investigates the possibilities using the SLDV in a continuous scanning mode [3] technique capable of avoiding some of these problems (i.e. time-consuming and massive data storage) which are always present in the conventional techniques. The new techniques are referred to as "CSLDV technology".

### *1.2.2 Need for Non –Contact Measurements Devices*

In conventional vibration tests, accelerometers are commonly used to acquire acceleration time histories at selected locations. These devices are a source of error when lightweight structures are examined because the local mass loading of the sensor may distort the results or when fluid flows are studied since the introduced transducer disturbs the flow itself. In the first case, a non-contact sensor is essential and in the second a non-invasive transducer is needed. The Laser Doppler Vibrometer (LDV) introduced by Yeh and Cummins (1964), [4], is an optical velocity-measuring device which satisfies both the characteristics demanded above. This device is based on the measurement of the Doppler shift of the frequency of laser light scattered by a moving object. One of the first applications of the LDV in vibration measurement fields was in the context of extremely lightweight objects such as fibre velocities measurement in spinning and drawing processes in man-made fibre production, [5].

### *1.2.3 Need for Spatially–Dense Measurements*

Many applications of structural vibration tests require spatially dense measurements, where a surface is surveyed with high spatial resolution and a lot of points over the area need to be investigated. The velocity distribution measured over the surface at a given frequency and referred to a reference signal is called “Operating Deflection Shape” (ODS) or simply, less precisely, “Mode Shape”. In this case the mode shape is the vibration pattern on the surface and it is different from the normal modes or eigenvectors which represent the free-vibration solution, together with the eigenvalues (natural frequencies and damping factors). A two-dimensional ODS can be measured over a grid of measurement points using several accelerometers or a SLDV (i.e. the laser beam moves discretely point by point). The latter technique permits a higher resolution because the laser spot dimension is smaller than an accelerometer, but the measurement process is still time-consuming. Alternatively, by using a CSLDV, scans along a line or across an area can be performed enabling mode shapes to be defined along the line or over the area

with only one measurement, [3]. In this way, the LDV can simulate a multitude of transducers located at the area where the scanning is acted, see Figure 1.1. Note that when the laser is scanning continuously the red points become closer and closer.

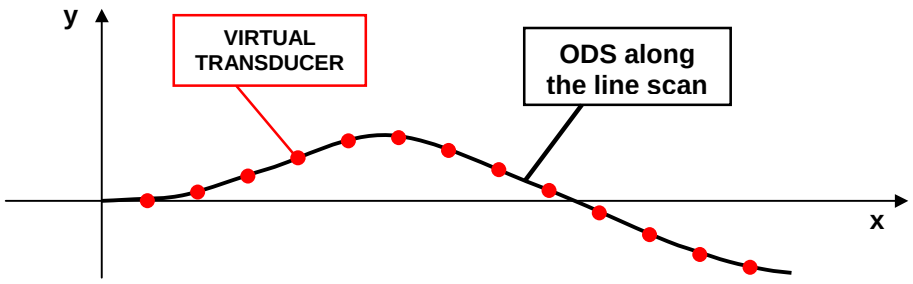


**Figure 1. 1** Virtual transducers location along the laser beam scan line.

The result of the measurement process is a modulated velocity time history with the spatial variation in vibration amplitude being the modulation signal. The physical meaning of the continuous scan is evident if the line scan is seen as a series of consecutive points where the laser beam is moving discretely. When the number of points increases towards infinity the scan becomes continuous. The first point in the scanning line is the first location and the laser returns to this point every cycle, the period of which is the inverse of the scanning rate. In the first cycle the laser measures the first sample of the first, second, third … points along the scanning line; on the second cycle the second sample of the same points is acquired and so on. Without scanning continuously, the velocity sensor is just waiting between samples, on the other hand, with scanning continuously, it scans a number of measurement locations during this waiting period. The response for a number of locations requires the same time to obtain a single response on the discrete scanning technique. Moreover, when a set of transducers are employed and they are positioned at discrete points along the scan line, as the red dots show in Figure 1.1, even if the accuracy of the measurement at each point is 100 %, there will be always an inaccuracy where the measurement is not performed (between the transducers). On the contrary, by scanning continuously, the ODS along the line can be recovered from the

time signal measured, after some signal processing. The spatial definition of the measurement points is, ideally, like going to infinity. In reality, the resolution will be determined by the number of samples used in the acquisition of the time history which could be very large with current commercially-available data acquisition boards (above 500 KSamples per second).

### *1.2.4 Need for Continuous–Field Measurements*

As described above, a SLDV is a measurement system which is potentially useful in mapping the spatial velocity distribution of vibrating surfaces. The spatial resolution should be increased, theoretically, up to infinity if a continuous scan is performed. A good application of this technique is in crack detection, for instance, where it is important not to miss the defect otherwise the tested structure's state is not detectable, and such an occurrence is always a likelihood when measurements are only made at discrete points.

### *1.2.5 Need for Multiple DOFs Measurements*

Sinusoidal vibration of a point on a test structure is defined by a velocity vector in magnitude and phase, that can be expressed by six components on the *x*, *y*, *z* orthogonal Cartesian co-ordinate axes. These components are the so-called Degrees of Freedom (DOFs) related to the point's velocity. Here, velocities are considered because LDV systems characteristics is that they measure velocity, and not acceleration or displacement, owing to the physical principle in which they are based. The velocity components, each in magnitude and phase, will be three translations in the axes directions, $V_x$, $V_y$, $V_z$, and three rotations about the axes themselves, $\dot{\theta}_x, \dot{\theta}_y$ and $\dot{\theta}_z$. An explanation must be made regarding the rotational DOFs; in fact, a point cannot have rotational degrees of freedom, but here the point is rather treated as an infinitesimal element of structure, at the point concerned, where rotations can be defined. The hypothesis that should be made is that the surface element behaves as a rigid body, i.e. in the surrounding

of the specific point the surface is planar and is not subjected to any deformation. Information related to the 'rotational degrees of freedom' (or RDOF) is often required, for example when acquiring data for sub-structure coupling calculations.

If an LDV beam scans continuously along a short line or around a circle over a small element (with linear dimension sufficiently small, i.e. the surface is treated as rigid body) of a harmonically-vibrating surface, its output will be modulated in such a way that can be used to analyse structural vibration in more than one DOF. Linear scanning enables two vibration components to be measured: the translation velocity in the direction perpendicular to the surface and the angular velocity about the direction lying on the surface plane and perpendicular to the line scan. Using circular scanning, two angular vibration DOFs about two mutual orthogonal axes lying in the plane of the test surface can be derived directly from the frequency spectrum of the laser output, together with the translational DOF in the direction perpendicular to the surface itself. A further continuous scanning technique is one where the laser beam scans on a circle over a short-focus lens so that the focal point is scanned in a circular cone. This technique will be named conical scan and it will be applied to recover three translation vibration DOFs at the point where the cone vertex is hitting the test surface, i.e. the measurement point.

### *1.3. Objectives of Research Project*

The specific objectives of this research work derive from the intention of investigating the CSLDV technique which can be the answer to the demands of the advanced applications highlighted in the previous section. These objectives can be summarised as:

1. development of the CLSDV techniques for MDOF vibration response and ODS measurements;
2. simulation of the CSLDV techniques;
3. experimental validation of the CSDLV techniques;
4. application of the CSLDV techniques in industrial cases

### *1.4. Literature Review*

The aim of this thesis is to give a comprehensive description in both mathematical and experimental points of view of continuous scanning laser Doppler vibrometry. Moreover, the work done within this research includes the development of the software to perform the control and the acquisition processes during a CSLDV test.

Previous work found in the literature are mostly done by A. B. Stanbridge [49] who first, used a microphone scanning on a circular pattern near a disc-like structure in 1979, at Rolls-Royce Small Engine Division.

Early works concerning continuous scanning laser Doppler vibrometer were realised by Sriram and al. in 1990-92 when the laser beam was made to scan by means of an oscillating external mirror, [10], [11] and [12].

The use of an LDV was applied to the continuous circular scan performed on rotating disc in 1994 by Bucher et al. in [6] and in 1995 by Stanbridge and Ewins, [7]. MDOF vibration response measurements were first attempted in 1996 by Stanbridge and Ewins by using small linear and circular scans, [8], and a conical scan [9]. The first stage of the research on ODS measurement was carried out in 1996 [3].

Further investigations of the CSLDV technology were undertaken within the BRITE/EURAM project VALSE, [13], by Stanbridge, Martarelli and Ewins and the research developed were published in several papers ([14]- [19]) and technical reports ([20]- [23]).

### *1.5. Structure of Thesis*

The work reported in this thesis has been divided into four main sections:

a) an introduction to laser Doppler vibrometry, which is dealt in Chapter 2, and, in particular, a critical assessment of the state-of-the-art of the scanning laser Doppler technique as applied in some commercially-available LDV such as the Polytec LDVs. The description of this is addressed in Chapter 3;

b) the analysis of the continuous scanning laser Doppler technology used for MDOF vibration response measurement (described in Chapter 4) and for ODS measurement (to which Chapter 5 is entirely devoted). This section constitutes the heart of the thesis where each CSLDV technique is critically analysed and validated being applied to simulated and experimental data;
c) the numerical simulation of a complete CSLDV test which is helpful to rehearse the experiment before going to the laboratory. This operation, so-called “virtual testing”, is described in Chapter 6;
d) the application of the CSLDV techniques to practical cases used to prove the functionality of the techniques in operating conditions. Chapter 7 describes the experimental cases studied and the different CSLDV techniques used.

A summary of each chapter is given here.

**Chapter 2** describes, first, the principles on which the laser Doppler vibrometry is based such as the Doppler effect and the laser light behaviour. Considerable emphasis is given to the analysis of speckle noise, which is an unavoidable phenomenon occurring when a coherent light beam is scattered back from an optically rough surface. The effects produced on measured data by the speckle noise are studied and, in particular, the frequency broadening of the LDV output spectrum is addressed. This effect is markedly visible in the experimental data, and so a through understanding of the phenomenon is important. Secondly, the principal LDV configurations are presented: the Michelson’s and the Mach-Zender interferometer. Finally, the working principles of two LDV systems available on the market, the Polytec and the Ometron LDVs, are outlined and a comparison between the two is deduced by applying them to an identical experimental case.

**Chapter 3** presents the scanning technology applied to the LDV systems and, specifically, the technology used by the commercial system produced by Polytec. This chapter aims to describe the state-of-the-art of the scanning LDV where the term “scan” means that the laser beam moves point-by-point in a

grid of discrete points recording at each time the velocity of the point. The laser beam acts as a transducer which measures at different positions over the tested structure with the advantages of its non-contact nature and the automation of the acquisition on the whole set of points. Several additional features available in the Polytec system for improving the quality of measurement data are addressed as well.

**Chapter 4** is completely devoted to the mathematical investigation, simulation and experimental validation of CSLDV techniques, when applied to MDOF vibration response measurement. Since the laser beam is scanned continuously along short pattern (lines or circles) in the proximity of the measurement target point on the test structure in order to derive from the LDV output the translational and angular vibration at that point, these CSLDV techniques are classified as short scanning techniques. They include:

(i) short linear scan for measuring one translational and one angular component of the velocity at a point;

(ii) small circular scan for measuring two translational and one angular component of the velocity at a point;

(iii) conical scan for measuring the three translational components of the velocity at a point;

(iv) conical-circular scan for measuring the three translational and two angular components of the velocity at a point.

The calibration process of the technique is described, here, in order to provide a definition of the performance of CSLDV technology and an outline of the accuracy of the measured data. The analysis of speckle noise in relation to experimental parameter settings as the scan speed is included, this noise being the most important parameter affecting the accuracy of the measurement.

**Chapter 5** is focused on the description of the CSLDV techniques used for ODS measurement. In this case the laser beam is scanned continuously over a long line or a large circle or even on a 2-dimensional pattern across a whole area. While the laser beam travels along the test surface, the velocity measurement is

acquired continuously and from these data the ODS of this surface can be derived. The final result, achieved in few seconds, is an ODS plotted with any desired resolution over the measured surface. Different techniques (linear scan, circular scan and area scan) are illustrated.

A large part of the chapter is devoted to the modal analysis applied to "frequency response functions" (i.e. FRFs) data measured by the CSLDV technique, with step-sine tests. The aim of this section is to prove the advantages of using such kinds of FRF, specifically, the small amount of data needed to be recorded and the time saving in both the acquisition and the modal analysis processes.

**Chapter 6** presents a numerical simulation of a complete CSLDV test. The mathematical model of an ideal test is, first, derived and, subsequently, models of the sources of noise are included with emphasis given to speckle noise. Comparison between experimental simulated data and real measured data is carried out in order to establish the level of agreement between numerical and measured results.

**Chapter 7** consists of a collection of experimental applications. Several experimental structures were studied and different CSLDV techniques were applied on them:

(i) short-line and small-circular scanning techniques for MDOF vibration response measurement;

(ii) uniform-rate straight-line scan for ODS direct measurement via demodulation of the LDV time history;

(iii) sinusoidal straight-line scan for polynomial ODS recovery;

(iv) parallel sinusoidal straight-line scan for 2-dimensional polynomial ODS recovering;

(v) uniform-rate area scan for 2-dimensional ODS direct measurement via demodulation;

(vi) sinusoidal area scan for 2-dimensional polynomial ODS determination.

# Chapter 2 LDV Theory

## *2.1. Introduction*

Laser Doppler Vibrometry is a well-established technique, based on the Doppler effect, as its name suggests. This phenomenon appears in any form of wave propagation where relative motion of source and receiver causes frequency shifts related to the relative velocity; by measuring the frequency change the velocity may be easily derived. In the LDV technique there is no relative movement of source and receiver: the moving object is a solid surface placed between them where the light is scattered. Rearranging the Doppler formulae in the case of scattering the velocity of this surface, which constitutes the tested object, can be recovered.

Only the invention of lasers made the exploitation of the Doppler technique to measure velocities possible since the existing electromagnetic radiations (infra-red, visible regions and beyond) could not be generated in a controlled way: by using thermal sources, referring on the thermodynamics principles, there is always a limit to the concentration of energy that imply random amplitude and phase fluctuations of the emitted radiation. On the other hand, lasers are

suitable to produce single frequency and constant amplitude oscillations in the optical region with an increased energy density and, more importantly, with a long coherence length.

Velocity measurement based on the Doppler effect cannot be applied directly, being velocities commonly encountered very small with respect to the light velocity and then Doppler shifts produced are small. In fact, the Doppler frequency resulting from a velocity *v* of a solid surface can be derived from the following linear relationship

$$f_D = \frac{2v\cos(\vartheta)}{\lambda} \qquad \textbf{(2. 1)}$$

*v cos* (ϑ) being the velocity component along the direction of illumination of the laser beam when it is directed at the tested surface, see Figure 2.1, where a schematic configuration of a LDV (Michelson arrangement) is shown. In most cases the light reflected by the moving target is collected by a detector placed on the same part of the source with respect to the target. Such receptive modality is defined as “backscattering”.

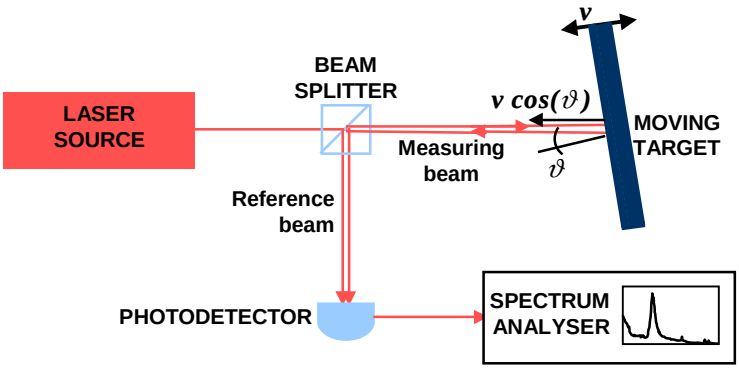


**Figure 2. 1** Basic LDV arrangement.

Assuming the solid surface of the moving target to be perpendicular to the optical axis of the laser source (*cos* (ϑ) = 0° ) and its velocity to be 1 m / s, λ being the wavelength of the light (632.8 nm for a He-Ne laser source) the correspondent Doppler shift will have a value of 3.17 $10^6$ Hz which is extremely small in comparison to the He-Ne laser frequency 4.74 $10^{14}$ Hz. Such a small

resolution can not be measured electronically; the highest resolution optical spectrometer is neither suitable to detect such a small change in frequency. Moreover, direct optical spectroscopy is an impractical technique, which is exceptionally relegated to measure high velocities (i.e. supersonic). Only by mixing the scattered light with a reference beam derived from the same coherent source on the surface of a light detector producing an heterodyne or beat of two frequencies in the output intensity, it is possible to recover from this output the Doppler shift. In fact, the frequency of the signal coming from the photodetector after the beating process is the difference between the two beam frequencies and it is just the Doppler frequency. The photodetector is an opto-electronic device which converts into an electrical signal proportional to the variation of the optical signal intensity and therefore to the velocity of moving scattering object. Using a conventional spectrum analyser, it is possible to determine the beat frequency, bearing in mind that high frequency ranges may be needed.

It is important to emphasize at this point that the optical beating technique can be regarded as an interferometry principle and this is the reason why Laser Doppler systems are usually called interferometers. Although this analogy should be made only when optical surfaces are prepared in such a way to be specularly reflective or, more likely, when tested objects move slowly, in the thesis the term “interferometer” will generally be employed.

In this chapter, fundamental physical principles related with LDV methods are addressed as the Doppler phenomenon (which constitutes the basis of the measurement operation) and laser speckle, which is a property of coherent monochromatic light scattered back from a rough surface on the scale of the optical wavelength. The most common configurations of the LDV are then described, i.e. Michelson and Mach-Zehnder Interferometer), together with some devices, which are capable of discriminating the direction of the velocity which is a peculiar problem in all beating techniques. Acousto-optic devices, such as the Bragg cell, are the most commonly used for this purpose and they

are hereafter afforded special attention. In conclusion, the two LDVs, which are commercially available are highlighted: Polytec and Ometron systems.

## *2.2. Doppler Effect*

### *2.2.1 Introduction*

The so-called “Doppler shift” is a phenomenon which arises when there is a relative motion of the source and the receiver of a wave propagating from one of them: the effect is a change in apparent frequency of the wave seen by the receiver. Such situation may be achieved having a stationary source and a moving observer or a moving source and a static observer but it can be extended to the case where the moving part is an intermediate object through which wave motion is transmitted from the source to the receiver. The latter is the common phenomenon realised in Laser Doppler devices, [4].

### *2.2.2 Stationary Source-Moving Observer*

A stationary source *S* of light waves of wavelength λ and velocity *c* and a moving observer *O*, endued with velocity *u* are considered, see Figure 2.2. The wave-front of the light in the neighborhood of *O* is supposed to be plane, the distance *SO* being large. With the observer *O* travelling towards the source, it will intercept the wave fronts at a higher frequency, the frequency shift being $\Delta f$.

$$\Delta f = \frac{u\cos(\vartheta)}{\lambda} = f\,\frac{u\cos(\vartheta)}{c} \qquad \textbf{(2. 2)}$$

where ϑ is the angle between the direction of the observer motion and the direction of the wave propagation and *f* is the frequency of the emitted wave.

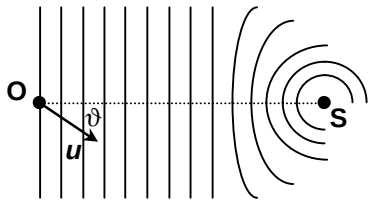


**Figure 2. 2** Doppler effect (Stationary Source-Moving Observer).

### *2.2.3 Moving Source-Stationary Observer*

The opposite situation deals with a moving source which transmits lightwaves of frequency *f* and velocity *c*, to a stationary observer; the relative motion of transmitter and receiver is the same in both cases but the formula describing the frequency shift appears more complicated:

$$\frac{\Delta f}{f} = \frac{\frac{u}{c}\cos(\vartheta)}{1-\frac{u}{c}\cos(\vartheta)} \qquad \textbf{(2. 3)}$$

This expression can be made to agree with the previous one, with the assumption of *u* being small velocity compared with *c*, by expanding it in Taylor power series in $u/c$ and neglecting the higher order addends:

$$\frac{\Delta f}{f} = \frac{u}{c}\cos(\vartheta) + \left(\frac{u}{c}\right)^2 \cos^2(\vartheta) + \left(\frac{u}{c}\right)^3 \cos^3(\vartheta) + \ldots \qquad \textbf{(2. 4)}$$

### *2.2.4 Scattering Condition*

The third Doppler situation occurs when a lightwave is emitted from a stationary source and received by a moving object, which then retransmits to a stationary observer. This circumstance can be visualised as split into two stages: in the first step, there are a stationary source and a moving observer (which is

the inert object) and in the second step, the inert object behaves as moving source, by reflecting to the receiver the incident wave. This is a combination of the two previous configurations and can be described as a "double Doppler shift" and is illustrated in Figure 2.3.

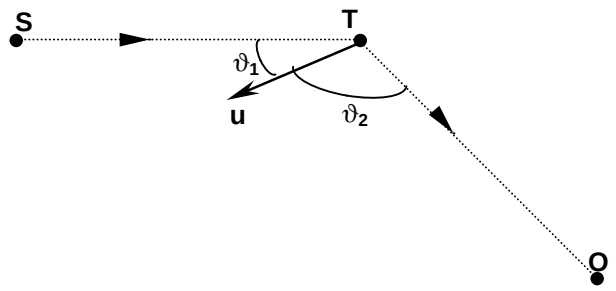


**Figure 2. 3** Doppler effect (Scattering Condition).

The global situation can be decomposed into two configurations, i.e. (i) and (ii):

(i) A stationary source *S* emits lightwaves at frequency *f* and velocity *c*, which are scattered by an observer *T* moving at velocity *u*. The wave frequency received by this latter would be shifted following Equation (2.1) and it will be $f+\Delta f$:

$$f' = f + \Delta f = f + f\frac{u}{c}\cos(\vartheta_1) = f\left(1+\frac{u}{c}\cos(\vartheta_1)\right) \qquad \textbf{(2. 5)}$$

$\vartheta_1$ being the angle between the direction of motion and the direction of waves coming from *S*.

(ii) Now the target *T* re-emits the light at frequency *f '* and it behaves as moving source which is reflecting the waves towards the steady observer *O* with a frequency shift given by Equation (2.2). The final frequency will be:

$$f'' = f' + \Delta f' = f' + f' \frac{\frac{u}{c}\cos(\vartheta_2)}{1 - \frac{u}{c}\cos(\vartheta_2)} = f' \left( 1 + \frac{\frac{u}{c}\cos(\vartheta_2)}{1 - \frac{u}{c}\cos(\vartheta_2)} \right) = f' \left( \frac{1}{1 - \frac{u}{c}\cos(\vartheta_2)} \right) \quad \textbf{(2. 6)}$$

Introducing Equation (2.3) into (2.6) the final Doppler frequency will become:

$$f'' = f \left( \frac{1 + \frac{u}{c}\cos(\vartheta_1)}{1 - \frac{u}{c}\cos(\vartheta_2)} \right) \quad \textbf{(2. 7)}$$

and, for small velocities compared with *c*, expansion in a Taylor power series can be applied, so that, neglecting higher order terms:

$$\frac{f''}{f} = 1 + \left. \frac{d\left(\frac{f''}{f}\right)}{d\left(\frac{u}{c}\right)} \right|_{\frac{u}{c}=0} \frac{u}{c} + \left. \frac{d^2\left(\frac{f''}{f}\right)}{d^2\left(\frac{u}{c}\right)} \right|_{\frac{u}{c}=0} \left(\frac{u}{c}\right)^2 + \ldots =$$

$$= 1 + \left. \frac{\left(1 - \frac{u}{c}\cos(\vartheta_2)\right)\cos(\vartheta_1) + \left(1 + \frac{u}{c}\cos(\vartheta_1)\right)\cos(\vartheta_2)}{\left(1 - \frac{u}{c}\cos(\vartheta_2)\right)^2} \right|_{\frac{u}{c}=0} \frac{u}{c} = \quad \textbf{(2. 8)}$$

$$= 1 + \left(\cos(\vartheta_1) + \cos(\vartheta_2)\right)\frac{u}{c}$$

The final expression for the scattering Doppler shift results as:

$$\Delta f = f'' - f = f \frac{u}{c}\left(\cos(\vartheta_1) + \cos(\vartheta_2)\right) = \frac{2u}{\lambda}\cos\frac{\vartheta_1 + \vartheta_2}{2}\cos\frac{\vartheta_1 - \vartheta_2}{2} \quad \textbf{(2. 9)}$$

In the special case when the source and the receiver are positioned close to each other, as in the LDV configurations available, $\vartheta_1$ and $\vartheta_2$ coincide and the conventional formula returns:

$$\Delta f = \frac{2u}{\lambda}\cos\vartheta \qquad \textbf{(2. 10)}$$

Velocity measurements made by means of an LDV exploit the above-illustrated physical principle where the wave source is a laser and the receiver is a photodetector which measures the target surface velocity related to the Doppler shift.

### *2.3. Laser Light*

Light is an electromagnetic wave arising from interaction of electric and magnetic fields, although in optics magnetic component fluctuation is negligible. The propagation of the light is, then, expressed by the solution of Maxwell's equations, which is, for a plane monochromatic wave of frequency *f* and wavelength λ propagating in *z* direction, neglecting polarization effects:

$$E(z,t) = E_0 \cos\left(\frac{2\pi}{\lambda} z + 2\pi\, f\, t + \varphi\right) \qquad \textbf{(2. 11)}$$

where φ is a phase constant, $E_0$ the amplitude of the electric field and $2\pi/\lambda$ is the so-defined wave-number *k*. Such a wave is an idealisation, which is satisfactorily approached by laser sources.

As the wave advances, the sinusoidal pattern moves along *z* at velocity *c* that depends on the propagation medium. If it is the vacuum *c* will assume the value of $2.997\ 10^8$ m / s. The wave oscillation is described in Figure 2.4.

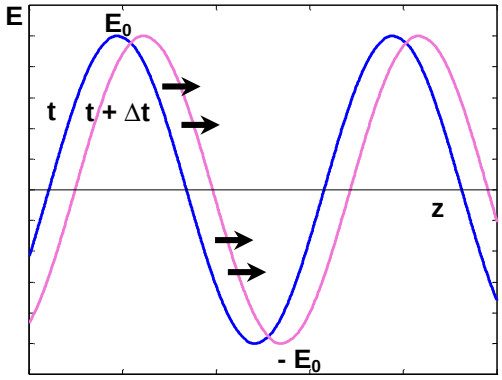


**Figure 2. 4** Electric field fluctuation along its direction of propagation.

In lightwaves theory, in order to simplify the analytical dealing with the electric field, a complex notation is introduced:

$$E(z,t) = \mathrm{Re}\{ E_0 \exp[\, i\,(kz + 2\pi\, f\, t + \varphi)\,]\} \qquad \textbf{(2. 12)}$$

The physical quantity electric field is represented by the real part of the complex expression $E_0 \exp[i\,(\,kz + 2\pi f\, t + \varphi\,)]$. Calling $A$ the complex amplitude of the lightwave:

$$A(z) = E_0 \exp[\, i\,(kz + \varphi)\,] \qquad \textbf{(2. 13)}$$

the analytical signal describing the electric field is

$$\mathrm{E} = A \exp[i\, 2\pi f\, t] \qquad \textbf{(2. 14)}$$

whose real component represent the physical quantity.

Light is then regarded as the oscillation of the electric field described above. In LDV techniques the light contains the sought velocity information; having this oscillation too high frequency to be oserved by available detectors, it is usual to

record its intensity that result to be proportional, by the light velocity, to the square of its complex amplitude:

$$I \propto AA^* \qquad \textbf{(2. 15)}$$

In order to perform velocity measurements using the beating of two lightwaves these latter must have long coherence length, that is the length of the optical path in which a constant phase relation exists between the two lightwaves. In fact interference phenomena can only be observed with coherent waveforms. Another requirement for the light source is to be single frequency. The spectral purity of the light source influences indeed the broadening of the measured Doppler spectrum, together with other factors such as optical imperfections, and velocity fluctuations. The broadening effect consists on a spread of the Doppler signal spectrum around the Doppler frequency; if this widening of the frequency peak becomes too large the spectrum can not be clearly interpreted to give the velocity information.

Laser sources meet these requirements with their spatial and chromatic coherence. They operate by the principle of Light Amplification by Stimulated Emission of Radiation. The amplifying medium, commonly an atomic or molecular gas at low pressure, is contained inside a long discharge tube. When the electric discharge is operated the gas excitation becomes a light amplifier. A cascade process starts: spontaneous emission causes stimulated emission which is amplified as it reflects back and forth many times through the amplifying medium by two high-reflectivity mirrors placed at the ends of the discharge tube. The space contained between the two mirrors is called optical resonator cavity. The resonator action of the optical cavity swamps out the random nature of the spontaneous emission and the light passing through the end-mirrors owns high spatial coherence. In practice lasers own a multi-mode frequency output although there is a dominant transverse mode, which allows to neglect all the others. This uniphase mode, so-called $TEM_{00}$ , yields a Gaussian light intensity distribution circularly symmetrical for the output beam. However

lasers operating in multi-mode are employed especially for large power requirements.

A monochromatic electromagnetic radiation with Gaussian profile of width $w$ and radius of curvature $\sigma$ at a point $\boldsymbol{r}$ in the space ($\boldsymbol{r}$ is the vector position), see Figure 2.5, can be expressed as:

$$E(\mathrm{r}) = E_0 \exp\left(\frac{ik\,\mathrm{r}^2}{2\sigma}\right)\exp\left(-\frac{\mathrm{r}^2}{w^2}\right) \qquad \textbf{(2. 16)}$$

The width $w$ at the point $\boldsymbol{r}$ away from the laser beam waist of the distance $z$ could be expressed as a function of $w_0$ or beam width at its waist.

$$w = w_0\sqrt{1+\frac{z^2}{a^2}} \qquad \textbf{(2. 17)}$$

where

$$a = \frac{\pi\, w_0^{\,2}}{\lambda} \qquad \textbf{(2. 18)}$$

and $\lambda$ is the laser wavelength.

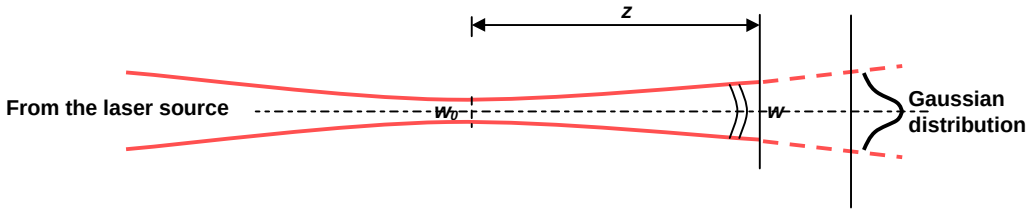


**Figure 2. 5** Gaussian light beam profile.

## *2.4. Laser Speckle*

When coherent light is scattered from an optically rough surface a laser speckle pattern is formed in space in front of the target, [24]. Optically rough surface is a requirement, which is accomplished when the micro-size of the surface roughness is equal or bigger than the wavelength of the illuminating source, according to the “Rayleigh criterion”, which says that a surface tend to be effectively smooth only if the ratio between its irregularities height and the wavelength of the incident beam tends to zero. Thus all but the quite highly polished optical surfaces are candidate to realise the condition for speckle pattern formation, hinting at the conclusion that speckle is unavoidable. The usual appearance of speckle pattern is granular since it is produced by the constructive and destructive interference of the coherent light scattered by the optically rough surface within the illuminated area of the structure. The phenomenon occurs because each microscopic element of the scattering surface within the laser spot acts like a point source of coherent light. At a point in space, individual scattered wavelets from these sources interfere constructively or destructively to produce the bright or dark speckle observed on the screen. The speckle pattern is a continuous random distribution of light amplitude and phase although in practice the quantity observed is the corresponding intensity distribution. The speckle effects are characteristic of monochromatic light and are particularly noticeable with laser sources. When the light contains a broad band of frequencies the speckle patterns for the different frequencies will differ and the effect averages out.

In Speckle Interferometry laser speckles are the information carriers: when the surface moves, the speckle created by the surface also moves, and the resulting changes in phase relationships within individual speckles cause changes in the speckle irradiances. In speckle interferometries, the irradiance change in each speckle is used to measure the displacement (deformation) of the object at that speckle. Thus the essence of the measurement is the monitoring of brightness

changes in each and every speckle, corresponding roughly to each pixel, in a video image of the object.

On the other hand, Laser Doppler Vibrometry investigate the resultant Doppler beat signal coming from the diffusely reflecting object. The signal is then deteriorated by the so-called "speckle noise", which appears as a dropouts of the signal when the light intensity is low ("dark" speckle). The speckle pattern dynamics, reducing accuracy of measurement, limits the performance of the laser system, indeed.

The most important property of the speckle that influences LDV measurements range is the speckle size[1] defined as a statistical average of the distance between adjacent regions of maximum and minimum brightness. This property can be statistically estimated from the space correlation function of the light scattered from a rough surface. Statistical properties of dynamic speckles produced by a diffuse object, which undergoes constant velocity motion within its own plane, have been intensively studied by E. Jackeman, J. G. McWhirter, [25], T. Asakura and N. Takai, [26] and J. H. Churnside, [27]. It is important to remark that if the object illuminated by the coherent light is motionless the scattered light forms a "stationary speckle pattern" which becomes "dynamic" when the object starts to move with an in-plane velocity. In fact the speckle pattern will move in the same direction of the target motion.

As the diffuse reflecting object, where the light is scattered, a model of the deep random phase screen is very often employed: recurring to light-scattering theory, the deep random phase screen is defined as a thin scattering layer which introduces randomly fluctuating path differences into an incident electromagnetic wave. The random phase fluctuations are considered to be Gaussian distributed. The diffuse object is supposed to move with a constant velocity at the object plane. In this situation two different fundamental motions of speckles are produced:

[1] LDV measurements are also influenced by the speckle amplitude and, in particular, phase since most commercial instruments work with one speckle on the detector. If the speckle moves off the detector and is replaced by another, a dark speckle will produce a drop out. If a series of different bright speckles move within the detected area the phase distribution will change randomly [50].

1. for considerable displacement of the diffuse object the speckles move as whole and their shape remains unchanged. This type of speckle motion is called *translation* of speckles.
2. in other cases, as the diffuse object moves, the individual speckles deform, disappear, and reappear without appreciable displacement of their positions. This type of speckle motion is called *boiling* of speckles.

These motions are strictly related to the diffuse object movement but also to the optical parameters ($w$, $\sigma$) and to the distance between the object and the detector ($R$). In practise the speckle translation appears in near-field conditions (observation position close to the object), while the boiling is predominant when the detector is far apart from the moving target (far-field conditions).

Dynamic speckles are then investigated in the diffraction field with the Fresnel diffraction approximation:

1. the distance between the observation plane, where the detector receiving the scattered light from the object is placed, and the diffuse object is finite;
2. the distance between the observation plane and the diffuse object is greater than the largest linear dimension of the lluminated region on the target; and
3. the propagating wave is assumed to be spherical.

A complex Gaussian beam, see Equation (2.16), will be employed for illumination since such a Gaussian beam can be easily obtained with a $TEM_{00}$ mode for the laser. The light scattering configuration is described in Figure 2.6.

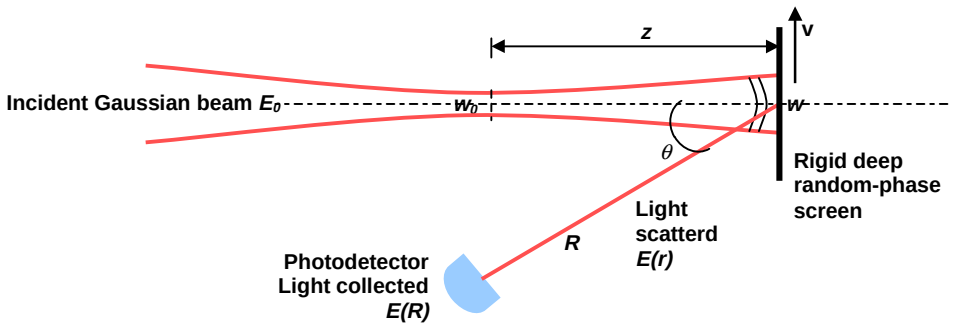


**Figure 2. 6** Light scattering and light collection process.

When the diffuse object moves with the in-plane velocity **v** the light emerging from it will be:

$$E(\mathrm{r},t) = E_0(\mathrm{r})\exp\left[i\phi(\mathrm{r}-\mathbf{v}t)\right]\exp(-i\omega t) = \\ = E_0\exp\left[\frac{ik\,\mathrm{r}^2}{2\sigma}\right]\exp\left(-\frac{\mathrm{r}^2}{w^2}t\right)\exp\left[i\phi(\mathrm{r}-\mathbf{v}t)\right]\exp(-i\omega t) \qquad \textbf{(2. 19)}$$

where $\phi(\boldsymbol{r})$ is the randomly varying position-dependent phase shift caused by transmission through the moving screen and $\boldsymbol{r}$ being the position of the object where the beam is scattered. The phase fluctuation $\phi$ produced by the diffuse object is strictly related to its velocity **v**.

In accordance with the Huygens-Fresnel principle, [28], the field in the observation point, defined by the vector position $\boldsymbol{R}$ (being $R$ its amplitude), is:

$$E(\mathrm{R},t) = \frac{1}{2\lambda}\int_{-\infty}^{\infty} E(\mathrm{r},t)(1+\cos\theta)\exp\left(\frac{i\pi}{\lambda R}|\mathrm{R}-\mathrm{r}|^2\right)d^2\,\mathrm{r} \qquad \textbf{(2. 20)}$$

where the propagation in the mean between screen and detector is assumed in the Fresnel approximation (i.e. the observing screen of the scattered wave is at a finite distance from the scattering surface). The propagation function is then expressed as:

$$h(\mathrm{r},\mathrm{R}) = \exp\left(\frac{i\pi}{\lambda R}|\mathrm{R}-\mathrm{r}|^2\right) \qquad \textbf{(2. 21)}$$

After some manipulations the field detected at **R** will become:

$$E(\mathrm{R},t) = \frac{E_0(1+\cos\theta)}{2\lambda}\exp(-i\omega t)\int_{-\infty}^{\infty}\exp\left(i\phi(\mathrm{r}-\mathbf{v}t)\right)\exp\left(-\frac{\mathrm{r}^2}{w^2}\right)\exp\left(\frac{ik\,\mathrm{r}^2}{2\sigma}\right)\exp\left(\frac{i\pi}{\lambda R}|\mathrm{R}-\mathrm{r}|^2\right)d^2\,\mathrm{r}$$

**(2. 22)**

Dependence on the angle θ, between the optical axis of the incident beam and the detector direction, appears on the observed field expression.

The speckle intensity detected at the point ***R*** on the detector surface will fluctuate randomly in space and in time being scattered by the diffuse object. Under the hipotesys of incident Gaussian beam with zero mean the space-time correlation of the speckle intensity detected can be formulated as:

$$\left\langle E(\mathrm{R}_1;t)E^*(\mathrm{R}_2;t+\tau)\right\rangle \qquad \textbf{(2. 23)}$$

where ⟨⟩ stands for an ensamble average. The correlation is done between the field in two points on the detector surface $R_1$ and $R_2$ and in two instants $t$ and $t+\tau$.

Normalising the previous expression:

$$g(\mathrm{R}_1,\mathrm{R}_2;\tau)=\frac{\left\langle E(\mathrm{R}_1;t)E^*(\mathrm{R}_2;t+\tau)\right\rangle}{\left\langle E(0;t)\right\rangle\left\langle E(0;t)\right\rangle}=\frac{\left\langle E(\mathrm{R}_1;t)E^*(\mathrm{R}_2;t+\tau)\right\rangle}{I(0;t)} \qquad \textbf{(2. 24)}$$

being

$$I(0;t)=[E(0;t)]^2 \qquad \textbf{(2. 25)}$$

and substituting Equation (2.22) in (2.24) the final formulation for the correlation function can be derived:

$$g(\mathrm{R}_1,\mathrm{R}_2;\tau)=\exp\left(-\frac{v^2\tau^2}{w^2}\right)\exp\left[-\frac{\pi^2w^2}{\lambda^2R^2}\left|\mathrm{R}_2-\mathrm{R}_1-\sigma\mathbf{v}\tau\right|^2\right] \qquad \textbf{(2. 26)}$$

The in-plane velocity **v** of the screen appears in the previous expression thus it is experienced by the detected light which constitue the signal output from the detector.

The statistical properties generally analysed are the correlation time length $\tau_C$ obtained by putting $\boldsymbol{R}_1$ and $\boldsymbol{R}_2$ equal zero in the space-time correlation function (time-correlation function $g(0,0;\tau)$) and the correlation length $\Delta x$ obtained by setting $\tau$ equal zero in the same function, i.e. the space correlation function $g(\mathbf{R}_1, \mathbf{R}_2;0)$ is derived.

The time correlation function will be

$$g(0,0;\tau) = \exp\left(-\frac{v^2\tau^2}{w^2}\right)\exp\left(-\frac{\pi^2 w^2}{\lambda^2 R^2}\left|-\sigma\mathbf{v}\,\tau\right|^2\right) = \exp\left(-\frac{\tau^2}{\tau_c^2}\right) \qquad \textbf{(2. 27)}$$

from which the time correlation lenght $\tau_c$ can be derived. This parameter has the phisycal meaning of the transit time of a single speckle across the detector (i.e. time taken for a speckle grain to advance across the receiving area on the detector by one speckle length).

The space correlation function will be

$$g(\mathrm{R}_1, \mathrm{R}_2;0) = \exp\left(-\frac{\pi^2 w^2}{\lambda^2 R^2}\left|\mathrm{R}_2 - \mathrm{R}_1\right|^2\right) \qquad \textbf{(2. 28)}$$

where the quantity

$$S = \frac{\lambda R}{\pi w} \qquad \textbf{(2. 29)}$$

is the correlation length which is strictly related to the speckle size formed in the diffraction field. Within this correlation region the amplitude and phase of the light may be assumed to be constant. In fact, intutitively, if the speckle is larger (larger $S$) the two detectors placed in $\mathbf{R}_1$ and $\mathbf{R}_2$ will measure the same speckle then the speckle intensity correlation is bigger. At points on the

observing screen closer than *S* there is a consistent phase relation between light received from all scattering particles and thus the intensity of illumination is substantially constant. For points far apart, phase correlation is lost and the intensity is in general different. Thus “speckly” illumination is obtained.
For a Helium-Neon laser source of wavelength of 632.8 nm and beam width at its waist of 0.08mm, if the laser source is placed at such a distance from the object that the beam waist is away from it of the length of 300 mm, the laser beam width on the object is 0.7556 mm (*w*). Placing the detector at 1 m from the object it is easy to calculate the average speckle size which is 0.2667 mm.

To the speckle pattern is related the Laser noise which affects measurements in fact, if the detector observes more than one speckle there is a large likelihood that bright and dark areas are detected then the light intensity collected will fluctuate between a minimum and a maximum. Because the device where the analog velocity waveform is derived from the Doppler signal requires that the Doppler signal exceeds an amplitude threshold, below this value the velocity output will be dropped to zero or to a value less than reality and this effect is called “drop-out”, see Figure 2.7.

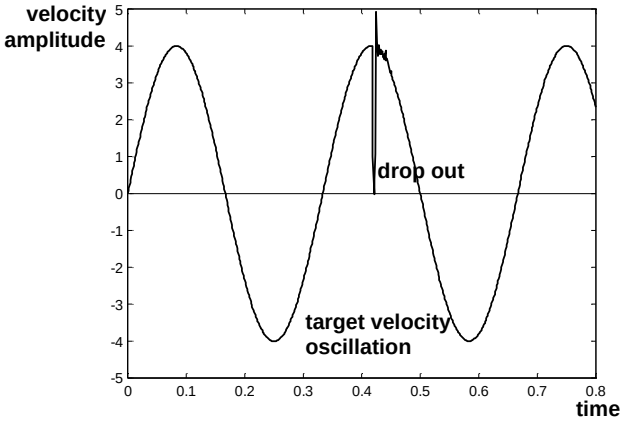


**Figure 2. 7** Velocity Drop out.

Signal dropouts affecting accuracy of the measurement appear if operation distances are not optimal, the test surface is poor reflective or the measuring beam is mis-focused, i.e. spot size on the object is large.

The measurement laser spot should be as small as possible: the ideal situation is achieved when the spot size is exactly the speckle size, allowing the detector to receive just one bright speckle and the coherence to be maximum. Moreover if the surface undergoes a sideways motion the illuminated area is changing during the vibration and the speckle pattern varies at the same time. This causes amplitude and phase detected become random. Increasing the measuring spot size, the sensitivity to surface tilt increases as well, i.e. maintaining the beam focused is an important task. An helpful expedient to realise this task is to treat the structure's surface in order to make it highly diffusely retroreflective and then to increase the intensity of backscattered light. The most commonly applied treatment is the surface coating with a developer spray or retroreflective paper provided by LDV manufacturers. The result is that the surface appear covered with fine matte particles which tend to concentrate more of the scattered light into a restricted angle centered along the laser beam line-of-sight. The Doppler signal level undergoes then an increase, in average, which makes the signal itself more robust to changes in speckle intensities resulting from the speckle motions generated during the motion of the vibrating structure.

Because the speckle pattern, although random, does not change with time unless the test surface is moved relative to the measuring beam, the occurrence of dropouts is spatial and not temporal in nature, [29]. But there are cases where the object is moving relatively to the beam (in-plain vibration or tilts) or vice versa when the beam is scanning along the surface in which case the occurrence of dropouts become periodic. If the surface is subjected to a sideways vibration or if the laser beam is moving the speckle pattern will move with them. Then a further kind of interference on the detected signal will occur: the so-called speckle pattern motion, which is caused by the relative rotation or in-plane translation of the illuminated area. The speckle motion will appear in the output Doppler signal and it will affect the velocity measurement in such a way as a pseudo-vibration, [50], is added to the true one, which is the target motion. This motion mostly appears close to the structure nodes where the vibration is

almost zero but it involves rotation of the surface plane, then the sideways motions are larger.

Speckle noise level found experimentally is always around 1% of the full scale of measurement (-40 dB) as the application chapters show.

### *2.5. Frequency Broadening related to the Laser Speckle*

The speckle intensity fluctuations produced in the diffraction field from an out-of-plane vibrating object scattering a laser light (assumed to have a Gaussian profile) is statistically investigated here. An effect strictly related to the speckle can be identified which is the so-called “frequency broadening” of the detected signal averaged power spectrum. This phenomenon is so-named since, under certain conditions, the frequency spectrum of the LDV output contains not only the component at the vibration frequency of the target, but also all its harmonics. The analysis shows that the behaviour of the averaged spectrum is determined by two physical parameters:

- the derivative value of the amplitude of the object vibration, and
- the beam width of light used for illumination.

It is especially noticed that the power spectral broadening width increases linearly with the increase of these two factors.
Dynamic speckles were studied in detail by T. Asakura and N. Takay, [30], since they were interested in applications to metrology. In fact, speckles produced by a diffuse object contain information about its motion because the space-time statistical properties of dynamic speckles depend on the velocity of the moving object.
The intensity distribution of the speckle pattern formed at a certain receiving plane (see Figure 2.8) in the diffraction field varies as a function of space and time. This quantity is described in terms of:

- the intensity distribution of the illuminating beam arriving on the moving object surface,
- the microscopic surface structure (roughness) of the illuminated object,
- the object vibration, and
- the propagation function of the linear optical system ( *h(R,r)* ), *R* and *r* being the spatial position of the scattered laser light at the vibrating object surface and the spatial position of the detected laser light on the receiver surface, see Figure 2.8.

The illumination of the vibrating object will be modulated in two different ways:

- one is a space-dependent phase modulation due to the surface roughness of the object, and
- the second one is a space- and time-dependent phase modulation due to the vibration of the object.

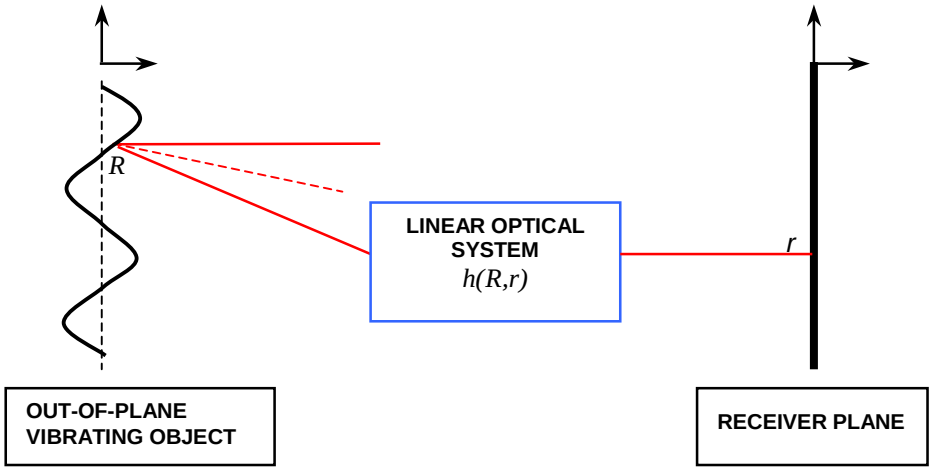


**Figure 2. 8** Schematic of the laser optical path.

The amplitude of speckle fluctuations detected at point $r$ and time $t$ may be expressed as:

$$e(t,r) = \int_{-\infty}^{\infty} E_0(R)\exp[i\phi(R)]\exp[i\psi(t,R)]h(R,r)dR \qquad \textbf{(2. 30)}$$

where $E_0(R)$ denotes the amplitude distribution of laser light illuminating the vibrating object,

$\phi(R)$ is a random phase variable obeying the microscopic random structure of the surface roughness, i.e. it represents the space-dependent phase modulation due to the surface roughness,

$\psi(t\ ,\ R)$ is the vibrating phase term linked to the object vibration, i.e. it represents the space- and time-dependent phase modulation due to the vibration of the moving object, and

$h\ (R, r)$ is the propagation function of the point object from the object plane to the receiving plane, characterising the light propagation.

The vibrating phase term in cases of reflection can be given as:

$$\psi(t,R) = \frac{4\pi}{\lambda}V(R)\sin(\omega_0 t + \theta_0) \qquad \textbf{(2. 31)}$$

$V(R)$ being the vibrating amplitude of the object,

$\omega_0$ the angular frequency of the vibration,

$\theta_0$ the initial phase of the vibrating object, and

$\lambda$ the wavelength of light used for illumination.

Note that the spatial variation of $\psi(t,\mathrm{R})$ depends on the vibration mode of the object and is generally much less than the variation of $\phi(R)$ characterised by the surface roughness of the object [30].

The intensity variation of the speckle will be given by:

$$i(t,r)=e(t,r)e^{*}(t,r)=\int_{-\infty}^{\infty}\int E_0(R_1)E_0^{*}(R_2)\exp\{i[\phi(R_1)-\phi(R_2)]\}$$
$$\exp\{i[\psi(t,R_1)-\psi(t,R_2)]\}h(R_1,r)h^{*}(R_2,r)dR_1dR_2 \qquad \textbf{(2. 32)}$$

Substituting Equation (2.31) into Equation (2.32), the term $\psi(t,R)$ will appear as:

$$\exp\{i[\psi(t,R_1)-\psi(t,R_2)]\}=\exp\left\{i\frac{4\pi}{\lambda}[V(R_1)\sin(\omega_0 t+\theta_0)-V(R_2)\sin(\omega_0 t+\theta_0)]\right\}=$$
$$=\exp\left\{i\frac{4\pi}{\lambda}\sin(\omega_0 t+\theta_0)[V(R_1)-V(R_2)]\right\}=\sum_{n=-\infty}^{\infty}J_n\left\{\frac{4\pi}{\lambda}[V(R_1)-V(R_2)]\right\}\exp[in(\omega_0 t+\theta_0)] \qquad \textbf{(2. 33)}$$

where the exponential term is expanded with respect to time into the Bessel series, which is:

$$\exp(ir\sin\theta)=\sum_{n=-\infty}^{\infty}J_n(r)\exp(in\theta) \qquad \textbf{(2. 34)}$$

$J_n(r)$ being the $n^{\text{th}}$ Bessel function of the first kind. If the vibration amplitude is small within the illuminating light spot on the object the argument $[V(R_1)-V(R_2)]$ of the Bessel function can be approximated by

$$V(R_1)-V(R_2)=V'(R_0)(R_1-R_2)+\frac{1}{2}V''(R_0)\left[(R_1-R_0)^2-(R_2-R_0)^2\right]+$$
$$+\frac{1}{3!}V'''(R_0)\left[(R_1-R_0)^3-(R_2-R_0)^3\right]+\ldots \qquad \textbf{(2. 35)}$$

where $V(R_1)$ and $V(R_2)$ are expanded in a Taylor series around the central point $R_0$ of the beam. Assuming the vibration amplitude $V(R)$ around $R_0$ always small, higher derivatives can be neglected, and Equation (2.32) becomes, then:

$$i(t,R)=\sum_{n=-\infty}^{\infty}\exp[in(\omega_0 t+\theta_0)]\iint_{-\infty}^{\infty}E_0(R_1)E_0^*(R_2)\exp\{i[\phi(R_1)-\phi(R_2)]\}$$
$$J_n\left[\frac{4\pi}{\lambda}\gamma_0(R_1-R_2)\right]h(R_1,r)h^*(R_2,r)dR_1dR_2 \qquad \textbf{(2. 36)}$$

$\gamma_0$ being the first derivative of the vibration amplitude of the object $V'(R_0)$ (i.e. its vibration slope at the central position $R_0$).

The power spectrum of the speckle intensity fluctuation detected at the point $r$ is obtained as:

$$I(\omega,r)=\int_{-\infty}^{\infty}i(t,R)\exp(-i\omega t)dt=\sum_{n=-\infty}^{\infty}\int_{-\infty}^{\infty}\exp(-i\omega t)\exp[in(\omega_0 t+\theta_0)]dt\iint_{-\infty}^{\infty}E_0(R_1)E_0^*(R_2)$$
$$\exp\{i[\phi(R_1)-\phi(R_2)]\}J_n\left[\frac{4\pi}{\lambda}\gamma_0(R_1-R_2)\right]h(R_1,r)h^*(R_2,r)dR_1dR_2=$$
$$\sum_{n=-\infty}^{\infty}\int_{-\infty}^{\infty}\exp[-i(\omega-n\omega_0)\ t]\exp(in\theta_0)dt\iint_{-\infty}^{\infty}E_0(\xi_1)E_0^*(\xi_2)$$
$$\exp\{i\ [\phi(R_1)-\phi(R_2)]\ \}J_n\left[\frac{4\pi}{\lambda}\gamma_0(R_1-R_2)\right]h(R_1,r)h^*(R_2,r)dR_1dR_2 \qquad \textbf{(2. 37)}$$

The time integral can be represented by the Dirac delta and Equation (2.37) can be written as:

$$I(\omega,r)=\sum_{n=-\infty}^{\infty}\delta(\omega-n\omega_0)\exp(in\theta_0)\iint_{-\infty}^{\infty}E_0(R_1)E_0^*(R_2)$$
$$\exp\{i[\phi(R_1)-\phi(R_2)]\}J_n\left[\frac{4\pi}{\lambda}\gamma_0(R_1-R_2)\right]h(R_1,r)h^*(R_2,r)dR_1dR_2 \qquad \textbf{(2. 38)}$$

This is the power spectrum of the intensity of the speckle fluctuation at one point at the detector surface; thus, in order to consider all the speckles an averaged spectrum of the time-varying vibrating speckle intensity fluctuations has to be performed:

$$\left\langle |I(\omega,r)|^2 \right\rangle = \sum_{n=-\infty}^{\infty} \sum_{n'=-\infty}^{\infty} \delta(\omega - n\omega_0)\delta(\omega - n'\omega_0)\exp[i(n-n')\theta_0]$$
$$\int \int_{-\infty}^{\infty} \int\int E_0(R_1)E_0^*(R_2)E_0(R_3)E_0^*(R_4)$$
$$\left\langle \exp\{i[\phi(R_1)-\phi(R_2)-\phi(R_3)+\phi(R_4)]\}\right\rangle \qquad \textbf{(2. 39)}$$
$$J_n\left[\frac{4\pi}{\lambda}\gamma_0(R_1-R_2)\right]J_{n'}\left[\frac{4\pi}{\lambda}\gamma_0(R_3-R_4)\right]$$
$$h(R_1,r)h^*(R_2,r)h^*(R_3,r)h(R_4,r)dR_1dR_2dR_3dR_4$$

where the average is operated only in terms of the random phase variable $\phi(R)$, which represents the roughness of the object surface. From the property of the $\delta$ function the terms in the sum will be non-zero only if $n = n'$ and therefore the averaged power spectrum will become:

$$\left\langle |I(\omega,r)|^2 \right\rangle = \sum_{n=-\infty}^{\infty} \delta(\omega - n\omega_0)$$
$$\int \int_{-\infty}^{\infty} \int\int E_0(R_1)E_0^*(R_2)E_0(R_3)E_0^*(R_4)$$
$$\left\langle \exp\{i[\phi(R_1)-\phi(R_2)-\phi(R_3)+\phi(R_4)]\}\right\rangle \qquad \textbf{(2. 40)}$$
$$J_n^2\left[\frac{4\pi}{\lambda}\gamma_0(R_1-R_2)\right]$$
$$h(R_1,r)h^*(R_2,r)h^*(R_3,r)h(R_4,r)dR_1dR_2dR_3dR_4$$

From the previous equation it can be seen that the averaged power spectrum consists of discrete contributions of line spectra at angular frequencies as:

$$\omega = n\omega_0 \qquad \textbf{(2. 41)}$$

which shows the property of periodically vibrating speckle intensity fluctuations with the same periodicity as that of the vibrating object motion. The magnitude of the averaged power spectrum at the spectral lines $n\omega_0$ is:

$$\int \int_{-\infty}^{\infty} \int \int E_0(R_1)E_0^*(R_2)E_0(R_3)E_0^*(R_4)$$
$$\left\langle \exp\{ i[\phi(R_1)-\phi(R_2)-\phi(R_3)+\phi(R_4)]\}\right\rangle \qquad \textbf{(2. 42)}$$
$$J_n^2\left[\frac{4\pi}{\lambda}\gamma_0(R_1-R_2)\right]$$
$$h(R_1,r)h^*(R_2,r)h^*(R_3,r)h(R_4,r)dR_1dR_2dR_3dR_4$$

The amplitude of the Fourier components depends on the Bessel function of the corresponding order and on the vibration slope $\gamma_0$.

Equation (2.42) can be simplified by making some assumptions:

**1.** The phase variable $\phi(R)$ characterising the roughness of the vibrating object surface follows a Gaussian behavior:

$$\phi(R)=\frac{1}{\sigma\sqrt{2\pi}}\exp\left(-\frac{(R-\mu)^2}{2\sigma^2}\right) \qquad \textbf{(2. 43)}$$

where $\sigma=\sqrt{\left\langle\left[\phi(R)-\left\langle\phi(R)\right\rangle\right]^2\right\rangle}$ and $\mu=\left\langle\phi(R)\right\rangle$ are the standard deviation and the mean value of the distribution $\phi(\xi)$, respectively.

**2.** The random phase variable $\phi(R)$ is spatially stationary (i.e. $\sigma$ and $\mu$ do not depend on the spatial variable $R$ ) and the surface is optically rough (i.e. the roughness of the object surface is extremely fine compared to the size of the illuminating beam). It can be then concluded that the phase variable $\phi(R)$ has an extremely short correlation in space. Under these conditions, the surface roughness is considered to have no correlation between two points, which means that the normalised correlation may be set to

$$\frac{\left\langle\phi(R_1)\phi(R_2)\right\rangle}{\left\langle\phi^2(R)\right\rangle}=\begin{cases}1 & \text{if} \quad R_1=R_2\\ 0 & \text{if} \quad R_1\neq R_2\end{cases}$$

and the same can be written for the other positions ($R_3$ and $R_4$).

**3.** Under the hypothesis of the diffraction field, the propagation function between the object and the receiving plane is given by:

$$h(R,r) = \exp\left[\left(\frac{i\pi}{\lambda \bar{R}}\right)(R-r)^2\right] \qquad \textbf{(2. 44)}$$

$\bar{R}$ being the distance between the object and the receiving plane and λ the wavelength of the propagating light. The absolute value of this function always equals unity whatever the receiving position is.

**4.** The illuminating light beam follows a Gaussian behaviour therefore the intensity scattered out from the object will be:

$$I_0(\xi) = \bar{I}_0 \exp\left[\frac{-(R-R_0)^2}{w^2}\right] \qquad \textbf{2. 45}$$

where $\bar{I}_0$ and $R_0$ are the central intensity and the central position of the Gaussian beam, respectively, and $w$ is the width of the beam at its intersection with the object surface.

Equation (2.40), representing the averaged power spectrum of the speckle fluctuation intensity, can be rewritten as [30]:

$$\left\langle |I(\omega,r)|^2 \right\rangle = \sum_{n=-\infty,\, n\neq 0}^{\infty} \delta(\omega - n\omega_0)\bar{I}_0^2 \int_{-\infty}^{\infty} \exp\left(-\frac{R^2}{w^2}\right) J_n{}^2\left[\frac{4\pi}{\lambda}\gamma_0 R\right] dR \qquad \textbf{(2. 46)}$$

and its magnitude can be deduced as:

$$\sum_{n=-\infty,\, n\neq 0}^{\infty} \bar{I}_0^2 \int_{-\infty}^{\infty} \exp\left(-\frac{R^2}{w^2}\right) J_n{}^2\left[\frac{4\pi}{\lambda}\gamma_0 R\right] dR \qquad \textbf{(2. 47)}$$

The parameters influencing the amplitude of the Fourier components are clearly *w* and $\gamma_0$ . No matter what values *n* assumes, if *w* (i.e. the size of the laser spot) increases these Fourier amplitude components increase because the term $\exp\left(-\frac{R^2}{w^2}\right)$ in Equation (2.47), see Figure 2.9.

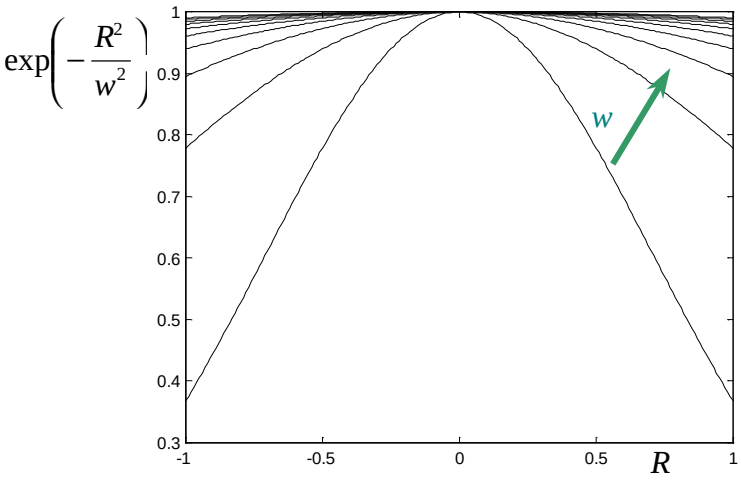


**Figure 2. 9** Gaussian function behavior varying the parameter *w*.

The parameter $\gamma_0$ (the slope of the vibrating surface) is included within the Bessel function that can be expressed as:

$$J_n\left(\frac{4\pi}{\lambda}\gamma_0 R\right) = \sum_{s=0}^{\infty} \frac{(-1)^s}{s!(n+s)!}\left(\frac{4\pi}{2\lambda}\gamma_0 R\right)^{n+2s} \qquad \textbf{(2. 48)}$$

If $\gamma_0$ is small $J_1$ is bigger with respect to $J_2$ , $J_3$ , $J_4$... The amplitude of the higher harmonics are, then, small and they can be neglected. That does not happen when $\gamma_0$ is large, see Figure 2.10.

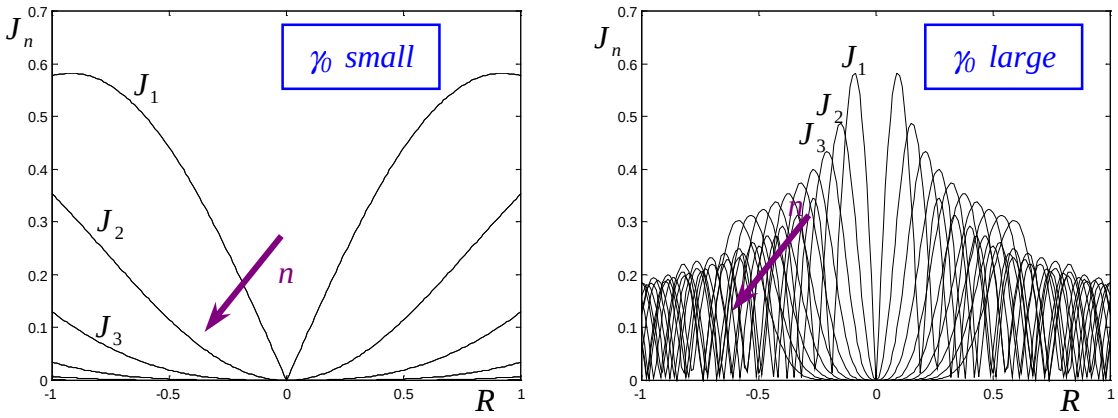


**Figure 2. 10** Bessel function behavior depending on the factor $\gamma_0$.

This means that if the vibration slope is large (i.e. large in-plane vibration component) a large number of harmonics appear in the detected signal spectrum and the so-called "frequency broadening" phenomenon arises. This effect is emphasised if the laser spot on the measurement surface is big (i.e. *w* large, see below).

It is possible to derive the amplitude of the Fourier components of the averaged power spectrum from Equation (2.47). This is, for *n = 1,2,3,...*:

$$\bar{I}_0^2 \int_{-\infty}^{\infty} \exp\left(-\frac{R^2}{w^2}\right) J_n{}^2\left[\frac{4\pi}{\lambda}\gamma_0 R\right] dR \qquad \textbf{(2. 49)}$$

Therefore, for $n=1$ $I_1 = \bar{I}_0^2 \int_{-\infty}^{\infty} \exp\left(-\frac{R^2}{w^2}\right) J_1{}^2\left[\frac{4\pi}{\lambda}\gamma_0 R\right] dR$,

for $n=2$ $I_2 = \bar{I}_0^2 \int_{-\infty}^{\infty} \exp\left(-\frac{R^2}{w^2}\right) J_2{}^2\left[\frac{4\pi}{\lambda}\gamma_0 R\right] dR$,

and so on.

Two cases are considered:

① $w = 1$ and $\gamma_0 = 1$

② $w = 10$ and $\gamma_0 = 10$

For the two cases the functions inside the integral are studied and they are:

$$f_1 = \exp\left(-\frac{R^2}{w^2}\right) \qquad \textbf{(2. 50)}$$

and

$$f_2 = J_n^2\left[\frac{4\pi}{\lambda}\gamma_0 R\right] \qquad \textbf{(2. 51)}$$

Figure 2.11 shows the behaviour of $f_1$ ( see the first plot) and $f_2$ for $n = 1, 2, 3$ ( see the second plot) in the first case ($w$ = 1 and $\gamma_0$ = 1). Figure 2.12 shows the product $f_1 f_2$ and it is clear that this product quickly decreases as soon as $n$ (the order of the Fourier components) increases. In other words, the amplitude of the averaged power spectrum is negligible for the higher harmonics.

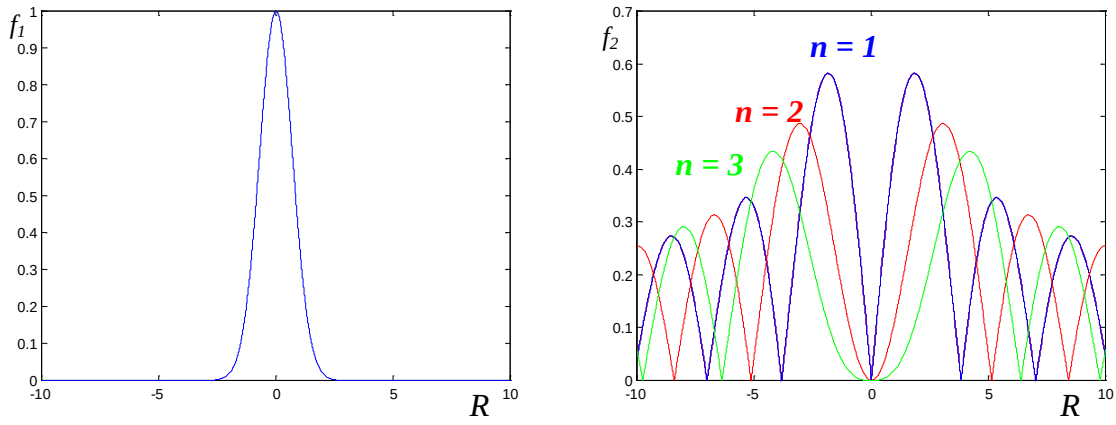


**Figure 2. 11** Gaussian and Bessel functions in the first case study.

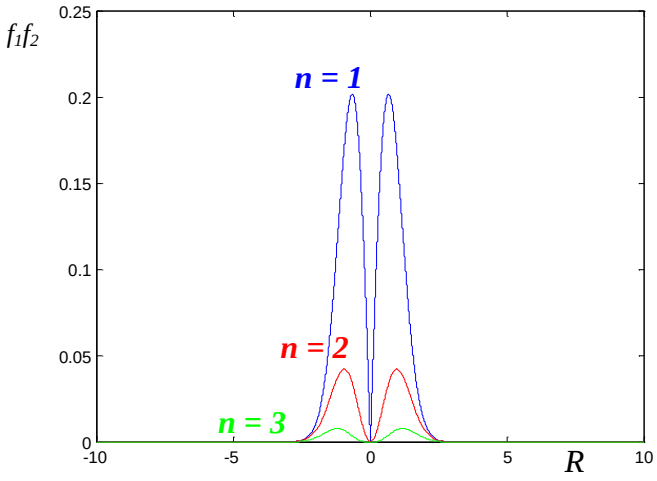


**Figure 2. 12** Product of $f_1$ and $f_2$ for the first case study.

Figures 2.13 and 2.14 show the same functions $f_1$ , $f_2$ and their product for the second case ($w$ = 10 and $\gamma_0$ = 10):

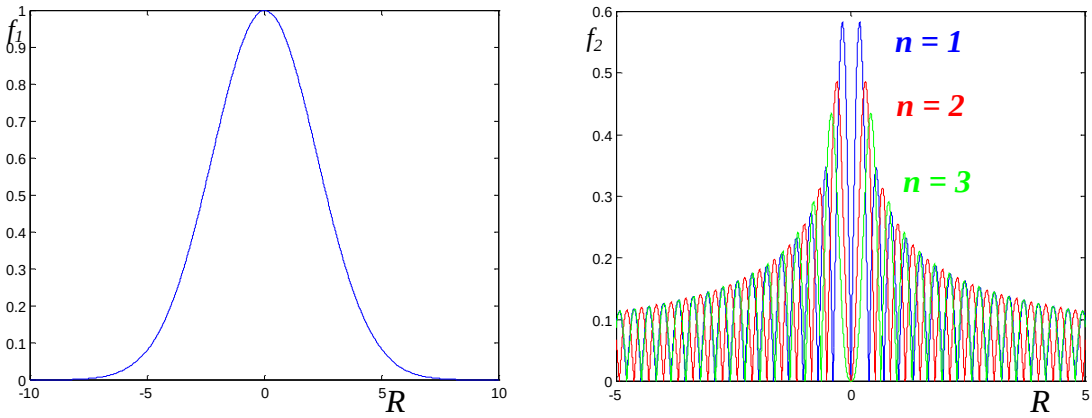


**Figure 2. 13** Gaussian and Bessel functions in the second case study.

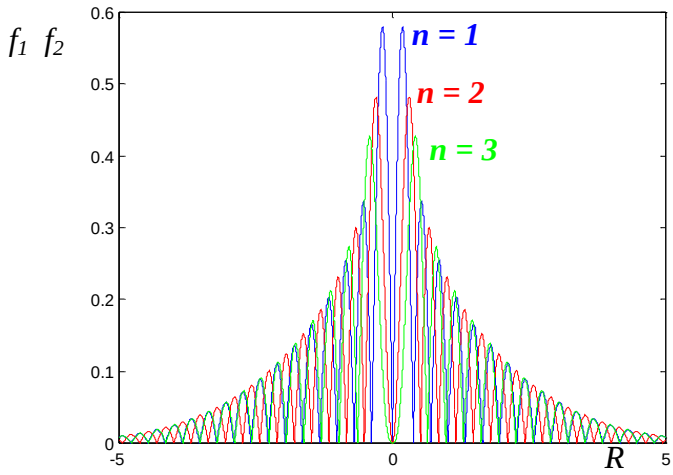


**Figure 2. 14** Product of $f_1$ and $f_2$ for the second case study.

It can be concluded that if *w* is small the spectral component at the fundamental frequency (i.e. for *n = 1*) is dominant since the broadening of the Gaussian function involved in the integral is small (see first plot in Figure 2.11). On the other hand, for relatively large values of *w* the higher order spectral components become more important as shown in Figure 2.14.

The amplitude of the averaged power spectrum is then shown for two more realistic cases:

① $w = 10\ \mu m$ and $\gamma_0 = 0.0016$ rad

② $w = 100\ \mu m$ and $\gamma_0 = 0.0028$ rad

and Figure 2.15 shows the first 15 components of the averaged Fourier spectrum. Note that in the second case the higher harmonics become significant. The most important parameter which leads the analyisis is the laser beam width, *w*. In fact, this latter governs the broadening of the Gaussian function $exp(-R^2 / w^2)$. If the broadening of the Gaussian function is small it does not matter how big the Bessel functions are (i.e. how large the vibration slope is)

because the product of the two functions ($f_1$ $f_2$) will emphasise only the centre of the Bessel functions where the first order only has importance.

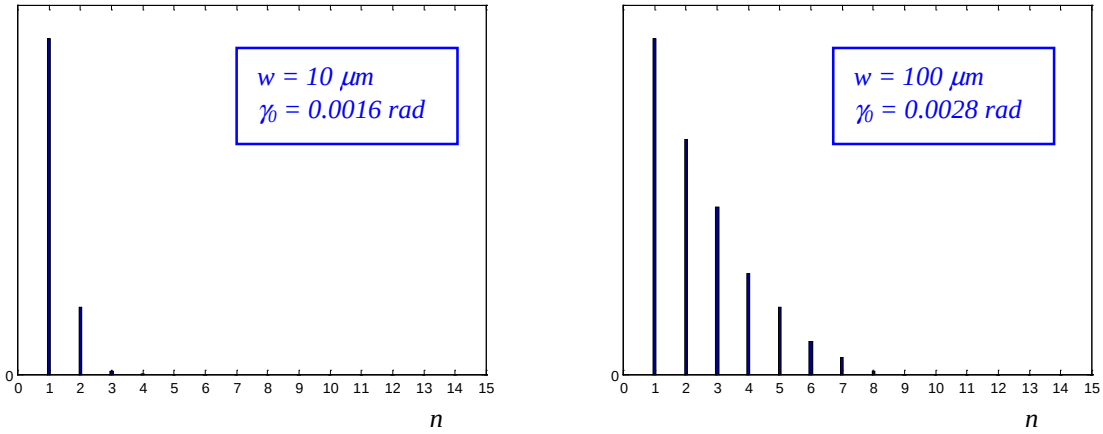


**Figure 2. 15** Averaged power spectrum components for the two cases study.

Now, the laser beam illuminating the object plane is assumed to move along a short straight line while the object vibrates out-of-plane at the frequency $\omega_0$. The vibration experienced by the laser will be affected also by the rotation of the object represented by the vibration slope $\gamma$.

The vibrating phase term as given by Equation (2.31) will be:

$$\psi(t,R)=\frac{4\pi}{\lambda}\left[V(R)\sin(\omega_0 t)+l\cos(\Omega t)\gamma(R)\sin(\omega_0 t)\right] \qquad \textbf{(2. 52)}$$

where $V(R)$ is the vibration amplitude of the object,

$\gamma(R)$ is the vibration slope,

$\omega_0$ is the angular frequency of the vibration,

$\Omega$ is the scan speed of the laser beam,

$l$ is the scanned line length, and

$\lambda$ is the wavelength of the light used for illumination.

$\theta_0$ is the initial phase datum, that is assumed zero.

Expanding out Equation (2.32) it will become:

$$\psi(t,R)=\frac{4\pi}{\lambda}\left\{V(R)\sin(\omega_0 t)+\frac{l}{2}\gamma(R)[\sin((\omega_0+\Omega)t)-\sin((\omega_0-\Omega)t)]\right\} \quad \textbf{(2. 53)}$$

The exponential term including the vibration phase, $\psi(R)$, examinated in Equation (2.33) can be written as:

$$\exp\{i[\psi(t,R_1)-\psi(t,R_2)]\}=\exp\{i\{\frac{4\pi}{\lambda}[V(R_1)\sin(\omega_0 t)+\frac{l}{2}\gamma(R_1)[\sin((\omega_0+\Omega)t)-$$
$$\sin((\omega_0+\Omega)t)]-V(R_2)\sin(\omega_0 t)+\frac{l}{2}\gamma(R_2)[\sin((\omega_0+\Omega)t)-\sin((\omega_0+\Omega)t)]]\}\}=$$
$$=\exp\left\{i\frac{4\pi}{\lambda}\left[\sin(\omega_0 t)[V(R_1)-V(R_2)]+\frac{l}{2}[\gamma(R_1)-\gamma(R_2)][\sin((\omega_0+\Omega)t)-\sin((\omega_0+\Omega)t)]\right]\right\}=$$
$$=\exp\left\{i\frac{4\pi}{\lambda}[\sin(\omega_0 t)[V(R_1)-V(R_2)]]\right\}$$
$$\times\exp\left\{i\frac{4\pi}{\lambda}\frac{l}{2}[[\gamma(R_1)-\gamma(R_2)][\sin((\omega_0+\Omega)t)-\sin((\omega_0+\Omega)t)]]\right\}$$
**(2. 54)**

By applying the trasformation in Bessel series, Equation (2.54) becomes:

$$\exp\{i[\psi(t,R_1)-\psi(t,R_2)]\}=\sum_{n=-\infty}^{\infty}J_n\left\{\frac{4\pi}{\lambda}[V(R_1)-V(R_2)]\right\}\exp(i n\omega_0 t)$$
$$\times\sum_{s=-\infty}^{\infty}J_s\left\{\frac{2\pi l}{\lambda}[\gamma(R_1)-\gamma(R_2)]\right\}\exp[i s(\omega_0+\Omega)t] \quad \textbf{(2. 55)}$$
$$\times\sum_{q=-\infty}^{\infty}J_q\left\{-\frac{2\pi l}{\lambda}[\gamma(R_1)-\gamma(R_2)]\right\}\exp[i q(\omega_0-\Omega)t]$$

It is again assumed that the vibration amplitude can be approximated by the slope and, moreover, that slope can be approximated by the curvature $\beta_0 = \gamma_0' = V_0''$ as seen in Equation (2.35). It can be, then, written:

$$V(R_1)-V(R_2)=V'(R_0)(R_1-R_2)=\gamma_0(R_1-R_2) \quad \textbf{(2. 56)}$$

and

$$\gamma(R_1)-\gamma(R_2)=\gamma'(R_0)(R_1-R_2)=V''(R_0)(R_1-R_2)=\beta_0(R_1-R_2) \quad \textbf{(2. 57)}$$

Substituting Equation (2.56) and (2.57) in Equation (2.55), this latter appears as:

$$\begin{aligned}\exp\{i[\psi(t,R_1)-\psi(t,R_2)]\}&=\sum_{n=-\infty}^{\infty}\sum_{s=-\infty}^{\infty}\sum_{q=-\infty}^{\infty}\exp\{i[(n+s+q)\omega_0+(s-q)\Omega]t\}\\ &\times J_n\left\{\frac{4\pi}{\lambda}\gamma_0(R_1-R_2)\right\}J_s\left\{\frac{2\pi l}{\lambda}\beta_0(R_1-R_2)\right\}J_q\left\{-\frac{2\pi l}{\lambda}\beta_0(R_1-R_2)\right\}\end{aligned} \quad \textbf{(2.58)}$$

The speckle intensity fluctuation obtained in Equation (2.36) is now:

$$\begin{aligned}i(t,R)=&\sum_{n=-\infty}^{\infty}\sum_{s=-\infty}^{\infty}\sum_{q=-\infty}^{\infty}\exp\{i[(n+s+q)\omega_0+(s-q)\Omega]t\}\\ &\int_{-\infty}^{\infty}\int E_0(R_1)E_0^*(R_2)\exp\{i[\phi(R_1)-\phi(R_1)]\}\\ &J_n\left[\frac{4\pi}{\lambda}\gamma_0(R_1-R_2)\right]J_s\left[\frac{2\pi l}{\lambda}\beta_0(R_1-R_2)\right]J_q\left[\frac{2\pi l}{\lambda}\beta_0(R_1-R_2)\right]\\ &h(R_1,r)h^*(R_2,r)dR_1dR_2\end{aligned} \quad \textbf{(2. 59)}$$

From the intensity fluctuation the power spectrum is derived as the following equation shows:

$$\begin{aligned}I(\omega,r)=&\sum_{n=-\infty}^{\infty}\sum_{s=-\infty}^{\infty}\sum_{q=-\infty}^{\infty}\delta\{\omega-[(n+s+q)\omega_0+(s-q)\Omega]\}\\ &\int_{-\infty}^{\infty}\int E_0(R_1)E_0^*(R_2)\exp\{i[\phi(R_1)-\phi(R_1)]\}\\ &J_n\left[\frac{4\pi}{\lambda}\gamma_0(R_1-R_2)\right]J_s\left[\frac{2\pi l}{\lambda}\beta_0(R_1-R_2)\right]J_q\left[\frac{2\pi l}{\lambda}\beta_0(R_1-R_2)\right]\\ &h(R_1,r)h^*(R_2,r)dR_1dR_2\end{aligned} \quad \textbf{(2. 60)}$$

By applying the same approximations used above in this section, the averaged power spectrum can be derived:

$$\left\langle \left| I(\omega,r) \right|^2 \right\rangle = \sum_{n=-\infty}^{\infty} \sum_{s=-\infty}^{\infty} \sum_{q=-\infty}^{\infty} \delta\{\omega - [(n+s+q)\omega_0 + (s-q)\Omega]\}$$
$$\bar{I}_0^2 \int_{-\infty}^{\infty} \exp\left(-\frac{R^2}{w^2}\right) J_n{}^2\left[\frac{4\pi}{\lambda}\gamma_0 R\right] J_s{}^2\left[\frac{2\pi l}{\lambda}\beta_0 R\right] J_q{}^2\left[-\frac{2\pi l}{\lambda}\beta_0 R\right] dR \qquad \textbf{(2. 61)}$$

It is immediate to notice that the amplitude of the Fourier components of the averaged speckle intensity spectrum does not depend only on the laser beam width, *w*, and the vibration slope, $\gamma_0$, but also on the vibration curvature, $\beta_0$, and the line scan length, *l*. Larger the vibration slope and the line scan length are bigger the amplitudes of the averaged power spectrum higher harmonics are. However, as above stated, the most important factor determining the frequency broadening of the averaged power spectrum is the laser beam width at its intersection with the object surface (*w*). Consequently, if this latter can be mantained small, by well-focusing the laser beam, the Gaussian function $exp(-R^2/w^2)$ will be enough sharp that its product with the Bessel functions - see Equation (2.61) - will give emphasis to the first order of harmonic only.

## *2.6. Michelson's Interferometer*

The basic interferometer design (Figure 2.16) was developed by Michelson; it is also called two beams interferometer and it allows detecting displacements, velocities and surface shapes.

Light from the laser source is split by a beam splitter, namely a half-silvered mirror, in the measuring and reference beam, both of them with the same amplitude. The first is directed towards the moving surface velocity of which must be measured, whereas the second one is diverted onto the fixed target. The reflected beams pass again through the beam splitter and they go to feed the photodetector where they are recombined. At this stage, then the optical beating or heterodyning of the two laser beams takes place. The process of optical heterodyning, well known in radio techniques, consists on adding two

signals in a non-linear circuit element such as a detector. The electrical non-linearity of the detector means that its output is proportional to the intensity of the incident light, i.e. to the square of the electrical field.

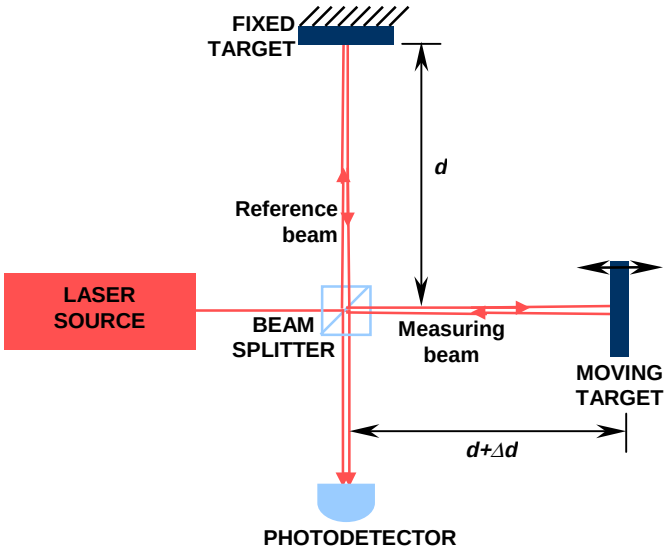


**Figure 2. 16** Schematic representation of Michelson's interferometer.

Considering the laser light produced by the source as a plane wave of frequency *f*, at the time *t* its analytical expression [31] is:

$$E_0(t) = A\exp(i2\pi f\, t) \qquad \textbf{(2. 62)}$$

where *A* is the complex amplitude of the electrical field.

The beam splitter divides this beam in two electrical fields of same amplitude and they are the measuring beam ($E_1$) and the reference beam ($E_2$):

$$E_1(t) = \frac{A}{2}\exp(i\,2\pi f\, t)$$
$$E_2(t) = \frac{A}{2}\exp(i\,2\pi f\, t) \qquad \textbf{(2. 63)}$$

After the beam splitter the two beams follow different optical paths: *d* being the distance between the fixed target and the beam splitter the reference beam will

travel a path long *d*; d+Δ*d* being the distance between the moving target and the beam splitter the measuring beam will cover the distance *d*+Δ*d*. The global difference of optical path traveled by the two beams will be *2*Δ*d*. Since the tested surface is moving, say at velocity *u*, Δ*d* can be expressed, at the instant *t*, as *ut*. The light incident on the photodiode will be:

$$E_1(t) = \frac{A}{2}\exp(i2\pi f\ t)$$
$$E_2(t) = \frac{A}{2}\exp(i2\pi f\ t + i\,2\pi f\ \Delta t\ ) \qquad \textbf{(2. 64)}$$

where Δ*t* is the time necessary to the measuring beam to cover the path difference *2*Δ*d*. Travelling the laser light at the velocity *c* this time interval corresponds to *2*Δ*d*/*c* and, consequentially, *2ut*/*c*. Taking into account the last considerations, Equation (2.64) will became:

$$E_1(t) = \frac{A}{2}\exp(i\ 2\pi f\ t)$$
$$E_2(t) = \frac{A}{2}\exp\left[i\ 2\pi\left(\ f\ +\ f\ \frac{2u}{c}\ \right)t\right] \qquad \textbf{(2. 65)}$$

The output intensity of the detector is the square of the result of the beating between these two electrical fields:

$$I(t) = K\left\{\frac{A}{2}\exp(i\,2\pi f\ t\ ) + \frac{A}{2}\exp\left[i\,2\pi\left(\ f\ +\ f\ \frac{2u}{c}\ \right)t\right]\right\}$$
$$\times\left\{\frac{A}{2}\exp(i\,2\pi f\ t\ ) + \frac{A}{2}\exp\left[i\,2\pi\left(\ f\ +\ f\ \frac{2u}{c}\ \right)t\right]\right\}^{*} \qquad \textbf{(2. 66)}$$

where *K* is the detector sensitivity constant related to its efficiency. Expanding out:

$$I(t) = K\left[\frac{A^2}{2} + \frac{A^2}{4}\exp\left(i\,2\pi f\,\frac{2u}{c}t\right) + \frac{A^2}{4}\exp\left(-i\,2\pi f\,\frac{2u}{c}t\right)\right] \quad \textbf{(2. 67)}$$

Introducing the Euler formula:

$$e^{i\theta} + e^{-i\theta} = 2\cos\theta \quad \textbf{(2. 68)}$$

and considering that $c/f = \lambda$ and $I_0$ is the intensity of the original field, which correspond to the square of its amplitude $A$, i.e. $I_0 = A^2$ :

$$I(t) = \frac{1}{2}KI_0\left[1 + \cos\left(2\pi\frac{2u}{\lambda}t\right)\right] \quad \textbf{(2. 69)}$$

The output contains a beat frequency that is the Doppler frequency $f_D$ , see Equation (2.10), and it holds the surface velocity information.

## *2.7. Mach-Zehnder Interferometer*

A second slightly different LDV configuration is presented in this section, see Figure 2.17. As the Michelson interferometer, this device can be named division amplitude interferometer because the laser beam coming from the source is split in two beams of same amplitude by a beam splitter. Then the measuring beam is reflected by the moving object and the reference one by the fixed target and both of them carry on their travel towards a second beam splitter which directs them onto two photodetectors where they are made to beat. The beams undergo a heterodyning process similar to the one illustrated in the previous section. The difference with the Michelson interferometer consists on the use of two photodetectors where the output intensities are out-of-phase each other. Namely in the first detector will occur a constructive beating, by summing the two incident electric fields ($E_1$ and $E_2$), while in the second a destructive interference will take place by subtracting the same fields.

$$I_1(t) = K_1\left\{\frac{A}{2}\exp(i2\pi f\,t) + \frac{A}{2}\exp\left[i2\pi\left(f + f\frac{2u}{c}\right)t\right]\right\}$$
$$\times\left\{\frac{A}{2}\exp(i2\pi f\,t) + \frac{A}{2}\exp\left[i2\pi\left(f + f\frac{2u}{c}\right)t\right]\right\}^* = \quad \textbf{(2. 70)}$$
$$= \frac{1}{2}K_1 I_0\left[1 + \cos\left(2\pi\frac{2u}{\lambda}t\right)\right]$$

The intensity $I_2$ at the second detector can be simply derived using the principle of energy conservation, i.e. the output intensities from the second beam splitter should be globally $A^2$ at every point in time.

$$I_2(t) = K_2\left\{\frac{A}{2}\exp(i\ 2\pi f\,t) - \frac{A}{2}\exp\left[i2\pi\left(f + f\frac{2u}{c}\right)t\right]\right\}$$
$$\times\left\{\frac{A}{2}\exp(i\ 2\pi f\,t) - \frac{A}{2}\exp\left[i2\pi\left(f + f\frac{2u}{c}\right)t\right]\right\}^* = \quad \textbf{(2. 71)}$$
$$= \frac{1}{2}K_2 I_0\left[1 - \cos\left(2\pi\frac{2u}{\lambda}t\right)\right]$$

Therefore subtracting the two signals the common noise spoiling the system is reduced.

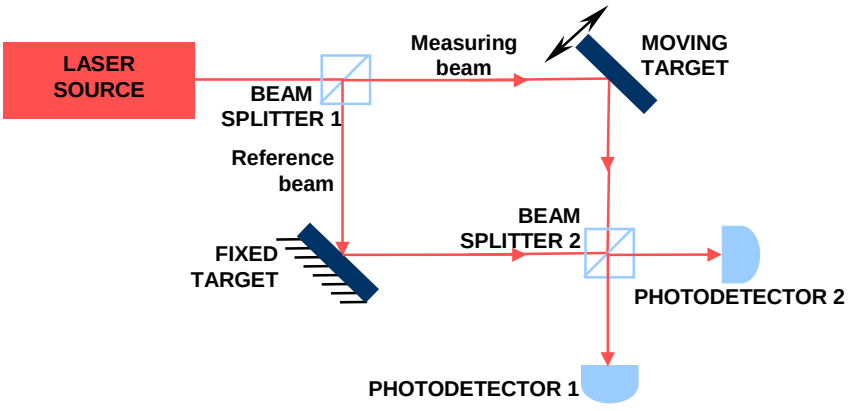


**Figure 2. 17** Schematic representation of Mach-Zehnder interferometer.

## *2.8. Velocity direction investigation*

Determining the sign of the velocity owned by a solid surface is an insoluble question by simple means of LDV arrangements described above: examining formulae 2.70 and 2.71, it is immediately noticeable that a change of sign of $u$, does not provoke any variation on the light intensity collected by the photodetector. In fact, the beating operation, whose feature is that the beat frequency appears as a difference of two frequencies, does not allow to detect which frequency is higher and to associate a sign to their difference. Only by analysing the Doppler signal it is not possible to distinguish whether the testing surface is moving away from or towards the detector. Two means to solve this problem are illustrated in this section: the simplest operation involves the detection of two signals produced from the same light beam but with a phase difference, while the most common makes use of a frequency shift introduced on the laser beams.

The simplest method used for the sake of determining whether the Doppler beat frequency is positive or negative is to duplicate the reference beam in two beams, identical except for a phase difference of 90°, equivalent to an optical path difference of $\lambda/4$, and to make them to beat with the measuring beam in two distinct channels. A determination of which channel leads onto the other gives the directional information required. Considering the laser light as a plane wave linearly polarised it can be analytically described by a single scalar quantity, without loosing generality with respect to the complex representation given by Equation (2.62):

$$E_0(t) = A\cos(2\pi f\, t) \qquad \textbf{(2. 72)}$$

This electrical field constitutes one reference beam, while the other one will be obtained by shifting it of 90°, then:

$$\begin{aligned} E_{1COS} &= A\cos(2\pi f\, t) \\ E_{1SIN} &= A\sin(2\pi f\, t) \end{aligned} \qquad \textbf{(2. 73)}$$

The measuring beam will contain the target velocity information, in term of the Doppler shift $f_D$ see Equation 2.65:

$$E_2 = A\cos[2\pi(f + f_D)t] \qquad \textbf{(2. 74)}$$

The first reference beam $E_{1COS}$ is directed to the first photodetector where the beating with the measuring beam takes place. The same happens in the second photodetector for the reference beam $E_{1SIN}$. The first detector will collect a signal due to the beating between $E_{1COS}$ and $E_2$, while the second one will collect the beat between $E_{1SIN}$ and $E_2$, i.e.

$$\begin{aligned} E_{1COS} + E_2 &= A\cos(2\pi f\, t) + A\cos[2\pi(f + f_D)t] \\ E_{1SIN} + E_2 &= A\sin(2\pi f\, t) + A\cos[2\pi(f + f_D)t] \end{aligned} \qquad \textbf{(2. 75)}$$

Plots of these two signals are shown in Figure 2.18: it is straightforward to notice what channel is leading the other.

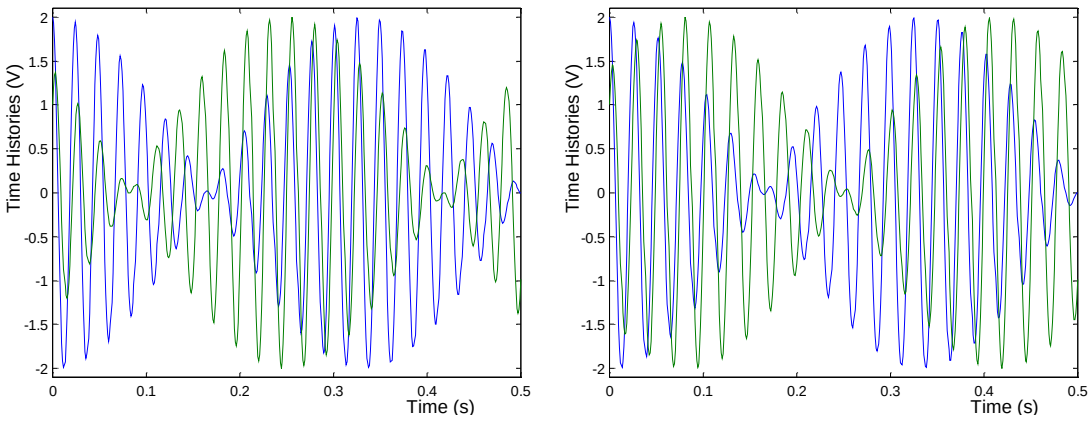


**Figure 2. 18** Plot of the output signal from the first detector (blue) and the output signals from the second detector (green) being $f_D$ positive in the first picture and negative in the second one.

From the previous figure it is clear that in the first case ( $f_D$ positive) the first channel signal leads the second channel one while in the second case ( $f_D$ negative) the opposite situation is realised.

Calculating the intensity output on the detector 1, whose sensitivity constant is $K_1$ , and taking into account trigonometric relationships:

$$I_1 = K_1(E_{1COS} + E_2)^2 = A^2\left[\cos^2(2\pi f\, t) + \cos^2(2\pi(f + f_D)t) + 2\cos(2\pi f\, t)\cos(2\pi(f + f_D)t)\right] =$$
$$= A^2\left\{\left[\frac{1+\cos(4\pi f\, t)}{2}\right] + \left[\frac{1+\cos(4\pi(f + f_D)t)}{2}\right] + \cos(2\pi f_D\, t) + \cos(2\pi(2f + f_D)t)\right\} \quad \textbf{(2. 76)}$$

and neglecting high frequency components which the detector can not observe,

$$I_1 = K_1 I_0[1 + \cos(2\pi f_D\, t)] \quad \textbf{(2. 77)}$$

A same process can be applied to the intensity recorded by the second photodetector, of sensitivity constant $K_2$:

$$I_2 = K_2 I_0[1 + \sin(2\pi f_D\, t)] \quad \textbf{(2. 78)}$$

Again it can be noticed that the current variation in channel 2 leads that into channel 1 by 90°, but if the Doppler frequency sign inverts into a negative value the current oscillation in channel 2 becomes:

$$I_2 = K_2 I_0[1 - \sin(2\pi f_D\, t)] \quad \textbf{(2. 79)}$$

then it is channel 1, which leads into channel 2.

For this system to work it is indispensable that each channel receives exactly similar samples of the scattered light which will be mixed with the reference beams shifted in phase, in such a way that the phase difference between the

channels remains constant. Common optical paths for the two channels must be used and their distinction will reside only in a different polarisation. Division of scattered light into two channels phase-shifted is carried out in optical way, by using a polarising beam splitter whose axes are oriented at 45° to the original plane of polarisation of the light. Conventionally here the plane of polarisation will be described as the plane containing the electric field and the direction of propagation, bearing in mind that in electromagnetic theory an oscillating electric field is always transverse to its propagation direction.

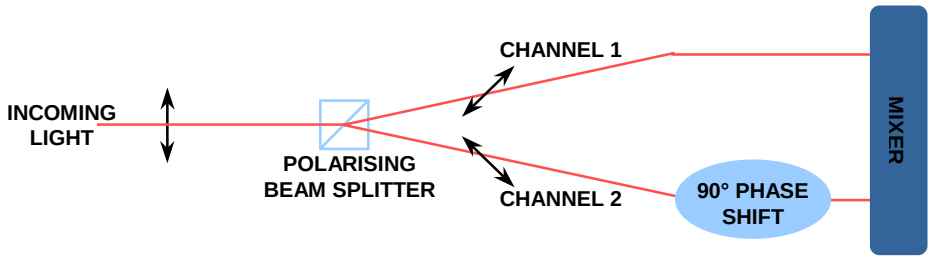


**Figure 2. 19** Schematic of the optical light split and phase shift between the two channels and the mixing of the two outputs after a second phase shift.

It is easier to register the phase difference between the output signals from the two diodes by mixing them: a phase shift of 90° is introduced then into the output of one detector. The phase between the signals applied to the mixer will then be 0° or 180°, depending on the direction of the velocity. The output of the mixer results positive or negative according with the velocity sign. Some smoothing of the output is needed to discriminate against noise but the response must be rapid enough to follow the fluctuations of the tested surface motion as closely as required.

The other method applied to remove velocity directional ambiguity is the so-called frequency shifting technique because the reference beam or both the reference and the measuring one undergo a change in frequency of some tens of MHz. Only a detector is needed in this case and no modification to the optics and signal processing should be made; an additional advantage is that it does

not involve polarisation and, at the end, that it is suitable to follow any velocity fluctuations smoothly through zero.

Producing a frequency shift of reference signal the initial frequency of the two beams will differ of $f_S$ , see Equation (2.65):

$$E_1(t) = \frac{A}{2}\exp[i\,2\pi(f + f_S)t]$$
$$E_2(t) = \frac{A}{2}\exp[i\,2\pi(f \pm f_D)t] \qquad \textbf{(2. 80)}$$

The corresponding beat intensity is given by:

$$I = [E_1 + E_2][E_1 + E_2]^* = \frac{A^2}{2}\{1 + \cos[2\pi(f_S \mp f_D)t]\} = \frac{I_0}{2}\{1 + \cos[2\pi(f_S \mp f_D)t]\} \qquad \textbf{(2.81)}$$

where the beat frequencies are ( $f_S$ + $f_D$ ) and ( $f_S$ - $f_D$ ). This device eliminates the ambiguity of the Doppler frequency sign making directional discrimination possible. The use of a frequency shift greater than the Doppler shift frequency corresponding to the maximum velocity occurring in a series of measurements ensures that ( $f_S$ - $f_D$ ) does not change sign, enabling an unambiguous relation between velocity and signal frequency to be obtained. Figure 2.20 shows the spectrum of the detector intensity output: the shift frequency $f_D$ provides a carrier frequency which is modulated from the targt surface velocity. Tracking the frequency modulation a time-resolved analogue signal can be recorded in both amplitude and phase.

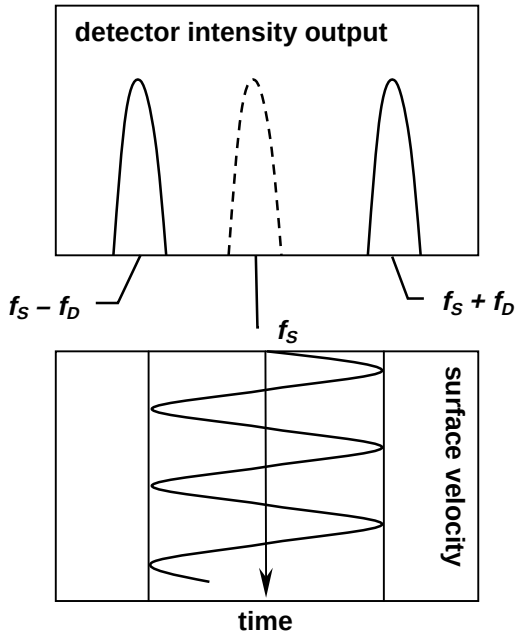


**Figure 2. 20** Frequency shifting and time-resolved velocity, [32].

The cheapest and straightforward technique of shifting the frequency of a laser beam is to make it to pass through a rotating grating which diffracts the incident light wave and makes it to emerge with a frequency change proportional to the rotation speed by the diffraction order and the number of lines of the grating. Tha main problem of this method is that high frequency shifts can not be realised unless high rotational speeds are achieved, but there is always a limit owing to vibration reasons. Then the maximum shift reachable is 5MHz.

When higher frequency shifts are requiered acousto-optic devices are recommended. They are based upon the principle of diffraction of light by acoustic waves that travel inside a cell the most common of which is called Bragg cell. This device operats in the Bragg mode to yield one beam with a frequency and direction different from the incident beam. The cell contains an acousto-optic medium in which acoustic waves are travelling producing a small-scale density variation. This effect generates inside the medium zones with different refraction index and the optical beam travelling throught these zones will be diffracted into several orders. This means that the incoming light

is divided in several beams deviated of an angle and undergone a frequency shift proportional to the acoustic wave frequency. If the incident beam intersects the acoustic waves at the Bragg angle the light intensity tends to be concentrate in just one order of diffraction, specifically the first order for Quartz media. In this way the emerging beam frequency undergoes a shift coincident with the acoustic wave frequency. The commercially available solid medium arrangements provide shifts around 40MHz which generally gives best results and diffraction efficiency.

The Bragg cell introduction is usefull to avoid a further inconvinient: the sensitivity of the system depends upon the phase shift between reference and measuring beams, i.e. when the output intensity is maximum or zero the sensitivity is zero. In fact that quantity is given by the intensity's deviation against the phase shift (that actually is the Doppler frequency):

$$\sigma = \frac{dI}{df_D} = \frac{d}{df_D}\left\{\frac{1}{2} I_0 [1 + \cos(2\pi\ f_D\ t)]\right\} = -\frac{1}{2} I_0 t \sin(2\pi\ f_D\ t) \qquad \textbf{(2. 82)}$$

When $I$ is maximum or zero ($t = n\,\pi\ /\ f_D$ where $n = 0,1,2...$ $I$ will be maximum for even values of $n$ and zero for odd values of $n$) $\sigma$ is zero. Introducing a frequency shift of $f_S$ , $\sigma$ will depend on the sine of ( $f_S + f_D$ ), i.e. it is never zero although measured velocity is such.

### *2.9. Polytec Laser Doppler Vibrometer*

Commercial LDV systems consist of two major components: the optical sensor / controller processor and the scan control / data acquisition system. The optical sensor contains the actual laser, the optical elements, and electrical components needed to spatially position the laser beam. The controller processor, containing the electronic components needed to process the velocity information provided by the optical sensor, constitutes the interface between

the interferometer and the scan control/data acquisition computer. The scan control/data acquisition system consists of the equipment and software needed to manipulate the scan mirrors and to acquire the velocity data. In this section only the first component will be treat, addressing the scan subject in the third chapter.

Commercial systems nowadays available are essentially two: VPI Sensor System manufactured by Ometron and the PSV Polytec product.

The Polytec system is a modified Mach-Zehnder interferometer (Figure 2.21), which allow the laser beam to exit from the "inner" interferometer cell and to hit the external target. A linearly polarised He-Ne laser is employed as a light source, which has polarisation orientated at 45° to the horizontal plane.

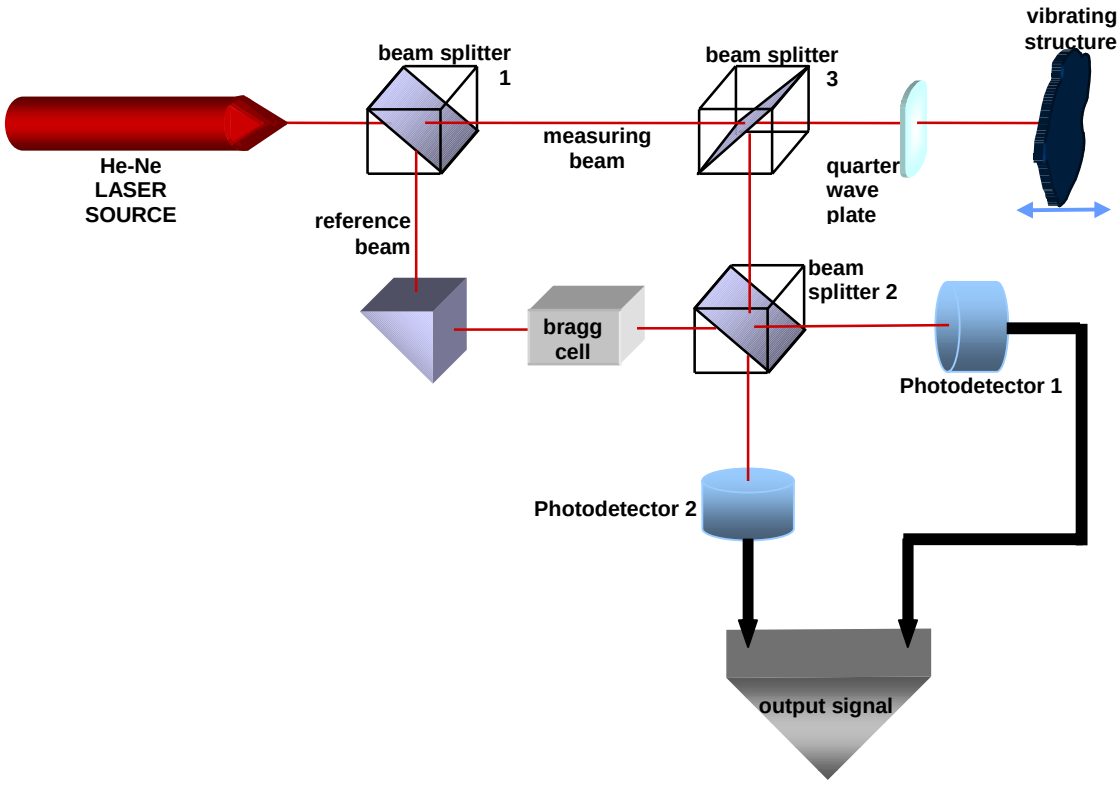


**Figure 2. 21** Polytec LDV arrangement.

Polytec uses as coherent light source a multi-mode (in the longitudinal direction) Helium-Neon laser, linearly polarised with an output power between 2.2 and 3.0 mW. This fact means that there are several modes of oscillation, with

different wavelengths, in the laser length (longitudinal axis), while only a transverse mode is dominant in the distribution of light across the beam and this is the uniphase mode $TEM_{00}$ (characterised by its Gaussian profile and circular symmetry). It is important that in the transverse direction only one mode occurs, since other transverse modes have frequencies slightly different from the $TEM_{00}$ mode and their beating may be then confused with the Doppler signal. On the contrary the occurrence of multi-modes in the longitudinal direction is not so critical, because they can be distinguished by their distinct numbers of wavelengths within the laser length. In order to privilege one mode (say the one with wavelength $\lambda$) the optical path length travelled by the wave that is twice the cavity length (distance between the mirrors placed in the laser oscillator system) must equal a whole number of wavelengths:

$$2L_c = n\lambda \qquad \textbf{(2. 83)}$$

where $L_c$ is the cavity length and $n = 1, 2, \ldots$ .

In this case the wave passing backwards and forwards between the mirrors reinforces itself each time around because each successive passage is in phase. The cavity lenght in the Polytec laser head is 205 mm. In order to assure that the same longitudinal mode will be enphasised during the travel of the laser beam towards to and backwards from the object tested the path followed ($L_p$) must be an integer multiple of the cavity length:

$$L_p = nL_c \qquad \textbf{(2. 84)}$$

wher now $n = 2, 3, \ldots$ since te minimum optical path of the beam must be at least twice the cavity length. $L_p$ can be seen as a sort of 'coherence repeat distance' because is the length where the Doppler interference is maximum and the signal output from the laser is so.

Therefore, if during the operation, a signal level minima is encountered, i.e. fluctuations of signal level occur mostly in the course of the laser warm-up, a

change of the operating distance of half cavity length should resolve the problem.

Configuration shown in Figure 2.17 is changed introducing at the place of the actual moving target a third polarising beam splitter with a quarter wave plate in order to realise a directional coupling: the light coming from the laser is directed straight through the object, while the reflected beam is deflected downwards to the second beamsplitter. The quarter wave plate is used as optical insulator, in order to avoid that the light reflected by the target can return towards the laser source. This optical element, also called retardation plate, has the main characteristic to modify the polarisation of the wave incident. In the case of quarter wave plate the polarisation direction is deviated of $\lambda/4$, i.e. 45°. The entry beam, coming from the polariser beam splitter, see Figure 2.22, owns a polarisation of 45° with respect to the plate axis, then it is transformed in a circularly polarised beam inside the plate. Being reflected back by the target surface the rotation is inverted and the travel across the plate will transmit to the beam a polarisation of 45° but on the opposite direction. Owing this polarisation the light can not pass again inside the beam splitter and it is deviated downwards.

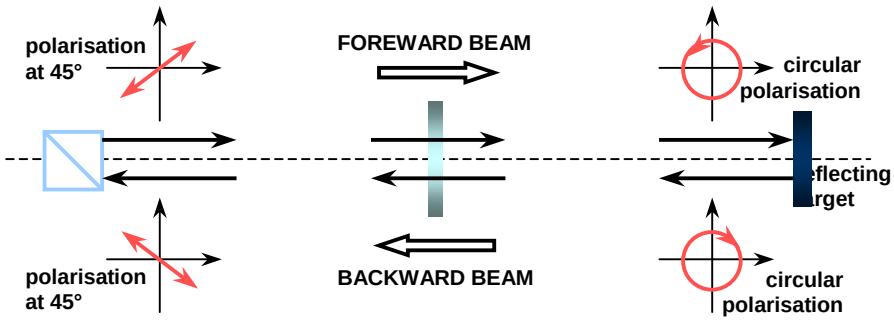


**Figure 2. 22** Quarter wave plate working principle.

Therefore, a second difference with the Mach-Zehnder configuration is the insertion of a Bragg cell as a device to discriminate the target velocity direction. The frequency shift introduced is 40 MHz.

The light intensities $I_1$ and $I_2$ seen by the photodetectors can be derived by the formulae written for the Mach-Zehnder interferometer - Equation (2.70) and (2.71) - taking into account the presence of Bragg cell and then Equation (2.81).

$$I_1 = \frac{1}{2} K_1 I_0 \{1 + \cos[2\pi (f_S \mp f_D) t]\} \quad \textbf{(2. 85)}$$

$$I_2 = \frac{1}{2} K_2 I_0 \{1 - \cos[2\pi (f_S \mp f_D) t]\} \quad \textbf{(2. 86)}$$

Both output signals from the photodetectors, which actually are photodiodes, are converted to electrical signals. Combining them together using a differential pre-amplifier stage the resulting output voltage is given:

$$V = K \cos[2\pi (f_S + f_D) t] \quad \textbf{(2. 87)}$$

where $K$ indicated the conversion efficiency.

The voltage $V$ constitutes the output signal of the interferometer and it is transmitted to the processor controller where the Doppler signal is frequency demodulated to extract the velocity information.To improve the signal quality, affected by velocity drop-outs, the Polytec system has introduced in the controller an optional device, which is the tracking filter[2]. The continuous nature of the Doppler signal from a solid surface measurement allows frequency tracking demodulation. To obtain real time demodulation of photodetector signal giving voltage proportional to instantaneous velocity component a tracking filter is activated instead of using a conventional spectrum analyzer. The tracking scheme is applying the principle of PLL (phase locked loop), where a Voltage-Controlled Oscillator (VCO), controlled via the feedback loop, tracks the incoming Doppler signal. A mixer at the input stage

[2] The frequency tracker allows demodulating the Doppler-signal in order to clean the signal itself from drop-outs. Therefore, it does not enhance signal quality itself. The demodulator must be designed in such a way that it is able to distinguish between a signal drop-out and a vibration's low level when the signal disappears.

produces an “error” signal between the Doppler and VCO frequencies which is band-pass filtered and weighted before being integrated and used to control the oscillator to drive the error to a minimum. The feedback loop has an associated “slew rate” which limits the frequency response of the processor. The overall effect of the tracker is to act as a low pass filter, which output the VCO voltage as a time, resolved voltage analogue of the changing frequency. The frequency range of interest for most vibration measurements is well within the range of this form of frequency demodulation. The tracker incorporates weighting networks, which tailor the control of the VCO according to the signal to noise ratios of the incoming signal. The network will hold the last value of Doppler frequency being tracked if the amplitude of the signal drops below a pre-set level. In this way the Doppler signal effectively drops out and careful consideration must be given to the statistics of what is essentially a sampled output, especially when high frequency information of the order of a dropout period is required. Fortunately for most practical applications this period, typically 0.2 μs, is negligible.

At last another option provided within the Polytec LDV is the auxiliary filter, which is applied to the force-signal to compensate for filter gain and phase-shifts. No such compensation is available in anyone else commercial instrument

### *2.10. Ometron Laser Doppler Vibrometer*

The operating principle is based on the Michelson interferometer technique with the only difference constituted by the introduction of a device to eliminate the ambiguity on the velocity direction of the structural motion along the laser line-of-sight. In the VPI sensor this is done by frequency shifting the frequency-coded velocity information and the shift is accomplished by electronic mixing: the recombined beam is split into two detection channels which are optically configured in such a way that one channel receives interferometric modulation that is effectively shifted by one-quarter wavelength ($2\pi/4 = \pi/2 = 90°$) relative to the other channel. This results in a 90° phase shift between the channels,

which are denoted as “sin” and “cos”. The direction of motion is then determined by which signal phasewise leads the other. Schematic of the VPI Sensor unit is shown in Figure 2.23.

Light emitted by the source reaches the first beam splitter that splits it in two beams of same amplitude, ideally. The first beam ① goes on towards a fixed target (reference beam) while the second ② is deflected to the vibrating structure (measuring beam). Then they are back reflected from the surfaces they hit and they are recombined in the same beam splitter.

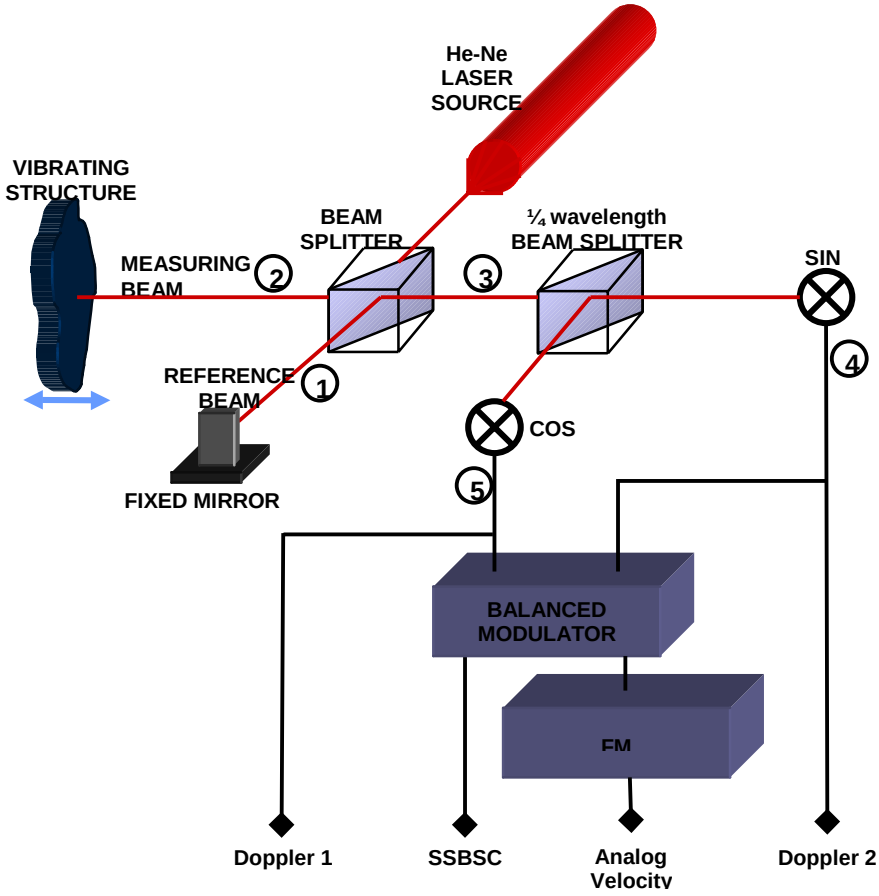


**Figure 2. 23** Ometron VPI configuration.

Being the electric field produced by the laser source $A\ exp\ (-i\omega t)$ , after the split the two fields would have the same amplitude $\frac{1}{2}\ A$ . Because they follow different path, say the one towards the fixed target takes a time as $T_r$ , while the one towards the vibrating object $T_r + T_m$ ($T_m$ is named the time delay associated to the measuring beam), the fields in ① and in ② would have the following expression respectively:

$$E_r = \frac{1}{2} A \exp(i\omega t) \exp(i\omega T_r)$$
$$E_m = \frac{1}{2} A \exp(i\omega t) \exp[i\omega (T_r + T_m)] \qquad \textbf{(2. 88)}$$

After recombination ③ the field detected by the sensor is

$$E_f = \frac{1}{2} A \exp(i\omega t) \exp(i\omega T_r) + \frac{1}{2} A \exp(i\omega t) \exp[i\omega (T_r + T_m)] =$$
$$= \frac{1}{2} A \exp(i\omega t) \exp(i\omega T_r) [1 + \exp(i\omega T_m)] \qquad \textbf{(2. 89)}$$

where $exp\ (\ i\omega T_r\ )$ is a constant depending on the construction specifications of the optical components and $\omega T_m$ is the optical path difference between the reference beam and the measuring one. If the path covered by the measuring beam to shot the vibrating structure is larger than the one followed by the reference beam to reach the fixed object and the difference is $z$ , the comprehensive distance would be $2z$ (for and backward). Then

$$\omega T_m = \frac{2\pi c}{\lambda} \frac{2z}{c} = \frac{4\pi z}{\lambda} \qquad \textbf{(2. 90)}$$

being ω the light frequency ($2\pi\ c/\ \lambda$) , λ its wavelength and $c$ the light velocity. Besides $T_m$ is the time the light needs to cover the distance $2z$ , being its speed $c$. The distance $z$ will depend upon the velocity of the vibrating object in the straightforward way: $z = v\ t$. This leads to the final expression:

$$\omega T_m = \frac{4\pi z}{\lambda} = \frac{4\pi v}{\lambda} t = 2\pi \frac{2v}{\lambda} t = 2\pi f_D t \qquad \textbf{(2. 91)}$$

where the Doppler frequency is easily recognizable $f_D = 2v\ /\ \lambda$ .
Substituting this value in the electric field formulation:

$$E_f = \frac{1}{2} A \exp(i 2\pi f t) \exp(i 2\pi f T_r) [1 + \exp(i 2\pi f_D t)] \qquad \textbf{(2.92)}$$

which is the electric field at position ③ .

If the photodetector is placed at this point (without having any shift of the beam) the intensity that will be decoded is:

$$\begin{aligned} I = E_f E_f^{*} &= \left\{ \frac{1}{2} A \exp(i 2\pi f t) \exp(i 2\pi f T_r) [1 + \exp(i 2\pi f_D t)] \right\} \\ &\times \left\{ \frac{1}{2} A \exp(-i 2\pi f t) \exp(-i 2\pi f T_r) [1 + \exp(-i 2\pi f_D t)] \right\} = \\ &= \frac{1}{4} A^2 [1 + \exp(i 2\pi f_D t) + \exp(-i 2\pi f_D t) + 1] \end{aligned} \qquad \textbf{(2. 93)}$$

From the Euler formulae the measured intensity expression can be simplified as:

$$I = \frac{1}{4} A^2 [2 + 2\cos(2\pi f_D t)] = \frac{1}{2} I_0 [1 + \cos(2\pi f_D t)] \qquad \textbf{(2. 94)}$$

being $I_0$ the intensity of the initial field. The intensity of the electrical field measured is not sensitive to the sign of velocity, which does not produce difference in frequency. The technique used here for the discrimination of the velocity direction is the shifting the frequency of light beams.

The recombined beams are duplicated in two channels, identical except for a phase difference of 90° equivalent to an optical path difference of $\lambda/4$, introduced into one of the beams. A determination of which channel leads onto the other gives the directional information required. This mode of operation is similar to the working principle of frequency trackers manufactured by Cambridge Consultants and by Communications and Electronics Ltd., [32]. The

photodetector signal (in this case $E_f$ at position ③) is divided and mixed separately with two components of a Voltage Control Oscillator (VCO), which produce two outputs at the frequency *f* having a 90° phase relationship with each other. The two mixed signals are low-pass filtered to remove the high frequency components.

Calling the fields in the two channels $E_{SIN}$ and $E_{COS}$ they would result from the mix of the photodetector signal $E_f$ and the outputs form the VCO.

$$E_{SIN} = \frac{1}{4} A \exp(i 2\pi f t) \exp(i 2\pi f T_r)[1 + \exp(i 2\pi f_D t)] \sin(2\pi f t)$$
$$E_{COS} = \frac{1}{4} A \exp(i 2\pi f t) \exp(i 2\pi f T_r)[1 + \exp(i 2\pi f_D t)] \cos(2\pi f t) \quad \textbf{(2.95)}$$

Using the generalised Euler formula:

$$E_{SIN} = \frac{1}{8i} A \exp(i 2\pi f t) \exp(i 2\pi f T_r)[1 + \exp(i 2\pi f_D t)][\exp(i 2\pi f t) - \exp(-i 2\pi f t)]$$
$$E_{COS} = \frac{1}{8} A \exp(i 2\pi f t) \exp(i 2\pi f T_r)[1 + \exp(i 2\pi f_D t)][\exp(i 2\pi f t) + \exp(-i 2\pi f t)] \quad \textbf{(2. 96)}$$

Multiplying and filtering out the high frequency component:

$$E_{SIN} = i \frac{1}{8} A \exp(i 2\pi f T_r)[1 + \exp(i 2\pi f_D t)]$$
$$E_{COS} = \frac{1}{8} A \exp(i 2\pi f T_r)[1 + \exp(i 2\pi f_D t)] \quad \textbf{(2. 97)}$$

This two signals are called Doppler 1 and Doppler 2 and can be derived as output from the VPI sensor. Observing their plots in Figure 2.24 it is straightforeward to notice what channel is leading the other.

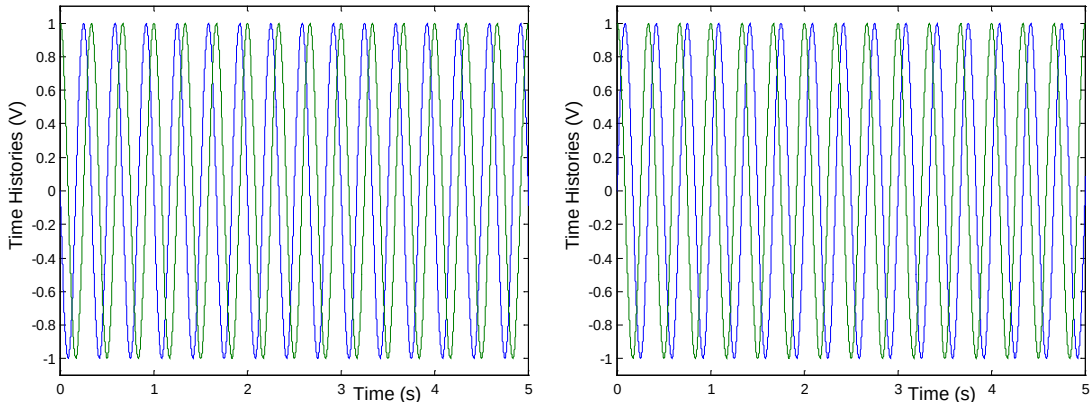


**Figure 2. 24** Doppler signals at the two detectors being the target velocity positive (first) and negative (second).

Being $E_{SIN}$ and $E_{COS}$ blue and green respectively and being $f_D$ positive in the first picture and negative in the second one, it is clear that in the first case $E_{COS}$ leads $E_{SIN}$ while in the second case, negative surface velocity, $E_{SIN}$ leads $E_{COS}$.

The operation mode above illustrated is the simplest one to discriminate velocity direction.

At this stage positions ④ and ⑤ are achieved where the two phase shifted fields enter in the dual-channel balanced modulator. Inside this device the beams are modulated by internally generated sine and cosine signals at a carrier frequency $f_C$ . Summation of the two modulated outputs yelds a frequency-shifted output at $f_{OUT} = f_C + f_D$ or $f_{OUT} = f_C - f_D$ . The mathematic process will be the following:

$$E_{SIN} = i\frac{1}{8}A\exp\left[i\,2\pi(f + f_C)T_r\right]\left\{1 + \exp\left[i\,2\pi(f_D + f_C)t\right]\right\}$$
$$E_{COS} = \frac{1}{8}A\exp\left[i\,2\pi(f + f_C)T_r\right]\left\{1 + \exp\left[i\,2\pi(f_D + f_C)t\right]\right\} \qquad \textbf{(2. 98)}$$

Summing out:

$$E_{OUT} = \frac{1+i}{8}A\exp\left[i\,2\pi(f + f_C)T_r\right]\left\{1 + \exp\left[i\,2\pi(f_D + f_C)t\right]\right\} \qquad \textbf{(2. 99)}$$

whose intensity is:

$$I_{OUT} = E_{OUT}E_{OUT}^{*} = \frac{A^2}{16}[1+\cos(2\pi(f_D + f_C)t)] = \frac{I_0}{16}[1+\cos(2\pi(f_D + f_C)t)] \quad \textbf{(2. 100)}$$

The output shows a frequency shift of $f_C + f_D$ or $f_C - f_D$ depending on the direction of the velocity *v*, see Figure 2.25. A positive velocity corresponds to a summed output signal which is above the carrier frequency, while a negative velocity corresponds to a summed output signal which is below the carrirer frequency.

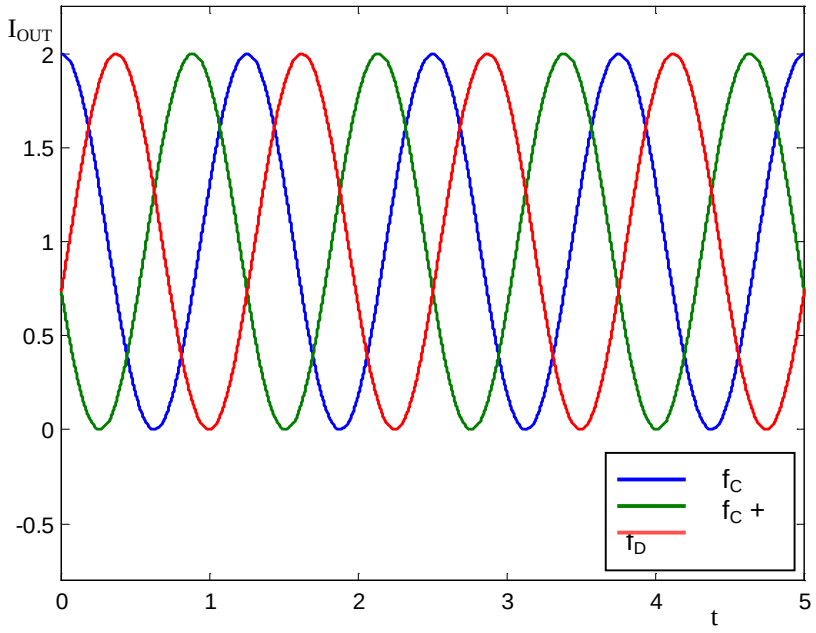


**Figure 2. 25** Intensity output for positive (green) and negative (red) target velocity.

From the picture it is noticeable that the waveform at frequency $f_C + f_D$ (green) is above the one at the carrier frequency $f_C$ (blue) and the waveform at frequency $f_C - f_D$ (red) is below it.

This combined signal is a frequency-coded velocity signal with a defined frequency offset, $f_C$ , and it is called the Single Side Band Suppressed Carrier (SSBSC). In order to obtain the instantaneous analog velocity, a FM-

demodulation circuit is employed. Instantaneous signals available to the user are: Doppler 1, Doppler 2, Analog Velocity and the SSBSC.

In the VPI Sensor the device where the analog velocity waveform is derived from the Doppler signal is a modulator-demodulator circuit which, as described in the manual, require that the Doppler signal exceeds an amplitude threshold (300 to 400 mV pk-pk referred to the external Doppler monitor sockets). Below this value the velocity output will be dropped to zero or to a value less than reality and this effect is the so-called dropout. As already stated, causes of dropouts are: operation in between optimum distances, using a test surface with poor reflectivity, misfocus of the measuring beam or operation at an incorrect range.

## *2.11. Conclusions*

This chapter has focused on a description of laser Doppler vibrometry with its fundamental principles (i.e. Doppler effect and laser light).

Considerable emphasis has been given to an investigation into the main problem affecting the measurement techniques, using coherent light as velocity detector, which is the “speckle noise”. Section 2.4 is entirely devoted to the laser speckle explaination as it can be found in literature, while Section 2.5 presents the well-known effect of the speckle which can be seen also in the experimental work done throughout this work (Chapters 5 and 7) and that is the frequency broadening of the LDV output spectrum. Starting from the work done by T. Asakura and N. Takai, [30], the treatement of the subject has been expanded in order to lighten the dependence of the phenomenon on some parameters which can be controlled during the experiment. In fact, it can be concluded that the most significant factor influencing the speckle noise is the laser beam width at its intersection with the tested object surface, which can be governed by focusing the laser spot on the structure. Morever, the investigation has been

extended to a laser beam which is moving along a line across the measured surface.

A description of the most common configurations of LDV is given in Sections 2.6 and 2.7 and commercial systems available (as the Polytec and Ometron vibrometers) are investigated in Sections 2.9 and 2.10.

# Chapter 3 SLDV Theory

## *3.1. Introduction*

The main purpose of this thesis is to investigate the continuous LDV scanning method of measuring vibration in all its facets, involving the short scan performance (to recover simultaneously the vibration responses in different directions at one point, see Chapter 4) and the long scan technique (to derive the operating deflection shape of a line or a surface where the scan is performed, see Chapter 5). In order to have a basis for comparison of the long scan method, the traditional point-by-point scanning technique was taken into consideration.

A definition of point-by-point and continuous scan would be helpful in understanding the difference between the two techniques. The point-by-point scan, also called “scanning technique at discrete points” or, simply, discrete or traditional scanning, is a way to measure the vibration velocity of a whole surface by measuring at a series of points, the geometric grid, on the surface itself. The overall measurement consists of a series of vibration responses (generally FRFs) obtained at each single point on the grid. The measurement

procedure starts with the laser beam pointing at the first point on the grid where the acquisition of the vibration response takes place. When the acquisition is finished, the laser beam moves to the next point and acquisition of the FRF at the second point starts. The procedure automatically carries on until the response at the last point on the grid is acquired. The test can be performed with different kinds of excitation, i.e. sine, broad-band or random excitation.

The continuous scanning technique is a method to measure the vibration velocity of a surface by sweeping it with a laser beam scanning continuously over the surface. Ideally, all the points constituting the surface will then be addressed, and a complete cycle of scan (in which the whole area is travelled) would be sufficient to reconstruct the operating deflection shape. During the scan, which can take few seconds, the acquisition of the time history measured by the moving laser beam is performed. From the time signal the Fourier coefficients can be recovered and transformed into polynomial coefficients describing the shape of the surface's vibration response. These data only are needed for the analysis; therefore a very small amount of data must be stored, depending on the order of the polynomial. From the recorded polynomial coefficients the spatial ODS of the tested surface is reconstructed with an arbitrary spatial resolution completely independent from the performed measurement. This is an important advantage of the continuous scanning technique, together with the small amount of stored data and the short acquisition time. In fact with the point-by-point scanning technique the spatial resolution defining the ODS derive from the number of points actually measured. Consequently, increasing the spatial resolution implies a larger amount of data to be recorded and a lengthening of the acquisition time. The continuous scanning tests described in this thesis involve mono-frequency sine excitations only and step-sine excitations when a range of frequencies is needed for the vibration analysis, which can become more time-consuming. However, continuous scanning techniques have been applied in structure excited with different kind of excitations as impact, see references [33] and [14], narrow-band, see references [3] and [8], and broad-band multi-sine excitation, [34].

In this chapter, the traditional scanning technique is addressed in order to better understand its features, since in the next chapters (specifically in Chapter 5 and in Chapter 7, with regards to the applications of the continuous scanning methods) the results of the point-by-point technique will be used for comparison with the results derived from the continuous scanning techniques.

## *3.2. Basics of SLDV technology*

Scanning Laser Doppler Vibrometry technology consists of an LDV with two moving mirrors, driven by galvanometric actuators. This technique allows us to measure accurately, from a remote position, selected point velocities where the laser beam can be directed automatically. Such an instrument can perform a series of velocity measurements across a grid of points defined over the surface under test, providing reductions in the time needed to carry out vibration tests, in contrast to traditional methods involving conventional transducers (i.e. accelerometers).

The first prototype of an SLDV was assembled by Dr. Stoffregen and Felske from Volkswagen AG in Germany, in 1981. They built a data acquisition and processing system which was used to drive the laser beam emitting from a conventional Laser Doppler sensor and process its velocity output. Moreover, their system was supplied with an integral video camera which monitored the location of the laser beam on the test item. The main advantage was that the measured results could be overlaid on an image of the tested surface itself. This design was found to be a significant help for SLDV applications and, consequently, it has been adopted by most manufacturers of Laser Doppler Vibrometers.

The system consists of a Laser Doppler sensor head, which performs the velocity measurement, and two galvanometer scanners that aim the laser beam at the pre-defined measurement position in two-dimensional space. Such a

vibrometer, which is now able to drive the beam by means of the two galvanometer motors, is controlled by a specialised computer hardware and software that complete the SLDV system. The computer drives the beam to scan, pauses for the time needed to take the measurement at each acquisition point, gathers signals proportional to velocity of the particular measurement point relative to a reference, and averages these signals, if necessary. The galvanometer-driven mirrors are then repositioned and data for the next measurement point are acquired. The data acquisition system includes an analogue-to-digital converter, which collects the analogue output voltage of the laser sensor and stores it in a digital manner in order to process it later. The result, obtained by video processing the acquired signals, is a bit-map of the velocity data for the entire scan area with a resolution which is determined by the user within the maximum range of the system (512 × 512 measurement points for Polytec systems). Software is used to control the sensor and to display the measurements in a variety of formats.

### *3.3. Scanning mirror system*

The scanning operation is performed by leading the laser beam emitting from the source towards two moving mirrors, which serve to aim the measuring beam at the specified location on the test surface, see Figure 3.1. The mirrors are driven by two galvanometer actuators: by applying a voltage to each of them, the mirrors will rotate about their axes of two angles related to the voltages by some constants defined via a prior calibration of the scanning system. Calling the voltages supplied to the horizontal mirror and the vertical one, $V_x$ and $V_y$ respectively, the mirrors' rotation angles (indicated as $\alpha_x$ and $\alpha_y$) will be described by the following relationship:

$$\begin{aligned} \alpha_x &= SV_x \\ \alpha_y &= SV_y \end{aligned} \qquad \textbf{(3. 1)}$$

*S* being the galvanometer static sensitivity (4 º/V from the manufacturer specifications), [35].

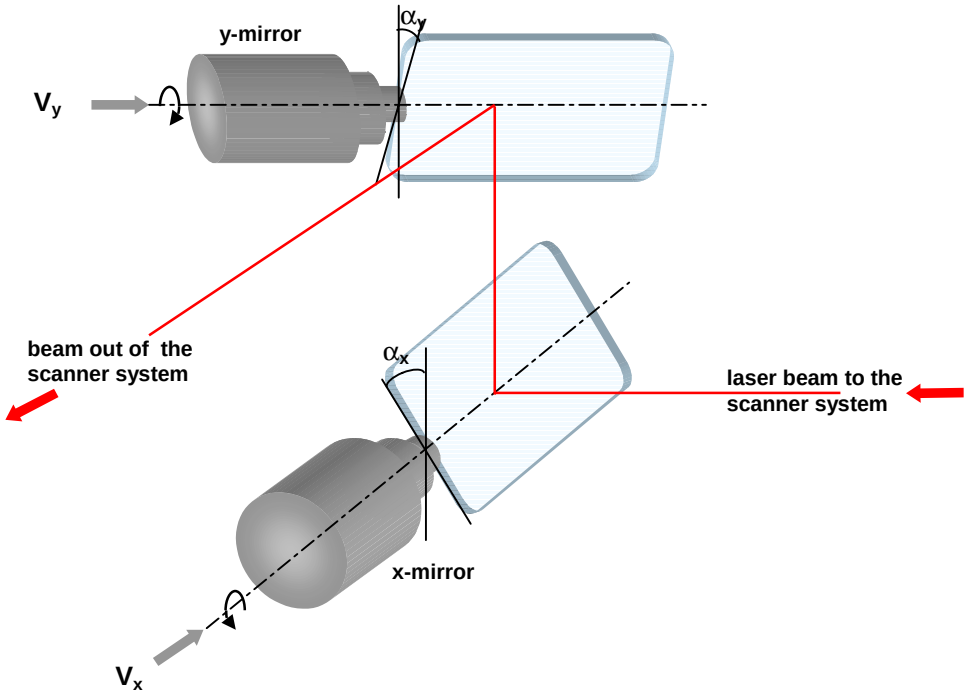


**Figure 3. 1** Schematic representation of the mirrors rotation.

The scanning angles, $\alpha_x$ and $\alpha_y$, can be decided by software and used as inputs for the scanner control which is basically an interface between the data acquisition / processing computer and the mirror driver motors, constituting of a digital-to-analogue converter (DAC). This transforms the digital value of the angles to voltages. The latter are applied to the galvanometer actuators to give the specific rotation to the mirrors and to deflect the laser beam to the sought position on the test item. The galvanometer scanner not only consists of the mirror and the actuator, but two further components are included in the device: a built-in capacitive rotation sensor to measure the actual angular shaft position of the mirror and a PID (Proportional, Integrative, Derivative) control system to generate a feedback control signal. This means that the galvanometers work within a closed loop control, as shown in the flow-chart illustrated in Figure 3.2, which allows it to determine precisely the spatial relationship between the test

structure and the SLDV system. It then accurately positions the laser beam on the desired location, [36].

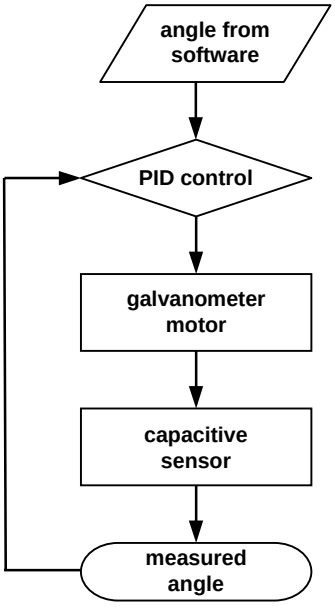


**Figure 3. 2** Flow-chart of the feedback control action.

The dynamic performance of the scanner system is related to the rotor and mirror inertias, actuator torque and PID control algorithm. Step response time depends on torque to inertia ratio and PID parameters. Mirror dimensions should be chosen as a compromise between the need for a large optical aperture for the scanning, and mirror inertia, in order to have a fast response of the mirror itself.

A typical optical scanner used by the SLDV manufacturers is model G325DT from *General Scanning Inc.*, whose common performance is reported in Table 3.1 and 3.2, [37].

| **Mirror** | | |
|---|---|---|
| Useable aperture. | 20 mm | 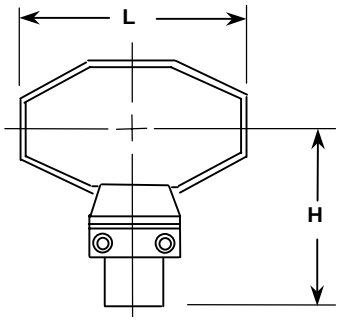 |
| Mirror+Mount Inertia. | 6.5 g- $cm^2$ | |
| '**L**' Dimension. | 29 mm | |
| '**H**' Dimension. | 37 mm | |



**Table 3. 1** Characteriscs of mirrors employed in low-inertia scanners.

| **Optical Scanner** | |
|---|---|
| *Parameters* | |
| Nominal accuracy of the | |
| motor / driver unit. | 0.01 deg / 0.175 mrad. |
| Specified scan resolution. | 0.0025 deg / 0.045 mrad |
| Pointing stability. | typ. 0.0035 deg / 0.06 rad |
| | *(after 1 hour warm-up over a period of 25* |
| Position repeatability. | typ. 0.001 deg / 0.018 rad |

**Table 3. 2** Performance of galvanometer scanners.

At present, the SLDV is only applied to displace a laser beam on a static grid of points, by driving the motors with discrete analogue voltages, which change point by point. The measurement acquisition is done for each point subsequently and only starts when the mirrors have come to rest. Because the galvanometer scanners are supplied by direct current, it is possible to drive them by voltages which vary continuously in order to make the laser beam follow a pre-determined trajectory and perform the so-called continuous scanning.

### *3.4. Polytec Discrete Scanning Utility*

SLDVs consist of a single point laser Doppler vibrometer, a scan unit and a data processing / management system.

The heart of the system is the optical sensor head (OFV-055) which consists of a single-point interferometer which focuses the laser beam towards the *x-y* scanner mirrors driven by the scanner driver electronics. Further, a compact video camera is installed on the case of the head for the visual observation of the test item and the scanning procedure. In fact, by means of a video control box settled on the PSV computer, the grid of measurement points to be followed over the structure surface is defined on top of the video image displayed on the computer monitor. In order to perform a correct measurement, the laser beam must be aligned to the video image and this is done by a calibration routine included in the Polytec software (PSV-200). This routine automatically corrects parallax errors and distortions to allow accurate positioning of the beam. In conjunction with the optical head there is the electronic signal processor / controller unit (OFV-3001-S) which controls the measuring parameters and processes the output of the laser sensor in order to derive the velocity information.

### *3.5. Speckle Noise and its Improvement by the Exploitation of Commercial Devices (Tracking filter and Signal Enhancement Facility)*

Since speckle noise is an intrinsic physical effect linked to coherent light backscattered from an optical rough surface, its occurrence cannot be avoided. As seen in Chapter 2, it appears on the LDV signal as dropouts, i.e. sudden drops in the laser light intensity, which deteriorates the signal, reducing the accuracy of measurement.

The tracking filter is a device based on the PLL (Phase Locked Loop) principle and it is used to bypass the signal losses owing to dropouts. At its heart is a

Voltage Controlled Oscillator whose output variations are the same as the Doppler signal (i.e. it is locked to the signal). When a dropout occurs in the signal intensity, the tracker freezes the frequency of the Voltage Controlled Oscillator during the dropout period, then, as the signal reappears, it locks in again to the signal. The tracker behaves as a “flywheel” that follows the signal and holds its intensity as it was before the intermittence of a dropout occurs. The device only works properly if the measurement area does not undergo excessive accelerations, which are the product of frequency and velocity of the surface vibration. Also, the losses of signal should not be too long, i.e. the signal amplitude reduction is only limited to a small number of samples. The latter is always realised in the case of the measurement of solid surface vibration by using a steady laser beam as a sensor. Alternatively, when the beam is sweeping across a vibrating surface (case of continuous scanning technique), the output signal amplitude is modulated by the deflection shape of the surface itself. When the beam is passing through areas which undergo a low vibration level, the amplitude of the time signal will reduce to lower values and the tracking filter will cease to work. In conclusion, the tracking filter is unhelpful in the case of continuous scans.

An additional option incorporated in Polytec SLDV systems is the Signal Enhancement system, a sophisticated routine which can improve data quality. The most important cause of speckle noise is the change of speckle pattern received by the detector during the measurement time. This change is strictly related to the relative motion between tested structure and laser beam, usually a sideways motion perpendicular to the laser line of sight. This occurrence is practically unavoidable when the structure is vibrating because the laser spot cannot be kept completely fixed at the specific position. With the Signal Enhancement device activated the PSV software estimates the SNR of the actual measured signal and, if this parameter is below a certain threshold level, the laser beam is moved slightly from its position and the measurement taken again. The measurement procedure can be repeated up to seven times at different points around the actual measurement point chosen within the

geometric grid. By performing a weighting average of the measured data at the different positions, the acquired signal quality is optimised, the only disadvantage being an increase in measurement time.

Because this algorithm is incorporated in the PSV Software which can be used exclusively in the fixed position mode of operation it is not possible to take advantage of it, when a continuous scan is performed. However, its philosophy could be applied to the continuous scanning technique by performing several scans along, say, different lines which are slightly apart from each other and by making an average of the signals acquired.

### *3.6. Vibration Measurements by Discrete Scanning*

Two-dimensional vibration Operating Deflection Shapes (ODSs) of structures can be derived by measuring FRFs on a grid of points selected over the test structure. The measurement philosophy is the same as that which uses accelerometers moved across the grid. The evident advantage is the use of a non-contact transducer, as in a laser sensor, and the automation of the measurement technique together with the time saving that can be achieved.

In order to understand the application of the point-by-point technique, an experiment was performed on a simple steel rectangular plate, 174 × 199 mm, cantilevered at one edge and excited in a range of frequencies between 0 and 2 kHz, using a pseudo-random excitation via an electromagnetic shaker attached off-centre on the structure, as shown in Figure 3.3. The same structure will be employed to test the continuous scanning method for deriving ODSs, as will be shown in Chapter 5.

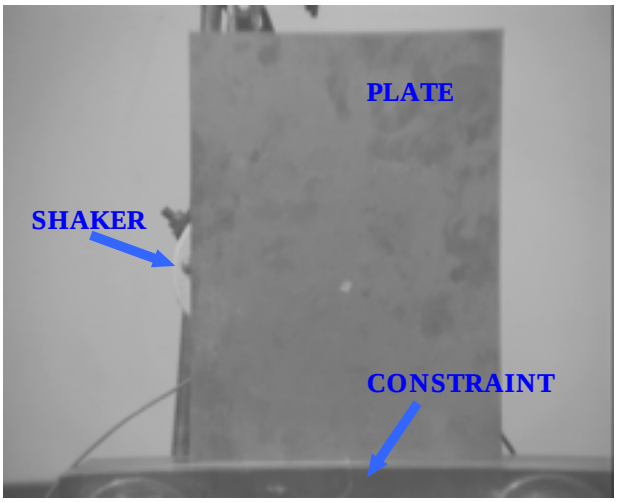


**Figure 3. 3** Experimental configuration.

The laser was made to scan step by step over a grid of 546 points (see Figure 3.4).

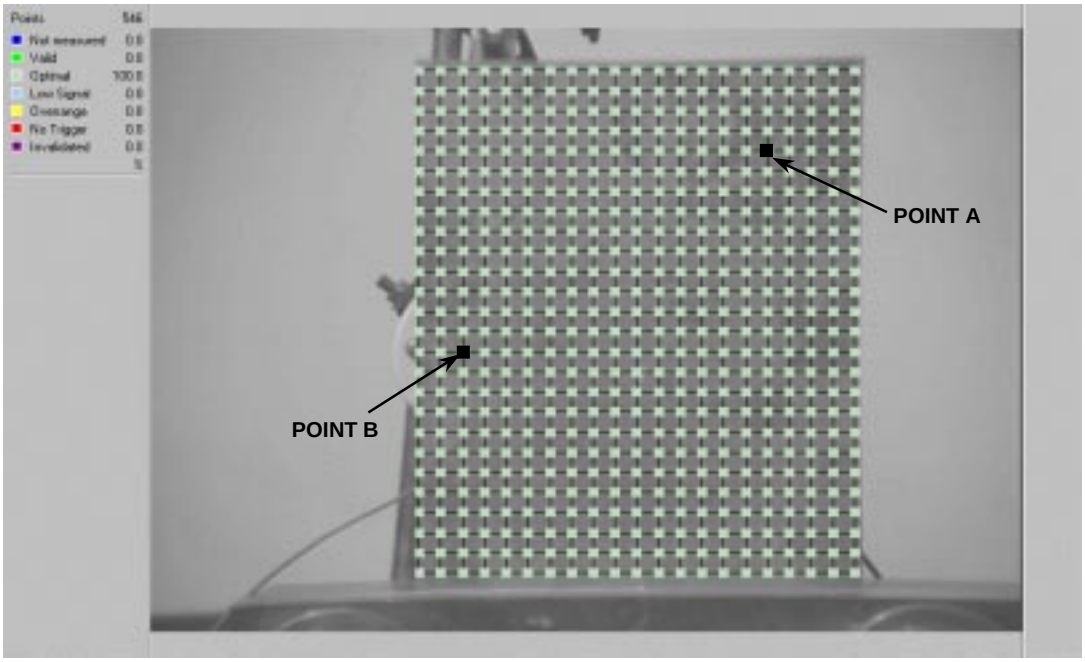


**Figure 3. 4** Measurement points grid.

The velocity range set for the velocity decoder was 125 mm/s/V which represents the scale factor between the actual point velocity and the vibrometer output voltage.

The acquisition was performed by activating the tracking filter and the 'Signal Enhancement' routine to improve the signal quality. Furthermore, a third option was selected via software: the so-called 'Remeasure' option whose purpose is to reject measurement points which do not have a valid status (i.e. during the acquisition there was an over-range or the signal level was low) and to remeasure again in the same location until the signal quality is acceptable. 'Signal Enhancement' and 'Remeasure' routines have the sole disadvantage of increasing the acquisition time of the test but it is worth using them to achieve good output signals for most of the points on the grid. In order to minimise the noise level, averages were also performed; in the experiment included here five averagings were found to be sufficient to obtain the optimal output signals.

Vibrometer output signals and reference signals, acquired from a force transducer attached to the plate, were measured at each point with an anti-aliasing low-pass filter activated. The analogue signal had to be sampled for a certain amount of time with a suitable sampling frequency, namely 2.56 times bigger than the frequency bandwidth chosen for the measurement (2 kHz). The number of samples which the analogue signal will be cut into are defined, again, as 2.56 times the FFT lines set in the PSV data acquisition (6400 lines in the actual experiment). From these data the time required to measure the velocity at one point could be calculated as:

$$time\ window = \frac{number\ of\ samples}{sample\ frequency} = \frac{6400 \cdot 2.56}{2000 \cdot 2.56} = 3.2\ s$$

An important parameter, which is a comparison term between discrete and continuous scans across an area, is the total time necessary for the test to be completed. For an area scan, the total measurement time can be derived as the following product:

$$total\ time = time\ window \times n.of\ measurement\ points \times n.of\ averagings = 3.2 \cdot 546 \cdot 5 = 2.43\ hours$$

In reality, together with this ideal quantity, additional times must be considered:

- time required for remeasuring measurement points which do not have a valid status;
- time necessary for waiting until the scanner mirror is at rest, which is set by default at 10 ms. The so-called settling time must be greatly emphasised as the mirrors should be in a stable position before the measurement starts, otherwise the laser spot on the structure will not be steady on the selected measurement point and the relative motion between laser beam and tested surface will produce speckle pattern motions with consequential dropouts.

The measurement time will increase further if additional facilities for signal quality improvement (i.e. signal enhancement) are selected. The total acquisition time for the actual test (564 points) was in excess of 4 hours.

The further parameter used to compare discrete and continuous scanning techniques is the ODS representation resolution, which coincides with the number of grid points in the fixed position mode of operation. In the test performed here, the geometry grid resolution consisted of 546 measurement points.

During the acquisition, an on-line processing of the data could be carried out. In the PSV software FRFs were stored for each point on the grid. They were derived at each measurement point by dividing the Fourier spectrum of the vibrometer output, at the actual acquisition point, by the reference signal, taking into account the averages. Since the quantity measured by the laser is a velocity, the resulting FRF will be a mobility, estimated with averaged measurement values (*H1* estimator), i.e. output noise on vibrometer channel is suppressed. The transfer mobility between the measurement point **A** and the excitation point **B**, illustrated in Figure 3.4, is shown in Figure 3.5.

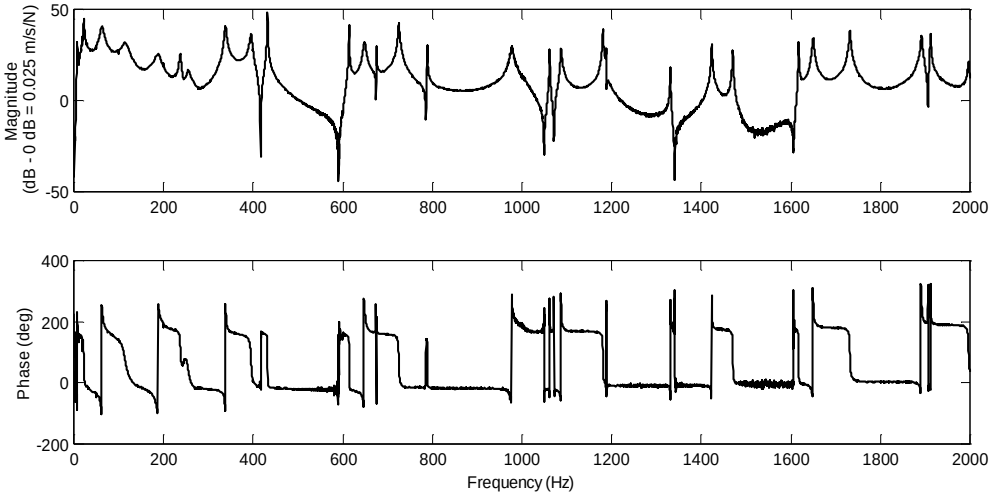


**Figure 3. 5** Transfer mobility at point **A**.

After the area scan had taken place, FRFs for all valid measurement points would be saved in order to be post-processed by using the standard PSV200 presentation module. Velocity maps for each resonance frequency chosen within the average spectrum of all grid points could be displayed. These patterns could be seen as ODSs at the selected frequency. Modal analysis was not performed on the data acquired, and therefore it is not appropriate to use the expression of "mode shapes". Two frequencies were selected: 181.9 Hz ($4^{th}$ resonance) and 239.1 Hz ($5^{th}$ resonance). ODSs at the same frequencies will be derived with the continuous scan operation mode in Chapter 5.

Values of instantaneous velocity at each measurement point are shown in Figures 3.6 and 3.7, plotted against the x and y coordinates of the points in a 3-D reference system.

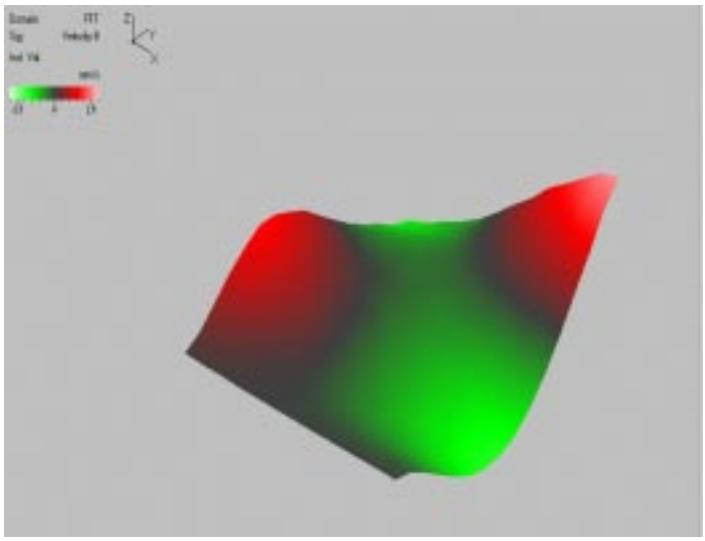

**Figure 3. 6** ODS at 181.9 Hz.

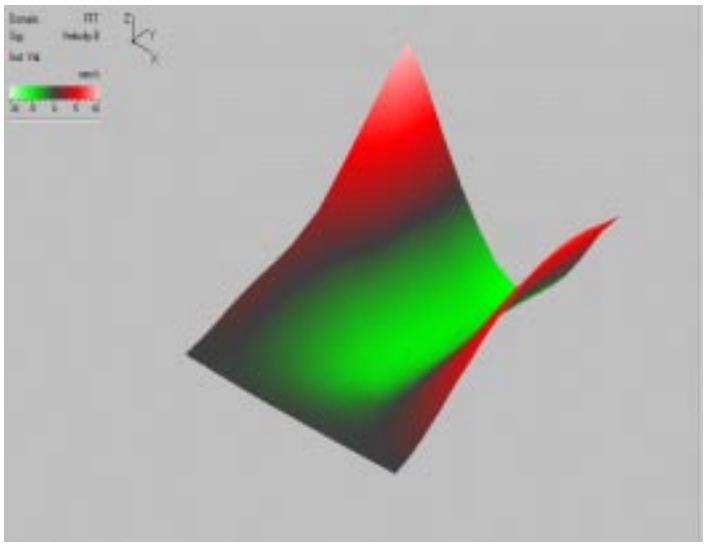

**Figure 3. 7** ODS at 239.1 Hz.

These results will be compared with those obtained using the continuous area scan technique in Chapter 5, in order to prove the efficiency of the second technique and to examine accuracy of both methods.

At the moment, ODSs measured can be correlated with the ones derived analytically, i.e. with mode shapes predicted from the classical theory. As a simplification, an isotropic square plate has been considered, with an edge-length of 0.199 m (the longest side of the experimental plate), cantilevered on one edge, with a Poisson's coefficient $\nu = 0.3$. The experiment described in this

chapter was done in a different moment of the one described in Chapter 5, in fact it can be noticed that the clamping conditions are different, specifically here the plate was deeper-clamped (its length is 0.199 mm while in the experiment in Chapter 5 the length is 0.244 mm). The analytical calculation was, then, made with different parameters. The resonance frequencies changes as well, even if slightly: 181.9 Hz and 239.1 Hz instead of 202.4 Hz and 242.68 Hz (see Section 5.5.4.2). The mode shapes are given by:

$$W(x,y)=\sum_{m=1}^{p}\left\{A_{m1}+A_{m2}\sqrt{3}\left(1-2\frac{y}{l}\right)+\sum_{n=3}^{q}A_{mn}\left[\cosh\frac{\varepsilon_n y}{l}+\cos\frac{\varepsilon_n y}{l}-\alpha_n\left(\sinh\frac{\varepsilon_n y}{l}+\sin\frac{\varepsilon_n y}{l}\right)\right]\right\} \quad \textbf{(3. 2)}$$
$$\left[\cosh\frac{\varepsilon_m x}{l}-\cos\frac{\varepsilon_m x}{l}-\alpha_m\left(\sinh\frac{\varepsilon_m x}{l}+\sin\frac{\varepsilon_m y}{l}\right)\right]$$

where $l$ is the plate dimension, $A_{mn}$ , $\alpha_m$, $\varepsilon_m$, $\alpha_n$, $\varepsilon_n$, are coefficients whose values are given in Table 4.45 and 4.46 in reference [38]. Representations of mode 4 and mode 5 are easily found numerically, using the same grid of coordinates (x, y) applied for the plots of the mode shapes derived experimentally by Discrete Area Scan.

Figure 3.8 and 3.9 show theoretical and experimental area-scan ODSs for the two frequencies analysed.

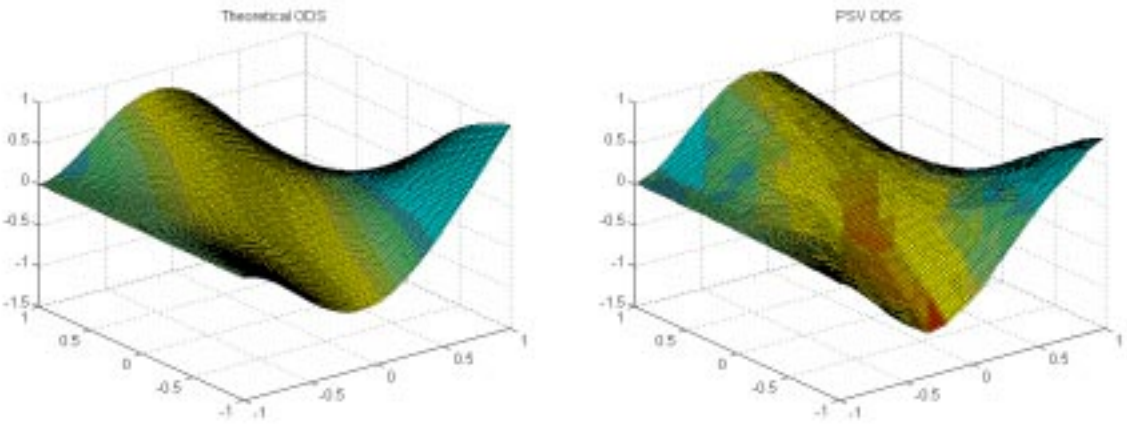


**Figure 3. 8** ODS at 181.9 Hz (4th Mode).

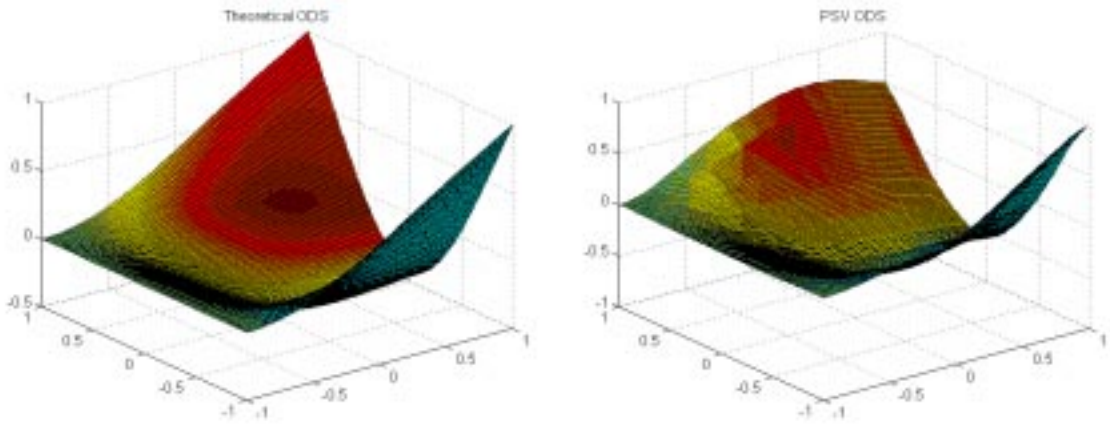


**Figure 3. 9** ODS at 239.1 Hz (5th Mode).

For both modes, theoretical and PSV ODSs can be plotted together to emphasise the areas on the plate where the measured data do not follow the prediction. This is done in Figure 3.10.

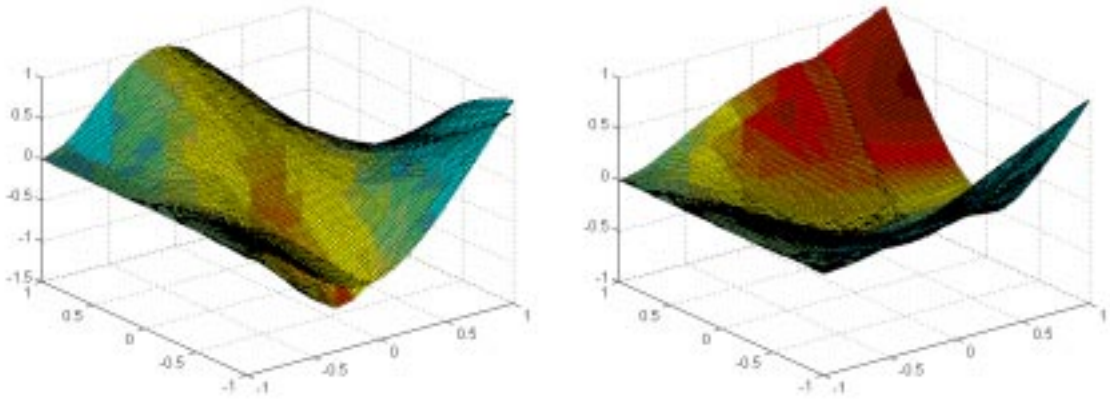

**Figure 3. 10** Measured and theoretical ODSs overlaid for mode 4th (left) and mode 5th (right).

The maximum shift between the two sets of data is concentrated on the free-end of the plate and on the right-side of the cantilevered end. The latter means that the constraint is not perfectly realised.

### *3.7. Fast Scan Option*

The Fast Scan procedure measures in a narrow band frequency only, centered on the frequency selected. The frequency bandwidth can be chosen also and will coincide with the bandpass filter bandwidth employed for acquisition. Because Fast Scan aims to speed-up the measurement process, the options 'Averagings' and 'Signal Enhancement' are disabled.

With this capability activated, speeds up to 100 discrete points/sec can be achieved.

In the PSV200 Presentation Mode there is no longer any need to select a frequency band as the ODS at the central frequency will automatically be displayed.

Acquisitions had been performed in this mode of operation by choosing center frequencies close to the ones analysed in the previous section and a bandwidth of 20 Hz, in such a way to be sure to include the resonance frequency. The first scan was done at 185 Hz and the second one at 237 Hz. Measurement parameters had been kept unchanged, i.e. the number of points on the grid is still 546. Total time needed for the complete acquisition was 3 min and 30 sec for the first scan and 2 min and 28 sec for the second one. Time had been stretched because the option 'Remeasure all invalid points' was activated. ODSs derived in the frequency bandwidth measured were displayed automatically by opening Presentation Mode and they are shown in Figure 3.11 and 3.12. Note that they completely reproduce the ODS recovered by the conventional Discrete Area Scan (Figure 3.6 and 3.7).

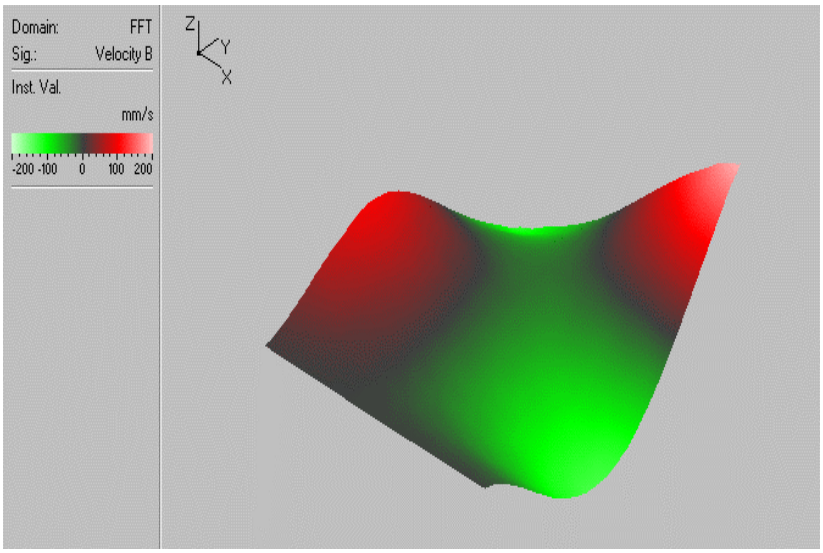


**Figure 3. 11** ODS at 181.9 Hz.

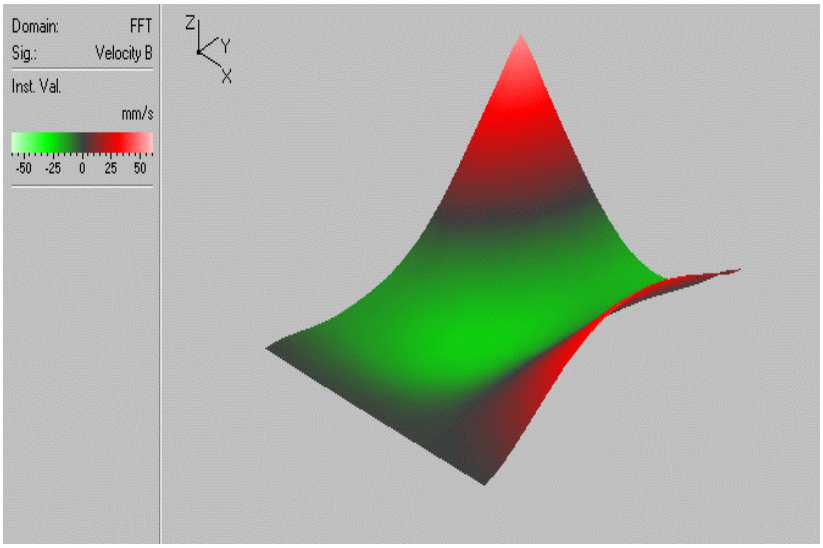


**Figure 3. 12** ODS at 239.1 Hz.

### *3.8. Conclusions*

In summary, this chapter's aim has been to describe the use of a commercially available system, such as the Polytec scanning vibrometer, which is able to measure operating deflection shapes of 3D structures. The system has been employed to perform a vibration measurement on a test piece, such as a simple plate, and the results obtained were compared with the ones obtained using the

continuous scanning technique as will be shown in the following Chapters of this thesis.

Some early conclusions about the differences between the two techniques, i.e. the point-by-point and the continuous scanning ones, can be drawn. The point-by-point scanning technique is more time-consuming because measurements must be made at a large number of points in order to have enough spatial resolution, while in the continuous scanning technique the spatial resolution used for the representation of the polynomial deflection shape is completely independent of the acquisition. However the continuous scanning technique is suitable with sine excitations only, at least as far as the work done in this thesis is concerned. In this case we must compare the results with the ones obtained by using the fast scan option included in the Polytec system, where the measurement is performed at one frequency and the acquisition is greatly speeded up (i.e. it could take seconds as the continuous technique does). However, the spatial resolution of the recovered ODS always depends on the geometric grid and an increase of the measurement points will slow down the measurement itself, while the ODS derived by the continuous scanning technique can be represented with an arbitrary resolution, indeed.

# Chapter 4 Continuous Scanning Technique Applied on MDOF Vibration Response Measurements

## *4.1. Measurement Methodology*

Continuous Scanning Laser Doppler Vibrometry (CSLDV) is a further feature of the scanning methodology applied to an optical sensor as a laser vibrometer, with its intrinsic advantage of being non-contacting and non-invasive. The philosophy of measuring vibration response of a structure by moving the measurement position continuously across its surface can be applied with any transducer, with the possibility to find in the future a sensor not sensitive to the speckle noise which is the main disadvantage affecting laser vibrometers, see references [8], [9], and [20]. Continuous scans can be made in different ways as mentioned in Section 3.2, by driving the *x*, *y*, beam-deflection mirrors in the LDV head with analog signals. A classification of the different trajectories the laser beam can be made to follow is outlined in Tables 4.1 and 4.2. A first distinction between them can be made in terms of long and short scan lengths, i.e. large or small amplitudes of the waveforms applied to the mirrors.

| MIRROR DRIVER SIGNALS | SCAN TYPE | | APPLICATION |
|---|---|---|---|
| One sinewave or triangular wave | Line scan | 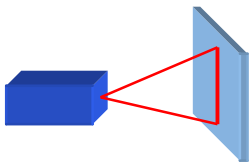 | • One-dimensional structures (beams)<br>• Raster scans across a plate |
| Two sinewaves at the same frequency | Circular scan | 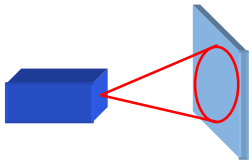 | 2-D structures:<br>Circular scan on a plate or a disc |
| Two sinewaves at different frequencies not fractionally related | Area scan (Lissajous trajectory) | 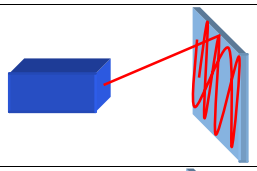 | 2-D structures (plates) |
| Two triangular waves at different frequencies not fractionally related | Area scan | 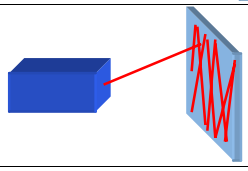 | 2-D structures (plates) |
| A triangular wave and a sinewave at different frequencies not fractionally related in polar coordinates | Circular area scan | 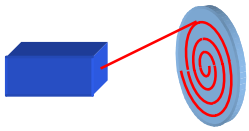 | 2-D structures (discs) |

**Table 4. 1** Long scans.

| MIRROR DRIVER SIGNALS | SCAN TYPE | | APPLICATION |
|---|---|---|---|
| One sinewave | Line scan | 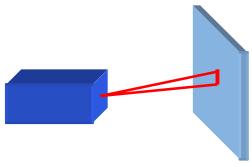 | Point measurement:<br>Translational and one angular vibration recovering |
| Two sinewaves at the same frequency | • Circular scan<br>• Conical scan | 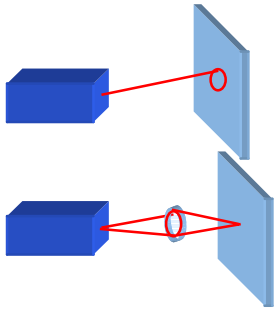 | Point measurement:<br>• Translational and two angular vibrations<br>• Three translational vibrations |

**Table 4. 2** Short scans.

In this chapter only short scans applied to MDOF vibration response measurement at a point, as shown in Table 4.2, will be addressed. Using conventional transducers such as accelerometers, only one DOF can be measured in one go: the component of the vibration response on the accelerometer axis. Although the desired response is usually translational, nowadays requirements to derive angular vibrations increase, first in substructure coupling and also in updating finite element models where rotary inertias, relayed to the rotations, cannot be neglected. Rotational degrees of freedom (RDOFs) can be measured also by the discrete scanning technique: considering a Cartesian reference system, *x, y, z,* and the rotation about *x* being approximated by the first derivative of the translations in the normal direction, *z*, the rotation can be derived from the difference between the translations at two points divided by their separation distance. This technique requires two translational response measurements and it will be more time-consuming than a continuous linear scan, but in this chapter it will be performed in order to be compared with the results obtained by the continuous scanning methods in order to evaluate the accuracy of the latter method.

In order to describe the techniques shown in Table 4.2, in more detail, and to identify vibration components derived with each of them, the velocity vector associated with the vibration which the measurement point is undergone must be defined in a Cartesian coordinate system *x, y, z.* A sinusoidal translational vibration, *V*, can be described in magnitude and phase by its projections on the Cartesian axes $V_x$, $V_y$, $V_z$ and are generally complex quantities, comprising real and imaginary parts.

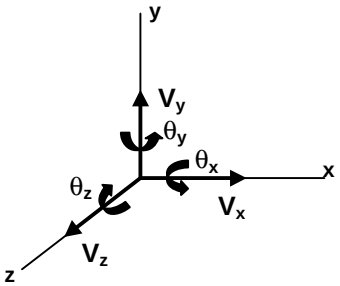


**Figure 4. 1** Vibration decomposition in the Cartesian system of coordinates.

Considering an infinitesimal element of structure at the point concerned, three angular vibration components of the point can be also described. Assuming the infinitesimal area to behave as a rigid body, i.e. to be a planar, non-deforming surface, the rotational sinusoidal vibration components on the Cartesian system $\theta_x$, $\theta_y$, $\theta_z$ can be defined (see Figure 4.1).

As shown in Table 4.2, three kinds of short scan can be realised:

- short line scans to recover one translational and one angular vibration, e.g. $V_z$ and $\theta_x$, respectively, when the scan lies along the *y* - direction;
- small circular scans to derive one translational and two angular vibrations, e.g. $V_z$ and $\theta_x$ and $\theta_Y$ respectively if the scanned circle is contained in *x*,*y* plane;
- conical scans, i.e. circular scans on a short-focus lens which focuses the beam on the point of interest. The laser beam is now moving in a cone with the vertex in the addressed point, and because its characteristic is to measure at the direction of its line of sight, the measurement direction is continuously changing during the rotation. Since three different directions independent from each other would be enough to derive the three translational components of the velocity vector, by performing the conical scan these three DOFs will be recovered in one go. The three translational vibration components will be $V_x$, $V_y$, $V_z$.

The experimental procedures described above can also be combined together in order to measure the greatest number of DOFs with the lowest possible number of measurements. For instance, a conical-circular scan, see Figure 4.2, where the structure is moved away from the lens focal plane in order to have a circular path, will be addressed. This technique allows the measurement of 5 DOFs in only two scans (i.e. the three translational vibration components $V_x$, $V_y$, $V_z$ and two angular vibration about two orthogonal axes lying in the plane of the tested surface, say $\theta_x$ and $\theta_y$).

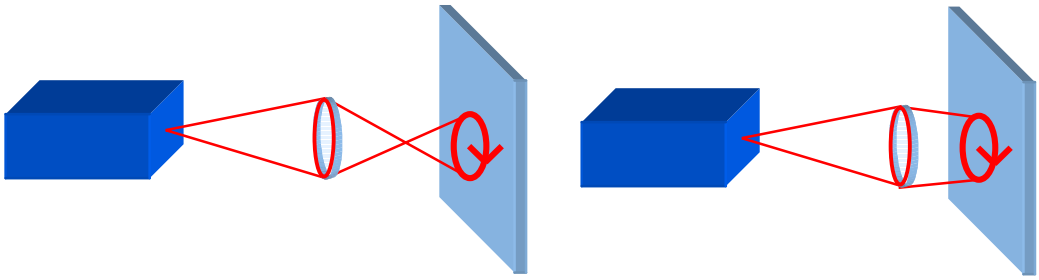

**Figure 4. 2** Circular-Conical scan.

These techniques suppose that the structure tested undergoes to a sinusoidal vibration, say, at frequency ω, and it can be assumed to be such that all six DOF responses are sinusoidal and at the same frequency (though not necessarily in phase). In this case, describing the laser beam scan frequency as Ω, the LDV response signal comprises three components: at frequencies ω, $(\omega + \Omega)$ and $(\omega - \Omega)$. Since the Fourier component at $(\omega - \Omega)$ is necessary for the analysis, it is important that the LDV scan rate Ω is lower than the vibration frequency, or else this component appears as a negative frequency, and is not picked up. Furthermore, a low scan frequency is advantageous, in that it avoids excessive mechanical loading on the mirror drive system, and minimises mirror-drive phase shift or delays due to the inertia of the mirrors, an effect which becomes more important at higher speeds of scanning. Scans in the range 5 Hz to 20 Hz are generally most satisfactory.

In a continuous scan, the laser spot position is an important datum which needs to be known. In long scans, whose goal is to recover the ODS along the trajectory traveled by the beam, only by the identification of the instantaneous measurement points on the trajectory is it possible to associate the velocity output to the geometry scanned. In short scans, the position of the measurement beam at the start of the data acquisition phase allows one to determine the orientation of the *x* and *y* axes on the tested surface and to identify the velocity vector components completely. This requirement is really important in circular and conical scans where two angular vibrations or three translations, respectively, are derived and they need to be distinguished by relating them to the *x* and *y* directions. In the linear scan, it is straightforward to recover the angular vibration without using any coordinate system convention:

the rotation will be simply about the axis perpendicular to the line scan independently from the definition of *x* and *y*. In the circular scan the position of the laser spot along the circle scanned can be tracked easily by triggering the acquisition with one of the mirror driver signals. Now, a start position of the spot in the circle must be defined. At this stage, it is assumed that the mirrors do not have any inertia and they deflect the laser beam with the same law as the one they are fed with, i.e. assume that the laser spot will move according to the sinewaves that drive the mirrors, without any delay, see Figure 4.3. Then the start point in the circle is point 1 in Figure 4.4 and the direction of the beam is the one marked in the picture.

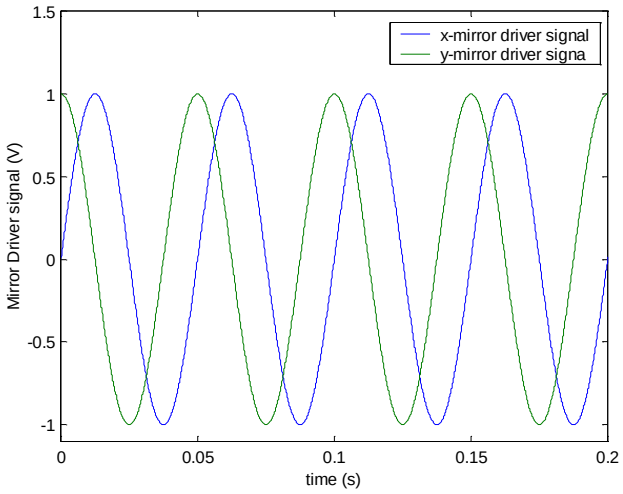


**Figure 4. 3** Mirror's driver signals.

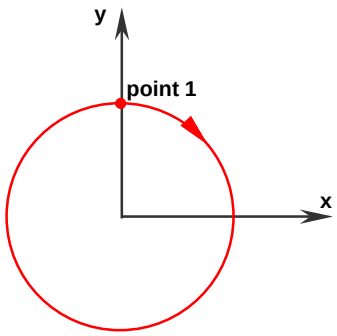


**Figure 4. 4** Circular scan configuration.

In order to start the acquisition when the laser spot is in position 1, the LDV signal acquired must be triggered when the *x*-axis mirror signal has zero

amplitude and positive slope. The coordinate system defined in Figure 4.4 can be then used for the circular scan procedure.

In practice, because there is a time-delay between a mirror position and its input drive signal, the trigger point usually requires adjustment after data acquisition, taking into account and phase delay in the LDV output. Provision is made for calibration to achieve this and the required offset is an input parameter, supplied before measurement. The calibration can be made to recover the time delay for both mirrors using a short line scan since the LDV output spectrum, in the ideal condition, is known a priori. In fact, for a straight-line scan performed in the ideal condition (there is no time delay in the mirror) the magnitudes of the sidebands, both real and imaginary components are equal in magnitude and opposite in sign (see Section 4.2). Generally, the time dalays for *x*- and *y*- mirrors are different, and there will be a relative delay between the two. However, this relative phase does not need a calibration to be determined because it can be set by adjusting the relative phase between the signal mirror drivers. Only when the trajectory of the laser spot on the surface is a perfect circle, and not an ellipse, will the relative delay between the two mirrors be zero. At this stage, just the delay of the other mirror will be necessary to define completely the trigger offset to be applied.

Continuous scanning techniques were applied to a simple structure as a cube to enable them to be demonstrated and to provide a basis for estimation of measurement accuracy. Figure 4.5 depicts the test set-up configuration. The tested item was an aluminium cube, 87 × 87 × 87 mm, suspended in a free-free condition by elastic bands. An electro-magnetic shaker attached off-centre, via a force transducer, was used to excite the structure at 158 Hz. At this frequency, the cube could be assumed to be moving as a rigid body, simplifying the validation of the vibration measurements.

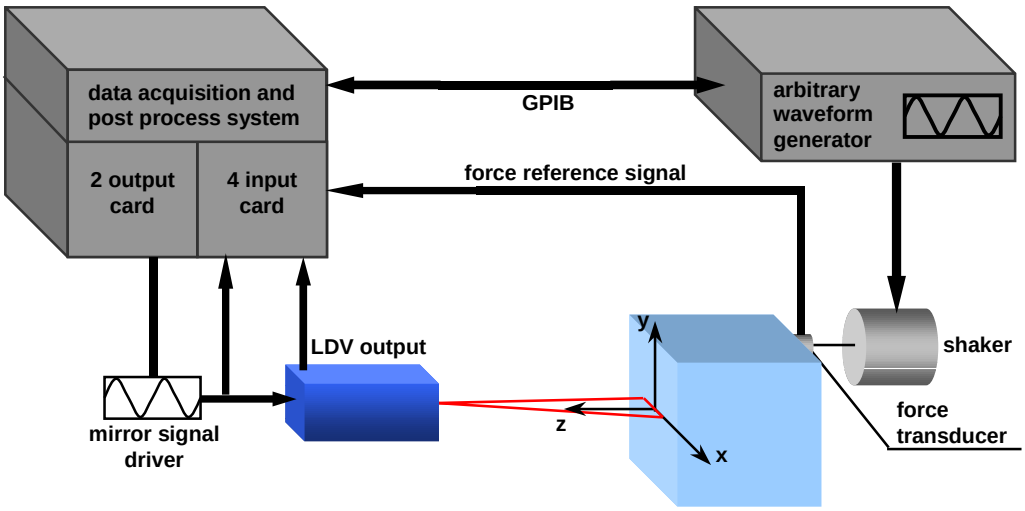


**Figure 4. 5** Schematic of the tested structure and the measurement equipment.

The equipment employed consisted of a Polytec Laser Doppler Vibrometer (optical unit and controller) used as a velocity transducer and made to work as a CSLDV by driving the scanning system with analogue signals: sinewaves, in practice. An associated computer hardware and software controlled the scanner system, driving an arbitrary waveform generator to provide the sinusoidal excitation and performed the acquisition and the post-process of the measured data. The output generator / data acquisition and post-processing PC was provided with:

- a two-channel output card which produced suitable sinewaves to supply the scanner control driver;
- a GPIB interface to control the sinusoidal force produced via the arbitrary waveform generator;
- a four-channel input card to acquire the LDV output signal, carrying the velocity information, the reference signal from the force transducer and the mirror drive signals to derive the actual position of the laser spot on the test surface.

In the following sections, the analysis of the LDV signal stored in order to derive angular and translational vibration at the point of interest is addressed. If the laser beam scans at frequency, Ω, this frequency will modulate the

vibration response of the LDV, giving an output spectrum characteristic for the occurrence of two sidebands apart from the excitation frequency of $\pm\Omega$. From the response at the sideband frequencies angular deflections can be obtained, while the translational component is straightforward measured from the response at the center frequency, i.e. the excitation frequency, $\omega$. Real and imaginary components of the LDV output spectrum at the mentioned frequencies, $\omega$, $(\omega+\Omega)$ and $(\omega-\Omega)$, are automatically derived from the SLDV time-record, without passing through a time-consuming FFT process. In fact, the time history is multiplied by sine and cosine waves at each of these frequencies in turn, since these frequencies are precisely known a priori. This procedure has a further advantage which is the small amount of data required to be stored: rather than record the whole LDV spectrum at each FFT line, only three (complex) values need to be saved.

### *4.2. Analysis of Linear Scan and Experimental Validation*

Scanning continuously with an LDV beam along a line on a vibrating surface, the transducer's output is a modulated signal which indicates the structure's vibration. If the mirror driving the beam is fed via a sine wave at frequency $\Omega$, and assuming the ideal condition where mirror delays can be neglected, the laser spot will follow a straight line of length $2l$ over the surface (see Figure 4.6).

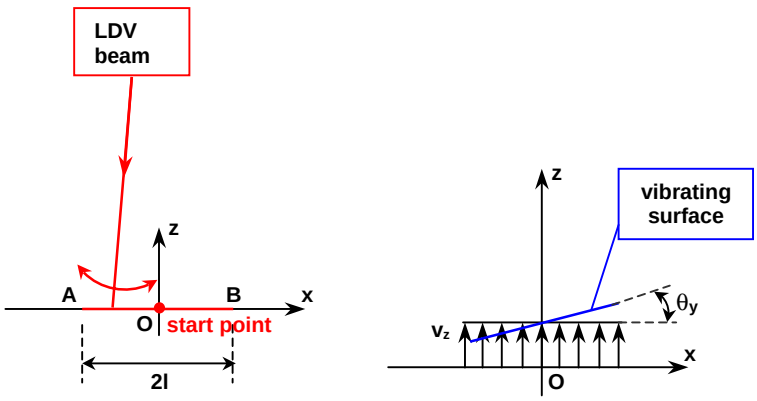


**Figure 4. 6** Laser beam scan and vibration DOFs associated to the surface.

The position of the spot on the line can be defined at each time instant, *t*, by:

$$x(t) = l\cos\Omega t \qquad \textbf{(4. 1)}$$

A suitable Cartesian coordinate system can be introduced as shown in Figure 4.6: the origin **O** is at the scan mid-point, the *z*-direction is the LDV scan-beam axis and the *x*- and *y*-axes are (if set up correctly) parallel to the LDV mirror deflection axes. The structure vibration at the origin can be derived from the LDV response, bearing in mind that the line scan must be sufficiently short such that the structure may be assumed to vibrate as a plane surface. Point **O** in Figure 4.6 is then supposed to undergo only to a translational velocity, $v_z$, and an angular velocity, $\theta_y$. At a generic point along the line scan the total velocity can be written as:

$$v(x) = v_z + x\theta_y \qquad \textbf{(4. 2)}$$

If a structure's deflections are sinusoidal at frequency, ω, in general, at any point:

$$v_z = V_{zR}\cos\omega t + V_{zI}\sin\omega t \qquad \theta_y = \Theta_{yR}\cos\omega t + \Theta_{yI}\sin\omega t \qquad \textbf{(4. 3)}$$

Introducing Equations (4.1) and (4.3) into the Equation (4.2) the structure's velocity becomes:

$$v(t) = V_{zR}\cos\omega t + V_{zI}\sin\omega t + (l\cos\Omega t)(\Theta_{yR}\cos\omega t + \Theta_{yI}\sin\omega t) \qquad \textbf{(4. 4)}$$

After some manipulation, the response measured by the laser can be shown to be as:

$$
\begin{aligned}
v(t) &= V_{zR}\cos\omega t + V_{zI}\sin\omega t + \\
&+\frac{1}{2}l\Theta_{yI}\cos(\omega-\Omega)t - \frac{1}{2}l\Theta_{yR}\sin(\omega-\Omega)t + \\
&-\frac{1}{2}l\Theta_{yI}\cos(\omega+\Omega)t + \frac{1}{2}l\Theta_{yR}\sin(\omega+\Omega)t
\end{aligned}
\qquad \textbf{(4. 5)}
$$

The LDV output comprises components at the vibration frequency, whose real and imaginary parts are labelled $R_\omega$ and $I_\omega$, and at a pair of sidebands $R_{\omega-\Omega}$ and $I_{\omega-\Omega}$ and $R_{\omega+\Omega}$ and $I_{\omega+\Omega}$ . The sideband components show a characteristic behaviour: real parts of the left and right sidebands have the same magnitude but opposite signs, and the same happens for the imaginary components. This recurrence can be used to calibrate the mirrors, since it is not perfectly realised when there is a delay of the mirror itself, see Section 4.6. The complex components of the *z*-axis translation ($V_{zR}$ and $V_{zI}$) and *x*-axis rotations ($\Theta_{xR}$ , $\Theta_{xI}$) may be derived from these Fourier components of the LDV spectrum:

$$
\begin{aligned}
V_{zR} &= R_\omega & V_{zI} &= I_\omega \\
\Theta_{yR} &= \frac{2I_{\omega+\Omega}}{l} = -\frac{2I_{\omega-\Omega}}{l} & \Theta_{yI} &= -\frac{2R_{\omega+\Omega}}{l} = \frac{2R_{\omega-\Omega}}{l}
\end{aligned}
\qquad \textbf{(4. 6)}
$$

Experiments have been carried out in the structure described in Section 4.1 and illustrated in Figure 4.5. In order to validate the results and to estimate the reliability of the continuous technique, the conventional discrete procedure has been performed to measure the translational and angular velocities at point **O**, by measuring with the non-scanning LDV at two points **A** and **B** (separated by the same distance as the length of the scan, 2*l*, see Figure 4.6) using the force signal as reference. In fact, the rotational DOF can be approximated by the first derivative of the translations in the normal *z*-directions, the first derivative approximation giving:

$$
\theta_y = \frac{\partial v_z}{\partial y} \approx \frac{v_z(A) - v_z(B)}{2l}
\qquad \textbf{(4. 7)}
$$

By measuring the LDV response (translational velocity along the *z*-axis) in two steps using the single point LDV working in the conventional way, the RDOF at the mid point in the conjunction of **A** and **B** can be derived. Moreover, the translational response at **O** can be obtained as the average of the measurements at **A** and **B**. Two DOFs are then obtained in three shots while the continuous technique achieves the same result with only one measurement.

In order to compare both amplitude and phase of the two vibration DOFs measured, it is customary to divide the response by the input forcing to obtain the FRF, i.e. to refer the vibration to a time datum that is the sinusoidal excitation. Therefore, forces applied in the continuous scan and in the discrete point measurement must be acquired at the same time as the corresponding velocity response.

In the experiments, a drive voltage has been applied to the *y*-axis laser beam deflection mirror, so as to scan at 20 Hz along a vertical line 16 mm long, centred on point **O**, see Figure 4.7. The translation DOF in the *z*-direction and rotation about *x* were deduced from the $\omega, (\omega + \Omega)$ and $(\omega - \Omega)$ complex components using Equations (4.6).

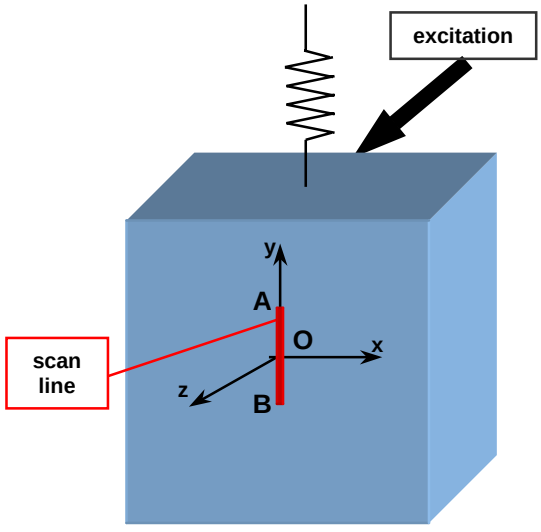


**Figure 4. 7** Linear scan set up.

Taking into account the mirror delay that always occurs in reality, by triggering the acquisition of the LDV signal, this latter appeared to have a modulated time

history exactly in phase with the mirror driver signal itself (Figure 4.8, where a slight phase shift can be noticed due to the delay).

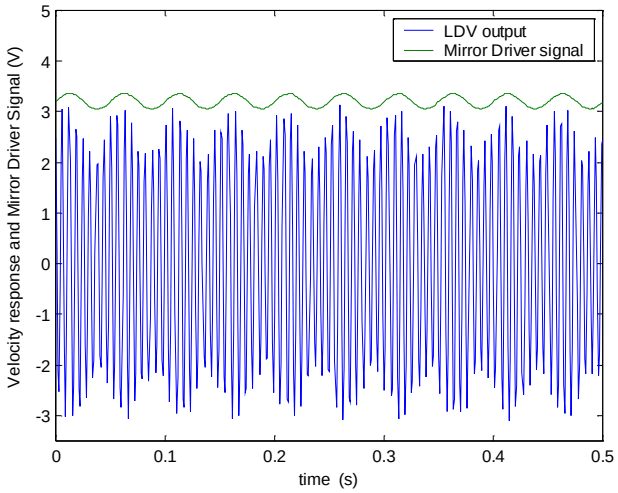


**Figure 4. 8** LDV output and Mirror Drive Signal plotted together.

By multiplying the velocity response by sine and cosine of the known frequencies ω, $(\omega+\Omega)$ and $(\omega-\Omega)$, i.e. 158 Hz, 178 Hz and 138 Hz respectively, the complex Fourier components can be derived and it can be noticed, as expected, that the real parts of the left and right sidebands are approximately equal in amplitude and opposite in sign, and similarly for the imaginary part.

$$\begin{array}{lll} R_{\omega-\Omega}=-0.00508 & R_{\omega}=2.57850 & R_{\omega+\Omega}=0.00682 \\ I_{\omega-\Omega}=0.25353 & I_{\omega}=0.07259 & I_{\omega+\Omega}=-0.25670 \end{array} \quad \textbf{(4. 8)}$$

Introducing these values into Equation (4.6), translational and angular vibration amplitudes can be derived and compared with those obtained by point measurements. Response magnitudes are quoted in the Table 4.3 where phase data, relative to the force-input signal in each case, are introduced as well:

| | STEADY MEASUREMENT | SCANNING MEASUREMENT |
|---|---|---|
| Translation in z (mag [mm/s]) | 12.936 | 12.911 |
| Translation in z (phase º) | -116.89 | -117.09 |
| Rotation about x (mag [rad/s]) | 0.151 | 0.159 |
| Rotation about x (phase º) | -116.99 | -117.26 |

**Table 4. 3** 2DOF measurement at point **O** via linear scan at 20Hz.

The maximum absolute phase discrepancy was 0.27º on the phase of the *x*-rotation (around 0.2%). The discrepancy in the measured velocity magnitude was 0.025 mm/s on the *z*-translation, inducing again an error of 0.2%. Whereas the percentage error related to the rotation magnitude was bigger (5.2%) and this is due to the small amplitude of the angular rotation; in fact, the absolute discrepancy in the measured rotation magnitude was 0.008 rad/s.

### *4.3. Analysis of Circular Scan and Experimental Validation*

If the laser beam is scanned continuously at a speed, Ω, in a circle of radius, *R*, centred on the nominal measurement point, the vibration response measured at an arbitrary position on the circle, say, **Q**, of general coordinates *x*,*y* will be:

$$v(x,y) = v_z + \theta_x y + \theta_y x \qquad \textbf{(4. 9)}$$

Positive directions of rotations $\theta_x$ and $\theta_y$ are shown in Figure 4.9.

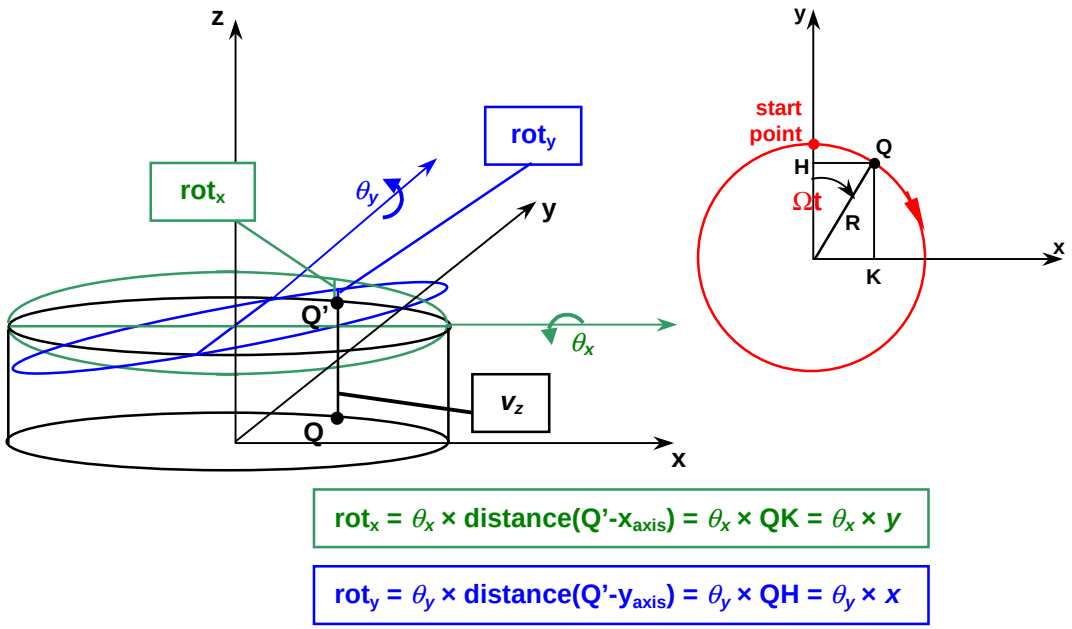


**Figure 4. 9** Circular scan configuration.

The laser spot is moving around the circle at speed, Ω, and so the angle swept when it is passing through **Q** will be Ω*t*. The coordinates of the point **Q** expressed in terms of scan speed are:

$$\begin{aligned} x &= R\sin(\Omega t) \\ y &= R\cos(\Omega t) \end{aligned} \qquad \textbf{(4. 10)}$$

*R* being the circle radius. Equation (4.9) will then become:

$$v(t) = v_z + \theta_x R\cos\Omega t + \theta_y R\sin\Omega t \qquad \textbf{(4. 11)}$$

If the surface vibration is harmonic, at frequency ω, the translational and rotational components can be expressed as:

$$\begin{aligned} v_z &= V_{zR}\cos\omega t + V_{zI}\sin\omega t \\ \theta_x &= \Theta_{xR}\cos\omega t + \Theta_{xI}\sin\omega t \qquad\qquad \theta_y = \Theta_{yR}\cos\omega t + \Theta_{yI}\sin\omega t \end{aligned} \qquad \textbf{(4. 12)}$$

So, Equation (4.11) can be rewritten as:

$$
\begin{aligned}
v(t) = {} & V_{zR}\cos\omega t + V_{zI}\sin\omega t + \\
& + \Theta_{xR}\cos\omega t R\cos\Omega t + \Theta_{xI}\sin\omega t R\cos\Omega t + \\
& + \Theta_{yR}\cos\omega t R\sin\Omega t + \Theta_{yI}\sin\omega t R\sin\Omega t
\end{aligned}
\qquad \textbf{(4. 13)}
$$

Expanding:

$$
\begin{aligned}
v(t) = {} & V_{zR}\cos\omega t + V_{zI}\sin\omega t + \\
& + \frac{1}{2}R(\Theta_{xR} + \Theta_{yI})\cos(\omega - \Omega)t + \frac{1}{2}R(\Theta_{xI} - \Theta_{yR})\sin(\omega - \Omega)t + \\
& + \frac{1}{2}R(\Theta_{xR} - \Theta_{yI})\cos(\omega + \Omega)t + \frac{1}{2}R(\Theta_{xI} + \Theta_{yR})\sin(\omega + \Omega)t
\end{aligned}
\qquad \textbf{(4. 14)}
$$

whence,

$$
\begin{aligned}
V_{zR} &= R_{\omega} & V_{zI} &= I_{\omega} \\
\Theta_{xR} &= \left(\frac{R_{\omega-\Omega} + R_{\omega+\Omega}}{R}\right) & \Theta_{xI} &= \left(\frac{I_{\omega-\Omega} + I_{\omega+\Omega}}{R}\right) \\
\Theta_{yR} &= \left(\frac{I_{\omega+\Omega} - I_{\omega-\Omega}}{R}\right) & \Theta_{yI} &= \left(\frac{R_{\omega-\Omega} - R_{\omega+\Omega}}{R}\right)
\end{aligned}
\qquad \textbf{(4. 15)}
$$

The real and imaginary components of the *z*-axis translation ($V_{zR}$ and $V_{zI}$) and the *x*- and *y*-axis rotations ($\Theta_{xR}$, $\Theta_{xI}$, $\Theta_{yR}$, $\Theta_{yI}$) are easily derived from the real and imaginary components of the LDV response using Equations (4.15) (the *z*-axis being the central axis around which the laser scan rotates).

Measurements have been again made on the cube test piece to validate the analysis of small-radius circular scanning. The same set up shown in Figure 4.5 has been used here. Drive voltages have been applied to the *x*- and *y*- laser beam deflection mirrors, so as to scan the beam at 20 Hz around a circle of 16 mm diameter, centred on point **O**, see Figure 4.10.

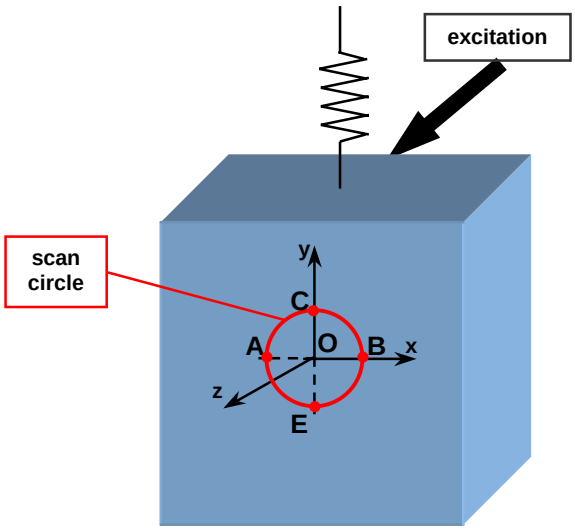


**Figure 4. 10** Circular scan set up.

The translation DOF, $V_z$, and the rotational DOFs $\Theta_x$ and $\Theta_y$, were derived using Equation (4.15) from the real and imaginary components of the LDV output spectrum recovered by multiplying the time acquired history by sines and cosines at the usual frequencies (138 Hz, 158 Hz and 178 Hz). The same procedure followed in Section 4.2 to validate the continuous technique has been applied here as well, i.e. via a non-scanning LDV, and translational vibration at four points **A**, **B**, **C**, **E** (Figure 4.10) were measured using the force signal as reference. The distances **A-B** and **C-E** were the same as the circle-scan diameter. Translation and rotation DOF derivation using measurements from four points is based on the same procedure as for two points (Section 4.2).

Steady measurements are compared with the results from the circular scan in the Table 4.4 (phase data are again relative to the corresponding force input signal stored in each case).

| | STEADY MEASUREMENT | SCANNING MEASUREMENT |
|---|---|---|
| Translation in z (mag [mm/s]) | 12.970 | 13.101 |
| Translation in z (phase º) | -116.97 | -117.05 |
| Rotation about x (mag [rad/s]) | 0.043 | 0.061 |
| Rotation about x (phase º) | 67.91 | 68.35 |
| Rotation about y (mag [rad/s]) | 0.290 | 0.299 |
| Rotation about y (phase º) | 62.87 | 64.32 |

**Table 4. 4** MDOF measurement at point O via circular scan at 20Hz.

In these measurements, the difference in the measured translation velocity magnitude was 0.131 mm/s ( 1.01 %), the maximum phase discrepancy was 1.45º (rotation about *y*). The worst rotation magnitude discrepancy was 0.018 rad/s (6.2%). Rotation measurement uncertainty obviously depends on the scan radius; in this case 0.018 rad/s uncertainty in $\Theta_x$ corresponds to a translational uncertainty of 0.14mm/s, 1.11% of the overall signal amplitude.

### *4.4. Analysis of Conical Scan and Experimental Validation*

The three translational degrees of freedom at a point in a vibrating structure, $V_x$ $V_y$ $V_z$, can be measured by a tri-axial accelerometer but the same result can be achieved by using an LDV with the advantage of overtaking the well-known mass-loading effect. The translational velocity components may be recovered by performing three separate non-contact measurements at different directions (each mutually independent, i.e. not belonging at the same plane) via a conventional single-axis laser vibrometer focused to the same measurement point. Moreover, an LDV can be directed at the target point while the laser beam exercises a conical scan; the philosophy is the same as the three directional measurements procedure but the three directions are now swept with one shot.

In practice, the laser beam is scanned in a circle, at frequency **Ω**, the circular scan being diverted by an annular mirror or a short-focus lens so that the focal

point is scanned in a circular cone with an angle of incidence Φ, as shown in Figure 4.11.

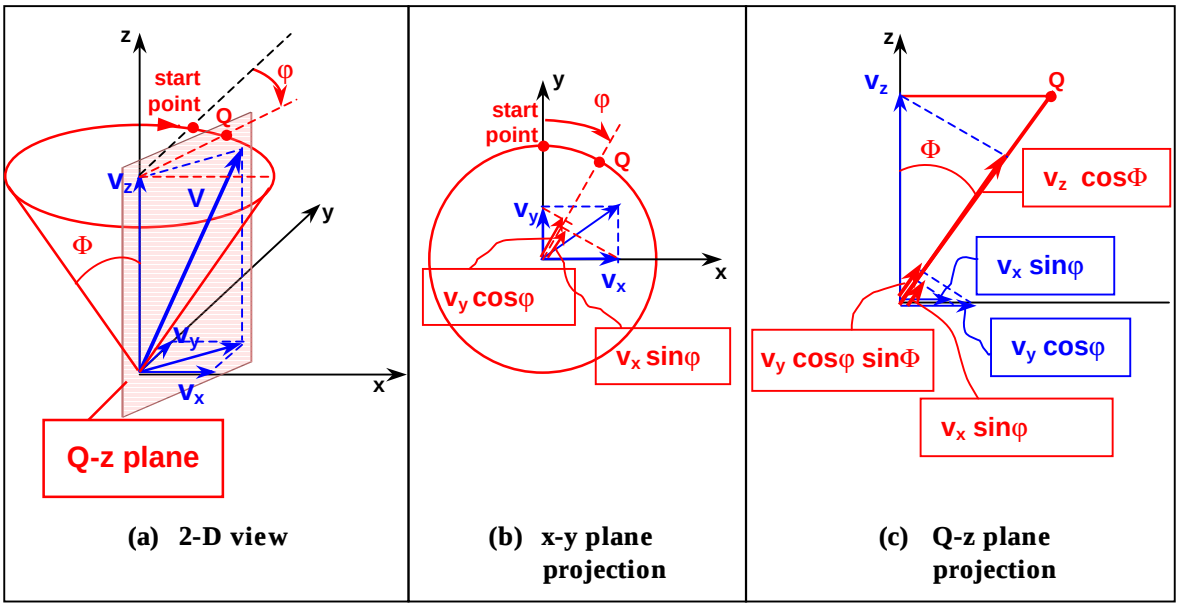


**Figure 4. 11** Conical scan configuration.

With the scan arranged as in Figure 4.11, specifically see detail (b), the vibration signal detected at an arbitrary angular position, φ, along the scan cone is

$$v_{\varphi}(t) = v_z(t)\cos\Phi + v_x(t)\sin\varphi(t)\sin\Phi + v_y(t)\cos\varphi(t)\sin\Phi \qquad \textbf{(4. 16)}$$

where, Φ, is the lens deviation angle (cone angle) and, φ, is the scanned angle or $\Omega t$, $\Omega$ being the scan speed. The mirrors are driven following again Equation (4.10) with a suitable radius, *R*, in order to make the laser beam scan in a circle inside the lens.

Considering the surface to be vibrating sinusoidally at frequency, ω, the three translational components can be written as:

$$\begin{aligned} v_x &= V_{xR}\cos\omega t + V_{xI}\sin\omega t \\ v_y &= V_{yR}\cos\omega t + V_{yI}\sin\omega t \\ v_z &= V_{zR}\cos\omega t + V_{zI}\sin\omega t \end{aligned} \qquad \textbf{(4. 17)}$$

Introducing the previous expressions in Equation (4.16), the vibration velocity will appear as:

$$v(t) = \left(V_{zR}\cos\omega t + V_{zI}\sin\omega t\right)\cos\Phi + \left(V_{xR}\cos\omega t + V_{xI}\sin\omega t\right)\sin\Omega t\sin\Phi + \left(V_{yR}\cos\omega t + V_{yI}\sin\omega t\right)\cos\Omega t\sin\Phi \quad \textbf{(4. 18)}$$

Expanding:

$$\begin{aligned} v(t) = {} & V_{zR}\cos\Phi\cos\omega t + V_{zI}\cos\Phi\sin\omega t + \\ & + \frac{1}{2}(V_{xI} + V_{yR})\sin\Phi\cos(\omega-\Omega)t + \frac{1}{2}r(V_{yI} - V_{xR})\sin\Phi\sin(\omega-\Omega)t + \\ & + \frac{1}{2}(V_{yR} - V_{xI})\sin\Phi\cos(\omega+\Omega)t + \frac{1}{2}(V_{xR} + V_{yI})\sin\Phi\sin(\omega+\Omega)t \end{aligned} \quad \textbf{(4. 19)}$$

The LDV output has a single sideband-pair spectrum and, using the same notation as before, the real and imaginary components of the velocities in the Cartesian system of reference may be derived:

$$\begin{aligned} V_{xR} &= \frac{I_{\omega+\Omega} - I_{\omega-\Omega}}{\sin\Phi} & V_{xI} &= \frac{R_{\omega-\Omega} - R_{\omega+\Omega}}{\sin\Phi} \\ V_{yR} &= \frac{R_{\omega-\Omega} + R_{\omega+\Omega}}{\sin\Phi} & V_{yI} &= \frac{I_{\omega+\Omega} + I_{\omega-\Omega}}{\sin\Phi} \\ V_{zR} &= \frac{R_{\omega}}{\cos\Phi} & V_{zI} &= \frac{I_{\omega}}{\cos\Phi} \end{aligned} \quad \textbf{(4. 20)}$$

Translational velocity has been measured at a point **O** on the cube: the free-free cube excited at the natural frequency of 158 Hz. The laser beam was scanned continuously in a conical path directed at the target point, see Figure 4.12.

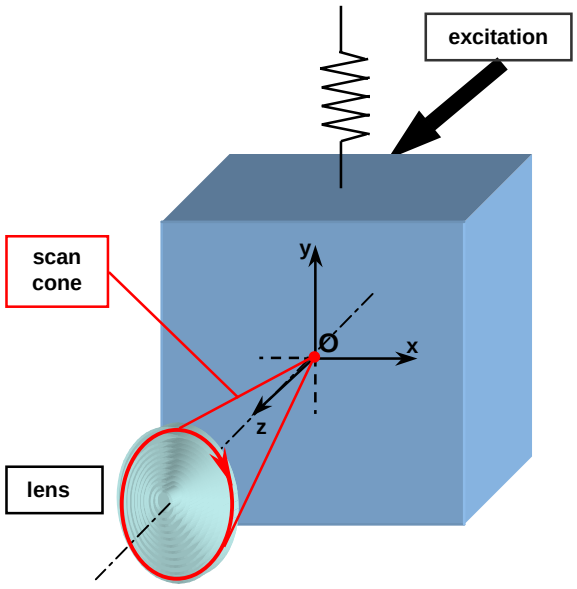


**Figure 4. 12** Conical scan set up.

The conical scan was realised by employing a single-element 67 mm diameter, plano-convex condenser lens with a focal length of about 45 mm. The maximum scan angle, Φ, that could be achieved with this lens was 36.66°, when the scan was performed at the lens edge as shown in Figure 4.13.

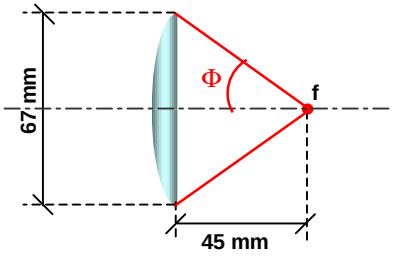


**Figure 4. 13** Lens deviation angle.

The cone angle can be determined precisely by calibration, see Section 4.6, but it was found that this angle was always fluctuating around 30º if the scan circle on the lens was set at about 2 mm from its circumferential edge.

The laser beam was driven to follow a circular path by feeding the *x*- and *y*-mirrors via two sinewaves 90º phase shifted described by Equations (4.10),

where $R$ is the scan circle radius (about 31.5 mm) and $\Omega$ is the scan speed that was chosen to be 10 Hz.

The focusing process was easily carried out, in fact, since the laser beam is constituted of coherent monochromatic light, and if it is made to scan around a circle centred on the lens's optical axis, no aberration fluctuations are produced. The standoff distance was adjusted until, when scanning, the circle produced on the illuminated surface degenerated to a point.

Curve fitting the modulated LDV output signal at 158 Hz and 158 ± 10 Hz real and imaginary components at the excitation and sideband frequencies are recovered ($R_\omega$, $I_\omega$, and $R_{\omega-\Omega}$, $I_{\omega-\Omega}$, $R_{\omega+\Omega}$, $I_{\omega+\Omega}$). By applying Equation 4.20, translational DOFs can be established in amplitude and phase relative to the force input signal. Their values are reported in Table 4.5.

| | **Amplitude** (mm/s) | **Phase** (º) |
|---|---|---|
| Translation in x | 9.720 | -124.03 |
| Translation in y | 0.926 | 56.16 |
| Translation in z | 6.517 | -119.02 |

**Table 4. 5** MDOF measurement at point O via conical scan at 10Hz.

An alternative analysis of the conical scanning technique in cylindrical coordinates, see reference [9], may be helpful to facilitate the processing of the data acquired. It is possible to derive the velocity magnitude, $V$, and its vector orientation angles, $\gamma$ and $\delta$, knowing magnitude and phase values of the central peak and sidebands in the velocity spectrum. In order to do this it is necessary to transform the formulae previously derived in cylindrical coordinates into Cartesian coordinates. The vibration vector, $\boldsymbol{v}$, expressed by the coordinates ($v_x$, $v_y$, $v_z$) in the Cartesian reference system, will be now identified by the cylindrical co-ordinates ($V$, $\delta, \gamma$). A relationship between rectangular and cylindrical coordinates can be easily established by geometrical considerations, see Figure 4.14. Note that this visualisation can be made only if the vibration velocity vector lies on a straight line in the $x,y$ plane, i.e. if the $x$- and $y$-components of the vibration response are in- or out-of-phase with each other.

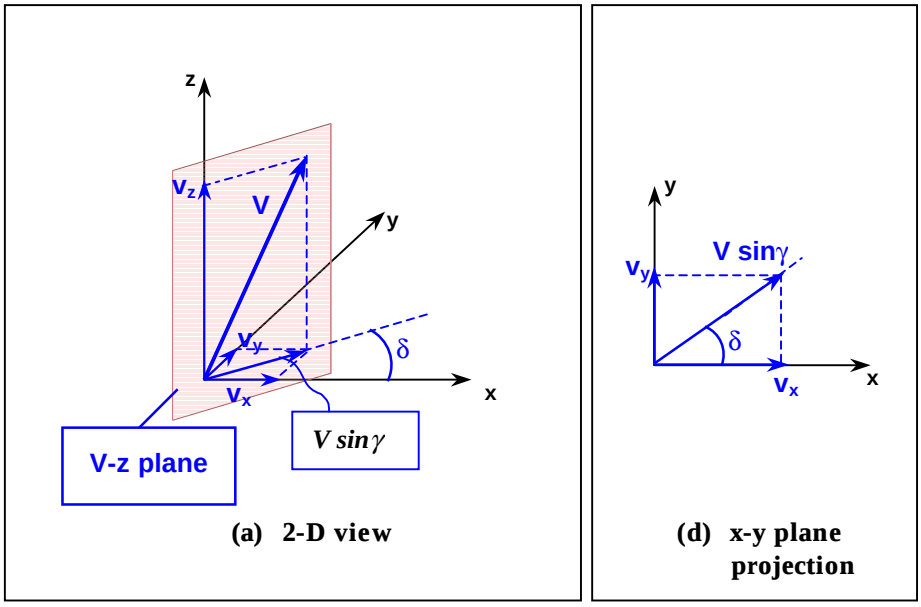


**Figure 4. 14** Cylindrical representation of vibration vector.

The velocity Cartesian components can be written in terms of the cylindrical coordinates:

$$\begin{aligned} v_z &= V\cos\gamma \\ v_x &= V\sin\gamma\cos\delta \\ v_y &= V\sin\gamma\sin\delta \end{aligned} \qquad \textbf{(4. 21)}$$

Because the amplitude vibration is harmonic, it can be represented as:

$$V = V_R\cos\omega t + V_I\sin\omega t \qquad \textbf{(4. 22)}$$

Introducing Equation (4.22) into (4.21), and in Equation (4.16), the full expression for the velocity at time *t* can be derived:

$$\begin{aligned} v_\theta(t) = &\left(V_R\cos\omega t + V_I\sin\omega t\right)\cos\gamma\cos\Phi + \\ &+\left(V_R\cos\omega t + V_I\sin\omega t\right)\sin\gamma\cos\delta\sin\varphi(t)\sin\Phi + \\ &+\left(V_R\cos\omega t + V_I\sin\omega t\right)\sin\gamma\sin\delta\cos\varphi(t)\sin\Phi \end{aligned} \qquad \textbf{(4. 23)}$$

Bringing $\Omega t$ into the place of $\varphi$, and expanding out in the usual trigonometric way:

$$\begin{aligned} v_\theta(t) = {} & V_R \cos\gamma\cos\Phi\cos\omega t + V_I \cos\gamma\cos\Phi\sin\omega t + \\ & + \frac{1}{2}\left(V_I\cos\delta + V_R\sin\delta\right)\sin\gamma\sin\Phi\cos(\omega-\Omega)t + \\ & + \frac{1}{2}\left(V_I\sin\delta - V_R\cos\delta\right)\sin\gamma\sin\Phi\sin(\omega-\Omega)t + \\ & + \frac{1}{2}\left(-V_I\cos\delta + V_R\sin\delta\right)\sin\gamma\sin\Phi\cos(\omega+\Omega)t + \\ & + \frac{1}{2}\left(V_R\cos\delta + V_I\sin\delta\right)\sin\gamma\sin\Phi\sin(\omega+\Omega)t \end{aligned} \qquad \textbf{(4. 24)}$$

Real and imaginary parts of the response components at frequency, $\omega$, and at sideband frequencies, $(\omega-\Omega)$, and, $(\omega+\Omega)$, can be deduced:

$$\begin{aligned} V_{\omega R} &= V_R\cos\gamma\cos\Phi \\ V_{\omega I} &= V_I\cos\gamma\cos\Phi \\ V_{(\omega-\Omega)R} &= \frac{1}{2}\left(V_I\cos\delta + V_R\sin\delta\right)\sin\gamma\sin\Phi \\ V_{(\omega-\Omega)I} &= \frac{1}{2}\left(-V_R\cos\delta + V_I\sin\delta\right)\sin\gamma\sin\Phi \\ V_{(\omega+\Omega)R} &= \frac{1}{2}\left(-V_I\cos\delta + V_R\sin\delta\right)\sin\gamma\sin\Phi \\ V_{(\omega+\Omega)I} &= \frac{1}{2}\left(V_R\cos\delta + V_I\sin\delta\right)\sin\gamma\sin\Phi \end{aligned} \qquad \textbf{(4. 25)}$$

In magnitude terms, calling $\overline{V}$ the vibration vector amplitude, the spectral amplitude at the central and at the sideband frequencies will be:

$$\begin{aligned} \overline{V}_\omega &= \sqrt{V_{\omega R}^2 + V_{\omega I}^2} = \sqrt{V_R^2 + V_I^2}\cos\Phi\cos\gamma = \overline{V}\cos\Phi\cos\gamma \\ \overline{V}_{(\omega-\Omega)} &= \sqrt{V_{(\omega-\Omega)R}^2 + V_{(\omega-\Omega)I}^2} = \frac{1}{2}\sqrt{V_R^2 + V_I^2}\sin\Phi\sin\gamma = \frac{\overline{V}\sin\Phi\sin\gamma}{2} \\ \overline{V}_{(\omega+\Omega)} &= \sqrt{V_{(\omega+\Omega)R}^2 + V_{(\omega+\Omega)I}^2} = \frac{1}{2}\sqrt{V_R^2 + V_I^2}\sin\Phi\sin\gamma = \frac{\overline{V}\sin\Phi\sin\gamma}{2} \end{aligned} \qquad \textbf{(4. 26)}$$

$\overline{V}$ and $\gamma$ may be derived from the previous equations considering the following relationships:

$$\begin{aligned} \frac{\overline{V}_{\omega}}{\cos\Phi} &= \overline{V}\cos\gamma \\ \frac{\overline{V}_{(\omega-\Omega)} + \overline{V}_{(\omega+\Omega)}}{\sin\Phi} &= \overline{V}\sin\gamma \end{aligned} \qquad \textbf{(4. 27)}$$

By squaring and summing the previous two equations, the velocity vector magnitude is deduced:

$$\overline{V} = \sqrt{\left(\frac{\overline{V}_{\omega}}{\cos\Phi}\right)^2 + \left(\frac{\overline{V}_{(\omega-\Omega)} + \overline{V}_{(\omega+\Omega)}}{\sin\Phi}\right)^2} \qquad \textbf{(4. 28)}$$

Using Equations (4.27), the angular position with respect the *z*-direction can be established as well, by:

$$\gamma = \tan^{-1}\left(\frac{V_{(\omega-\Omega)} + V_{(\omega+\Omega)}}{V_{\omega}}\frac{1}{\tan\Phi}\right) \qquad \textbf{(4. 29)}$$

Angle $\delta$ may be derived from the measured phase data at the sideband frequencies. The calculation is made easier if the sinusoidal vibration -depicted in Equation (4.22)- is written in terms of amplitude and phase instead of real and imaginary components:

$$V = \overline{V}\cos(\omega t + \alpha) \qquad \textbf{(4. 30)}$$

$\alpha$, being the response phase angle relative to a reference that is usually the applied forcing input.

In order to make Equations (4.30) and (4.22) coincide, real and imaginary components must be expressed in terms of magnitude and phase of the vibration vector:

$$V_R = \overline{V}\cos\alpha$$
$$V_I = \overline{V}\sin\alpha \qquad \textbf{(4. 31)}$$

Introducing Equation (4.31) into (4.25), the LDV spectral components at ω , (ω–Ω) and (ω+Ω) are derived in terms of vibration amplitude and phase, $\overline{V}$ and δ:

$$\begin{aligned}
V_{\omega R} &= \overline{V}\cos\alpha\cos\gamma\cos\Phi \\
V_{\omega I} &= \overline{V}\sin\alpha\cos\gamma\cos\Phi \\
V_{(\omega-\Omega)R} &= \frac{1}{2}\left(\overline{V}\sin\alpha\cos\delta + \overline{V}\cos\alpha\sin\delta\right)\sin\gamma\sin\Phi \\
V_{(\omega-\Omega)I} &= \frac{1}{2}\left(-\overline{V}\cos\alpha\cos\delta + \overline{V}\sin\alpha\sin\delta\right)\sin\gamma\sin\Phi \\
V_{(\omega+\Omega)R} &= \frac{1}{2}\left(-\overline{V}\sin\alpha\cos\delta + \overline{V}\cos\alpha\sin\delta\right)\sin\gamma\sin\Phi \\
V_{(\omega+\Omega)I} &= \frac{1}{2}\left(\overline{V}\cos\alpha\cos\delta + \overline{V}\sin\alpha\sin\delta\right)\sin\gamma\sin\Phi
\end{aligned} \qquad \textbf{(4. 32)}$$

After some manipulation, Equation (4.32) can be written as:

$$\begin{aligned}
V_{\omega R} &= \overline{V}\cos\alpha\cos\gamma\cos\Phi \\
V_{\omega I} &= \overline{V}\sin\alpha\cos\gamma\cos\Phi \\
V_{(\omega-\Omega)R} &= \frac{1}{2}\overline{V}\sin(\alpha+\delta)\sin\gamma\sin\Phi \\
V_{(\omega-\Omega)I} &= -\frac{1}{2}\overline{V}\cos(\alpha+\delta)\sin\gamma\sin\Phi \\
V_{(\omega+\Omega)R} &= -\frac{1}{2}\overline{V}\sin(\alpha-\delta)\sin\gamma\sin\Phi \\
V_{(\omega+\Omega)I} &= \frac{1}{2}\overline{V}\cos(\alpha-\delta)\sin\gamma\sin\Phi
\end{aligned} \qquad \textbf{(4. 33)}$$

Phase angles of each component can be calculated, using the quantities in Equation (4.33):

$$\angle V_{\omega} = \tan^{-1}\left(\frac{V_{\omega I}}{V_{\omega R}}\right) = \tan^{-1}\left(\frac{V_I}{V_R}\right) = \tan^{-1}\left(\frac{V\sin\alpha}{V\cos\alpha}\right) = \alpha$$

$$\angle V_{(\omega-\Omega)} = \tan^{-1}\left(\frac{V_{(\omega-\Omega)I}}{V_{(\omega-\Omega)R}}\right) = \tan^{-1}\left(\frac{-\cos(\alpha+\delta)}{\sin(\alpha+\delta)}\right) = \tan^{-1}\left(-\frac{\sin\left[\frac{\pi}{2}-(\alpha+\delta)\right]}{\cos\left[\frac{\pi}{2}-(\alpha+\delta)\right]}\right) = \alpha+\delta-\frac{\pi}{2}$$

$$\angle V_{(\omega+\Omega)} = \tan^{-1}\left(\frac{V_{(\omega+\Omega)I}}{V_{(\omega+\Omega)R}}\right) = \tan^{-1}\left(\frac{\cos(\alpha-\delta)}{-\sin(\alpha-\delta)}\right) = \tan^{-1}\left(-\frac{\sin\left[\frac{\pi}{2}-(\alpha-\delta)\right]}{\cos\left[\frac{\pi}{2}-(\alpha-\delta)\right]}\right) = \alpha-\delta-\frac{\pi}{2}$$

**(4. 34)**

It can be noticed that the phase at the excitation frequency corresponds directly to the vibration phase while the third angular coordinate of the vibration vector is established from the difference of the phases at the sideband frequencies:

$$\delta = \frac{\angle V_{(\omega-\Omega)} - \angle V_{(\omega+\Omega)}}{2} \qquad \textbf{(4. 35)}$$

From Equations (4.28), (4.29) and (4.35) the three cylindrical components of the vibration vector ($\overline{V}$ , γ, δ) can thus be obtained.

The accuracy of the method has been checked by comparing the conical scanning results with corresponding velocities measured by a single-axis accelerometer directly mounted on the vibrating platform of a shaker, see Figure 4.15. With this set-up the velocity of the top surface of the accelerometer was expected to be in a direction perpendicular to its surface. The point **O**, shown in Figure 4.12, was, in this case, the centre point of the accelerometer's top surface.

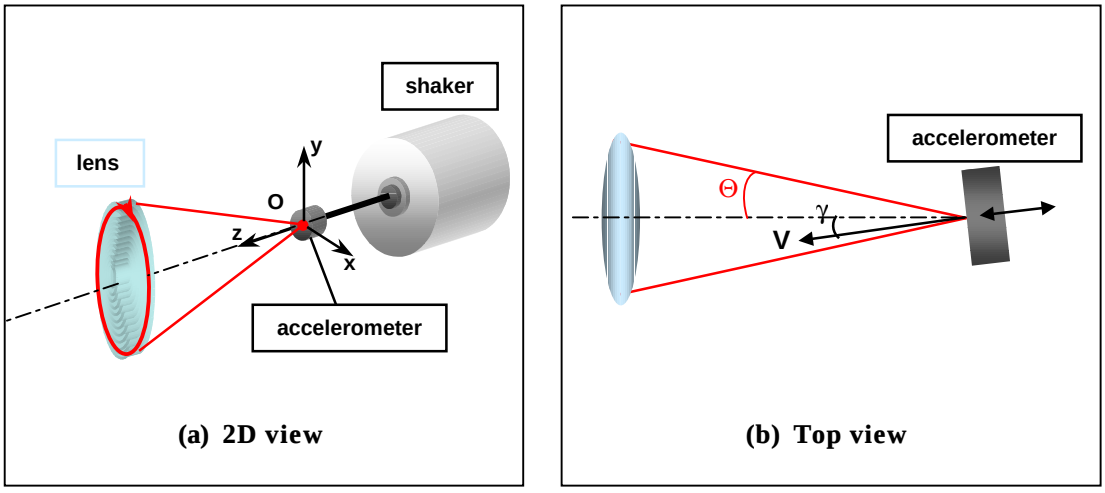


**Figure 4. 15** Accelerometer / Shaker set-up for Conical Scan trial.

Vibration velocities were measured simultaneously using both the accelerometer and the conical-scanning LDV, changing the angle of incidence of the laser beam axis to the surface of the accelerometer (γ) in order to visualise the measurement accuracy at different direction of acquisition. For conical scanning, the LDV beam was made to follow a circular trajectory by supplying sine and cosine signals at 20 Hz to the mirror drive inputs, the voltages being adjusted to scan in a circle near the periphery of the lens.

From Equation (4.20), vibration magnitudes $V_x$ , $V_y$ , $V_z$ , in the *x*-, *y*-, *z*-directions can be obtained combining real and imaginary components. The velocity vector modulus $\overline{V}$ is:

$$\overline{V} = \sqrt{V_x^2 + V_y^2 + V_z^2} \qquad \textbf{(4. 36)}$$

This value was compared with the velocity magnitude derived from the accelerometer with the results shown in Table 4.6. In Figure 4.16 the velocity outputs of the LDV and of the accelerometer, listed in the second and third columns of Table 4.6 respectively, are plotted against the incidence angle, γ.

| ANGLE (º) | From LDV OUTPUT (mm/s) | From ACCELEROMETER OUTPUT (mm/s) | DISCREPANCY (%) |
|---|---|---|---|
| 0 | 29.049 | 28.404 | 2.278 |
| 5 | 30.215 | 28.562 | 5.784 |
| 10 | 30.507 | 28.615 | 6.612 |
| 15 | 30.753 | 28.545 | 7.735 |
| 20 | 27.924 | 27.473 | 1.641 |
| 25 | 28.309 | 26.224 | 7.951 |
| 30 | 27.578 | 26.223 | 5.163 |
| 35 | 28.828 | 28.443 | 1.353 |
| 40 | 29.008 | 28.615 | 1.373 |
| 45 | 29.094 | 28.478 | 2.163 |
| 50 | 27.88 | 28.439 | 1.965 |

**Table 4. 6** Vibration velocity amplitudes measured with a conical scan LDV and an accelerometer.

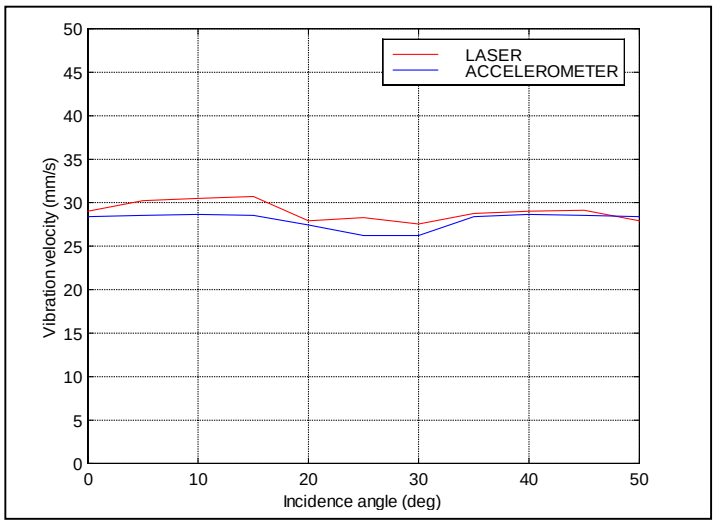


**Figure 4. 16** Vibration velocity amplitude measured with a conical scan LDV and an accelerometer.

With this test set-up, it was found that the vibration vector was not exactly in the direction of the accelerometer's axis. In fact, there were sidebands to the LDV response even if the scan axis was perpendicular to the accelerometer's top surface. This means that the LDV was observing also sideways velocities $V_x$ and $V_y$. The reason was found to be because the motion of the shaker platform was not exactly perpendicular to its mounting plane. The deviation varied with excitation frequency, being as low as 2° at 400Hz. Therefore discrepancies

between the two measurements appeared to be rather significant (up to around 8%).

In order to improve the accuracy test, a second check was performed with a different test specimen and with the purpose in investigating the accuracy of the angle (γ) measured. The alternative way of recovering the vibration vector in cylindrical coordinates was used in this case, see Equation (4.29).

Tests were conducted using an aluminium cantilever beam, 25 mm wide, 6.5 mm thick and 180 mm long, clamped at one end to a heavy block to produce, essentially, a simple cantilever, Figure 4.17. When excited at its lowest natural frequency, 84.5Hz, the motion was expected to be perpendicular to the face of the beam.

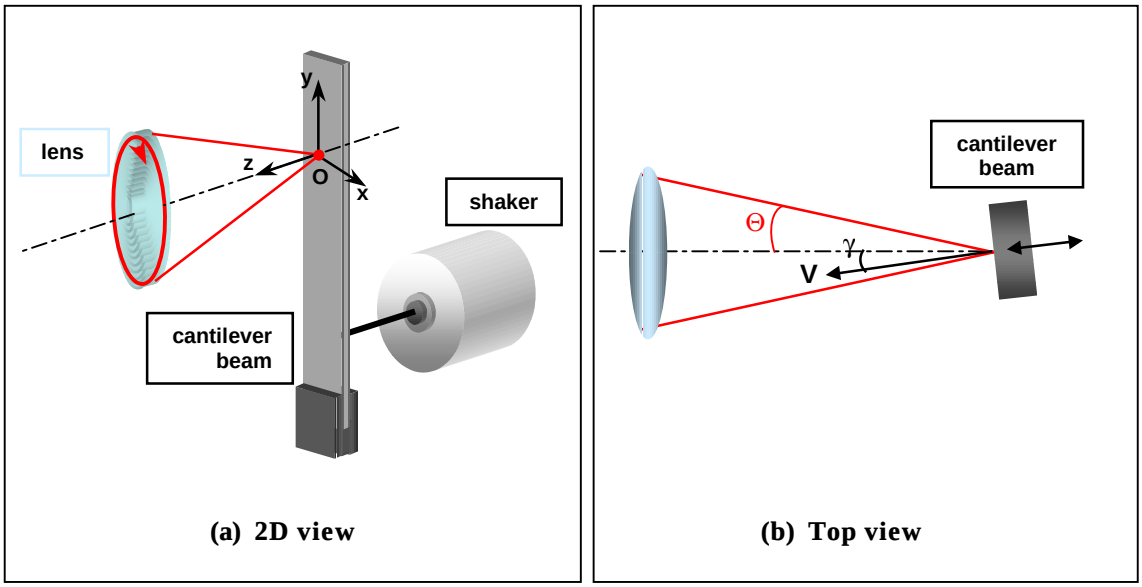


**Figure 4. 17** Conical scan set-up on the beam.

The cantilever beam was inclined to the conical scan axis in a series of different set-ups with angles of incidence between 0º and 55º in steps of 5º and at each step the (corresponding) angle γ was calculated using Equation (4.29). The results are listed in Table 4.7.

| TRUE ANGLE γ (º) | MEASURED ANGLE γ (º) | ERROR (º) |
|---|---|---|
| 0 | 2.11 | 2.11 |
| 5 | 4.951 | 0.049 |
| 10 | 8.394 | 1.606 |
| 15 | 15.039 | 0.039 |
| 20 | 18.599 | 1.401 |
| 25 | 24.827 | 0.173 |
| 30 | 31.022 | 1.022 |
| 35 | 34.642 | 0.358 |
| 40 | 41.569 | 1.569 |
| 45 | 46.688 | 1.688 |
| 50 | 52.466 | 2.466 |
| 55 | 58.238 | 3.238 |

**Table 4. 7** Measured angles using conical scan.

Measured values are plotted against the true ones in the following graph (Figure 4.18):

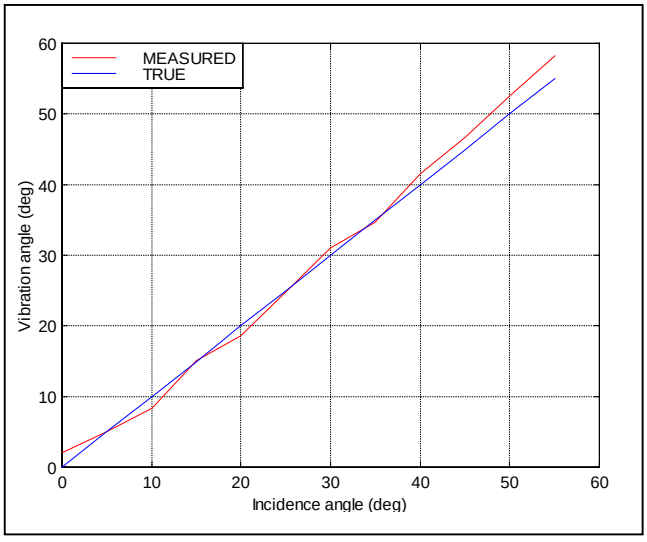


**Figure 4. 18** Accuracy of Vibration Direction measured by Conical Scan.

The worst discrepancies were obtained at the smallest and the largest angles. Uncertainties associated with the measurements at high incidence angles may be associated with an apparent increase in speckle noise in the LDV output. It is clearly impossible to apply a conical scan at angles of incidence to a surface greater than the cone scan angle. At high angles of incidence, the light returned to the laser unit was reduced and the LDV signal was heavily polluted with

signal dropouts. The speckle noise was generally low below a nominal incidence of 40º but increased above this (Figure 4.19), as the scan angle on one side approached grazing incidence. There was also considerable difficulty in focusing the laser spot on the test surface when its inclination to the cone axis was high. Measurement accuracy was optimized by using retro-reflective tape attached at the test point on the structure.

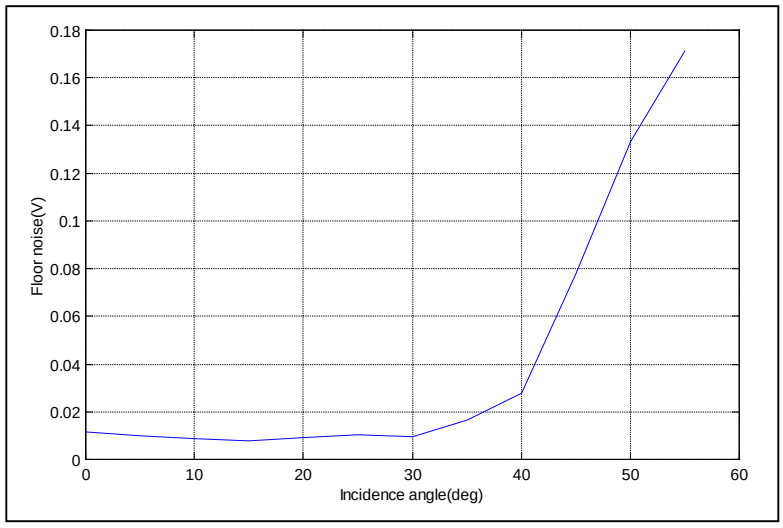


**Figure 4. 19** Noise floor outline.

At small angles of inclination, the sidebands, which represent the test surface rotation angle, are relatively small and the analysis error becomes larger, as the sidebands become confused with the noise.

An accuracy analysis can be applied to the angle derived if the uncertainty of the peak amplitudes in the LDV output spectrum is known. Ten measurements of the central peak and sideband amplitudes were acquired using the set-up shown in Figure 4.17, with an inclination angle of 10º. The errors relative to the main value of each parameter have been calculated as a standard deviation and are reported in Table 4.8:

| | **STANDARD DEVIATION** (V) | **MEAN VALUE** (V) |
|---|---|---|
| $\overline{V}_{\omega}$ | $\varepsilon_{\omega}$ = 3.8887e-3 | $\overline{V}_{m}$ = 4.0623 |
| $\overline{V}_{(\omega-\Omega)}$ | $\varepsilon_{-}$ = 4.2239e-3 | $\overline{V}_{m-}$ = 0.1065 |
| $\overline{V}_{(\omega+\Omega)}$ | $\varepsilon_{+}$ = 4.2241e-3 | $\overline{V}_{m+}$ = 0.1071 |

**Table 4. 8** Uncertainty associated with Conical Scan measurements.

The uncertainty associated with γ, which is a function of $\overline{V}_{\omega}$, $\overline{V}_{(\omega-\Omega)}$, and $\overline{V}_{(\omega-\Omega)}$, may be deduced from the following equation:

$$\varepsilon_{\gamma}=\sqrt{\varepsilon_{-}^{2}\left(\frac{\partial\gamma}{\partial\overline{V}_{(\omega-\Omega)}}\right)^{2}_{\overline{V}_{m},\overline{V}_{m-},\overline{V}_{m+}}+\varepsilon_{\omega}^{2}\left(\frac{\partial\gamma}{\partial\overline{V}_{\omega}}\right)^{2}_{\overline{V}_{m},\overline{V}_{m-},\overline{V}_{m+}}+\varepsilon_{+}^{2}\left(\frac{\partial\gamma}{\partial\overline{V}_{(\omega+\Omega)}}\right)^{2}_{\overline{V}_{m},\overline{V}_{m-},\overline{V}_{m+}}} \qquad \textbf{(4. 37)}$$

The final result, $\varepsilon_{\gamma}$, the standard deviation in γ, is 0.00247, which corresponds to a $3\varepsilon_{\gamma}$ uncertainty of 0.00741 rad, or 0.42°. This uncertainty, it may be noticed, is less than the discrepancies shown in Figure 4.18. The latter include errors in setting the actual beam vibration angle, which might well account for a significant proportion of the discrepancies in the graph. This measurement uncertainty is acceptable for most purposes, and should be achievable provided the conical scan axis is not inclined too far from the normal to the surface. Accuracy also depends on the conical scan angle, Φ. It will be worse if Φ is less than 30°, as used here.

## *4.5. Analysis of Conical-Circular Scan and Experimental Validation*

If a conical scan is set up and the target surface then moved away from the point of focus, towards the lens, the scan traces a circle on the vibrating surface, as shown in Figure 4.20, where the cone angle is Φ. This configuration will be called a circular scan 'inside the focus' because the test structure surface is lying in a position before the focus with respect to the lens. If the vibrating surface is

moved away from the lens, a circular scan 'outside the focus' will be realised; in fact, the test structure surface is now positioned beyond the focal plane of the lens. If the distance between the focus and the structure surface in both the configurations is the same (*d*), the circle scanned by the laser will be similar (same radius *R*) but the start point in the circle will undergo to a shift of 180º. In Figure 4.20 it can be noticed that the start point in the inside-focus configuration is situated in the first quadrant while in the outside-focus configuration it is in the third one.

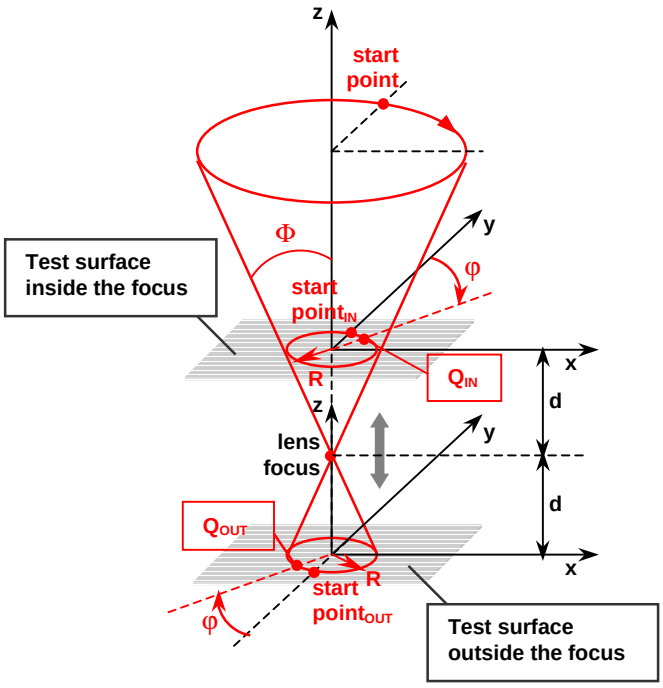


**Figure 4. 20** Conical-circular scan configuration.

Two measurements of this type enable *z*-axis translation and *x*-axis and *y*-axis translation and rotation DOFs to be resolved.

For the inside-focus configuration, at time instant *t*, the laser spot will coincide with the point $\mathbf{Q}_{IN}$ defined by its at angular position, $\varphi(t)$. If the scan speed is $\Omega$, the angle $\varphi$ is expressed by $\Omega t$. At point $\mathbf{Q}_{IN}$, the laser beam, whose measurement direction is dictated by the cone angle $\Phi$, will be then sensitive to the three translational DOFs ($v_x$, $v_y$, $v_z$) and the two rotation DOFs ($\theta_x$ , $\theta_y$),

which are, in a vectorial representation, $\theta_x R\cos\varphi$ and $\theta_y R\sin\varphi$: see Figure 4.9 in Section 4.3. The velocity measured at point $\mathbf{Q_{IN}}$ will be:

$$v_{IN\,\varphi}(t) = v_z(t)\cos\Phi + v_x(t)\sin\varphi(t)\sin\Phi + v_y(t)\cos\varphi(t)\sin\Phi + \\ + \theta_x(t)R\cos\varphi(t)\cos\Phi + \theta_y(t)R\sin\varphi(t)\cos\Phi \qquad \textbf{(4. 38)}$$

The complete vibration signal, given in the previous equation, can be deduced geometrically as shown in Figure 4.21.

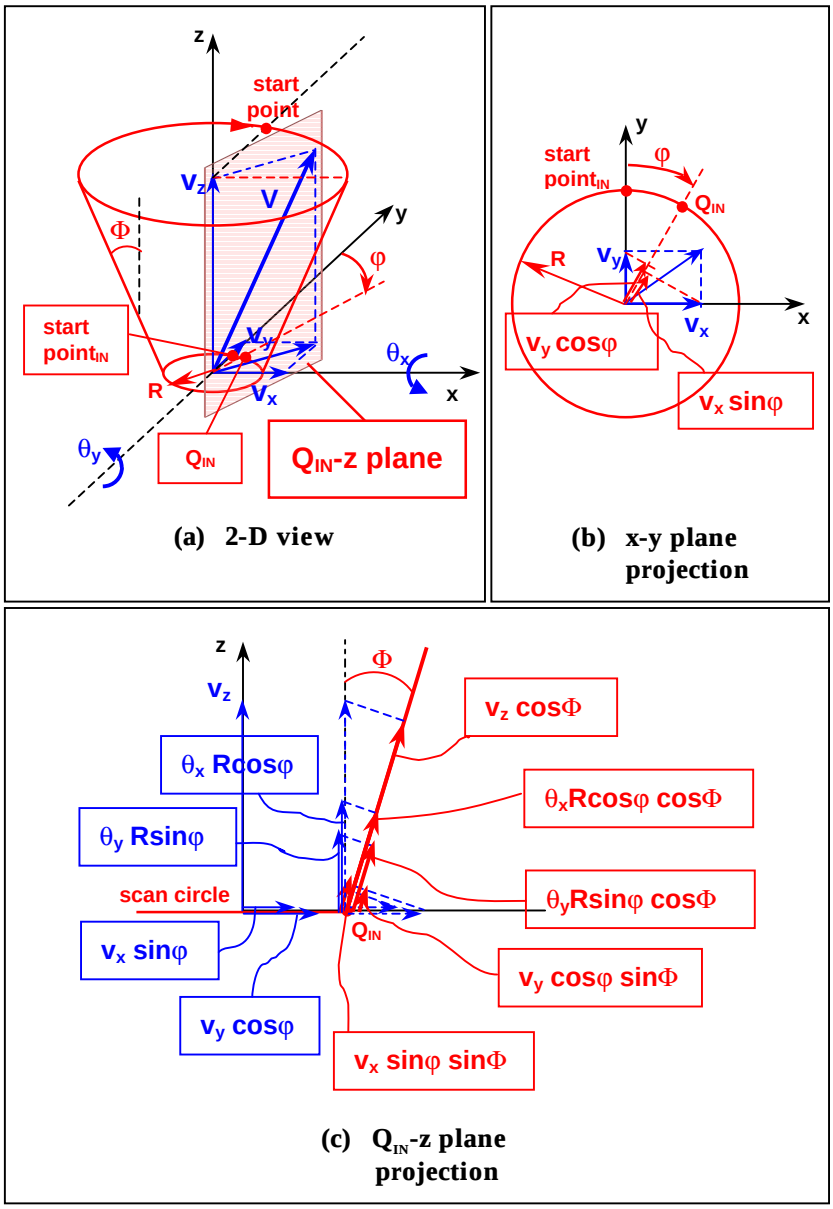


**Figure 4. 21** Inside-focus conical-circular scan.

Considering the test structure to be undergoing a complex sinusoidal motion, the vibration DOFs, in terms of their real and imaginary components, can be expressed as:

$$\begin{aligned} v_x(t) &= V_{xR}\cos\omega t + V_{xI}\sin\omega t & \theta_x(t) &= \Theta_{xR}\cos\omega t + \Theta_{xI}\sin\omega t \\ v_y(t) &= V_{yR}\cos\omega t + V_{yI}\sin\omega t & \theta_y(t) &= \Theta_{yR}\cos\omega t + \Theta_{yI}\sin\omega t \\ v_z(t) &= V_{zR}\cos\omega t + V_{zI}\sin\omega t \end{aligned} \qquad \textbf{(4.39)}$$

These quantities can be substituted into the vibration velocity expression given by Equation (4.38) and the following relationship developed:

$$\begin{aligned} v_{IN}(t) = {} & V_{zR}\cos\Phi\cos\omega t + V_{zI}\cos\Phi\sin\omega t + \\ & + V_{xR}\sin\Phi\cos\omega t\sin\Omega t + V_{xI}\sin\Phi\sin\omega t\sin\Omega t + \\ & + V_{yR}\sin\Phi\cos\omega t\cos\Omega t + V_{yI}\sin\Phi\sin\omega t\cos\Omega t + \\ & + \Theta_{xR}R\cos\Phi\cos\omega t\cos\Omega t + \Theta_{xI}R\cos\Phi\sin\omega t\cos\Omega t + \\ & + \Theta_{yR}R\cos\Phi\cos\omega t\sin\Omega t + \Theta_{yI}R\cos\Phi\sin\omega t\sin\Omega t \end{aligned} \qquad \textbf{(4. 40)}$$

where the quantity $\Omega t$ takes the place of the scanned angle, φ. Expanding out, we obtain:

$$\begin{aligned} v_{IN}(t) = {} & V_{zR}\cos\Phi\cos\omega t + V_{zI}\cos\Phi\sin\omega t + \\ & + \left[\frac{1}{2}\left(V_{yR}+V_{xI}\right)\sin\Phi + \frac{R}{2}\left(\Theta_{xR}+\Theta_{yI}\right)\cos\Phi\right]\cos\left(\omega-\Omega\right)t + \\ & + \left[\frac{1}{2}\left(V_{yI}-V_{xR}\right)\sin\Phi + \frac{R}{2}\left(\Theta_{xI}-\Theta_{yR}\right)\cos\Phi\right]\sin\left(\omega-\Omega\right)t + \\ & + \left[\frac{1}{2}\left(V_{yR}-V_{xI}\right)\sin\Phi + \frac{R}{2}\left(\Theta_{xR}-\Theta_{yI}\right)\cos\Phi\right]\cos\left(\omega+\Omega\right)t + \\ & + \left[\frac{1}{2}\left(V_{yI}+V_{xR}\right)\sin\Phi + \frac{R}{2}\left(\Theta_{xI}+\Theta_{yR}\right)\cos\Phi\right]\sin\left(\omega+\Omega\right)t \end{aligned} \qquad \textbf{(4. 41)}$$

The real (cosine term) and imaginary (sine term) parts of the components at the centre and sideband LDV output frequencies are thus:

$$
\begin{aligned}
R_{\omega IN} &= V_{zR}\cos\Phi & I_{\omega IN} &= V_{zI}\cos\Phi \\
R_{(\omega-\Omega)IN} &= \frac{1}{2}\left(V_{yR}+V_{xI}\right)\sin\Phi+\frac{R}{2}\left(\Theta_{xR}+\Theta_{yI}\right)\cos\Phi \\
I_{(\omega-\Omega)IN} &= \frac{1}{2}\left(V_{yI}-V_{xR}\right)\sin\Phi+\frac{R}{2}\left(\Theta_{xI}-\Theta_{yR}\right)\cos\Phi \\
R_{(\omega+\Omega)IN} &= \frac{1}{2}\left(V_{yR}-V_{xI}\right)\sin\Phi+\frac{R}{2}\left(\Theta_{xR}-\Theta_{yI}\right)\cos\Phi \\
I_{(\omega+\Omega)IN} &= \frac{1}{2}\left(V_{yI}+V_{xR}\right)\sin\Phi+\frac{R}{2}\left(\Theta_{xI}+\Theta_{yR}\right)\cos\Phi
\end{aligned}
\qquad \textbf{(4. 42)}
$$

In this system of equations there are eight unknowns ($V_{xR}$, $V_{xI}$, $V_{yR}$, $V_{yI}$, $\Theta_{xR}$, $\Theta_{xI}$ $\Theta_{yR}$, $\Theta_{yI}$) but only four equations. However by using ones derived for the second conical-circular scan configuration (outside-focus configuration), a further four equations are developed and the system can be solved. This situation is described in Figure 4.22, where it is possible to note that at point $\mathbf{Q_{OUT}}$ the sensitivity to $v_x$, $v_y$, and $v_z$, are unchanged, but the responses to $\theta_x$, and $\theta_y$ are phase-reversed because the scanned point is at the opposite end of a diameter of the scan circle.

Equation (4.38) therefore becomes:

$$
\begin{aligned}
v_{OUT\,\varphi}(t) = {} & v_z(t)\cos\Phi + v_x(t)\sin\varphi(t)\sin\Phi + v_y(t)\cos\varphi(t)\sin\Phi + \\
& -\theta_x(t)R\cos\varphi(t)\cos\Phi - \theta_y(t)R\sin\varphi(t)\cos\Phi
\end{aligned}
\qquad \textbf{(4. 43)}
$$

The LDV response components are hence given by a small modification of Equations (4.42):

$$R_{\omega OUT} = V_{zR}\cos\Phi \qquad I_{\omega OUT} = V_{zI}\cos\Phi$$

$$R_{(\omega-\Omega)OUT} = \frac{1}{2}\left(V_{yR} + V_{xI}\right)\sin\Phi - \frac{R}{2}\left(\Theta_{xR} + \Theta_{yI}\right)\cos\Phi$$

$$I_{(\omega-\Omega)OUT} = \frac{1}{2}\left(V_{yI} - V_{xR}\right)\sin\Phi - \frac{R}{2}\left(\Theta_{xI} - \Theta_{yR}\right)\cos\Phi \qquad \textbf{(4. 44)}$$

$$R_{(\omega+\Omega)OUT} = \frac{1}{2}\left(V_{yR} - V_{xI}\right)\sin\Phi - \frac{R}{2}\left(\Theta_{xR} - \Theta_{yI}\right)\cos\Phi$$

$$I_{(\omega+\Omega)OUT} = \frac{1}{2}\left(V_{yI} + V_{xR}\right)\sin\Phi - \frac{R}{2}\left(\Theta_{xI} + \Theta_{yR}\right)\cos\Phi$$

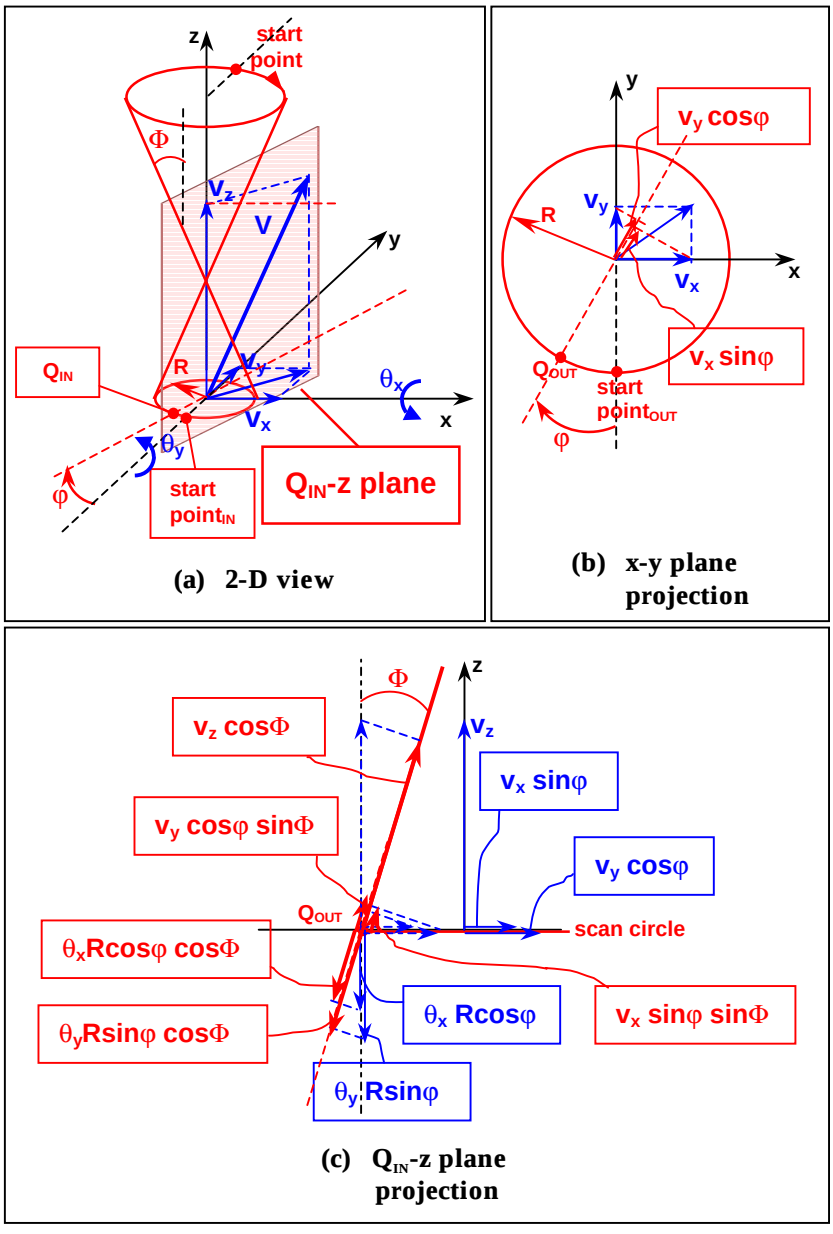


**Figure 4. 22** Outside-focus conical-circular scan.

Combining Equations (4.42) and (4.44) together, there is sufficient information to extract the required five DOF vibration components, the unknowns $V_x$, $V_y$, $V_z$, $\Theta_x$, and $\Theta_y$.

$$V_{zR} = \frac{R_{\omega IN}}{\cos\Phi} = \frac{R_{\omega OUT}}{\cos\Phi} \qquad V_{zI} = \frac{I_{\omega IN}}{\cos\Phi} = \frac{I_{\omega OUT}}{\cos\Phi}$$

$$V_{xR} = \frac{I_{(\omega+\Omega)IN} - I_{(\omega-\Omega)IN} + I_{(\omega+\Omega)OUT} - I_{(\omega-\Omega)OUT}}{2\sin\Phi} \qquad V_{xI} = \frac{R_{(\omega-\Omega)IN} - R_{(\omega+\Omega)IN} - R_{(\omega+\Omega)OUT} + R_{(\omega-\Omega)OUT}}{2\sin\Phi}$$

$$V_{yR} = \frac{R_{(\omega+\Omega)IN} + R_{(\omega-\Omega)IN} + R_{(\omega+\Omega)OUT} + R_{(\omega-\Omega)OUT}}{2\sin\Phi} \qquad V_{yI} = \frac{I_{(\omega+\Omega)IN} + I_{(\omega-\Omega)IN} + I_{(\omega+\Omega)OUT} + I_{(\omega-\Omega)OUT}}{2\sin\Phi}$$

$$\Theta_{xR} = \frac{R_{(\omega+\Omega)IN} + R_{(\omega-\Omega)IN} - R_{(\omega+\Omega)OUT} - R_{(\omega-\Omega)OUT}}{2R\cos\Phi} \qquad \Theta_{xI} = \frac{I_{(\omega+\Omega)IN} + I_{(\omega-\Omega)IN} - I_{(\omega+\Omega)OUT} - I_{(\omega-\Omega)OUT}}{2R\cos\Phi}$$

$$\Theta_{yR} = \frac{I_{(\omega+\Omega)IN} - I_{(\omega-\Omega)IN} - I_{(\omega+\Omega)OUT} + I_{(\omega-\Omega)OUT}}{2R\cos\Phi} \qquad \Theta_{yI} = \frac{R_{(\omega-\Omega)IN} - R_{(\omega+\Omega)IN} - R_{(\omega-\Omega)OUT} + R_{(\omega+\Omega)OUT}}{2R\cos\Phi}$$

**(4. 45)**

It is worth emphasising that circular and conical scans are special cases of the conical-circular scan theory, and this section therefore serves as a derivation for Equations (4.15) and (4.20) respectively.

If the cone angle, Φ, approaches zero, the test set up becomes equivalent to a circular scan situation and Equations (4.45) will take the form of Equations (4.15). The circular scan can thus be seen as a particular conical-circular scan where the lens has a focal plane at infinite distance (see Figure 4.23). This produces the effect of moving the outside-focus configuration to infinity as well and then of preventing its use in the process.

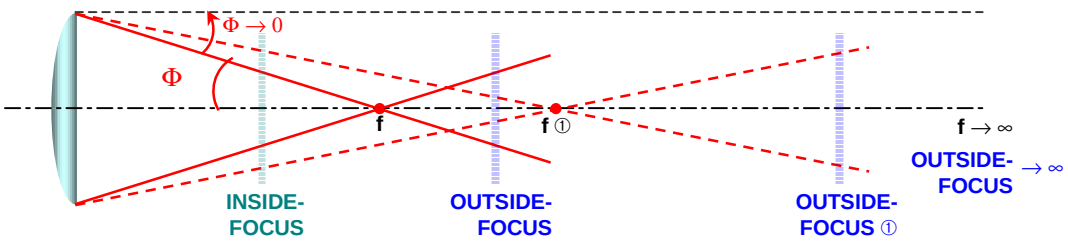


**Figure 4. 23** Conical-circular scan degeneration for Φ going to zero.

Only Equation (4.41) will then be available but it will be sufficient to solve the remaining DOFs $V_{zR}$, $V_{zI}$, $\Theta_{xR}$, $\Theta_{xI}$, $\Theta_{yR}$, $\Theta_{yI}$ , since the other ones -$V_{xR}$ , $V_{xI}$ , $V_{yR}$ , $V_{yI}$- disappeared, being multiplied by sin$\Phi$, which is zero. Therefore, Equation (4.41) will become the same as Equation (4.14), representing the vibration velocity in the case of a circular scan, and from it the relevant DOF components can be derived.

Similarly, if the scan radius becomes zero, that leads to a conical scan, the two circles degenerating to a point coincident with the lens focus, and Equations (4.45) simplify to those of Equations (4.20) in Section 4.4. In fact, components in the outside-focus configuration will assume the same values of the ones in the inside-focus configuration: $R_{\omega\ IN} = R_{\omega\ OUT}$ , $I_{\omega\ IN} = I_{\omega\ OUT}$ , $R_{(\omega-\Omega)\ IN} = R_{(\omega-\Omega)\ OUT}$ , $I_{(\omega-\Omega)IN} = I_{(\omega-\Omega)OUT}$ , $R_{(\omega+\Omega)IN} = R_{(\omega+\Omega)OUT}$ , $I_{(\omega+\Omega)IN} = I_{(\omega+\Omega)OUT}$ , and then $V_{xR}$, $V_{xI}$, $V_{yR}$, $V_{yI}$, $V_{zR}$, $V_{zI}$ can be derived from Equations (4.20) while, if $R$ = 0, the remaining DOFs - $\Theta_{xR}$, $\Theta_{xI}$, $\Theta_{yR}$, $\Theta_{yI}$- will become meaningless.

In order to prove the validity of the mathematical derivation of the multiple DOFs hereby described tests were conducted using both the set-ups described in Figures 4.21 and 4.22. A lens moving between two positions ① and ② (see Figure 4.24) was emploied in order to make the laser beam perform two circle scans of the same scan radius, $R$. As in the previous experiments, the test specimen was the aluminium cube excited at 158 Hz. The scan speed was set at 10 Hz, the measurement direction 30°, that is the deflection angle of the lens, and the scan radius 8 mm in both the configuration (namely the outside-focus and the inside focus). Two vibration signals were then acquired and post-processed in order to recover the five DOFs by using Equations (4.45).

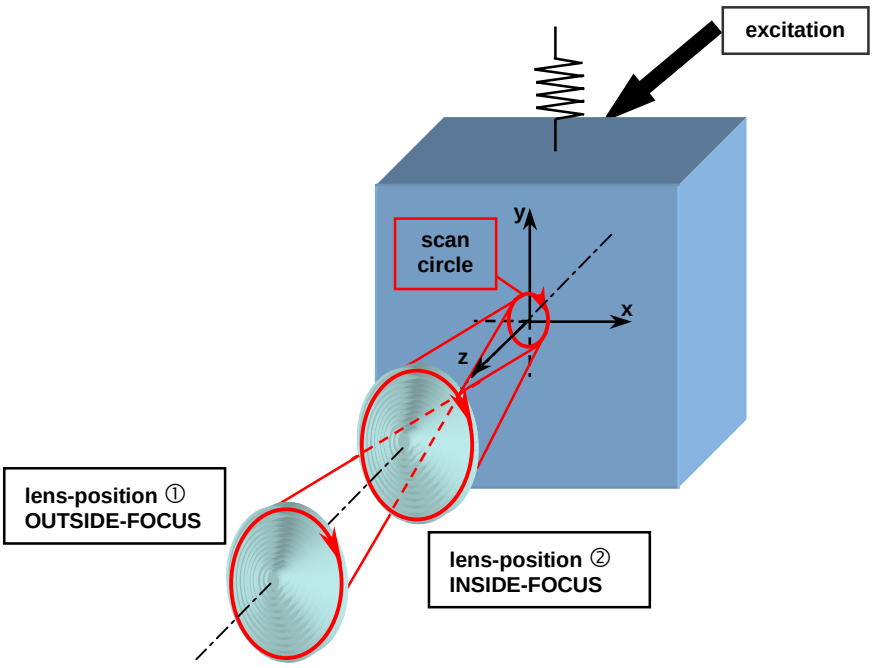


**Figure 4. 24** Conical-Circular scan set-up.

In order to check the reliability of the technique, single point measurements were performed with the LDV directed at three positions lying on the scan circle (see Figure 4.25) . Moreover, for each position, measurements were taken in two different directions, specifically at ± 45° with respect to the axis perpendicular to the tested surface. From these six point velocities, all the DOFs at point **O** (scan circle centre), can be derived and compared with ones obtained by the continuous technique (i.e. conical-circular scan), where only two acquisitions were required.

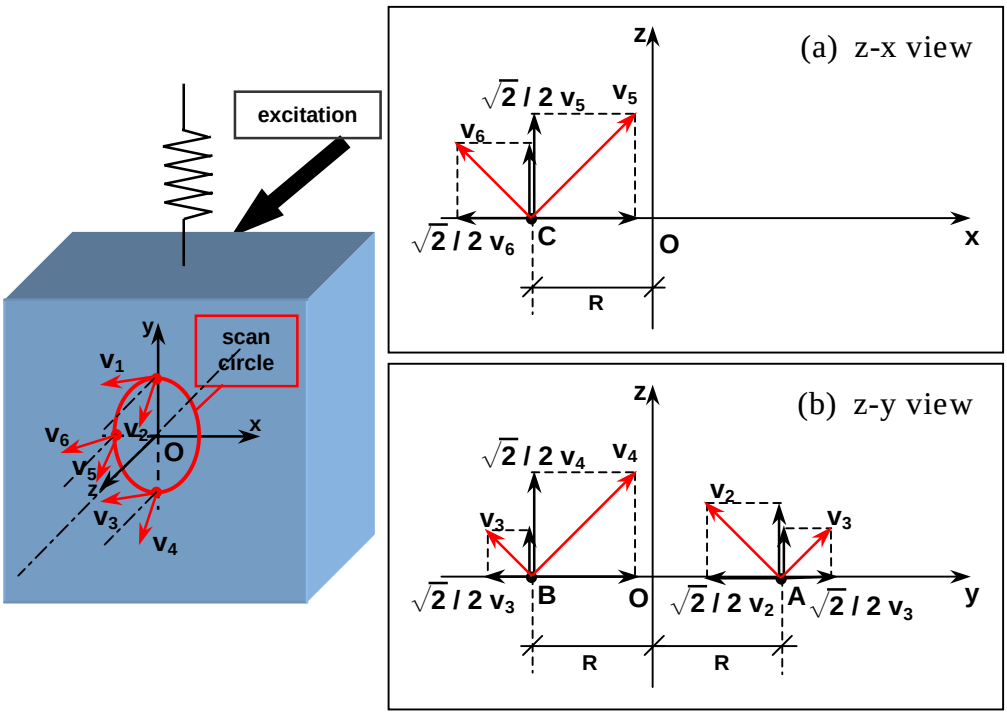


**Figure 4. 25** Single point measurements configuration.

Real and imaginary components of the required DOFs can be derived applying geometric considerations, which lead to the following formulae:

$$
\begin{aligned}
v_x &= \frac{\sqrt{2}}{2}(v_5 - v_6) \\
v_y &= \frac{\sqrt{2}}{2}(v_1 - v_2) \\
v_z &= \frac{v_z(A) + v_z(B)}{2} = \frac{\sqrt{2}}{4}(v_1 + v_2 + v_3 + v_4) \\
\theta_x &= \frac{v_z(A) - v_z(B)}{2R} = \frac{\sqrt{2}}{4R}(v_1 + v_2 - v_3 - v_4) \\
\theta_y &= \frac{v_z(0) - v_z(C)}{R} = \frac{v_z - v_z(C)}{R} = \frac{1}{R}\left[\frac{\sqrt{2}}{4}(v_1 + v_2 + v_3 + v_4) - \frac{\sqrt{2}}{2}(v_5 + v_6)\right] = \\
&= \frac{\sqrt{2}}{4R}(v_1 + v_2 + v_3 + v_4 - 2v_5 - 2v_6)
\end{aligned}
\qquad \textbf{(4. 46)}
$$

Table 4.9 reports the values of DOFs recovered with the different techniques of single points and continuous conical-circular scan, respectively. The third column of Table 4.9 contains the value of discrepancy between the results obtained by performing steady measurements at different points and the ones derived by using the conical-circular scanning method. The vibration responses found out at each DOFs by employing the steady technique were considered the valid ones and they were taken as reference to which the vibration responses determined by the continuous scanning method were compared. The discrepancies give in the third column of Table 4.9 were, then, calculated by subtracting the two corresponding vibration responses at each DOF and dividing the difference by the maximum vibration response which was the translation in the *z*-direction (4.8478 mm). In order to make comparable discrepancies between steady and continuous techniques associated to rotational and translational DOFs the first one must be multiplied by the scan radius (8 mm).

| | **STEADY MEASUREMENT** | **SCANNING MEASUREMENT** | **ERROR** (%) |
|---|---|---|---|
| Translation in x (mag [mm/s]) | 3.173 | 2.5211 | 13.44 |
| Translation in y (mag [mm/s]) | 1.2573 | 1.9995 | 15.31 |
| Translation in z (mag [mm/s]) | 4.8478 | 5.3283 | 9.91 |
| Rotation about x (mag [rad/s]) | 0.0093 | 0.0508 | 6.84 |
| Rotation about y (mag [rad/s]) | 0.9416 | 0.7995 | 23.44 |

**Table 4. 9** MDOF measurement at point O via conical-circular scan at 10Hz-Magnitude of the vibrational response.

The greatest difference in the translation velocity was found in the *y*-direction (0.7422 mm/s) to which was associated a percentage error of about 15 % (normalised with respect to the *z*-translation velocity). The largest discrepancy in rotation DOF was in *y*-direction (0.1421 rad/s) leading to a rotational discrepancy of 1.1368 mm/s (now given in the same unit of the translational

DOF). The percentage error is now, then, much higher, specifically of about 23 %.

Concerning the phase the maximum difference was 1.49° (translation in *y*-direction) and all the phase responses and associated errors are reported in Table 4.10.

| | **STEADY MEASUREMENT** | **SCANNING MEASUREMENT** | **ERROR** (º) |
|---|---|---|---|
| Translation in x (phase º) | 53. 87 | 55.29 | 1.42 |
| Translation in y (phase º) | -128.88 | -130.37 | 1.49 |
| Translation in z (phase º) | -125.77 | -124.81 | 0.96 |
| Rotation about x (phase º) | -119.92 | -121.13 | 1.21 |
| Rotation about y (phase º) | 53.81 | 54.44 | 0.63 |

**Table 4. 10** MDOF measurement at point O via conical-circular scan at 10Hz - Phase of the vibrational response.

Errors can be due to the difficulties related to the setting of the single point measurements. In fact, positioning the laser beam accurately in the different directions required a major effort and it was difficult to guarantee that the laser line-of-sight formed with the test specimen surface angles was exactly 45°.

From Table 4.10 it is possible to observe that the phase assumed approximately the same value for each DOF, or it is shifted by 180°. This happens for the special, but common, case where the mode shape is real, so that imaginary and real components of $V_x$, $V_y$, $V_z$, $\Theta_x$ and $\Theta_y$ are all in the same ratio. Therefore, the (temporal) phase angle, which is the inverse of the tangent of this ratio, will be such that motion in all DOFs is in phase (or 180° out of phase).

## *4.6. Calibration of Continuous Scanning Techniques*

### *4.6.1 Mirror Calibration*

As emphasised in Section 4.1, a mirror calibration must be performed a priori in order to derive the delay associated with these mechanical devices, together with the rotors which drive them. In practice the delay is due to the global inertia of both the mirror and the rotor.

In fact, considering the horizontal mirror, which moves the beam in the x-direction, it is possible to show that, the sinewave, $x(t)$, produced by the software piloting the electronic card, whose output drives the mirror is

$$x(t) = V\sin(2\pi\Omega t) \qquad \textbf{(4. 47)}$$

where $V$ is the amplitude in volts and $\Omega$ is the scan frequency in Hz. Also if the laser mirror is fed by $x(t)$, the real position of the laser spot on the structure depend on several others parameters associated to the chain of devices presents in between the output of the electronic board and the scanning system. Following each step of the process through which the driving signal passes, the spot position can be related to $x(t)$. The analog output of the electronic board, $x(t)$, is sent to the laser scanner placed in the laser head via an interface or Analog-Digital converter which generates discrete data. The galvanometer optical scanners are then driven by discrete voltages, which control the angular movement of the mirror, $\alpha(t)$:

$$\alpha(t) = AV\sin(2\pi\Omega t + \varphi) \qquad \textbf{(4. 48)}$$

In this relationship $A$ represents the static sensitivity of the scanners and it is expressed in (rad/V), being a ratio between mirror angle and driving signal,

while φ is the angular delay due to the scanner system inertia. It is worth noting that if the interface produces discrete data, the mirrors are moving following a typical 'staircase', but this stepwise characteristic is heavily filtered out by the mirror inertia for the amplitudes and scan speeds commonly used. The angular position of the mirror may be then related to the scanning plane coordinate which defines the laser spot position on the target specimen by a geometrical parameter, *B*, which depends on the mirrors' position in the laser head and on the optics characteristics, as the separation distance of the two mirrors surface in the direction of the laser beam. The laser spot coordinate will be:

$$x(t) = ABV\sin(2\pi\Omega t + \varphi) \qquad \textbf{(4. 49)}$$

where $B$ is in mm / rad.

In Section 4.2, an ideal situation was assumed where the mirrors were not subjected to any delay and the position of the laser spot was supposed to be, simply:

$$x_{IDEAL}(t) = l\sin(2\pi\Omega t) \qquad \textbf{(4. 50)}$$

$l$ being the scan length. In order to make Equations (4.49) and (4.50) agree, and to render Equation (4.50) general the parameters $A$, $B$ and φ must be determined a priori by calibration. Knowing the applied voltage $V$, the length of the scan on the structure can be derived; although the amplitude calibration is not important since a straight-line scan length is easily determined approximately simply by using a scale on the scanned surface (idem for the radius on a circular scan), see reference [36] and [40].

Instead what is necessary to determine exactly is the angular delay, which defines the true position of the laser spot along the scan line or circle. Setting φ at the value derived by calibration the start point of the continuous scan is the point (called start point) marked in Figures 4.6, 4.9, 4.11, 4.20 for the different

situations (linear scan, circular scan, conical scan, conical - circular scan respectively). It is possible to demonstrate that the mirror delay depends only on the scan velocity because, considering the mirror together with its mounting rotor as a rigid body with moment of inertia with respect to the rotation axis *J*, the kinetic energy with which it reacts, when a rotational motion is imposed on it, is:

$$T = \frac{1}{2} J\Omega^2 \qquad \textbf{(4. 51)}$$

where Ω is the imposed scan speed. Then, a calibration process can be performed varying only the scan speed, i.e. the rotation velocity of the mirror. For each frequency a phase or time delay can be determined. This quantity will be recovered by adjusting the relative phase of the LDV output time history and the mirror signal, in order to make them perfectly in phase to each other, see Figure 4.26.

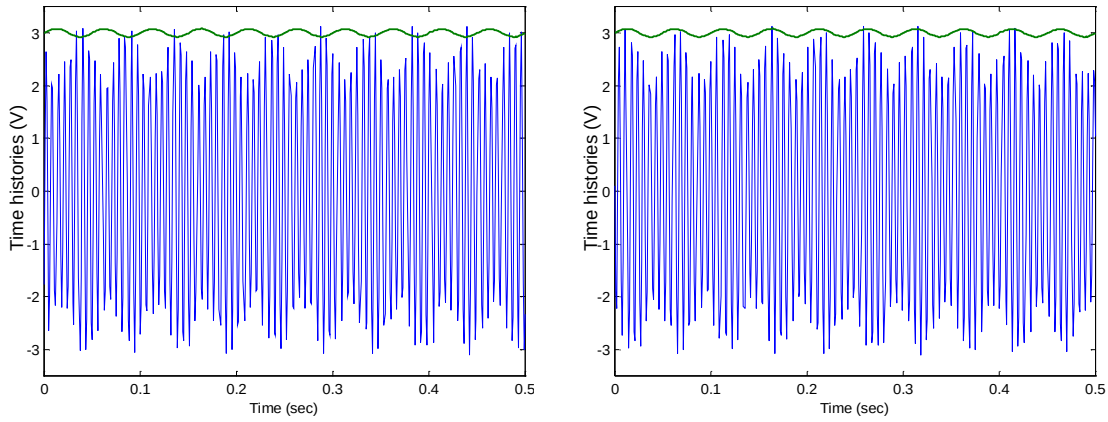


**Figure 4. 26** LDV output signal before and after applying the mirror delay correction.

It can be noticed that in the second plot of Figure 4.26 the LDV output and the sinewave indicating the laser spot position are in phase with each other because the mirror delay correction has been performed. When this condition is reached, both the real and the imaginary parts of the upper and lower sidebands of the

LDV output, obtained by a line scan measurement, are equal but opposite in sign, as was highlighted in Section 4.2. Following this recurrence, the calibration can be preformed on the basis of a line scan test.

It is preferable to calibrate using a test piece, such as the cube used for the demonstrations described in the previous sections, for which a pure rocking mode can be established. The test set-up was the same as the one shown in Figure 4.5 and the structure excitation was again at 158 Hz. To calibrate the *x*-mirror, a small horizontal straight line scan of length of 18 mm was performed by driving the *x*-scanning system with a sinewave of suitable amplitude and of frequency set at different values (0.5, 0.7, 1, 1.5, 2, 3, 4, 5, 10, 15, 20, 25, 30 Hz). The LDV acquisition was triggered with the mirror signal, i.e. when the scanning sinewave passes through zero with positive slope and, therefore, if there was no delay in the mirror, the laser spot position should follow perfectly the driving signal and the LDV time history should be completely in phase with the mirror signal, as shown in the right-hand plot in Figure 4.26. Then, by performing a curve-fit of the LDV output, the derived sidebands' complex components must realise the recurrence above mentioned. In practice, this recurrence does not happen at any scan speed imposed to the mirror driving the laser beam, because a delay exists also at low frequencies. The LDV output is then shifted by a phase angle, $\alpha$, until its complex sideband components are equal and opposite in sign: this angle represents the mirror delay. From this, the time delay is simply deducible by dividing it by $(360\ \Omega)$, $\Omega$ being the scan frequency.

The *x*-mirror delay values are listed in Table 4.11 and plotted against the scan speed in Figure 4.27.

| SCAN FREQUENCY (Hz) | PHASE ANGLE (°) | TIME DELAY (sec) |
|---|---|---|
| 0.5 | 2.28 | $1.2667\ 10^{-2}$ |
| 1 | 2.77 | $7.6944\ 10^{-3}$ |
| 2 | 3.95 | $5.4861\ 10^{-3}$ |
| 3 | 5.14 | $4.7593\ 10^{-3}$ |
| 4 | 4.32 | $3.0000\ 10^{-3}$ |
| 5 | 6.33 | $3.5167\ 10^{-3}$ |
| 10 | 7.52 | $2.0889\ 10^{-3}$ |
| 15 | 10.83 | $2.0056\ 10^{-3}$ |
| 20 | 12.8 | $1.7778\ 10^{-3}$ |
| 25 | 14.32 | $1.5911\ 10^{-3}$ |
| 30 | 16.81 | $1.5565\ 10^{-3}$ |

**Table 4. 11** Phase angles and relative time shifts associated to the *x*-mirror delay.

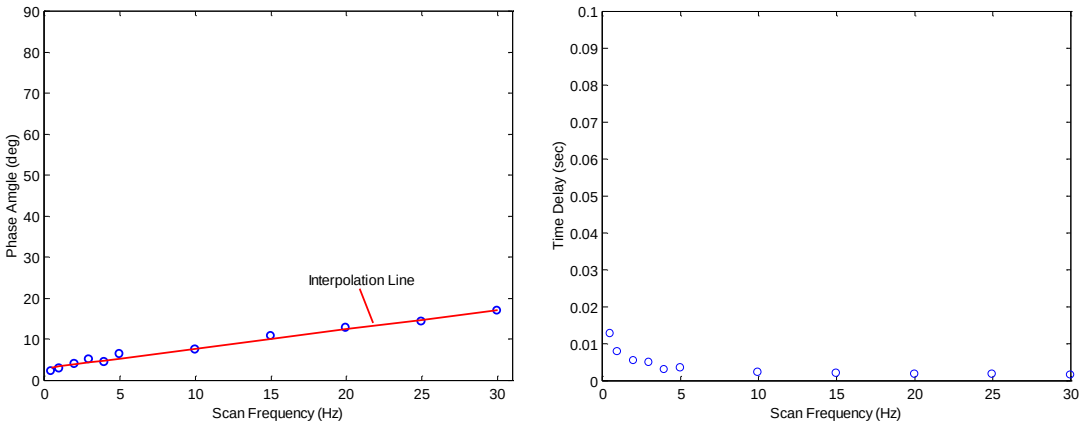


**Figure 4. 27** Phase angles and relative time shifts plotted against the scan frequency.

The interpolation line shown in the first plot of Figure 4.27 is determined by a least-squares method; if the line is

$$y = a + b\,\Omega \qquad \textbf{(4. 52)}$$

the line coefficients are

$$a = \frac{\sum \Omega_i^2 \sum \alpha_i - \sum \Omega_i \alpha_i \sum \Omega_i}{n\sum \Omega_i^2 - \left(\sum \Omega_i\right)^2} \qquad \text{and} \qquad b = \frac{n\sum \Omega_i \alpha_i - \sum \Omega_i \sum \alpha_i}{n\sum \Omega_i^2 - \left(\sum \Omega_i\right)^2} \qquad \textbf{(4. 53)}$$

where Ω is the scan frequency vector and α the phase angle vector consisting of *n* elements (which are 11, see Table 4.11). The same procedure was conducted to calibrate the *y*-mirror and Table 4.12 and Figure 4.28 show its behaviour.

| **SCAN FREQUENCY** (Hz) | **PHASE ANGLE** (°) | **TIME DELAY** (sec) |
|---|---|---|
| 0.5 | 2.68 | $1.4889\ 10^{-2}$ |
| 1 | 4.77 | $1.3250\ 10^{-2}$ |
| 2 | 5.95 | $8.2639\ 10^{-3}$ |
| 3 | 7.14 | $6.6111\ 10^{-3}$ |
| 4 | 4.32 | $3.0000\ 10^{-3}$ |
| 5 | 6.50 | $3.6111\ 10^{-3}$ |
| 10 | 5.42 | $1.5056\ 10^{-3}$ |
| 15 | 8.83 | $1.6352\ 10^{-3}$ |
| 20 | 9.05 | $1.2569\ 10^{-3}$ |
| 25 | 9.92 | $1.1022\ 10^{-3}$ |
| 30 | 12.49 | $1.1565\ 10^{-3}$ |

**Table 4. 12** Phase angles and relative time shifts associated to the *y*-mirror delay.

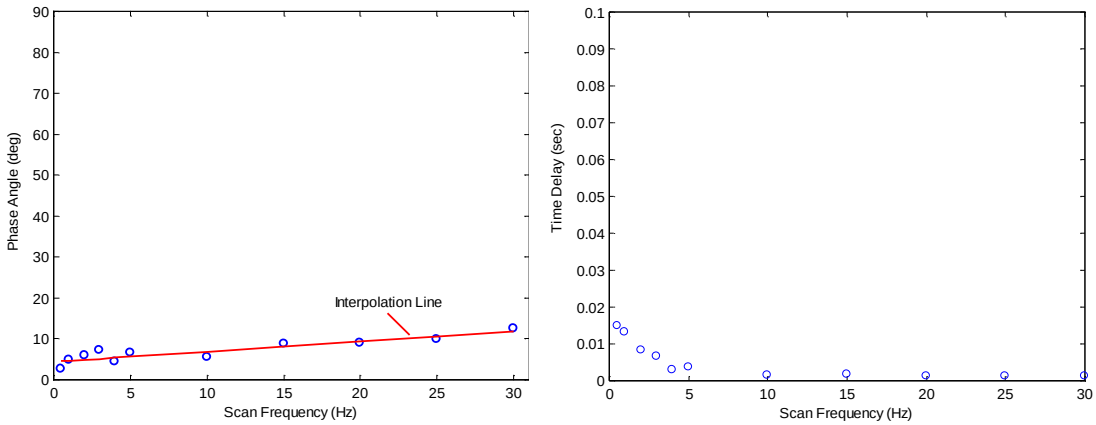


**Figure 4. 28** Phase angles and relative time shifts plotted against the scan frequency.

Comparing Table 4.11 and Table 4.12, it is possible to deduce that the *x*-mirror is more sensitive to the scan speed increase: the delay increases faster, i.e. the

slope of the line interpolating the angle values is greater by comparison with the one associated with the *y*-mirror calibration values, see Figure 4.29.

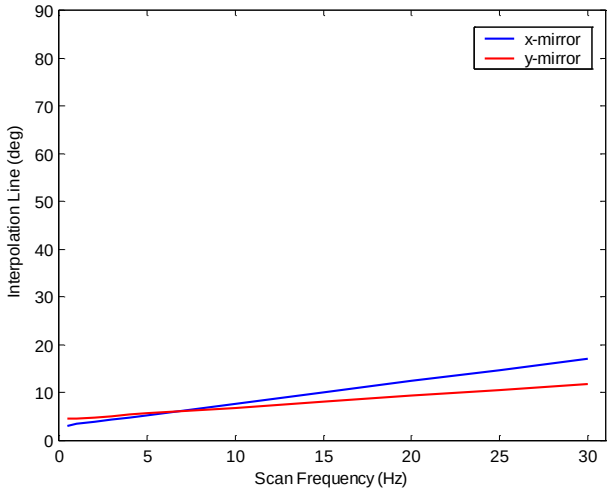


**Figure 4. 29** Comparison of phase angles associated to the delay of both the mirrors.

The discrepancy between the two mirrors is unexpected, since the mirrors are ostensibly identical and so their inertias should be alike. This difference can be explained taking into account uncertainty sources connected to the hardware systems as non-linearity of the galvanometer device and the position sensor which constitutes the feedback control system, optical and mechanical inaccuracy (i.e. mirrors misalignment) and electronic problems (such as errors in D / A conversion).

In addition to the previous general calibration, additional ones must be conducted for each scanning technique; some can be avoided, as the line scan length derivation, since they can be easily determined by direct measurement, but some are indispensable.

### *4.6.2 Line-Scan Calibration*

In spite of what has been said above, however, it is difficult to measure the scan line length to, say, 1% by this means. The angle of vibration can then be derived

from two non-scanning point measurements, and the effective line length derived by using Equation (4.6) on a line-scan measurement. Assuming linearity, i.e. that the parameters $A$ and $B$ are constant, see Equations (4.49) and (4.50), the scan length / drive voltage ratio ($l/V$ ) can be used to produce any scan line length desired.

In order to find the parametric relationship between line scan length $l$ and voltage $V$, sent to the mirror, a simple calibration was done, by setting different voltage amplitudes for the sinewave driving the $x$-mirror and directly measuring, via a rule, the length of the line scanned on the surface. Naturally, this relationship will depend on the distance between the laser head and the scanned surface and such a type of calibration must be repeated each time the object is moved. But, by transforming the relationship in terms of angles instead of line length the generality can be restored. In the case of a target surface set at 2667 mm ($D$) away from the laser head, the amplitude in Volts of the sinewave sent to the $x$-mirror and the scan length measured are given in Table 4.13:

| VOLTAGES | LINE SCAN LENGTH (mm) |
|---|---|
| 0.03 | 13 |
| 0.05 | 20 |
| 0.07 | 27 |
| 0.09 | 34 |
| 0.11 | 41 |
| 0.15 | 55 |
| 0.19 | 69 |
| 0.23 | 83 |
| 0.27 | 97 |

**Table 4. 13** Line scan lengths and correspondent voltages feeding the mirror.

A linear relationship can fit these values precisely

$$l = 350V + 2.5 \qquad \textbf{(4. 54)}$$

where $l$ is expressed in mm. Since $l$ can be written in terms of the angle scanned by the laser beam, $\alpha$:

$$l = 2D\tan\alpha = 2D\alpha \qquad \textbf{(4. 55)}$$

$\alpha$ being small, due to the fact that $D >> l$, the more general relationship will become:

$$\alpha = \frac{350}{2D}V + \frac{2.5}{2D} = 3.758V + 0.026 \qquad \textbf{(4. 56)}$$

where $\alpha$ is expressed in degrees.

Equation (4.56) was found to be valid also for the *y*-mirror, and consequently for circular scan.

As already stated, this calibration method must be repeated every time the scanning LDV settings (specifically, the distance from the object) are changed. However, the procedure is general and it is suitable for all the scanning laser systems available in commerce.

### *4.6.3 Circular-Scan Calibration*

As for a line scan, approximate scan circles can be arrived at by eye, adjusting the *x*- and *y*-axis drive voltages and relative phase to suit. For best accuracy, however, equal scan amplitudes should be set for both mirrors using the straight-line scan procedure.

The phase shift in the mirror drive may not be exactly the same for both mirrors. One method of countering this is to set the relative phase between *x* and *y* mirror drives to produce a single diagonal line. The *y*-axis drive voltage is then shifted by exactly 90° to achieve a circle.

It is assumed in the analysis carried out above that the direction of scan is clockwise on the surface, viewed from the laser head. This can be conveniently

checked with a circular scan frequency temporarily reduced to a low value (i.e. 2 Hz).

### *4.6.4 Conical-Scan Calibration*

For a conical scan, with the LDV scanning in a circle near the periphery of a short-focus lens, the circle should be set up as described for the circular scan calibration and the deviation angle of the lens will require in situ calibration. This may be achieved by comparing the vibration of a surface moving parallel to the scan axis as measured by the conical scan and by a fixed-point, non-scanning LDV.

If $V_z$is the vibration velocity amplitude measured by a static beam in a direction perpendicular to the vibrating surface, and $V_C$ is the amplitude measured by conical scanning, the geometric configuration shown in Figure 4.30 allows the angle Θ to be deduced.

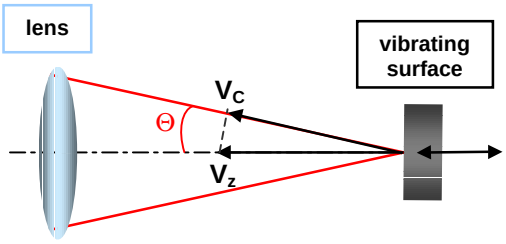


**Figure 4. 30** Conical scan configuration.

The scan semi-angle Θ is:

$$\Theta = \cos^{-1}\left(\frac{V_C}{V_z}\right) \qquad \textbf{(4. 57)}$$

and this angle depends on the lens characteristic (i.e., focal length) and the set-up parameters (i.e. distance between lens and object).

## *4.7. Conclusions*

Continuous scanning techniques for determining MDOF vibrational responses have been described mathematically, simulated numerically and tested experimentally on a simple laboratory specimen (an aluminum cube made for the purpose) in this chapter.

The continuous scanning techniques have been applied the so-called 'short scan' methods, where the laser is made to scan on different paths as (i) lines, (ii) circles, (iii) cones. Different MDOF vibration measurements can, then, be performed using the suitable type of scan:

1. Linear Scan for one translational and one angular DOFs recovery;
2. Circular Scan for one translational and two angular DOFs recovery;
3. Conical Scan for three translational DOFs recovery;
4. Conical-Circular Scan for three translational and two angular DOFs recovery.

The accuracy of the CSLDV techniques have been studied by comparing the experimental results with ones obtained by single-point measurements. The greatest discrepancies found between the results from the two techniques were around 10%. For a detailed comparison analysis, see Section 4.2 (short line scans), Section 4.3 (small circular scans), Section 4.4 (conical scans) and Section 4.5 (conical-circular scans).

Problems related to the continuous scanning methods employed in the short scan fashion were treated in detail, by giving the most emphasis to the mirror scanning system calibration. Some practical applications on industrial case study will be examined with particular detail in Section 7.2 in Chapter 7.

# Chapter 5 Continuous Scanning Technique Applied to Operational Deflection Shape Measurements

## *5.1. Introduction*

This chapter investigates continuous scanning techniques when scans are performed over long straight-lines, large circles or whole 2D surfaces (see Table 4.1, Chapter 4, for the schematic summary). In order to follow the development of the chapter, a map of its structure can be helpful as a breakdown of the treated topics.

First the linear scan is addressed and the analysis is split as shown in Table 5.1. The second topic is the circular scan: its treatment breakdown is illustrated in Table 5.2. Subsequently, in Section 5.5 the two-dimensional scan (area scan), whose topics are summarised in Table 5.3, is described. The last major subject is the Modal Analysis on FRF data acquired by using the continuous area scanning technique and its breakdown is depicted in Table 5.4.

<table>
<tr><td colspan="5">UNIFORM STRAIGHT-LINE SCAN</td></tr>
<tr><td colspan="3">Numerical simulation</td><td colspan="2">Experimental validation</td></tr>
<tr><td colspan="5">SINUSOIDAL STRAIGHT-LINE SCAN</td></tr>
<tr><td rowspan="2">Mathematical investigation</td><td colspan="3">Numerical simulation</td><td rowspan="2">Experimental validation</td><td rowspan="2">Experimental validation using the point-by-point technique</td></tr>
<tr><td>Real vibration response</td><td>Imaginary vibration response</td><td>Mirror delay effect</td></tr>
</table>

**Table 5. 1** Linear scan topics.

| Mathematical investigation | |
|---|---|
| Numerical simulation | |
| On a rectangular plate | On a disc |
| Experimental investigation | |

**Table 5. 2** Circular scan topics.

<table>
<tr><td colspan="6">AREA SCAN ON A RECTANGULAR SURFACE</td></tr>
<tr><td colspan="6">Two-dimensional uniform scan</td></tr>
<tr><td colspan="6">Sinusoidal parallel straight-line scans</td></tr>
<tr><td colspan="6">Two-dimensional sinusoidal scan</td></tr>
<tr><td rowspan="2">Mathematical investigation</td><td colspan="3">Numerical simulation</td><td colspan="2">Experimental validation</td></tr>
<tr><td>Real vibration response</td><td>Imaginary vibration response</td><td>Mirror delay effect</td><td>Plate's 4$^{th}$ resonance</td><td>Plate's 5$^{th}$ resonance</td></tr>
<tr><td colspan="6">AREA SCAN ON A CIRCULAR SURFACE</td></tr>
<tr><td colspan="2">Mathematical investigation</td><td colspan="2">Numerical simulation</td><td colspan="2">Experimental validation</td></tr>
</table>

**Table 5. 3** Area scan topics.

| MODAL ANALYSIS ON CSLDV FRFs DATA |
| --- |
| Experimental modal analysis on the GARTEUR structure |
| Concluding remarks |

**Table 5. 4** Modal analysis on CSLDV FRFs data.

## *5.2. Measurement Methodology*

A number of new ODS measurement techniques are described here, applying the LDV scanned continuously over the surface of a sinusoidally-excited structure. Under these conditions, the LDV output is an amplitude-modulated sinewave from which the ODS, defined along the scan pattern, can be derived. If the scan speed is uniform, the structure's deflection shape can be directly recovered by demodulating the LDV output time history. Actually, in this case, the ODS is the envelope of the modulated LDV output signal. Otherwise, if the laser beam is scanning sinusoidally, the LDV output spectrum can be analysed in the frequency domain where it is represented by spectral lines centered on the excitation frequency and spaced at multiple of the scan frequency. It is worth noting that the number of terms comprising the LDV output spectrum will be limited only if the ODS is smooth, i.e. if no discontinuities occur within the vibration pattern where the laser is scanning. The sideband amplitudes give a series of coefficients for the mode shape defined along the scan path: Fourier coefficients for a circular scan or, via a simple transform, polynomial coefficients for a sinusoidal straight line or area scan.

Demodulation techniques will be addressed in this chapter for line and area scans at uniform speed, obtained by driving one or both at the scanning mirrors respectively, by triangular waveforms. Frequency-domain techniques described here are straight-line and circular scans, in which the scanning mirrors, again one or both of them, are fed with sinewaves. Applications of circular scans to the measurement of vibration of rotating discs are included. The use of line scan theory can then be widened to recover of two-dimensional ODSs that can be

produced either from sets of straight-line scans or by performing a continuous two-dimensional sine scan.
Previous works done in the CSLDV technique can be found in literature, see references [16], [41] and [42] for straight-line scanning techniques. As concerning 2-dimensional ODS measurement previous developed works are described in references [15] and [17]. [39]. For modal analysis on FRF data measured by CSLDV see references [39] and [19].

All the continuous scanning techniques employed in ODS recovering involve sinusoidal excitation of the structure: experimental structures are excited by sinusoidal input forcing so that the response at any point, measured at any direction, is also sinusoidal at the same frequency, assuming the structure to be effectively linear. The response, in general, is not in-phase with the force and it does not necessarily have a uniform phase across the scan.
By directly applying these techniques, ODSs can be determined, these being forced vibration patterns of the structure and not natural or “normal” mode shapes. In fact, ODSs have contributions from more than one natural mode, each with a different mode shape and phase-shift between the motions in all the measurement locations (if the mode is real, all the points are in phase with each other or 180° out of phase). A perfectly real ODS is normally produced on undamped structures, however, in the case of damped structures, it is possible to generate a real ODS if a multiple-input normal mode test is made. However, in practice, lightly-damped structures, vibrating at a frequency close to the natural frequency, assume nearly real ODSs which are normally the same as the undamped natural mode shapes. In other cases, particularly if there are close natural frequencies, or with heavily-damped structures, an ODS may be markedly complex. If frequency responses are available, modal analysis may be applied, a process which eliminates the contributions from extraneous modes, extracting the natural mode shapes.

## *5.3. Analysis of a Linear Scan*

### *5.3.1 Introduction*

This technique involves a one-dimensional scan along a line that can be swept by the laser moving at a uniform speed or sinusoidally-varying. The first option is the so-called demodulation method which is straightforward to apply since the ODS along the line is directly derived by demodulating the LDV output in the time domain. The second option is to work in the frequency domain and employs a sinusoidal linear scan in order to avoid the discontinuities at the end of each scan that otherwise occur whenever the scan direction reverses. In fact, even if the scan speed is constant along the scan line, when the laser beam changes direction it suddenly passes from a positive velocity to a negative one, causing a discontinuity. In contrast, if the scan is sinusoidal, the velocity of the laser beam reduces smoothly to zero at the ends of the scan line. This arrangement allows it to work with Fourier spectra of the LDV output. However, with the uniform rate scan, the LDV signal in the frequency domain does not contain any useful information.

### *5.3.2 Uniform straight-line scan*

#### *5.3.2.1 Numerical Simulation*

Firstly, the method applying the continuous scan at a uniform rate is studied mathematically and simulated in order to foresee how a simple structure will behave during vibration tests. An experimental case will be then analysed.

A simple specimen can be considered as a free-free beam undergoing a sinusoidal vibration at a frequency $\omega$, see Figure 5.1. The vibration, which is expressed here as velocity in the $z$-direction, perpendicular to the beam surface

nominally in the *x*, *y* plane, and measured at a point *x* along the scan line, will be:

$$v_z(x,t) = V_R(x)\cos\omega t + V_I(x)\sin\omega t \qquad \textbf{(5. 1)}$$

$V_R$ and $V_I$ being the real and imaginary components of the vibration, relating to some datum that is usually the input force.

If the laser beam is scanned continuously at a uniform rate, *v*, at each instant, *t*, the position of the laser spot along the scanned line, can be represented by the quantity $x = vt$, so that the vibration velocity can be considered as a function of time only.

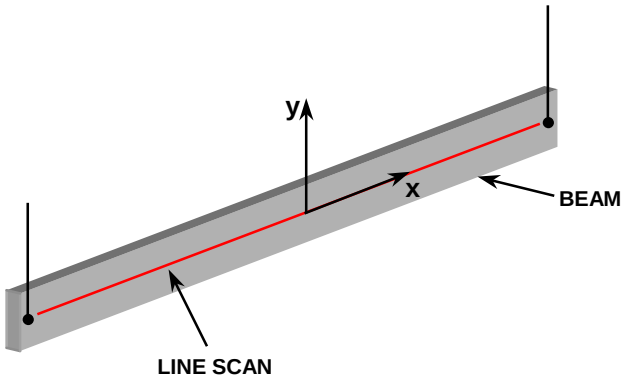


**Figure 5. 1** Laser linear scan on the beam.

Assuming that the beam is vibrating at the second natural frequency, the second mode shape can be simulated following the Timoshenko theory on simple beam transverse vibrations theory for free-ends conditions, [43]. The solution of the motion equation is:

$$V(x) = C_1(\cos kx + \cosh kx) + C_2(\sin kx + \sinh kx) \qquad \textbf{(5. 2)}$$

Applying the boundary conditions for the free-ends beam, assumed to have a unitary length of 1 m, constants *k* and the ratio $C_1 / C_2$ are derived as:

$$k = 7.853$$
$$\frac{C_1}{C_2} = -0.99922$$

The second bending mode shape is then described by Equation (5.2), by introducing the constant values on it and it is visualised along the length of the beam in Figure 5.2. Assuming that the mode is completely real, i.e. that $V_R(x) = V(x)$ and $V_I(x) = 0$, Equation (5.1) can be written as:

$$v_z(x,t) = V(x)\cos\omega t = \left[-0.99922\left(\cos 7.853x + \cosh 7.853x\right) + \sin 7.853x + \sinh 7.853x\right] \times\cos\left(2\pi\omega_2 t\right) \quad \textbf{(5. 3)}$$

where $\omega_2$ is the natural frequency, which can be derived from the simple beam theory.

$$\omega_2 = \frac{k_2^2}{2\pi}\sqrt{\frac{EI}{\rho A}} \quad \textbf{(5. 4)}$$

*EI* being the flexural rigidity of the beam, *A* its cross-section area, and ρ the mass density of the material. Considering a beam of cross-section 0.005×0.05 m, with the larger dimension in *y*-direction, and made of steel, the flexural rigidity will be 114.58 $Nm^2$ and the mass density 7810 $kg/m^2$. The natural frequency can therefore be calculated: $\omega_2$ = 472.43 Hz.

The beam position, *x*, depends on time, *t*, according to the following relationship:

$$x = vt = 2l\Omega t \quad \textbf{(5. 5)}$$

where Ω is the scan frequency and *l* the beam length, i.e. within a complete scan period the beam will be swept twice forward and backward. Substituting

Equation (5.5) in Equation (5.3), the vibration velocity can be expressed in function of time only:

$$v_z(t) = \{-0.99922[\cos(2 \cdot 7.853\Omega t) + \cosh(2 \cdot 7.853\Omega t)] + \sin(2 \cdot 7.853\Omega t) + \sinh(2 \cdot 7.853\Omega t)\} \times \cos f_2 t \quad \textbf{(5. 6)}$$

where the beam length is normalised to 1.

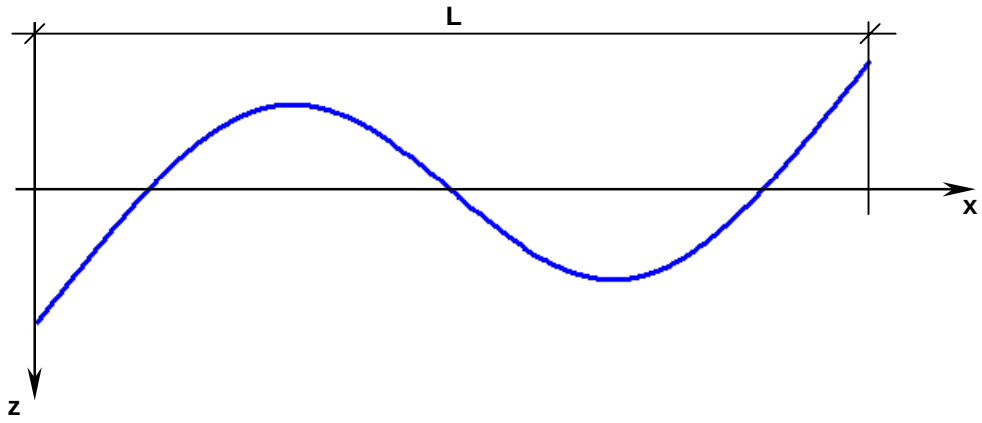


**Figure 5. 2** Second mode deflection shape.

Deriving $v_z$ from Equation (5.3), with $\omega_2$ = 472.43 Hz, and assuming the laser beam to scan at a frequency, Ω, of 0.5 Hz, a time signal is found, and this is the signal at the output of the LDV whose laser beam is scanning along the length of the beam. The vibration time vector is shown in Figure 5.3, where the envelope modulation, i.e. the mode shape, is emphasised.

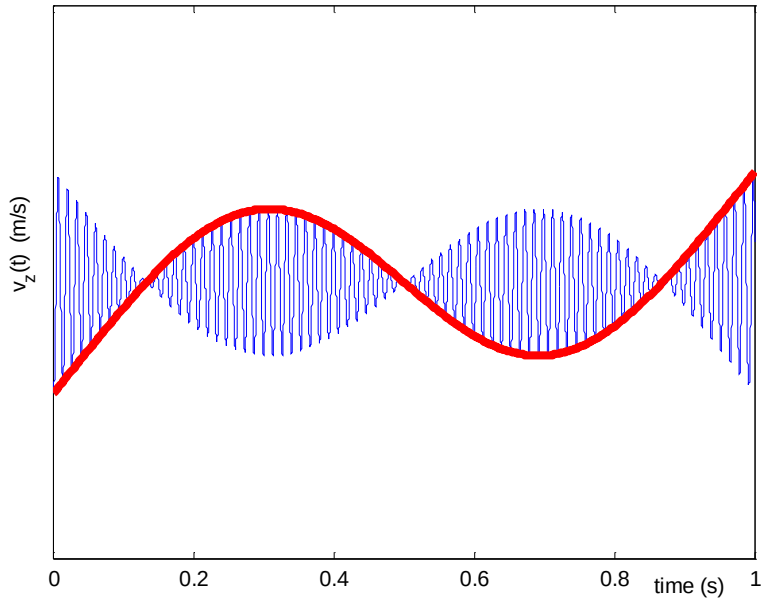


**Figure 5. 3** LDV output modulated by the bending mode shape of the beam (red line).

From the simulation it can be deduced that the ODS may be obtained by demodulating the SLDV output signal. A convenient method to perform the demodulation is simply to multiply the LDV output signal alternately by cosine and sine waves at the excitation frequency.

$$V_R(t)\cos^2\omega t + V_I(t)\sin\omega t\cos\omega t = \frac{1}{2}V_R(t) + \frac{1}{2}V_R(t)\cos 2\omega t + \frac{1}{2}V_I(t)\sin 2\omega t$$
$$V_R(t)\sin\omega t\cos\omega t + V_I(t)\sin^2\omega t = \frac{1}{2}V_I(t) + \frac{1}{2}V_R(t)\sin 2\omega t - \frac{1}{2}V_I(t)\cos 2\omega t \quad \textbf{(5. 7)}$$

If the scan speed is sufficiently slow, the signal components at the frequency 2ω can be removed by using a low-pass filter and the real and imaginary coefficients of the ODS can be derived in the time domain. The complex vibration pattern is then obtained with a resolution that depends on the sampling rate set during the acquisition and the scan rate. In practice, cross-talk interference may occur at the excitation frequency, so it is convenient to set the filter cut-off below this frequency value.

#### *5.3.2.2 Experimental Validation*

The uniform straight-line scanning technique can be applied experimentally by driving the horizontal scanning mirror with a triangular wave so that the laser beam will sweep along a straight line alternately in opposite directions with uniform speed.

Software for the control, data-acquisition and post processing has been developed in LabVIEW in order to have in output of it directly the ODS real and imaginary components. This routine is composed of several sub-routines, consisting of:

- a control program which generates the sinewave to be sent to the shaker for the structure's excitation. The excitation frequency and amplitude are the only parameters that are to be set (see Appendix A.1.1 for the control panel of the LabVIEW program driving the shaker).
- a control program used to produce the triangular wave driving the scanning mirror. The amplitude of the waveform should be set according to the length of the scan required and the scan frequency must be carefully chosen. It has to be sufficiently slow with respect to the excitation frequency (see Appendix A.1.2 for the control panel of the LabVIEW program driving the mirrors).
- an acquisition program where the sample rate chosen must follow the Nyquist theorem and the number of samples to acquire must be set so that the time length of the signal coincides exactly with the scan period. In this situation the mode shape will be swept twice (see Appendix A.1.3 for the control panel of the LabVIEW program used for the acquisition).
- a post-process program which performs the multiplication of the signal acquired by sine and cosine at the excitation frequency and applies a low pass filter whose threshold frequency must be fixed (see Appendix A.1.4 for the control panel of the LabVIEW program performing the demodulation procedure).

The last part of the program can also be performed using a `Matlab` routine, leaving to the `LabVIEW` software only the tasks of control and acquisition.

An experimental example has been carried out using as a measurement specimen a free-free steel beam, 32 mm wide, 10.05 mm thick and 1000 mm long. Measurements involved a half-scan, from the centre to one end, for modes 1, 3, and 5 found experimentally at 58 Hz, 311 Hz and 766 Hz, respectively.

For the first ODS recovery, the scan frequency was set at 0.5 Hz and, since the sample rate was chosen to be 1000 Hz, the LDV output signal was sampled with 2000 samples in order to have a time window as long as the scan period (i.e. 2 s). The time signal acquired is shown in Figure 5.4 while Figure 5.5 depicts the in-phase and out-of-phase ODS components referred to an initial datum, which is the phase of the vibration when its real component is maximum. Using this procedure the phase is adjusted to minimise the output to give the effectively zero imaginary part of the ODS and then, shifted by $\pi/2$, to give the real component. The low-pass-filter frequency was fixed at 20 Hz.

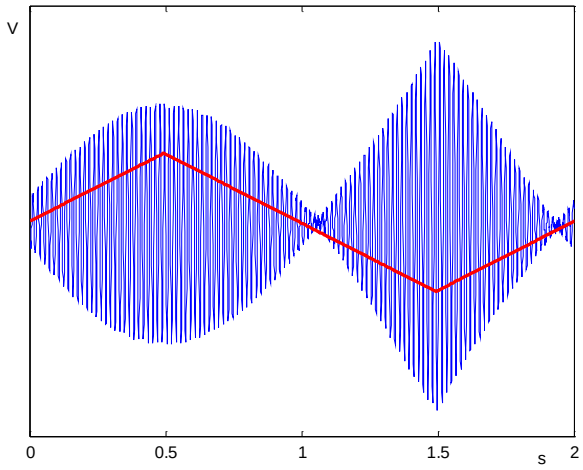


**Figure 5. 4** LDV output signal (blue) and mirror driving signal (red).

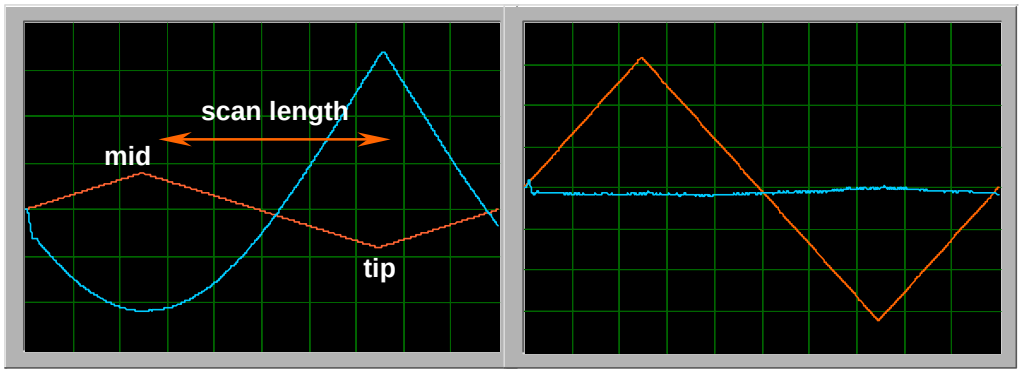


**Figure 5. 5** In-phase and out-of-phase components of the ODS at 58 Hz.

The same procedure was followed on the ODSs recovered at the higher frequencies of 311 and 766 Hz. In-phase and out-of-phase components are depicted in Figures 5.6 and 5.7.

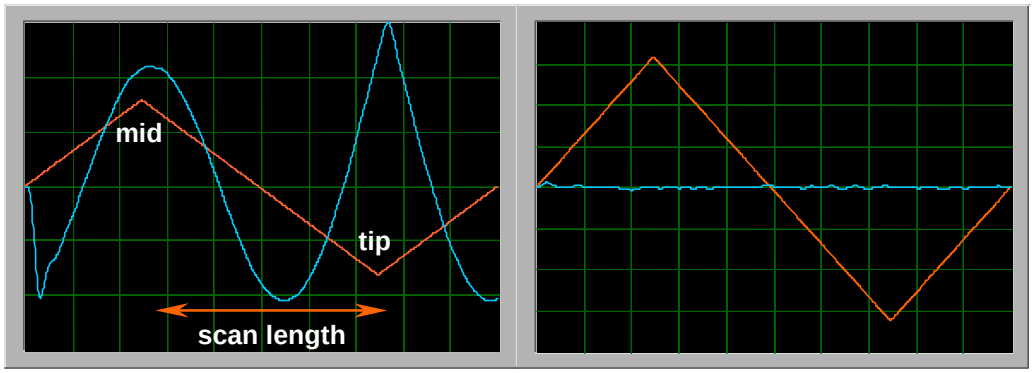


**Figure 5. 6** In-phase and out-of-phase components of the ODS at 311 Hz.

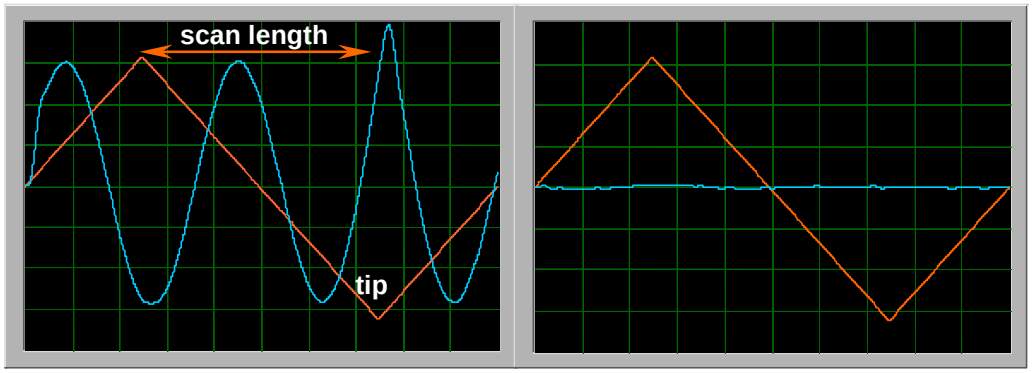


**Figure 5. 7** In-phase and out-of-phase components of the ODS at 766 Hz.

A comparison can be made between ODSs recovered by demodulation and analytical mode shapes derived by Timoshenko theory, whose frequencies are calculated from Equation (5.4), knowing the constant *k*. Table 5.5 summarises values of *k* and natural frequencies ω, for modes 1, 3 and 5 the factor $\sqrt{\frac{EI}{\rho A}}$ assuming the value of 16.08 $m^2/s$, with *E* and ρ the Young modulus and the mass density of steel.

| MODE NUMBER | $k$ ($m^{-1}$) | $\omega$ (Hz) | EXPERIMENTAL FREQUENCY (Hz) |
|---|---|---|---|
| 1 | 4.730 | 57.28 | 58.00 |
| 3 | 10.996 | 309.57 | 311.00 |
| 5 | 17.279 | 764.42 | 766.00 |

**Table 5. 5** Analytical natural frequencies.

Mode shapes are established by Equation (5.2) using for each mode the corresponding constant *k* and ratio $C_1/C_2$. The vibration velocity will then be:

$$\begin{aligned} v_z(x) &= \cos 4.73x + \cosh 4.73x - 0.9822\left(\sin 4.73x + \sinh 4.73x\right) \\ v_z(x) &= \cos 10.996x + \cosh 10.996x - 0.999966878\left(\sin 10.996x + \sinh 10.996x\right) \\ v_z(x) &= \cos 17.279x + \cosh 17.279x - 0.9999999329\left(\sin 17.279x + \sinh 17.279x\right) \end{aligned} \quad \textbf{(5. 8)}$$

which are for modes 1, 3 and 5 respectively. They are plotted together with the ODSs derived by demodulation at the same frequency as Figures 5.8, 5.9 and 5.10 show.

It can be noticed that nodal points are coincident for each mode and the relative ODSs since all of them are mostly real; on the other hand the amplitude is different because the ODS represent the absolute deformed shape dependent on the actual force applied. On the contrary, the mode shape is not dependent on the measurement system being derived from an FRF namely the structure vibration velocity divided by the input force.

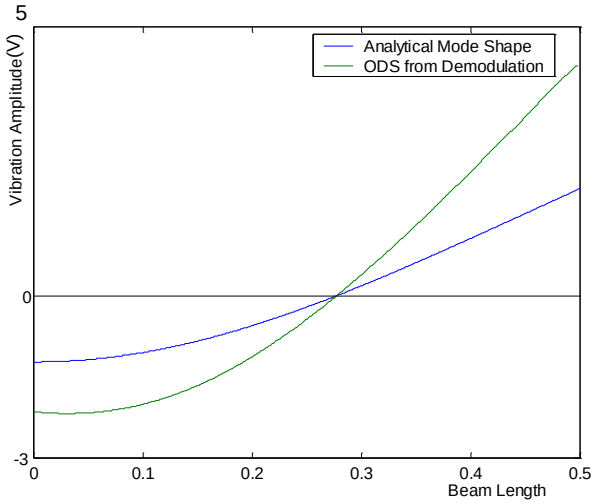


**Figure 5. 8** Analytical mode shape and ODS at 58 Hz.

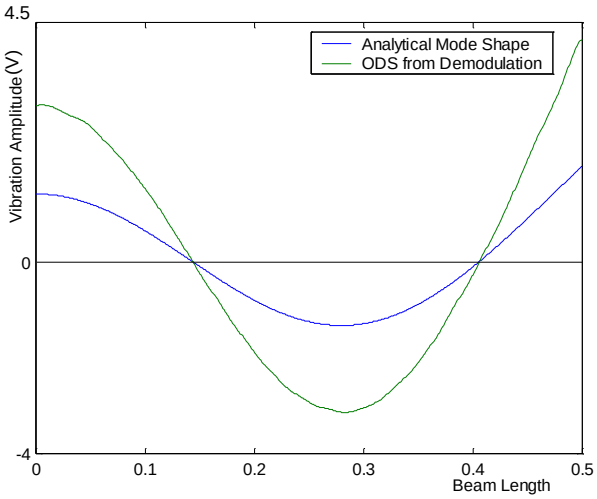


**Figure 5. 9** Analytical mode shape and ODS at 311 Hz.

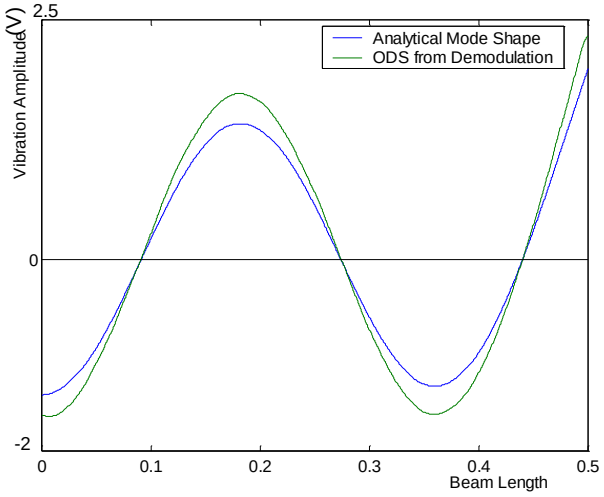


**Figure 5. 10** Analytical mode shape and ODS at 766 Hz.

A disadvantage of the uniform-rate straight-line scans is the instantaneous reversal in velocity at each end of the sweep that taxes the capability of the mirror drive electronics but, more importantly, provokes distortions near the scan end-points. There are no such sudden reversals with a sinusoidal straight-line scan but distortions can still occur, and may be particularly difficult to detect.

### *5.3.3 Sinusoidal straight-line scan*

#### *5.3.3.1 Mathematical Investigation*

The mode shape contributions $V_R(x)$ and $V_I(x)$ in Equation (5.1) can be expanded as spatial Fourier series, along the scan line. However, if the laser beam moves at uniform speed, difficulties can arise during the Fourier transform because of the discontinuities at the end of the scan, where the scan direction reverses. The end-point discontinuities can be avoided by employing a sinusoidal linear scan so that the scan velocity reduces smoothly to zero at these ends.

Assuming the complex operational deflection shape of the beam to be a smooth deflection pattern, it can be described as a polynomial which is, in the general case, of $p^{th}$ order. The vibration in the *z*-direction will consist then of two components, real and imaginary:

$$V_R(x) = \sum_{n=0}^{p} V_{Rn} x^n$$
$$V_I(x) = \sum_{n=0}^{p} V_{In} x^n \qquad \textbf{(5. 9)}$$

*x* being the normalised position vector representing all the points along the line. It goes from –1 to 1 considering the zero position the center of the line and

normalising at 2 its total length. $V_{Rn}$ is the $n^{th}$ polynomial coefficient describing the velocity pattern along the line. The vibration can be written following the principle of Equation (5.1):

$$v_z(x,t) = \sum_{n=0}^{p} V_{Rn} x^n \cos(\omega t) + \sum_{n=0}^{p} V_{In} x^n \sin(\omega t) \qquad \textbf{(5. 10)}$$

ω being the angular frequency of vibration. If the measurement points are continuously scanned sinusoidally at frequency Ω along the line of length normalised at 2, the instantaneous position of the laser spot over that line would be represented by the sinewave of equation:

$$x(t) = \cos(\Omega t) \qquad \textbf{(5. 11)}$$

Consequently, Equation (5.10) becomes:

$$v_z(t) = \sum_{n=0}^{p} V_{Rn} \cos^n(\Omega t)\cos(\omega t) + \sum_{n=0}^{p} V_{In} \cos^n(\Omega t)\sin(\omega t) \qquad \textbf{(5. 12)}$$

Expanding out trigonometrically, multiple terms arise at frequencies $(\omega \pm n\Omega)$, which are called upper and lower sidebands. Their value, in magnitude and phase, is the same for both the real and imaginary components, i.e. both the real and the imaginary Fourier spectra are symmetrical with respect to the central frequency or excitation one. The vibration can be expressed as:

$$v_z(t) = \sum_{n=0}^{p} A_{R(\pm n)} \cos[(\omega \pm n\Omega)t] + \sum_{n=0}^{p} A_{I(\pm n)} \sin[(\omega \pm n\Omega)t] \qquad \textbf{(5. 13)}$$

$A_{R0}$ being the spectrum component at the excitation frequency ω and $A_{R\pm1}$ the spectrum sidebands amplitude at $(\omega \pm \Omega)$, and so on up to $n = p$. Deriving

the sideband coefficients $A_{R,6n}$ from the polynomial coefficients $V_{Rn}$ it can be shown that $A_{R,-n} = A_{R,+n}$, see below. Then Equation (5.13) becomes:

$$v_z(t) = \sum_{n=0}^{p} A_{Rn} \cos[(\omega \pm n\Omega)t] + \sum_{n=0}^{p} A_{I\,n} \sin[(\omega \pm n\Omega)t] \qquad \textbf{(5. 14)}$$

After some manipulations the sideband coefficients, $A_R$ and $A_I$, can be seen as related to the corresponding polynomial coefficients, $V_R$ and $V_I$, by a simple matrix transform [T].

$$\begin{aligned} \{V_R\} &= [T]\{A_R\} \\ \{V_I\} &= [T]\{A_I\} \end{aligned} \qquad \textbf{(5. 15)}$$

where, for 15th order polynomials, [T] is:

$$[T] = \begin{bmatrix}
1 & 0 & -2 & 0 & 2 & 0 & -2 & 0 & 2 & 0 & -2 & 0 & 2 & 0 & -2 & 0 \\
0 & 2 & 0 & -6 & 0 & 10 & 0 & -14 & 0 & 18 & 0 & -22 & 0 & 26 & 0 & -30 \\
0 & 0 & 4 & 0 & -16 & 0 & 36 & 0 & -64 & 0 & 100 & 0 & -144 & 0 & 196 & 0 \\
0 & 0 & 0 & 8 & 0 & -40 & 0 & 112 & 0 & -240 & 0 & 440 & 0 & -728 & 0 & 1120 \\
0 & 0 & 0 & 0 & 16 & 0 & -96 & 0 & 320 & 0 & -800 & 0 & 1680 & 0 & -3136 & 0 \\
0 & 0 & 0 & 0 & 0 & 32 & 0 & -224 & 0 & 864 & 0 & -2464 & 0 & 5824 & 0 & -12096 \\
0 & 0 & 0 & 0 & 0 & 0 & 64 & 0 & -512 & 0 & 2240 & 0 & -7168 & 0 & 18816 & 0 \\
0 & 0 & 0 & 0 & 0 & 0 & 0 & 128 & 0 & -1152 & 0 & 5632 & 0 & -19968 & 0 & 57600 \\
0 & 0 & 0 & 0 & 0 & 0 & 0 & 0 & 256 & 0 & -2560 & 0 & 13824 & 0 & -53760 & 0 \\
0 & 0 & 0 & 0 & 0 & 0 & 0 & 0 & 0 & 512 & 0 & -5632 & 0 & 33280 & 0 & -140800 \\
0 & 0 & 0 & 0 & 0 & 0 & 0 & 0 & 0 & 0 & 1024 & 0 & -12288 & 0 & 78848 & 0 \\
0 & 0 & 0 & 0 & 0 & 0 & 0 & 0 & 0 & 0 & 0 & 2048 & 0 & -26624 & 0 & 184320 \\
0 & 0 & 0 & 0 & 0 & 0 & 0 & 0 & 0 & 0 & 0 & 0 & 4096 & 0 & -57344 & 0 \\
0 & 0 & 0 & 0 & 0 & 0 & 0 & 0 & 0 & 0 & 0 & 0 & 0 & 8192 & 0 & -122880 \\
0 & 0 & 0 & 0 & 0 & 0 & 0 & 0 & 0 & 0 & 0 & 0 & 0 & 0 & 16384 & 0 \\
0 & 0 & 0 & 0 & 0 & 0 & 0 & 0 & 0 & 0 & 0 & 0 & 0 & 0 & 0 & 32768
\end{bmatrix}$$

**(5. 16)**

The matrix can be derived simply by expanding the real or the imaginary component of Equation (5.12). In fact, considering $n$ = 0...3, for each value of $n$ the equation addends will be:

$$\begin{aligned}
&for \quad n=0 && V_{R0}\cos(\omega t)\\
&for \quad n=1 && \frac{V_{R1}}{2}\cos[(\omega\pm\Omega)t]\\
&for \quad n=2 && \frac{V_{R2}}{4}\cos[(\omega\pm 2\Omega)t]+\frac{V_{R2}}{2}\cos(\omega t)\\
&for \quad n=3 && \frac{V_{R3}}{8}\cos[(\omega\pm 3\Omega)t]+\frac{3V_{R3}}{8}\cos[(\omega\pm\Omega)t]
\end{aligned}$$

For a generic $n$ it can be written, [44]:

$$\frac{V_{Rn}}{2^{(n-1)}}\{\cos[(\omega\pm n\Omega)t]+\binom{n}{1}\cos[(\omega\pm(n-2)\Omega)t]+\binom{n}{2}\cos[(\omega\pm(n-4)\Omega)t]+..$$
$$..+\binom{n}{\frac{n-1}{2}}\cos[(\omega\pm\Omega)t]\}$$

In the frequency domain the LDV output will, then, have components at the usual frequencies with the following amplitudes, called $A$ (as mentioned above the spectral amplitudes at the frequencies ($\omega \pm n\Omega$) are the same):

$$\begin{aligned}
&at \quad \omega && A_{R0}=V_{R0}+\frac{V_{R2}}{2}\\
&at \quad \omega\pm\Omega && A_{R1}=\frac{V_{R1}}{2}+\frac{3V_{R3}}{8}\\
&at \quad \omega\pm 2\Omega && A_{R2}=\frac{V_{R2}}{4}\\
&at \quad \omega\pm 3\Omega && A_{R3}=\frac{V_{R3}}{8}
\end{aligned}$$

which can be written as

$$\begin{Bmatrix} A_{R0} \\ A_{R1} \\ A_{R2} \\ A_{R3} \end{Bmatrix} = \begin{bmatrix} 1 & 0 & 1/2 & 0 \\ 0 & 1/2 & 0 & 3/8 \\ 0 & 0 & 1/4 & 0 \\ 0 & 0 & 0 & 1/8 \end{bmatrix} \begin{Bmatrix} V_{R0} \\ V_{R1} \\ V_{R2} \\ V_{R3} \end{Bmatrix}$$

The polynomial coefficients can be expressed in function of the spectral amplitude only by inverting the matrix transform, which will then, coincide with [T].

Note that the sensitivity to higher polynomial components diminishes rapidly as *n* increases.

#### *5.3.3.2 Numerical Simulation*

##### *5.3.3.2.1 Real Vibration Response*

The vibration velocity $v_z(t)$ can be simulated, assuming it is associated with the same beam shown in Figure 5.1, where the LDV is now scanning sinusoidally along the straight line. The beam is again supposed to vibrate at the second natural frequency, i.e. 472.43 Hz as derived above. First, the beam vibration is considered to be real (standing wave on the beam), later (subsection 5.3.3.2.2) the complex case (travelling wave along the beam) will be analysed, where the vibration along *z* consists of two components, real and imaginary ones.

The second flapwise bending mode is again simulated using the Timoshenko theory and Equation (5.2) with values for *k* and $C_1/C_2$ given. Considering the real component only:

$$V_R(x) = -0.99922\left(\cos 7.853x + \cosh 7.853x\right) + \sin 7.853x + \sinh 7.853x \quad \textbf{(5. 17)}$$

this can be approximated by a polynomial of, say, the $10^{th}$ order.

$$V_R(x) = 2.26e^{-6}x^{10} - 0.5601x^9 + 2.92e^{-4}x^8 + 3.8972x^7 - 3.10e^{-4}x^6 - 10.5870x^5 + 2.19e^{-3}x^4 + 14.6450x^3 - 4.84e^{-4}x^2 - 5.3949x + 2.21e^{-4} \quad \textbf{(5. 18)}$$

The vibration response assumes the form of a standing wave, i.e. nodal points are spatially fixed, as shown in Figure 5.11.

$$v_z(x,t) = V_R(x)\cos(\omega t) = (2.26e^{-6}x^{10} - 0.5601x^9 + 2.92e^{-4}x^8 + 3.8972x^7 - 3.10e^{-4}x^6 + -10.5870x^5 + 2.19e^{-3}x^4 + 14.6450x^3 - 4.84e^{-4}x^2 - 5.3949x + 2.21e^{-4})\cos(\omega t) \quad \textbf{(5. 19)}$$

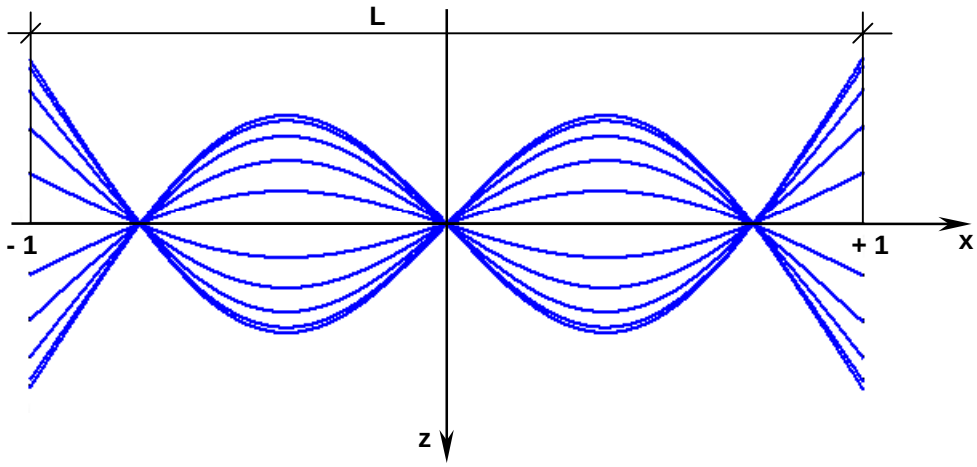


**Figure 5. 11** Vibration pattern at different time instants.

If the measurement points are continuously scanned sinusoidally at a frequency of 10 Hz along the beam assumed to have a length of 2 m, the velocity will depend on time only.

$$v_z(t) = (2.26e^{-6}\cos^{10}(2\pi 10t) - 0.5601\cos^9(2\pi 10t) + 2.92e^{-4}\cos^8(2\pi 10t) + 3.8972\cos^7(2\pi 10t) - 3.10e^{-4}\cos^6(2\pi 10t) - 10.5870\cos^5(2\pi 10t) + 2.19e^{-3}\cos^4(2\pi 10t) + 14.6450\cos^3(2\pi 10t) - 4.84e^{-4}\cos^2(2\pi 10t) + -5.3949\cos(2\pi 10t) + 2.21e^{-4})\cos(2\pi 472.43t) \quad \textbf{(5. 20)}$$

where $\omega = 472.43$ Hz.

Considering a time vector sampled at a sample rate of 10000 Hz at 100000 points the LDV output signal $v_z(t)$ can be plotted as in Figure 5.12.

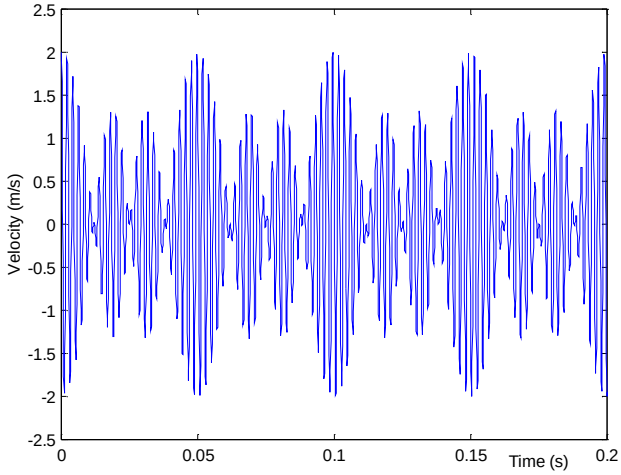


**Figure 5. 12** Velocity response.

Looking at the spectrum of the LDV time signal, sideband components appear at frequencies far apart from the excitation 472.43 Hz of 10 Hz. Their phases, as expected, are 0° or 180°, because a structure vibrating in a real mode will have all the points constituting it vibrating in-phase or in anti-phase with each other. Figure 5.13 shows magnitude and phase of the spectrum of the velocity time signal.

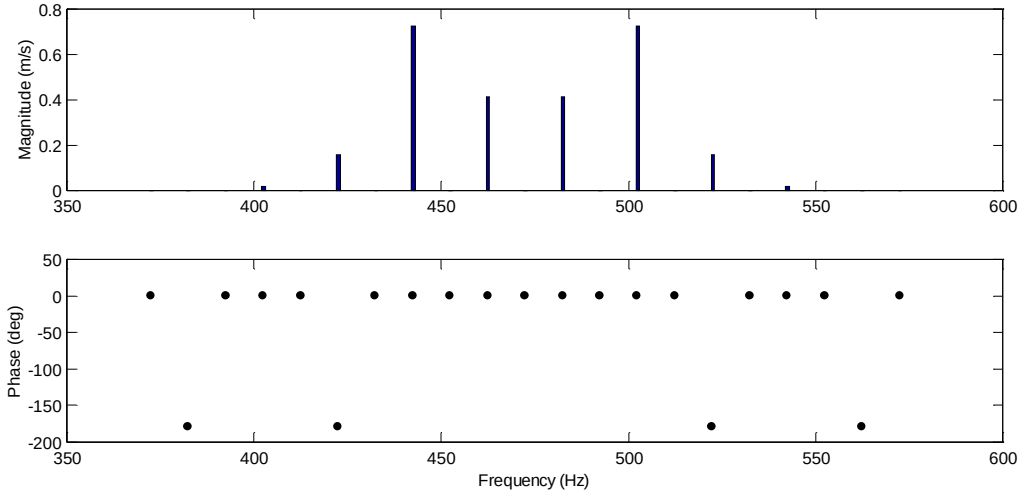


**Figure 5. 13** Velocity spectrum.

The amplitudes of the spectrum at the components 472.43 ± $n$ 10 Hz, for $n$ = 0 ... 10 (the polynomial being of the 10th order) are associated with a conventional sign of + if their phase is 0° and – if it is –180°. They can be converted again in polynomial coefficients applying the matrix transformation [T] as in Equation (5.15).

The vector {A} is measured directly from the spectrum at the precisely known frequencies:

$$\{A\} = \{\ 8.26\ e^{-4}\quad 0.4138\quad 4.59\ e^{-4}\quad 0.7239\quad 1.80\ e^{-4}\quad -0.1570\quad 4.44\ e^{-5}\quad 0.0206\quad 4.12\ e^{-5}\quad -0.0010\quad 4.00\ e^{-5}\}\ (\mathrm{m/s})$$

and applying the transformation (5.14) the vector $\{V_R\}$ is recovered as

$$\{V_R\} = \{\ 1.81\ e^{-4}\quad -5.3944\quad 0.0019\quad 14.6380\quad -0.0202\quad -10.5600\quad 0.0714\quad 3.8562\quad -0.0919\quad -0.5396\quad 0.0410\ \}\ (\mathrm{m/s})$$

that compared with the initial values

$$\{V_R\} = \{\ 2.21\ e^{-4}\quad -5.3949\quad -4.84\ e^{-4}\quad 14.6450\quad 0.0022\quad -10.5870\quad -3.10\ e^{-4}\quad 3.8972\quad -2.92\ e^{-4}\quad -0.5601\quad 2.26\ e^{-6}\ \}\ (\mathrm{m/s})$$

shows a real error of:

$$\mathrm{err} = \{\ 0.0007\quad 0.0090\quad 0.0445\quad 0.1190\quad 0.4156\quad 0.4985\quad 1.3300\quad 0.7611\quad 1.7100\quad 0.3802\quad 0.7600\ \}\ \%$$

The error is calculated as

$$err = \frac{\left| V_{R\,initial} - V_{R\,derived} \right|}{\left| V_{R\,initial\,1} \right|} \times 100 \qquad \textbf{(5. 21)}$$

where $V_{R\ initial\ 1}$ = - 5.3949 m / s, the reference value.

*5.3.3.2.2 Complex Vibration Response*

Now, the more general case of complex vibration is taken into analysis: the beam's second flapwise ODS is supposed to be composed of real and imaginary components, $V_R(x)$ and $V_I(x)$, that can be approximated by two polynomial of the 10th order:

$$\begin{aligned} V_R(x) &= 2.26e^{-6}x^{10} - 0.5601x^9 + 2.92e^{-4}x^8 + 3.8972x^7 - 3.10e^{-4}x^6 - 10.5870x^5 \\ &\quad + 2.19e^{-3}x^4 + 14.6450x^3 - 4.84e^{-4}x^2 - 5.3949x + 2.21e^{-4} \\ V_I(x) &= -0.0380x^{10} - 0.2472x^9 + 0.2933x^8 + 1.9277x^7 - 1.48e^{-4}x^6 \\ &\quad - 6.3049x^5 + 3.1198x^4 + 10.3360x^3 - 3.2832x^2 - 4.6495x + 0.4578 \end{aligned} \quad \textbf{(5. 22)}$$

The ODS real and imaginary components are shown together in Figure 5.14. In this case the vibration appears as a travelling wave that can be emphasised plotting the complex mode shape at different time instants as in Figure 5.15. Note that nodal points travel along the line.

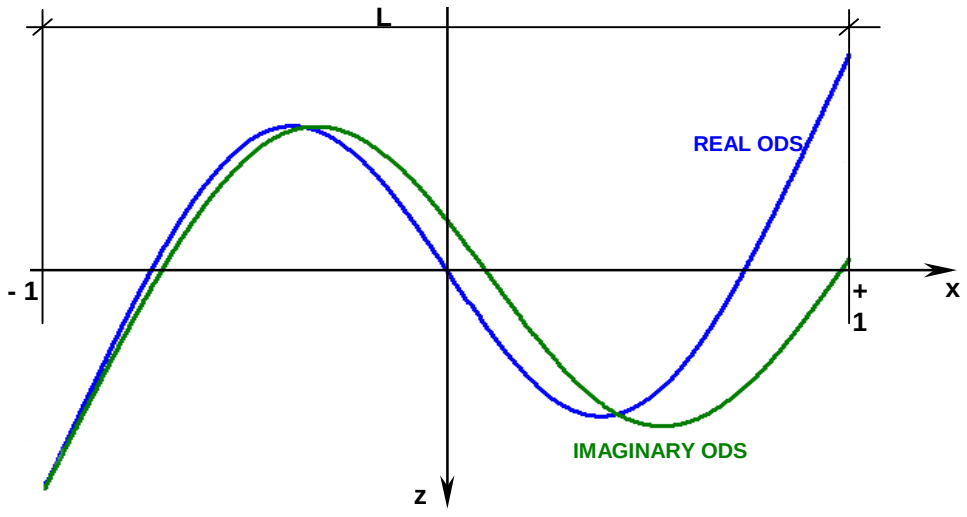


**Figure 5. 14** Polynomial description of the real and imaginary components of the vibration.

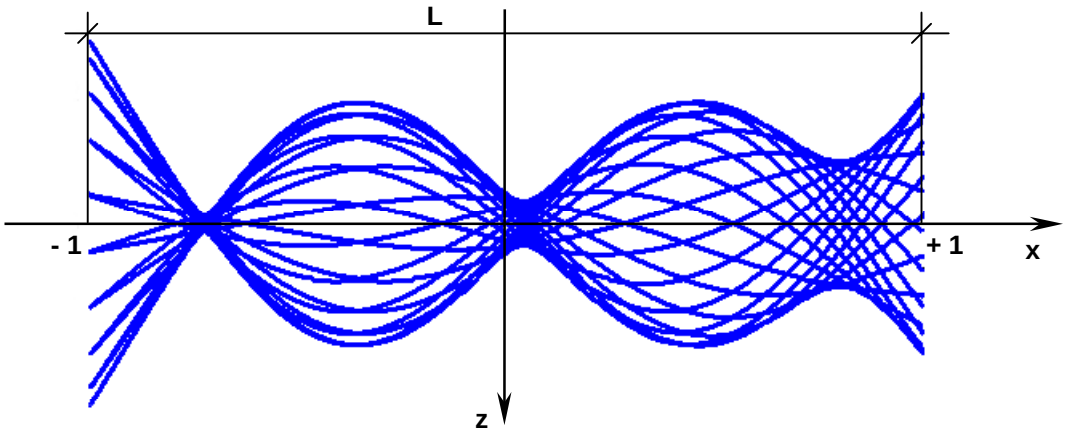


**Figure 5. 15** Vibration pattern at different time instants.

The vibration is then given by:

$$v_z(x,t) = V_R(x)\cos(\omega t) + V_I(x)\sin(\omega t) \qquad \textbf{(5. 23)}$$

As assumed before, the excitation frequency will be ω = 472.43 Hz and the spatial vector, $x = \cos(2\pi 10t)$, then the time dependent velocity vector will become:

$$\begin{aligned} v_z(t) = (&2.26e^{-6}\cos^{10}(2\pi 10t) - 0.5601\cos^{9}(2\pi 10t) + 2.92e^{-4}\cos^{8}(2\pi 10t) + \\ &+ 3.8972\cos^{7}(2\pi 10t) - 3.10e^{-4}\cos^{6}(2\pi 10t) - 10.5870\cos^{5}(2\pi 10t) + \\ &+ 2.19e^{-3}\cos^{4}(2\pi 10t) + 14.6450\cos^{3}(2\pi 10t) - 4.84e^{-4}\cos^{2}(2\pi 10t) + \\ &- 5.3949\cos(2\pi 10t) + 2.21e^{-4})\cos(2\pi 472.43t) \\ &+ (-0.0380\cos^{10}(2\pi 10t) - 0.2472\cos^{9}(2\pi 10t) + 0.2933\cos^{8}(2\pi 10t) + \\ &+ 1.9277\cos^{7}(2\pi 10t) - 1.48e^{-4}\cos^{6}(2\pi 10t) - 6.3049\cos^{5}(2\pi 10t) + \\ &+ 3.1198\cos^{4}(2\pi 10t) + 10.3360\cos^{3}(2\pi 10t) - 3.2832\cos^{2}(2\pi 10t) + \\ &- 4.6495\cos(2\pi 10t) + 0.4577)\sin(2\pi 472.43t) \end{aligned}$$

**(5. 24)**

Considering the same time vector used to derive the velocity response shown in Figure 5.12, the LDV output signal $v_z(t)$ can be derived and depicted in Figure 5.16. In this situation, the ODS being complex, the vibration amplitudes measured at different points are not necessarily in phase and from the phase spectrum of the time signal obtained the effect is clear, see Figure 5.17.

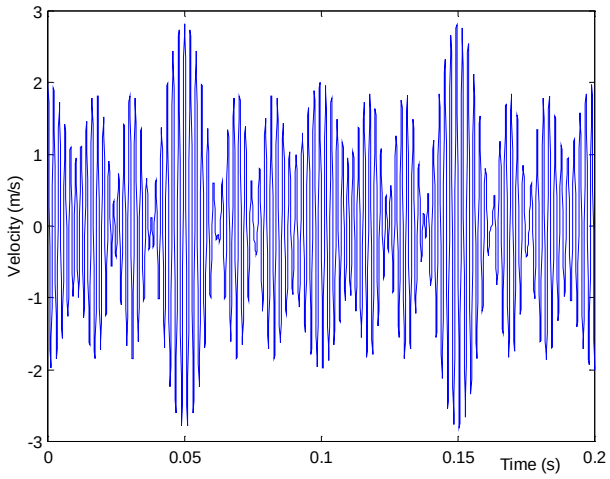


**Figure 5. 16** Complex velocity response.

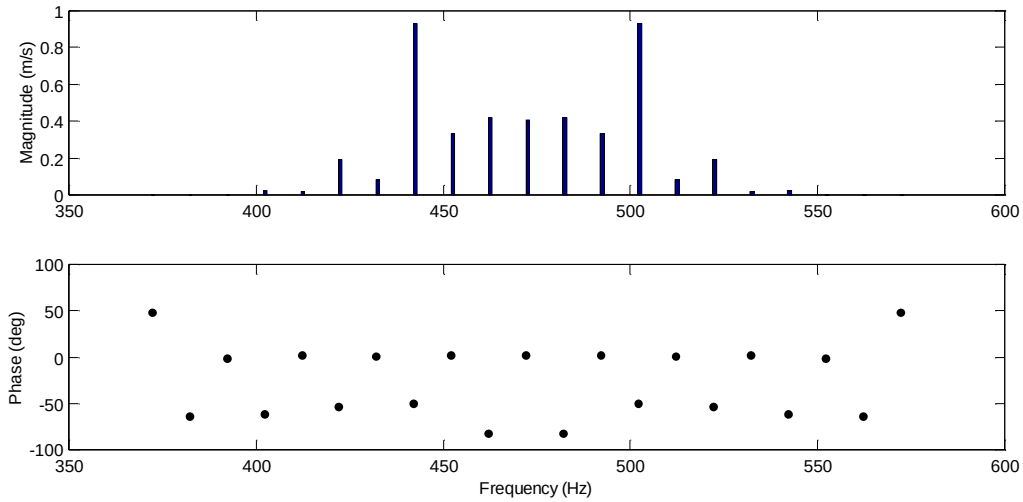


**Figure 5. 17** Velocity spectrum.

It is possible to note the sideband phases are not lined up at exactly 0° or -180°. The sign of these sidebands, then, can not be derived from the spectrum and the analysis cannot be done in terms of amplitude and phase but in terms of real and imaginary part of the sidebands.

The real and imaginary spectrum values at the sideband frequencies of 472.43 ± $n$ 10 Hz, for $n$ = 0 ... 10 are:

$\{A_R\}$ = { 8.26 $e^{-4}$ 0.4138 4.59 $e^{-4}$ 0.7239 1.80 $e^{-4}$ -0.1570 4.44 $e^{-5}$ 0.0206 4.12 $e^{-5}$ -0.0010 4.00 $e^{-5}$} (m / s)

$\{A_I\}$ = { 0.4078 -0.0472 0.3330 -0.5825 -0.0832 0.1089 0.0157 -0.0107 -7.74 $e^{-4}$ 4.82 $e^{-4}$ 3.71 $e^{-5}$ } (m / s)

Applying the matrix transformation [T] to both the real and imaginary sideband values, polynomial coefficients can be recovered:

$\{V_R\}$ = { 1.81 $e^{-4}$ -5.3944 0.0019 14.6380 -0.0202 -10.5600 0.0714 3.8562 -0.0919 -0.5396 0.0410 } (m / s)

$\{V_I\}$ = { 0.4578 -4.6495 -3.2832 10.3360 3.1198 -6.3048 -1.4872 1.9277 0.2933 -0.2472 -0.0380 } (m / s)

that compared with the initial values

$\{V_R\}$ = { 2.21 $e^{-4}$ -5.3949 -4.8402 $e^{-4}$ 14.6450 0.0022 -10.5870 -3.10 $e^{-4}$ 3.8972 -2.92 $e^{-4}$ -0.5601 2.26 $e^{-6}$ } (m / s)

and

$\{V_I\}$ = { 0.4578 -4.6495 -3.2832 10.3360 3.1198 -6.3049 -1.4872 1.9277 0.2933 -0.2472 -0.0380 } (m / s)

give the following corresponding errors calculated with the previous Equation (5.20):

real err = { 0.0007 0.0090 0.0445 0.1190 0.4156 0.4985 1.3300 0.7611 1.7100 0.3801 0.7600 } %

imaginary err = { 0.0010 0.0066 0.0331 0.1538 0.0041 0.0221 0.0015 0.0063 0.0008 0.0023 0} %

#### *5.3.3.2.3 Mirror Delay Effect Investigation*

As seen in Figure 5.13 and 5.17 the phase spectrum of the LDV output is always symmetrical with respect to the excitation frequency, although the sidebands phase values do not lie on two horizontal lines, 180° apart; that only happens in the real case. In practice, the experimental LDV output never appears like that: the corresponding sideband phases are not equal and they lie on inclined lines over the horizontal axis. Phase errors are related to the initial position of the LDV scan at the start of data acquisition. A delay, described already in Chapter 4, is always present because of the inertia of the mirrors, so that there is a time gap between the instant when the mirror signal driver is at zero and the instant when the laser spot is starting its scan in the surface. Although the acquisition is triggered with the mirror driver signal when it passes through zero with positive slope, i.e. when the laser spot should be in the middle of the scanned line, a shift between the two time signals always occurs. In Figure 5.18 two simulated LDV outputs are plotted together with the mirror driver signal which comes from Equation (5.11), using a scan speed of 10 Hz. The first time history is due to an ideal acquisition where no delays occur and it is obtained from Equation (5.14), assuming the ODS real and then only the first part of the formula existing. Considering again the second flapwise bending mode of the beam, approximated by the polynomial represented by Equation (5.18), the sideband vector $A_n$, to be inserted in Equation (5.14), can be derived by applying the inverse of Equation (5.15).

If

$V_R$ = { 2.26 $e^{-6}$ -0.5601 2.92 $e^{-4}$ 3.8972 -3.10 $e^{-4}$ -10.5870 2.19 $e^{-3}$ 14.6450 -4.84 $e^{-4}$ -5.3949 2.21 $e^{-4}$ }

then, applying

$$\{A\}=[T]^{-1}\{V\}$$

the sideband vector will be:

$A_R$ = { 7.83 $e^{-4}$ 0.4137 4.18 $e^{-4}$ 0.7238 1.40 $e^{-4}$ -0.1571 4.38 $e^{-6}$ 0.0206 1.16 $e^{-6}$ - 0.0011 2.20 $e^{-9}$ }

and the ideal LDV output:

$$v_z(t)=\sum_{n=0}^{p} A_{Rn}\cos[(\omega \pm n\Omega)t] \qquad \textbf{(5. 25)}$$

with ω = 472.43 Hz and $n$ = 0..10.

If now a delay, δ, of the mirror is taken into consideration the mirror drive signal will be given by a sinewave of equation:

$$x(t)=\cos(\Omega t+\delta) \qquad \textbf{(5. 26)}$$

Consequently the vibration response as depicted in Equation (5.10) becomes:

$$v_z(t)=\sum_{n=0}^{p} V_{Rn}\cos^n(\Omega t+\delta)\cos(\omega t)+\sum_{n=0}^{p} V_{In}\cos^n(\Omega t+\delta)\sin(\omega t) \qquad \textbf{(5. 27)}$$

and expanding out trigonometrically the vibration appears to have a similar expression to that obtained for the ideal case ( Equation (5.25) ), with the same upper and lower sidebands but with sine and cosine term arguments containing the delay value.

$$v_z(t) = \sum_{n=0}^{p} A_{Rn} \cos\left[(\omega \pm n\Omega)t \pm n\delta\right] + \sum_{n=0}^{p} A_{In} \sin\left[(\omega \pm n\Omega)t \pm n\delta\right] \qquad \textbf{5. 28}$$

Assuming, again, the ODS to be real and using the previous sideband vector, the LDV output considering the mirror delay will be

$$v_z(t) = \sum_{n=0}^{p} A_{Rn} \cos\left[(\omega \pm n\Omega)t \pm n\delta\right] \qquad \textbf{(5. 29)}$$

where $\delta$ is supposed to be $\pi/8$. Ideal and actual LDV outputs are plotted in Figure 5.18 together with the ideal mirror driver signal to emphasise the shift due to the delay, see lower plot.

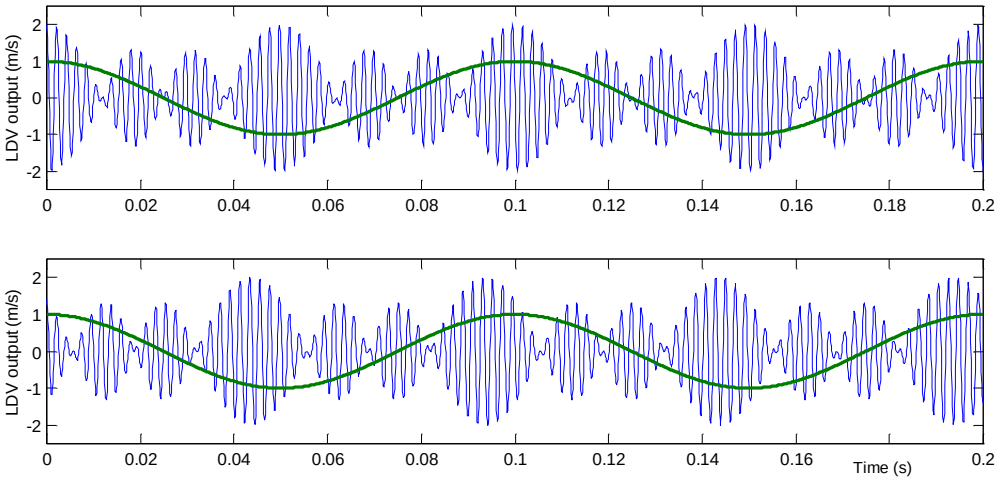


**Figure 5. 18** LDV output in the case of ideal and real mirror plotted together with the mirror driver signal.

Sidebands coefficients can be recovered from the ideal LDV output in the usual way, by multiplying the time signal by sine and cosine at $(\omega \pm n\Omega)$, see Figure 5.19. If the same curve fitting is applied to the LDV output, obtained in the case of the mirror delay considered, the argument of the sine and cosine must be $(\omega \pm n\Omega)t \pm n\delta$, supposing the delay is known, i.e. $\pi/8$ in this circumstance. If the delay is not taken into account, the expected phase spectrum occurs, so that the phase values lie on inclined lines over the horizontal axis, see Figure 5.20. Figure 5.21 shows the curve fitted spectrum of the LDV output when the delay is considered.

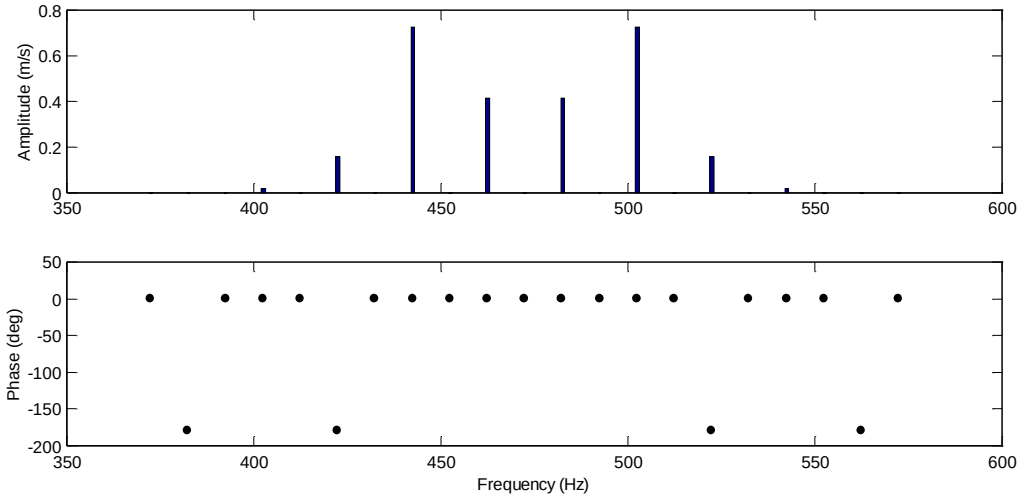


**Figure 5. 19** LDV spectrum in the ideal situation.

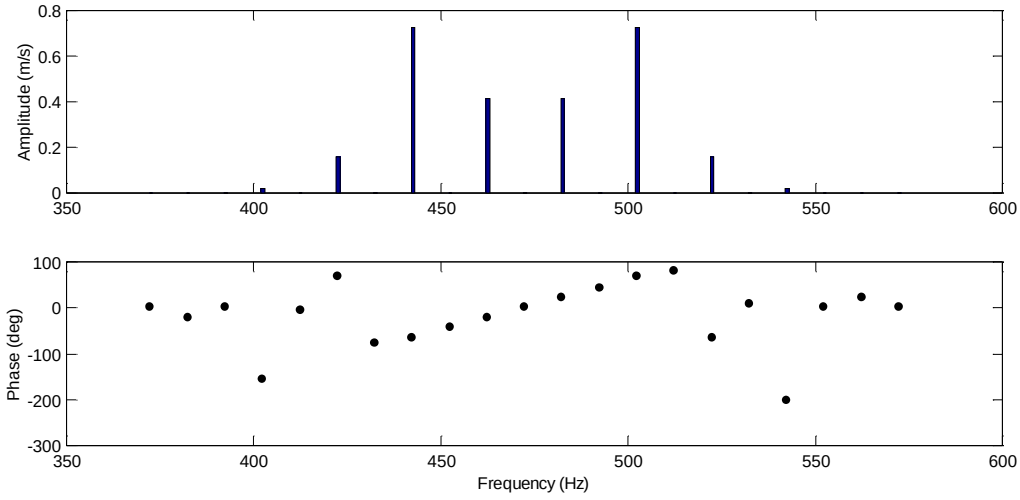


**Figure 5. 20** LDV spectrum in the real situation without considering the mirror delay in the curve-fit.

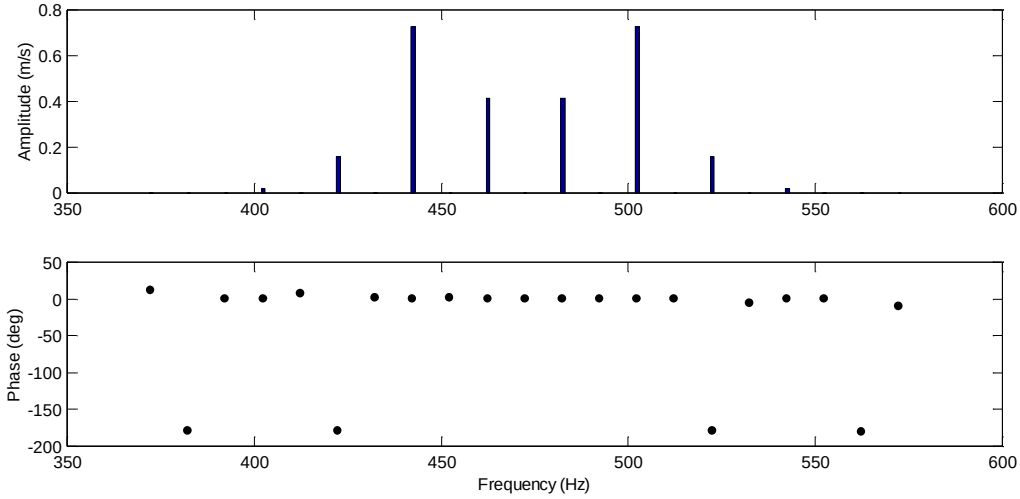


**Figure 5. 21** LDV spectrum in the real situation considering the mirror delay in the curve-fit.

### *5.3.3.3 Experimental Validation*

The straight-line scan technique has been applied to the same beam employed in Subsection 5.3.2 and measurements have again been performed by scanning on half the length of the beam when it is excited at the experimental natural frequencies of 58 Hz, 311 Hz and 766 Hz corresponding to the first, third, and fifth mode respectively.

A similar software to the one produced in `LabVIEW` for the uniform scan technique was used to control, acquire and post-process measurement data. The shaker control and acquisition programs are completely identical to the ones described in subsection 5.3.2.2 (see Appendix A.1.1 for the control panel of the `LabVIEW` program driving the shaker and Appendix A1.3 for the control panel of the `LabVIEW` program used for the acquisition). The mirror control routine is different from the one used for uniform straight-line scans, since the waveform employed to drive the mirror is a sinewave (see Appendix A.1.5 for the control panel of the `LabVIEW` program driving the mirrors). The post-process routine, to which a `Matlab` version also exists, performs the curve fit of the LDV output at the known frequencies. Inputs of this program must be the number of sidebands required and the mirror delay used to correct the phase spectrum

and lined up horizontally phase values. The number of sidebands can be decided after having a quick look at the spectrum of the LDV output, which is derived and plotted by the program itself. The mirror delay is defined after some trials until the phase values are lying horizontally and the spectrum becomes symmetrical.

First, the beam vibrating at its first mode, 58 Hz, was measured with the LDV scanning continuously at 10 Hz. The acquisition was triggered with the mirror-driving signal, when it passed through zero, positively going, see Figure 5.22.

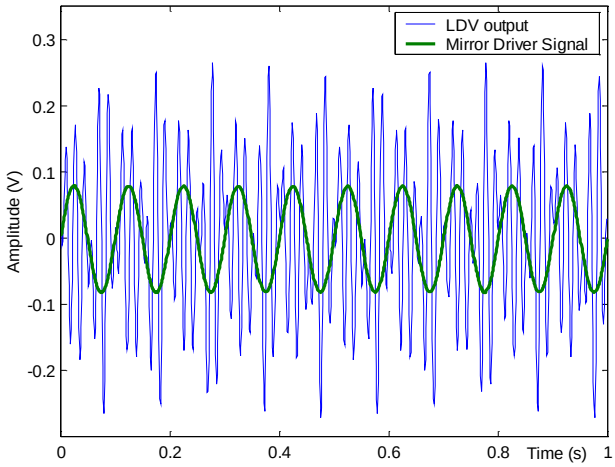


**Figure 5. 22** Acquired time signals.

A curve fit was performed at the frequencies ($\omega \pm n\Omega$) with $n$ = 0..5 ($n$ can not be bigger than 5 in order not to go up to negative frequencies. However, observing the LDV output spectrum during the acquisition it can be noticed that after the fourth order the sideband amplitudes are negligible). With this operation the mirror delay is not taken into account and in the LDV spectrum the phase values misalignment can be seen, see Figure 5.23. On the contrary, assuming for that delay a value of 1.42 rad, the phase spectrum becomes correct as shown in Figure 5.24, where phase unwrapping is applied as well.

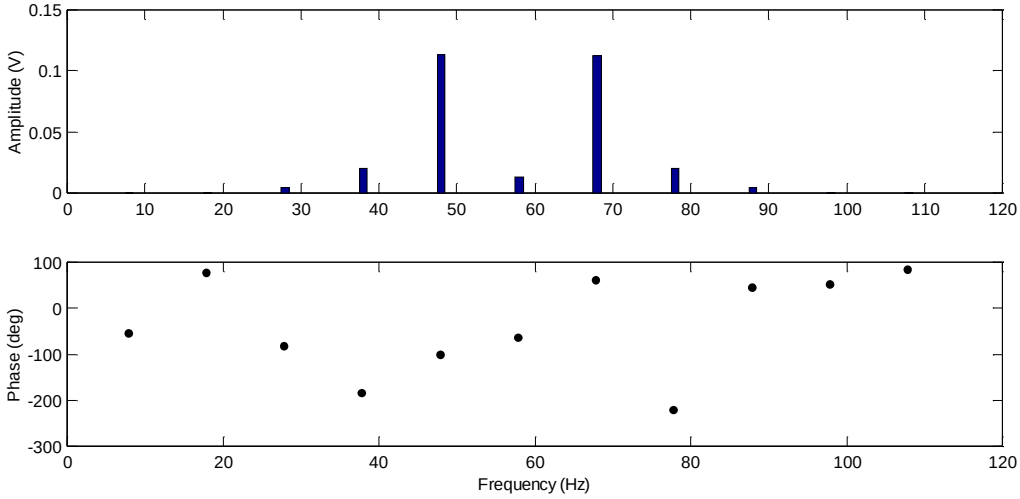


**Figure 5. 23** LDV output spectrum without considering the mirror delay.

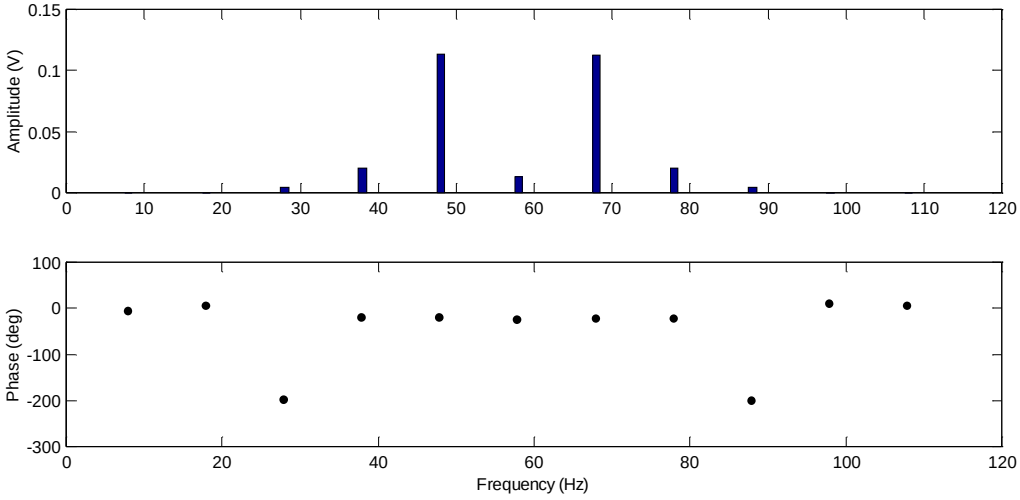


**Figure 5. 24** Correct LDV output spectrum.

The sideband spectrum is not perfectly symmetrical and this can be related to the fact that, in reality, the ODS is not completely real and a complex analysis must be performed. However, the discrepancy is very small (1.3 %) and the assumption can be kept. The signed sideband vector will be

$$\{A\} = \{\, 0.013410 \quad 0.11231 \quad 0.019779 \quad -0.0042793 \quad 3.0066\, e^{-4} \quad 7.5285\, e^{-5} \,\}$$

where it was assumed positive sign if the sideband phases were 0° and negative if they were -180°.

Applying the transformation described in Equation (5.15) the polynomial coefficients for the ODS can be recovered:

$\{V\} = \{ -0.025821 \quad 0.25104 \quad 0.079245 \quad -0.037246 \quad -0.0083580 \quad 0.0024091 \quad 0.008779\}$.

These values can be compared with the coefficients of the polynomial approximating the mode shape described by the Timoshenko theory which expression is given by the first Equation of the set (5.8). Note that the polynomial approximation must be taken for half beam only.

$\{V\} = \{ -0.19332 \quad 1.8657 \quad 0.60723 \quad -0.28019 \quad -0.015749 \quad 0.030399 \quad 0.003298 \}$.

In order to have a sensible comparison, the two sets were scaled with the corresponding maximum component and, subtracting the first from the second one, a percentage error was calculated.

$err = \{ 0.07 \quad 0 \quad 0.98 \quad 0.18 \quad 2.48 \quad 6.69 \quad 3.32 \}$

The two polynomials are plotted together in Figure 5.25.

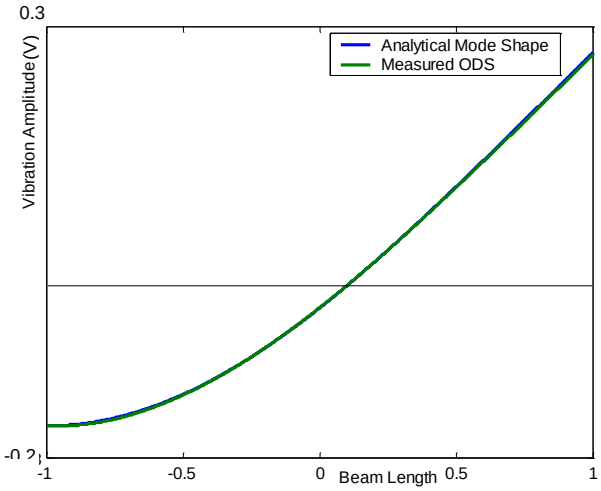


**Figure 5. 25** Analytical mode shape and measured ODS at 58 Hz.

The same procedure can be followed to recover the third and fifth mode shapes: the ODSs derived by continuous scans and the mode shape simulated by the Timoshenko theory are plotted together in Figures 5.26 and 5.27 for the natural frequencies 311 and 766 Hz respectively.

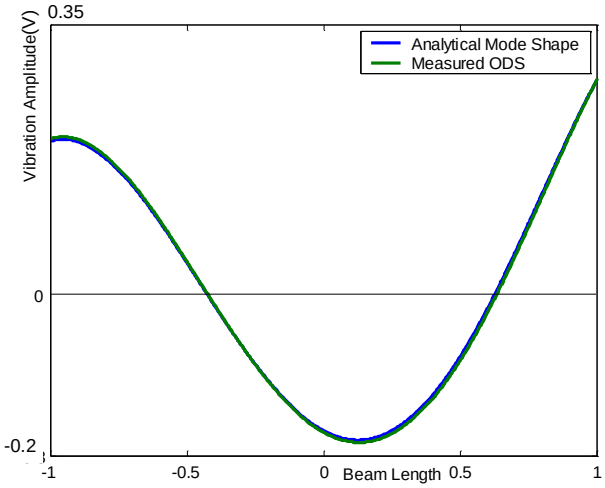


**Figure 5. 26** Analytical mode shape and measured ODS at 311 Hz.

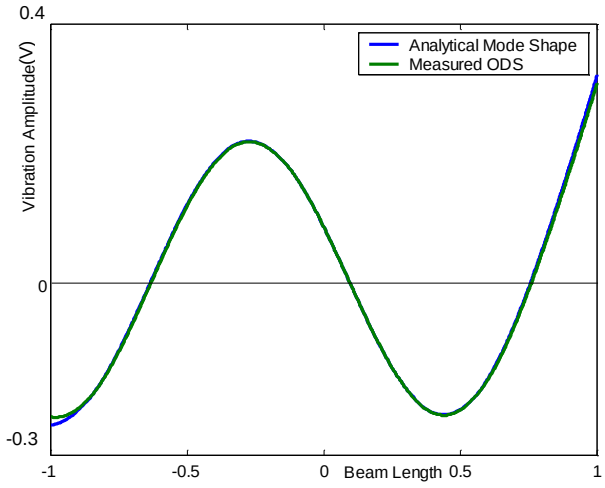


**Figure 5. 27** Analytical mode shape and measured ODS at 766 Hz.

### *5.3.3.4 Experimental Investigation using the Point-by-Point Technique*

Experiments have been carried out in a set of discrete points as well using the conventional software available from Polytec PSV200. Measurements have been

performed in the same set-up employed for continuous scanning tests and, in practice, 47 points, uniformly distributed along the line scan, have been addressed, see Figure 5.28.

Results are plotted together with the associated ODSs, derived by the CSLDV technique, in Figures 5.29, 5.30 and 5.31 for the first, third and fifth modes respectively. Dots in the plot represent the exact position of the laser spot along the line during the measurement. Resonance frequencies found during the PSV test were slightly different from the ones observed during the continuous scanning and their values are reported in Table 5.6.

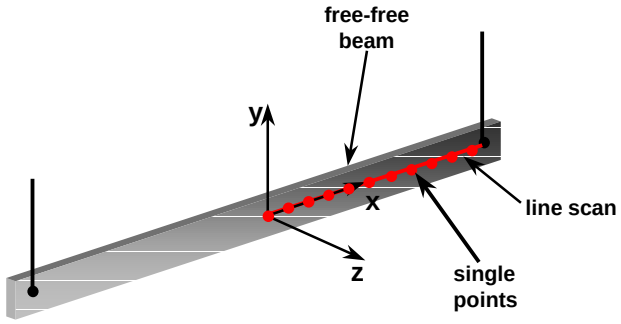


**Figure 5. 28** Single points location.

| | Single Points Test | Continuous Scan Test |
|---|---|---|
| **FIRST MODE** | 58.12 Hz | 58 Hz |
| **THIRD MODE** | 312.81 Hz | 311 Hz |
| **FIFTH MODE** | 770.01 Hz | 766 Hz |

**Table 5. 6** Resonance frequencies observed in both the tests performed.

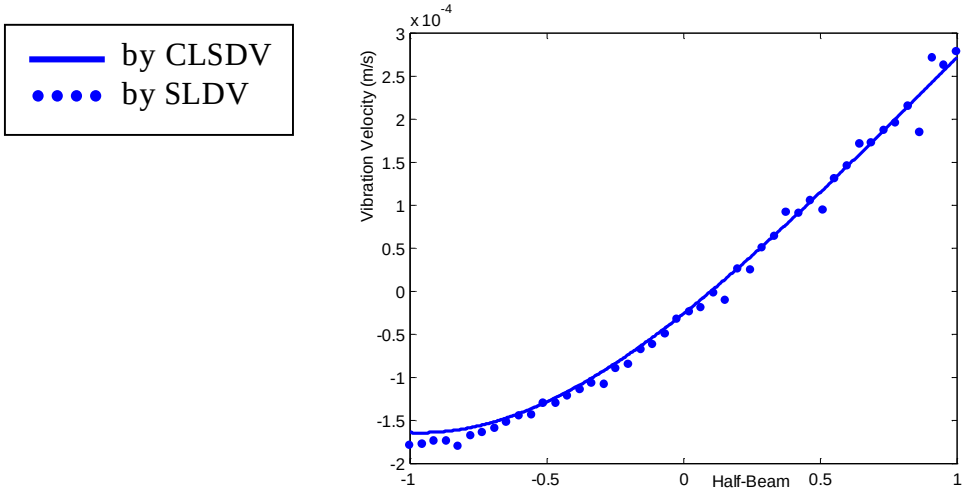


**Figure 5. 29** ODS corresponding to the first mode.

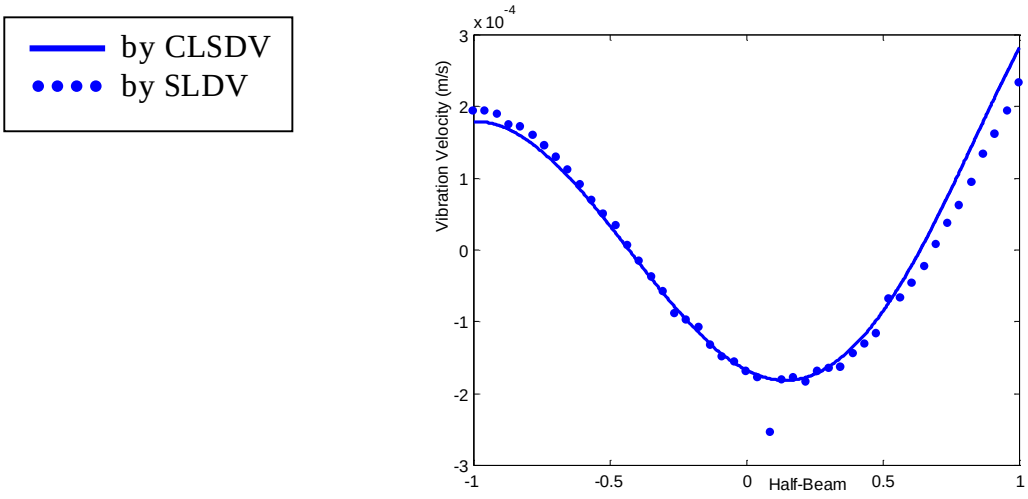


**Figure 5. 30** ODS corresponding to the third mode.

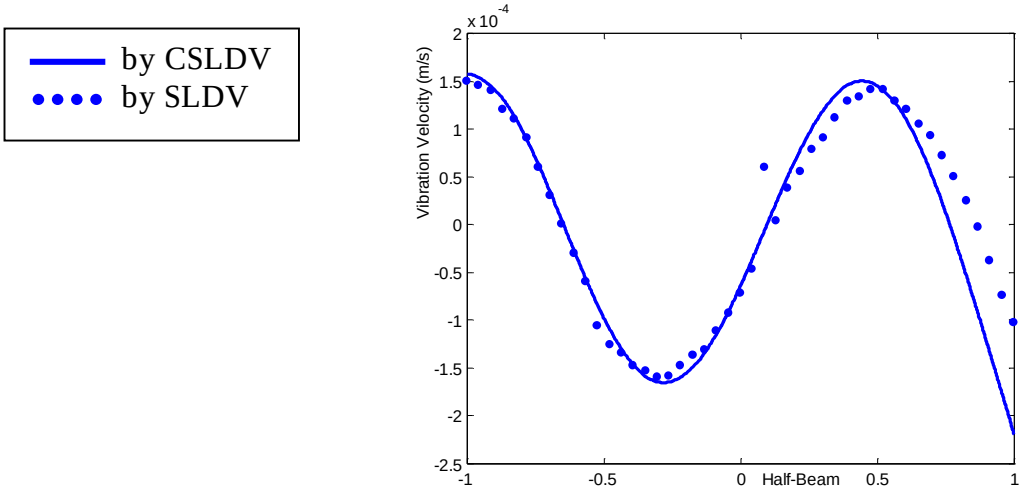


**Figure 5. 31** ODS corresponding to the fifth mode.

The results clearly correspond closely, but the coarse resolution of the point-by-point survey is very marked as is the irregularity of the shape.

## *5.4. Analysis of Circular Scan*

### *5.4.1 Introduction*

The continuously-scanning laser Doppler vibrometry can be extended to two-dimensional structures such as plates of any shape by forcing the laser beam to move on a trajectory covering the structure surface and following a 2-D path. In order to realise this, the second mirror in the scanning system of the LDV must be employed. Driving both mirrors with two sinewaves of different amplitudes, phases and frequencies, an arbitrarily trajectory can be built to be imposed to the laser spot, either in Cartesian or polar co-ordinates. However, the easiest 2-D path that the laser can follow is a large circular scan which covers the greatest amount of the surface possible, see Figure 5.32. This type of scanning is an extension of the straight-line scan where the line is now a circle. Moreover, the velocity of the laser spot following the circle is uniform; specifically, the angular velocity is Ω, which is the scan speed. The ODS along the circular line can then be recovered in a straightforward fashion by demodulating the LDV output, as

seen in Subsection 5.3.1. Also, if it is possible that the mode shape along the circular path can be expanded as a spatial Fourier series in the circular coordinate, then the CSLDV output spectrum will have a known sideband-like appearance from which the ODS can be directly recovered. This technique can be applied for measuring out-of-plane vibration of plates, discs or disc-like components steady or rotating, see references [6], [7] and [18].

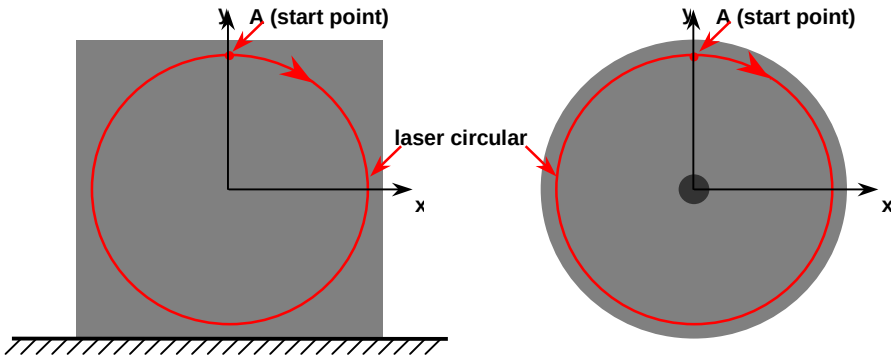


**Figure 5. 32** Cantilever square plate and disc together with the laser beam trajectory.

### *5.4.2 Mathematical Investigation*

It is again assumed that the structural vibration or the motion of any point on the test specimen is approximately sinusoidal at the specific frequency, ω. The vibration velocity in the *z*-direction, namely the direction perpendicular to the vibrating surface, nominally in the plane *x*,*y*, is a function of the spatial position and the time according to the customary relationship:

$$v_z(s,t)=V_R(s)\cos(\omega t)+V_I(s)\sin(\omega t) \qquad \textbf{(5. 30)}$$

*s*, being the circular coordinate around the scan line from a datum position which is fixed as the start point of the scan. As stated in Section 4.1, if the laser beam is driven by horizontal and vertical mirrors fed by two sinewaves of equations $R\sin(\Omega t)$ and $R\cos(\Omega t)$, respectively, *R* being the circle radius, the

initial point over the circle will be determined by the intersection of the circle with the *y*-axis, point **A** in Figure 5.32. Under this condition, the laser beam scans uniformly at a rotational speed of Ω. Therefore, the coordinate around the scan trajectory may be written as $s=\Omega t$, so that, the real and imaginary mode shape contributions $V_R$ and $V_I$, which are functions of the position of the point on the structure, *s*, can be expressed in terms of time only. Their spatial representation can be expanded as Fourier series in the circular coordinate, this series being upper limited up to, say, the $p^{th}$ terms if the deflection shape is smooth. It can be then written:

$$V_R(s)=\sum_{n=0}^{p} V_{Rn}\cos ns$$
$$V_I(s)=\sum_{n=0}^{p} V_{In}\sin ns \qquad \textbf{(5. 31)}$$

$V_{Rn}$ and $V_{In}$ being the n$^{th}$ spatial Fourier coefficients of the real and imaginary mode shape components. Substituting the spatial coordinate *s* with Ω*t*, the mode shape contributions can be expressed as functions of time only as the following equation illustrates:

$$V_R(t)=\sum_{n=0}^{p} V_{Rn}\cos n(\Omega t)$$
$$V_I(t)=\sum_{n=0}^{p} V_{In}\sin n(\Omega t) \qquad \textbf{(5. 32)}$$

At this point, the vibration velocity can be written as:

$$v_z(t)=\sum_{n=0}^{p} V_{Rn}\cos n(\Omega t)\cos(\omega t)+\sum_{n=0}^{p} V_{In}\sin n(\Omega t)\sin(\omega t) \qquad \textbf{(5. 33)}$$

The previous equation can be expanded to give:

$$v_z(t) = V_{R0}\cos(\omega t) + V_{I0}\sin(\omega t) + \\ + \sum_{n=1}^{p}\left\{\frac{V_{Rn}}{2}\left[\cos(\omega t + n\Omega t) + \cos(\omega t - n\Omega t)\right] + \frac{V_{In}}{2}\left[\cos(\omega t - n\Omega t) - \cos(\omega t + n\Omega t)\right]\right\}$$

**(5. 34)**

where the corresponding terms can be collected to produce:

$$v_z(t) = V_{R0}\cos(\omega t) + V_{I0}\sin(\omega t) + \sum_{n=1}^{p}\left\{\frac{V_{Rn} + V_{In}}{2}\cos(\omega - n\Omega)t + \frac{V_{Rn} - V_{In}}{2}\cos(\omega + n\Omega)t\right\}$$

**(5. 35)**

The vibration velocity then consists of harmonic components at frequencies ($\omega \pm n\Omega$) and its spectrum can be seen as a collection of sideband pairs spaced at $\pm n\Omega$ about the vibration frequency, $\omega$. If the ODS is real, the imaginary coefficients are all zero ($V_{In} = 0$) so that each pair of sideband components have equal amplitudes. From Equation (5.35) we can conclude that the Fourier coefficients describing the operating deflection shape of the structure at the actual excitation frequency can be directly recovered from the spectrum of the LDV output without passing through the transformation needed in case of linear scans.

### *5.4.3 Numerical Simulation on a Rectangular Plate*

A circular scan on a rectangular plate, which is illustrated in the first plot of Figure 5.32, can be simulated by assuming that the vibration pattern along the scan circle is known and, that it follows the Equation (5.31), i.e. it can be represented as a Fourier series of the circular coordinate *s*. Supposing that the vibration pattern is real only, a set of coefficients $V_{Rn}$ can be introduced, specifically 8, i.e. $n = 0...7$.

Around the circle, the spatial representation of the ODS real component is then expressed by Equation (5.36) and it is depicted in Figure 5.33.

$$V_R(s)=1.778+0.100\cos(s)-0.224\cos(2s)-1.584\cos(3s)+0.562\cos(4s)-0.224\cos(5s)$$
$$+0.031\cos(6s)+0.056\cos(7s) \qquad \textbf{(5. 36)}$$

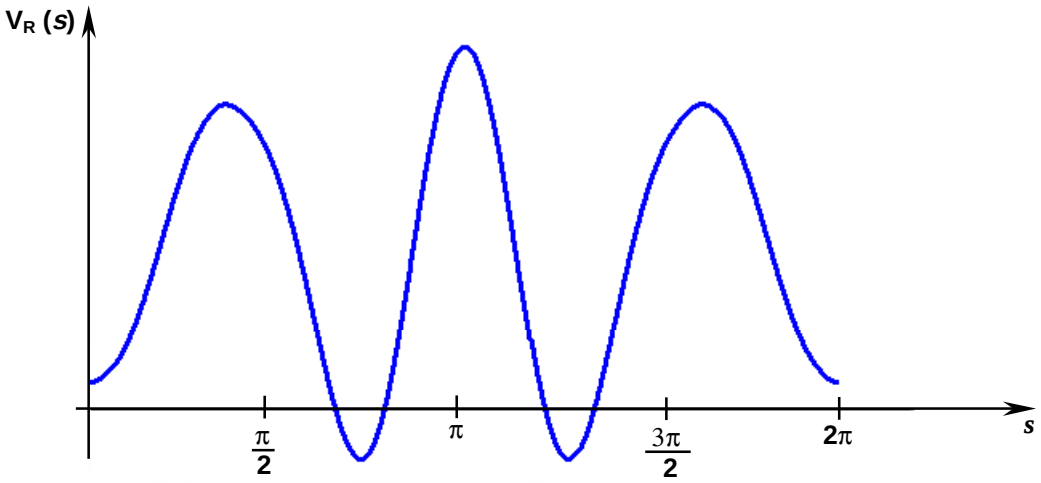


**Figure 5. 33** Polynomial ODS along the rectified circle scanned on the plate.

If the laser beam scans in that circle at a speed of 10 Hz, i.e. $s = 2\pi 310t$ , the LDV will measure a time signal modulated by the mode shape, and it will then be sensitive to a vibration velocity whose expression is given by Equation (5.33), adapted to the actual situation:

$$v_z(t)=\{1.778+0.100\cos(2\pi 10t)-0.224\cos[2(2\pi 10t)]-1.584\cos[3(2\pi 10t)]+$$
$$+0.562\cos[4(2\pi 10t)]-0.224\cos[5(2\pi 10t)]+0.031\cos[6(2\pi 10t)]+ \qquad \textbf{(5. 37)}$$
$$+0.056\cos[7(2\pi 10t)]\}\cos(2\pi 211t)$$

In the previous equation, it was considered that the resonance frequency, ω, of the actual ODS was 211 Hz. If the LDV signal is acquired using 20000 samples at a sample rate of 20000 Hz, the time vector *t* can be introduced in the previous equation and the time history will appear as Figure 5.34 shows.

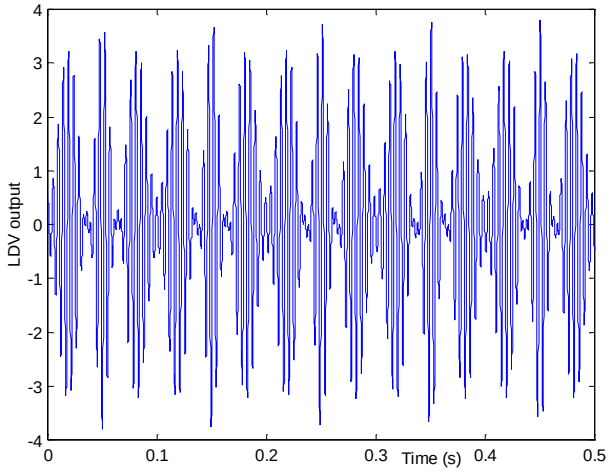


**Figure 5. 34** LDV time history modulated by the circumferential mode shape.

By multiplying the LDV time signal by sine and cosine at the well known frequencies of $2\pi(211 \pm n310)$ Hz, with $n$ = 0...8, real and imaginary spectral components are derived, the imaginary ones being negligible since the original ODS is completely real. The spectral components are illustrated as magnitude and phase in Figure 5.35.

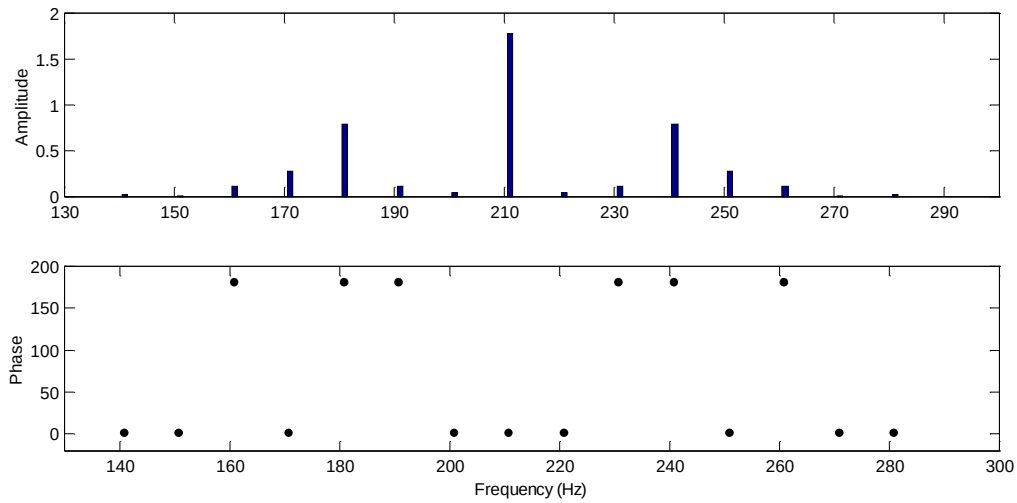


**Figure 5. 35** LDV output spectral components amplitude and phase (°).

On the basis of Equation (5.35), the polynomial coefficients $V_{R\,n}$ can be recovered from the sideband amplitudes $A_{R\,n}$ and sign, following the convention that the

sign will be positive if the sideband phase is 0° and negative if it is 180° shifted. From Figure 5.35 the following sideband vector is derived:

$\{ A_R \} = \{1.778 \quad 0.050 \quad -0.112 \quad -0.792 \quad 0.281 \quad -0.112 \quad 0.016 \quad 0.028 \}$

and then it will be $V_0 = A_0 = 1.778$ and $V_n = 2\ A_n$ for $n = 1..7$, therefore:

$\{ V_R \} = \{1.778 \quad 0.100 \quad -0.224 \quad -0.158 \quad 0.562 \quad -0.224 \quad 0.032 \quad 0.056 \}$

which are the same as those that appeared in Equation (5.36), which is the expression describing the ODS over the scan circle. As already mentioned, the deflection shape along the line scanned can be directly recovered from the LDV output time history without passing through its Fourier decomposition, by simply demodulating the time signal itself and filtering out the higher harmonics, see Subsection 5.3.2. In this case, the scan frequency cannot be too high as explained above (Subsection 5.3.2); a scan speed of 1 Hz is then considered. The LDV output will be simulated by Equation (5.37) again with the only difference being that now the scan frequency is 1 Hz and not 10 Hz. The time history obtained is shown in Figure 5.36, where a time vector of samples acquired with a 5000 Hz sample rate is considered.

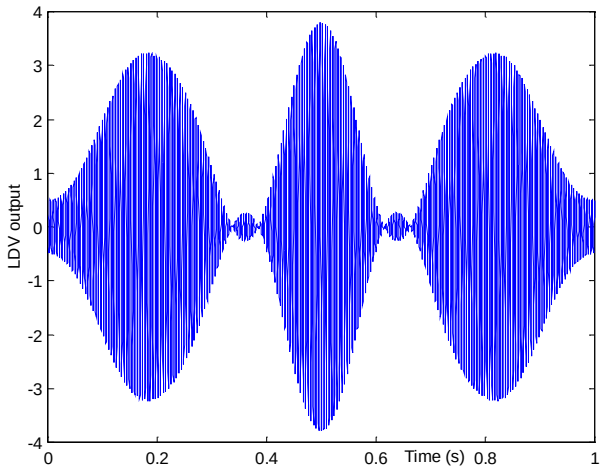


**Figure 5. 36** LDV output time history zoomed within a scan period (1 sec).

By demodulating this signal at the excitation frequency (211 Hz) and applying a suitable low-pass filter the ODS can be straightforwardly recovered as shown in Figure 5.37. Note that the picture shows two scan cycles of the laser beam around the circle, which will take 2 seconds.

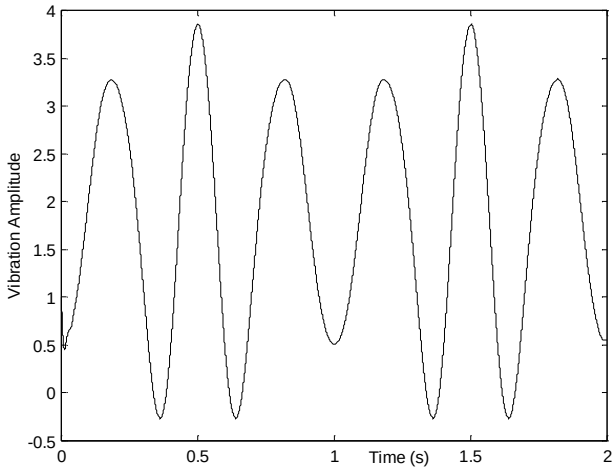


**Figure 5. 37** ODS of the plate around the circle where the laser beam scans.

### *5.4.4 Numerical Simulation on a Disc*

In the context of a vibrating circular disc, $V_{R\ n}$ and $V_{I\ n}$ represent spatially orthogonal, uniform cosine and sine, *n*-nodal diameter circumferential amplitude distributions. In fact, provided that the disc is axi-symmetric, its natural modes occur in pairs, with coincident natural frequencies and nodal diameters but orthogonal. This results from the solution of the equation describing the transverse vibration of an axi-symmetric thin disc, which is:

$$v_z(\theta,t) = V_{Rn}\cos(n\theta)\cos(\omega t) + V_{In}\sin(n\theta)\sin(\omega t) \qquad \textbf{(5. 38)}$$

$v_z$ being the circumferential mode shape including the mode pairs sine and cosine, and θ the circumferential coordinate.

Only when the disc has some slight asymmetry does the so-called mistuning phenomenon occur and the pairs of orthogonal modes appear at slightly different natural frequencies. They are then excited to different extents at both natural frequencies.

In any case, there is always a single value of $n$ and the response mode shape therefore has $n$ sinewaves around the circumference and $2n$ equispaced nodes. In Equation (5.32), the summation will disappear, existing for only a single value of $n$ and the same will happen for Equation (5.35) implicating that the CSLDV output spectrum will contain only one pair of sidebands at frequencies, $(\omega - n\Omega)$ and $(\omega + n\Omega)$, $\Omega$ being the scan speed of the laser beam around a circle on the periphery of the disc.

If $V_{In}$ is zero, so that the response mode shape is completely real and visualised as a pure standing wave fixed with respect to the disc (see Figure 5.38) the sideband amplitudes are equal (see the top plot in Figure 5.41).

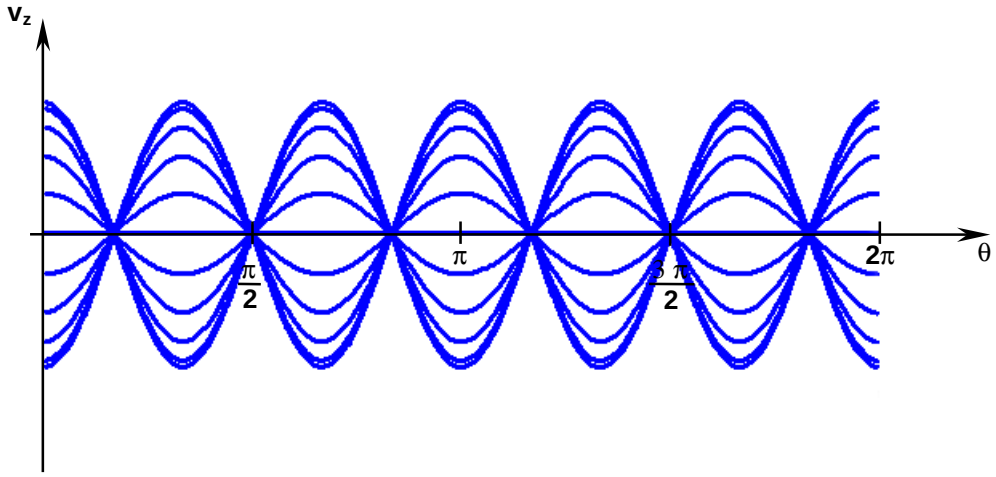


**Figure 5. 38** Standing wave on the disc circumference, case of 3-diameter mode.

If $V_{In}$ and $V_{Rn}$ are equal, the response is a uniform travelling wave (Figure 5.39) with all points around the circle experiencing the same vibration amplitude, and there is only one frequency component in the LDV spectrum - at $(\omega - n\Omega)$, see the central plot in Figure 5.41.

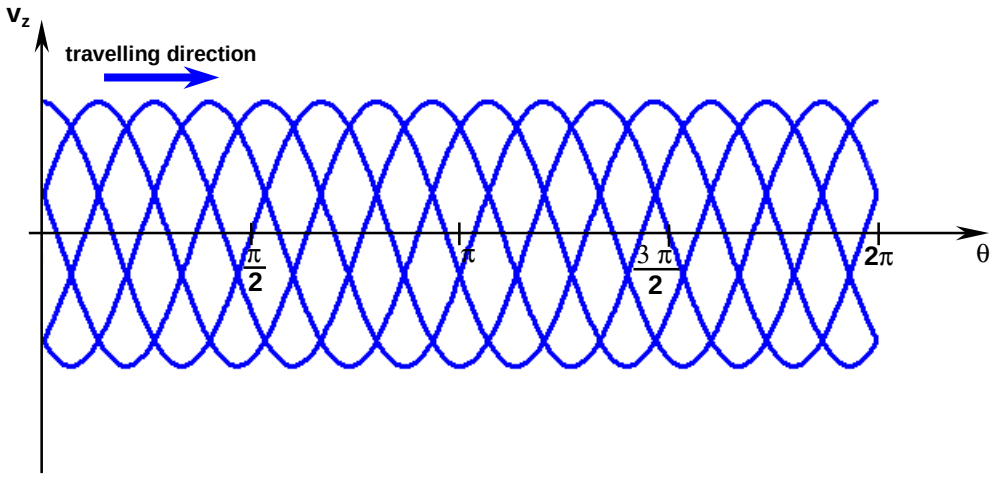


**Figure 5. 39** Travelling wave on the disc circumference, case of 3-diameter mode.

In Figure 5.40 a three-dimensional view of the travelling wave around the disc circumference is shown.

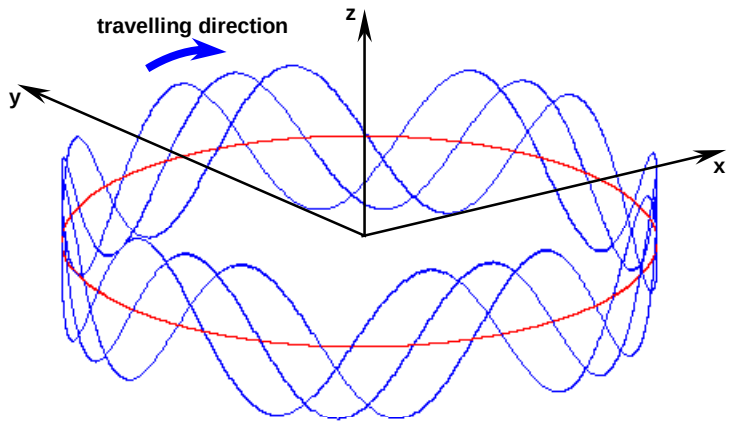


**Figure 5. 40** 2-D view of the travelling wave on the disc circumference.

If $V_{I\,n}$ and $V_{R\,n}$ assume different values the disc response will consists of a travelling and a standing wave. The LDV output spectrum appears, then, with two sidebands of different magnitudes at $(\omega - n\Omega)$ and $(\omega + n\Omega)$ and the amplitude difference give us an information about the percentage of the

contribution of the travelling wave to the whole complex ODS (see the bottom plot in Figure 5.41). In the pictures shown in Figure 5.41 it is assumed that the resonance frequency of the disc is 681 Hz and the ODS is a 3-diameter mode. If a scan frequency of 10 Hz is employed the sideband frequency are 651 and 711 Hz, when they occur both.

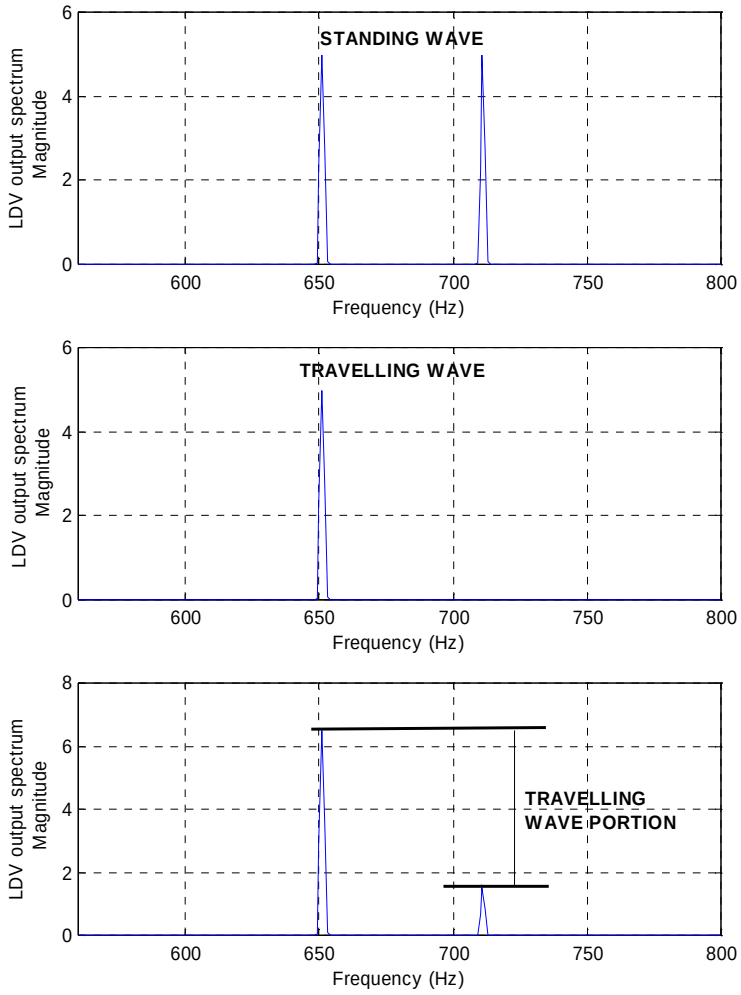


**Figure 5. 41** LDV output spectrum for $V_{In} = 0$ (top plot), $V_{In} = V_{Rn}$ (central plot) and $V_{In} \neq V_{Rn} \neq 0$ (bottom plot).

### *5.4.5 Experimental Investigation on a Disc*

The vibration of circular stationary discs has been studied using the circular-scanning LDV technique working through the same control, data acquisition and post-process program software developed in `LabVIEW` for the linear scanning described in subsection 5.3.2.2 and 5.3.3.3, with slight modifications.

It must be noted that a main source of systematic error, and one which can be difficult to calibrate out, is scan distortion. Input signal distortion or non-linearity in the LDV deflection mirror drive system may, in the case of "circular scan", produce distortion of the circular scan trace. This can be corrected but, even after such correction, it is difficult to guarantee that the circle is followed at precisely uniform rate.

The circular scanning technique was applied on a test piece that was taken from an application to the problems of disc-brake squeal, specifically a pin-on-disc rig, where an inclined pin is pressed against a rotating disc. If the pin arrangement is suitably adjusted, the disc will exhibit limit-cycle parametric vibration, the so-called 'squeal', even at very low speeds of rotation. The arrangement is simpler than for a vehicle brake disc assembly, there being, for instance, point contact rather than area contact where the pin and disc are pressed together. The phenomenon is essentially non-linear, being friction-induced, but the disc itself generally vibrates in a sinusoidal vibration with an *n*-diameter ODS. The disc has then been analysed under the condition of self-induced vibration due to the squeal excitation but also with discrete frequency input excitation by removing the pin and producing the input force via a shaker attached to the structure.

The disc tested was an aluminum 406 mm diameter and 25.4 mm thick uniform disc around whose circumference the LDV was set up to scan in a circle at 10 Hz rotational speed. In setting up the scanning, particular care must be taken of the alignment of the scan axis with the disc axis of rotation. In fact, the LDV measures the velocity of the point addressed, in the direction of the incident

measurement beam, which is not exactly perpendicular to the surface, the LDV being set up on the rotation axis of the disc. Therefore, it actually measures the vibration resolved onto an inclined line, but, since the angle involved is usually no more than about 10°, the correction is subsequently quite small. Of more importance it is the mentioned alignment if the measurement is to be made on a rotating disc, otherwise the LDV detects a proportion of the rotational velocity, apparent in the LDV output signal as a component at the LDV scan frequency. Disc peripheral speeds can be very high compared with the vibration velocities to be measured and this interference can be overwhelming unless the alignment is very precise.

First, the disc vibrating only under direct excitation was addressed; the schematic configuration of the experimental structure is sketched in Figure 5.42. The disc was excited at some of its resonance frequencies already known from a previous measurements campaign, and in particular these were chosen at 128, 130.9, 996, 1016, 2307, and 3887.68 Hz. Note that the lower frequencies appear in pairs and for each couple the same nodal diameter mode was excited. This means that the disc was slightly mistuned and the natural frequencies of each of the mode pairs did not coincide exactly. The spectrum amplitude for the above-listed frequencies are plotted in Figures 5.43, 5.44, 5.45 and 5.46 where in the first two pictures the coupled frequencies, 128 and 130.9 Hz, 996 and 1016 Hz are plotted together.

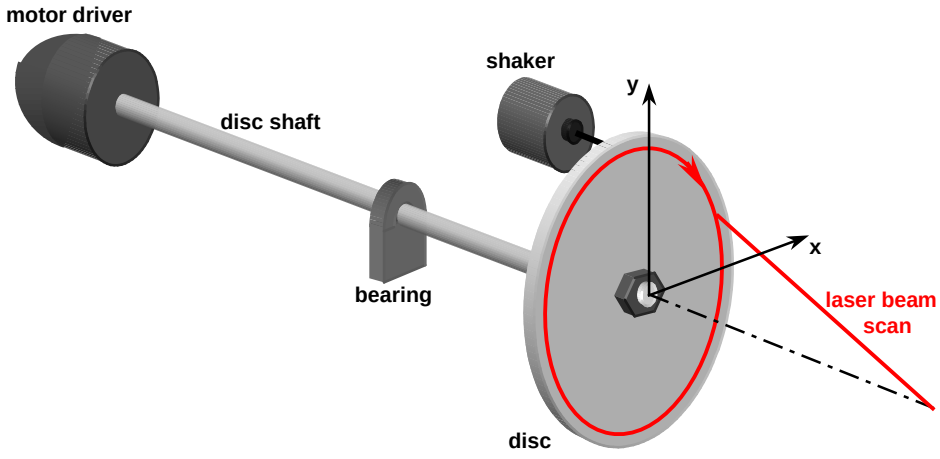


**Figure 5. 42** Disc under direct excitation (pin-on-disc rig).

As the first plot in Figure 5.43 shows, two sidebands of different amplitude occurred at 118 and 138 Hz, so that it can be recognised that the mode excited was the 1st diameter mode, as

$$n = \frac{\omega^{+} - \omega^{-}}{2\Omega} = 1 \qquad \textbf{(5. 39)}$$

where $\omega^{+}$ is the right sideband frequency (138 Hz), $\omega^{-}$ is the left sideband frequency (118 Hz) and $\Omega$ is the scan frequency (10 Hz). Since the sidebands' spectral amplitudes are different, the ODS is a combination of both the sine and cosine modes or, in other words, of forward and backward travelling waves, and it can then be concluded that the vibration is not a pure standing wave but combination of standing and travelling wave. This effect is even more evident when the excitation frequency is at 130.9 Hz, see second plot in Figure 5.43, where the contribution of the travelling wave is even larger (in fact, the difference of the sidebands' magnitude is larger).

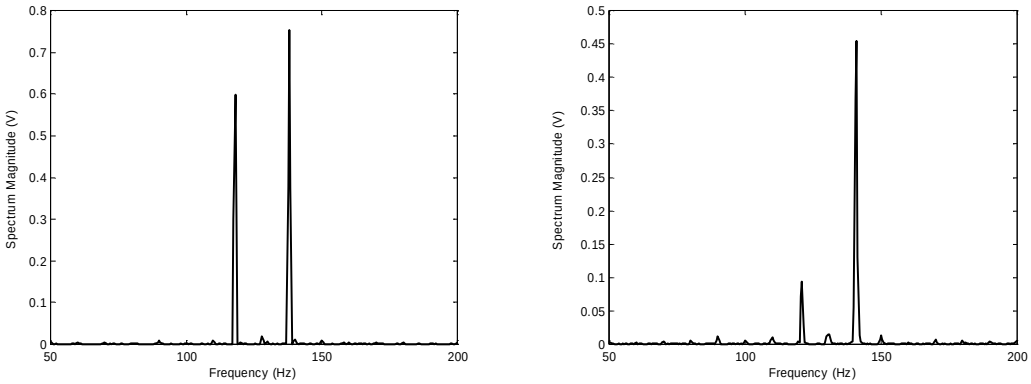


**Figure 5. 43** LDV spectrum amplitude (V) at the excitation frequency of 128 Hz (left) and 130.9Hz (right). 1-nodal diameter ODS.

In the first plot of Figure 5.44, it can be seen that excitation at 996 Hz forces a resonance with a 2-nodal diameter ODS, sidebands being at 976 and 1016 Hz, both of them apart from the central frequency by twice the scan speed.

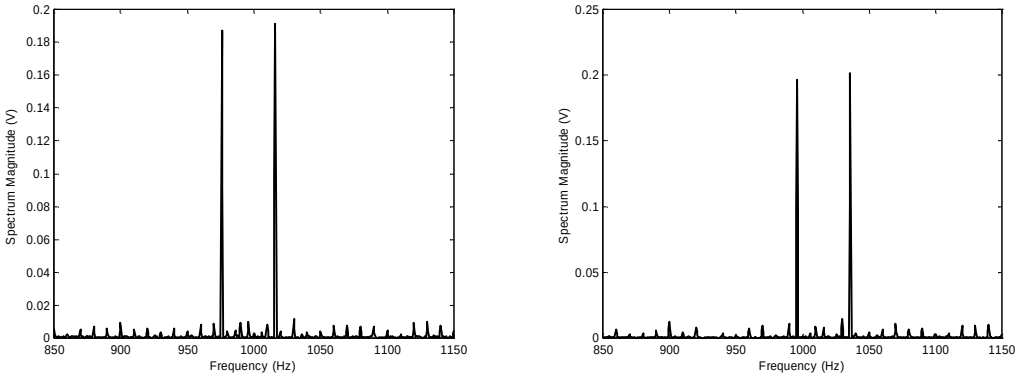


**Figure 5. 44** LDV spectrum amplitude (V) at the excitation frequency of 996 Hz (left) and 1016 Hz (right). 2-nodal diameter ODS.

Response sideband peaks at both the excitation frequencies of 996 and 1016 Hz have identical magnitude so that the corresponding ODSs are seen to be pure standing waves.

The third and fourth nodal diameter ODSs are excited, finally, at the frequencies of 2307 Hz and 3887.78 Hz and these are illustrated in Figures 5.45 and 5.46.

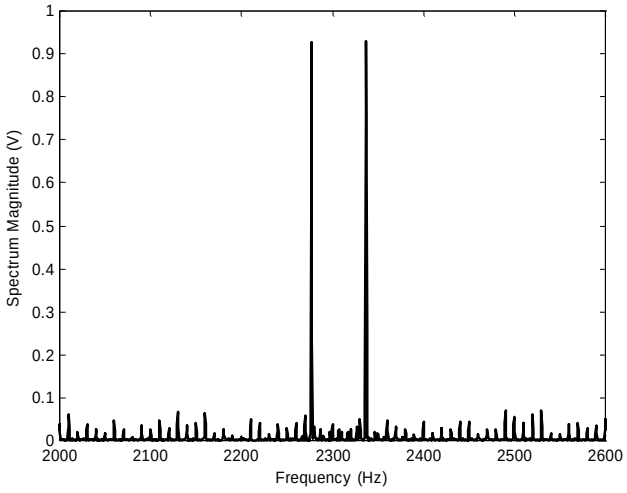


**Figure 5. 45** LDV spectrum amplitude (V) at the excitation frequency of 2307 Hz. 3-nodal diameter ODS.

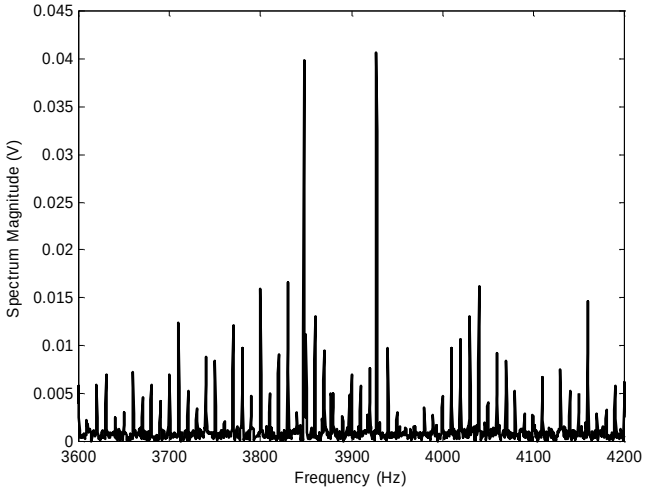


**Figure 5. 46** LDV spectrum amplitude (V) at the excitation frequency of 3887.68 Hz. 4-nodal diameter ODS.

Both the 3rd and 4th nodal diameter ODSs are pure standing waves, the sideband amplitudes being equal. From the LDV output spectrum shown in Figure 5.46 it can be noticed that the vibration amplitude at the resonance frequency of 3887.68 Hz was really low and the floor noise assumed more inportance.

The 3rd nodal diameter ODS at frequency of 2307 Hz is recovered following the mathematical procedure described in this section, strictly speaking Equation (5.35). From this it can be observed that the vibration velocity measured by the LDV contains the third component only ($n$ = 3). Then Equation (5.35) can be written as:

$$v_z(t) = \frac{V_{R3} + V_{I3}}{2}\cos(\omega - 3\Omega)t + \frac{V_{R3} - V_{I3}}{2}\cos(\omega + 3\Omega)t \qquad \textbf{(5. 40)}$$

where $\frac{V_{R3} + V_{I3}}{2}$ is the spectral amplitude at $(\omega - 3\Omega)$ = 2277 Hz and $\frac{V_{R3} - V_{I3}}{2}$ the spectral amplitude at $(\omega + 3\Omega)$ = 2337 Hz. Knowing the LDV sensitivity which is 5 mm/s/V the sideband amplitudes readable in Figure 5.45 can be expressed in terms of velocity:

$$A_{(\omega-3\Omega)} = A_{(\omega+3\Omega)} = 0.9286(V) \times 5\left(\frac{mm/s}{V}\right) = 4.6433\left(\frac{mm}{s}\right) \qquad \textbf{(5. 41)}$$

Then the polynomial coefficients $V_{R3}$ and $V_{I3}$ can be recovered from:

$$\begin{aligned} \frac{V_{R3} + V_{I3}}{2} &= 4.6433\left(\frac{mm}{s}\right) \\ \frac{V_{R3} - V_{I3}}{2} &= 4.6433\left(\frac{mm}{s}\right) \end{aligned} \qquad \textbf{(5. 42)}$$

so that,

$$V_{R3} = V_{I3} = 4.6433\left(\frac{mm}{s}\right) \qquad \textbf{(5. 43)}$$

Equation (5.38) then becomes:

$$v_z(\theta) = 4.6433\cos(3\theta) + 4.6433\sin(3\theta) \qquad \textbf{(5. 44)}$$

This equation represents the ODS along the circle scanned by the LDV and it is a pure standing wave, as depicted in Figure 5.47.

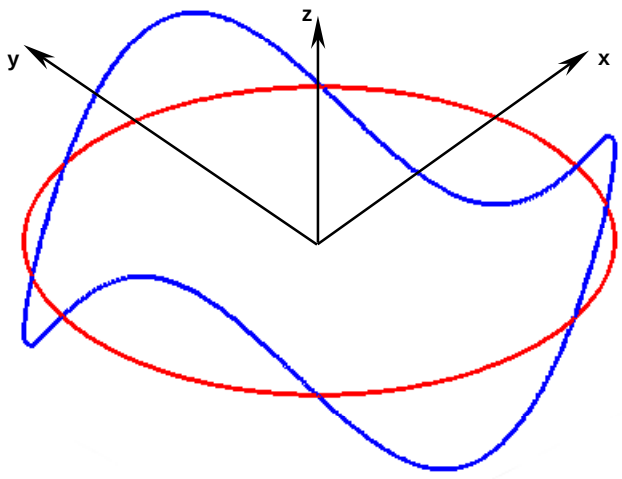


**Figure 5. 47** Standing wave along the scanning circle (3-nodal diameter ODS).

In the case of parametric excitation of the pin-on-disc rig (squeal), vibration is forced at the frequency of 2307 Hz and the involved ODS is then a standing wave fixed in space. The squeal was produced by pressing the pin against the disc rotating at 1.9 rpm (0.0317 Hz), see Figure 5.48.

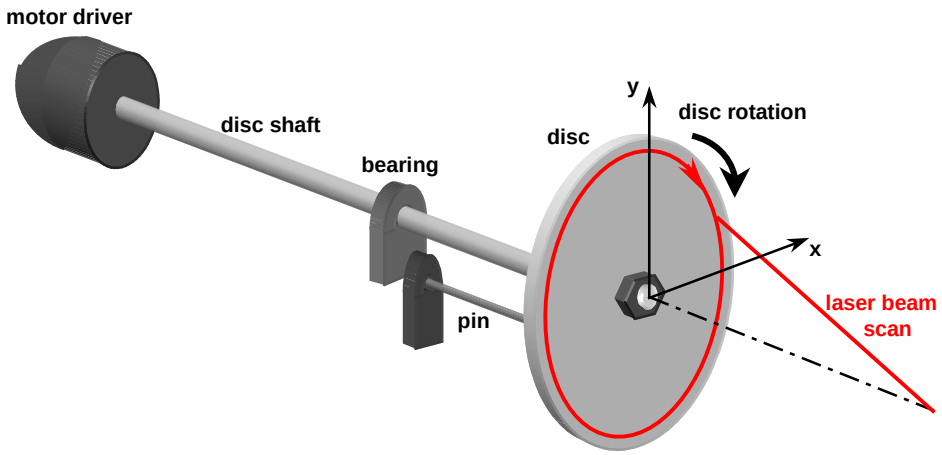


**Figure 5. 48** Pin-on-disc rig – "squeal" excitation.

Using again a circular LDV scan at 10 Hz, in the same direction of the disc rotation, the LDV squeal signal spectrum is acquired and it is virtually identical with the previous spectrum, for the case of shaker excitation, shown in Figure 5.45. The LDV time signal modulation was seen to be fixed in time relative to the mirror drive signals, Figure 5.49, with an anti-node at the pin contact position as Figure 5.50 clearly shows. The disc was therefore rotating slowly through a standing wave, which was fixed in the non-rotating frame of reference.

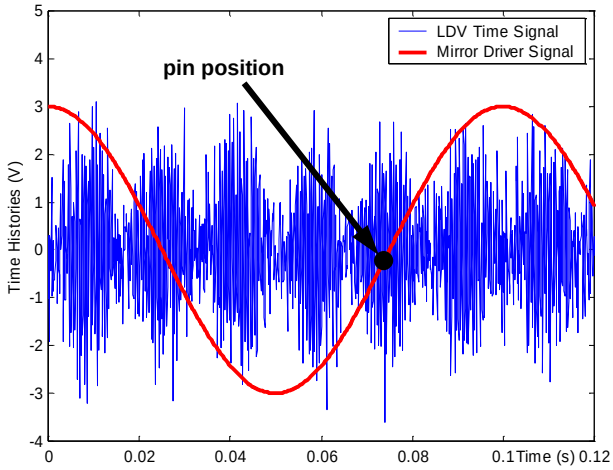


**Figure 5. 49** LDV Time signal and mirror drive signal.

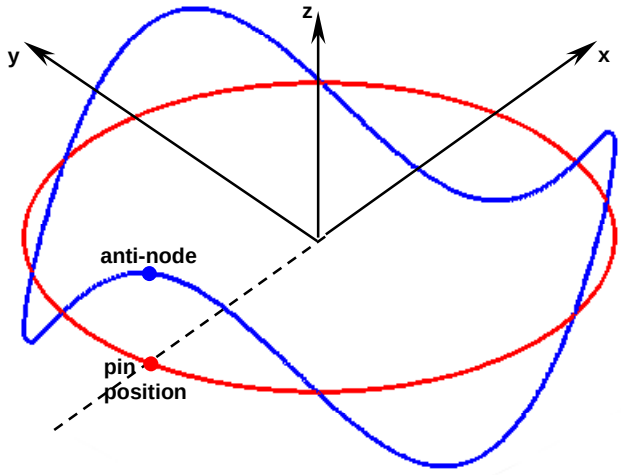


**Figure 5.50** 3-nodal diameter ODS at 2307 Hz. Standing wave with an antinode at the pin position.

This technique can be extended to the measurements of vibration of rotating discs, provided proper account is taken of the relative motion, since the response frequencies are modified by the disc rotation. In fact, if the disc is rotating at an angular speed $\Omega_D$ , assuming that is possible to apply sinusoidal vibration to it from a fixed point in space (such a kind of excitation can be realised in operating machines via non-contacting sources as magnetic fields or

aerodynamic forces), and if the applied excitation is at frequency ω, in the non-rotating frame of reference, *n*-diameter ODSs are excited, in the local, rotating disc coordinates at two distinct frequencies ($\omega \pm n\Omega_D$). Equation (5.38), will then contain four components:

$$\begin{aligned} v_z(\theta,t) = V_{Rn}^- \cos(n\theta)\cos[(\omega - n\Omega_D)\,t] + V_{Rn}^+ \cos(n\theta)\cos[(\omega + n\Omega_D)\,t] + \\ + V_{In}^- \sin(n\theta)\sin[(\omega - n\Omega_D)\,t] + V_{In}^+ \sin(n\theta)\sin[(\omega + n\Omega_D)\,t] \end{aligned} \quad \textbf{(5. 45)}$$

θ being the angular position of a point along the circumference of the disc. If the LDV laser beam scans around the circumference at an absolute speed $\Omega_L$, the laser beam angular position relative to the disc at the time instant *t* will be:

$$\theta = (\Omega_L - \Omega_D)t \quad \textbf{(5. 46)}$$

Substituting Equation (5.46) into (5.45) and expanding trigonometrically it will become:

$$\begin{aligned} v_z(\theta,t) = & \frac{V_{Rn}^- + V_{In}^-}{2}\cos[(\omega - n(2\Omega_D - \Omega_L))\,t] + \\ & + \frac{V_{Rn}^- - V_{In}^-}{2}\cos[(\omega - n\Omega_L)\,t] + \\ & + \frac{V_{Rn}^+ + V_{In}^+}{2}\cos[(\omega + n\Omega_L)\,t] + \\ & \frac{V_{Rn}^+ - V_{In}^+}{2}\cos[(\omega + n(2\Omega_D - \Omega_L))\,t] \end{aligned} \quad \textbf{(5. 47)}$$

As result, there are four frequency components in the SLDV output spectrum for each diametral order. They appear as sidebands, spaced by multiples of the laser beam speed relative to the disc, *n* ($\Omega_L - \Omega_D$), centered on the disc frequency ($\omega \pm n\Omega_D$). From the spectral component values, the unknown vibration amplitudes, $V_{Rn}^+$, $V_{Rn}^-$, $V_{In}^+$, $V_{In}^-$ can be easily recovered.

In many practical cases, excitation is due to steady forces fixed in a stationary frame of reference, i.e. $\omega = 0$, so that the disc experiences vibration at frequency $n\Omega_D$ and responses appear at frequencies $n\Omega_L$ and $n\ (2\Omega_D - \Omega_L)$. With a symmetrical disc, if $n\Omega_D$ coincides with a natural frequency, a backward travelling wave will be set up in the disc, or a standing wave in the non-rotating frame of reference. This is the so-called "critical speed" condition.

## *5.5. Analysis of Area Scan*

### *5.5.1 Introduction*

Out-of-plane vibration response ODS recovery by applying the CSLDV technique, can be extended to more general two-dimensional scans than the circular scan described in Section 5.4. Operational mode shapes of a rectangular or circular area vibrating under a sinusoidal excitation can be conveniently measured by scanning over the whole area. As for the linear scan, the technique can be divided into two main branches: a continuous scan at uniform speed, where the mode shape is directly recovered by demodulation, and a continuous sinusoidal scan, where the ODS, being approximated by a polynomial, the relevant series coefficients are derived from the LDV spectral components at the known discrete frequencies.

The process, involving the demodulation of the LDV output signal can be applied to any vibrating surface but, since the ODS is directly obtained from the LDV time history, the data pollution effect of speckle noise may be severe. To minimise the speckle, the uniform scan speed must, then, kept low. In order to have enough information from the LDV time history, the acquisition time must be sufficient for the laser beam to cover all the surface and consequently the acquisition can become very long. Moreover, a large amount of data may be generated by using the uniform scanning technique.

Alternatively, the sinusoidal area scan can be employed bearing in mind that its validity applies only if the mode shape is spatially smooth and without any

discontinuities, like, for instance, apertures or sudden changes in section, within the scanned area. The particular advantage of this technique is that the ODS can be represented by a smaller data set which consists of the polynomial coefficients only.

The various test techniques were proven to work in practice with reference to a simple test piece as the beam was for the linear scan. This consists of a cantilevered steel plate 172 × 225 × 1 mm thick excited at some of the specific frequencies where the response was maximum, by a small electro-dynamic shaker attached off-center to the structure, see Figure 5.51. The plate was the same as the one used for the test described in Chapter 3 (Section 3.6) but, in this case it was clamped more deeply and, therefore, the results obtained were different. In order to validate the continuous-scanning technique the plate was first tested using the PSV200 software in its conventional mode: a discrete LDV scan on a grid of points covering the structure surface in reasonable detail. The plate was excited in a range of frequencies between 0 and 2 kHz, using a pseudo-random excitation and the laser was scanned step-by-step in a grid of 546 points (see Figure 5.52).

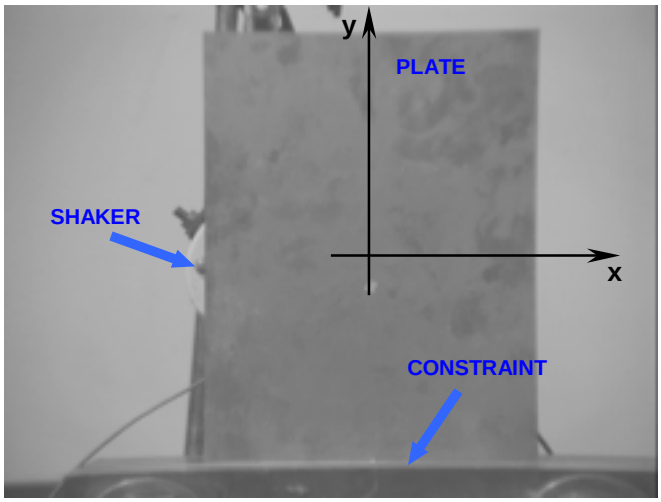


**Figure 5. 51** Experimental configuration.

After the measurement acquisition (which took almost three hours) was completed, the velocity patterns were derived at the resonant frequencies by

using the standard PSV200 presentation module. A transfer FRF measured between the points **A** and **B** (excitation position) - shown in Figure 5.52 - is depicted in Figure 5.53. Only the ODSs at some resonances, corresponding to the ones analysed by the continuous scanning techniques were taken into consideration.

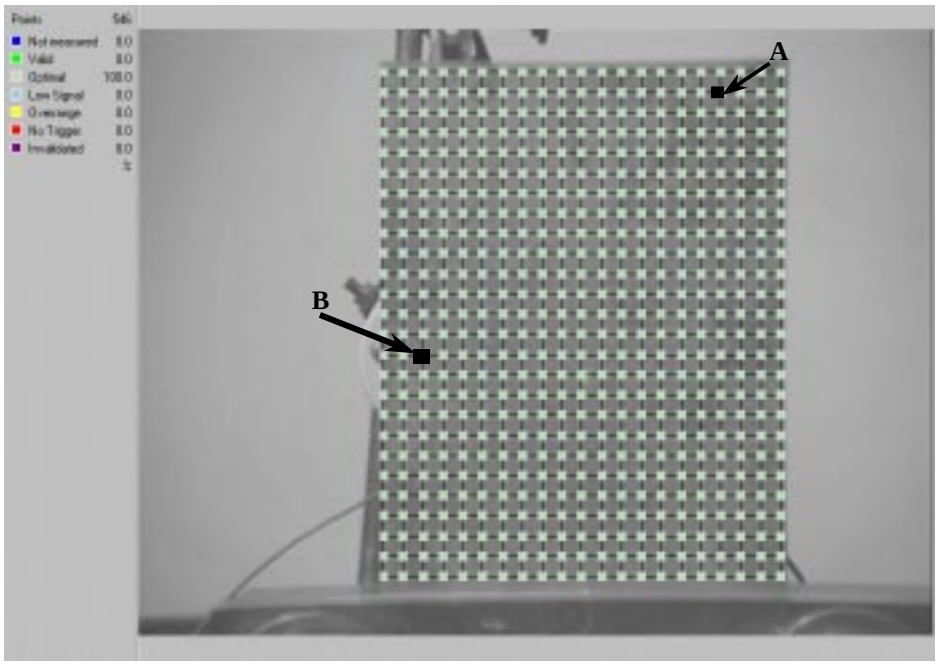


**Figure 5. 52** Measurement points grid.

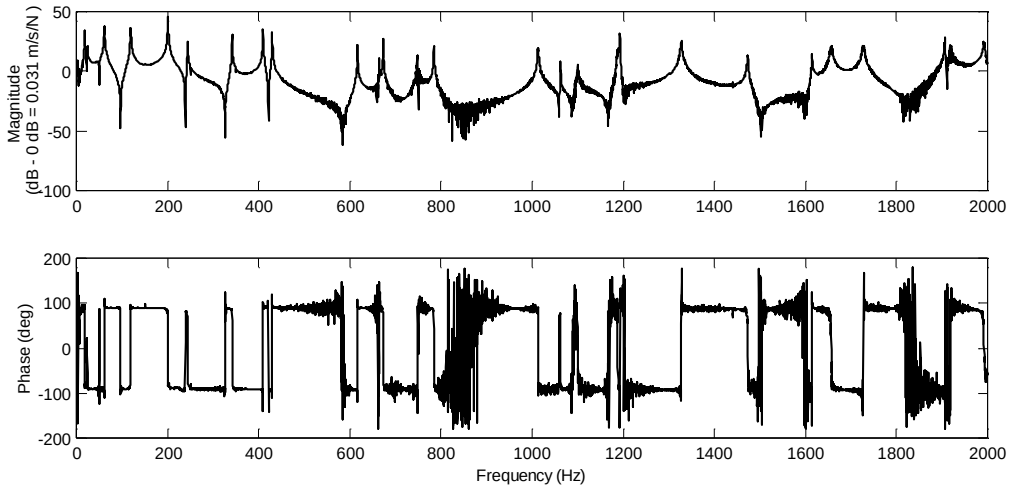


**Figure 5. 53** Transfer FRF at point **A** on the plate.

Resonant frequencies investigated were these at 202.5, 241.25 and 628.8 Hz.

### *5.5.2 Two-Dimensional Uniform Scan*

In making the laser beam scan at a uniform rate, parallel to one side of a rectangular surface, and simultaneously at a slower uniform rate, parallel to its other side, the whole area will be covered with a spatial resolution depending on the data acquisition sampling rate and the two scan rates. In fact, if the slowest scan frequency is, say, 0.01 Hz, the laser beam will perform a complete scan in 50 seconds (one pass over the line scanned) and the acquisition of the LDV output signal must last at least 50 seconds. Since the acquisition time is determined by the ratio between the number of samples acquired and the acquisition sampling rate, the number of samples, namely the ODS spatial resolution, will be 50 times the sample rate. The slower the scan rate, the larger is the spatial resolution, but the acquisition becomes more time consuming. Demodulating the LDV time history a two-dimensional ODS is derived with the spatial position being the time axis. If the demodulated signal is then plotted against the mirrors' drive signals, recorded simultaneously with the LDV output, since they represent the laser spot spatial position over the surface at each time instant, a three-dimensional surface representing the ODS can be visualised.

The procedure followed for demodulation is the same as that described in Subsection 5.3.2 ( Equation (5.7) ) for a one-dimensional scan, the only difference with the latter is the presentation of results, since the demodulated signal is now plotted against two spatial position vectors defined by the mirrors drive time signals.

As an example, the cantilever plate depicted in Figure 5.51 was analysed under a sinusoidal excitation at 628.8 Hz. Mirrors, driving the laser beam to scan over the surface of the plate, were fed via two triangular waves in order to force the laser spot to sweep the *x*-axis at a uniform rate of 0.12 Hz and the *y*-axis at 7 Hz. The pattern followed by the laser beam across the plate's surface is visualised in Figure 5.54.

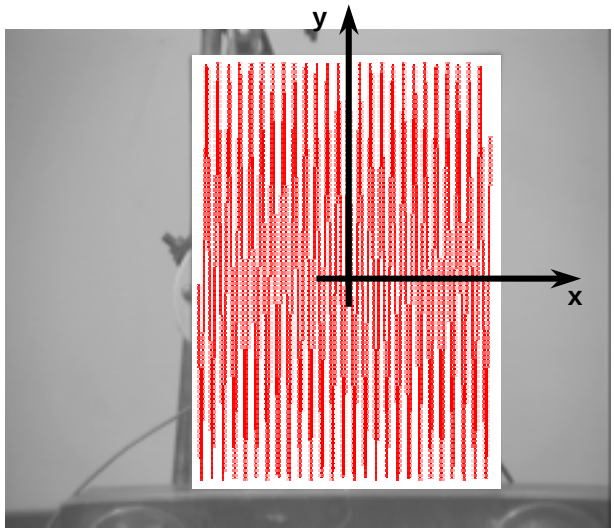


**Figure 5. 54** Scan pattern over the plate.

Under these conditions the laser will take 4.1667 s to perform a complete scan (in one go) along *x*. Within this time it will cover several lines along the *y*-direction since it needs only 0.0714 s to perform a scan along *y*, specifically the number of lines travelled will be $\frac{4.1667\,s}{0.0714\,s} = 58.33 \approx 58$. The response ODS derived is shown in Figure 5.55, where only the real component is plotted since the ODS was almost exactly real and the imaginary part was, then, negligible.

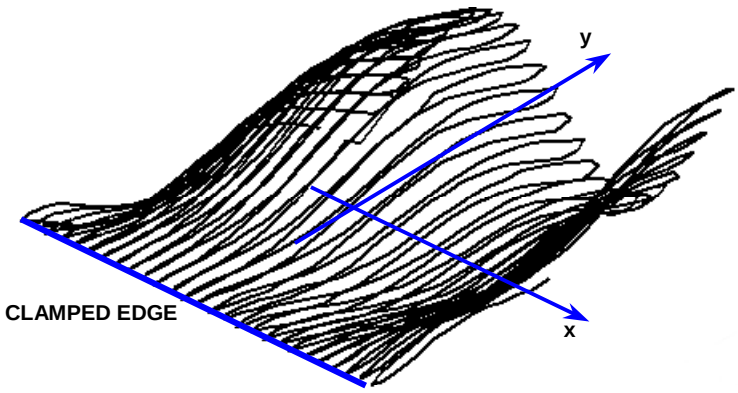


**Figure 5. 55** ODS from demodulation of the LDV output signal with the laser beam scanning at uniform rate across the plate surface.

### *5.5.3 Sinusoidal Parallel Straight-Line Scans*

The sinusoidal scanning technique can also be applied to area scans, where the easiest way to do it is to make the laser beam to scan on a set of parallel lines along which polynomial mode shapes can be defined. The method straightforwardly applies the sinusoidal straight-line scanning technique (Subsection 5.3.3 and Equation (5.15) ), the line scanned being parallel to the *y*-axis but, in addition, this technique is repeated for several parallel lines evenly spaced in the *x*-direction in order to cover all area of the specimen under test. Plotting in the same diagram the polynomial ODS recovered along each of these lines, a two-dimensional picture representing the global ODS of the structure is obtained.

As an example, the usual plate, vibrating at the same excitation frequency of 628.8 Hz, was studied and twenty straight-lines parallel to the *y*-axis were scanned at a rate of 10 Hz on its surface. From each scan the LDV time signals were acquired and curve fitted at the set of frequencies given by $(\omega \pm n\Omega)$ with $n = 0...p$ and $p$ the polynomial order. From the spectral amplitudes at these frequencies ($A_n$), applying Equation (5.15), the polynomial coefficients ($V_n$) were derived and, plotting the ODSs together in a same diagram, Figure 5.56 was obtained. Again only one plot is shown, the ODS being almost exactly real.

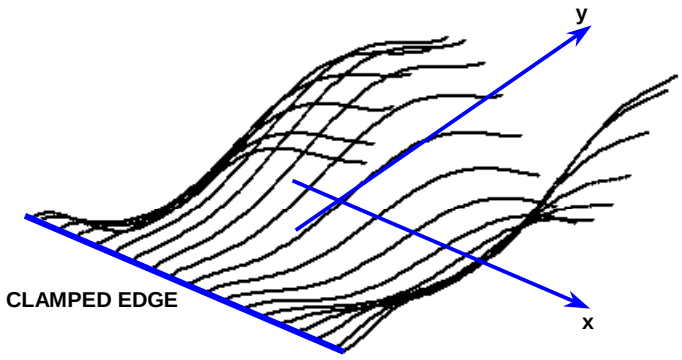


**Figure 5. 56** Polynomial ODSs recovered from the LDV output signal in the frequency domain with the laser beam scanning sinusoidally along a set of parallel straight-lines covering the plate surface.

For example, when the first line was scanned the LDV output spectral amplitudes at ($628.8 \pm n\ 10$), where $n = 0...6$ , transformed by the matrix [T] gave a set of coefficients series which could be written as the following $6^{th}$ order polynomial expression:

$$v(y) = 0.9254 + 2.7827y + 6.5628y^2 - 1.1782y^3 - 10.0128y^4 + 0.3760y^5 + 4.5248y^5 \quad \textbf{(5. 48)}$$

A similar expression can be derived for each LDV output acquired.

### *5.5.4 Two-Dimensional Sinusoidal Scans*

#### *5.5.4.1 Mathematical Investigation*

From the parallel straight lines technique, it can be concluded that, instead of plot a different set of one-dimensional polynomial series together, which requires one to perform a number of measurements corresponding to the number of line scans realised, a two-dimensional polynomial can be obtained directly in one measurement.

In order to perform an area scan, the laser beam of an LDV must scan at frequency of $\Omega_x$ in *x*-direction and a frequency of $\Omega_y$ in *y*-direction. If these two frequencies are not fractionally related - and they must be so, as it will be explained later - the scan describes an open Lissajou figure over the scanned area which can be completely covered after a conveniently short time period. In order to sweep a normalised area of dimensions $2 \times 2$, with the zero position the center of the square, the mirror drivers should be fed by two sinewaves of equations:

$$x(t)=\cos(\Omega_x t)$$
$$y(t)=\cos(\Omega_y t) \qquad \textbf{(5. 49)}$$

The complex amplitudes of the ODS appearing in Equation (5.1) can be written as two-dimensional polynomial series:

$$V_R(x,y)=\sum_{n,m=0}^{p,q} V_{Rn,m}\, x^n y^m$$
$$V_I(x,y)=\sum_{n,m=0}^{p,q} V_{In,m}\, x^n y^m \qquad \textbf{(5. 50)}$$

*p* and *q* being the polynomial order in *x*- and *y*-direction respectively.
The vibration velocity, following the principle of Equation (5.1), translated to a two-dimensional structure, becomes:

$$v_z(x,y;t)=V_R(x,y)\cos(\omega t)+V_I(x,y)\sin(\omega t) \qquad \textbf{(5. 51)}$$

Substituting Equation (5.49) in (5.50) and again in (5.51), Equation (5.51) itself can be rewritten as:

$$v_z(t)=\sum_{n,m=0}^{p,q} V_{Rn,m}\cos^n(\Omega_x t)\cos^m(\Omega_y t)\cos(\omega t)+\sum_{n,m=0}^{p,q} V_{In,m}\cos^n(\Omega_x t)\cos^m(\Omega_y t)\sin(\omega t) \qquad \textbf{(5. 52)}$$

Expanding out trigonometrically, as was done for the linear scan mathematics in Subsection 5.3.3.1, the following representation of the vibration signal is derived:

$$v_z(t)=\sum_{n,m=0}^{p,q} A_{Rn,m}\cos\left[\left(\omega \pm n\Omega_x \pm m\Omega_y\right)t\right]+\sum_{n,m=0}^{p,q} A_{In,m}\sin\left[\left(\omega \pm n\Omega_x \pm m\Omega_y\right)t\right] \qquad \textbf{(5. 53)}$$

It can be deduced that the transformation to recover the polynomial coefficients from the spectral amplitudes of the LDV output is:

$$\begin{aligned}\{V_R\}&=[T]\{A_R\}[T]^T\\ \{V_I\}&=[T]\{A_I\}[T]^T\end{aligned} \qquad \textbf{(5. 54)}$$

The previous equation can be demonstrated by expanding, again, the relationship (5.52), considering $n$ = 0...3 and $m$ = 0...3.

| | | | | |
|---|---|---|---|---|
| *for* | $n=0$ | *and* | $m=0$ | $V_{R00}\cos(\omega t)$ |
| *for* | $n=0$ | *and* | $m=1$ | $\frac{V_{R01}}{2}\cos[(\omega\pm\Omega_y)t]$ |
| *for* | $n=0$ | *and* | $m=2$ | $\frac{V_{R02}}{4}\cos[(\omega\pm 2\Omega_y)t]+\frac{V_{R02}}{2}\cos(\omega t)$ |
| *for* | $n=0$ | *and* | $m=3$ | $\frac{V_{R03}}{8}\cos[(\omega\pm 3\Omega_y)t]+\frac{3V_{R03}}{8}\cos[(\omega\pm\Omega_y)t]$ |
| *for* | $n=1$ | *and* | $m=0$ | $\frac{V_{R10}}{2}\cos[(\omega\pm\Omega_x)t]$ |
| *for* | $n=1$ | *and* | $m=1$ | $\frac{V_{R11}}{4}\cos[(\omega\pm\Omega_x\pm\Omega_y)t]$ |
| *for* | $n=1$ | *and* | $m=2$ | $\frac{V_{R12}}{8}\cos[(\omega\pm\Omega_x\pm 2\Omega_y)t]+\frac{V_{R12}}{4}\cos[(\omega\pm\Omega_x)t]$ |
| *for* | $n=1$ | *and* | $m=3$ | $\frac{V_{R13}}{16}\cos[(\omega\pm\Omega_x\pm 3\Omega_y)t]+\frac{3V_{R13}}{16}\cos[(\omega\pm\Omega_x\pm\Omega_y)t]$ |
| *for* | $n=2$ | *and* | $m=0$ | $\frac{V_{R20}}{4}\cos[(\omega\pm 2\Omega_x)t]+\frac{V_{R20}}{2}\cos(\omega t)$ |
| *for* | $n=2$ | *and* | $m=1$ | $\frac{V_{R21}}{8}\cos[(\omega\pm 2\Omega_x\pm\Omega_y)t]+\frac{V_{R21}}{4}\cos[(\omega\pm\Omega_y)t]$ |
| *for* | $n=2$ | *and* | $m=2$ | $\frac{V_{R22}}{16}\cos[(\omega\pm 2\Omega_x\pm 2\Omega_y)t]+\frac{V_{R22}}{8}\cos[(\omega\pm 2\Omega_x)t]+$ $+\frac{V_{R22}}{8}\cos[(\omega\pm 2\Omega_y)t]+\frac{V_{R22}}{4}\cos(\omega t)$ |
| *for* | $n=2$ | *and* | $m=3$ | $\frac{V_{R23}}{32}\cos[(\omega\pm 2\Omega_x\pm 3\Omega_y)t]+\frac{3V_{R23}}{32}\cos[(\omega\pm 2\Omega_x\pm\Omega_y)t]+$ $+\frac{V_{R23}}{16}\cos[(\omega\pm 3\Omega_y)t]+\frac{3V_{R23}}{16}\cos[(\omega\pm\Omega_y)t]$ |
| *for* | $n=3$ | *and* | $m=0$ | $\frac{V_{R30}}{8}\cos[(\omega\pm 3\Omega_x)t]+\frac{3V_{R30}}{8}\cos[(\omega\pm\Omega_x)t]$ |
| *for* | $n=3$ | *and* | $m=1$ | $\frac{V_{R31}}{16}\cos[(\omega\pm 3\Omega_x\pm\Omega_y)t]+\frac{3V_{R31}}{16}\cos[(\omega\pm\Omega_x\pm\Omega_y)t]$ |

$$\textit{for} \quad n=3 \quad \textit{and} \quad m=2 \qquad \frac{V_{R32}}{32}\cos\left[\left(\omega \pm 3\Omega_x \pm 2\Omega_y\right)t\right]+\frac{V_{R32}}{16}\cos\left[\left(\omega \pm 3\Omega_x\right)t\right]+$$
$$\frac{3V_{R32}}{32}\cos\left[\left(\omega \pm \Omega_x \pm 2\Omega_y\right)t\right]+\frac{3V_{R32}}{16}\cos\left[\left(\omega \pm \Omega_x\right)t\right]$$

$$\textit{for} \quad n=3 \quad \textit{and} \quad m=3 \qquad \frac{V_{R33}}{64}\cos\left[\left(\omega \pm 3\Omega_x \pm 3\Omega_y\right)t\right]+\frac{3V_{R33}}{64}\cos\left[\left(\omega \pm 3\Omega_x \pm \Omega_y\right)t\right]+$$
$$\frac{3V_{R33}}{64}\cos\left[\left(\omega \pm \Omega_x \pm 3\Omega_y\right)t\right]+\frac{9V_{R33}}{64}\cos\left[\left(\omega \pm \Omega_x \pm \Omega_y\right)t\right]$$

The LDV output spectrum will then have components at the frequencies ($\omega \pm n\Omega_x \pm m\Omega_y$) with the following amplitudes, called $A_{nm}$:

$$\textit{at} \quad \omega \qquad A_{R00}=V_{R00}+\frac{V_{R02}}{2}+\frac{V_{R20}}{2}+\frac{V_{R22}}{4}$$

$$\textit{at} \quad \omega \pm \Omega_y \qquad A_{R01}=\frac{V_{R01}}{2}+\frac{3V_{R03}}{8}+\frac{V_{R21}}{4}+\frac{3V_{R23}}{16}$$

$$\textit{at} \quad \omega \pm 2\Omega_y \qquad A_{R02}=\frac{V_{R02}}{4}+\frac{V_{R22}}{8}$$

$$\textit{at} \quad \omega \pm 3\Omega_y \qquad A_{R03}=\frac{V_{R03}}{8}+\frac{V_{R23}}{16}$$

$$\textit{at} \quad \omega \pm \Omega_x \qquad A_{R10}=\frac{V_{R10}}{2}+\frac{V_{R12}}{2}+\frac{3V_{R30}}{8}+\frac{3V_{R32}}{16}$$

$$\textit{at} \quad \omega \pm \Omega_x \pm \Omega_y \qquad A_{R11}=\frac{V_{R11}}{4}+\frac{3V_{R13}}{16}+\frac{3V_{R31}}{16}+\frac{9V_{R33}}{64}$$

$$\textit{at} \quad \omega \pm \Omega_x \pm 2\Omega_y \qquad A_{R12}=\frac{V_{R12}}{8}+\frac{3V_{R32}}{32}$$

$$\textit{at} \quad \omega \pm \Omega_x \pm 3\Omega_y \qquad A_{R13}=\frac{V_{R13}}{16}+\frac{3V_{R33}}{64}\,at$$

$$\textit{at} \quad \omega \pm 2\Omega_x \qquad A_{R20}=\frac{V_{R20}}{4}+\frac{V_{R22}}{8}$$

$$\textit{at} \quad \omega \pm 2\Omega_x \pm \Omega_y \qquad A_{R21}=\frac{V_{R21}}{8}+\frac{3V_{R23}}{32}$$

$$\textit{at} \quad \omega \pm 2\Omega_x \pm 2\Omega_y \qquad A_{R22}=\frac{V_{R22}}{16}$$

$$\textit{at} \quad \omega \pm 2\Omega_x \pm 3\Omega_y \qquad A_{R23}=\frac{V_{R23}}{32}$$

$$\textit{at} \quad \omega \pm 3\Omega_x \qquad A_{R30}=\frac{V_{R30}}{8}+\frac{V_{R32}}{16}$$

$$at \qquad \omega \pm 3\Omega_x \pm \Omega_y \qquad A_{R31} = \frac{V_{R31}}{16} + \frac{3V_{R33}}{64}$$

$$at \qquad \omega \pm 3\Omega_x \pm 2\Omega_y \qquad A_{R32} = \frac{V_{R32}}{32}$$

$$at \qquad \omega \pm 3\Omega_x \pm 3\Omega_y \qquad A_{R33} = \frac{V_{R33}}{64}$$

which can be written as

$$\begin{bmatrix} A_{00} & A_{01} & A_{02} & A_{03} \\ A_{10} & A_{11} & A_{12} & A_{13} \\ A_{20} & A_{21} & A_{22} & A_{23} \\ A_{30} & A_{31} & A_{32} & A_{33} \end{bmatrix} = \begin{bmatrix} 1 & 0 & 1/2 & 0 \\ 0 & 1/2 & 0 & 3/8 \\ 0 & 0 & 1/4 & 0 \\ 0 & 0 & 0 & 1/8 \end{bmatrix} \begin{bmatrix} V_{00} & V_{01} & V_{02} & V_{03} \\ V_{10} & V_{11} & V_{12} & V_{13} \\ V_{20} & V_{21} & V_{22} & V_{23} \\ V_{30} & V_{31} & V_{32} & V_{33} \end{bmatrix} \begin{bmatrix} 1 & 0 & 0 & 0 \\ 0 & 1/2 & 0 & 0 \\ 1/2 & 0 & 1/4 & 0 \\ 0 & 3/8 & 0 & 1/8 \end{bmatrix}$$

The polynomial coefficients matrix can then be derived:

$$\begin{bmatrix} V_{00} & V_{01} & V_{02} & V_{03} \\ V_{10} & V_{11} & V_{12} & V_{13} \\ V_{20} & V_{21} & V_{22} & V_{23} \\ V_{30} & V_{31} & V_{32} & V_{33} \end{bmatrix} = \begin{bmatrix} 1 & 0 & -2 & 0 \\ 0 & 2 & 0 & -6 \\ 0 & 0 & 4 & 0 \\ 0 & 0 & 0 & 8 \end{bmatrix} \begin{bmatrix} A_{00} & A_{01} & A_{02} & A_{03} \\ A_{10} & A_{11} & A_{12} & A_{13} \\ A_{20} & A_{21} & A_{22} & A_{23} \\ A_{30} & A_{31} & A_{32} & A_{33} \end{bmatrix} \begin{bmatrix} 1 & 0 & 0 & 0 \\ 0 & 2 & 0 & 0 \\ -2 & 0 & 4 & 0 \\ 0 & -6 & 0 & 8 \end{bmatrix}$$

where the first numeric matrix appearing, in the left-hand-side of the algebraic equation, is a truncation of the transform matrix [T] ( see Equation (5.16) ) and the second matrix is its transpose.

### *5.5.4.2 Numerical Simulation*

#### *5.5.4.2.1 Real Vibration Response*

In order to predict how the output time signal of an LDV will appear when it scans over the surface of a plate vibrating at one of its natural frequencies, a simulation of this situation will be performed. First, analytical mode shapes of

the plate used as an experimental specimen will be calculated together with the associated natural frequencies, then one of this modes will be approximated by a polynomial in order to derive the coefficients series to be inserted in Equation (5.52) and to derive the LDV time history.

Since this analysis is coming from an analytical calculation, the mode shape is completely real, and therefore only the first sum appearing in Equation (5.52) will be taken into account, each imaginary coefficient $V_{In,m}$ being zero.

Within the analytical derivation, natural frequencies and mode shapes were calculated with reference to the plate shown in Figure 5.51. Natural frequencies were determined from the frequency parameters λ given by:

$$\lambda = 2\pi\omega b^2\sqrt{\frac{\rho h}{D}} \qquad \textbf{(5. 55)}$$

where ω is the natural frequency in Hz, *b* is the length of the cantilever side of the plate (172 mm), ρ is the mass density per unit of volume of the plate (6040 $kg/m^3$ for steel material), *h* is the thickness of the plate (1 mm), and *D* the flexural rigidity defined as:

$$D = \frac{Eh^3}{12(1-\nu^2)} \qquad \textbf{(5. 56)}$$

*E* being the Young's modulus (2.2 $10^{11}$ $N/m^2$ for steel), and ν the Poisson's ratio assumed to be 0.3.

Frequency parameters can be found in literature [38] for a rectangular canteliver plate, with aspect ratio *b/a* of 0.75, *a* and *b* being the plate dimensions, specifically *b* is the length of the cantilever edge, i.e. *a* = 224 mm and *b* = 172 mm. Table 5.7 summarises the analytical values of natural frequencies obtained

from the frequency parameters taken from references which are also illustrated in this table.

| MODE | Reference | Frequency Parameter λ | Natural Frequency ω (Hz) |
|---|---|---|---|
| **1** | Table 4.51 – symmetric mode | 1.946 | 19.21 |
| **2** | Table 4.52 – antisymmetric mode | 5.99 | 58.85 |
| **3** | Table 4.51 – symmetric mode | 12.09 | 118.79 |
| **4** | Table 4.52 – antisymmetric mode | 20.6 | 202.40 |
| **5** | Table 4.51 – symmetric mode | 24.7 | 242.68 |

**Table 5. 7** Analytical values of natural frequencies.

The mode shapes equation is given in literature, [38]:

$$w(x,y)=\sum_{m=1}^{p}\left\{A_{m1}+A_{m2}\sqrt{3}\left(1-2\frac{y}{a}\right)+\sum_{n=3}^{q}A_{mn}\left[\cosh\frac{\varepsilon_n y}{b}+\cos\frac{\varepsilon_n y}{b}-\alpha_n\left(\sinh\frac{\varepsilon_n y}{b}+\sin\frac{\varepsilon_n y}{b}\right)\right]\right\}\times$$
$$\times\left[\cosh\frac{\varepsilon_m x}{a}-\cos\frac{\varepsilon_m x}{a}-\alpha_m\left(\sinh\frac{\varepsilon_m x}{a}-\sin\frac{\varepsilon_m x}{a}\right)\right]$$

**(5. 57)**

where the values of $A_{mn}$ and those of α and ε are given in literature as well. The fourth anti-symmetric mode shape (at a frequency of 202.4 Hz) is then calculated and its plot is shown in Figure 5.57.

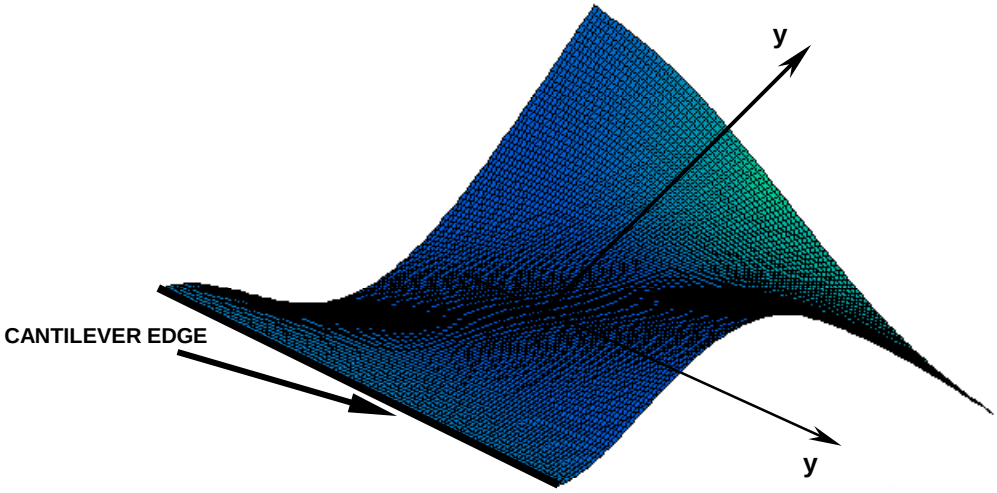


**Figure 5. 57** Analytical mode shape at the natural frequency of 202.4 Hz.

In order to apply Equation (5.52), the mode shape is approximated by a two-dimensional polynomial of, say, the 6th order in both the dimensions:

$$V(x,y)=\sum_{n,m=0}^{6,6} V_{n,m}\, x^n y^m \qquad \textbf{(5. 58)}$$

with the coefficients matrix:

$$V_{nm}=\begin{bmatrix} -0.0332 & -2.4478 & -0.0002 & 0.2360 & 0.0005 & -0.1436 & -0.0003 \\ -0.0568 & 1.9297 & -0.0007 & -0.6186 & 0.0005 & 0.2975 & 0 \\ -0.0141 & 7.6566 & -0.0043 & -1.9595 & 0.0086 & 0.7443 & -0.0051 \\ 0.0078 & -0.5146 & 0.0038 & -0.7135 & -0.0058 & -0.0198 & 0.0030 \\ -0.0029 & -3.4327 & 0.0181 & 0.7667 & -0.0387 & -0.3147 & 0.0232 \\ 0 & 0.8637 & -0.0022 & 0.2376 & 0.0047 & 0.0581 & -0.0028 \\ 0.0013 & 0.4957 & -0.0136 & -0.1416 & 0.0295 & 0.0494 & -0.0177 \end{bmatrix} \qquad \textbf{(5. 59)}$$

Considering now a laser beam scanning in the *x*-direction at 1.1 Hz and at 20 Hz in the *y*-direction, the *x* and *y* position can be related to the time so that:

$$x(t)=\cos(2\pi 1.1t)$$
$$y(t)=\cos(2\pi 20t) \qquad \textbf{(5. 60)}$$

and the LDV will measure a time-dependent velocity signal of the following form:

$$v_z(t)=\sum_{n,m=0}^{6,6} V_{n,m}\cos^n(2\pi 1.1t)\cos^m(2\pi 20t)\cos(2\pi 202.4t) \qquad \textbf{(5. 61)}$$

the natural frequency associated with the mode shape being 202.4 Hz.

The time history to be measured by the LDV is shown in Figure 5.58, assuming that the acquisition is performed at 20000 samples with a sampling rate of 2000 Hz. Figure 5.59 illustrates the pattern followed by the laser beam on the plate, if its position is driven by Equation (5.60).

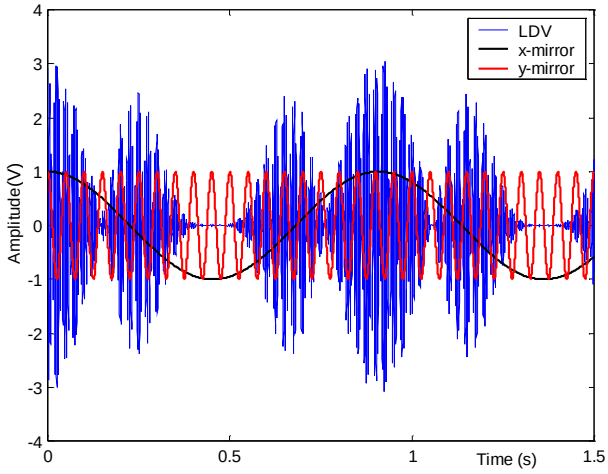


**Figure 5. 58** Simulated time histories of the velocity response, together with the time-dependent position of the laser beam on the plate.

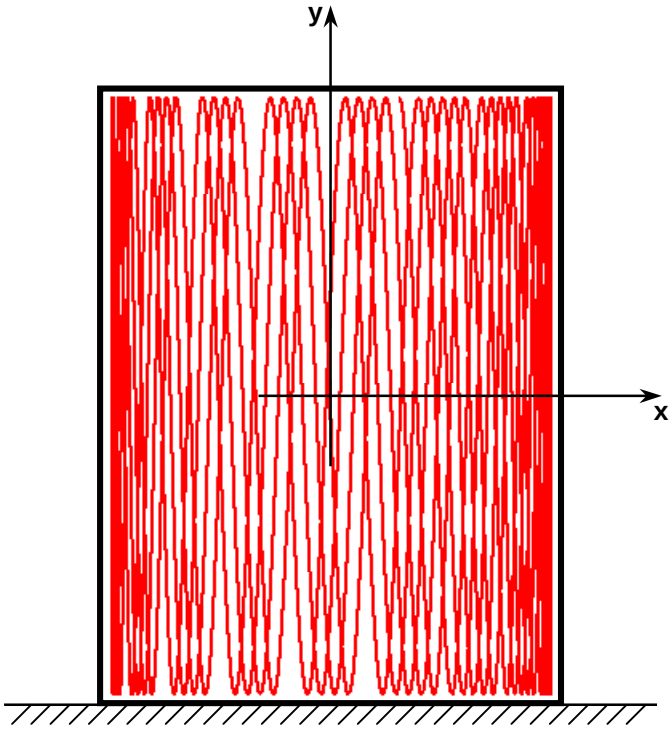


**Figure 5. 59** Laser beam pattern.

The LDV output time signal can be now post-processed following the mathematics manipulation summarised in Equation (5.53). By curve-fitting the time signal at the known frequencies of $\left(\omega \pm n\Omega_x \pm m\Omega_y\right)$, where $\Omega_x$ = 1.1 Hz and $\Omega_y$ = 20 Hz, the spectral amplitudes $A_{n,m}$ can be deduced and by applying the [T] transformation, the polynomial coefficients, $V_{n,m}$, can be recovered. The curve-fit was done by multiplying the LDV time history by sine and cosine of the mentioned frequencies, the real and imaginary components of the signal in the frequency domain were then derived. In Figure 5.60 these components are shown; it must be noticed how small the imaginary parts are in comparison with the real parts. This is understandable, as the simulated mode shape being completely real. In Figure 5.61, magnitude and phase of the LDV output spectrum are illustrated.

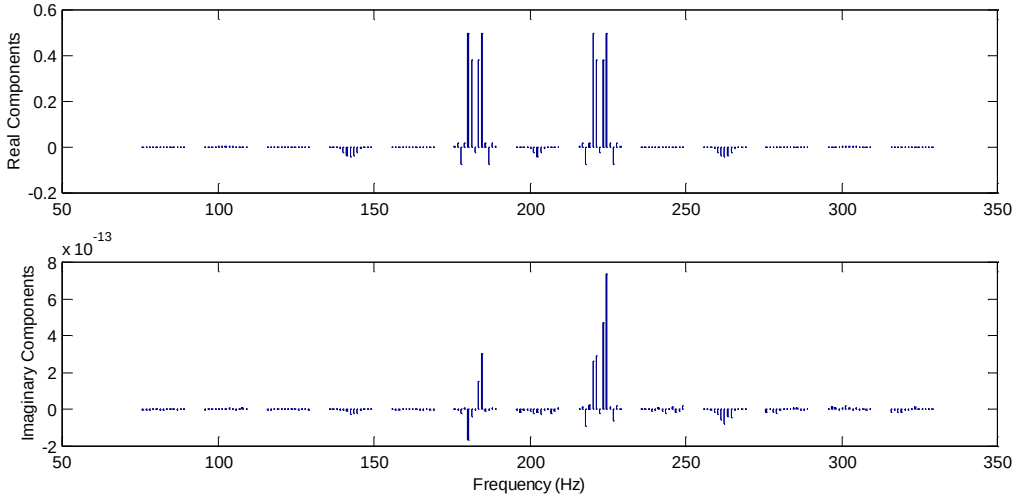


**Figure 5. 60** Real and imaginary components (in V) of the LDV output spectrum.

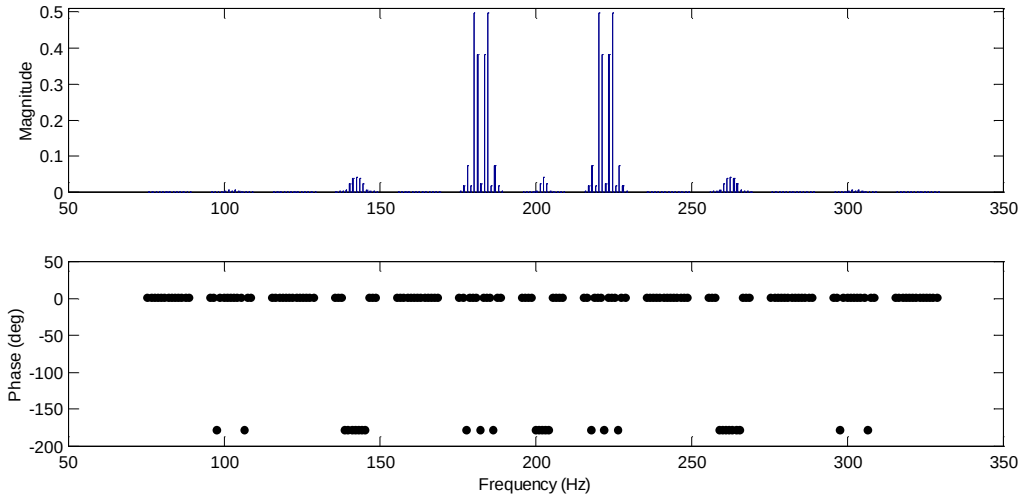


**Figure 5. 61** Magnitude (in V) and phase of the LDV output spectrum.

The sideband matrix $A_{n,m}$, which is unique in this case, since the mode is real, can be derived from the magnitude of the LDV output spectrum and its sign from the phase. This matrix is associated with the spectral components as is explained in the diagram of Figure 5.62. If

$$A_{n,m} = \begin{bmatrix} A_{00} & A_{01} & A_{02} & . & . & A_{0m} \\ A_{10} & A_{11} & A_{12} & . & . & A_{1m} \\ A_{20} & A_{21} & A_{22} & . & . & A_{2m} \\ . & . & . & . & . & . \\ . & . & . & . & . & . \\ A_{n0} & A_{n1} & A_{n2} & . & . & A_{nm} \end{bmatrix}$$

the spectral components can then be named as in Figure 5.62.

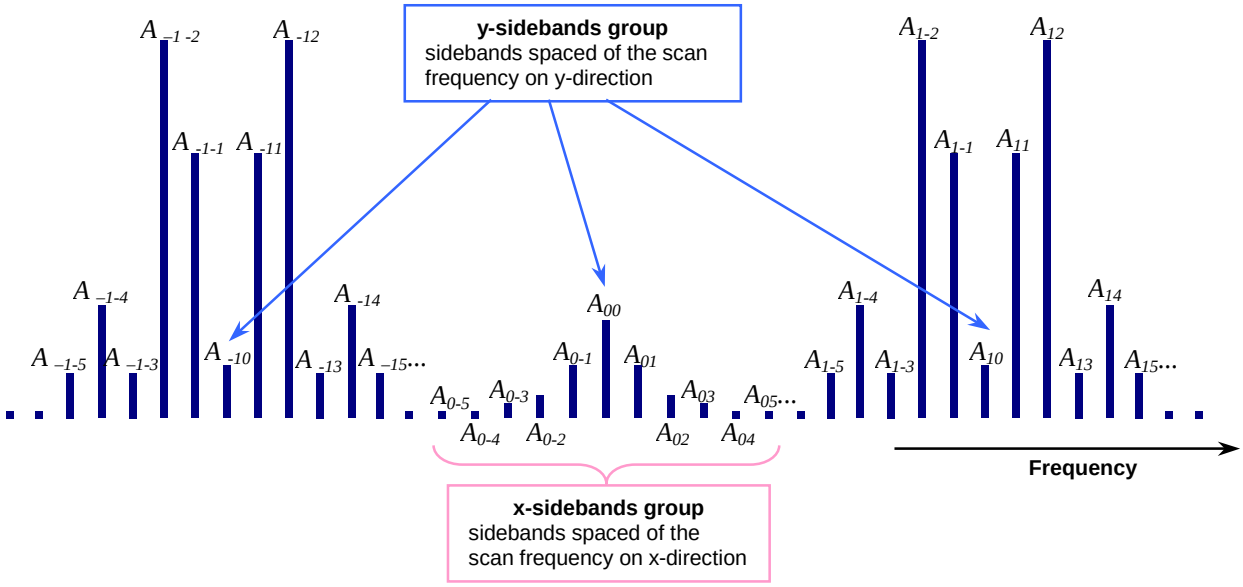


**Figure 5. 62** Association between the LDV spectral amplitudes and the sideband matrix components.

As has been demonstrated mathematically, in the case of purely real mode shapes, the symmetrical sideband components have identical amplitudes so the sideband matrix can then be composed of only one component of each sideband's pair. The *x*-sidebands group ($A_{00}$, $A_{01}$, $A_{02}$ ..., and $A_{10}$, $A_{11}$, $A_{12}$ ...) will be the columns of the sidebands matrix, while the *y*-sidebands group ($A_{00}$, $A_{10}$, $A_{20}$ ..., and $A_{01}$, $A_{11}$, $A_{21}$ ...) will be the rows of this matrix.

Each matrix element can be associated with a positive or negative sign by observing the spectral phase of the LDV output. In fact, all the spectral components are in phase with each other or they have a shift of 180°. Referring all the component's phase to that of the central component, it can be

conventionally postulated that the sidebands with phase equal to the central component phase have a negative sign, whereas the sidebands shifted of 180° have a positive sign.

Following the procedure described hereby, the sidebands matrix can be derived for the LDV spectrum simulated and shown in Figure 5.61. This will be:

$$A_{nm} = \begin{bmatrix} -0.0407 & -0.0239 & 0.0003 & -0.0425 & 0.0003 & 0.0042 & 0.0003 \\ -0.0251 & 0.3825 & 0.0003 & -0.0376 & 0.0003 & 0.0053 & 0.0003 \\ -0.0036 & 0.4992 & 0.0003 & -0.0225 & 0.0003 & 0.0040 & 0.0003 \\ 0.0013 & 0.0181 & 0.0003 & -0.0051 & 0.0003 & 0.0005 & 0.0003 \\ 0.0002 & -0.0754 & 0.0003 & 0.0023 & 0.0003 & -0.0002 & 0.0003 \\ 0.0003 & 0.0171 & 0.0003 & 0.0015 & 0.0003 & 0.0003 & 0.0003 \\ 0.0003 & 0.0004 & 0.0003 & 0.0001 & 0.0003 & 0.0003 & 0.0003 \end{bmatrix}$$

Applying the [T] transform ( Equation (5.54) ), the polynomial coefficients series can be recovered:

$$V_{nm} = \begin{bmatrix} -0.0329 & -2.4494 & -0.0072 & 0.2454 & 0.0239 & -0.1529 & -0.0190 \\ -0.0586 & 1.9401 & 0.0041 & -0.6748 & -0.1401 & 0.3538 & 0.1126 \\ -0.0211 & 7.6984 & 0.1644 & -2.1845 & -0.5540 & 0.9694 & 0.4451 \\ 0.0172 & -0.5708 & -0.2213 & -0.4133 & 0.7445 & -0.3199 & -0.5972 \\ 0.0204 & -3.5733 & -0.5142 & 1.5170 & 1.8371 & -0.9651 & -1.4774 \\ -0.0094 & 0.9199 & 0.2224 & 0.06253 & -0.7456 & 0.3583 & 0.5974 \\ -0.0174 & 0.6082 & 0.4366 & -0.7418 & -1.4711 & 0.6497 & 1.1828 \end{bmatrix}$$

which can be compared with the initial polynomial coefficients given by Equation (5.59) and rewritten here:

$$V_{nm,\,INITIAL} = \begin{bmatrix} -0.0332 & -2.4478 & -0.0002 & 0.2360 & 0.0005 & -0.1436 & -0.0003 \\ -0.0568 & 1.9297 & -0.0007 & -0.6186 & 0.0005 & 0.2975 & 0 \\ -0.0141 & 7.6566 & -0.0043 & -1.9595 & 0.0086 & 0.7443 & -0.0051 \\ 0.0078 & -0.5146 & 0.0038 & -0.7135 & -0.0058 & -0.0198 & 0.0030 \\ -0.0029 & -3.4327 & 0.0181 & 0.7667 & -0.0387 & -0.3147 & 0.0232 \\ 0 & 0.8637 & -0.0022 & 0.2376 & 0.0047 & 0.0581 & -0.0028 \\ 0.0013 & 0.4957 & -0.0136 & -0.1416 & 0.0295 & 0.0494 & -0.0177 \end{bmatrix}$$

The derived polynomial coefficients, $V_{n,m}$, can be used to recover the ODS already shown in Figure 5.57.

#### *5.5.4.2.2 Complex Vibration Response*

A more general case, where the simulated mode shape is complex, is addressed next. It is assumed that the real and imaginary components of the mode shape, again at 202.4 Hz (ω), are equal and they can be approximated by the same polynomial and the polynomial coefficients series $V_{Rnm}$ and $V_{Inm}$ are the same (Equation (5.59) ). Both the two addenda of Equation (5.52) must be considered in this case and they will produce an LDV output $v_z(t)$ whose spectrum is, now complex, i.e. real and imaginary components are comparable (Figure 5.63).

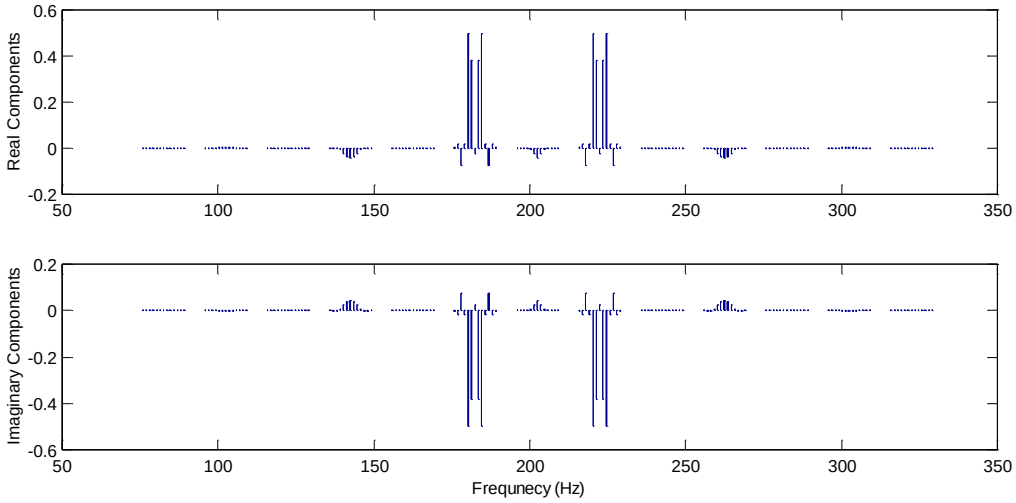


**Figure 5. 63** Real and imaginary components of the LDV output spectrum.

Observing the LDV output spectrum in amplitude and phase (Figure 5.64), it is possible to notice that all the points are no longer in phase with each other, or 180° phase-shifted. This is because the ODS measured is complex and the spatial points are not in phase with each other as well.

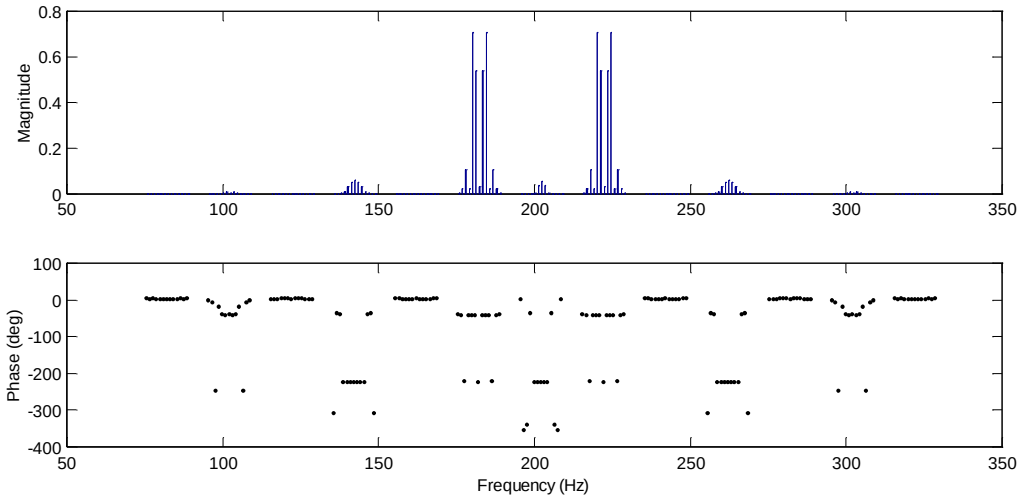


**Figure 5. 64** Magnitude and phase of the LDV output spectrum.

From the real and imaginary components of the LDV spectrum the sidebands matrix $A_{Rnm}$ and $A_{Inm}$ can be derived. The procedure to recover their sign is not necessary anymore because the real and imaginary components are now comprehensive of the sign.

$$A_{Rnm} = \begin{bmatrix} -0.0407 & -0.0239 & 0.0003 & -0.0425 & 0.0003 & 0.0042 & 0.0003 \\ -0.0251 & 0.3825 & 0.0003 & -0.0376 & 0.0003 & 0.0053 & 0.0003 \\ -0.0036 & 0.4992 & 0.0003 & -0.0225 & 0.0003 & 0.0040 & 0.0003 \\ 0.0013 & 0.0181 & 0.0003 & -0.0051 & 0.0003 & 0.0005 & 0.0003 \\ 0.0002 & -0.0754 & 0.0003 & 0.0023 & 0.0003 & -0.0002 & 0.0003 \\ 0.0003 & 0.0171 & 0.0003 & 0.0015 & 0.0003 & 0.0003 & 0.0003 \\ 0.0003 & 0.0035 & 0.0003 & 0.0001 & 0.0003 & 0.0003 & 0.0003 \end{bmatrix}$$

$$A_{Inm} = \begin{bmatrix} 0.0409 & 0.0242 & 0 & 0.0428 & 0 & -0.0039 & 0 \\ 0.0255 & -0.3822 & 0 & 0.0379 & 0 & -0.0049 & 0 \\ 0.0039 & -0.4989 & 0 & 0.0228 & 0 & -0.0037 & 0 \\ -0.0009 & -0.0178 & 0 & 0.0054 & 0 & -0.0002 & 0 \\ 0 & 0.0757 & 0 & -0.0019 & 0 & 0.0004 & 0 \\ 0 & -0.0168 & 0 & -0.0012 & 0 & 0 & 0 \\ 0 & -0.0033 & 0 & 0.0001 & 0 & 0 & 0 \end{bmatrix}$$

From the sidebands matrices the 2-D polynomial coefficients series are derived applying the transform in Equation (5.54):

$$V_{Rnm} = \begin{bmatrix} -0.0329 & -2.4494 & -0.0072 & 0.2454 & 0.0239 & -0.1529 & -0.0190 \\ -0.0586 & 1.9401 & 0.0041 & -0.6748 & -0.1401 & 0.3538 & 0.1126 \\ -0.0211 & 7.6984 & 0.1644 & -2.1845 & -0.5540 & 0.9694 & 0.4451 \\ 0.0172 & -0.5708 & -0.2213 & -0.4133 & 0.7445 & -0.3199 & -0.5972 \\ 0.0204 & -3.5733 & -0.5142 & 1.5170 & 1.8371 & -1.0651 & -1.4774 \\ -0.0094 & 0.9199 & 0.2224 & 0.06253 & -0.7456 & 0.3583 & 0.5974 \\ -0.0174 & 0.6082 & 0.4366 & -0.7418 & -1.4711 & 0.6497 & 1.1828 \end{bmatrix}$$

$$V_{Inm} = \begin{bmatrix} 0.0332 & 2.4477 & 0.0002 & -0.2361 & -0.0005 & 0.1435 & 0.0003 \\ 0.0568 & -1.929 & 0.0007 & 0.6185 & -0.0005 & -0.2975 & 0 \\ 0.0141 & -7.6562 & 0.0043 & 1.9594 & -0.0087 & -0.7443 & 0.0051 \\ -0.0078 & 0.5145 & -0.0038 & 0.7134 & 0.0058 & 0.0198 & -0.0030 \\ 0.0029 & 3.4326 & -0.0181 & -0.7134 & 0.0387 & 0.3147 & -0.0232 \\ 0 & -0.8637 & 0.0026 & -0.2376 & -0.0047 & -0.0581 & 0.0028 \\ -0.0013 & -0.4956 & 0.0013 & 0.1416 & -0.0295 & -0.0494 & 0.0178 \end{bmatrix}$$

Real and imaginary components of the ODS given by the previous polynomial coefficients series are shown in Figures 5.65 and 5.66 respectively.

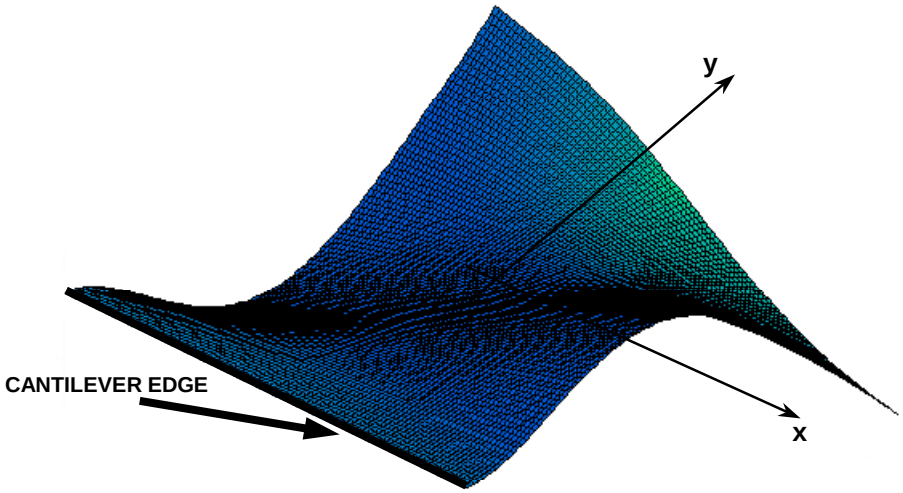


**Figure 5. 65** Real components of the recovered ODS.

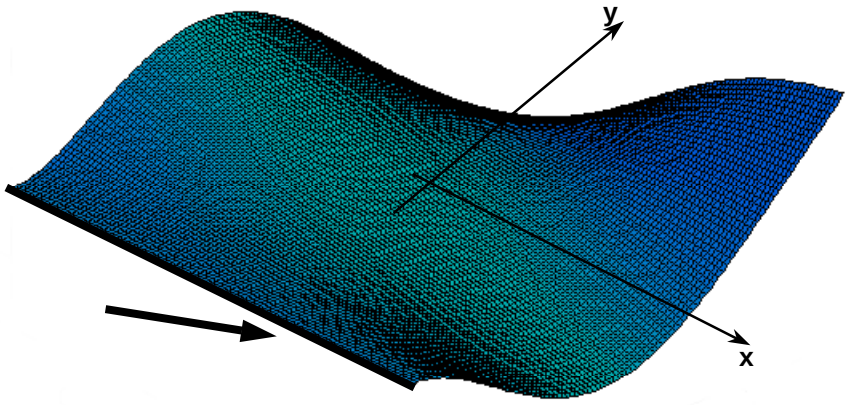


**Figure 5. 66** Imaginary components of the recovered ODS.

*5.5.4.2.3 Mirror Delay Effect*

A further detail which must taken into account is the mirror delay already discussed in Chapter 4 (Section 4.6). In practice, the sinewaves followed by the laser beam over the plate surface are never completely equal to the ones driving the mirrors and given by Equation (5.49). Usually, the laser beam presents a

slight delay, which can be called $\delta_x$ in *x*-direction and $\delta_y$ in *y*-direction. The laser beam will then travel according to the following relationship:

$$\begin{aligned} x(t) &= \cos(\Omega_x t + \delta_x) \\ y(t) &= \cos(\Omega_y t + \delta_y) \end{aligned} \qquad \textbf{(5. 62)}$$

Equation (5.52) will become:

$$\begin{aligned} v_z(t) = & \sum_{n,m=0}^{p,q} V_{Rn,m} \cos^n(\Omega_x t + \delta_x)\cos^m(\Omega_y t + \delta_y)\cos(\omega t) + \\ & + \sum_{n,m=0}^{p,q} V_{In,m} \cos^n(\Omega_x t + \delta_x)\cos^m(\Omega_y t + \delta_y)\sin(\omega t) \end{aligned} \qquad \textbf{(5. 63)}$$

In terms of sideband components this can be written ( similarly to Equation (5.53) ):

$$\begin{aligned} v_z(t) = & \sum_{n,m=0}^{p,q} A_{Rn,m} \cos\left[\omega t \pm n(\Omega_x t + \delta_x) \pm m(\Omega_y t + \delta_y)\right] + \\ & + \sum_{n,m=0}^{p,q} A_{In,m} \sin\left[\omega t \pm n(\Omega_x t + \delta_x) \pm m(\Omega_y t + \delta_y)\right] \end{aligned} \qquad \textbf{(5. 64)}$$

which leads to:

$$\begin{aligned} v_z(t) = & \sum_{n,m=0}^{p,q} A_{Rn,m} \cos\left[(\omega \pm n\Omega_x \pm m\Omega_y)t \pm n\delta_x \pm m\delta_y\right] + \\ & + \sum_{n,m=0}^{p,q} A_{In,m} \sin\left[(\omega \pm n\Omega_x \pm m\Omega_y)t \pm n\delta_x \pm m\delta_y\right] \end{aligned} \qquad \textbf{(5. 65)}$$

This means that the mirror delay must be taken into consideration with the curve-fit process in order to determine the real value of the sideband matrices components $A_{Rnm}$ and $A_{Inm}$ to which Equation (5.54) can be applied without any

correction. In practical examples the last formulae derived will in any case be employed and the mirror delay always considered.

Such a situation can be simulated considering an *x*-mirror delay ($\delta_x$) of $\pi/8$ rad and a *y*-mirror delay ($\delta_y$) of $\pi/10$ rad. The LDV time history recovered for a purely real mode shape approximated by a polynomial with coefficients given by Equation (5.59) is shown in Figure 5.67, where the upper plot represents the time signal derived without any delay and using Equation (5.52), while the lower plot represents the LDV output in the real situation derived applying Equation (5.63). It can be noticed that the LDV time history is not in phase with the sinewaves (red and green) which are the signal driving the mirrors (not affected by the delay, since they are the signals drivers upstream of the inertia of the mirrors).

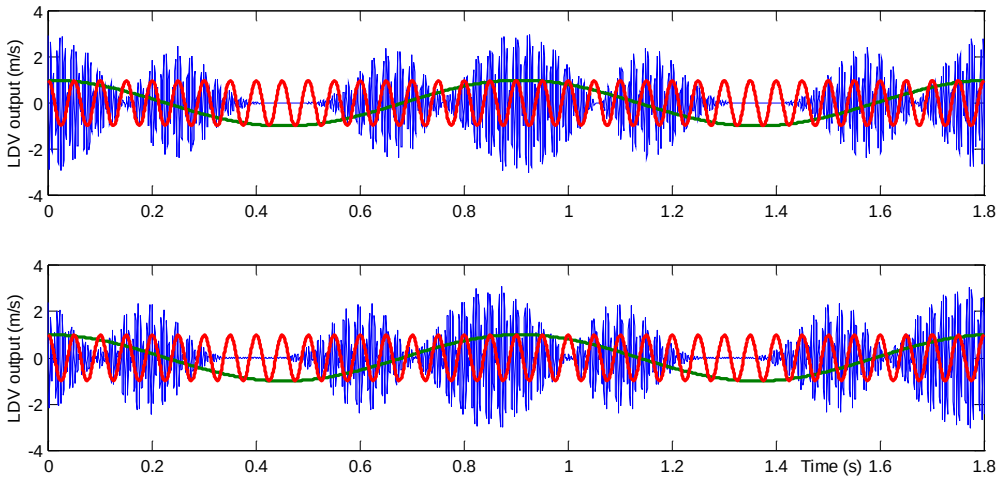


**Figure 5. 67** LDV output signal for the ideal and real situation, considering the delay of the mirrors, which are plotted as well (the *x*-mirror is green and the *y*-mirror is red).

By performing a curve-fit to the ideal time signal multiplying by sine and cosine of ($\omega \pm n\Omega_x \pm m\Omega_y$), the LDV spectrum will appear as shown in Figure 5.68; in contrast, if the time signal is the real one (i.e. the laser beam pattern is actually delayed) without taking into account the mirrors delay, a phase spectrum which is completely spread is recovered, see Figure 5.69. On the other

hand the spectrum is brought back to the ideal situation if the multiplication is done by sine and cosine of $[(\omega \pm n\Omega_x \pm m\Omega_y)t \pm n\delta_x \pm m\delta_y]$, see Figure 5.70.

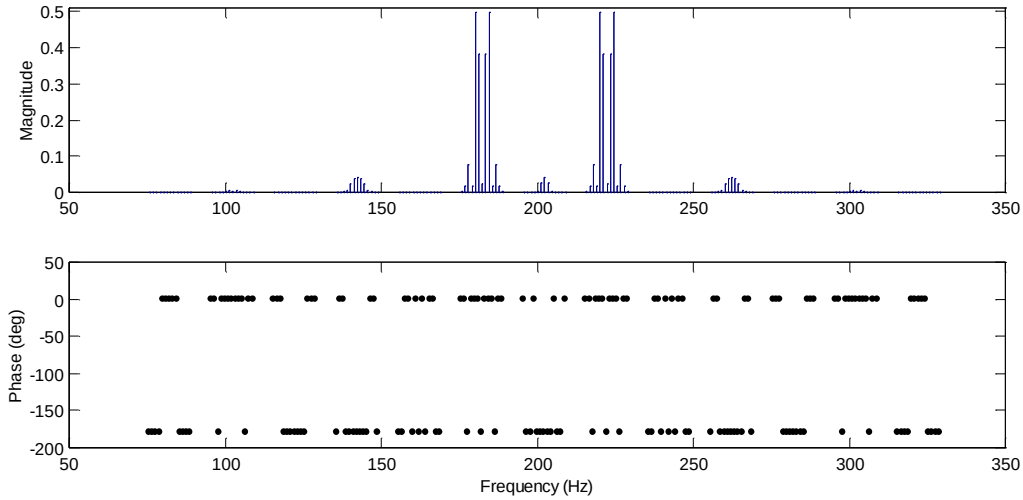


**Figure 5. 68** LDV spectrum in the ideal situation.

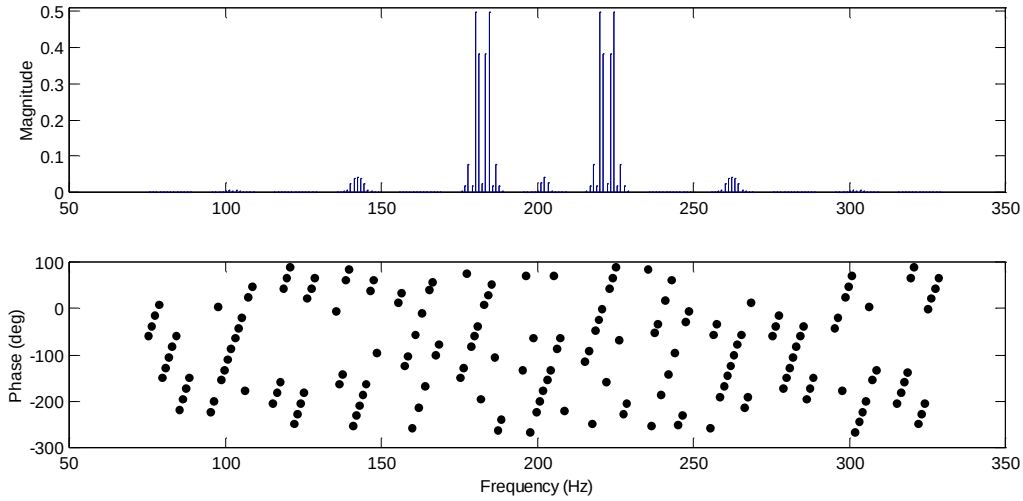


**Figure 5. 69** LDV spectrum in the real situation without considering the mirror delay.

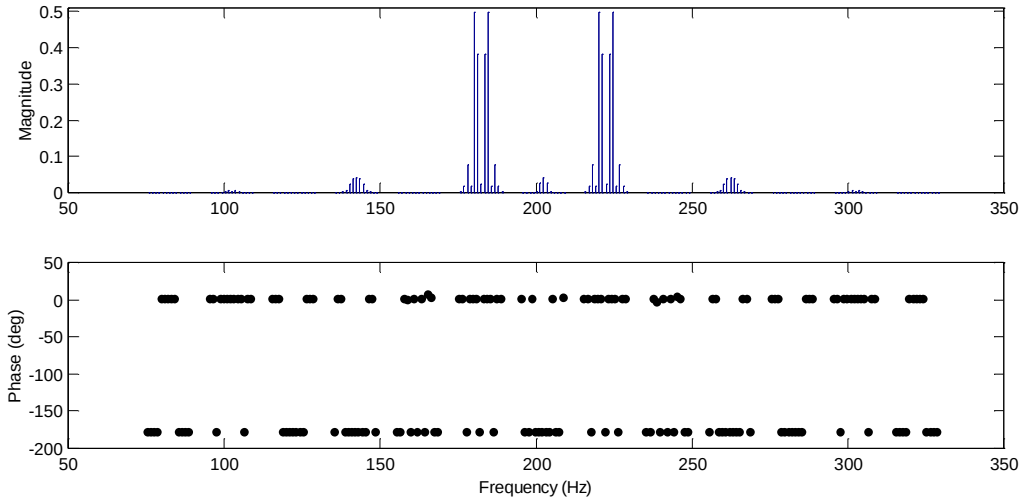


**Figure 5. 70** LDV spectrum in the real situation considering the mirror delay.

Since, in practice, the delay of the mirrors is unknown, the lined-up process can be used as a calibration to determine these delays from the correction parameters. In fact, if any correction is given during the curve-fit a spread-up phase spectrum as shown in Figure 5.69 is obtained. By trying several values for the correction those needed can be defined. In order to do this, the *x*- and *y*-sidebands groups must be considered separately. In Figure 5.71 the process is shown. First, each group of x-sidebands phases are lined-up, trying different offset values (0, $\pi$/16, $\pi$/8 rad). Note that with a correction corresponding to the mirror delay angle, i.e. $\pi$/8 rad, the phase components for the first plot lie on a straight line and they are 0° or 180° (blue dots in Figure 5.71). In the second plot the phase components are lined-up as well but they do not lie on a straight line and they are 0° or 180°, but their values is 18° and –162°. This means that all the components are translated of 18° and this depends on the *y*-correction that is not yet done. After the *x*-correction the complete sideband spectrum becomes as that shown in Figure 5.72. Now the trial for the *y*-correction can be applied as shown in Figure 5.73, where three different values of the delay are taken into consideration, specifically 0, $\pi$/20, $\pi$/10 rad. Note that when the best correction ($\pi$/10 rad) is used in *y*-direction as well, the phase spectrum (blue dots in Figure 5.73) is completely lined-up as it was in the ideal situation (Figure 5.68).

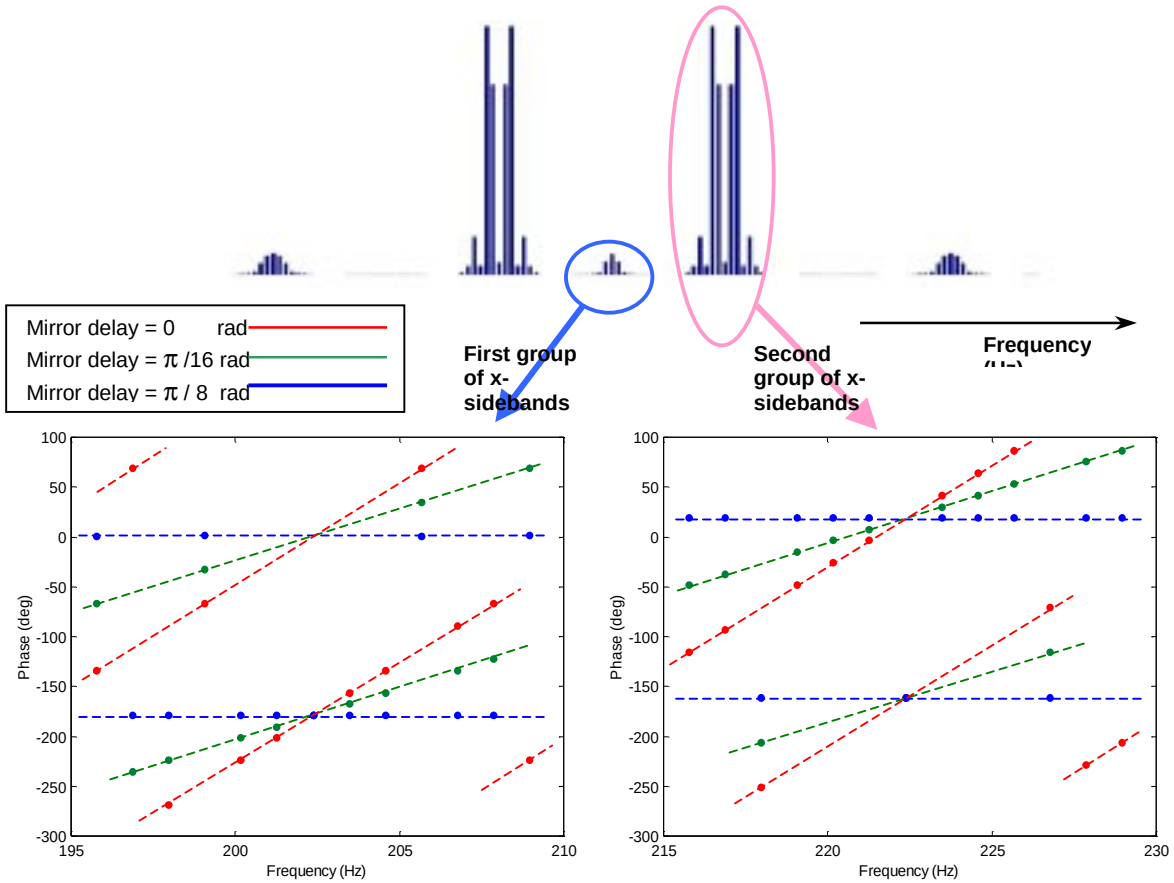


**Figure 5. 71** *x*-group sidebands correction using different values for the mirror delay.

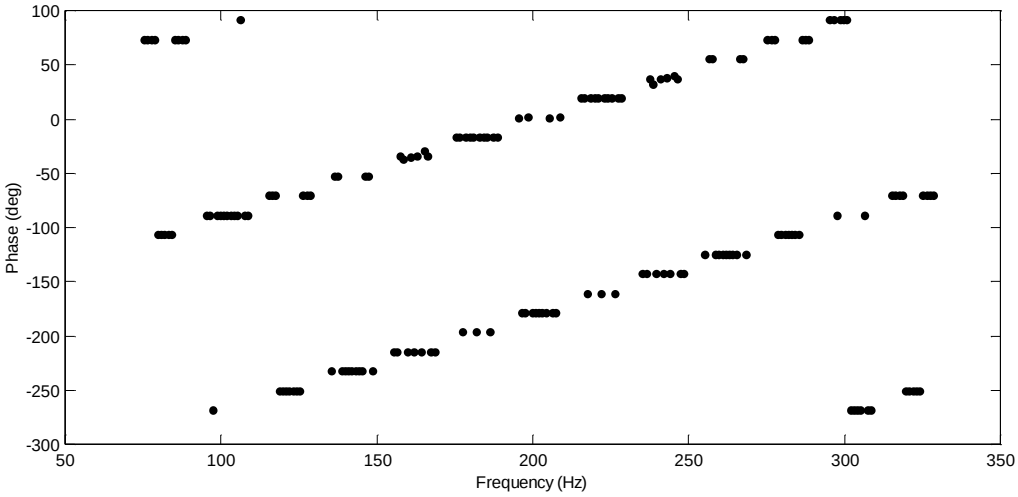


**Figure 5. 72** Complete phase spectrum after the *x*-correction procedure.

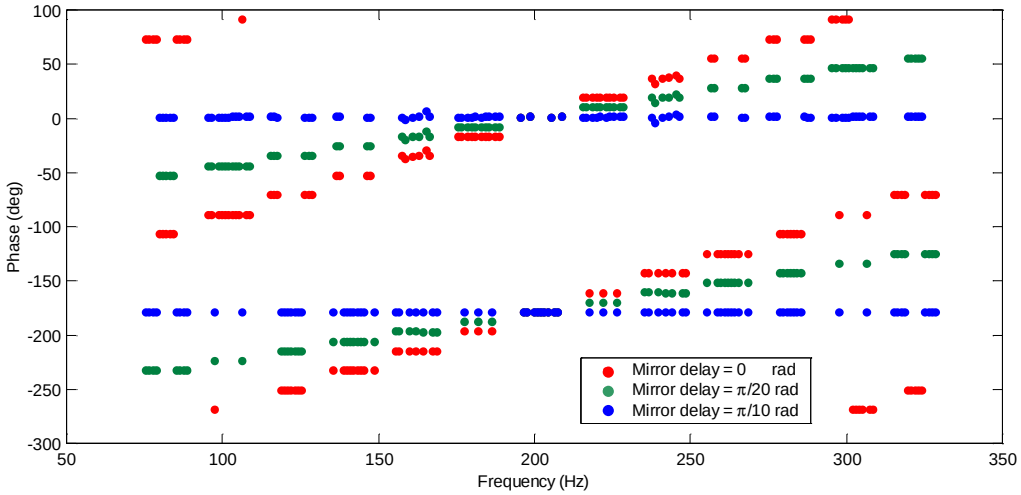


**Figure 5. 73** *y*- correction using different values for the mirror delay.

### *5.5.4.3 Experimental Validation*

#### *5.5.4.3.1 Experimental Set-up Description*

An experimental procedure to derive a two-dimensional area-scan ODS is now addressed in order to demonstrate the validity of the process hereby analysed. With reference to the test rig described in Figure 5.51 (i.e. cantilever plate with shaker attached on it rear surface), an area scan over the surface of the structure vibrating at a specific, known frequency, has been performed. The software used to set up the test and to acquire and post-process the measurement data consists of a set of `LabVIEW` programs whose philosophy can be summarised in brief:

1. Set Mirrors Drivers to make the mirrors scan the area to be tested (see Appendix A.1.5 for the control panel of the `LabVIEW` program driving the mirrors).
2. Set Arbitrarily Waveform Generator parameters according to the excitation input required (see Appendix A.1.1 for the control panel of the `LabVIEW` program driving the shaker).

3. Spectral Analysis. The LDV output spectrum is visualised in order to determine the number of the relevant sidebands present on it. The order of the polynomial, which will represent the ODS of the tested surface, can, then, be straightforwardly derived at this stage (see Appendix A.1.6 for the control panel of the `LabVIEW` program used as spectrum analyser).
4. Data Acquisition. The signals stored for post processing are: LDV output, which contains the surface velocity information, sinewave driving the x-mirror, sinewave driving the y-mirror and, optionally, the force cell signal (see Appendix A.1.3 for the control panel of the `LabVIEW` program used for the acquisition).
5. ODS determination using the settings defined previously and the data stored in the data acquisition step. The goal of this stage is to produce a plot of the deflected surface at the excitation frequency (see Appendix A.1.7 for the control panel of the `LabVIEW` program performing the post-processing of the LDV output signal in order to derive the ODS).

By applying the `LabVIEW` control-acquisition programs, the plate was tested at two frequencies of maximum response that were established by discrete scanning technique using the conventional Polytec PSV procedure, i.e. at 202.5 Hz ($4^{th}$ resonance) and 241.25 Hz ($5^{th}$ resonance).

The LDV mirrors were set in such a way as to describe a non-closed Lissajou pattern on the plate surface, perpendicular to the laser beam. The *x*-mirror was fed with a sine wave at 1.1 Hz and the *y*-mirror with a sine wave at 20 Hz (i.e. not an integral multiple of 1.1Hz). The amplitudes of these output signals were adjusted so that the whole surface was swept by the measurement beam. The acquisition took 10 seconds, i.e. 11 cycles of the laser beam in the direction scanned at lower speed (1.1 Hz in the *x*-direction) were covered.

*5.5.4.3.2 Test on the Plate at the Fourth Resonance*

By exciting the plate at the first frequency mentioned (202.5 Hz), the LDV output time history triggered with the sinewave driving one of the mirrors was stored together with the excitation force signal and the two mirror drive signals. These signals are shown in Figure 5.74, where a zoom of the acquisition start point (zero time instant) is given in order to illustrate that the trigger is performed with the *x*-mirror drive signal (red), which start at zero amplitude with positive slope.

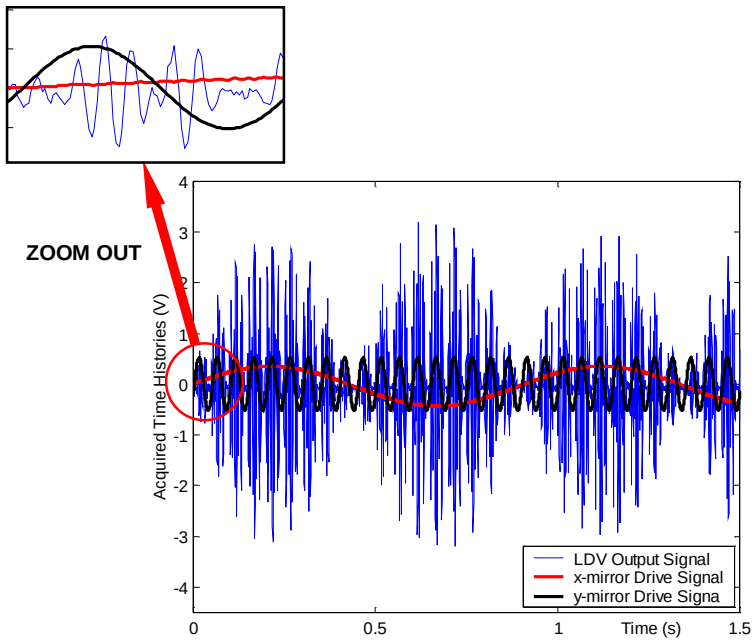


**Figure 5. 74** Measured time signals and zoom on the acquisition initial time instant which shows that the trigger signal employed is the x-mirror driver signal (red line).

The acquisition sample rate must be carefully chosen as it should be higher than twice the highest frequency component of the LDV output spectrum. This latter would be given by:

$$202.5 + n \times 1.1 + m \times 20$$

*n* and *m* being the number of *x*- and *y*-sidebands that should be chosen in the curve-fit process. Say that $n = m = 8$, the maximum frequency would be 371.3 Hz and the sample rate at least 750 Hz.

By observing the LDV signal spectrum (Figure 5.75) the number of *x*- and *y*-sidebands necessary to be taken into account in the curve-fitting process can be decided. It was noticed, that some small amplitude peaks were present in a high frequency region – above the group being considered here. Zooming in on this range (Figure 5.76) it is easy to see that these components are centered at 405 Hz, which is the second harmonic of the excitation frequency. This phenomenon is due to speckle noise, see Subsection 2.5, and if the beam was better focused, i.e. the beam width *w* of light used for illumination was smaller, the effect might be much reduced, or even disappear altogether. The phenomenon does not affect the analysis and can be neglected.

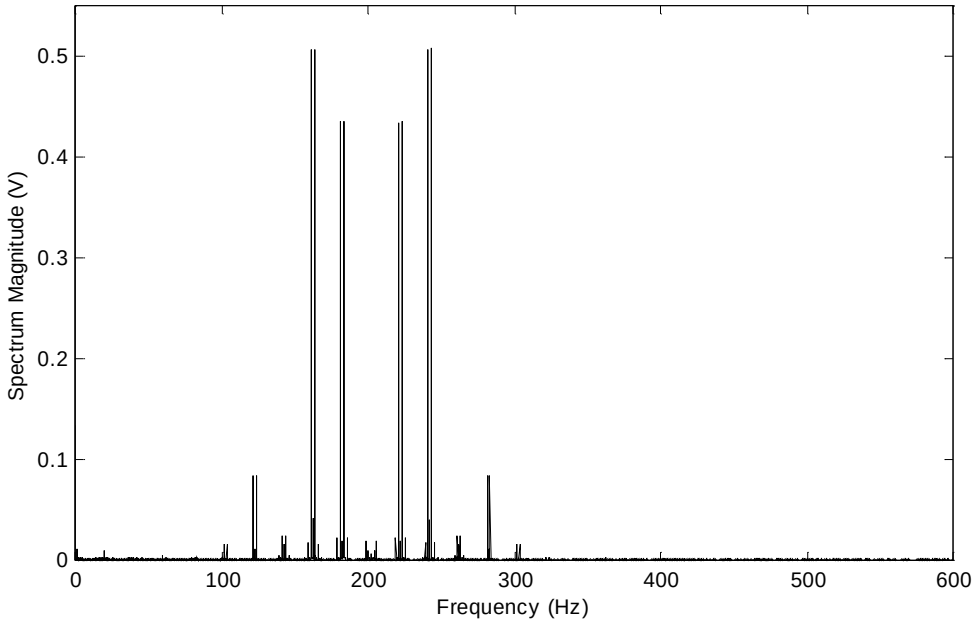


**Figure 5. 75** LDV Output Spectrum.

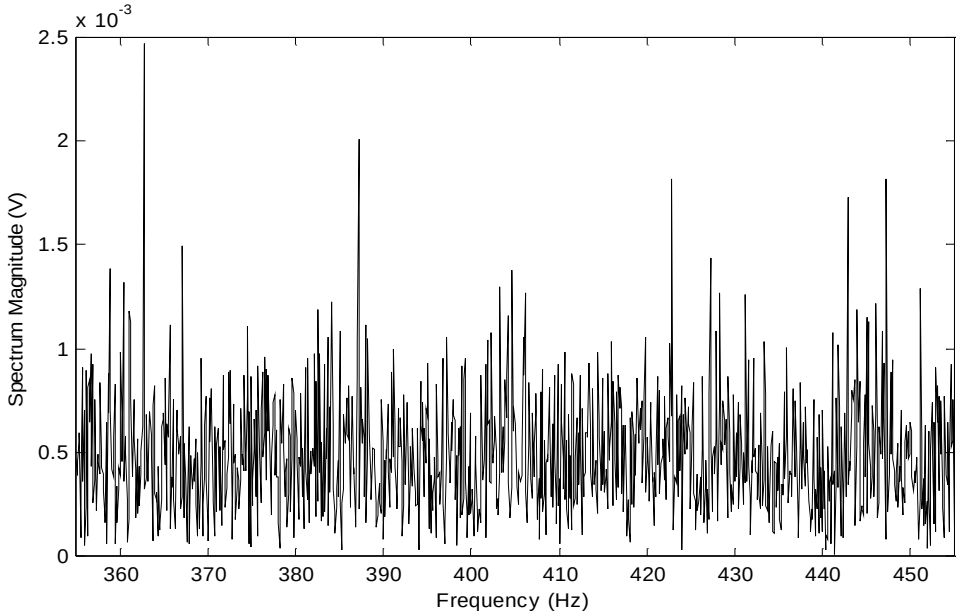


**Figure 5. 76** LDV Output Spectrum zoomed in the high frequency region.

By observing the spectrum in the region of interest (Figure 5.77) it can be decided the number of *x*- and *y*-sidebands to include, specifically 6 in both directions.

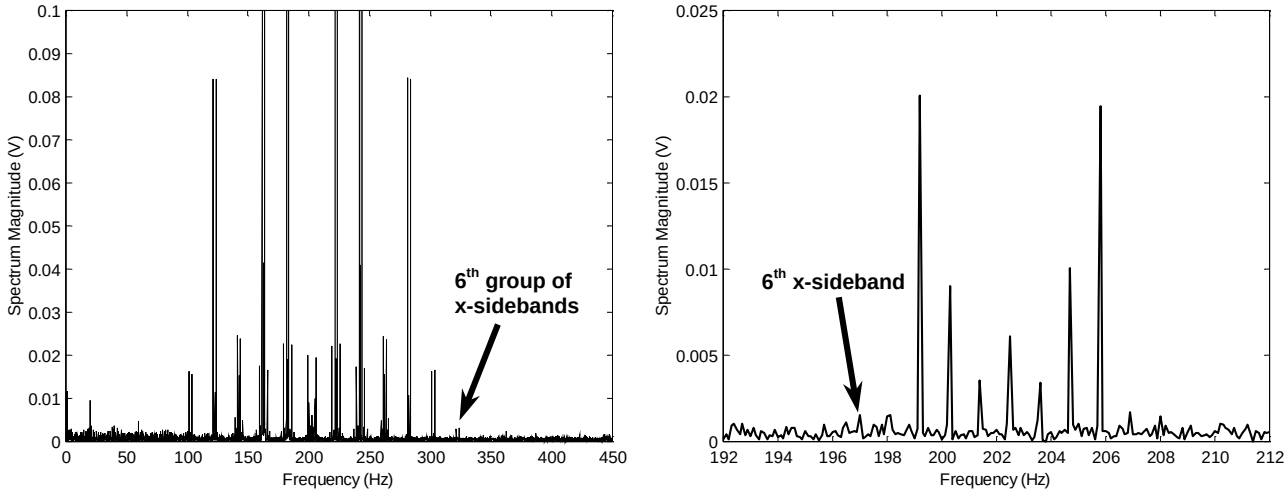


**Figure 5.77** LDV Output Spectrum zoomed in the region of interest (around the excitation frequency). Left plot shows all the x-sidebands groups (the last visible is the 6th one) while right plot is a zoom around the central group where sidebands are important up to the 6th only again.

By curve-fitting the LDV time history at the frequencies of $202.5 \pm n \times 1.1 \pm m \times 20$, for *n* and *m* assuming integer values from 0 up to 6. In order to have a phase spectrum with aligned components, the mirror delays must be considered; after some trials it was found that the best configuration was obtained when the delay associated with the *x*-mirror was 0.53 rad ($\delta_x$) and the one associated with the *y*-mirror was 0.803 rad ($\delta_y$). The curve fit was then performed by multiplying by sine and cosine of $202.5 \pm n \times 1.1 \pm m \times 20 \pm n \times \delta_x \pm m \times \delta_y$. Figure 5.78 shows the amplitude and phase spectrum recovered. Note, that the phase spectrum is still spread, even taking into account the mirrors delay. This occurs because the actual ODS of the plate is not completely real. In fact, observing the complex LDV output spectrum, Figure 5.79, it can be seen that the real and imaginary components are comparable.

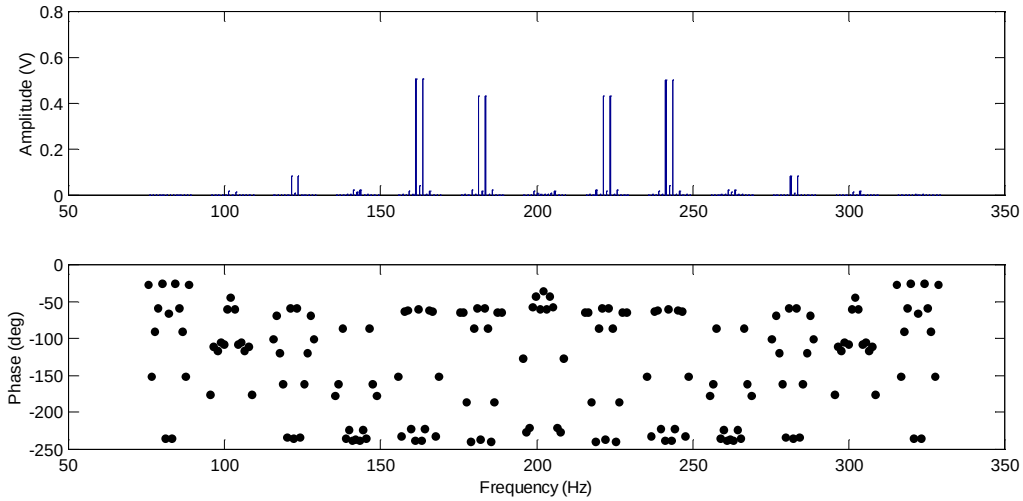


**Figure 5. 78** LDV output spectrum in magnitude and phase format.

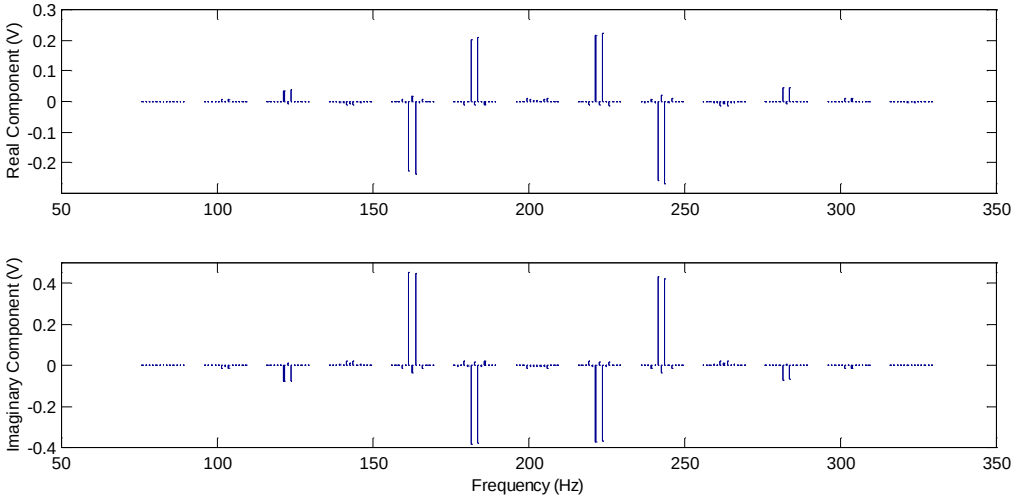


**Figure 5. 79** Real and imaginary components of the LDV output spectrum.

From the LDV output spectrum, in terms of real and imaginary components, sidebands matrices $A_{Rnm}$ and $A_{Inm}$ can be derived. Applying to these the [T] transform (Equation (5.54) ) real and imaginary polynomial coefficients series $V_{Rnm}$ and $V_{Inm}$ are established and the real and imaginary components of the ODS can be plotted as shown in Figure 5.80 and 5.81 respectively.

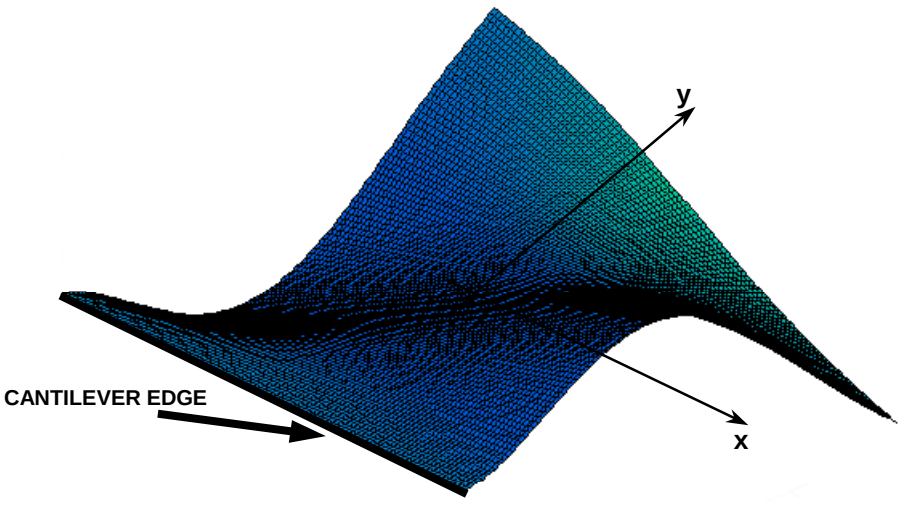


**Figure 5. 80** Plate ODS real component.

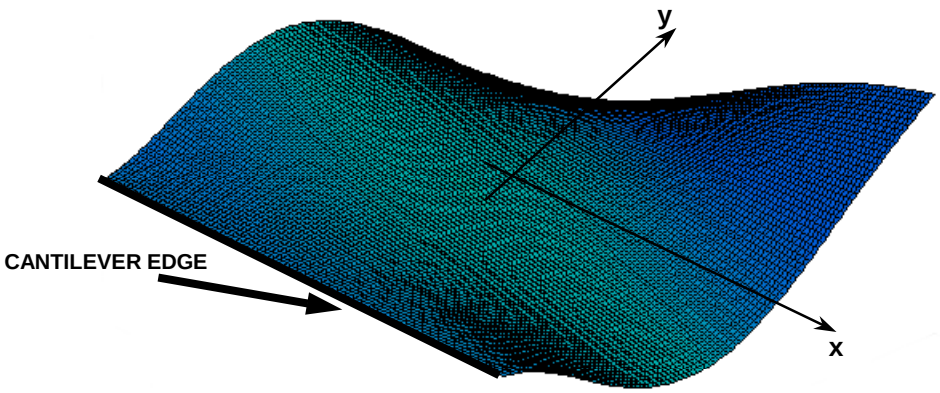


**Figure 5. 81** Plate ODS imaginary component.

In order to obtain a purely real ODS, the phase can be adjusted to minimise the output to effectively give zero imaginary parts of the ODS and then, shifted by $\pi/2$ to give the real component. This procedure is useful when the mode shape complexity, or lack of it, is to be demonstrated. The phase is then referred to one relative to the maximum imaginary component of the spectrum shown in Figure 5.79. Figures 5.82 and 5.83 show respectively the amplitude and translated phase spectrum and the complex spectrum recovered, specifically the in-phase and out-of-phase components.

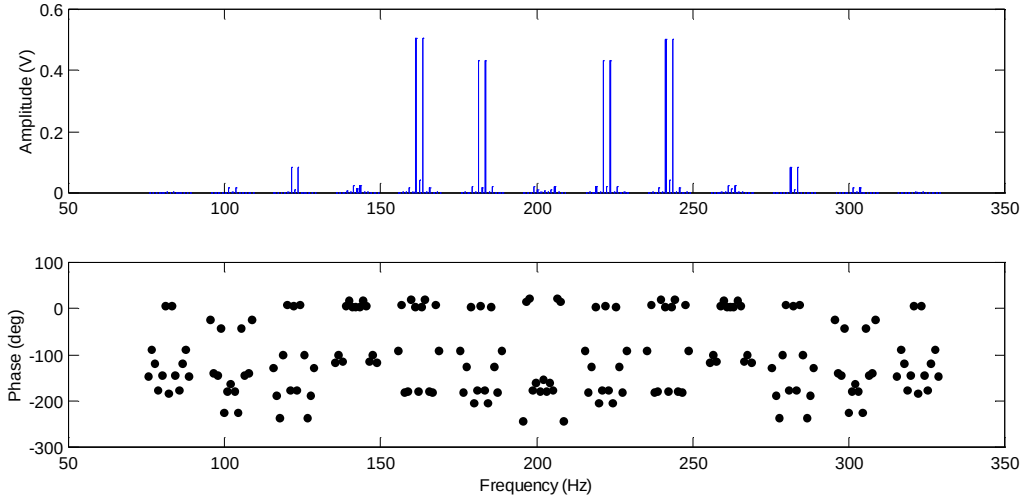


**Figure 5.82** Amplitude and Phase spectrum of the LDV output obtained for imaginary component minimising.

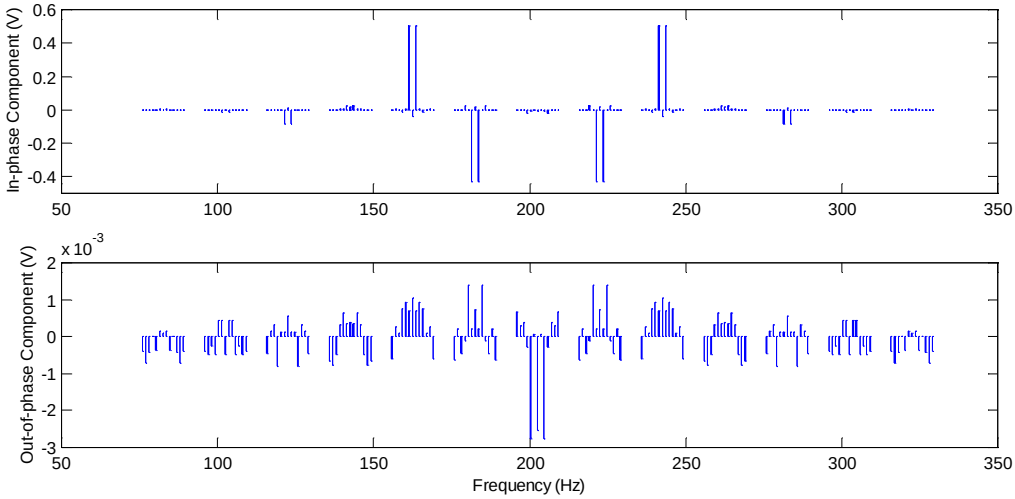


**Figure 5.83** In-phase and Out-of-phase components of the LDV output spectrum.

The ODS in-phase and out-of phase components are illustrated in Figure 5.84. Note that the ODS now represents the velocity pattern since it is given in mm/s. In fact, the polynomial coefficient series were multiplied by the laser sensitivity (5 mm/s/V) in order to have a response mode shape, comparable with the velocity pattern derived by using the conventional discrete area scanning technique, provided by the Polytec system (See Figure 5.52). Figure 5.85 shows both the ODSs at 202.5 Hz derived with Polytec and the continuous area scan.

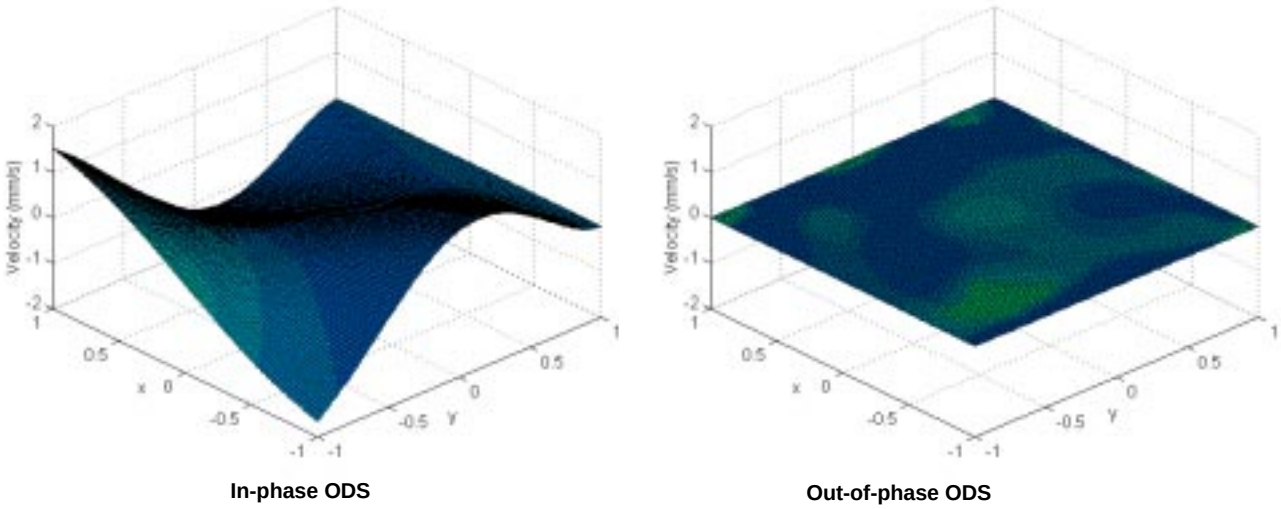


**Figure 5. 84** Vibration pattern from the contiuous area scan at 202.5 Hz.

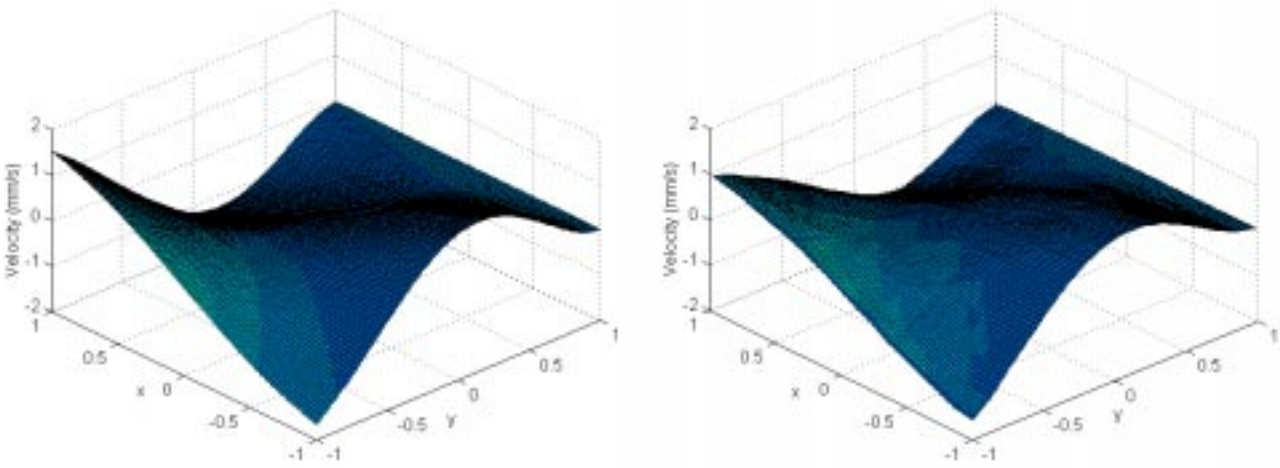


ODS from continuous area scan

ODS from discrete area scan

**Figure 5. 85** Vibration patterns at 202.5 Hz from continuous area scan and the conventional Polytec step-point area scan.

A validation parameter similar to the Modal Assurance Criterion (MAC) was calculated between the ODS derived by continuous area scan (**C**) and discrete area scan (**D**) following the MAC definition:

$$MAC(\mathbf{C},\mathbf{D}) = \frac{\sum_{i=1}^{n}\sum_{j=1}^{m} C_{ij} D_{ij}}{\sum_{i=1}^{n}\sum_{j=1}^{m} C_{ij}^2 \sum_{i=1}^{n}\sum_{j=1}^{m} D_{ij}^2} \qquad \textbf{(5. 66)}$$

where the sums are done for each point of the mode shape surface (then if the ODS is defined for $x$ = -1..0.02..1 and $y$ = -1..0.02..1, $n$ = $m$= 101). Note that the ODS were found to be purely real, therefore no complex notation is used in the MAC equation (5.66). The MAC value obtained was 87 %.

To validate the results the theoretical mode derived analytically by employing the theory for uniform plates, [38], was calculated using Equation (5.57) and its plot is shown in Figure 5.86. The MAC between theoretical mode and ODS from

continuous area scan was 98.4 % while the MAC between theoretical mode and ODS from discrete area scan was 82.7 %.

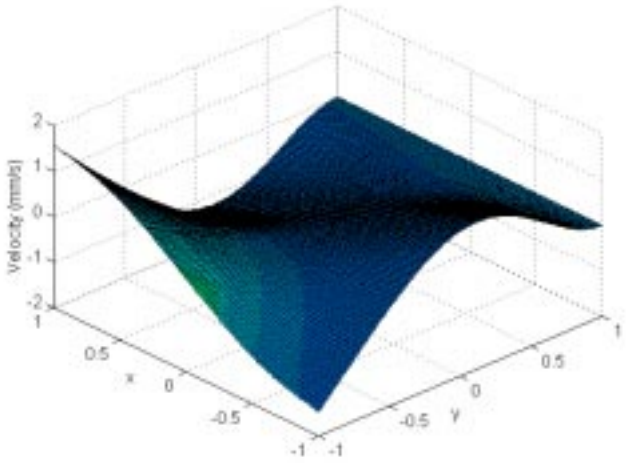


**Figure 5. 86** Analytical 4th mode shape at 202.4 Hz.

*5.5.4.3.3 Test on the Plate at the Fifth Resonance*

An area scan was performed on the plate vibrating at the fifth resonance, i.e. at 241.25 Hz, and following the same procedure described for the fourth resonance, in-phase and out-of-phase components of the ODS were derived as shown in Figure 5.87.

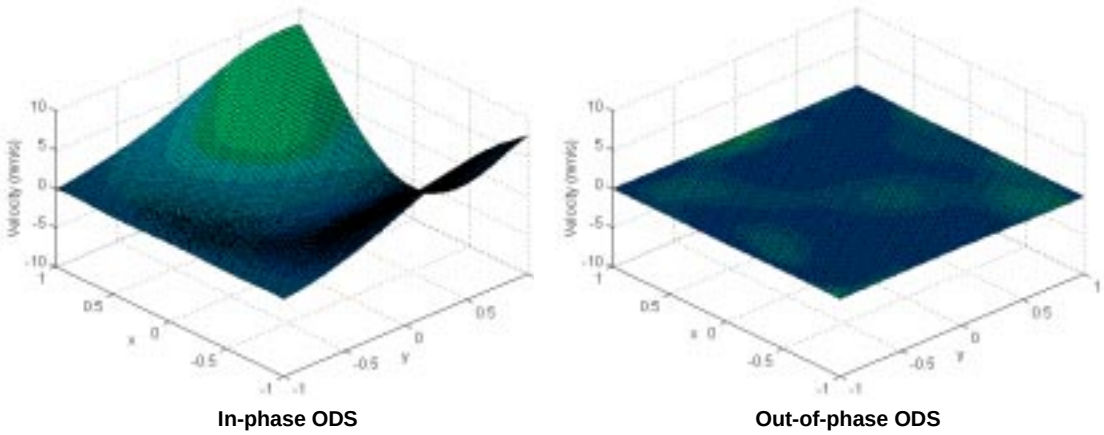


**Figure 5. 87** Vibration pattern from the continuous area scan at 241.25 Hz.

For comparison, the corresponding ODS was recovered from the stepped area scan which was done using the conventional Polytec facilities. In Figure 5.88 the ODSs derived with both techniques are shown.

The MAC parameter derived from the correlation between Polytec and continuous area scan results was 85.27 %. Again, the theoretical mode shape was determined and the correlation performed with the continuous area scan ODS first, and then with the discrete area scan. The MAC values derived were respectively 95.17 and 88.06 %. Figure 5.89 is the plot of the analytical mode shape at 242.68 Hz (see Table 5.7).

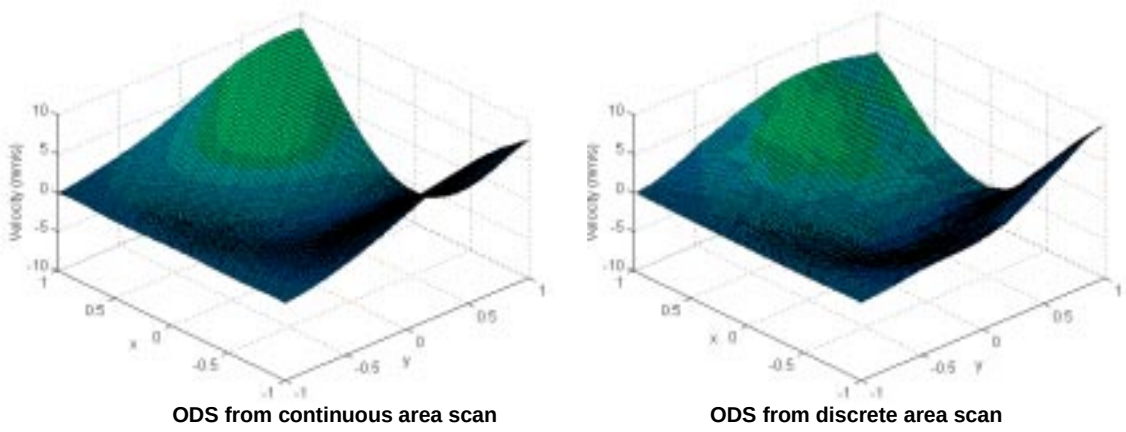


**Figure 5. 88** Vibration patterns at 241.25 Hz from continuous area scan and the conventional Polytec step-point area scan.

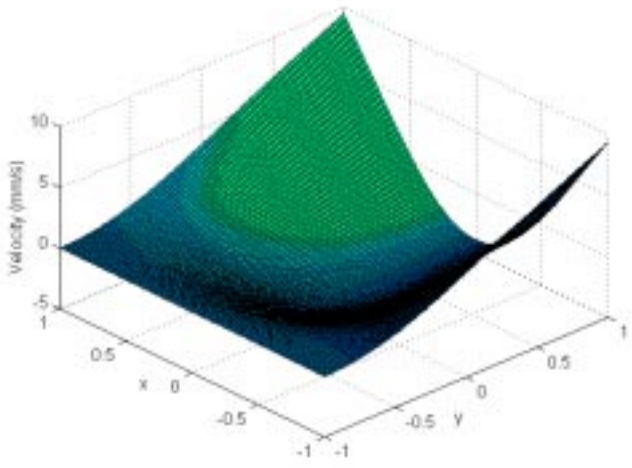

**Figure 5. 89** Analytical 5$^{th}$ mode shape at 242.68 Hz.

### *5.5.5 Sinusoidal Scan on a Circular Area*

#### *5.5.5.1 Mathematical Investigation*

A two-dimensional sinusoidal scan can not only be performed over a rectangular surface, but also on circular elements like discs, if the two directions where the scan is done, are no longer the axes of a 2-D Cartesian reference system but the axes of a polar system, i.e. the beam sweeps in the circumferential and radial directions.

As described in Section 5.4, a circular scan is achieved by directing the LDV measurement point around a circle with a radius *r* at a uniform rate, so that the circumferential direction will be swept at an angular velocity

$$\theta = \Omega_\theta \, t \qquad \textbf{(5. 67)}$$

The radius *r* can also be varied, for example so that $r = R_i....R_f$ , $R_i$ and $R_f$ being the initial and final radii. The radius can be expressed as:

$$r = \frac{R_f - R_i}{2} \cos\left(2\pi \Omega_r \, t\right) + \frac{R_f + R_i}{2} \qquad \textbf{(5. 68)}$$

If $\Omega_r$ is bigger than $\Omega_\theta$ the radial direction will be covered faster than the circumferential one, the laser beam will then cover a pattern like a “daisy”. If the opposite situation occurs the pattern will be a spiral, the circumferential direction being swept faster than the radial one, see Figure 5.90.
The *x*- and *y*-mirror drive signals required to achieve this, in a Cartesian representation, take the form of:

$$x = \left[\frac{R_f - R_i}{2}\cos(2\pi\,\Omega_r t) + \frac{R_f + R_i}{2}\right]\cos(2\pi\,\Omega_\theta t)$$
$$y = \left[\frac{R_f - R_i}{2}\cos(2\pi\,\Omega_r t) + \frac{R_f + R_i}{2}\right]\sin(2\pi\,\Omega_\theta t) \qquad \textbf{(5. 69)}$$

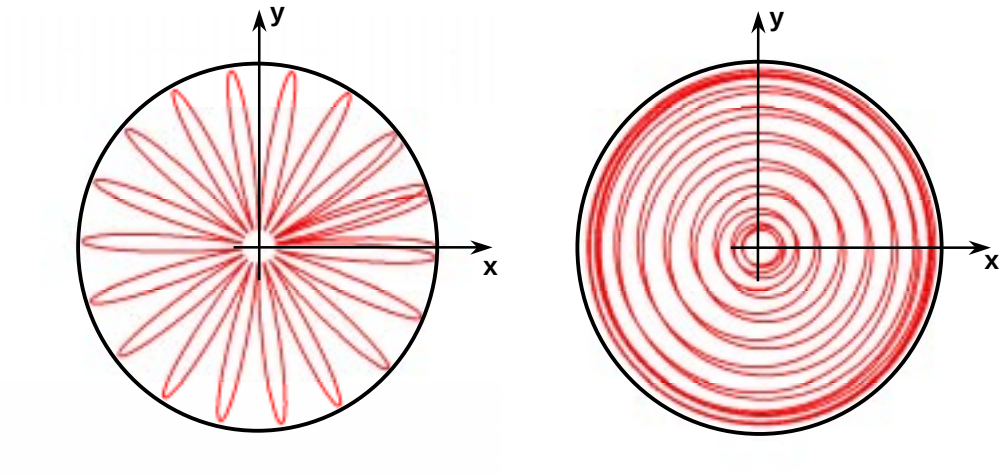


**Figure 5. 90** Laser beam pattern on a disc-like component for circumferential speed (1.1 Hz) lower than the radial (20 Hz) (left), and vice versa (right).

If the vibration pattern of the disc surface can be written as:

$$v(r,\theta,t) = v_{Rn}(r)\cos(n\theta)\cos(\omega\,t) + v_{In}(r)\sin(n\theta)\sin(\omega\,t) \qquad \textbf{(5. 70)}$$

and specifically, the radial mode shape may be expressed as a polynomial of the $p^{th}$ order, then:

$$v_{Rn}(r) = \sum_{i=0}^{p} V_{Rni}\,r^i$$
$$v_{In}(r) = \sum_{i=0}^{p} V_{Ini}\,r^i \qquad \textbf{(5. 71)}$$

If the laser is assumed to scan across a normalised pattern so that $r$ = -1..1 with the zero position in the center of the annular disc it will occur that $R_i$ = -1 and $R_f$ = 1 and the mirror driver signals will be:

$$\begin{aligned} r &= \cos\left(\Omega_r\, t\right) \\ \theta &= \Omega_\theta\, t \end{aligned} \qquad \textbf{(5. 72)}$$

To simplify the analysis, without any losses of generality, only the real component of Equation (5.70) (first addendum) is considered:

$$v(t) = \sum_{i=0}^{p} V_{Rni} \cos^i(\Omega_r t)\cos(n\Omega_\theta\, t)\cos(\omega t) \qquad \textbf{(5. 73)}$$

which can be transformed trigonometrically and written in terms of the sidebands components ($A_{Rn\ i}$) present in the LDV output at frequencies ($\omega \pm n\Omega_\theta \pm i\Omega_r$) with $i$ = 0..$p$ and $p$ the order of the radial polynomial.

$$v(t) = \sum_{i=0}^{p} A_{Rni} \cos\left[(\omega \pm n\Omega_\theta \pm i\Omega_r)t\right] \qquad \textbf{(5. 74)}$$

where $A_{Rn\,i}$ is related to the polynomial coefficients $V_{Rni}$ according to the partially changed usual transformation:

$$\{V_{Rn}\} = 2[T]\{A_{Rn}\} \qquad \textbf{(5. 75)}$$

In fact, expanding out Equation (5.73) for $p$ = 0...3 it will occur:

$$
\begin{aligned}
&for \quad i=0 && \frac{1}{2}V_{Rn0}\cos[(\omega\pm\Omega_\theta)t] \\
&for \quad i=1 && \frac{V_{Rn1}}{4}\cos[(\omega\pm\Omega_\theta\pm\Omega_r)t] \\
&for \quad i=2 && \frac{V_{Rn2}}{8}\cos[(\omega\pm\Omega_\theta\pm2\Omega_r)t]+\frac{V_{Rn2}}{4}\cos[(\omega\pm\Omega_\theta)t] \\
&for \quad i=3 && \frac{V_{Rn3}}{16}\cos[(\omega\pm\Omega_\theta\pm3\Omega_r)t]+\frac{3V_{R3}}{16}\cos[(\omega\pm\Omega_\theta\pm\Omega_r)t]
\end{aligned}
$$

In the frequency domain the LDV output will then have components at the usual frequencies with the following amplitudes:

$$
\begin{aligned}
&at \quad && \omega\pm\Omega_\theta && A_{Rn0}=\frac{V_{Rn0}}{2}+\frac{V_{Rn2}}{4} \\
&at \quad && \omega\pm\Omega_\theta\pm\Omega_r && A_{Rn1}=\frac{V_{Rn1}}{4}+\frac{3V_{Rn3}}{16} \\
&at \quad && \omega\pm\Omega_\theta\pm2\Omega_r && A_{Rn2}=\frac{V_{Rn2}}{8} \\
&at \quad && \omega\pm\Omega_\theta\pm3\Omega_r && A_{Rn3}=\frac{V_{Rn3}}{16}
\end{aligned}
$$

which can be written as:

$$
\begin{Bmatrix} A_{Rn0} \\ A_{Rn1} \\ A_{Rn2} \\ A_{Rn3} \end{Bmatrix} = \begin{bmatrix} 1/2 & 0 & 1/4 & 0 \\ 0 & 1/4 & 0 & 3/16 \\ 0 & 0 & 1/8 & 0 \\ 0 & 0 & 0 & 1/16 \end{bmatrix} \begin{Bmatrix} V_{Rn0} \\ V_{Rn1} \\ V_{Rn2} \\ V_{Rn3} \end{Bmatrix} = \frac{1}{2}\begin{bmatrix} 1 & 0 & 1/2 & 0 \\ 0 & 1/2 & 0 & 3/8 \\ 0 & 0 & 1/4 & 0 \\ 0 & 0 & 0 & 1/8 \end{bmatrix} \begin{Bmatrix} V_{Rn0} \\ V_{Rn1} \\ V_{Rn2} \\ V_{Rn3} \end{Bmatrix}
$$

The polynomial coefficients can be expressed as functions of the spectral amplitudes only, by inverting the matrix transform which will then coincide, again, with [T], the only difference being, with respect to linear scan process, of the multiplication by the factor 2.

*5.5.5.2 Numerical Simulation*

In order to simulate the vibration velocity experienced by the laser beam when it scans over the plane surface of a disc, the theory of thin discs (i.e. rotational inertia and shear effects are neglected) is taken into analysis. Specifically, the disc is an annular plate of internal radius 0.015 m and external radius of 0.15 m and it is clamped on the inside. The specimen is shown in Figure 5.91 with reference to a polar coordinate system with the origin coincident with the center of the disc. This configuration is the most common to find in practice, when an axi-symetric disc is fixed to a rotating shaft.

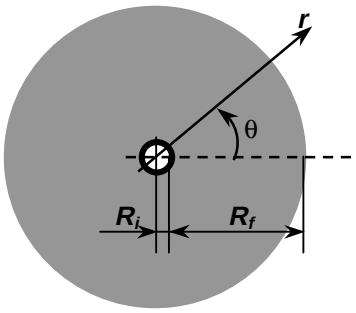


**Figure 5. 91** Annular disc clamped on inside and free on outside.

The solution of the equation of the disc transverse vibrations is given in reference [38] and, after some simplifications (i.e. the origin of the polar reference system coincides with the disc center and the boundary conditions possess symmetry with respect to one or more diameters of the disc), can be written as:

$$w(r,\theta) = \sum_{n=0}^{\infty} \left[ A_n J_n(kr) + C_n I_n(kr) \right] \cos(n\theta) \qquad \textbf{(5. 76)}$$

where $J_n$ is the Bessel function of the first kind,

$I_n$ is the modified Bessel function of the first kind,

$n$ = 0, 1, ... ∞ is the number of nodal diameters (diametral lines where the vibration is zero) of the mode shape,

$k$ is a factor depending on the natural frequency associated with the mode shape so that $k^2 = \omega\sqrt{\frac{\rho h}{D}}$, where ρ is the mass density of the disc, $h$ is its thickness and $D$ is the flexural rigidity, and $A_n$, $C_n$ are constants to be established by defining the boundary conditions on both the disc edges.

For a typical mode $n$, the radial component of the mode shape can be expressed as:

$$w_n(r) = A_n J_n(kr) + C_n I_n(kr) \qquad \textbf{5. 77}$$

and it must be understood that $n$ can take all values from 0 to ∞.

If the inside radius ($R_i$ ) of the disc is clamped all around, the boundary conditions at $r = R_i$ for every values of θ will be:

$$\begin{aligned} w(R_i) &= 0 \\ \left.\frac{dw(r)}{dr}\right|_{r=R_i} &= 0 \end{aligned} \qquad \textbf{5. 78}$$

By introducing Equation (5.77) in (5.78), the existence of a non-trivial solution yields the characteristic equation:

$$J_n(kR_i) I_{n+1}(kR_i) + I_n(kR_i) J_{n+1}(kR_i) = 0 \qquad \textbf{5. 79}$$

The eigenvalues $kR_i$ can be obtained by solving Equation (5.79) but they are tabulated [38] Considering a disc with an inside radius of 0.015m and an outside radius of 0.15 m ($R_i/R_f$ = 0.1) and assuming the mode shape to have 2

nodal diameters ($n$) and one nodal circumference ($s$) (i.e. circle where the vibration is zero), the value of $\lambda^2 = \omega R_i^2 \sqrt{\frac{\rho h}{D}}$ is 37 and then $kR_i = \lambda = 6.0828$.

The mode shapes of Equation (5.77) are determined from either Equations (5.78). Using the first equation the constants ratio will be derived:

$$\frac{A_n}{C_n} = -\frac{I_n(kR_i)}{J_n(kR_i)} = -1.0014 \qquad \textbf{(5. 80)}$$

The radial mode shape ( Equation (5.77) ) becomes then:

$$w_n(r) = -1.0014 J_n(6.0828\, r) + I_n(6.0828\, r) \qquad \textbf{(5. 81)}$$

which is shown in Figure 5.92.

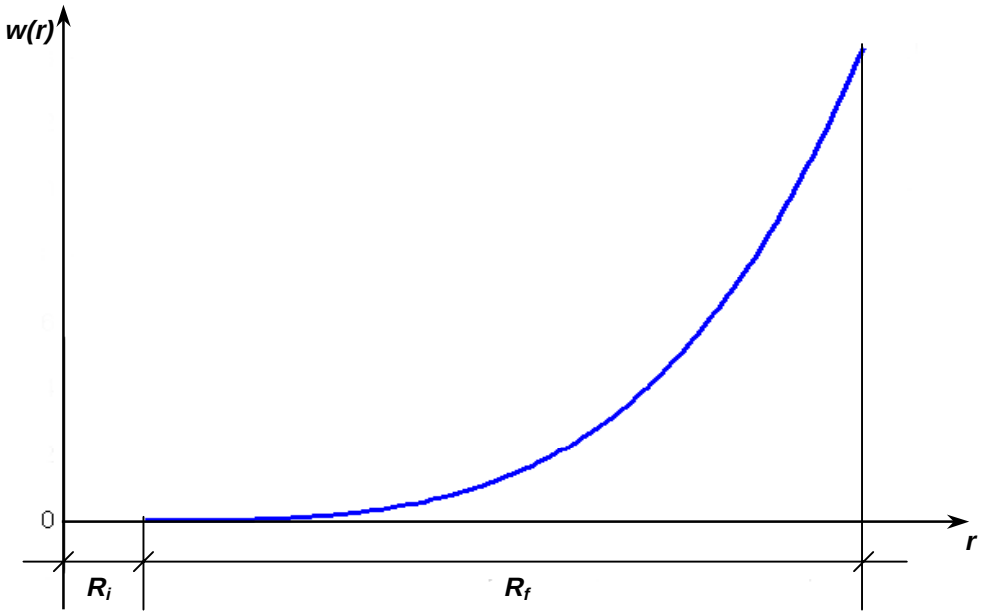


**Figure 5. 92** Radial mode shape.

The complete mode shape is given by Equation (5.76):

$$w_n(r,\theta) = [-1.0014 J_n(6.0828\, r) + I_n(6.0828\, r)]\cos(2\theta) \qquad \textbf{(5. 82)}$$

and this is shown in Figure 5.93.

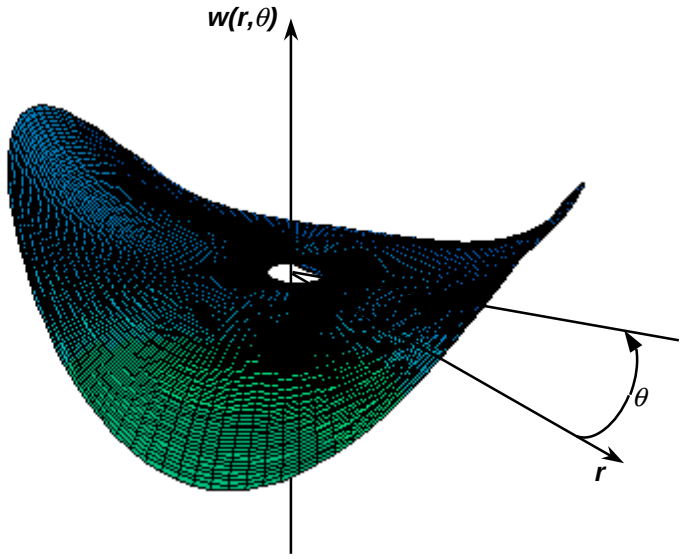


**Figure 5. 93** Mode shape of the disc with two nodal diameters and one nodal circumference.

In order to make it possible to apply the Fourier transform to the LDV output when this scans all over the disc surface and to recover from it the ODS of the disc itself, the mode shape must be written as a polynomial. The radial mode shape is then approximated by a 4$^{th}$ order polynomial and the two-dimensional mode shapes can be rewritten as:

$$w(r,\theta) = [28.63r^4 - 0.021623r^3 - 0.0046211r^2 - 0.000063543r + 7.0151e^{-7}]\cos(2\theta) \quad \textbf{(5. 83)}$$

If now an LDV scan is performed across the disc surface undergoing this vibration pattern, the laser beam will output a velocity signal of the form:

$$v(t) = [28.63r^4 - 0.021623r^3 - 0.0046211r^2 - 0.000063543r + 7.0151e^{-7}] \cos(2\theta)\cos(2\pi\omega t) \quad \textbf{(5. 84)}$$

which is exclusively dependent on the time coordinate, $r$ and θ being given by Equations (5.68) and (5.67).

The natural frequency, ω, can be determined from knowledge of the tabulated parameter, $\lambda^2 = 2\pi\omega R_i^2\sqrt{\frac{\rho h}{D}} = 37$, $D$ being $Eh^3/12\,(1\text{-}\nu^2)$. Assuming the disc is made from aluminum ($E$ = 6.75 $e^{10}$ N / m$^2$ and ρ = 2640 kg / m$^3$) and its thickness is 0.005 m the natural frequency will be 2026 Hz.

First, the laser beam is supposed to follow a spiral pattern at a circumferential speed of 20 Hz and a radial speed of 1.1 Hz; the LDV time history is shown then in Figure 5.94and its Fourier spectrum in Figure 5.96. If, successively, the laser is considered to perform a daisy on the disc surface with circumferential and radial speed reversed the LDV output time history and spectrum will become as shown in Figure 5.95 and 5.97.

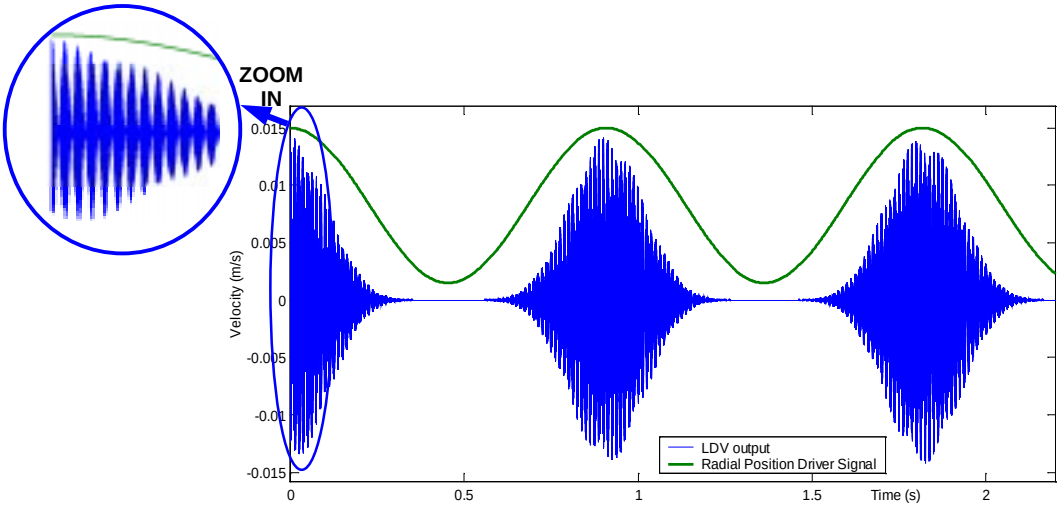


**Figure 5. 94** LDV output time history when the laser beam scans in a spiral pattern over the surface of the disc vibrating at the natural frequency of 2026 Hz. The zoom shows clearly the signal modulation given by the circumferential motion of the laser beam.

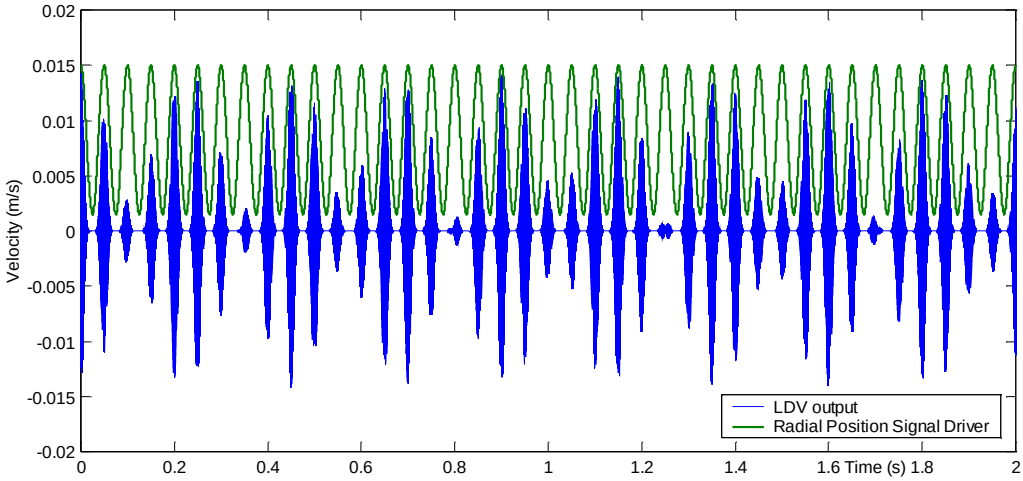


**Figure 5. 95** LDV output time history when the laser beam scans in a daisy pattern over the surface of the disc vibrating at the natural frequency of 2026 Hz. The modulation due to the circumferential motion of the laser beam is visible.

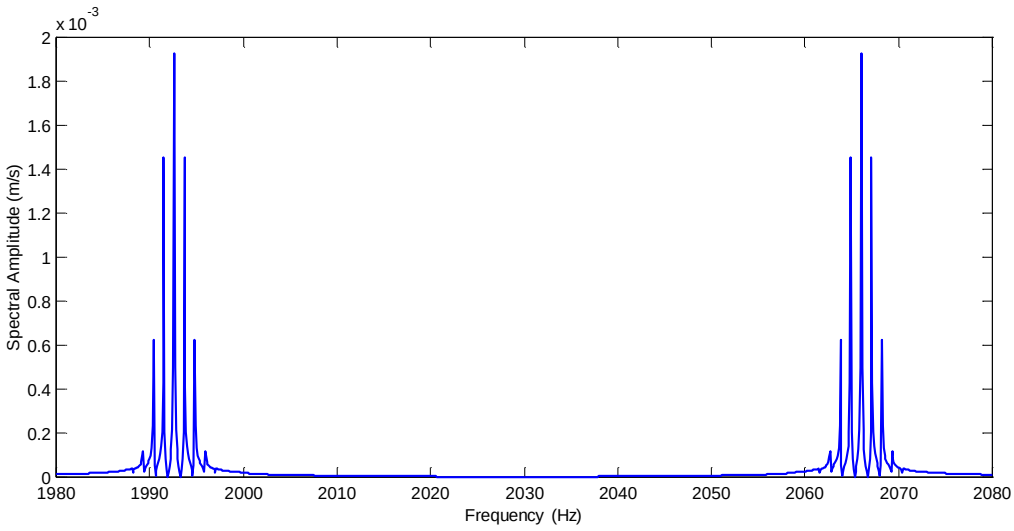


**Figure 5. 96** LDV output time history when the laser beam scans over a spiral pattern on the surface of the disc vibrating at the natural frequency of 2026 Hz.

When the laser beam scans in a spiral pattern the circumferential direction is swept at the speed of 20 Hz. Two groups of sidebands then appear spaced of 20 × 2 = 40 Hz from the excitation frequency since the nodal diameters are two.

Each group is formed by 4 pairs of sidebands 1.1 Hz (the radial speed) apart from each other, the radial polynomial mode shape being of the 4$^{th}$ order.

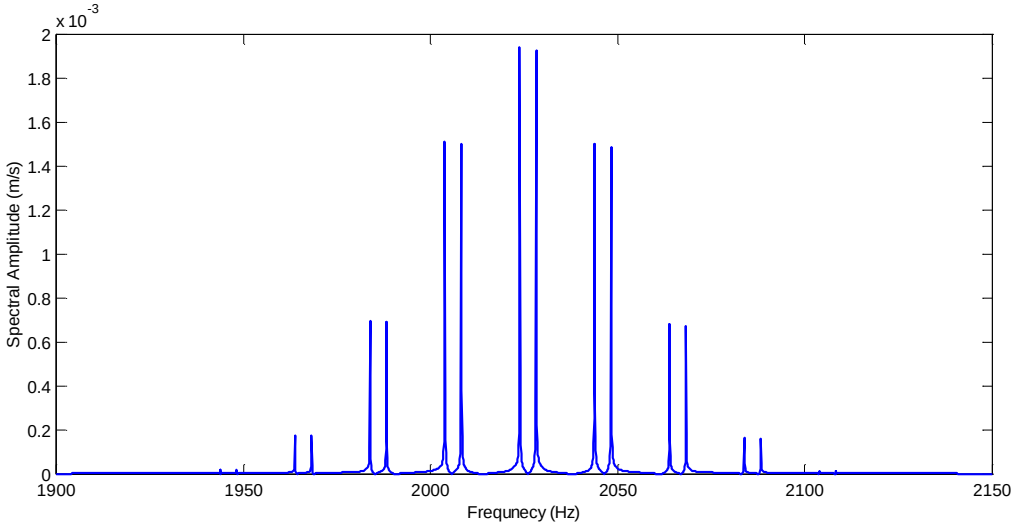


**Figure 5. 97** LDV output time history when the laser beam scans in a daisy pattern over the surface of the disc vibrating at the natural frequency of 2026 Hz.

Now the LDV spectrum consists of four pairs of sideband groups spaced 20 Hz (the radial frequency) from each other and each group then contains 2 sidebands spaced apart by $1.1 \times 2 = 2.2$ Hz, where 1.1 Hz is the circumferential speed, in which direction two nodal diameters are present.

The LDV output time history is then post-processed in the usual way by being multiplied by sine and cosine functions at frequencies ($2026 \pm 2 \times 1.1 \pm i \times 20$), considering the laser beam performing a daisy (LDV output spectrum shown in Figure 5.99), for $i = 0...4$. The LDV spectral components derived are depicted in amplitude and phase in Figure 5.98 and they are:

$$\{A_n\} = \{\ 2.071\ e^{-3}\ \ 1.607\ e^{-3}\ \ 7.347\ e^{-4}\ \ 1.814\ e^{-4}\ \ 1.885\ e^{-4}\ \}$$

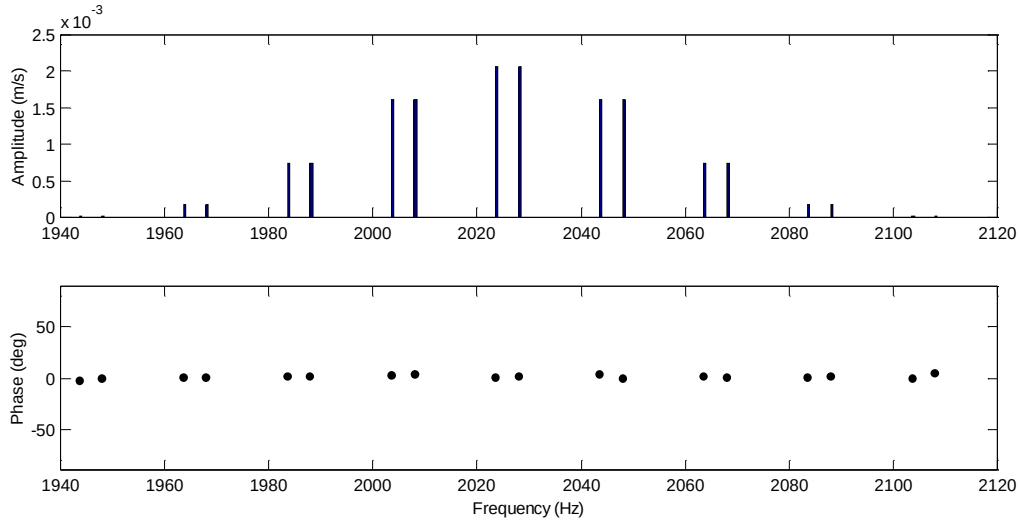


**Figure 5. 98** Curve fitted LDV output spectrum in amplitude and phase.

By applying to the sidebands amplitude vector to the transformation shown in Equation 5.75, the polynomial coefficients series $V_{ni}$ can be recovered:

$$\{V_n\} = \{\ 1.278\ e^{-3}\ \ 4.252e\ e^{-3}\ \ 5.274\ e^{-3}\ \ 2.903\ e^{-3}\ \ 6.034\ e^{-4}\}$$

The polynomial representing the radial mode shape can be derived, bearing in mind, that the radial position is normalised between –1 and 1, instead of going from the true dimensions of the disc (0.015 and 0.15 m). Then, if the spatial position is defined as *x* = -1...1, in order to recover the same plot as Figure 5.93 with *r* = 0.015...0.15 the radial mode shape should be written as

$$w(r) = 1.287\,e^{-3}\left(-1.222+14.815r\right)^4 - 4.252\,e^{-3}\left(-1.222+14.815r\right)^3 + \\ +5.274\,e^{-3}\left(-1.222+14.815r\right)^2 - 2.903e^{-3}\left(-1.222+14.815r\right) + 6.034\,e^{-4}$$

which can be approximated by a polynomial of *r* only :

$$w(r) = [29.0720\,r^4 - 0.1522\,r^3 - 0.0082\,r^2 - 0.0005\,r + 5.88e^{-6}]$$

This radial mode shape can be compared with the one given by Equation (5.81) which is the original and is shown in Figure 5.92.

The two dimensional disc mode shape is finally given by

$$w(r,\theta) = [29.0720\,r^4 - 0.1522\,r^3 - 0.0082\,r^2 - 0.0005\,r + 5.88\,e^{-6}]\cos(2\theta)$$

which completely matches the original mode shape given by Equation (5.82) and shown in Figure 5.93.

### *5.5.5.3 Experimental Validation*

As a practical example of circular area scans, a laboratory test was performed on the pin-on-disc rig described in Section 5.4, Figure 5.42, with the pin retracted and with direct excitation at a relevant 3$^d$-diameter mode resonance frequency (2271 Hz). The scan across the disc surface was achieved by driving the LDV mirrors by signals given by Equation (5.69) at the frequencies of 20 and 1.1 Hz and with external radius ($R_f$) coincident with the disc actual radius (0.406 m) and the internal one ($R_i$) as large as the bolt fixing the disc on the shaft could be avoided (i.e. 0.025 m). Under these conditions, the total time required by the laser scanning beam to cover the whole disc annular surface is about 1 sec, since the time to perform one cycle in the lower-speed (1.1 Hz) direction is 0.0909 secs. First a daisy pattern ($\Omega_r$ bigger than $\Omega_\theta$) was produced and the LDV spectrum obtained is shown in Figure 5.99.

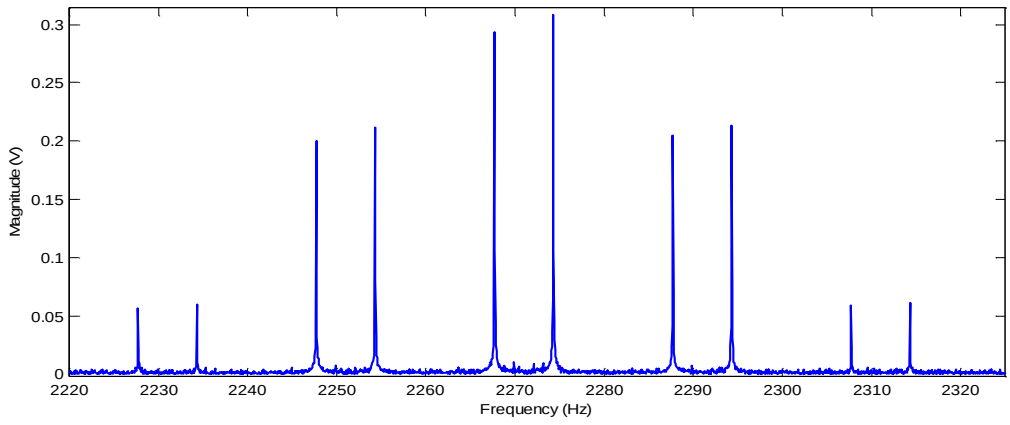


**Figure 5. 99** LDV signal spectrum for the daisy scan and excitation at 2271 Hz.

The LDV spectrum consists of only two sideband pairs on either side of the central pair, so that the radial distribution derived, will simply be a quadratic expression in *r*. Moreover, each group of sidebands is split in two, the spacing between each pair being $\pm 3\,\Omega_\theta$. Spectral components are then located at $2271 \pm 3 \times 1.1 \pm i \times 20$ Hz, with $i$ = 0, 1 and 2. They are shown, averaged out with respect to the central frequency, i.e. the excitation frequency 2271 Hz, in Figure 5.100.

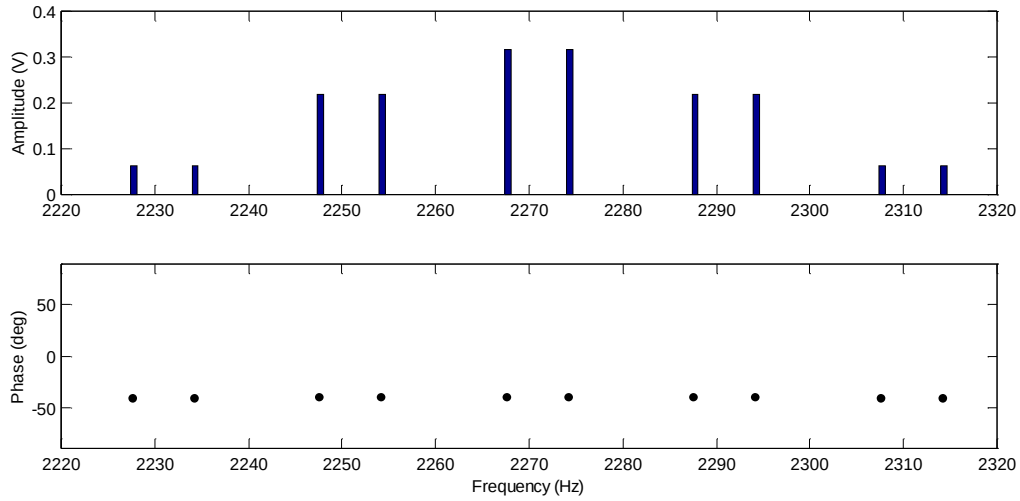


**Figure 5. 100** Sidebands spectral components of the LDV output.

The sideband matrix $\{A_n\}$ can then be recovered, considering only the radial components at $2271 + 3 \times 1.1 \pm i \times 20$ Hz. All of these will have the same sign (i.e. positive), the sideband components being in phase with each other:

$$\{A_n\} = \{0.3160 \quad 0.2192 \quad 0.0629\}\ (\mathrm{V})$$

By applying the transformation in Equation (5.75), the polynomial coefficients can be recovered and by multiplying by the LDV velocity range (5 mm/s/V) they can be expressed in terms of velocity:

$$\{V_n\} = \{1.9005 \quad 4.3846 \quad 2.5196\}\ (\mathrm{mm/s})$$

Then the radial mode shape will be

$$w(r) = 2.5196\,r^2 + 4.3846\,r + 1.9005$$

which is plotted, for a normalised radial position ($r$ = -1...1), in Figure 5.101.

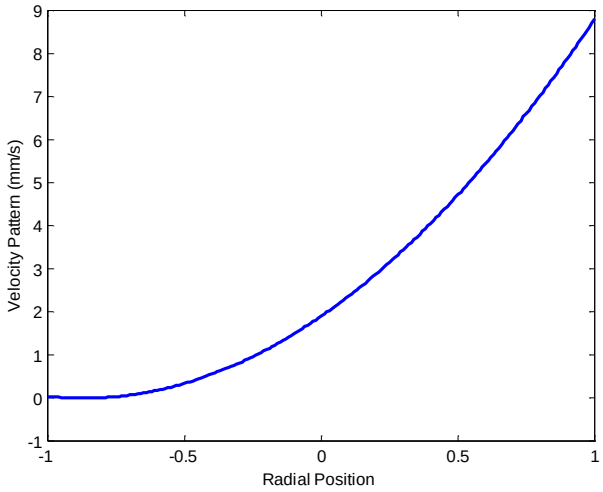


**Figure 5. 101** Radial ODS at 2271 Hz along the radius of the annular disc.

The global ODS will be:

$$w(r,\theta) = \left(2.5196\,r^2 + 4.3846\,r + 1.9005\right)\cos(3\theta)$$

which is plotted against the true dimension of the annular disc in Figure 5.102.

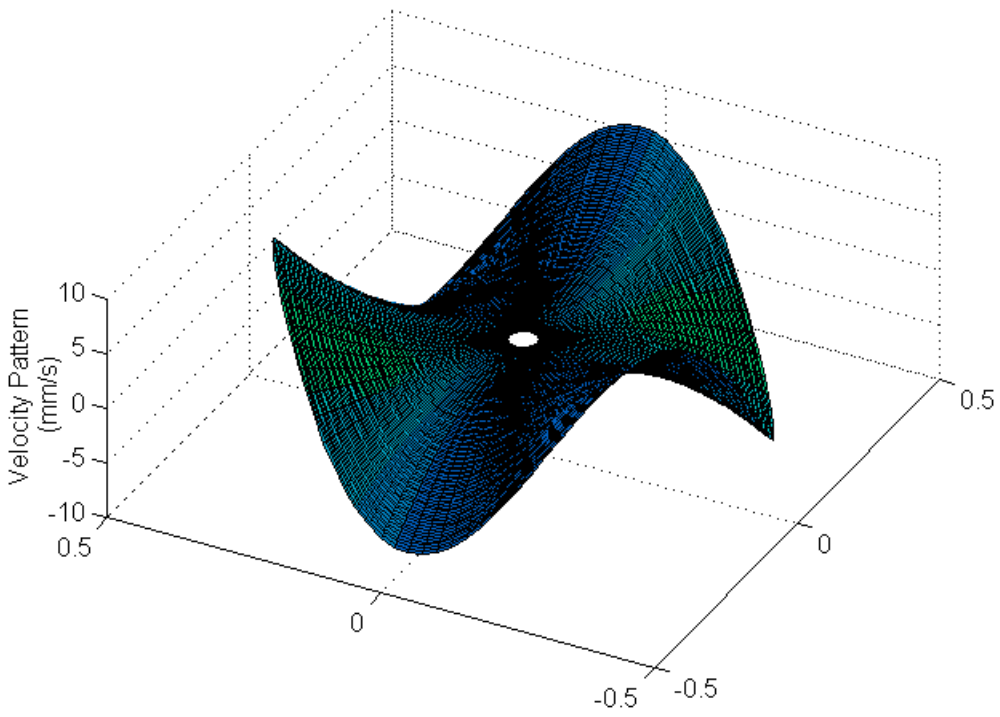


**Figure 5. 102** Two-dimensional ODS at 2271 Hz.

By performing a spiral pattern scan across the annular disc surface by substituting the radial frequency with the circumferential (i.e. $\Omega_r$ = 1.1 Hz and $\Omega_\theta$ = 20 Hz), and following the same procedure, an identical two-dimensional ODS can be recovered. The LDV output spectrum is shown in Figure 5.103.

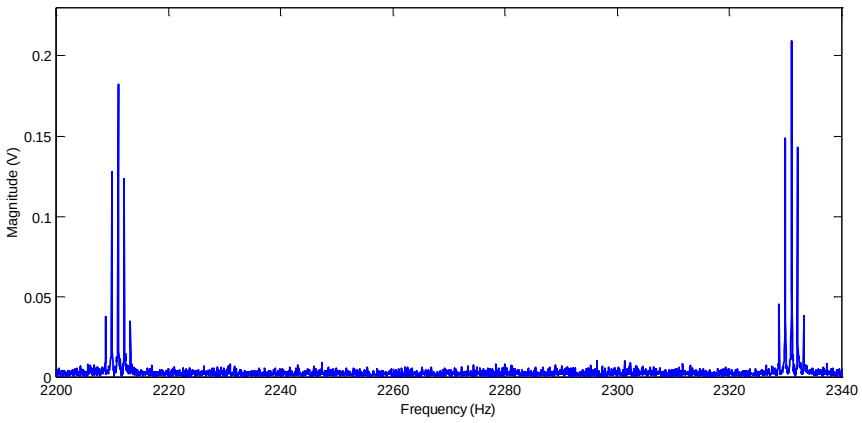


**Figure 5. 103** LDV signal spectrum for the spiral scan and excitation at 2271 Hz.

## *5.6. Modal Analysis of ODSs derived by Area Scan*

### *5.6.1 Introduction*

The CSLDV methods described in the previous sections give response measurements for sinusoidal excitation at a single frequency and yield real and imaginary ODSs to be recovered as polynomial series, over the area being scanned. If the process is repeated at a series of frequencies, with sufficient frequency resolution, as in a stepped-sine test, frequency response functions can be established over this range. By applying any conventional modal analysis process to these FRFs, natural frequencies, modal damping factors and modal constants may be evaluated. The modal analysis procedure can be applied to the sideband responses referred to the measured input force directly. These represent weighted summations of responses which form the eigenvectors in just the same way as any other grouping of DOFs, i.e. measured points on the structure which now corresponds to the sidebands on the spectrum, the latter giving the spatial information. The processing necessary to derive series coefficients for ODSs is then performed on the modal constants in order to obtain, this time, mode shapes, again as polynomial series. If multiple FRFs have been acquired by a sinusoidal area scan over a whole surface, this represents a considerable saving because a global modal analysis algorithm may be applied to the complete set of scan data.

It must be pointed out that the modal analysis process is, in this case, applied to sidebands referred to a derived natural frequency which is artificially translated by the scan procedure, i.e. for the *n,m* sideband the natural frequency will be $(\omega_r + n\Omega_x + m\Omega_y)$ where $\omega_r$ is the true natural frequency. This means that the "natural frequencies" derived from sideband FRFs are shifted by $n\Omega_x + m\Omega_y$. In consequence, estimates of modal damping factors and modal constants have to be multiplied by $\dfrac{\left(\omega_r + n\Omega_x + m\Omega_y\right)^2 - \left(\omega + n\Omega_x + m\Omega_y\right)^2}{\omega_r^2 - \omega^2}$.

In fact, the modal analysis procedure consists of applying the following formula to derive the modal constant, see reference [1]

$$H_{jk}(\omega) = \sum_{r=1}^{N} \frac{{}_{r}A_{jk}}{\omega_r^2 - \omega^2 + i\eta_r\omega_r^2} \qquad \textbf{(5. 85)}$$

where $H_{jk}$ is the FRF measured at the point *j* that now is the sideband location, i.e. *j* = *i,l* with *i*= 0 ... *n* and *l*= 0 ... *m* and *k* is the excitation point which is unique, the excitation being position in only one point;

${}_{r}A_{jk}$ is the modal constant relative to the $j^{th}$ (i.e. *n,m*) sideband FRF again *k* being constant;

$\omega_r$ the natural frequency of the natural mode included within the frequency range ω analysed, which usually is in the neighborhood of a maximum response frequency and then of the natural frequency;

$\eta_r$ the damping loss factor.

This relationship is exact in the case of the first FRF associated with the excitation frequency, which is not translated by the *x*- and *y*-scan speeds, but for the other FRFs corresponding to the sidebands this translation must be taken into account.

An example may clarify the somewhat unusual perspective on modal testing illustrated above.

### *5.6.2 Experimental Modal Analysis on the Garteur Structure*

A laser Doppler vibrometer was used to perform a continuous scan over a particular test piece, the GARTEUR structure, used as a test case for evaluating modal testing methods and FE analysis capabilities, see reference [19]. The

GARTEUR structure is a high-tail aircraft model, consisting of a beam assembly as shown in Figure 5.104. The dimension of the wing span is 2 m.

**Figure 5. 104** The GARTEUR structure.

The structure was hung from the ceiling with the tail on top. The front surface of the wing was scanned by the LDV and the excitation was applied from behind, at one end of and perpendicular to the wing surface, see in Figure 5.105.

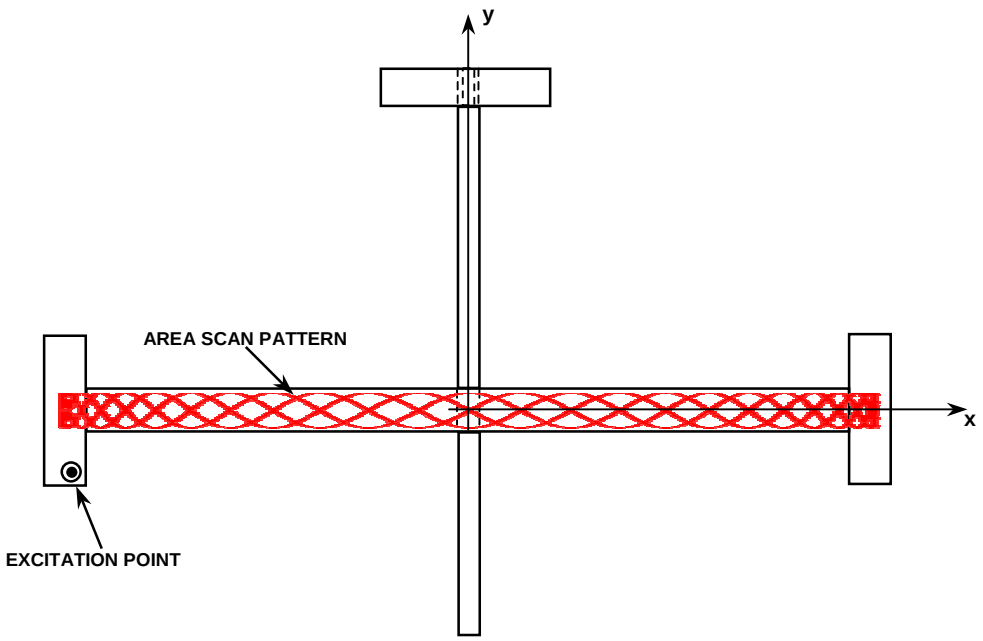


**Figure 5. 105** Excitation and LDV continuous-scan path.

The frequency range excited (30-40 Hz) was chosen so as to include a specific natural frequency of one of three close natural modes which had been located by performing a finite element analysis on the structure. These modes, all involving out-of-plane vibration of the wing part of the structure, have a predominantly wing bending mode at 32.58 Hz, a symmetric wing torsion at 33.11 Hz, and a skew-symmetric wing torsion at 33.38 Hz.

In the experimental set-up the structure was hung nose-down, so that the LDV could be directed at any point on the wing almost perpendicularly to measure its *z*-axis vibration. Response measurements were obtained with the LDV scanning over an area encompassing both wings, with an *x*-axis sinusoidal scan at 0.3 Hz ($\Omega_x$), and a simultaneous *y*-axis scan ($\Omega_y$) at 5.0 Hz. The frequency-domain spectrum of the LDV, then contains components at all frequencies ($\omega \pm n\Omega_x \pm m\Omega_y$), from which coefficients $V_{n,m}$ for the polynomial series $\Sigma V_{n,m} x^n y^m$ giving the spatial ODS may be derived. In this case, *y*-axis vibration only involved torsional-type motion, so only values of 0 and 1 needed to be included for *m* while values of *n* up to 7 were adequate to describe the ODS along *x*-axis direction.

By performing a conventional point measurement directing the laser beam in a steady position, corresponding to the excitation point a conventional magnitude, and phase point FRF is obtained (see Figure 5.106) which indicates a mode at 35.0 Hz comparable with the predicted natural frequencies 32.58, 33.11 and 33.38 Hz.

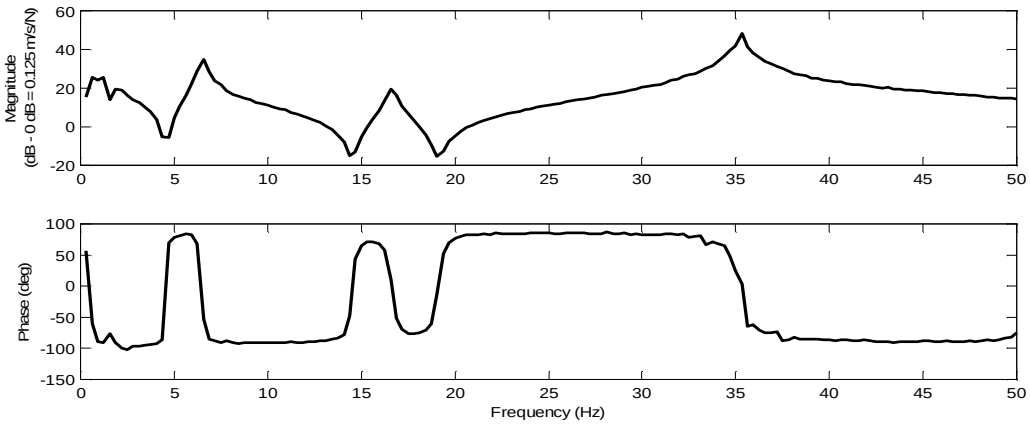


**Figure 5. 106** Point Mobility FRF.

When a continuous scan was performed over the area previously mentioned, the maximum vibration response was found at 34.8 Hz, corresponding roughly to the natural frequency. In order to determine the excitation frequency to have the maximum vibration, the frequency of the signal feeding the shaker was changed between 30 and 40 Hz and by observing the modulated LDV output signal the excitation could be decided. The natural frequency to be excited was the one corresponding to the excitation frequency which produces a maximum LDV output with a more emphasised modulation. This time history is illustrated in Figure 5.107 together with the mirror driver signals.

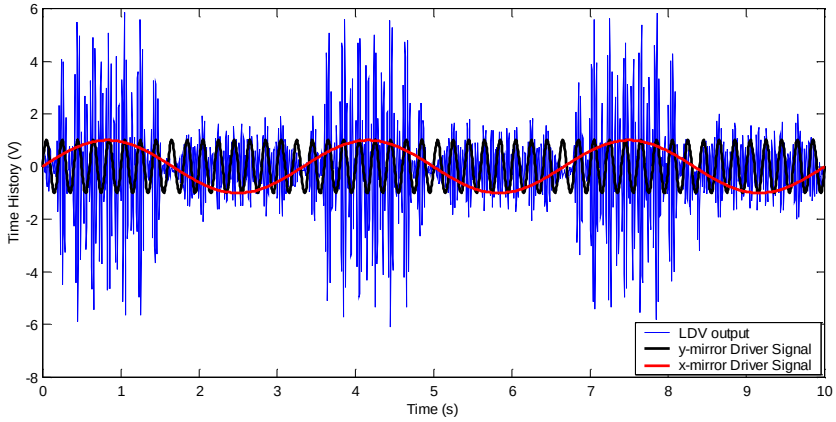


**Figure 5. 107** LDV time-signal obtained by area scan; and *x*-axis and y-axis mirror drive signals.

By post-processing the time signal in the usual way, the ODS at 34.8 Hz is recovered in order to have a basis of comparison with the corresponding mode shape which will be obtained by performing a modal analysis procedure on the set of measurement data acquired in the step-sine process described below. The complex spectrum of the LDV time signal is shown in Figure 5.108 in magnitude / phase format. It was extracted by multiplying the LDV time signal by suitably phase-shifted (depending on the mirrors delay) sine and cosine waves at each component frequency ( $34.8 \pm n\,0.3 \pm m\,5$, with $n = 0, 1$ and $m = 0, ..., 7$). It can be noticed that, for an ODS, the reference phase vector for real and imaginary components is arbitrary. It can conveniently be set, as it was

for the illustrations here, to minimise the imaginary component. All the components are then almost lined up at 0° and 180°. The spectrum consists of three sidebands groups: a central one, symmetrical, which describes the wing's translational vibration along the *x*-axis, the longest dimension, and two groups, similar to each other, spaced symmetrically about ($\omega \pm \Omega_y$), which describe the torsional vibration, along the shortest dimension (*y*).

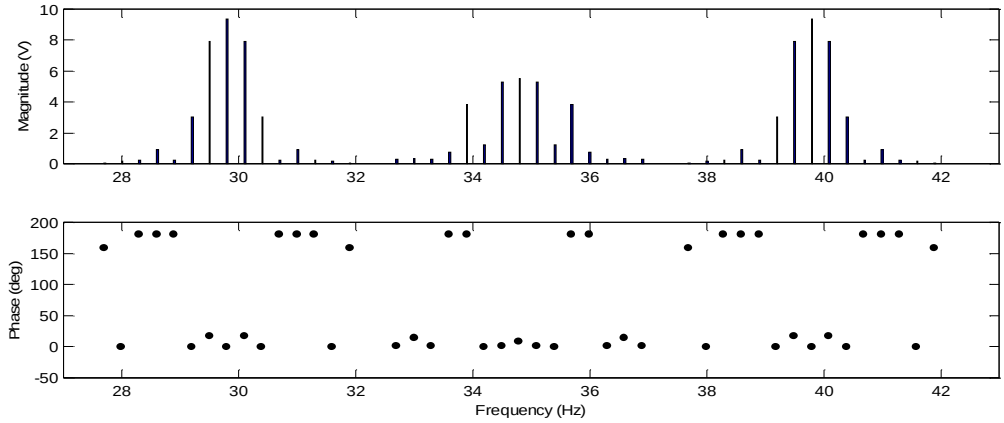


**Figure 5. 108** Area scan LDV signal spectrum components.

These sideband data were processed to give 16-term polynomial equations for real and imaginary ODS surfaces, which are plotted in Figure 5.109. This describes a complex ODS with, predominantly, a torsion mode of the left-hand wing, and some bending.

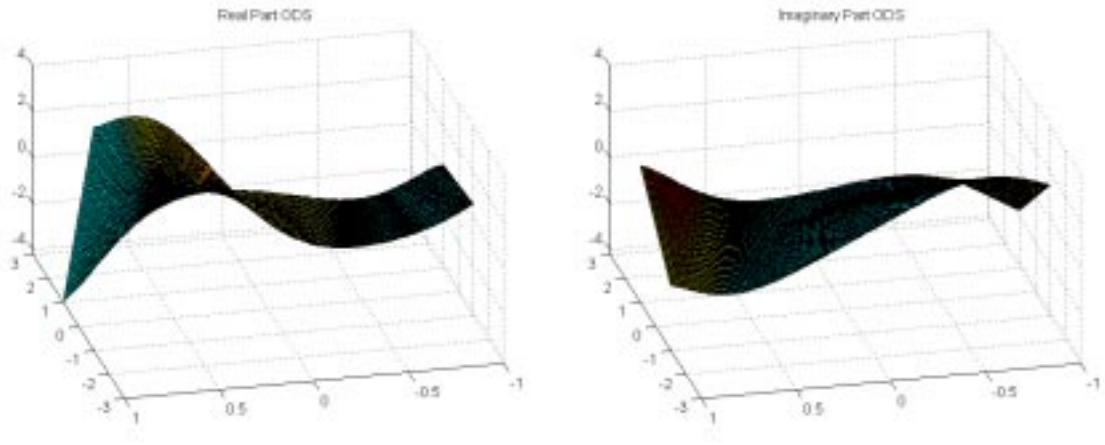

**Figure 5. 109** Real and imaginary ODS at 34.8 Hz.

Now, attention is concentrated on the sine-step procedure which was performed around the maximum response frequency of 34.8 Hz in order to undertake a modal analysis on it and to derive the normal mode shape. Sideband data were obtained at a series of frequencies between 33.7 and 37.7 Hz, with a 0.1 Hz step, then normalised to the input force signal and plotted to give a set of sideband FRFs (see Appendix A.2, Figures from A.10 to A.29, for the sideband FRFs at frequencies from 34 to 35.9 Hz, i.e. around resonance).

Note that the sideband FRF amplitudes increase in proximity to the maximum response frequency (34.8 Hz) and the maximum amplitude is indeed reached around this frequency (Figures A.17, A.18, A.19). A change in the phase of the sideband FRFs can be observed as well. In fact, passing through the maximum response frequency, the phase of each spectral component undergoes a 180° phase shift. For instance, if attention is concentrated on the central component, it can be seen that for frequencies smaller than 34.8 Hz, the phase assumes a value around -50° while for higher frequencies its value is around 100°, see Figures A.10 up to A.29. From these sideband FRFs, conventional FRFs can be derived: the conventional FRF on the frequency range between 33.7 and 37.7 Hz, where the sine-step test was performed, associated with each component of the sideband FRFs can be determined taking the amplitude and phase values corresponding to these components at each frequency step. For example, the conventional FRF corresponding to the central component of the sideband FRFs consists of the series of the central components of each sideband FRF. The first element will be the central component of the sideband FRF at 33.7 Hz, the second element will be the central component of the sideband FRF at 33.8 Hz, and so on up to the last sideband FRF at 37.7 Hz. This FRF is shown in Figure 5.110 in amplitude and phase within the frequency range studied. Some FRFs relative to further sidebands are plotted in Figures 5.111 (for the $4^{th}$ sideband of the central group), 5.112 (for the central sideband of the left sideband group) and 5.113 (for the second sideband of the sideband group) as shown in the small diagrams plotted in each picture.

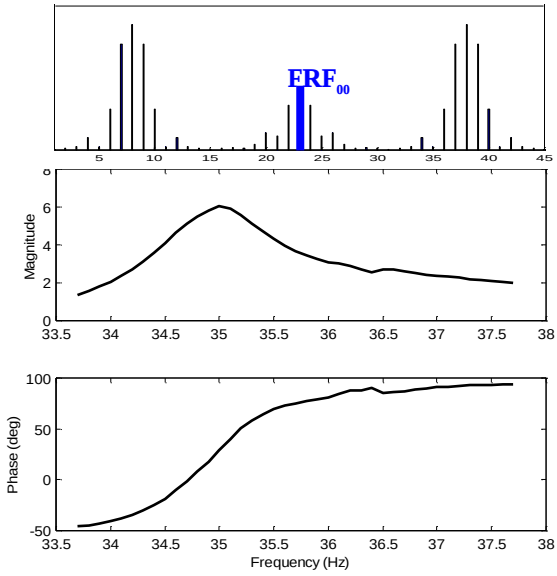


**Figure 5. 110** FRF relative to the central component of the LDV spectrum ($n = 0$, $m = 0$) as emphasised in the top diagram.

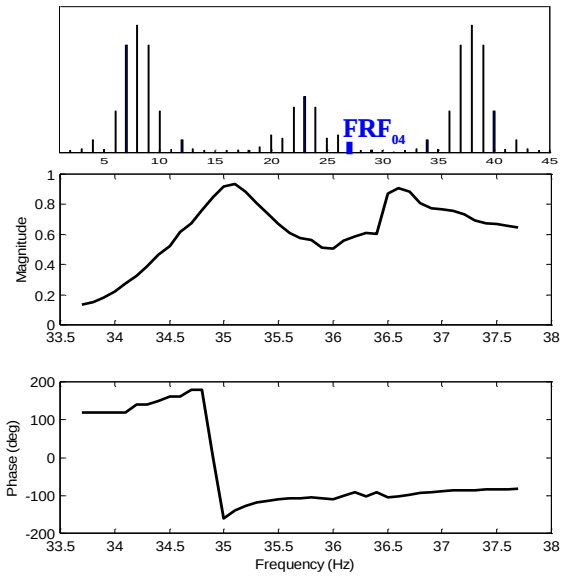


**Figure 5. 111** FRF relative to the 4$^{th}$ sideband on the central sidebands group in the LDV spectrum ($n = 0$, $m = 4$) as emphasised in the top diagram.

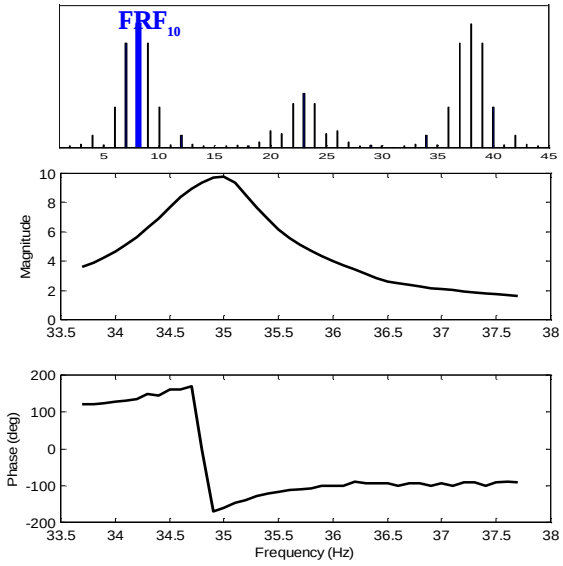


**Figure 5. 112** FRF relative to the central component of the left sidebands group in the LDV spectrum ($n$ = 1, $m$ = 0) as emphasised in the top diagram.

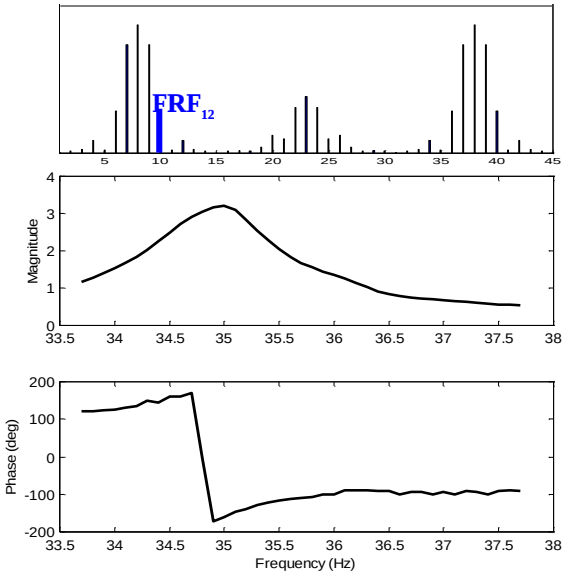


**Figure 5. 113** FRF relative to the second sideband of the left sidebands group in the LDV spectrum ($n$ = 1, $m$ = 2) as emphasised in the top diagram.

In order to have a two-dimensional view of the sideband FRFs and the conventional ones, it is helpful to plot all the sideband FRFs in a waterfall picture as shown in Figure 5.114. If the diagram is observed from its front view (i.e. parallel to the magnitude-sideband number plane) the sideband FRFs are obtained: each cross section corresponds to a frequency step on the sine-step test. If a lateral view of the diagram (i.e. parallel to the magnitude-frequency plane) is taken, the conventional FRFs assume prominence: each cross section is associated with a single sideband value. Figure 5.115 represents the top view of the waterfall diagram and highlights the zones where the vibration response is maximum, specifically the red zones.

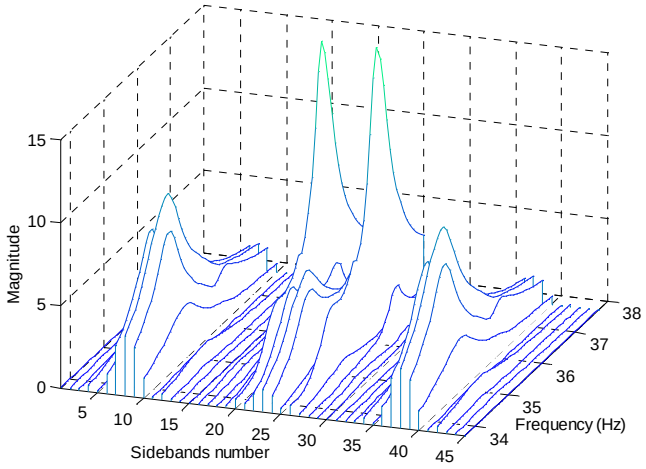


**Figure 5. 114** Waterfall diagram of all the sideband FRFs (amplitude).

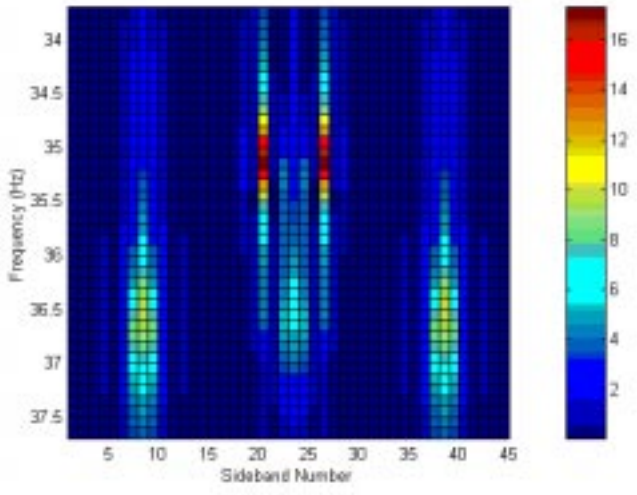


**Figure 5. 115** Color map of the overall plot of the sideband FRFs in magnitude (red color corresponds to the maximum vibration response).

The same kinds of plot (waterfall and top view color map) can be derived for the phase FRF as shown in Figures 5.116 and 5.117.

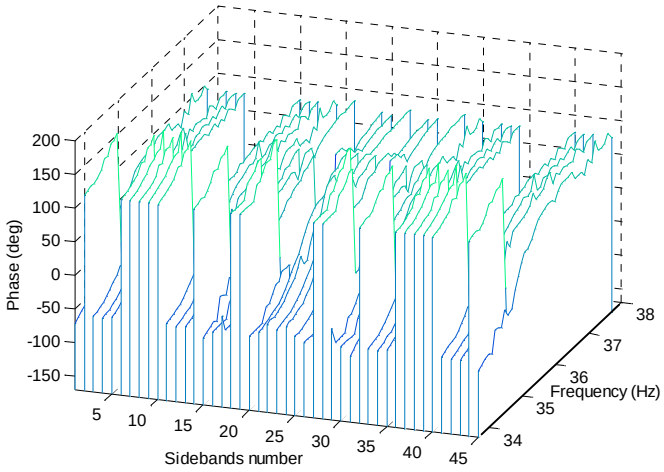


**Figure 5. 116** Waterfall diagram of all the sideband FRFs (phase).

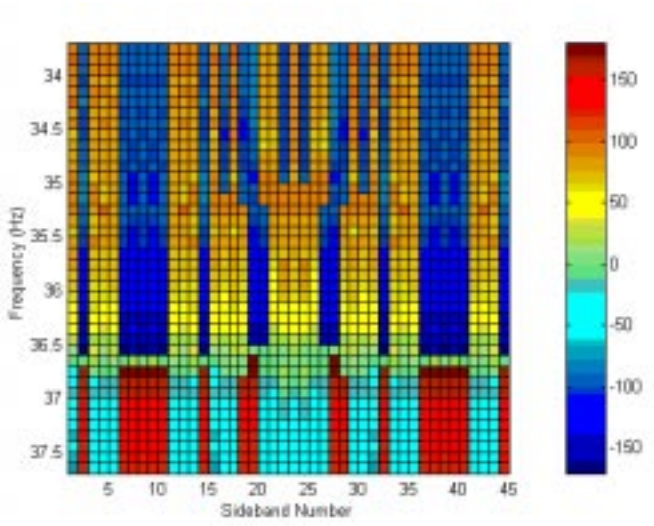


**Figure 5. 117** Color map of the overall plot of the sideband FRFs in phase.

Modal Analysis (using *ICATS MODENT*) was applied to a restricted set of conventional FRFs, taking advantage of the symmetry property of these FRFs with respect to the central spectral component. Table 5.8 describes the identification of the conventional FRFs from the sideband FRFs. $FRF_{00}$ is the conventional FRF associated with the central component of the LDV output spectra, $FRF_{01}$ is the one corresponding to the first right sideband of the central group, $FRF_{0\text{-}1}$ is the one related to the first left sideband of the central group, and

so on and $FRF_{10}$ is the conventional FRF associated with the central component of the right sidebands group, $FRF_{11}$ is the one corresponding to the first right sideband of the right sidebands group and so on.

| Conventional FRF name | x-sideband n° | y-sideband n° | |
|---|---|---|---|
| **$FRF_{-7-1}$** | -7 | -1 | 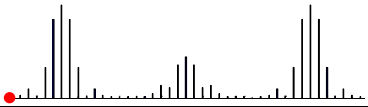 |
| **$FRF_{-6-1}$** | -6 | -1 | 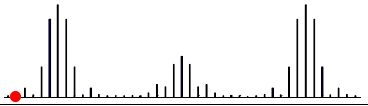 |
| **...** | ... | -1 | |
| **$FRF_{-1-1}$** | -1 | -1 | 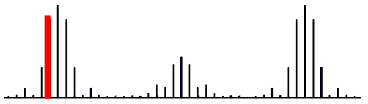 |
| **$FRF_{0-1}$** | 0 | -1 | 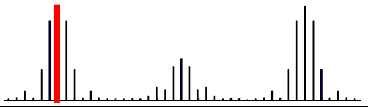 |
| **$FRF_{1-1}$** | 1 | -1 | 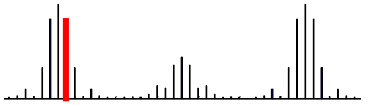 |
| **...** | ... | -1 | |
| **$FRF_{6-1}$** | 6 | -1 | 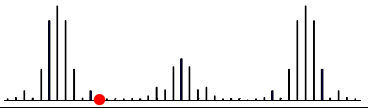 |
| **$FRF_{7-1}$** | 7 | -1 | 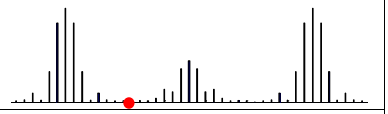 |
| **$FRF_{-70}$** | -7 | 0 | 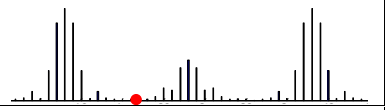 |
| | | | |
| **...**<br>**$FRF_{-10}$** | ...<br>-1 | 0<br>0 | 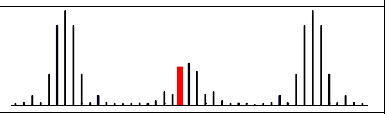 |
| **$FRF_{00}$** | 0 | 0 | 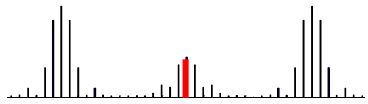 |
| **$FRF_{10}$** | 1 | 0 | 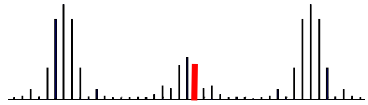 |
| **...** | ... | 0 | |
| **$FRF_{70}$** | 7 | 0 | 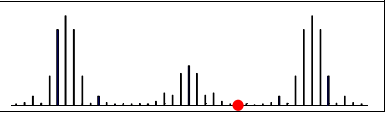 |

| | | | |
|---|---|---|---|
| **$FRF_{-71}$** | -7 | 1 | 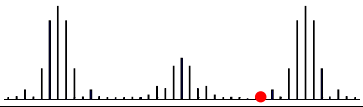 |
| **...** | ... | 1 | |
| **$FRF_{-11}$** | -1 | 1 | 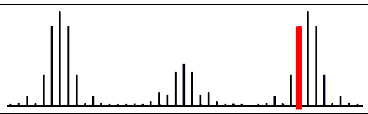 |
| **$FRF_{01}$** | 0 | 1 | 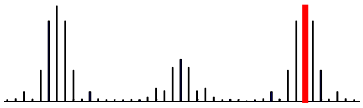 |
| **$FRF_{11}$** | 1 | 1 | 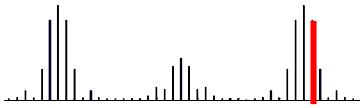 |
| **...** | ... | 1 | |
| **$FRF_{71}$** | 7 | 1 | 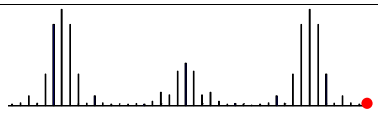 |

**Table 5. 8** Identification of the conventional FRFs.

From Table 5.8 and Figures 5.114 and 5.116 it is clear that:

for the central group sidebands

$$FRF_{01} = FRF_{0\text{-}1}$$
$$FRF_{02} = FRF_{0\text{-}2}$$
$$FRF_{03} = FRF_{0\text{-}3}$$
$$\ldots$$
$$FRF_{07} = FRF_{0\text{-}7}$$

for the sideband groups

$$FRF_{10} = FRF_{-10}$$
$$FRF_{-1\text{-}1} = FRF_{-11} = FRF_{1\text{-}1} = FRF_{11}$$
$$FRF_{-1\text{-}2} = FRF_{-12} = FRF_{1\text{-}2} = FRF_{12}$$
$$FRF_{-1\text{-}3} = FRF_{-13} = FRF_{1\text{-}3} = FRF_{13}$$
$$\ldots$$
$$FRF_{-1\text{-}7} = FRF_{-17} = FRF_{1\text{-}7} = FRF7_{17}$$

It is easier, then, to analyse $FRF_{00}$, $FRF_{01}$, ..., $FRF_{07}$, $FRF_{10}$, $FRF_{11}$, ... $FRF_{17}$ only, a set of 16 conventional FRFs. Figures 5.118 and 5.119 illustrate the first eight FRFs (corresponding to the central group of sidebands) and the last eight ones

(associated with the sideband group of sidebands) respectively in ICATS format (by using the software package *MODESH*).

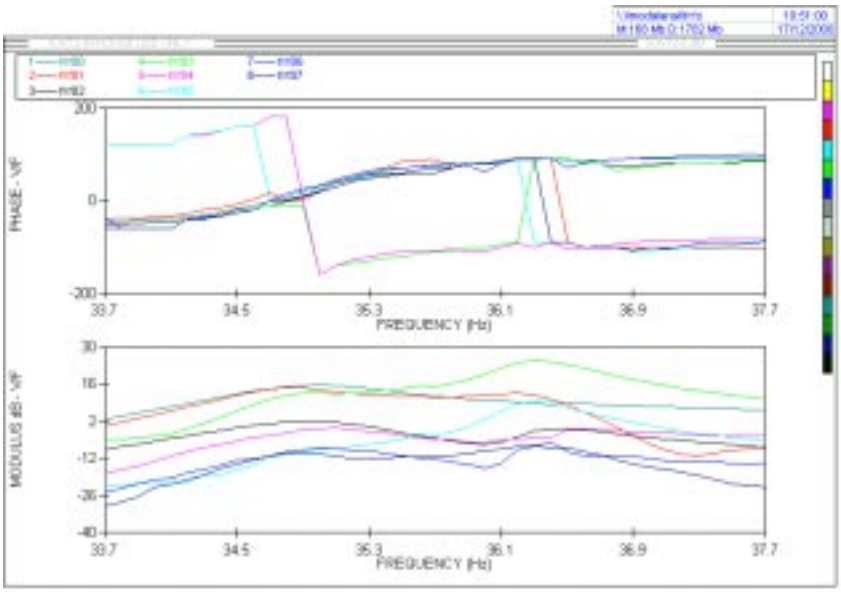


**Figure 5. 118** Conventional FRFs analysed by ICATS ($FRF_{00}$, $FRF_{01}$, ..., $FRF_{07}$).

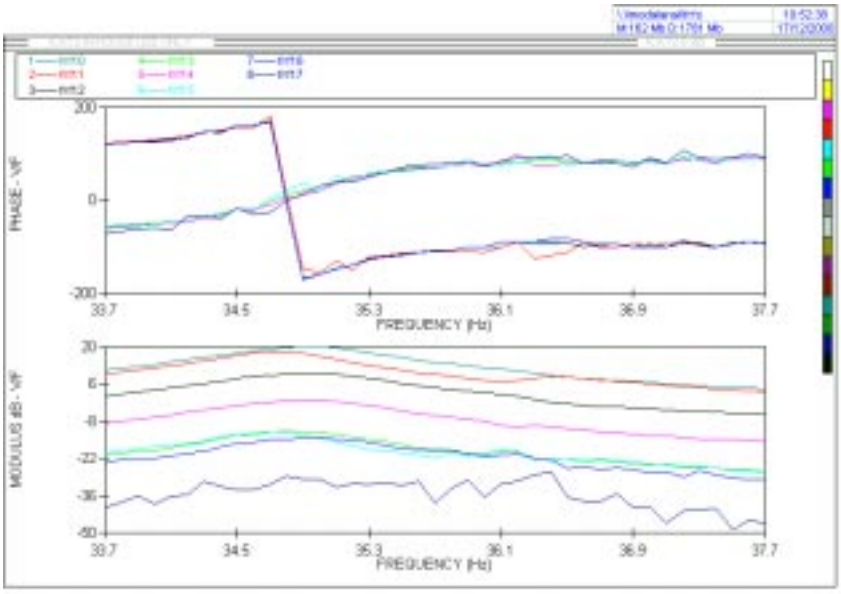


**Figure 5. 119** Conventional FRFs analysed by ICATS ($FRF_{10}$, $FRF_{11}$, ..., $FRF_{17}$).

Modal analysis was performed using ICATS software package *MODENT* in order to obtain modal constants associated to the predominant mode; FRFs were analysed one by one by applying the SDOF line–fit method included in *MODESH* and the modal constants found were validated by regenerating the FRF from them. Figure 5.120 shows the results for $FRF_{10}$ after SDOF line-fit has been run and Figure 5.121 the regenerated FRF from the modal constant derived.

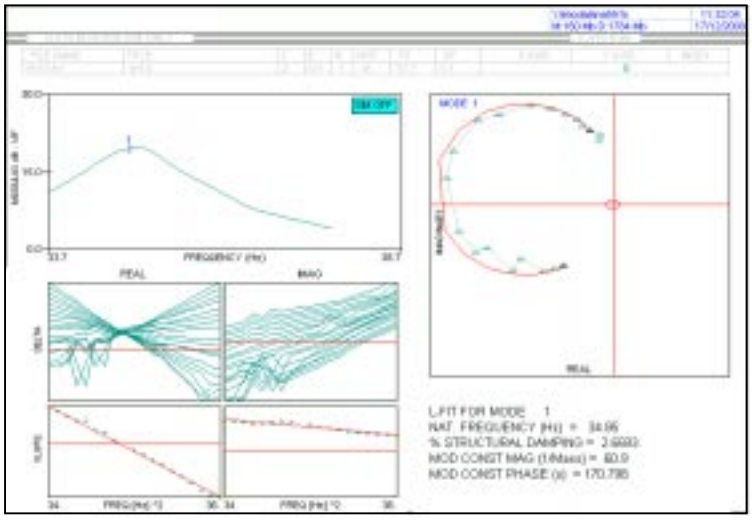


**Figure 5. 120** Modal Analysis by SDOF Line-fit (*ICATS-MODENT*) for $FRF_{10}$.

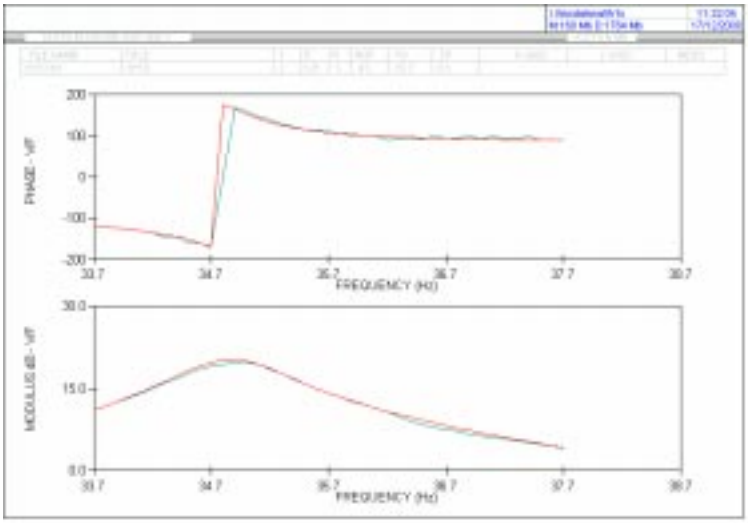


**Figure 5. 121** FRF regenerated from modal constant derived by SDOF line-fit to $FRF_{10}$.

During the modal analysis procedure a further natural mode shape was found at 36.55 Hz, which could already be noticed by observing the set of FRFs and, in particular, $FRF_{03}$. This was the most evident example since the mode at 36.55 Hz was predominant, see the green plot in Figure 5.118. The SDOF line-fit of $FRF_{03}$ is shown in Figure 5.122 and the regenerated FRF in Figure 5.123.

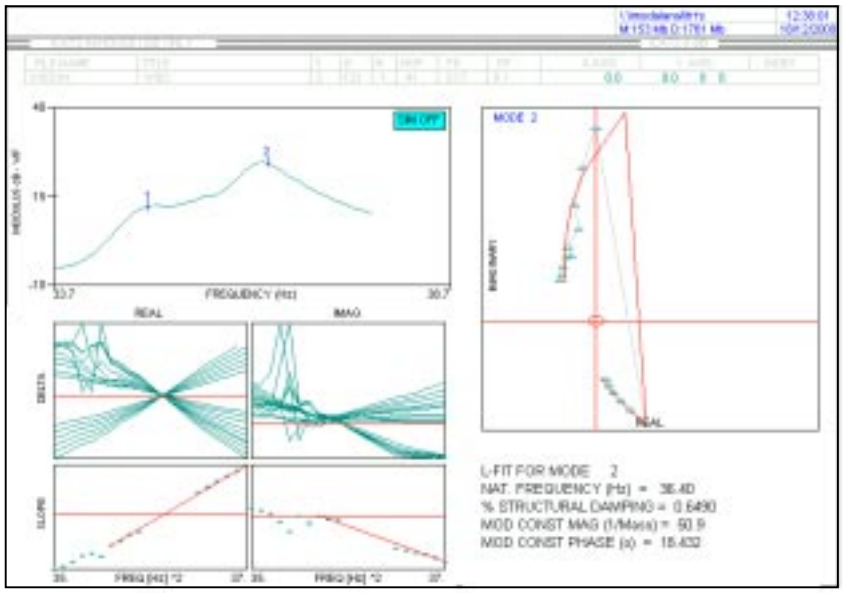


**Figure 5. 122** Modal Analysis by SDOF Line-fit (*ICATS-MODENT*) for $FRF_{03}$.

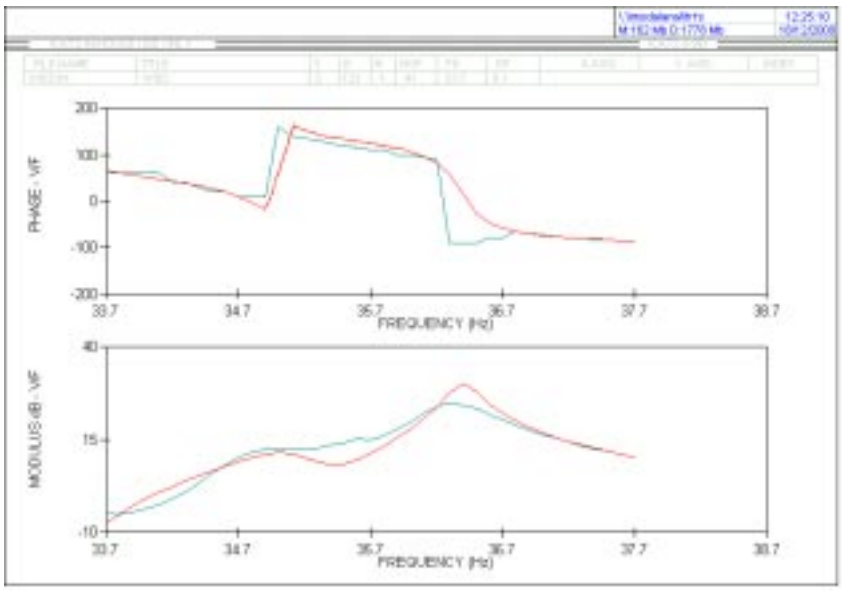


**Figure 5. 123** FRF regenerated from modal constant derived by SDOF line-fit to $FRF_{03}$.

The modal analysis process will end up with two sets of modal constants - one for each identified natural mode (at 34.86 and 36.55 Hz) - where each modal constant is associated with an individual FRF. These constants, which are complex parameters since they are derived from the FRFs that are complex quantities, are written in Table 5.9.

| | **MODE 1** (34.86 Hz) | | **MODE 2** (36.55 Hz) | |
|---|---|---|---|---|
| **Related FRF** | **Magnitude** | **Phase** (°) | **Magnitude** | **Phase** (°) |
| **$FRF_{00}$** | 33.6 | -9.55 | 0 | 0 |
| **$FRF_{01}$** | 36.5 | 5.136 | 4.31 | -169.619 |
| **$FRF_{02}$** | 6.49 | -7.849 | 0 | 0 |
| **$FRF_{03}$** | 8.03 | -26.367 | 88.2 | 4.631 |
| **$FRF_{04}$** | 4.19 | -176.223 | 2.06 | 135.902 |
| **$FRF_{05}$** | 0.772 | -99.2 | 7.33 | -165.748 |
| **$FRF_{06}$** | 2.4 | -2.793 | 0.786 | -145.536 |
| **$FRF_{07}$** | 1.46 | 18.52 | 2.1 | -48.497 |
| **$FRF_{10}$** | 62.8 | 170.325 | 0 | 0 |
| **$FRF_{11}$** | 40.7 | 173.912 | 18.7 | 53.138 |
| **$FRF_{12}$** | 20.5 | 168.341 | 0 | 0 |
| **$FRF_{13}$** | 1.84 | -22.047 | 0 | 0 |
| **$FRF_{14}$** | 6.64 | -11.329 | 0 | 0 |
| **$FRF_{15}$** | 1.23 | -18.149 | 0 | 0 |
| **$FRF_{16}$** | 1.32 | 172.546 | 0.511 | -58.073 |
| **$FRF_{17}$** | 0.26 | -2.677 | 0.0579 | -110.746 |

**Table 5. 9** Modal Constants in magnitude and phase format derived by Modal Analysis.

The resulting set of modal constants can be seen as sideband modal constants which can be transformed in the same way as the ODS sideband data to give an eigenvector of polynomial series modal constants. As already mentioned, however, a correction must be made before doing the usual transformation applying the matrix [T]. In fact, the modal analysis has been done considering

the frequency range of interest from 33.7 Hz to 37.7 Hz but this is true for the central spectral component FRF ($FRF_{00}$) only. The other FRFs are, in reality, given for a translated frequency range: for instance, $FRF_{01}$ is in the range of 33.7+0.3 and 37.7+0.3 Hz (because it is the first right sideband of the central group) and, similarly, $FRF_{12}$ is in the range of 33.7+5+2×0.3 and 37.7+5+2×0.3 Hz (because it is the first right sideband of the central group). In relation to Equation 5.85, the modal constants must be corrected by multiplying each of them for the corresponding factor given by:

$$\frac{\left(\omega_r + n\Omega_x + m\Omega_y\right)^2 - \left(\omega + n\Omega_x + m\Omega_y\right)^2}{\omega_r^2 - \omega^2}$$

i.e. $n = 0$ and $m = 2$ for the modal constant relative to $FRF_{02}$ and $\omega_r = 34.86$ Hz for the first mode. Two correction vectors can be derived, each associated with one natural mode. The corrected modal constants are then obtained by multiplying the original modal constants of each natural mode element by element and the relative correction vector. Table 5.10 depicts the new values for the modal constants.

| | **MODE 1** (34.86 Hz) | | **MODE 2** (36.55 Hz) | |
|---|---|---|---|---|
| **Related FRF** | **Magnitude** | **Phase** (°) | **Magnitude** | **Phase** (°) |
| **$FRF_{00}$** | 33.6 | -9.55 | 0 | 0 |
| **$FRF_{01}$** | 36.8 | 5.136 | 4.34 | -169.619 |
| **$FRF_{02}$** | 6.59 | -7.849 | 0 | 0 |
| **$FRF_{03}$** | 8.23 | -26.367 | 90.43 | 4.631 |
| **$FRF_{04}$** | 4.33 | -176.223 | 2.12 | 135.902 |
| **$FRF_{05}$** | 0.804 | -99.2 | 7.64 | -165.748 |
| **$FRF_{06}$** | 2.52 | -2.793 | 0.825 | -145.536 |
| **$FRF_{07}$** | 1.54 | 18.52 | 2.22 | -48.497 |
| **$FRF_{10}$** | 71.56 | 170.325 | 0 | 0 |
| **$FRF_{11}$** | 46.71 | 173.912 | 21.48 | 53.138 |
| **$FRF_{12}$** | 23.7 | 168.341 | 0 | 0 |
| **$FRF_{13}$** | 2.14 | -22.047 | 0 | 0 |
| **$FRF_{14}$** | 7.78 | -11.329 | 0 | 0 |
| **$FRF_{15}$** | 1.45 | -18.149 | 0 | 0 |
| **$FRF_{16}$** | 1.57 | 172.546 | 0.608 | -58.073 |
| **$FRF_{17}$** | 0.31 | -2.677 | 0.0694 | -110.746 |

**Table 5. 10** Corrected Modal Constants in magnitude and phase format.

Correction of phase is not so essential, the difference between original and corrected modal constants being imperceptible, see also Figure 5.124 and 5.125 where real and imaginary mode shapes at the natural frequency of 34.86 Hz derived from original and corrected modal constants are plotted together. The mode shape can be compared with the ODS found previously at the maximum response frequency of 34.8 Hz, see Figure 5.109. Both the ODS and the mode shape describe a predominantly torsional mode, mostly confined to the left-hand wing, where the excitation is located, with some bending component. It may be noted that the mode shape was very nearly a real mode, without any significant imaginary component (see Figure 5.125), unlike the imaginary part of the ODS which was significantly relevant in comparison to its real part, as shown in Figure 5.109.

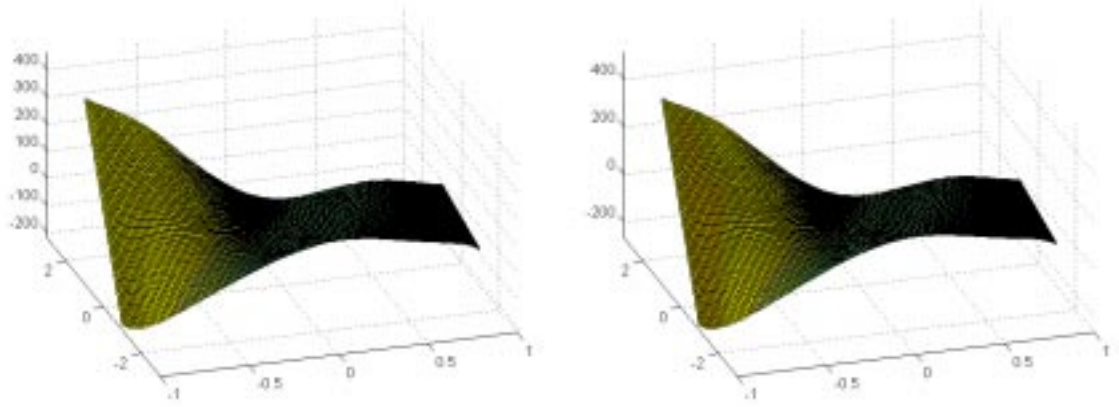

**Figure 5. 124** Real part of the mode shape at the natural frequency of 34.86 Hz derived from original (left) and corrected (right) modal constants.

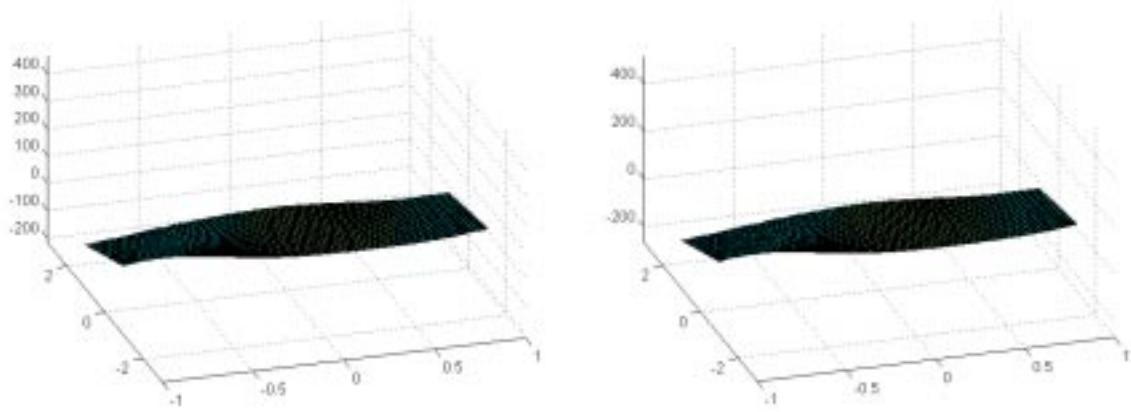

**Figure 5. 125** Imaginary part of the mode shape at the natural frequency of 34.86 Hz derived from original (left) and corrected (right) modal constants.

A “hybrid” correlation between the ODS ( **[ODS]** ) at the measured resonance frequency of 34.8 Hz (Figure 5.109) and the mode shape ( **[MODE]** ) derived via modal analysis at the natural frequency of 34.86 Hz (Figure 5.124) can be done [1] using the mode-response correlation parameter (MFAC) defined by the following equation:

$$MFAC([\mathbf{ODS}],[\mathbf{MODE}]) = \frac{\left|\sum_{i=1}^{n}\sum_{j=1}^{m} ODS_{i\,j} MODE^{*}_{i\,j}\right|^{2}}{\left(\sum_{i=1}^{n}\sum_{j=1}^{m} ODS_{i\,j} ODS^{*}_{i\,j}\right)\left(\sum_{i=1}^{n}\sum_{j=1}^{m} MODE_{i\,j} MODE^{*}_{i\,j}\right)} \quad \textbf{(5. 86)}$$

where $n$ is the number of DOFs in the $x$-direction and $m$ is the number of DOFs in the $y$-direction. Therefore, if the ODS and the mode shape are plotted for $x$ = -1..0.02..1 and $y$ = -1..0.02..1, it will be $n$ = $m$= 101. The degree of correlation (MFAC) between the operating deflection shape and the mode shape was 73.34 %.

Figure 5.126 shows real and imaginary components of the mode shape for the natural frequency of 36.55 Hz (corrected modal constants are used), while Figure 5.127 reports, for completeness, the ODS derived by the conventional continuous area scan performed at only one frequency, that of the maximum response, which was found at 36.6 Hz. Both the ODS and mode-shape corresponded to a real bending mode, largely uncontaminated by torsional motion.

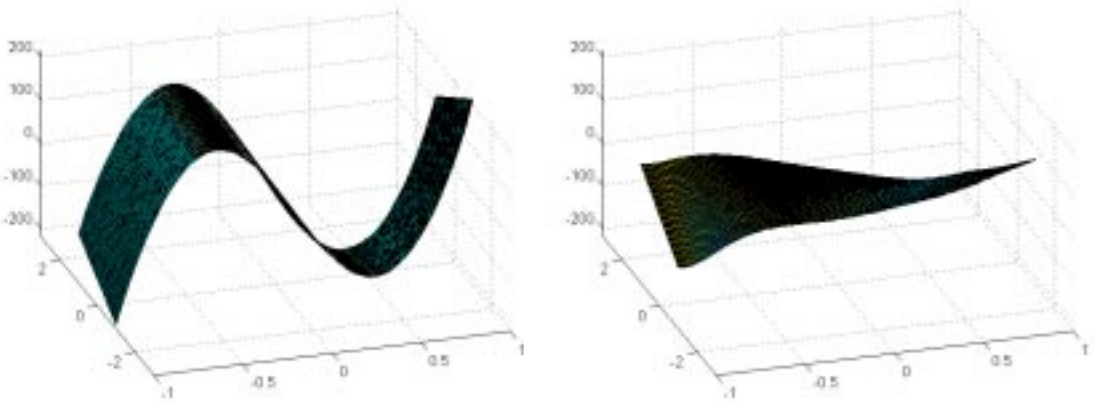

**Figure 5. 126** Real (left) and imaginary (right) part of the mode shape at the natural frequency of 36.55 Hz derived from corrected modal constants.

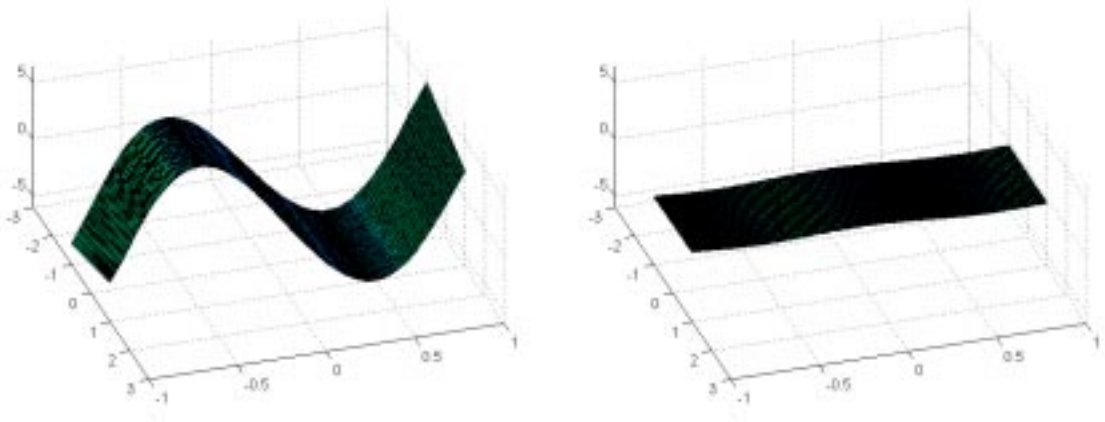

**Figure 5. 127** Real and imaginary ODS at 36.6 Hz.

### *5.6.3 Concluding Remarks*

In this last section, an unusual modal analysis performed on continuous area scan data obtained by conventional step-sine test experimental procedure has been described. In the end, it was shown that the modal analysis procedure can be used also in the standard way the correction needed, giving no remarkable difference.

The ODSs derived by continuous area scanning are generally complex, as there is a significant out-of-phase component in the dynamic deflected form. In general, the shape of the ODS, even at a natural frequency, depends to some extent on the position of the applied excitation, whereas the natural mode-shape does not. The ODS is complex because it is a combination of the mode shapes occurring at frequencies close to that of the excitation. It is then affected by the off-resonant contributions from the other modes. Natural mode shapes must therefore be derived from ODSs by modal analysis by performing a step-sine test, i.e. by extracting modal characteristics from frequency response functions (response / force ratio) data, measured at a succession of frequencies spaced suitably around the natural mode being analysed. In this context, the force input had to be quantified; it must therefore be acquired via a force cell

attached on the structure at the shaker position and sampled simultaneously with the LDV signal. Both signals are then subjected to the same post-processing: the force input recorded is multiplied by sine and cosine functions at the excitation frequency (ω) to determine magnitude and phase. FRFs are then derived by complex division and they are assembled together in order to have an FRF for each CSLDV sideband spectral component. The end result of a modal analysis of these FRFs is a rather novel eigenvector, not of individual point responses, but of polynomial coefficients representing the responses of the complete ensemble of points contained within the scanned area.

It must be emphasised that with the CSLDV area sine scan, modal analysis need only be applied to the polynomial coefficient data (or, indeed, to the averaged sideband data, before applying the transform to recover polynomial coefficients). The number of FRFs to be analysed is thus smaller than the number of FRFs that have to be taken into consideration when a point-by-point area scan is performed. The latter process is computationally intensive because of the large number of spatial positions to be addressed. The time saving on the analysis must be added to the saving on the acquisition time, as already stated in this Chapter. With the CSLDV technique used for modal analysis step-sine tests must be carried out. At each step-frequency excitation, only one acquisition has to be made. If the slower scan speed is of, say, 0.3 Hz, the acquisition time will be at least 3.33 secs, in order to cover the whole tested surface. The overall acquisition time (for a complete step-sine test) will be a number of times longer than the single-step acquisition time corresponding to the number of frequency-steps which are required. However, this time will be shorter than the time required to acquire the FRFs at all points defined in the discrete scanning technique.

Finally, it should be pointed out that the final resolution of the mode shape as it is plotted out is completely independent from the acquisition. While the spatial resolution of a mode shape derived from FRFs measured by using a point-by-point scan is represented by the number of points measured, the spatial

resolution of the mode shape obtained from CSLDV FRFs data is totally arbitrary. In fact, the mode shape is represented by a polynomial whose coefficients are derived from the post-processing of the measurement data. With these coefficients the polynomial can be plotted over whatever grid of points is required, i.e. with any resolution one choses. For example, in the plots of Figures 5.126, 5.127, 5.128 and 5.129 a resolution of 101 × 101 points was used.

## *5.7. Conclusions*

This chapter has covered a number of applications of a continuous-scan LDV to the measurement of response mode shapes (ODSs) using line (straight and circular lines) and area scanning. Single-frequency vibration, as produced with sinusoidal vibration of a linear structure, is assumed. Two basic methods of signal processing are described: (i) demodulation and (ii) sideband identification. The first of these will give an ODS with the resolution of the signal sampling, and to the accuracy of the basic LDV measurement. The second method produces a representation of the ODS in a polynomial series form. If the ODS is a smooth function of position, without discontinuities, higher terms in the series become insignificant, and the ODS may be represented with little error by a relatively small number of series coefficients. The continuous scan demodulation technique does not require, instead, that the mode shape is smooth within the scanned area. This approach can then be used on structures with discontinuities on the surface, i.e. apertures or corrugations. The disadvantage of this technique is that it is sensitive to the speckle noise which may limit its accuracy locally. Linear circular scans and circular area scans have been applied to disc-like structures in order to recover circumferential and 2-D mode shapes of the disc respectively.

For all these techniques, mathematical analysis has been performed, and then, they have been shown to work effectively by performing omparisons with experimental data measured on simple structures as beams, plates and discs.

For some methods (such as sinusoidal straight line scan and sinusoidal rectangular area scan), further analysis have been made by measuring the corresponding ODSs via the Polytec system applied in its conventional fashion (single point scan).

In the last section a procedure to recover mode shapes from data measured by the area scanning technique has been illustrated. Scanning LDV ODS coefficients may easily be repeated in a frequency-step sequence and converted into FRF form, so that modal analysis can be applied to extract modal constants. The method has been applied to a practical test specimen, i.e. the GARTEUR structure, in order to make the procedure clearer and easier to be followed.

# Chapter 6 Virtual Testing

## *6.1. Introduction*

The continuous scanning LDV technology, described and tested in all its facets in the previous chapters, is studied here from a different perspective. The aim of this part of the work is to simulate the experimental procedure which must carried out when a CSLDV measurement has to be performed. This technique, when applied to practical case studies, needs to be performed by specialists skilled in the LDV field, otherwise the setting-up process could become extremely time-consuming. The rehearsal of all the steps accomplished in the laboratory during a CLSDV experiment can be done via a numerical simulation which is called a “virtual test”. This process can be useful as a means (i) to optimise the actual test by selection of the best experimental parameters, a priori, and (ii) to train engineers on the fairly new continuous scanning philosophy.

## *6.2. Virtual Testing Technique*

Virtual testing is a new technique devised in order to make the actual tests more effective and less time-consuming, and thus to reduce their cost. In fact, nowadays experimental structures tend to be overbooked and the length of time which they can spend in a laboratory is limited.

In order to carry out a virtual test, a mathematical model of the whole test structure and set-up must be developed where a model of the dynamic properties of each element in the test set-up must be included. Such a model will simulate the input signals actually used in the real test, including the sources of noise as and where they are experienced by the acquisition sensors in real measurements. In these conditions, the derived response functions can be supposed to well reproduce the real data which would be measured by performing a true test.

The concept of virtual testing can be applied to continuous scanning laser Doppler vibrometry treated in this work in order to investigate ahead of time the applicability and the accuracy of the various techniques which depend on the conditions in which the system operates.

The simulation of a continuous scanning test is based on the application of the algorithms illustrated in detail in Chapters 4 and 5 for the different techniques by using numerical data rather than (or before) actual measured data. Parameters describing the operating conditions of the test are introduced into the numerical model of the measurement system in order to verify their effects and to allow forecasting the best settings of these parameters. The optimum test configuration and design can then be decided a priori before entering the laboratory.

The computer model of the structure under test will act as a realistic simulator that can yield computed LDV responses containing the various “errors” that

have been found to contaminate the data measured in real tests. The most important practical deviation from an ideal measurement by an LDV is due to the speckle noise to which the LDV is intrinsically sensitive. The speckle noise depends on interfering inputs of a random nature mostly related with the characteristics of the tested surface: it can actually be considered as a measurement of the roughness of the surface itself and as such cannot be avoided. It is important then to determine the reasons for the occurrence of this phenomenon (see Chapter 2) which distorts the LDV output signal, and thence the experimental parameter settings that can be manipulated in order to provide a prediction version of the optimal working conditions. This approach greatly improves the chances for a successful test and saves, simultaneously, time in "tuning" the experimental process.

The speckle noise effect will be treated briefly in next section, the subject having already been discussed in detail in Chapter 2. First, the occurrence of the speckle noise in a traditional single point LDV used for step-scanning over discrete points will be mentioned, and then its presence in a continuous scanning LDV operation will be considered. A mathematical model of the noise superimposed on the ideal signal will be developed in order to simulate the vagaries of real test data and to predict realistic LDV responses when the laser beam moves continuously over the test structure. In this software model a specific parameter is introduced which identifies the actual continuous scanning test adopted and which is the scan speed of the moving laser beam. In this way the optimal scan rate that should be employed to drive the scanning system can be decided a priori.

### *6.3. Mathematical Model*

The mathematical model of an experiment performed with an LDV system used in the continuous scan fashion will consist mainly of the algorithm described in Chapter 5 and employed to test analytically the post-processing techniques

used to recover ODSs from the simulated time histories. For instance, some previous simulations can be recalled:

(i) Equation (5.6), which produces a simulated LDV output when uniform straight-line scan is performed. A typical time signal is shown in Figure 5.3;

(ii) Equation (5.27), used to predict the time history which could be acquired by the vibrometer if the laser beam is scanning sinusoidally along a straight-line. Scanning mirror delays are also taken into account here. Figure 5.19 illustrates the time signal obtained; and

(iii) Equation (5.63), which simulates the LDV output in the time domain considering the laser scanning over a 2-D area (area scan) and including in the algorithm the mirror driver delay. For the simulated time signal see Figure 5.69 (bottom plot).

In order to complete the mathematical model to make a simulated velocity signal look like an experimental signal, the noise affecting real test data must be modeled as well. When an LDV system is used for measurement, the main source of pollution is the speckle noise or, in other words, the speckle noise prevails over all the other kinds of random noise. In the following section, a model for the speckle noise will be developed.

As already stated (see Section 2.4), speckle noise occurs when monochromatic, coherent light, scattered from an optically rough surface, is collected by a photodetector. In the detector's collecting surface a speckle pattern is formed. If the speckle pattern undergoes spatial and temporal changes these latter will modulate the Doppler signal which is the output from the photodetector. Such kind of changes are caused by target motions as tilt or in-plane translation, that produce a Doppler signal phase modulation, referred to as speckle noise.

For fixed-point measurements, in particular if there is a large vibratory displacement perpendicular to the LDV beam, speckle can cause severe problems because the speckle noise can become synchronous with the

vibration, leading to severe harmonic distortion. In fact, speckle noise is noted at certain points in the spatial field of the velocity information measured by the LDV. It appears as occasional velocity drop-outs which are unidirectional, always estimating velocity response closer to zero than reality. The areas of drop-out translate the data points of the velocity response into data points which are closer to the zero axis for both positive and negative velocities. Thus, the laser noise can be classified as a "biased-low" due to the fact that the drop-out effects in the velocity signal produce absolute velocity data which are lower than similar velocity signals which do not contain drop-out.

The drop-out areas have been seen to occur more predominantly at points of minimum linear velocity response with big local tilt components ("nodes" of the structure), see reference [29].

The occurrence of the speckle noise can be explained by the fact that during vibration the point illuminated by the laser is not identical through the entire period of motion, [4]. This results in the detector receiving a changing speckle pattern over the course of the periodic motion of the structure. When the speckle covered by the detector is "dark" or is "bright", but it scatters back towards the detector an insufficient intensity of light, the Doppler signal amplitude falls below the threshold of the demodulator circuit used to derive the analogue velocity waveform from the Doppler signal and velocity drop-outs are yield.

Since the noise appears at specific areas (vibrational node) its effect is commonly reduced either by averaging or by statistically smoothing the measured data. These methods have the disadvantage that they bias the data averaged because the speckle noise always appears as a drop towards zero of the velocity signal.

When the measuring laser beam is not steady over the surface to be measured, but scans continuously, and, for instance, it moves backward and forward along a straight-line a relative motion between structure and laser occurs. The speckle noise will then appear since the photodetector collecting the light scattered by the target surface experiences also the motion of the "dark" and

"light" speckles. The output signal will contain drop-outs when a "dark" speckle grain is encountered. The presence of "dark" or "light" speckles along the light is random since they depend on the light-scattering properties of the surface, i.e. on the surface roughness. But, if the laser beam travels along the same line all the time, then it meets always the same succession of "light" and "dark" speckles, and the photodetector will notice the same spatial distribution of speckle grains in each scan cycle. The noise effect will appear periodic with the laser scan frequency since in each scan cycle it will be located at the same phase value. The speckle noise can be seen, as the experimental data will demonstrate (see subsection 6.4.3), as it concentrates all its content at some frequencies which are, namely, the scan frequency and its harmonics. These harmonic frequencies, which constitute a sort of noise floor, are due to a so-called "pseudo-vibration", [50], because it is introduced by the laser motion. They should not coincide with the genuine vibration frequency and any relevant sideband frequencies otherwise their level, even low, will pollute the true vibration information. It is therefore essential that the scan speed is chosen carefully in order to be sure that none of its harmonics will overlap with the structural vibration frequency and its sidebands.

Consequently it can be deduced that the scan frequency becomes an important parameter which should be controlled in order to have the best measurement data (best SNR, since it is possible directly to interfere on the noise content of the LDV output).

## *6.4. Speckle Model*

### *6.4.1 Introduction*

The aim of this section is to present a model of the velocity signal measured by an LDV sensor which is continuously scanning over the target surface, taking into account the luminous intensity variation due to the random shifts caused

by the motion of the speckle pattern that is incident on the instrument's photodetector. In fact, the Doppler signal coming from the LDV is modulated by the changes of the speckle pattern formed by the light scattered back from the surface illuminated by the laser beam. Certain types of motion of the tested surface, such as rotation (see reference [45]) or in-plane motion (see reference [46]), produce spatial and temporal modifications of the speckle pattern and lead to a Doppler signal phase modulation clearly seen in the LDV output. In practice, since the speckle grains vary their spatial distribution, the photodetector will experience this motion as a shift in frequency similar to the shift due to the Doppler effect in which the information to be measured exists. The phenomenon commonly referred as "speckle noise" will produce an uncertainty in the derivation of the vibration response from the Doppler signal in output from the LDV. In the case with which this work deals, an in-plane relative motion can be still considered with the only difference that, now, the system which moves is not the target but the measurement laser beam. Since the laser beam travels sinusoidally around in circles or backwards and forwards along lines, its motion is periodic with a frequency which is the scan speed. This means that the speckle changes are periodic as well and their frequency content is concentrated at the fundamental motion frequency (the scan frequency) and its harmonics. For instance, if the laser beam travels along a line on the measured surface at a frequency of 10 Hz, the LDV output spectrum will show peaks at 10 Hz and its harmonics, also if the structure is not vibrating at all. It is possible to state, then, that there exists a "pseudo-vibration" due to the laser motion, and therefore due to the speckle pattern motion, which is indistinguishable from the genuine vibration. In order to reduce its importance, the speckle noise amplitude must be minimised otherwise it must be assured that its frequency content does not coincide with the vibration frequency and its sidebands. A theoretical model of the speckle noise has been developed in order to simulate the distortion that will be produced on the LDV output when the speckle pattern undergoes an in-plane motion and a validation of the model has been performed by comparing theoretical results with experimental data.

### *6.4.2 Theoretical Model of the Light Intensity Collected by the Photodetector*

First, an analytical representation of the light intensity received at the photodetector can be derived by recalling the formulae established in Section 2.8, Equations (2.80). In order to consider the speckle pattern motion, phase information should be included in the light intensity formulation. Writing the electric field associated to the reference beam as $E_1$ and $A_1$ and $\theta_1$ its amplitude and phase, respectively, and $E_{2i}$ the electric field associated to the measuring beam scattered back from the i$^{th}$ speckle grain ($A_{2i}$, and $\theta_{2i}$, are the amplitude and the phase of $E_{2i}$), Equations (2.80) will become:

$$\begin{aligned} E_1 &= A_1 \exp\{i[2\pi(f + f_S)t + \theta_1]\} \\ E_{2i} &= A_{2i} \exp\{i[2\pi(f - f_D)t + \theta_{2i}]\} \end{aligned} \qquad \textbf{(6. 1)}$$

where $f$ is the frequency of the laser source employed, $f_S$ is the frequency shift induced in the reference beam by the Bragg cell and $f_D$ is the Doppler frequency carrying the velocity information required. The resultant intensity scattered by the i$^{th}$ speckle and observed by the photodector, $I_i$, can be derived by the combination of the two beams intensities:

$$\begin{aligned} I_i &= KS_i [E_1 + E_{2i}][E_1 + E_{2i}]^* = KS_i \{A_1^2 + A_{2i}^2 + 2A_1A_{2i}\cos[2\pi(f_S + f_D)t + (\theta_1 - \theta_{2i})]\} = \\ &= KS_i \left\{ I_1 + I_{2i} + 2\sqrt{I_1 I_{2i}} \cos\left[ \omega_S t + \frac{4\pi}{\lambda} v t + (\theta_1 - \theta_{2i}) \right] \right\} \end{aligned}$$

**(6. 2)**

$\omega_S$ being the reference beam angular frequency shift, $\frac{2\pi}{\lambda}v$ the Doppler frequency, $f_D$, (with $\lambda$ the laser source wavelength and $v$ the target velocity) and $K$ the constant radiant sensitivity of the active area, $S_i$, on the photodetector which receives the light scatterd from the i$^{th}$ speckle.

The first component ($I_1 + I_{2i}$), also named intensity noise, is at a relatively low frequency and is often constant (DC), as it usually occurs in experimental tests, so it can be filtered out to leave the LDV output to represent the Doppler signal only:

$$I_i = 2KS_i\sqrt{I_1 I_{2i}}\cos\left[\omega_S t - \frac{4\pi}{\lambda}vt + (\theta_1 - \theta_{2i})\right] \qquad \textbf{(6. 3)}$$

If the active area on the photodetector is now considered, the area where the light intensities scattered from *n* speckle grains arrive, the total current generated by the detector will be:

$$I = \sum_{i=1}^{n} I_i = KI_{TOT}\cos\left[\omega_S t + \frac{4\pi}{\lambda}vt + \Theta_{TOT}\right] \qquad \textbf{(6. 4)}$$

From Equation (6.4) the angular beat frequency produced by the heterodyne process between the reference and the measuring beams, involved in the measurement in the LDV system, can be derived as:

$$\omega = \omega_S + \frac{4\pi}{\lambda}v + \frac{d\Theta_{TOT}}{dt} \qquad \textbf{(6. 5)}$$

Two cases can be then underlined:

(i) if the *n* speckle grains scattering the light towards the photodetector have constant phase, which happens when the speckle pattern does not undergo any spatial changes, the output spectrum of the LDV will contain peaks at the vibration frequency only, the term $\frac{d\Theta_{TOT}}{dt}$ being zero. This case occurs if any in-plane motion is imposed on the target structure.

(ii) if the speckle pattern experiences changes in its spatial and temporal characteristics (i.e. speckle "boiling" or/and "translation" occur ,see Section 2.4), the derivative $\frac{d\Theta_{TOT}}{dt}$ becomes non-zero and it will be the term related to the speckle noise which can be seen in the LDV output. The spectrum of this latter will still contain the peaks at the vibration frequencies but noise will be superimposed at frequencies corresponding to the spectral content of $\frac{d\Theta_{TOT}}{dt}$.

The second case occurs when a continuous scanning LDV technique is used. The speckle pattern will evolve in sympathy with the target motion, in this case with the relative movement between the target and the laser beam (here, it is the laser beam which actually moves). In this situation, where the laser beam scans continuously along a straght line, it can be assumed that the dominant motion which the speckle pattern undergoes is translation and, specifically, that it is a periodic translation following the motion of the laser beam. If the latter moves sinusoidally backwards and forwards along a straight line, the speckle grains will translate across the detector active area with the same frequency as the scanning beam motion. Figure 6.1 shows the spectral components of the simulated light intensity that would be recorded by the photodetector in both cases where the speckle phase fluctuation is zero and non-zero (left and right plots, respectively). The left-hand plot has been derived from Equation 6.4 for a beat frequency of approximately 403 MHz, considering a Bragg frequency shift of 40 MHz ($\omega_S$), a He-Ne laser source with wavelength of 633 nm ($\lambda$) and a vibration velocity occurring at a frequency of 115 Hz. On the other hand, the right-hand plot has been obtained for the situation when the measuring laser beam is continuously scanning along a line at a speed of $\Omega_L$ (say10 Hz). The speckle grains will then undergo a periodic motion with a periodicity of 10 Hz. If we introduce a simplified[1] model where it is assumed that the phase of the speckle pattern changes periodically as:

[1] In practice, the change of the speckle pattern phase is a periodogram at the scan frequency and higher order harmonics and it can be modeled as amplitude modulated comb function. Equation 6.6 is adopted for simplicity purpose.

$$\Theta_{TOT} = \sin(\Omega_L t) \qquad \textbf{(6. 6)}$$

and then its derivative will become non-zero.

The light intensity collected by the photodetector will then have a spectral content described by:

$$\omega = \omega_S + \frac{4\pi}{\lambda} v + \Omega_L \cos(\Omega_L t) \qquad \textbf{(6. 7)}$$

which means that the intensity appears as a frequency-modulated signal and its spectrum will contain sidebands at $\pm \Omega_L$ centered at the frequency of 403 MHz.

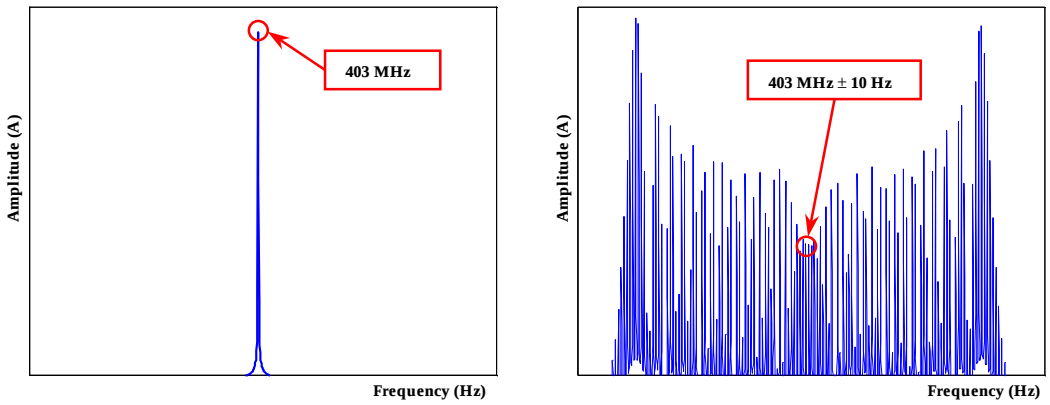


**Figure 6. 1** Simulated light intensity collected at the photodetector (which is sensitive to current signals, i.e. Ampere) for phase fluctuation zero (left) and non-zero (right).

In practice, when an LDV is employed for experiments, the instrument output is an analogue voltage derived by demodulating the Doppler signal represented by the light intensity collected at the photodetector. The voltage output represents the target vibration velocity directly. As it has been already outlined

(see Section 6.3), when a continuous scan is performed by using a scanning LDV the output spectrum contains the characteristic speckle noise peaks at the scan frequency and its harmonics.

### *6.4.3 Experimental Speckle Noise Analysis*

Before building a mathematical model which can reproduce the noise due to the speckle pattern displacement when a relative motion between surface to be measured and laser spot on the surface itself occurs (laser beam scanning continuously along the surface), an analysis of experimental data acquired in a real test has been performed. The analysis has been done on a structure used for a practical application where the noise analysis was needed before starting the real experimental work in order to derive the optimal scan speed which would allow us to have the best measurement data (higher SNR) The structure consisted of the rear panel of a lorry cab which was a case study within the BRITE/EURAM project VALSE, [13]. The analysis took into account two parameters that were thought to influence the speckle noise behaviour: (i) the laser beam scan speed and (ii) the scan length of the line traveled by the laser beam. By varying these parameters, the speckle noise experienced by the LDV sensor was studied.

The tested structure was the rear panel of an IVECO DAILY motor lorry cab, see Figure 6.2, where the continuous scanning techniques (specifically, long scan along a line) were applied in order to prove their proper functionality also in complex structures.

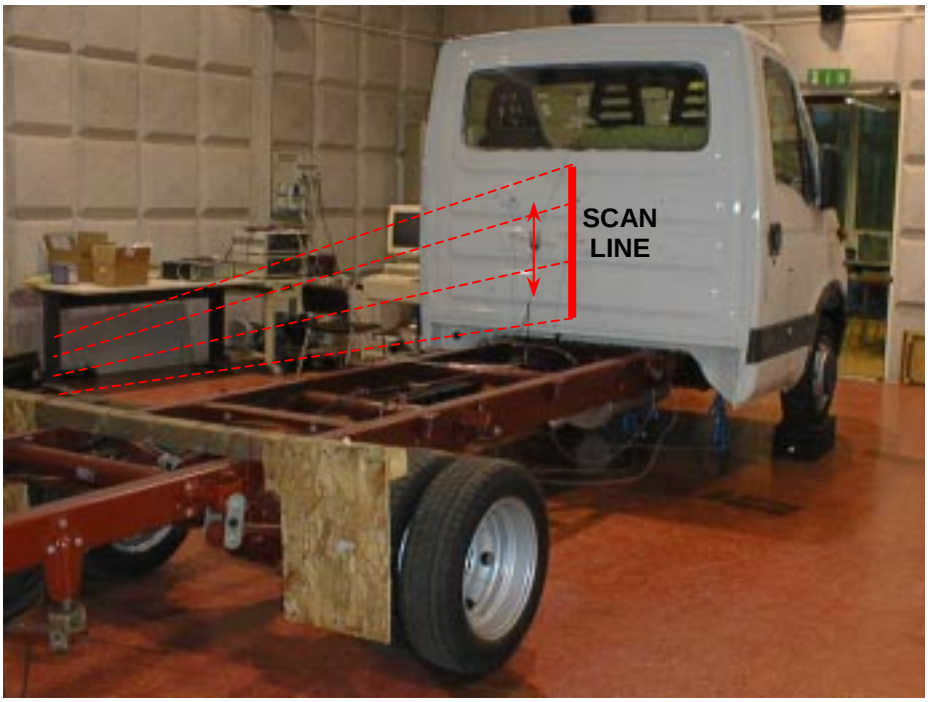


**Figure 6. 2** Experimental structure.

Before commencing the continuous-scan measurements, the opportunity was taken to assess the LDV noise at different scan rates and different scan lengths. First, different LDV output time histories were acquired at different scan speeds (i.e. at 0.2, 0.5, 1, 5, 10, 20 Hz) along a vertical line 740 mm long, on the lorry cab back panel, without exciting the panel. Two sets of measurements were recorded: one driving the mirror with a sine wave and the other with a triangular wave. Observing the FFTs of those signals for the sinusoidal scans (Figure 6.3), it is noticeable that the noise increases with the scan speed and is concentrated at the scan frequency and its harmonics. Figure 6.3 also shows zoomed LDV output spectra to highlight that there is a broad-band noise-floor, which also increases with scan rate. Note that in the left-hand plot of Figure 6.3 only the LDV spectra at 1, 5, 10, 20 Hz are reported in order to have a more legible figure. However, the spectra at 0.2 and 0.5 Hz have such a low noise content that they can be neglected.

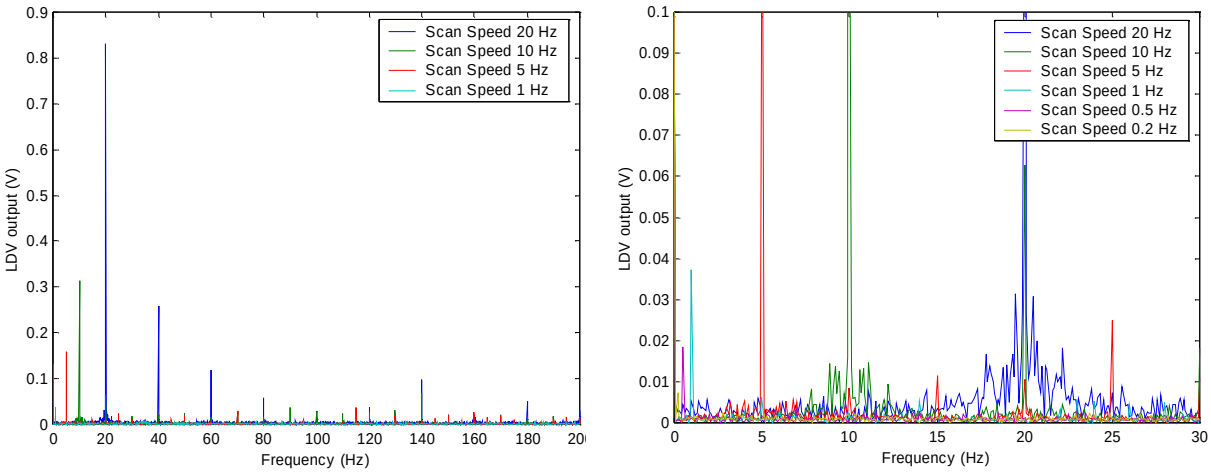


**Figure 6. 3** Measured LDV output spectrum, case of laser beam scanning sinusoidally.

The amplitude of the LDV spectrum component at the scan frequency increased with the scan speed, as shown in the left-hand plot of Figure 6.4. The noise floor amplitude, which is defined as the maximum amplitude of the LDV output spectrum, the peak at the scan frequency being excluded, is shown in the right-hand plot.

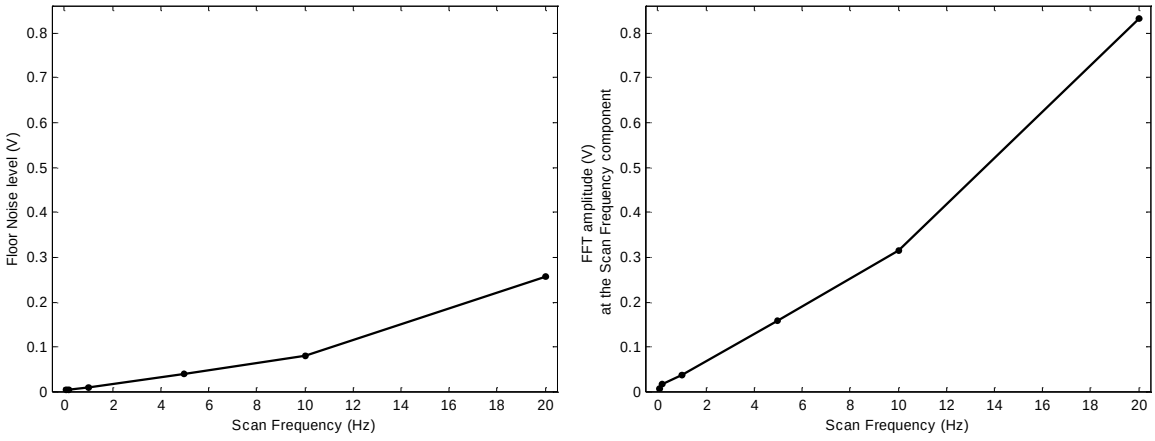


**Figure 6. 4** Noise, plotted against the scan frequency – sinusoidal scan.

In the second case, the mirror was driven by a triangular wave, i.e. scan at uniform rate (see in Figure 6.5 the LDV output spectra): the noise behaviour (Figure 6.6) is the same, the only difference being that it is a bit smaller - specifically 25 % less. This value was derived from the maximum noise level in both cases - sinusoidal (0.8317 V at 20 Hz) and uniform scan (0.6202 V at 20 Hz). Again, as in Figure 6.3, in the left-hand plot of Figure 6.5 the spectra at 0.2 and 0.5 Hz are not reported.

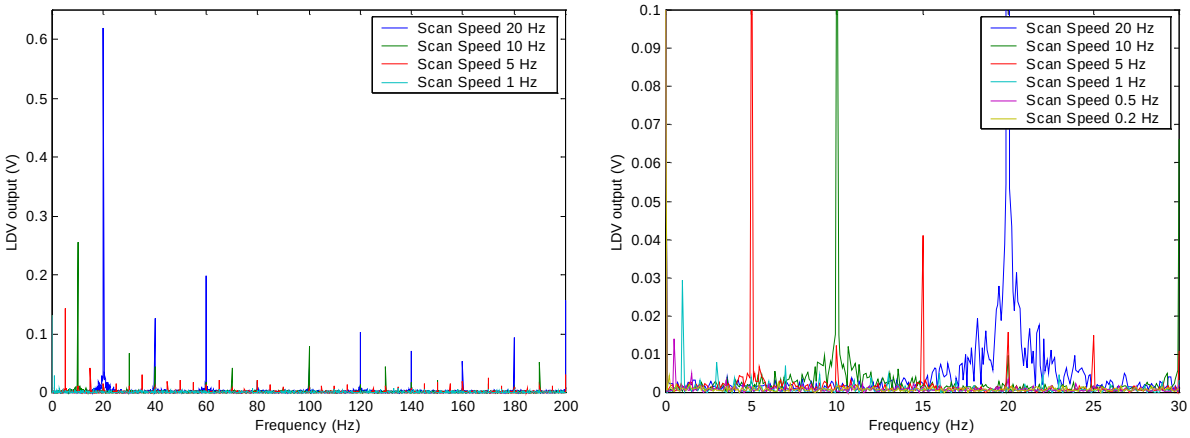


**Figure 6. 5** Measured LDV spectrum, case of laser beam scanning at uniform rate.

The noise behaviour is displayed in Figure 6.6 and, since the laser beam was scanning at uniform rate, it was plotted against the scan speed in m / s.

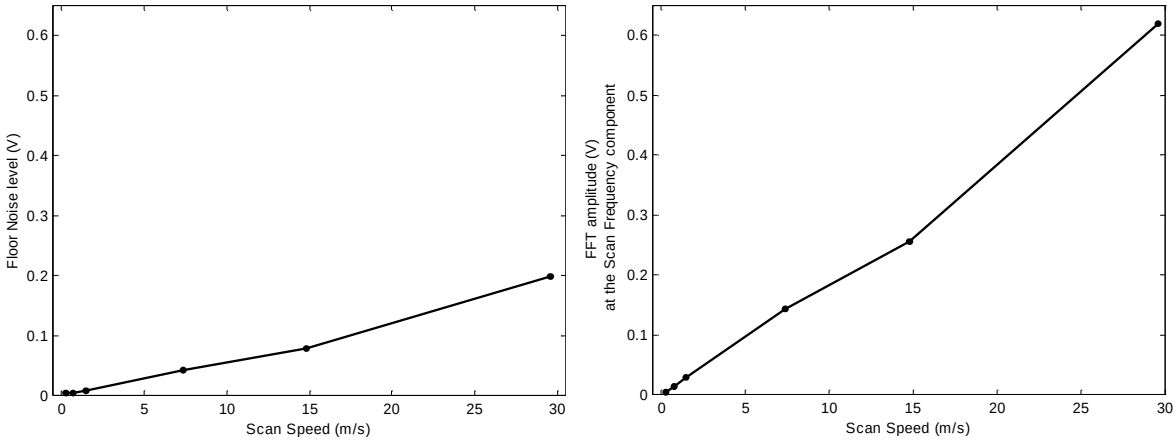


**Figure 6. 6** Noise, plotted against scan speed – scan at uniform rate.

These data were used to select suitable scan rates for the continuous-scan measurements.

By this noise analysis it was demonstrated that the scan speed is the most influential parameter on the noise behaviour. It was then deduced that the speckle model should be built on the basis of this parameter since, when varying the scan speed, the noise occurrence change consequently. The noise will appear at the scan frequency and its harmonics and its level will increase as the scan frequency increases. Therefore, when a continuous scanning LDV is employed, the laser beam scan speed will be chosen as a compromise: (i) it should be high (from 10 up to 20 Hz) so that, the noise being concentrated in its harmonics only, the presence of the noise itself will be limited and (ii) the scan frequency and all its harmonics must no coincide with the excitation frequency and its sidebands otherwise the derived response will be spoilt with the noise and cannot be reliable anymore. By arranging the scan speed in relation to the vibration frequency, the frequency range of interest, which includes the vibration response frequency with its sidebands, can be made to lie far apart from the scan speed harmonics. The spectral components used in the curve-fit analysis will then be unspoiled by the noise.

After the analysis at different scan speeds was completed, several LDV output acquisitions were performed by changing the scan length, which was taken at four values:

(i) 20 mm,
(ii) 30 mm,
(iii) 170 mm, and
(iv) 300 mm.

Figure 6.7 shows the amplitude of the noise level at 20 Hz and its harmonics for all the situations at different scan lengths. It can be noticed that the speckle noise is concentrated mostly at 20 Hz, where it increases as the scan length increases. On the other hand, at the higher harmonics the noise level decreases

no matter what scan length is used. This means that the noise assumes importance at the scan frequency only and this does not constitute a big problem since the scan frequency can always be made to be smaller than the vibration frequency. Therefore the noise does not necessarily pollute the information required (i.e. the vibration response) from the measured data. Figure 6.8 is a different, more compact, visualisation of the speckle noise contents at the different scan length and scan frequency harmonics. It can be seen, again, that its level is maximum at the scan frequency whatever the scan length is, but this value increases with the scan length. The noise content at the upper harmonics is always small. For a long scan the reduction is more noticeable than for small scans, see Table 6.1 for a quantitative representation of this reduction.

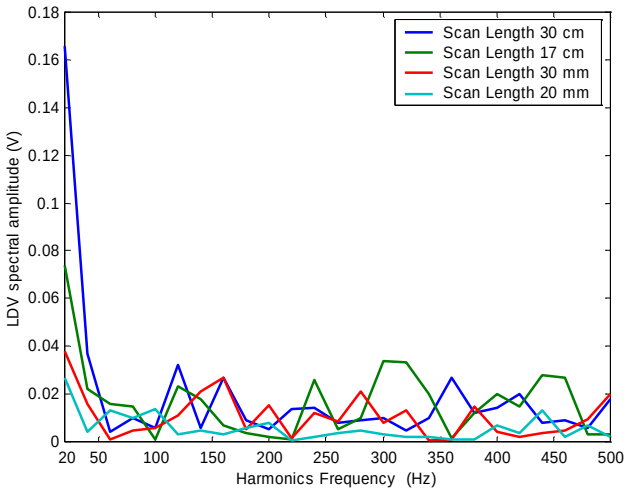


**Figure 6. 7** Speckle noise level plotted against the scan frequency and its harmonics for the different scan length.

Table 6.1 reports the difference between the noise level occurring at the scan frequency (20 Hz) and the noise level at the higher harmonics. This difference, called “noise reduction”, is obtained for each scan length by subtracting from the noise level at 20 Hz the averaged noise amplitude at all the higher harmonics and it is given as a percentage of the noise level at 20 Hz.

| **Scan Length** (m) | **Noise Reduction** (%) |
|---|---|
| 0.02 | 81.49 |
| 0.03 | 74.58 |
| 0.17 | 80.43 |
| 0.30 | 91.96 |

**Table 6. 1** Noise reduction at high-frequency range.

Figure 6.8 shows the noise content at the different harmonics of 20 Hz (i.e. the scan speed) and at the different scan lengths between 0.02 and 0.3 m.

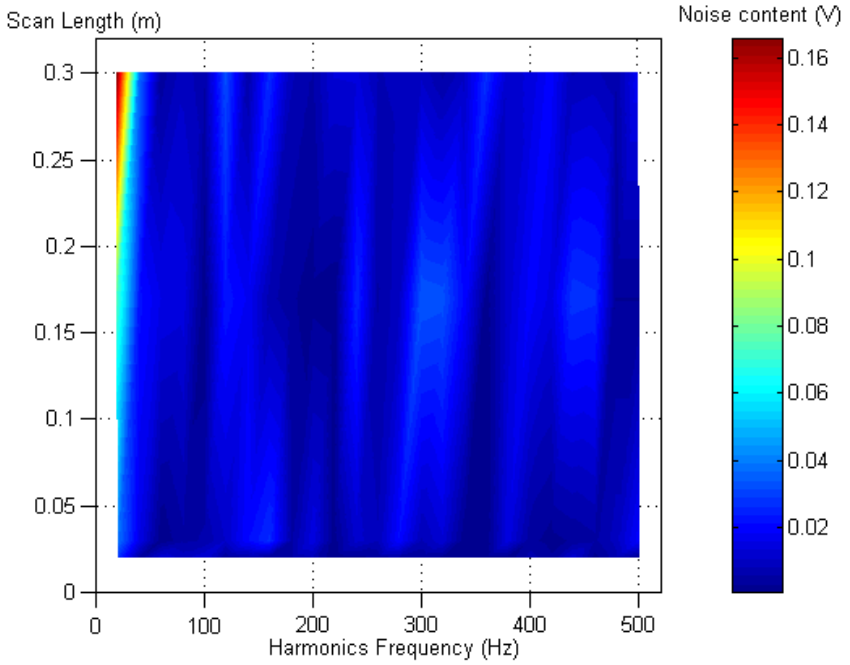


**Figure 6.8** Color-map of the speckle noise level simultaneously plotted against the scan length and the scan frequency and its harmonics.

From the experiment results described in this section, it can be noted that the noise at higher harmonics of 20 Hz is smaller by around 80-90 % with respect to the noise level at 20 Hz and it can be neglected. The scan length consequently influences the noise content at the scan frequency only and, as was already highlighted, the scan frequency component does not assume big importance within the complete LDV output spectrum. In fact, the information required,

namely the vibration response, is at the vibration frequency which is usually much higher than the scan frequency. It can thus be concluded that the scan length does not affect the quality of the measured data and it will not be included in the speckle noise model, which will take into account the scan speed only.

### *6.4.4 Simulated Speckle Noise*

If a measuring laser beam moving continuously along a line on a structure is considered, it must be clear that the speckle pattern seen by the laser would change since the surface swept is changing. The speckle noise characteristic that the experimental analysis has shown, i.e. the classical noise concentration at a scan frequency and higher harmonics, can be explained with regard to a simple model. It will be assumed that the laser beam scans sinusoidally at the speed of 10 Hz backwards and forwards along a straight-line and over this line all the speckles swept by the laser are “bright” with the exception of one, which is “dark”. When the laser beam passes through this speckle, the light scattered back towards the photodetector will experience a drop-out. The LDV output will then present a loss of the signal twice within a scan cycle since the laser is going backwards and forwards along the scan line. The LDV output and its spectral content are illustrated in Figure 6.9.

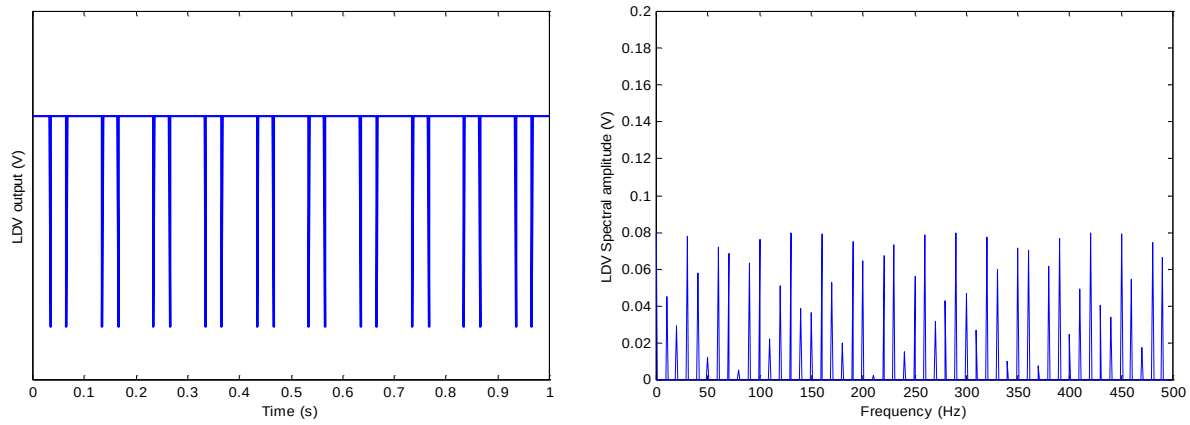


**Figure 6.9** Simulated LDV output time signal showing drop-outs and corresponding Fourier spectrum.

A model of the speckle noise can then be developed on the basis of the considerations derived from the experimental analysis that can be summarised as:

(i) speckle noise is concentrated at the scan frequency and its harmonics, and

(ii) the speckle noise at the scan frequency occurs with a higher level.

The model can be then written as:

$$rate\,of\ change\,of\ speckle\ phase = A_{SPECKLE\ at\ \Omega_L}\left[\cos\left(2\pi\,\Omega_L\,t\right) + b\sum_{n=2}^{n.of\ harm} v(n)\cos\left(n\,2\pi\,\Omega_L\,t\right)\right] \quad \textbf{(6. 8)}$$

$\Omega_L$ being the scan frequency of the measuring laser beam, $v$ a normalised random variable which represents the amplitude of the LDV spectrum at the harmonics of the scan frequency, $n$ is an integer which it depends on the number of harmonics of the scan frequency that it is decided to be included, $A_{SPECKLE\ at\ \Omega}$ is the amplitude of the speckle noise at the scan frequency and $b$ is a parameter which links the noise level at the scan frequency with the noise level at its harmonics (see the following analysis).

From the experimental noise analysis it is possible to deduce how the noise level occurring at scan frequency of the measuring laser beam and at its harmonics is related to the scan frequency itself.

First, it should be pointed out that the noise level at higher harmonics is always smaller than the noise amplitude at the scan frequency, as Table 6.2 shows. The “noise reduction“ is calculated as a percentage difference between the noise level at the scan frequency and the maximum noise level at the higher harmonics.

| **Scan Frequency** (Hz) | **Noise level at the Scan Frequency** (V) | **Maximum Noise level at the Higher Harmonics** (V) | **Noise Reduction** (%) |
|---|---|---|---|
| 0.2 | 0.0072 | 0.0049 | 32.41 |
| 0.5 | 0.0182 | 0.0058 | 68.13 |
| 1 | 0.0371 | 0.0105 | 71.62 |
| 5 | 0.1600 | 0.0393 | 75.43 |
| 10 | 0.3200 | 0.0800 | 75.00 |
| 20 | 0.8400 | 0.2600 | 69.05 |

**Table 6. 2** Noise amplitude at the scan frequency and at high-frequency harmonics, and relative reduction.

With the exception of a scan rate of 0.2 Hz, where the noise level at the scan frequency itself is very low, the difference between the noise amplitude at the scan frequency and that at the higher harmonics can be assessed around 72 %, ("noise reduction", from the third column of Table 6.2). It can be deduced then that the parameter *b* appearing in Equation (6.8) will assume a value of about 0.28.

Moreover, from the experimental noise analysis, and specifically from the graphic shown in the right-hand plot in Figure 6.4, a relationship between the scan frequency and the noise level at the scan frequency can be deduced. It can be noticed that the noise amplitude increases with the scan speed with a linear behaviour up to 10 Hz then a big rise occurs up to 20 Hz, see right-hand plot in Figure 6.4. The noise data plotted in this graph can be curve-fitted by a polynomial of the third degree, which can be written as:

$$A_{SPECKLE\ at\ \Omega_L} = 7.34e^{-5}\,\Omega_L^3 - 1.17e^{-3}\,\Omega_L^2 + 3.57e^{-2}\,\Omega_L + 1.11e^{-3} \qquad \textbf{(6. 9)}$$

Figure 6.10 shows the matching of this polynomial relationship with the measured data plotted in Figure 6.4 (right-hand plot).

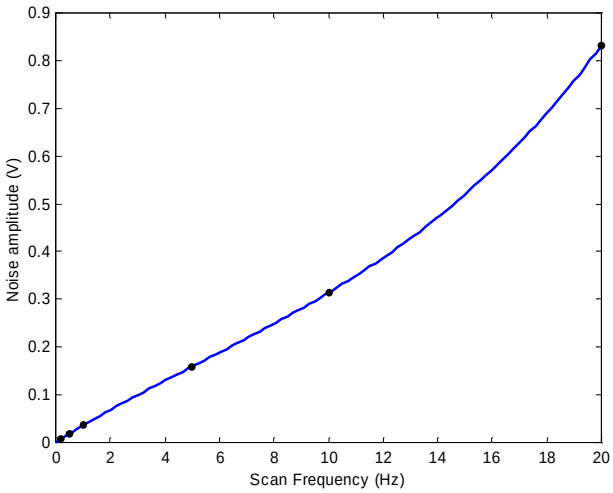


**Figure 6. 10** Measured noise level data (black dots) and their polynomial curve-fit (blue line).

Equations (6.8) and (6.9) can be used to build a speckle noise model.

The LDV output obtained by a measurement performed by a laser beam moving continuously at 10 Hz along a straight-line can be simulated, by using Equation (6.8) by setting $\Omega_L$ = 10 Hz, *n. of harmonics* = 100, $b$ = 0.28 , and $A_{SPECJKLE\ at\ \Omega_L} = 0.3138$ V, derived from Equation (6.9) for $\Omega_L$ = 10 Hz.

Some random noise, related to different types of 'error' inevitably contained in the real test data, is added to the model of the speckle noise as well.

The results are shown in Figure 6.11 where the left-hand plot shows the simulated time signal, which the model produced as LDV output, while the right-hand plot illustrates the real data measured in time domain (the measured time history is taken from the experiments described in Subsection 6.4.3, specifically for a scan speed of the laser beam of 10 Hz). In Figure 6.12 the relative LDV spectra are depicted, namely the left plot represents the spectrum of the simulated signal and the right plot the spectrum of the measured one.

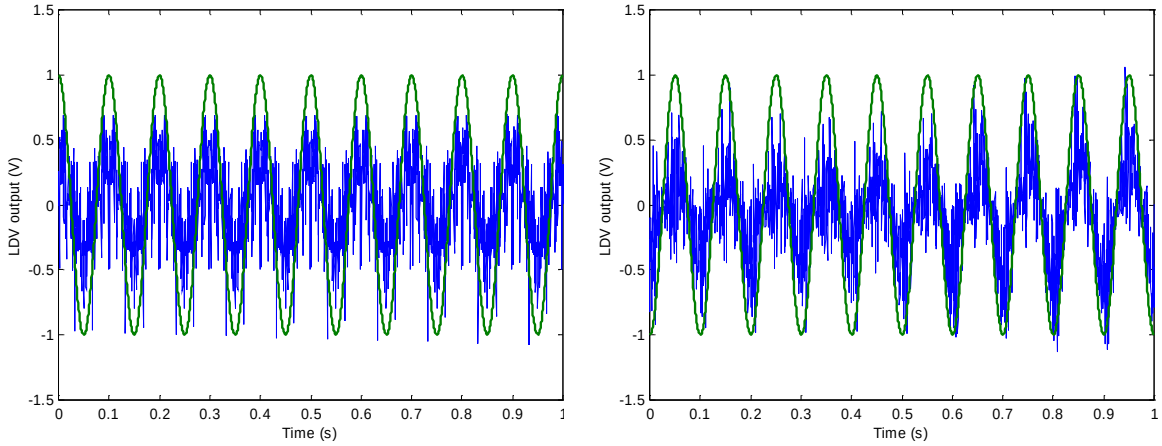


**Figure 6. 11** Simulated (left-hand plot) and measured (right-hand plot) LDV output time histories plotted together with the 10 Hz sinewave.

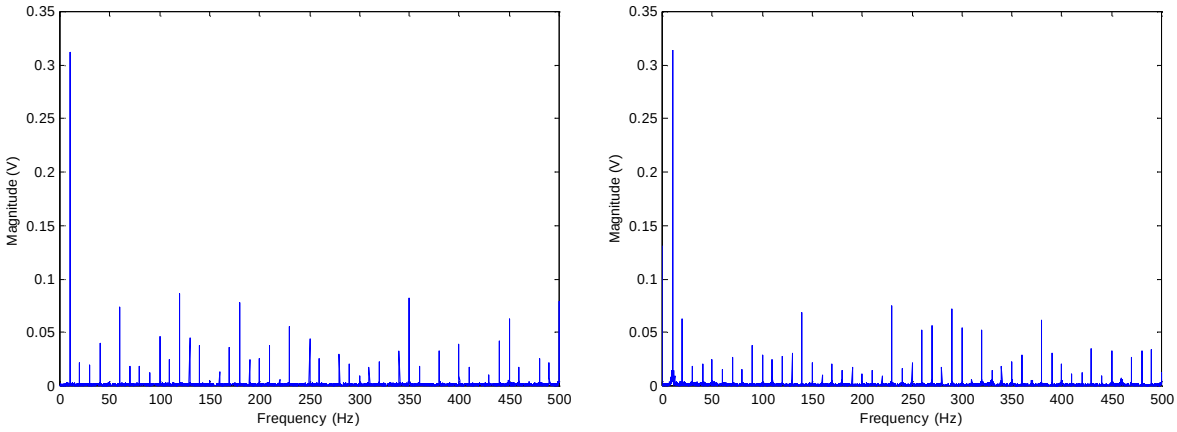


**Figure 6. 12** Simulated (left-hand plot) and measured (right-hand plot) LDV output spectrum.

### *6.5. Experiment Simulation using the Model developed and Comparison with the Real Measurement Data*

As shown in the previous section, the speckle noise model works when the simulated LDV output is compared with an experimental LDV output acquired on a stationary structure (Figures 6.11 and 6.12). In this section a complete CSLDV experiment is simulated when the structure under test is vibrating at one of its natural frequencies.

Specifically, a sinusoidal scan of the laser beam along a straight line will be considered and, in order to have a comparative term, real measured data will be taken into account, namely - the experimental data obtained by performing a linear continuos scan test on half of the length of the steel beam described in Subsection 5.3.3.3, and excited at its third natural frequency of 311 Hz.

The third mode shape of the beam whose material characteristics are known, can be derived by applying the second equation of (5.8) derived from the Timoshenko theory for a simple beam in transverse vibrations. It is plotted in Figure 6.13 with the *x*-axis representing the length of the beam normalised between –1 and 1.

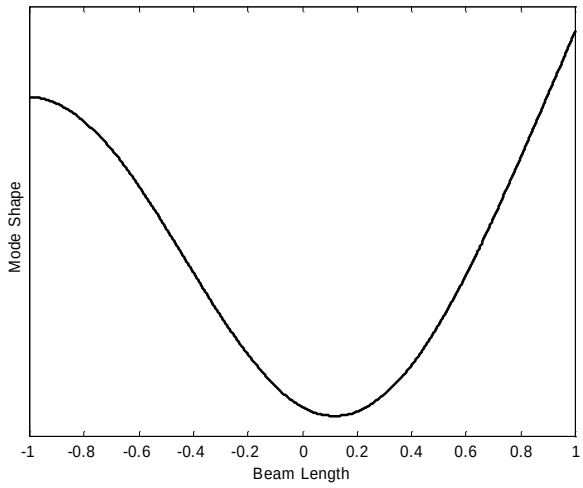


**Figure 6. 13** Third mode shape of the beam (311 Hz) derived from the second equation of (5.8) - Timoshenko theory.

The mode shape illustrated in Figure 6.13 can be curve-fitted by a polynomial of the 7$^{th}$ (optimal) order ($p$). The polynomial coefficients ($V_{Rn}$) can then be used to determine the transverse velocity that a laser beam moving continuously along the half length of the beam will measure, by using Equation (5.27). Only the first term of the sum in (5.27), being the mode shape calculated analytically real. The parameters to be set into the equation will then be:

- $V_{Rn}$ = { -1.24 -1.30 5.17 2.07 -2.87 -0.61 0.65 0.12 } mm / s ,
- $p$ = 7 ,

- $\Omega$ = 10 Hz (as it was set in the actual experiments),
- $\delta$ = 5.1° (mirror delay found by performing a mirror calibration),
- $\omega$ = 311 Hz, and
- $t$ the time vector built with the same parameters (sample rate and samples acquired, specifically 5000 Hz and 5000 samples) used in the real experiment.

The uncontaminated velocity of the beam, $v_z(t)$, is then obtained. To introduce the speckle noise, Equations (6.8) and (6.9) will be used with the following parameters:

- $A_{SPECKLE\ at\ \Omega}$ = 0.32 (V) as from Equation (6.9) which should be converted in (mm/s) as the vibration velocity is now given in its physical units. Considering that the experiments were performed by using a sensitivity of the laser of 5 mm/s/V, the value of $A_{SPECKLE\ at\ \Omega}$ can be set at 1.6 mm/s.
- $\Omega_L$ = 10 Hz,
- $b$ = 0.28,
- *number of harmonics* = 500, and
- $v$ = normalised random variable.

The velocity signal simulated is shown in Figure 6.14 together with the LDV output time history acquired during the real laboratory test, while their relative magnitude spectra are illustrated in Figure 6.15.

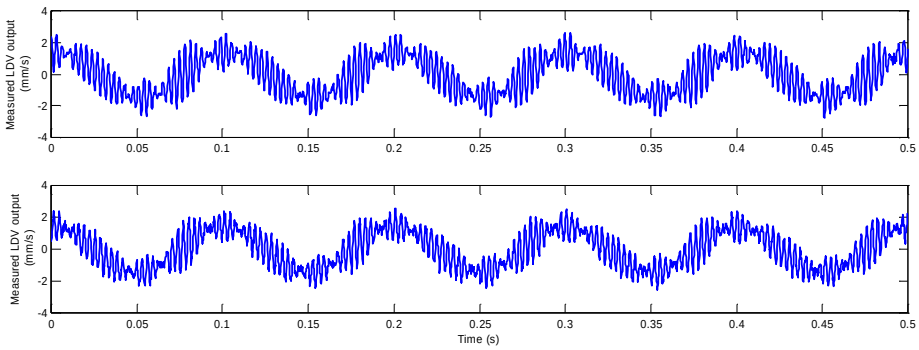


**Figure 6. 14** Measured (top) and simulated (bottom) LDV output time histories.

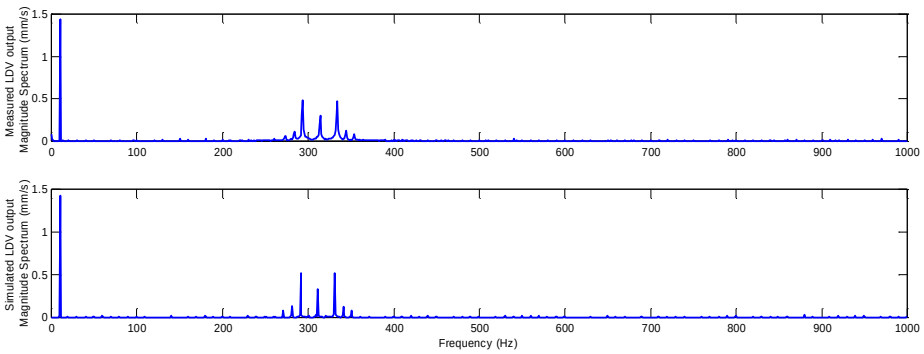


**Figure 6. 15** Measured (top) and simulated (bottom) LDV output magnitude spectra.

The phase spectra of the simulated and measured LDV outputs are plotted together in Figure 6.16. Note that the phase at the different sidebands frequencies are not aligned on a horizontal line and the misalignment is the same for both the simulated and the real data. This misalignment, as explained in Subsection 5.3.3.2.3, depends on the mirror delay which was included in the simulation as well .

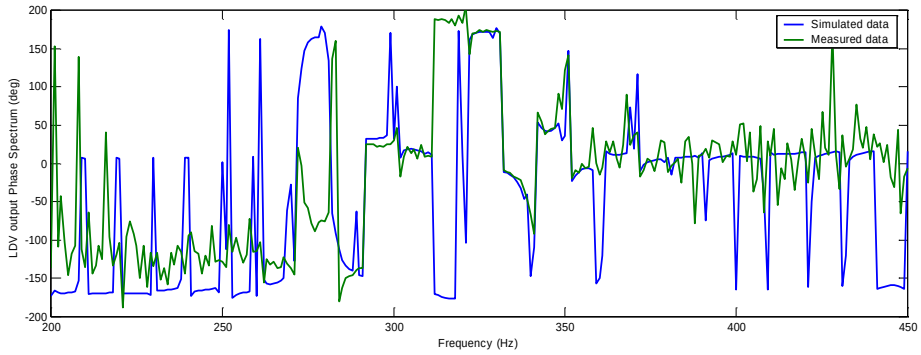


**Figure 6.16** Measured (green) and simulated (blue) LDV output phase spectra.

## *6.6. Averaging Procedure*

In the previous section it was demonstrated that the speckle noise affecting the measurements performed by continuous scanning techniques is periodic with a basic period at the frequency of the motion of the measuring laser beam, and, specifically, although the amplitude of the noise is random, its effect occurs located at the same phase datum. It was then thought that the easiest solution of the problem would be to average the time histories acquired each time within one complete scan (say backwards and forwards if it was considered a line scan) taking care to start the acquisitions always at the same position over the line (this is made possible by triggering the acquisition with the mirror driver signal). Another solution has been found in the use of velocity data acquired over several cycles of the laser scan. The signal could, then, be cut into a number of sub-signals, each of them corresponding to an unique complete cycle of scanning of the laser along the line traveled. Therefore, all these pieces could be averaged in order to remove the periodic noise and reassembled together again to give a new "filtered" time history free from the speckle noise.

As an example, where it was decided to show the feasibility of the idea of averaging, the time histories measured, when performing a straight-line scan at 10 Hz on the beam shown in Figure 5.1, were considered. The same experimental data used for the validation of the analysis of the line scan technique described in Subsection 5.3.3.3 were employed here, specifically the averaging procedure was applied to the time signal acquired when the beam was excited at the third and fifth natural frequencies (311 and 766 Hz).

Figure 6.17 illustrates the time history and the spectral content in magnitude of the LDV output when the beam was excited at 311 Hz.

From both plots, in the time and the frequency domains the important presence of the 10 Hz component is clear and from the zoomed FFT plotted in Figure 6.18 all the harmonics of 10 Hz are visible.

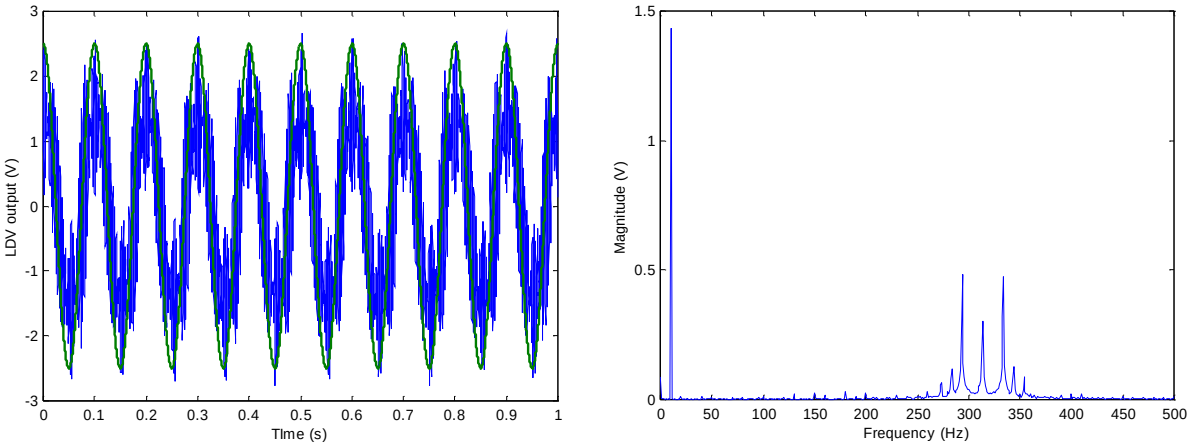


**Figure 6. 17** Measured LDV output spectrum (blue) shown together with the mirror driver signal (green) in the left-hand plot and LDV output spectrum magnitude in the right-hand – Resonance frequency at 311 Hz.

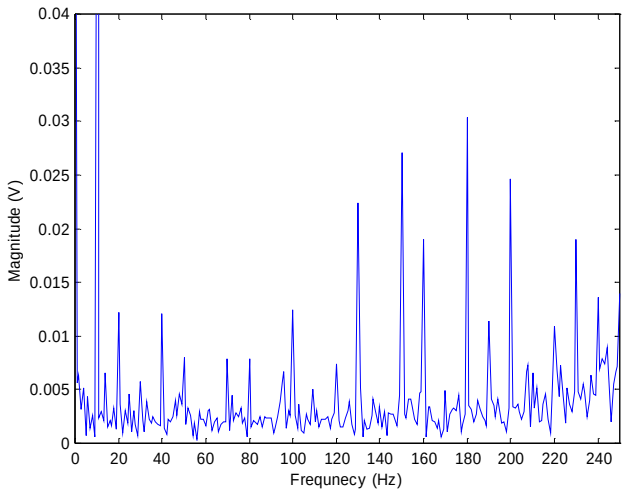


**Figure 6. 18** Zoomed LDV output spectrum in the low-frequency range to emphasize the harmonics of the scan frequency (10 Hz).

If the time history is now cut into ten samples (“sub-signals”), ten scan cycles being contained in the acquired data, and then averaged, all the non-periodic components will be taken out and a time signal consisting of the periodic noise only will be derived, see Figure 6.19. By subtracting this latter from the original measured data (left-hand plot of Figure 6.17), a new time signal unspoiled by

the noise is obtained, see Figure 6.20, where the right plot is a zoom of the left one.

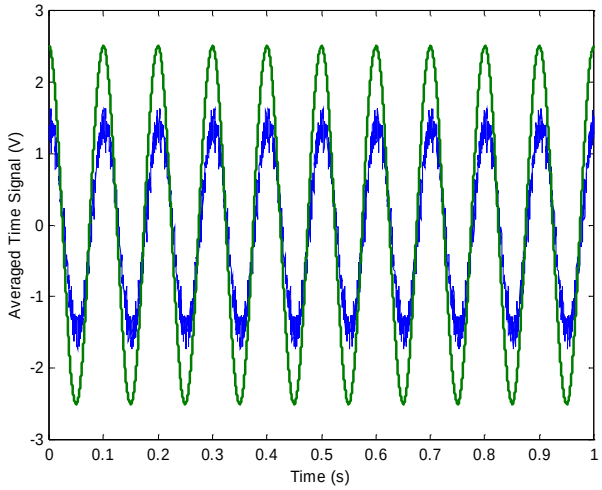


**Figure 6. 19** Averaged time signal (blue) and mirror driver signal (green).

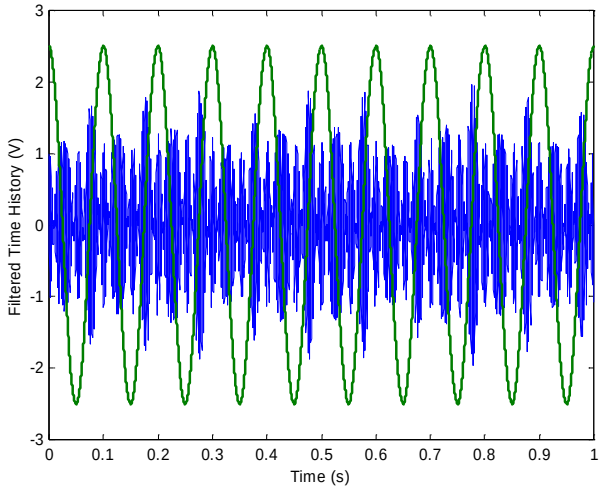


**Figure 6. 20** Time history deprived of the periodic noise (blue) and mirror driver signal (green) – Resonance frequency at 311 Hz.

It is already evident by inspecting the filtered time signal that the periodic component due to the speckle pattern motion at the same frequency of the scanning laser beam is completely eliminated. In Figure 6.21 the effect is emphasised: the spectral contents of the original time history and the processed

one are plotted together. The left-hand plot shows how the components at the excitation frequency (311 Hz) and its sidebands are completely coincident while the right-hand plot highlights that the filtered spectrum does not contain anymore any components at 10 Hz and its harmonics[2].

Figure 6.22 depicts the magnitude of the FFT of both the signals (original in the left plot and filtered in the right) in order to have a quantitative description of the floor noise reduction. In the measured signal the floor noise level was at –30 dB (40 dB less than the vibration peak which was at 10 dB); in the filtered signal the noise floor drop at –43 dB (53 dB less of the vibration peak which was not changed). The noise then drops from 1% re the vibration peak to 0.2 %.

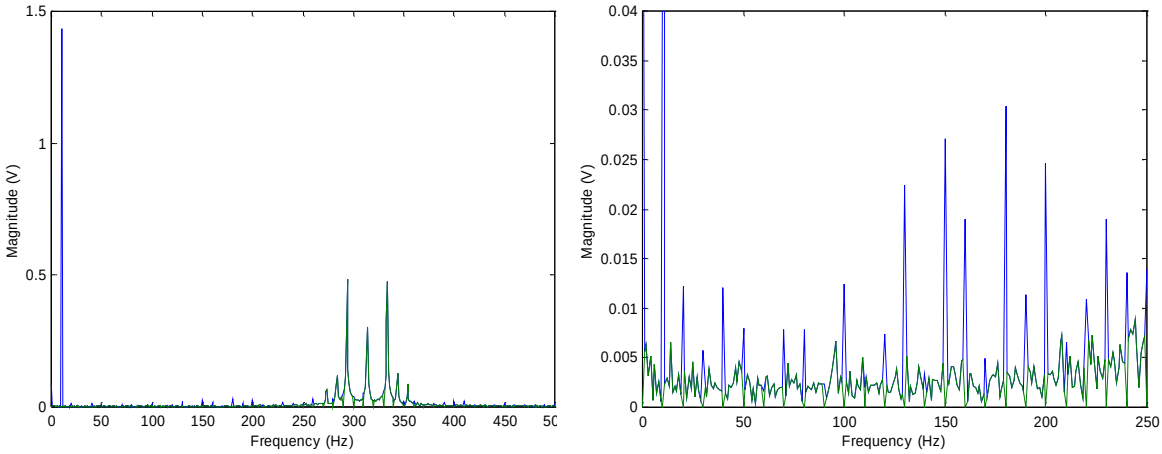


**Figure 6. 21** Spectral components of the original time history (blue) and the filtered one (green). The left plot is a zoom in the low-frequency range – Resonance frequency at 311 Hz.

[2] In this section it was stated that the averaging procedure allows eliminating the periodic component due to the speckle pattern motion. It should be highlighted again that the periodicity of the speckle noise concerns only the phase while its amplitude is random. Therefore, it is possible to get rid of the speckle noise by averaging. On the other hand the vibration component of the signal is periodic in amplitude and phase; the averaging will, then, not produce any effect on it.

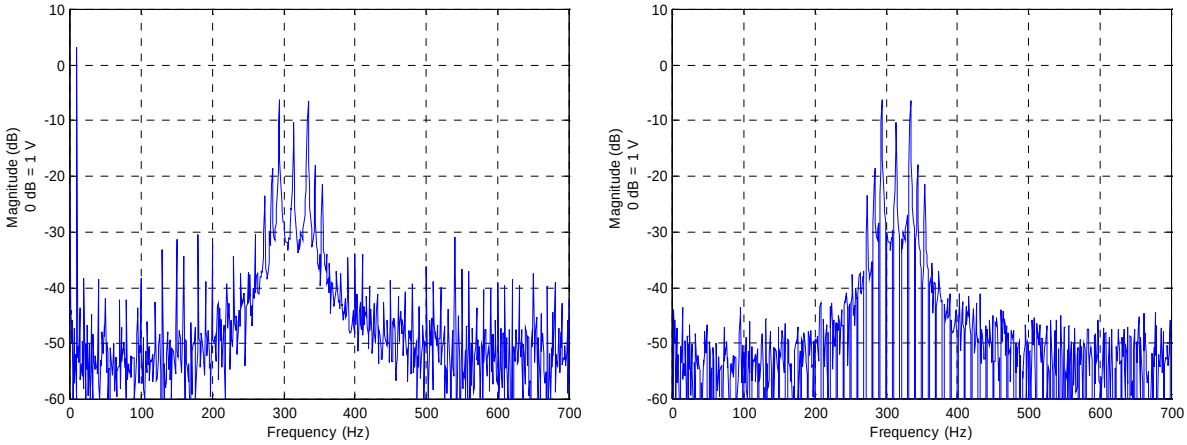


**Figure 6. 22** Fourier spectrum amplitude in dB for the original measured signal (left) and the filtered one (right) – Resonance frequency at 311 Hz.

The same procedure can be applied to the time history acquired when the beam was excited at 766 Hz, see Figure 6.23 where the LDV output is shown in the time (left) and frequency domain (right). This case is interesting since the level of the structural vibration was higher than the previous case (third natural frequency). Therefore, it was found to be hard to maintain the focus of the laser spot in the structure stable. The classical frequency broadening (as described in Section 2.5 and experimentally shown in Subsection 5.5.4.3, specifically in Figure 5.78) was noticed, namely the group of sidebands around the excitation frequency was repeated at the double of the excitation frequency value (1532 Hz), as it is clear in the right plot of Figure 6.23.

Since the spectral component at the double of the excitation frequency and its sidebands are due to the speckle noise which is periodic, one would expect that its contribution will be reduced if not completely eliminated. The right plot of Figure 6.24, where the FFT of the signal processed in the way described in this section is illustrated, prove this deduction since the spectral content in the high-frequency range is remarkably decreased. Moreover, as expected, the Fourier components at 10 Hz and its harmonics are almost absent (the spectral magnitude at 10 Hz was 3 V in the original measured signal while it drop to 0.3

V in the filtered one, 90% less), see also the left plot of Figure 6.24 where the time history deduced after averaging shows that the 10 Hz modulation is invisible.

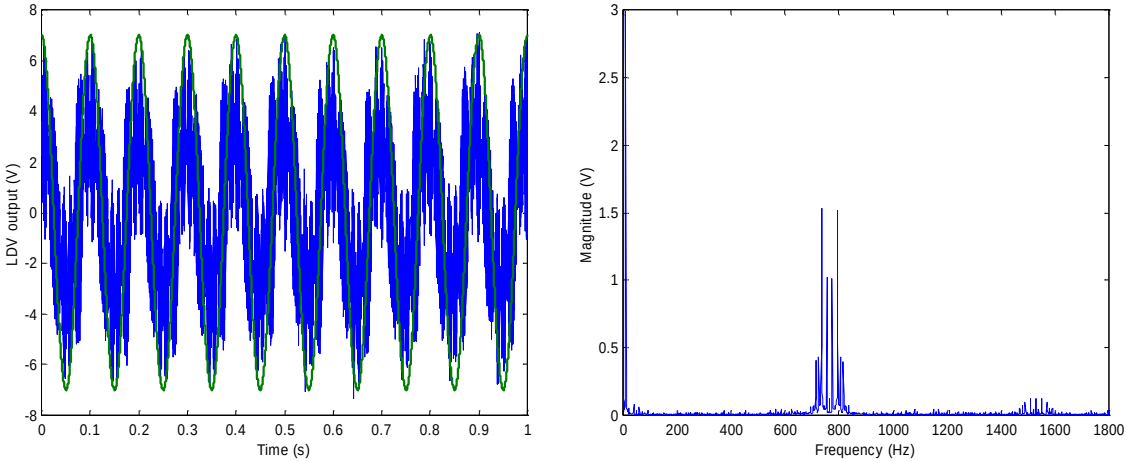


**Figure 6. 23** Measured LDV output spectrum (blue) shown together with the mirror driver signal (green) in the left-hand plot and LDV output spectrum magnitude in the right-hand – Resonance frequency at 766 Hz.

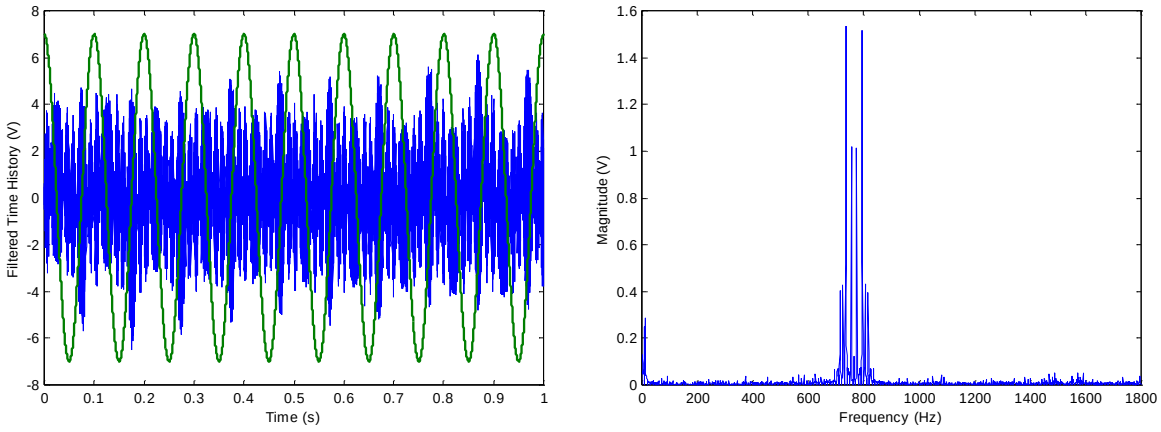


**Figure 6. 24** Time history deprived of the periodic noise (blue) after the averaging process and mirror driver signal (green) in the left-hand plot and its Fourier spectrum in the right-hand – Resonance frequency at 766 Hz.

In Figure 6.25 the spectra of both the measured and the processed signal in dB are reported to have again a quantitative representation of the noise floor reduction: the floor noise drop from –18 dB to –25.7 dB, the maximum vibration peak being at 3.6 dB. The noise then was reduced from 8.3% re the vibration peak to 3.4 %.

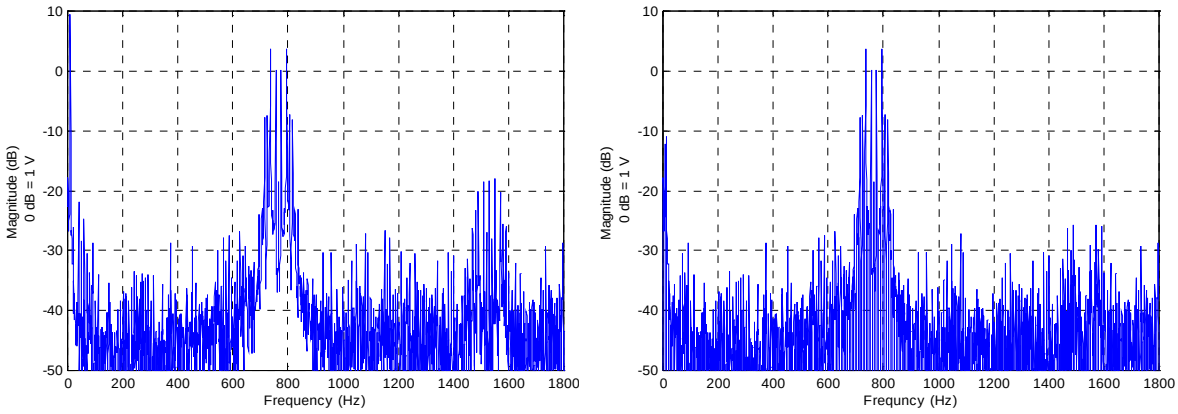


**Figure 6. 25** Fourier spectrum amplitude in dB for the original measured signal (left) and the filtered one (right).

## *6.7. Conclusions*

In this chapter the role of a “virtual” continuous scanning measurement has been investigated. In order to carry out a virtual test, a simulation of a real test has been performed by producing a mathematical model of the test which includes the actual tested object’s structural behaviour when excited at one of its natural frequencies, and the simulation of the noise that pollutes the LDV output signal. This latter has been found to depend mostly on the laser-related effect, which is the speckle noise. A detailed theoretical model of speckle has then been developed and tested by comparing analytical results with real experimental data.

From the study of speckle noise, which involved both a theoretical analysis and the experimental observation of the phenomenon, an important deduction was

made: when a continuous scanning technique is applied, the speckle noise is concentrated at the scan frequency and its harmonics. The scan frequency becomes then an important parameter which must be chosen in order to have the frequency components where the noise is concentrated far apart from the vibration frequency and its sidebands, which carry the vibration response information.

At the conclusion of the chapter, a technique to overcome the speckle noise and its effect in the measurement signal has been highlighted and, specifically, an averaging procedure that allows us to obtain a better SNR in the real experimental data.

# Chapter 7 Application of the Continuous Scanning Technique on Industrial Cases

## *7.1. Introduction*

In this chapter a collection of measurements obtained with the continuous-scanning measurement techniques described in Chapters 4 and 5 are illustrated. Different practical applications were investigated: some case studies were taken from structures under analysis within BRITE/EURAM projects running at Imperial College such as QUATTRO, [47], and VALSE, [13]. A number of different techniques were employed on these practical structures:

(i) short-line scan for 2-DOF recovery;
(ii) small-circular scan for 3-DOF determination;
(iii) long-line scan at uniform rate for direct ODS establishment, via demodulation;
(iv) sinusoidal long-line scan for the calculation of the ODS as a polynomial;
(v) parallel sinusoidal long-line (raster) scans over an area to derive 2D ODSs;
(vi) two-dimensional long-scan at uniform rate to recover the 2D ODS via demodulation;

(vii) two-dimensional sinusoidal long-scan to produce the ODS as a 2D polynomial.

## *7.2. Short-Line and Small-Circular Scanning Techniques Applied to Practical Cases (RDOF or Angular Motion Measurement)*

### *7.2.1 Experimental Set-up Description*

In order to validate the techniques introduced above in more general experimental cases, measurements have been performed using two general practical structures:

- a simple but representative structure (called the “1203” structure) consisting of two plates connected together by a third plate and two bars whose three-dimensional sketch is shown in Figure 7.1.

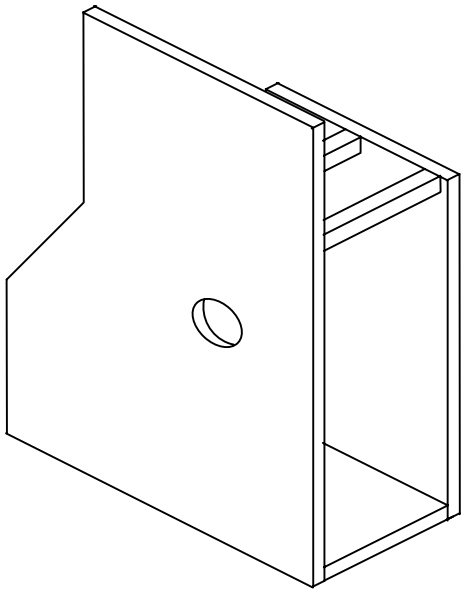

**Figure 7. 1** Three-dimensional view of the test specimen.

- the second specimen tested is a well-documented simple coupled structure, namely the 'breadboard', manufactured on purpose for the BRITE/EURAM program QUATTRO, see reference [47]. This structure consists of a brass plate and a beam which is joined to the plate along its

diagonal via two bolts, whose positions are shown in Figure 7.4. Figures 7.2 and 7.3 show the dimensions of plate and beam respectively.

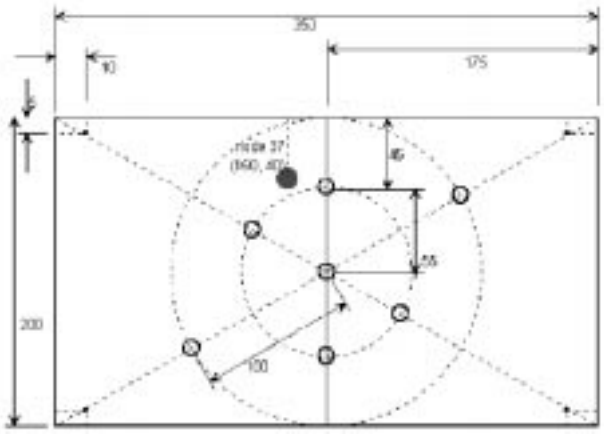


**Figure 7. 2** The brass plate.

The thickness of the plate is 3 mm. Seven holes with diameter 5 mm are drilled in the plate. Four small holes with 2 mm diameter are also made at the plate corners primarily for hanging the structure.

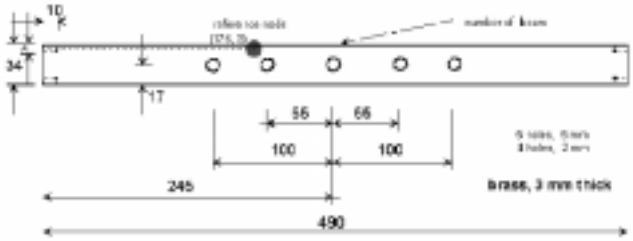


**Figure 7. 3** The brass beam.

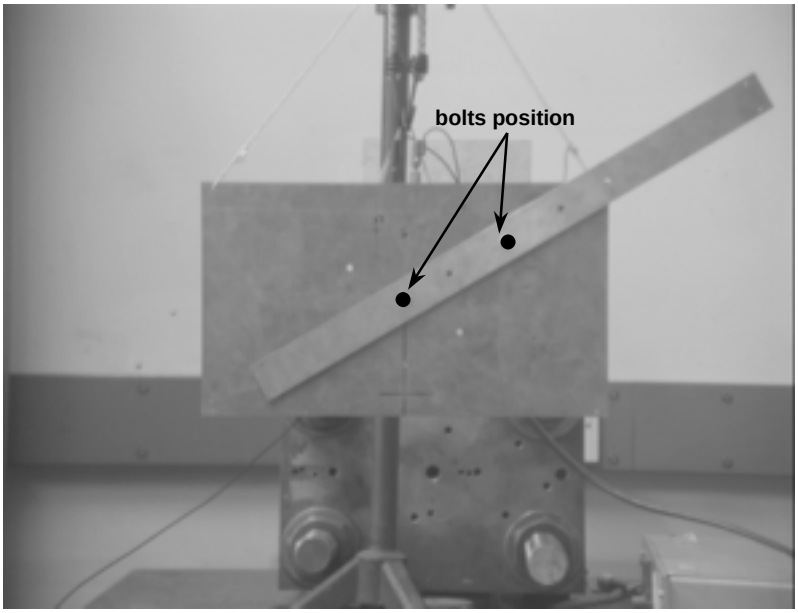


**Figure 7. 4** Assembled structure seen from the laser head position.

A system has been developed for measuring MDOF vibration of a point, exploiting the techniques described in the previous sections. A standard Polytec scanning vibrometer (laser head OFV-055 and controller OFV-3001-S) is used as the velocity transducer. The measurement process can be divided in two separate stages: (i) the scanning control and data acquisition, where the vibration signal from the CSLDV is stored as a time-history and (ii) the data post-processing, in which the derivation of the required DOF responses is made. The control and data-acquisition system has been designed using National Instrument boards controlled by a PC platform and the management software has been developed in LabVIEW. The control system generates the arbitrary waveforms that must be sent to the mirrors in order to perform the continuous scan by means of an NI two-output channels 12-bit resolution card driven by the LabVIEW routines. In this case, since linear or circular scans are employed, the routine is used to produce respectively one or two sinewaves of identical amplitude and frequency and a 90° phase shift (see Appendix A.1.5 for the control panel of the LabVIEW program driving the mirrors). The same PC controls, via a GPIB, an HP 33120A 15MHz Function / Arbitrary Waveform Generator which produces the excitation transmitted to the structure through a

shaker. The CSLDV output, the force signal coming from a force cell attached to the structure and the signals driving the mirrors, are then stored as time histories using an NI four-input channels Dynamic Signal Acquisition card. The excitation control and the acquisition steps are achieved by a `LabVIEW` routine which runs into a loop where the different excitation frequencies are swept (see Appendix A.1.8 for the control panel of the `LabVIEW` program which controls the excitation and the acquisition in the automatic step-sine test). With such a program, a step-sine test can be performed: the excitation can go through different frequencies within a range that can be set as a parameter of the routine together with the step frequency. At each frequency, the four inputs are stored by the system having waited the necessary transient time needed for the vibration to become stationary. Moreover, a trigger option is available in order to start the acquisition when the sinewave driving one of the mirrors is passing, positive going, through zero, as required for the continuous techniques, see Section 4.1. Parameters that need to be set at this stage, in addition to the excitation frequency bandwidth and step already mentioned, are the sample rate and the number of samples required for the acquisition. The stored time domain data can be post-processed later on in a different stand-alone PC. Data post-processing software has been written in `Matlab`. Figure 7.5 shows the schematic sketch of the measurement system set-up.

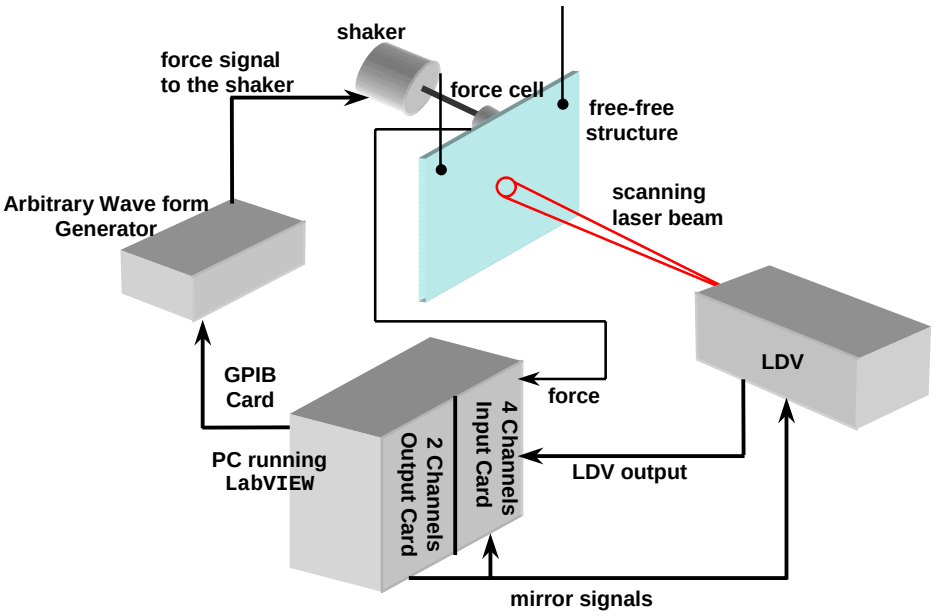


**Figure 7. 5** Schematic representation of measurement system.

### *7.2.2 Test of the "1203" Structure*

The first case study consisted of the structure depicted in Figure 7.1, that was used at the Imperial College laboratories for many comparative studies. A small circular scan was arranged around a position on the top plate where it was expected there would be a significant angular motion. In fact, via a previous analysis made with the two-dimensional uniform scanning technique, see subsection 5.5.2, a bending mode was found at 242 Hz, as shown in Figure 7.6.

The measurement set-up employed was the one shown in Figure 7.5: sinusoidal vibration was produced in the structure by driving the shaker, whose position is shown in Figure 7.6, in the frequency range of 200-300 Hz with an increment of 0.5 Hz, so that the bending mode at 242 Hz would be excited. Using the LabVIEW routines written for the purpose, the scanning mirrors were first made to scan continuously in a circle of 11 mm radius centered at the nominal measurement point and at a speed of 10 Hz. Then, the step-sine test was started and, at each step, the time history coming from the LDV, triggered with the mirror driving signal, and the output of a force cell interposed between the shaker and the structure, were acquired and stored.

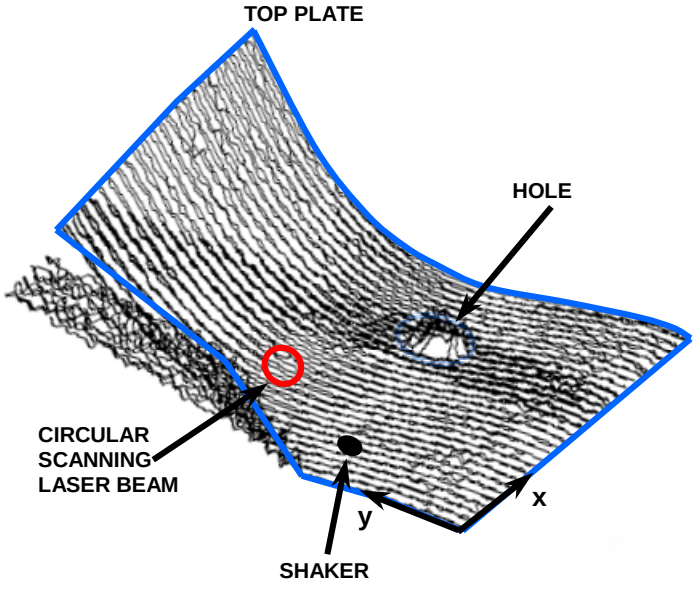


**Figure 7. 6** Plate bending mode and circular scan location.

Time-domain data were then post-processed by `Matlab` routines written for the purpose. The process consisted of a curve-fit of each LDV time signal at the corresponding excitation frequency, which varied from 200 Hz to 300 Hz with a step of 0.5 Hz, and at the sideband frequencies that were derived from the excitation one by subtracting and adding the scan frequency (10 Hz). Thus, the first time signal was multiplied by sine and cosine of 190, 200 and 210 Hz, and so on for the further data. As a result, real and imaginary components of the LDV output Fourier spectrum at each frequency step were derived: $R_{\omega}$, $I_{\omega}$, $R_{\omega-\Omega}$, $I_{\omega-\Omega}$, $R_{\omega+\Omega}$, $I_{\omega+\Omega}$, where, $\omega$, was the actual excitation frequency and $\Omega$ the scan speed. These Fourier components were then scaled with the spectrum component derived from a curve fit of the force driving signal at the relevant excitation frequency in order to produce transfer functions - mobilities, in this case. By applying Equation 4.15, real and imaginary components of the translation and rotation (about both *x*- and *y*-directions) mobilities were obtained (their magnitude plots are shown in Figures 7.7 and 7.8). RDOF mobilities are plotted together and are multiplied by the scan radius (0.011 m) in order to appear in the same units as the translation properties.

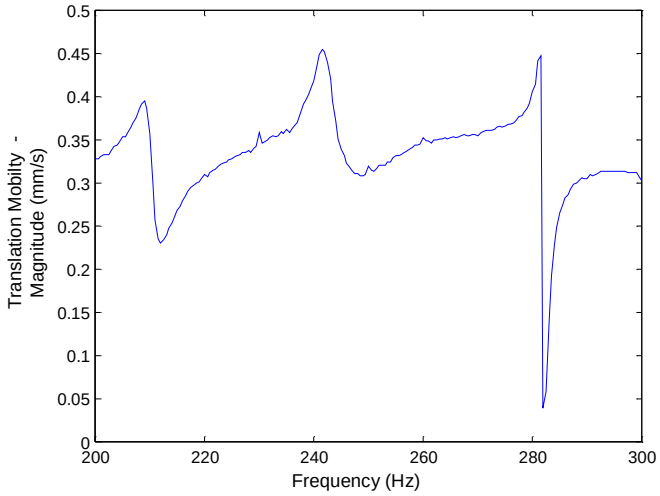


**Figure 7. 7** Translation mobility amplitude.

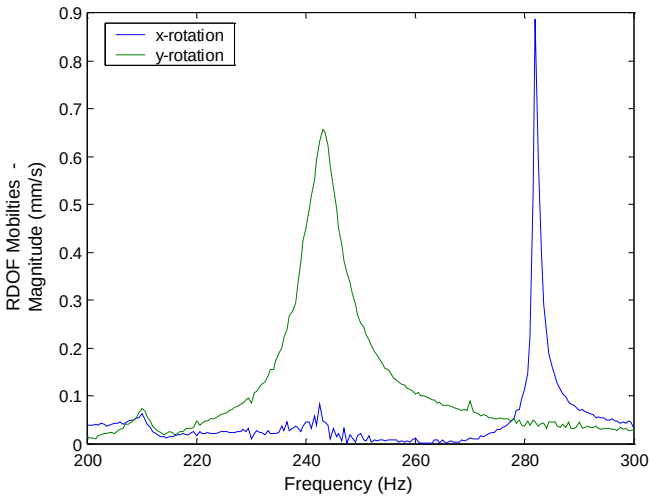


**Figure 7. 8** Angular mobilities amplitude.

As was expected from the previous analysis, which recovered a bending mode at the excitation frequency of 242 Hz (see Figure 7.6) and, moreover, since the bending was about the *x*-direction, the results from the small circular scan appeared reliable. Indeed, Figure 7.8 shows a clear predominance of the *x*-angular vibration.

Mobility data are visibly spoiled by noise but in order to have more accurate measurement it is necessary to increase the resolution of the step sine test (0.5 Hz is too high), implying a more time-consuming process.

### *7.2.3 Test of the "breadboard" Structure*

The second case study was of the so-called "breadboard" structure on which extensive measurement of rotational degrees of freedom (RDOFs) has been accomplished as part of the research about advanced techniques undertaken within the BRITE/EURAM project-QUATTRO, see references [47] and [48]. The goal of the experimental work reported here was to validate the continuous scan technique – specifically, the linear and circular scans - for RDOFs

recovered at a point in the structure. As a comparison technique, used to prove the reliability of the continuos scans, a discrete point measurement was employed with the single tested points located around the point where the angular velocity was deduced.

The "breadboard" structure was excited in the frequency range of 300-400 Hz with a resolution of 0.1 Hz via a shaker attached at point 37, as Figure 7.9 indicates. Then, translation and rotation degrees of freedom were derived at the same position, using the measurement set-up shown in Figure 7.5.

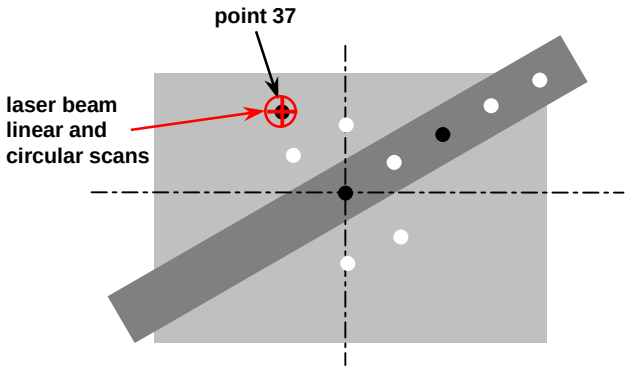


**Figure 7. 9** Point measurement on the "breadboard" structure.

Discrete point measurements were carried out in *z*-direction (perpendicular to the structure surface) around point 37, specifically at four points slightly apart from point 37 by a gap of 11 mm. Their positions are shown in Figure 7.10.

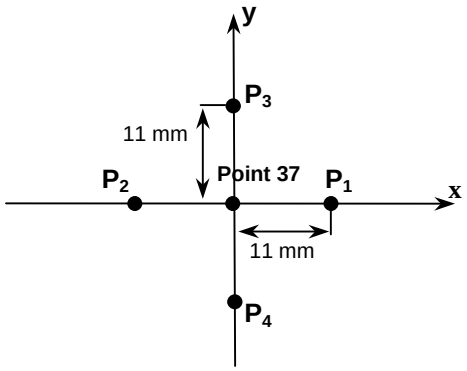


**Figure 7. 10** Point measurement position.

The *z*-direction translation mobility was directly measured by pointing the steady laser beam at point 37 (see Figure 7.11), while angular mobilities ($\dot{\theta}_x$ and

$\dot{\theta}_y$) were derived from point measurements at $\mathbf{P_1}$, $\mathbf{P_2}$, $\mathbf{P_3}$, and $\mathbf{P_4}$, using the formulae reported in Section 4.2 (Equation 4.7):

$$\dot{\theta}_x = \frac{\partial z\_frf}{\partial y} \approx \frac{z\_frf(\mathrm{P}_1) - z\_frf(\mathrm{P}_2)}{2d} \quad \textbf{(4. 1)}$$

$$\dot{\theta}_y = \frac{\partial z\_frf}{\partial x} \approx \frac{z\_frf(\mathrm{P}_3) - z\_frf(\mathrm{P}_4)}{2d} \quad \textbf{(4. 2)}$$

*d* being 11 mm. Rotational mobilities about the *x*- and *y*-directions are both shown in Figure 7.12.

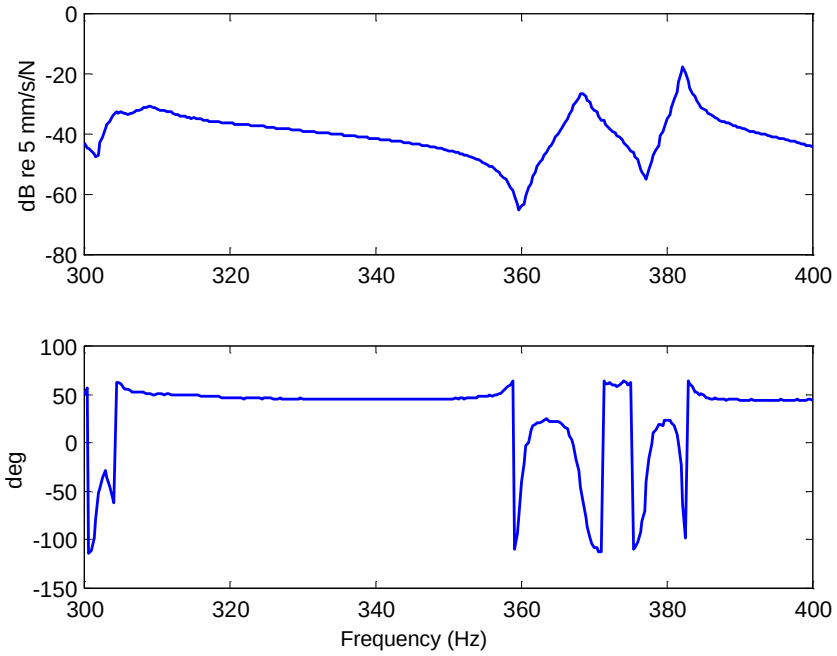


**Figure 7. 11** Translation mobility 37z37z – amplitude (top) and phase (bottom).

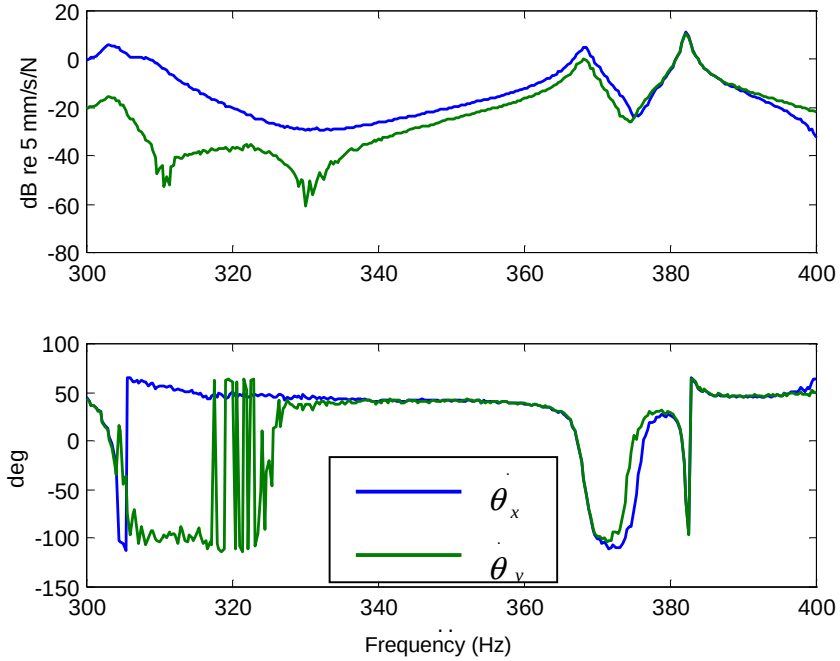


**Figure 7. 12** RDOF mobilities about *x*- and *y*-direction calculated from translational measurements around point 37 – amplitude (top) and phase (bottom).

Continuous linear and circular scans were directed around point 37 (see Figure 7.9) and translation and rotation degrees of freedom extracted from time-domain signals using the `Matlab` routines written for this purpose.

First, linear scanning was carried out in the vertical (*y*) direction along a line of 11 mm half-length and the out-of-plane translation and one rotational mobility (*z* and $\dot{\theta}_x$) were derived by applying Equation 4.6; these have been plotted together with the corresponding DOFs measured at discrete points, for reference, in Figures 7.13 and 7.14.

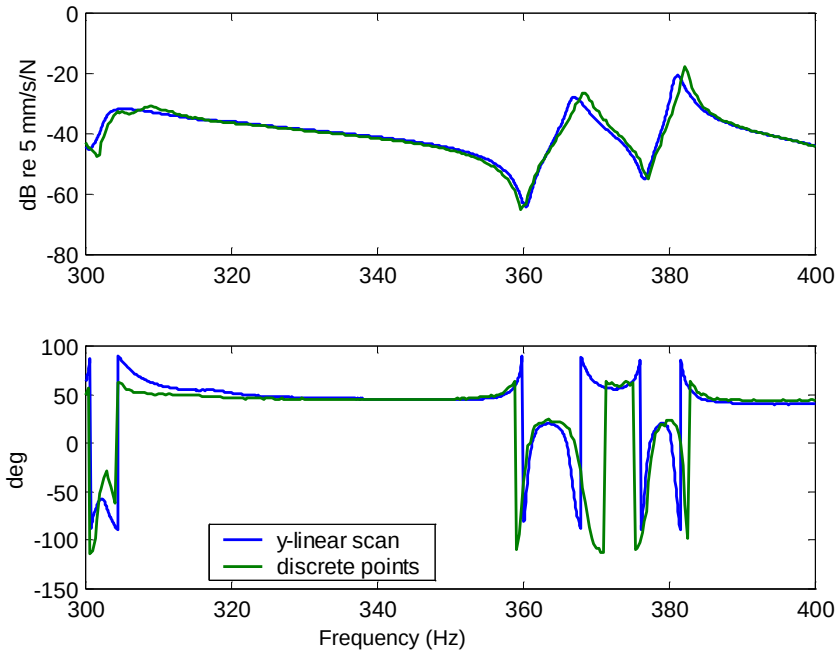


**Figure 7. 13** Translation mobility amplitude and phase derived at point 37 by vertical line scan.

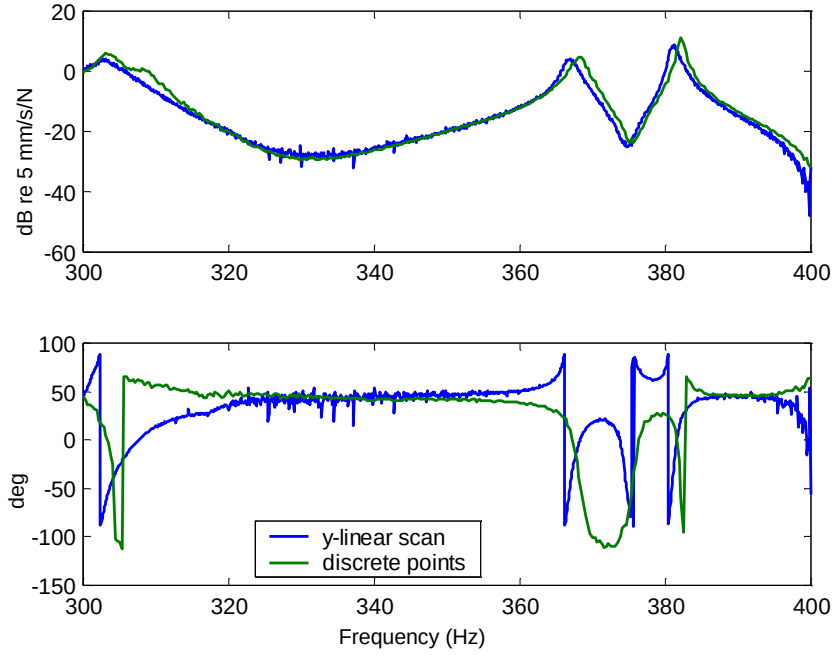


**Figure 7. 14** Rotation mobility in *x*-direction derived at point 37 by vertical line scan – amplitude (top) and phase (bottom).

Comparing translational mobilities found by discrete point measurements and by a linear scan, see Figure 7.15, it can be noticed that results are in good agreement: the only difference is in the narrow range between 300 to 315 Hz where two close modes exist. The discrete point measurements detect this feature while the linear scan in the *y*-direction fails to detect it. This can be explained by the fact that this is like a bending mode along the *y*-axis and therefore its deflection in the scan direction is negligible. Actually, it can be seen from Figures 7.15 up to 7.19 that the linear scan in the *x*-direction and the circular scan are more sensitive to the double modes and they can detect two peaks also, even if their amplitudes are rather small. Consequently, it can be deduced that the method is more accurate around than away the resonance as the signal is small at antiresonances and therefore the effects of noise are predominant.

Next, the same vibration responses has been measured by using a scan in the horizontal direction (*x*) with a scan frequency of 10 Hz and different half-length lines (*S* ) in order to investigate the effect of parameter *S* on the rotational mobility. The scan in the *x*-direction has been repeated for *S* = 8, 11 and 15 mm. The results are depicted in Figures 7.15 and 7.16 for the different values of *S*.

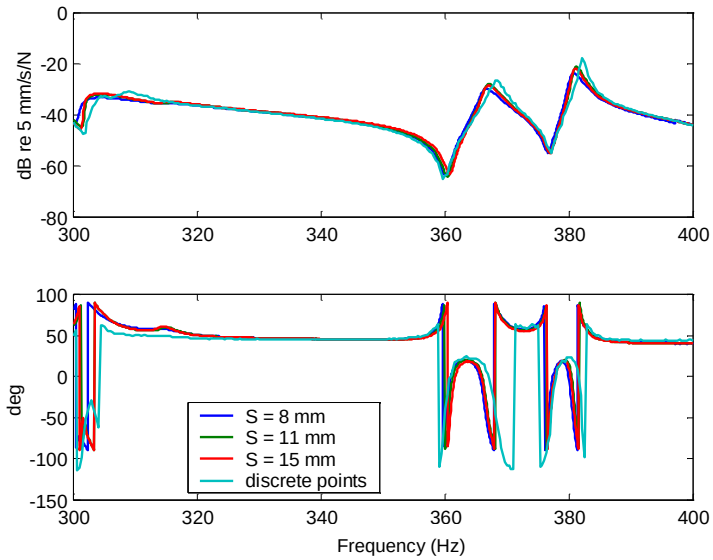


**Figure 7. 15** Translation mobility amplitude and phase derived at point 37 by horizontal line scan with different scan length.

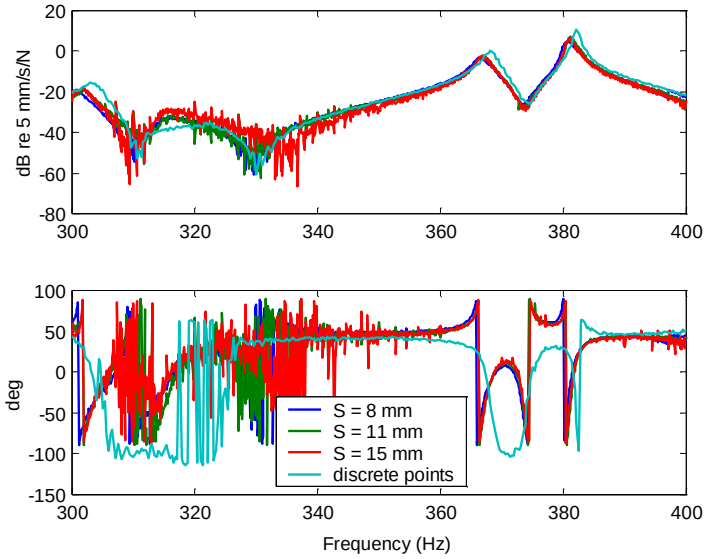


**Figure 7. 16** Rotation mobility in *y*-direction derived at point 37 by horizontal line scans – amplitude (top) and phase (bottom).

Comparing the appearance of the RDOF mobility (Figure 7.16) with the translational one (Figure 7.15), it can be seen that the first is significantly spoiled by the noise floor. This is due to the fact that rotational components are recovered from the Fourier spectrum sidebands whose levels are small and often covered by the noise floor in frequency ranges which are far from resonances.

In addition, rotational DOFs were extracted from data measured by continuous circular scanning techniques; in this case, rotations about both the *x*- and *y*-directions, i.e. $\dot{\theta}_x$ and $\dot{\theta}_y$, can be recovered using Equation 4.15. The beam was made to scan continuously in a circle of radius, *R*, which assumed different values (8, 11, 15 mm) in order to investigate the influence of this parameter into the measured data. Figures 7.17, 7.18 and 7.19 indicate the translational, *x*- and *y*-rotational mobilities obtained at the different scan radii. In each plot, the corresponding DOF derived by discrete measurements is shown as reference.

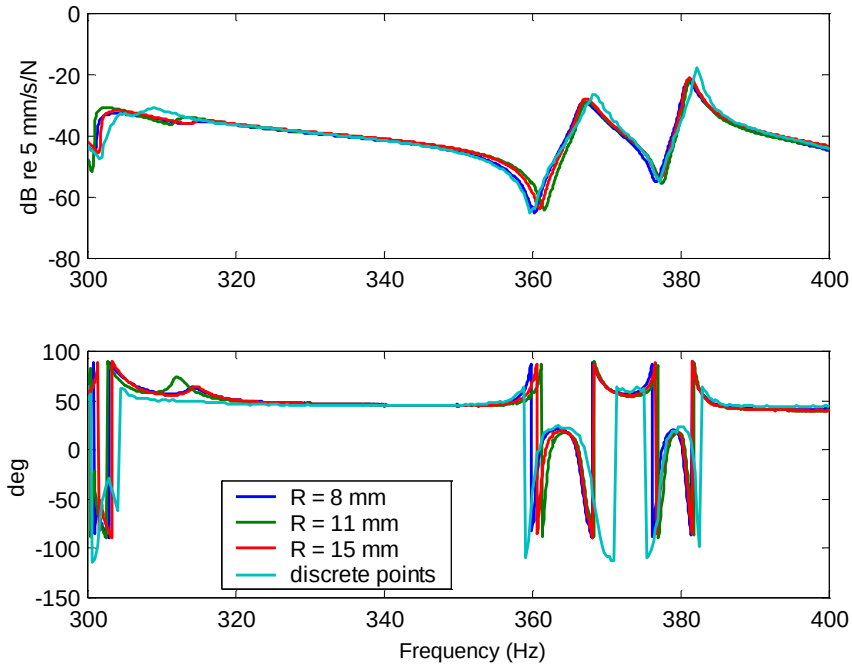


**Figure 7. 17** Translation mobility amplitude and phase derived at point 37 by circular scan with different scan radii.

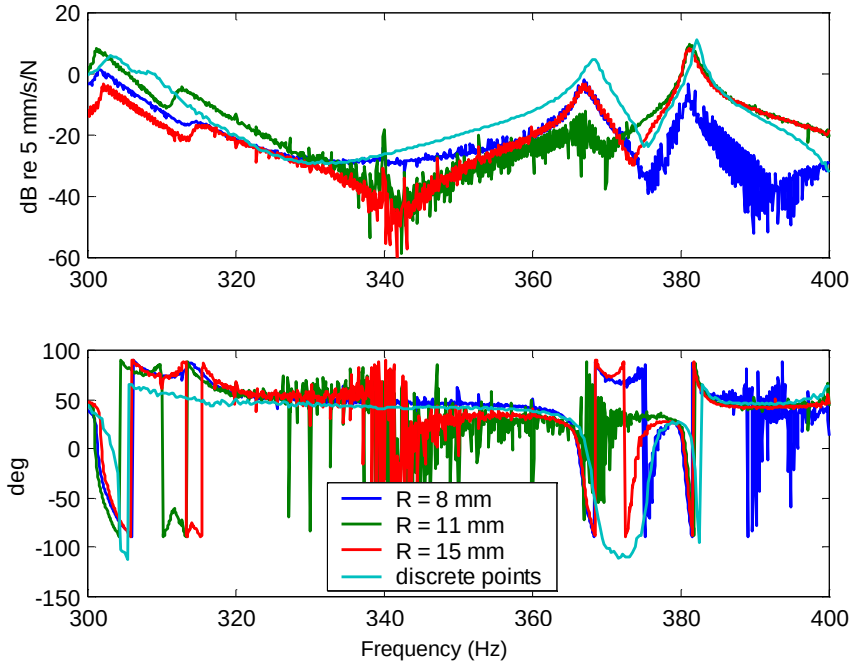


**Figure 7. 18** Rotation mobility in *x*-direction derived at point 37 by circular scanning – amplitude (top) and phase (bottom).

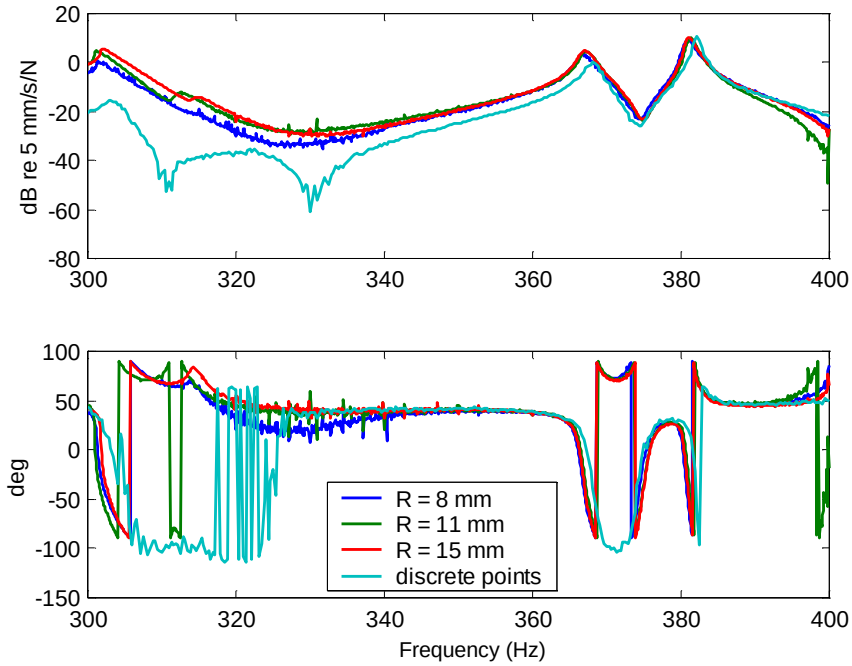


**Figure 7. 19** Rotation mobility in *y*-direction derived at point 37 by circular scanning- amplitude (top) and phase (bottom).

Overall, the effect of the scanning radius in a circular scan, or length in a linear scan, is not very significant, in the range examined here.

Next, the scan frequency was changed to 20 Hz and the measurements repeated with the scan radius kept at 11 mm. Figures 7.20, 7.21 and 7.22 show the effect of different scan frequencies, here 10 and 20 Hz, on the three DOFs.

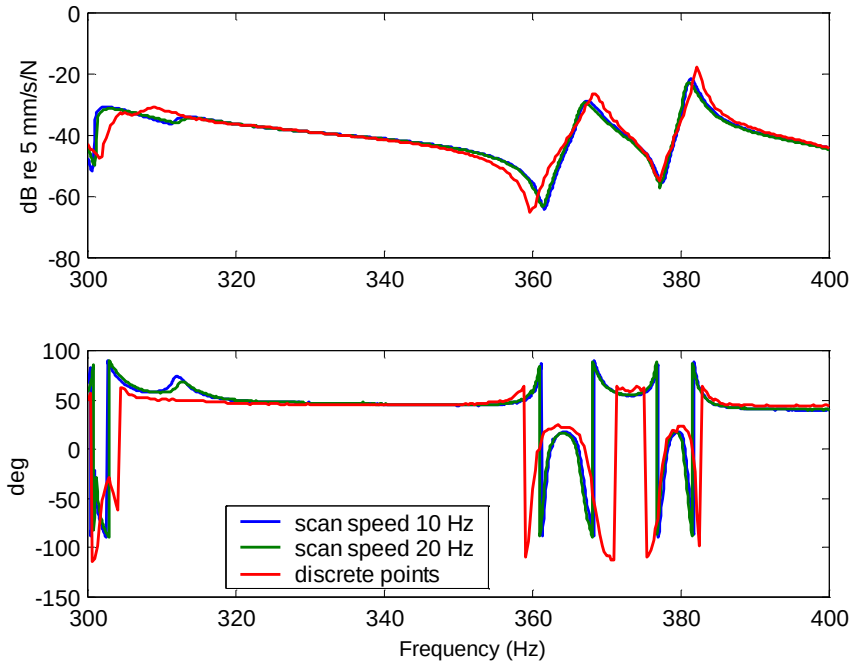


**Figure 7. 20** Translation mobility amplitude and phase derived at point 37 by circular scan with different scan speeds.

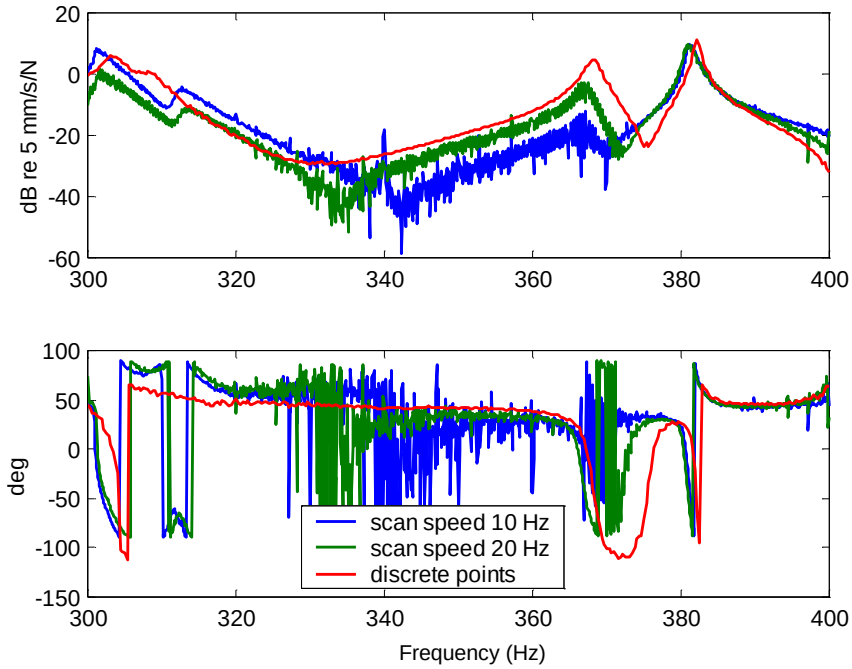


**Figure 7. 21** Rotation mobility in *x*-direction derived at point 37 by circular scanning- amplitude (top) and phase (bottom).

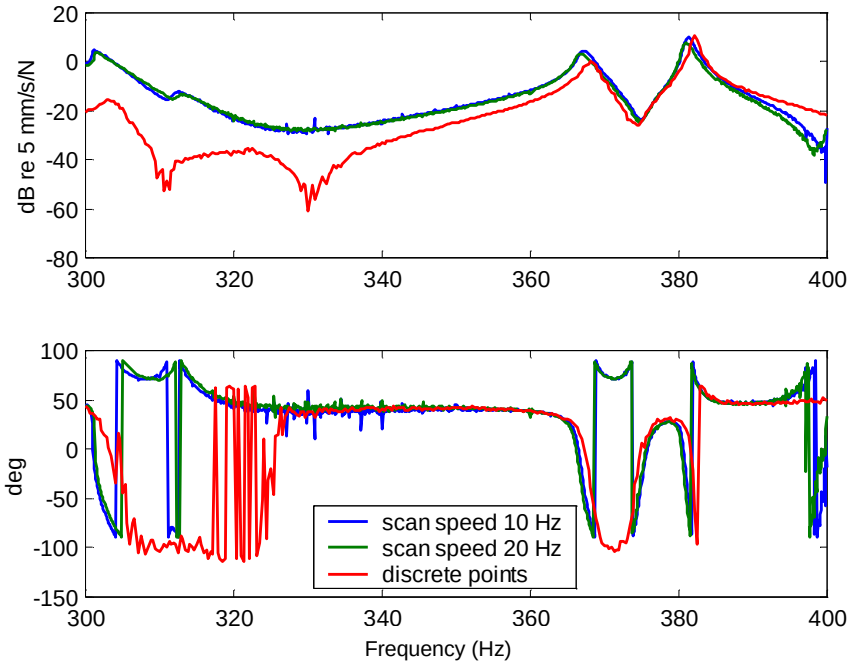


**Figure 7. 22** Rotation mobility in *y*-direction derived at point 37 by circular scanning – amplitude (top) and phase (bottom).

It was observed that by increasing the scan frequency, the resonance peaks drop slightly, particularly for the translational DOF and rotation about the *y*-direction. It is possible to explain this behaviour by referring to the speckle noise which produces a noise floor whose level increases with the scan frequency.

The continuous scan technique for measuring MDOF responses at a point is convenient to use, particularly after setting up. In fact, it is less time-consuming than a similar test done by single point measurements since with only one go, three DOFs can be recovered simultaneously. However, in order to achieve accurate results, the frequency step around resonances, in the step-sine acquisition routine, often needs to be very small and this makes the measurement time long.

## *7.3. One-Dimensional Long - Scan Technique Application in Practical Cases*

### *7.3.1 Experimental Set-up Description*

The following experimental examples are taken from practical demonstrations of the developed CSLDV techniques undertaken within the BRITE/EURAM project VALSE, [13], specifically as far as regard Task 4, i.e. demonstration of application on practical cases, see reference [23]. Measurements have been performed (by the author) at Centro Ricerche Fiat, the VALSE partner who leads the task related to the application to vibration transmission through vehicles structures. Two case studies, illustrated by general views in Figure 7.23, were investigated: the rear panel of an IVECO DAILY motor lorry cab (right) and the windscreen of a FIAT PUNTO 5door car (left). A number of different techniques were employed, but in this section only line scans will be considered: in particular, uniform-rate linear scans for direct ODS recovery by LDV signal demodulation, and linear sinusoidal scans, which give ODS polynomial coefficients.

**Figure 7. 23** Vehicles used as case studies**.**

In addition, for comparison purposes, conventional point-by-point vibration surveys were conducted using the same Polytec measurement system in its "standard" mode and software, PSV200.

As far as concerns the truck rear panel, vibration frequency response functions (FRFs) were measured at 375 different positions, as shown in Figure 7.24.

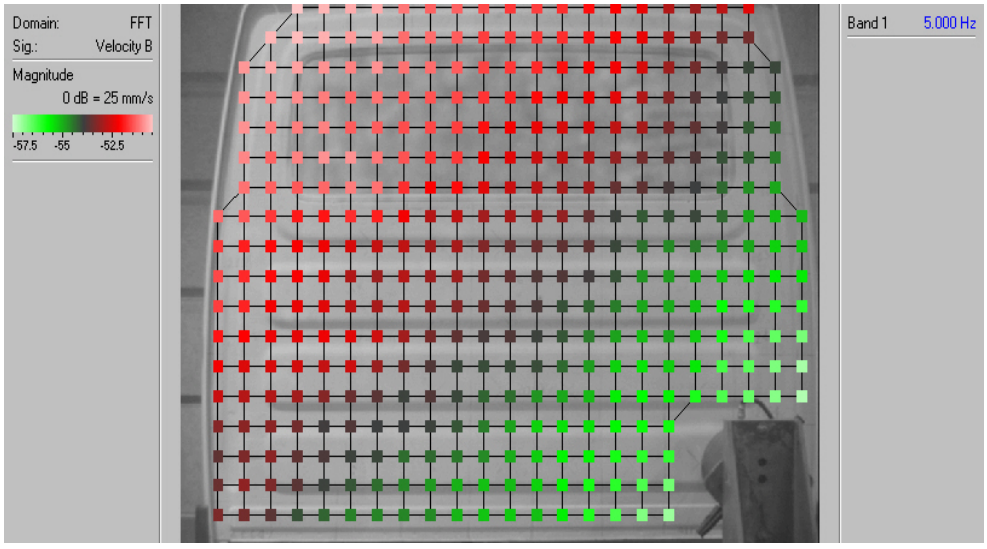


**Figure 7. 24** Acquisition points grid –rear panel of the lory cab.

The data acquisition was performed with a sample time of 0.8 s and employing the averaging option (specifically, five complex averages); the acquisition time was therefore, basically $(0.8 \times 5 \times 375)$ seconds., i.e. 25 mins. The actual elapsed time for the measurement was somewhat greater than this (about 30 mins) because of signal processing, LDV mirror reaction time, etc, see Section 3.6. Resonant frequencies observed were: 5, 13.75, 35, 37.5, 57.5, 85, 112.5, 126.3, 137.5, 146.3, 185, 191.3, 211.3, and 230 Hz.

Similar point-by-point surveys were conducted on the FIAT Punto car front-windscreen, to determine resonant frequencies. The screen was coated with *ADROX 9D6F* spray so as to obtain a diffusing surface giving the scattered light necessary for LDV operation. FRFs were measured on the windscreen at 382 different positions, Figure 7.25. Excitation was applied by a shaker attached on

the engine mounting. ODSs were measured at 25.63, 71.88, 77.5, 95, 113.1, 142.5, 185, and 240Hz, corresponding to peaks in the FRFs acquired.

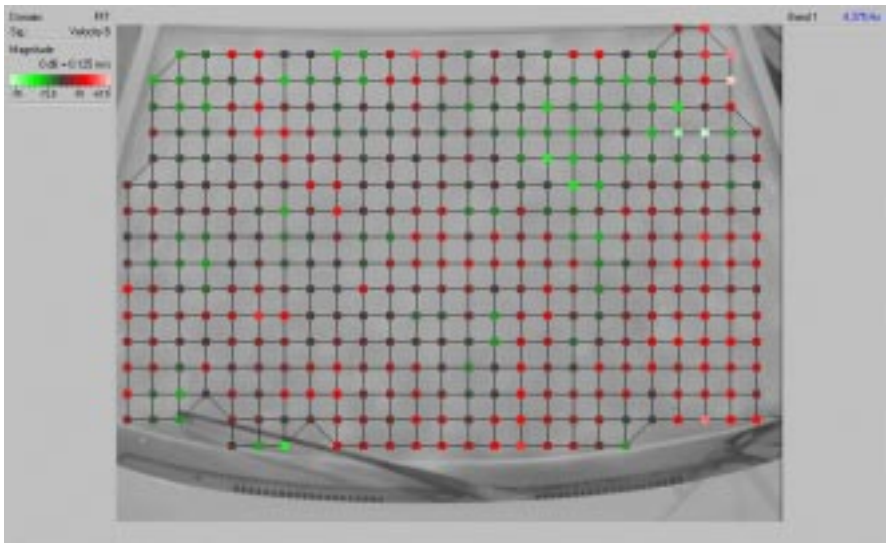

**Figure 7. 25** Acquisition points grid - windscreen.

For the CSLDV technique developed in this thesis the equipment used included the same Polytec measurement head and controller employed in the SLDV technique. In this case, however, the data acquisition, control and processing software was completely independent from the PSV200 and it was developed in `LabVIEW`. For the data post-processing `Matlab` routines are also available.

### *7.3.2 Uniform-Rate Straight-Line Scan on the IVECO DAILY Rear Panel*

Continuous linear scanning measurements have been made with the LDV head positioned about 2.5 m from the rear panel of the truck in such a way that the laser beam at its home position (i.e. without any deflection sent to the mirrors drivers) would be effectively perpendicular to the panel surface. The laser beam was scanned at a uniform rate along a line **A-B**, shown in Figure 7.26 (i.e. the mirror driver was fed with a triangular wave). The length of the scan was 1.406 m. The LDV output was acquired and post-processed for two different scan speeds of the laser beam, at 0.5 Hz (1.406 m/s), and 1 Hz (2.812 m/s). The structure was excited at one of its natural frequencies (146.3Hz) via a shaker attached at the bottom right of the panel, as shown.

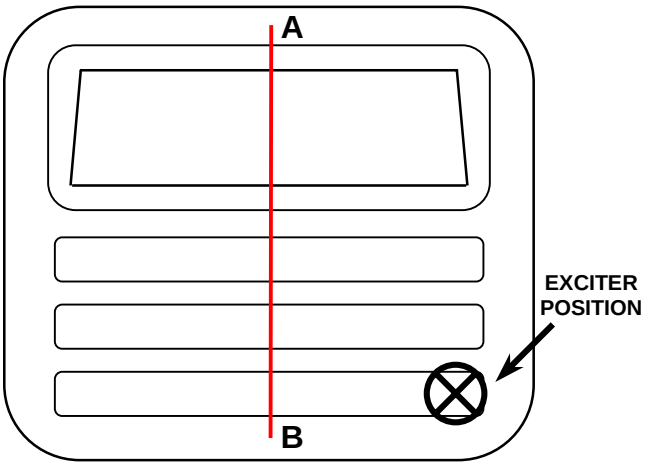


**Figure 7. 26** Linear scan at the middle of the panel.

By running the LabVIEW acquisition program, the LDV output, triggered with the mirror driving signal, the excitation force signal, and the triangular wave driving the mirror were stored (using 10000 samples for each signal and a sample rate of 1000 Hz). Data acquisition at one test frequency therefore took 10 seconds, although, strictly, only one half-scan is necessary, taking, at 0.5 Hz, just 1 sec, or 0.5 sec with at 1 Hz scan.

In order to have the same ODS information with the point-by-point technique a set of points lying along the line **A**-**B** must be measured. In the experiment shown in subsection 7.3.1 the line **A**-**B** contains 15 points, see Figure 7.27.

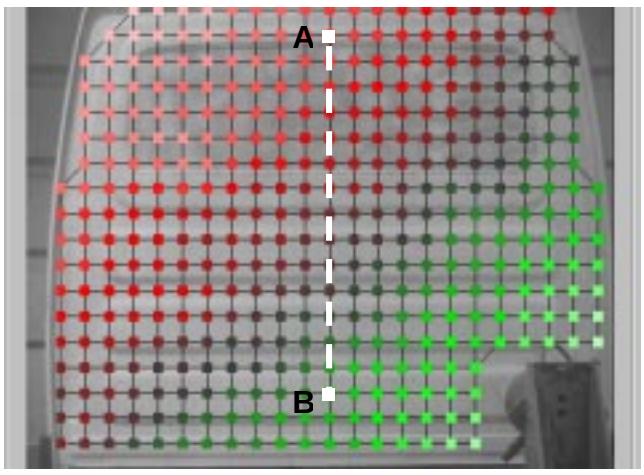


**Figure 7. 27** Line scan superimposed to the grid of points used in the point-by-point technique.

With the point-by-point technique (where the acquisition timeat each position of the laser beam was of 0.8 secs and 5 averages for each point were made), the overall time needed for the acquisition of 15 points would be 4 secs. However, as already stated (see Section 3.8), a comparison between the acquisition time required for the continuous scanning technique and the point-by-point technique is somewhat ambiguous. In fact, with a point-by-point technique a broad-band excitation is applied and, consequently, in one measurement a lot of data in the frequency domain are collected, i.e. several ODSs can be measured in one go. With a continuous scanning technique only one ODS at the time is measured, instead, since the excitation must be sinusoidal at the resonance frequency. On the other hand, with a CSLDV measurement a lot of data in the spatial domain can be collected, since the resolution of the recovered ODS depends, in the case of uniform-rate scan, on the scan speed and the sample rate set in the acquisition (i.e. in the actual experiment, where the scan speed was 0.5 Hz and the sample rate 1000 Hz the ODS was measured with a spatial resolution of 1000 points). On the contrary, with the point-by-point technique the spatial resolution depends on the measured number of points along the line.

Figure 7.28 shows the LDV output (black) and the mirror driver triangular wave (in red) for two complete scans and two half-scans for the 0.5 Hz scan (left) and the 1 Hz scan (right).

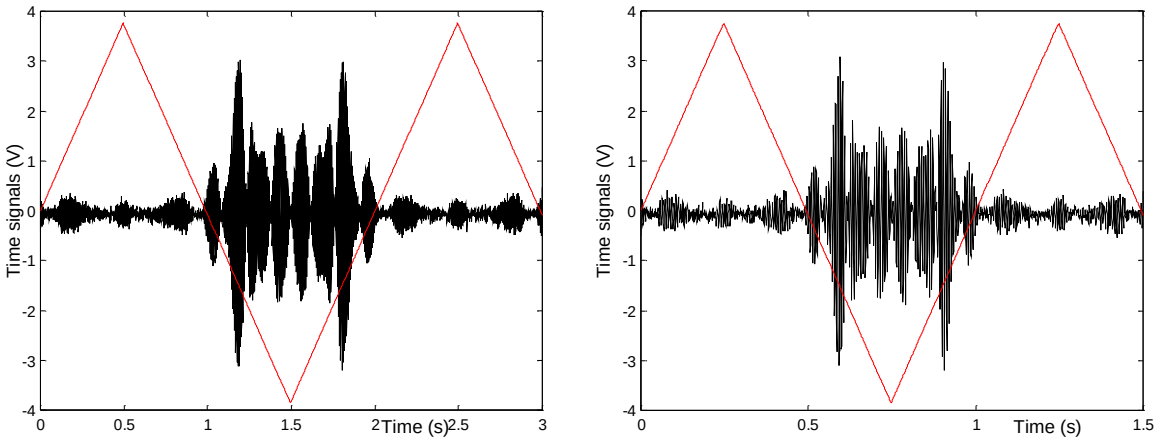


**Figure 7. 28** Time histories (V) for 0.5Hz (left) and 1 Hz (right) scan speed – LDV output (black), mirror driver signal (red).

The post-processing of the LDV output time history consisted simply of a demodulation at the excitation frequency together with a low-pass filtering, set at a 50 Hz cut off frequency to reject higher components at twice the excitation frequency. The derived ODS can easily be seen by plotting the demodulated signal during the length of one scan (half cycle of the triangular wave); in Figure 7.29 both the ODSs recovered for 0.5Hz scan speed and 1Hz scan speed are shown, in their in-phase and out-of-phase components.

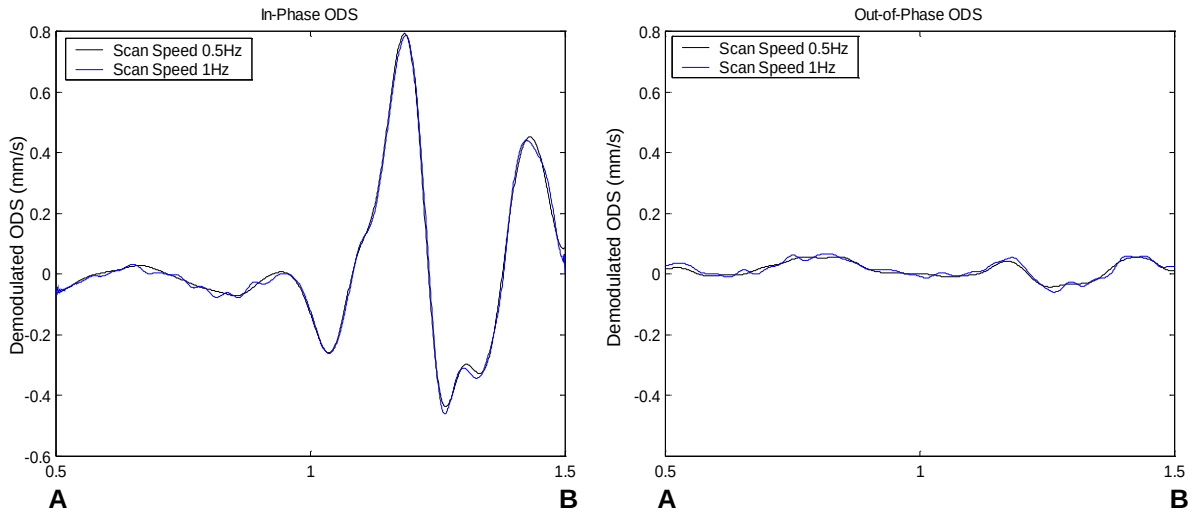


**Figure 7. 29** ODSs in-phase and out-of-phase components (mm / s).

It may be noticed in Figure 7.29 that the 1 Hz scan speed record appears to be less smooth than that from the 0.5 Hz scan. This is believed to be due to speckle noise, exaggerated by the higher scan speed.

Using the PSV200 facility of selecting a profile along the ODS found by the point-by-point scan described in subsection 7.3.1 it is possible to see the profile of the mode along the line **A**-**B**, see Figures 7.26 and 7.27, where the line scan was performed; Figure 7.30 shows the line where the profile was taken.

The real and imaginary components of the ODS in Figure 7.29 have been compared with results from the pint-by-point scan measurements, Subsection 7.3.1. Data corresponding to the vertical scan line were extracted from the data

set derived at a frequency of 146.3 Hz using PSV200 software, and are compared directly in Figures 7.31 and 7.32. The results clearly correspond closely, but the coarse velocity resolution of the point-by-point survey is very marked.

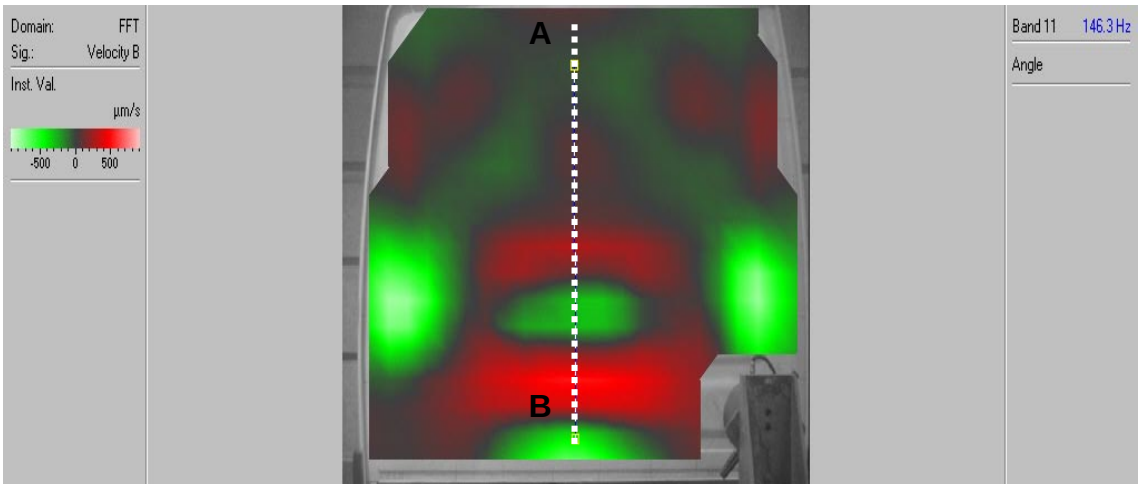


**Figure 7. 30** Profile selected.

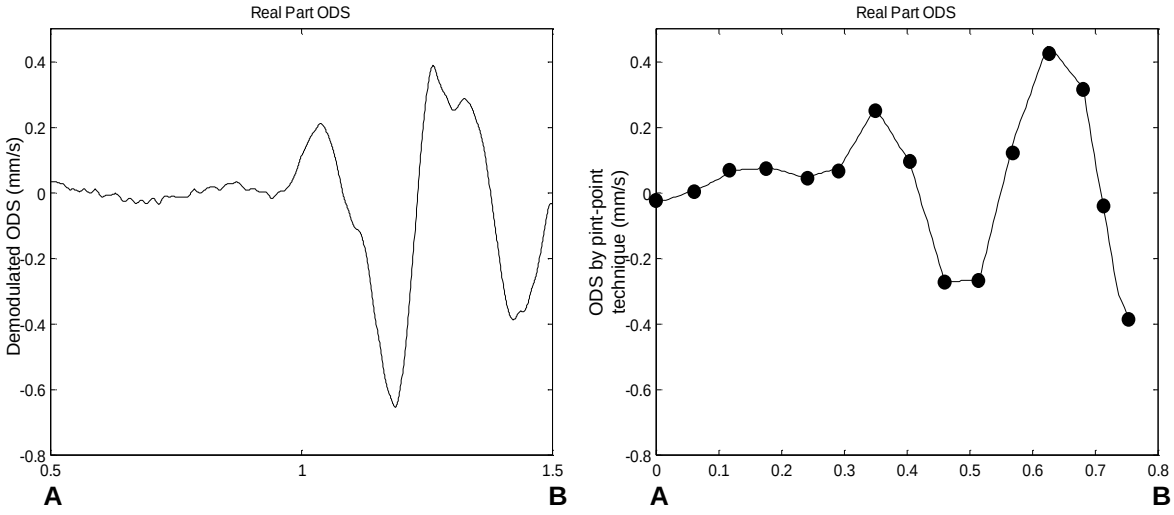


**Figure 7. 31** ODS Real component (mm/s) derived by demodulation (left) and point-by-point scan (right, the vibration response is measured at the marked points only, where the actual measurements have been acquired).

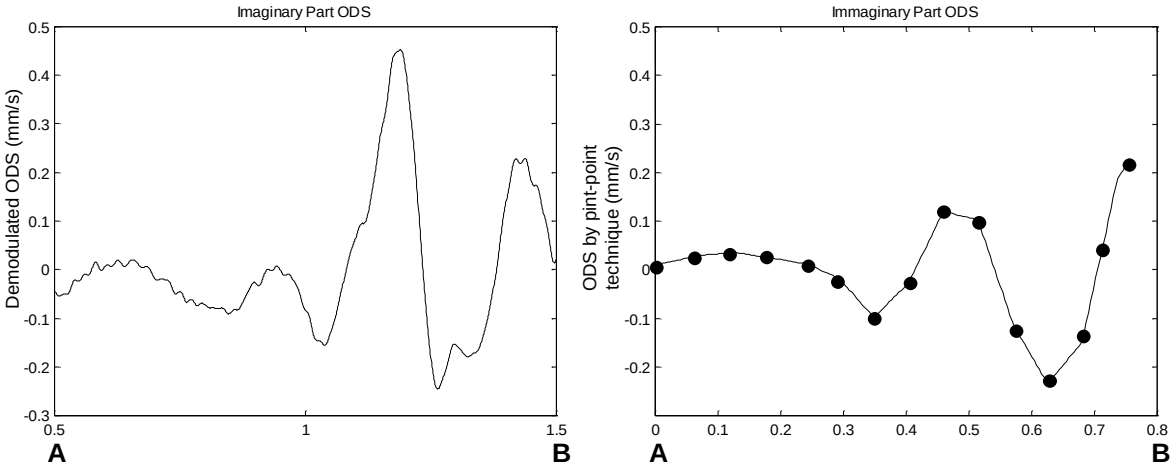


**Figure 7. 32** ODS Imaginary component (mm / s) derived by demodulation (left) and point-by-point scan (right, the vibration response is measured at the marked points only, where the actual measurements have been acquired).

It should be noted that the point-by-point survey real and imaginary data were normalised to the excitation force signal. The line scan data were adjusted similarly for Figures 7.31 and 7.32.

Another ODS, the resonant frequency of 57.5 Hz, was investigated using the same demodulation technique. The laser beam was scanned along a somewhat shorter line than before, avoiding the lorry window (Figure 7.33), at a uniform rate of 1 Hz.

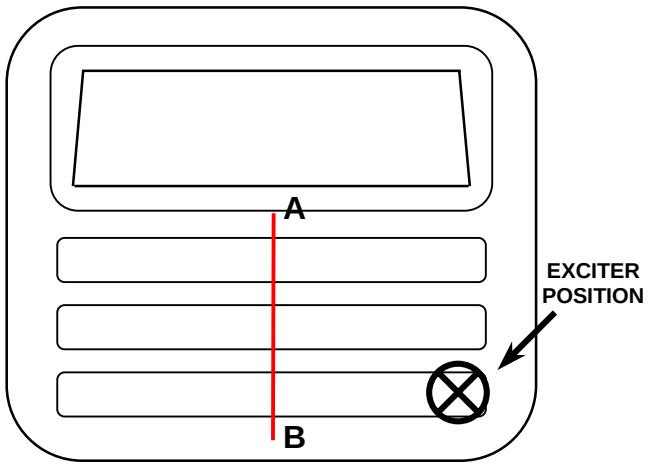


**Figure 7. 33** Line Scan on the panel.

The LDV output time signal together with the triangular wave driving the mirror is shown in Figure 7.34.

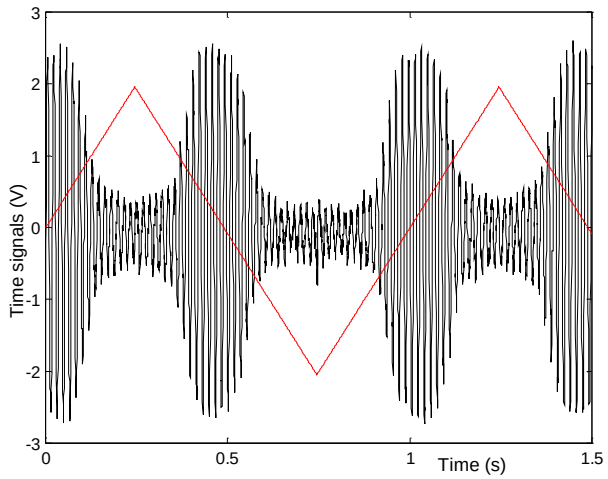


**Figure 7. 34** LDV output time history (V) at 57.5Hz resonant frequency.

The post-processing used was similar to that described above. In-phase and out-of-phase ODS components are shown in Figure 7.35. Figures 7.36 and 7.37 illustrate the comparison between real and imaginary components of ODS recovered via demodulation and by conventional Polytec PSV200 technique.

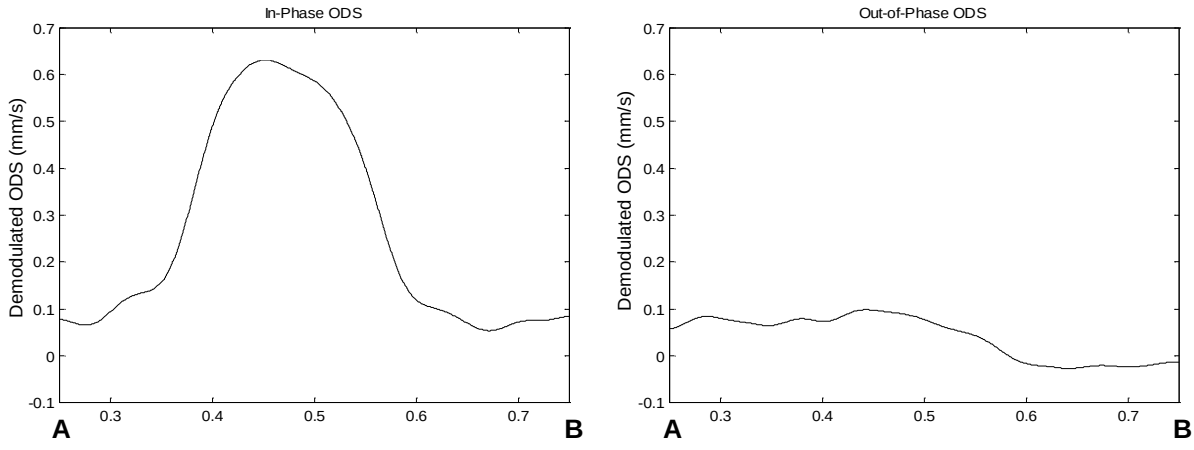


**Figure 7. 35** ODSs in-phase and out-of-phase components (mm / s).

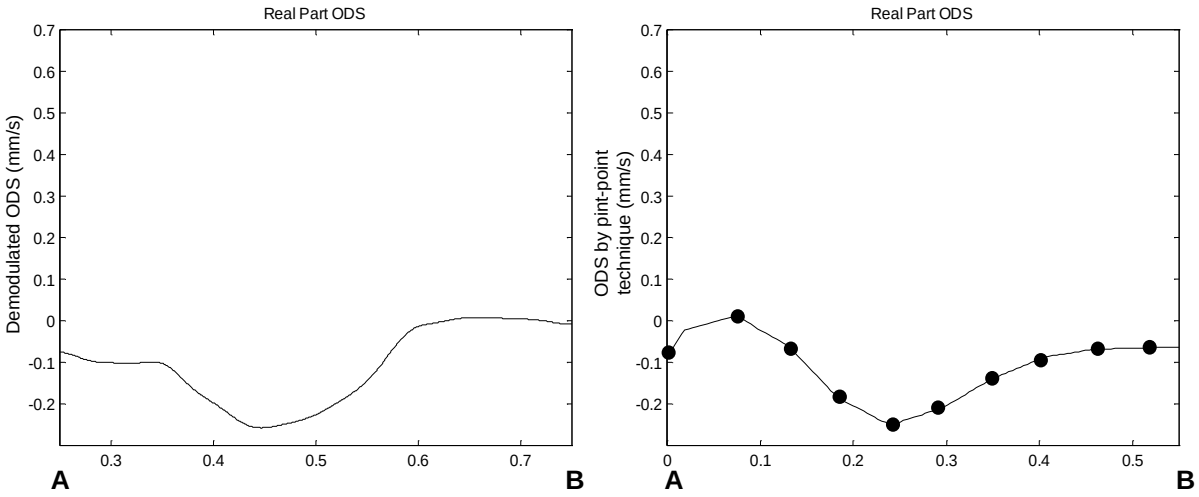


**Figure 7. 36** ODS Real component (mm / s) derived by demodulation (left) and point-by-point scan (right, the vibration response is measured at the marked points only, where the actual measurements have been acquired).

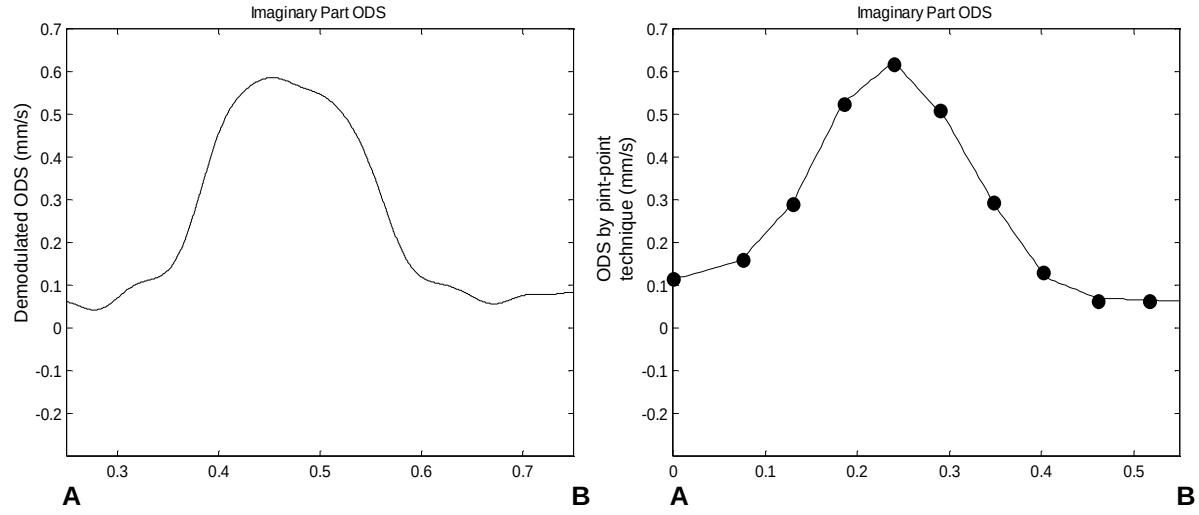


**Figure 7. 37** ODS Imaginary component (mm / s) derived by demodulation (left) and point-by-point scan (right, the vibration response is measured at the marked points only, where the actual measurements have been acquired).

### *7.3.3 Sinusoidal Straight-Line Scan on the IVECO DAILY Rear Panel*

A sinusoidal line scan technique was applied to the same structure, to recover ODSs defined as polynomial series. Polynomial coefficients derived from Fourier components of the LDV output spectrum at frequencies $(\omega \pm n\Omega)$, where $\omega$ is the excitation frequency, $\Omega$ the scan frequency and $n$ takes integer values from zero up to some limit set by the nature of the ODS. In order to apply this process successfully, the ODS should ideally be spatially smooth. Accordingly the rear panel of the lorry was excited at 57.5 Hz using the scan line in Figure 7.33, to allow a comparison of results of the two techniques. The laser beam was made to scan at a frequency of 1Hz.

The LDV output was acquired by running the `LabVIEW` program, written for the purpose, using 20000 acquisition points with 2000 Hz sample rate. Data acquisition, therefore, took 10 secs. The LDV time history, triggered with the mirror-drive signal, was stored together with the (excitation) force signal and the sinewave driving the mirror.

Part of the LDV output time signal is shown in Figure 7.38 where the mirror-drive sine wave is included.

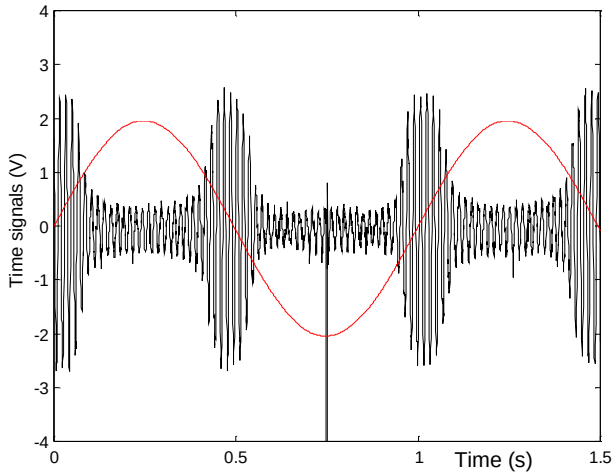


**Figure 7. 38** LDV output time history (V).

The LDV output spectrum, Figure 7.39, shows the sideband structure (seen more clearly in the zoomed, right-hand picture). Frequency broadening due to the speckle noise, see Section 2.5, can be seen if the vertical scale is expanded, Figure 7.40. As stated in Section 2.5, speckle noise introduces interference in the harmonics of the excitation frequency, in this case the second harmonic (115 Hz) is visible.

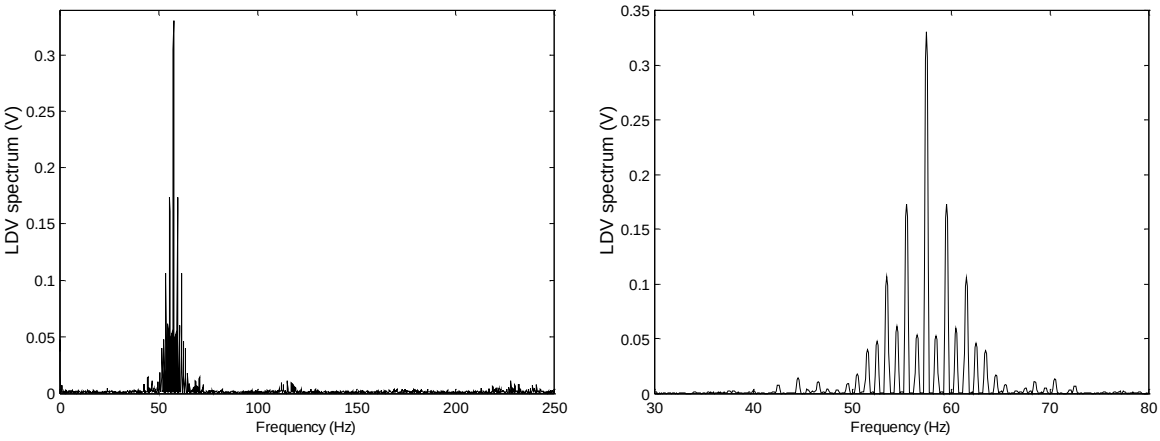


**Figure 7. 39** CSLDV output spectrum and its zoom around the excitation frequency 57.5 Hz.

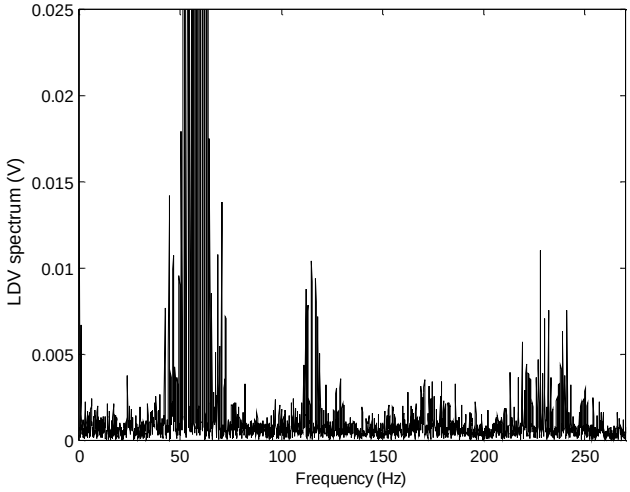


**Figure 7. 40** CSLDV output spectrum noise content.

Post-processing of the LDV output was done in LabVIEW, by setting the number of sidebands included in relation to the LDV spectrum, Figure 7.39. Fifteen sideband pairs can be seen, but they are of relatively small magnitudes

above $n$ = 8. Two cases have been then taken into consideration: polynomial ODS curve-fitted up to the 8$^{th}$ or 15$^{th}$ order. Extracted magnitude and phase data of the LDV spectrum at the known frequencies are illustrated, for 8 and 15 sidebands, in Figures 7.41 and 7.42.

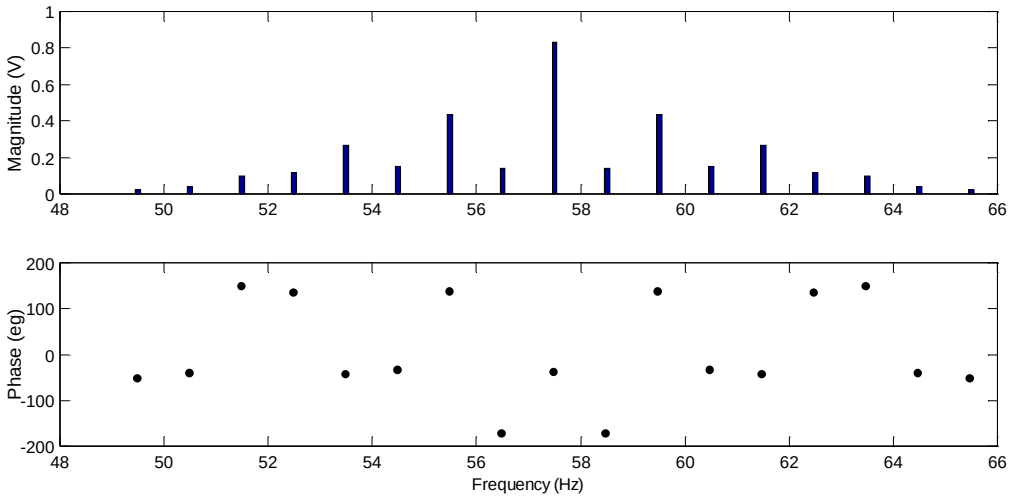


**Figure 7. 41** LDV spectrum magnitude and for ±8 sidebands.

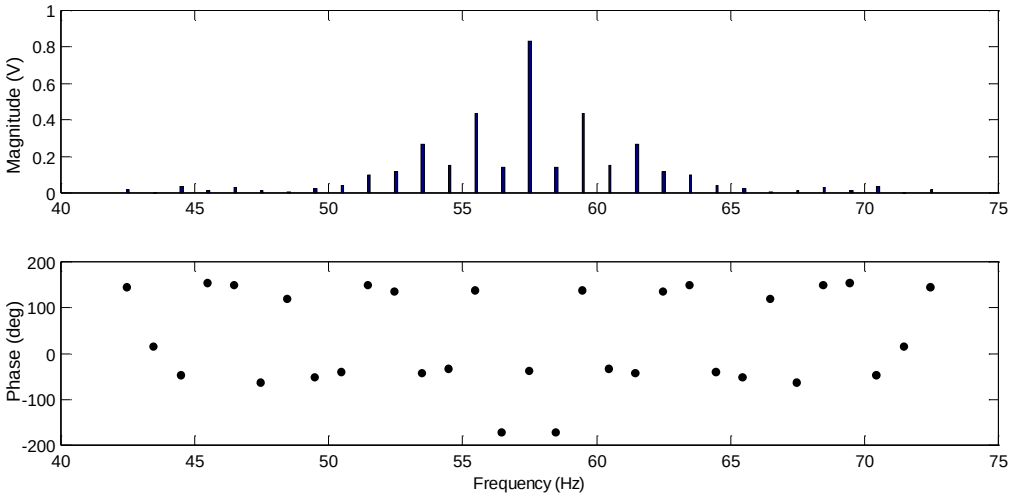


**Figure 7. 42** LDV spectrum magnitude and phase for ±15 sidebands.

ODSs recovered from the polynomial coefficients derived by transforming the ±8 and ±15 sideband vectors are compared in Figures 7.43 and 7.44. The result obtained using 15 sidebands is, arguably, more accurate than that using only 8 sidebands. These higher sidebands, though relatively insignificant in amplitude, do have a noticeable effect on the shape of the ODS.

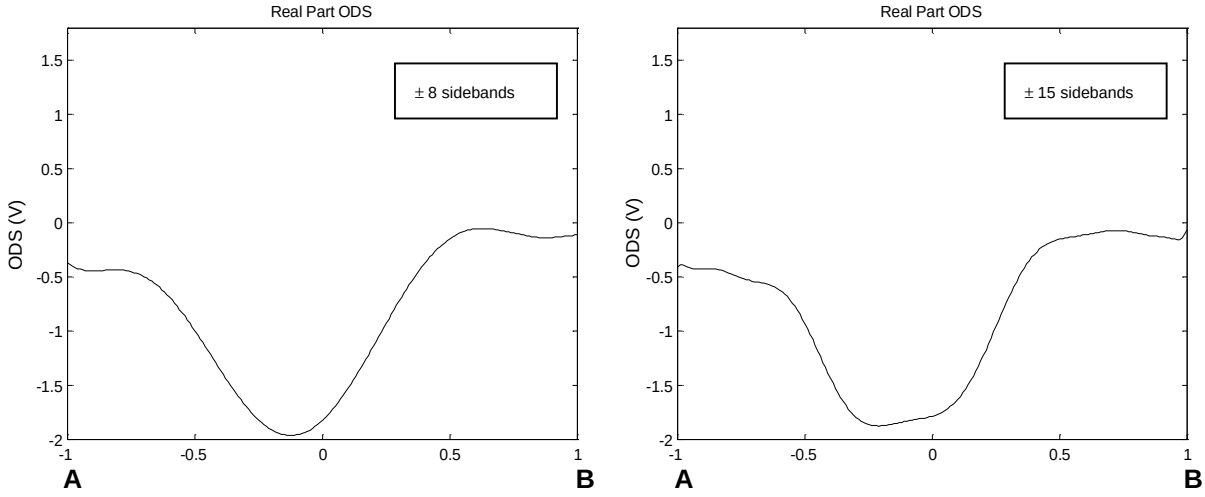


**Figure 7. 43** ODS real part derived by polynomial series using 8 (left) and 15 (right) sidebands.

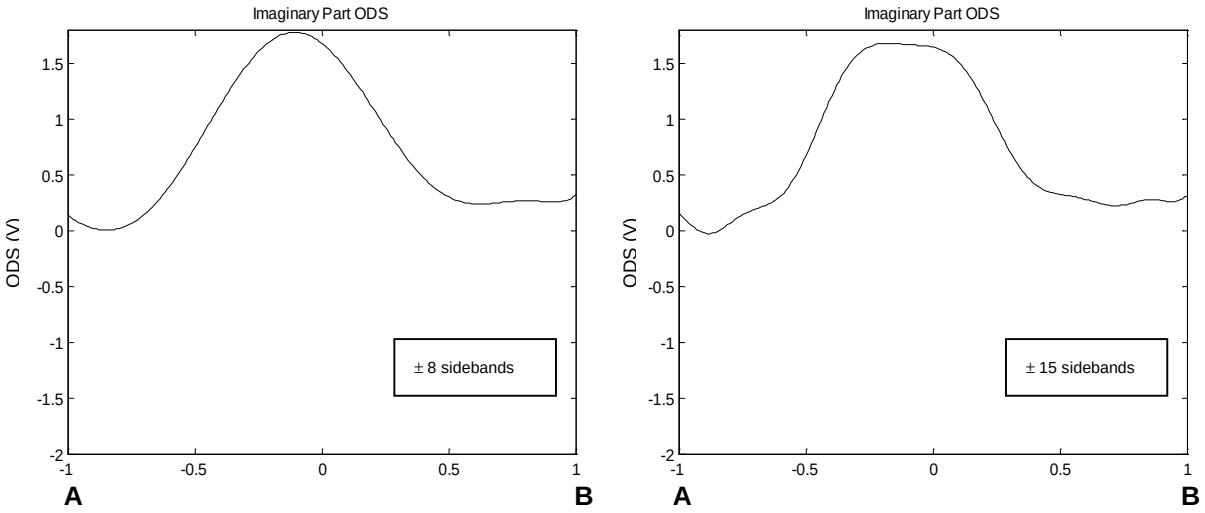


**Figure 7. 44** ODS imaginary part derived by polynomial series using 8 (left) and 15 (right) sidebands.

Finally, in Figure 7.45, the (15 sideband) sine-scan ODS is compared directly with that obtained by demodulation, shown previously in Figure 7.35.

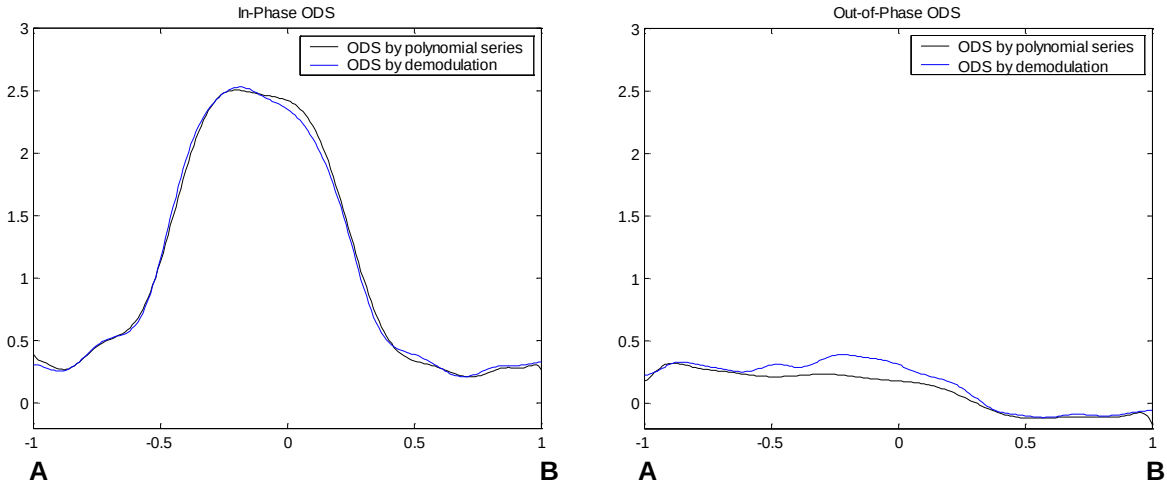


**Figure 7. 45** In-Phase and Out-of-Phase ODS (V) derived by polynomial series (± 15 sidebands) and demodulation.

### *7.3.4 Parallel Sinusoidal Straight-Line Scan on the FIAT PUNTO Windscreen*

The technique described in subsection 7.3.3 was applied to the FIAT PUNTO windscreen with the difference that now a series of several lines were scanned at different positions over the surface in order to recover a raster description of the ODS of the whole area. In practice, straight-line polynomial ODSs were recreated from 13 sinusoidal straight-line scans, illustrated in Figure 7.46, with excitation at 142.5 Hz and a scan speed of 1Hz. The scan lines were inclined, as shown, to avoid areas of the curved surface where the laser beam would had a large angle of incidence.

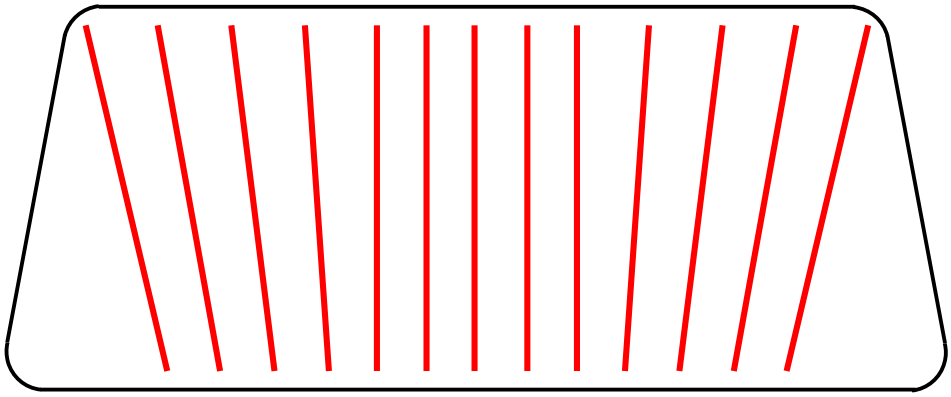

**Figure 7. 46** Windscreen sketch.

An ODS was derived for each line in the same way as described in subsection 7.3.3 for the lorry panel.

Three time histories were again acquired: specifically, the LDV output, triggered with the sinewave driving the mirror, the force and the mirror driver signals, using a sample rate of 1000 Hz and a number of samples of 10000 points.

Figure 7.47 shows the LDV output time signal and the mirror driver signal for the central scan line (i.e. 7$^{th}$ line), and its LDV signal spectrum. This line ODS was particularly simple in form, the spectrum has major components at only the centre frequency and two sideband pairs. Four sidebands were included in the signal processing in this case, to derive ODS real and imaginary components. The sideband data extracted are shown in Figure 7.48, and the real and imaginary ODS components in Figure 7.49.

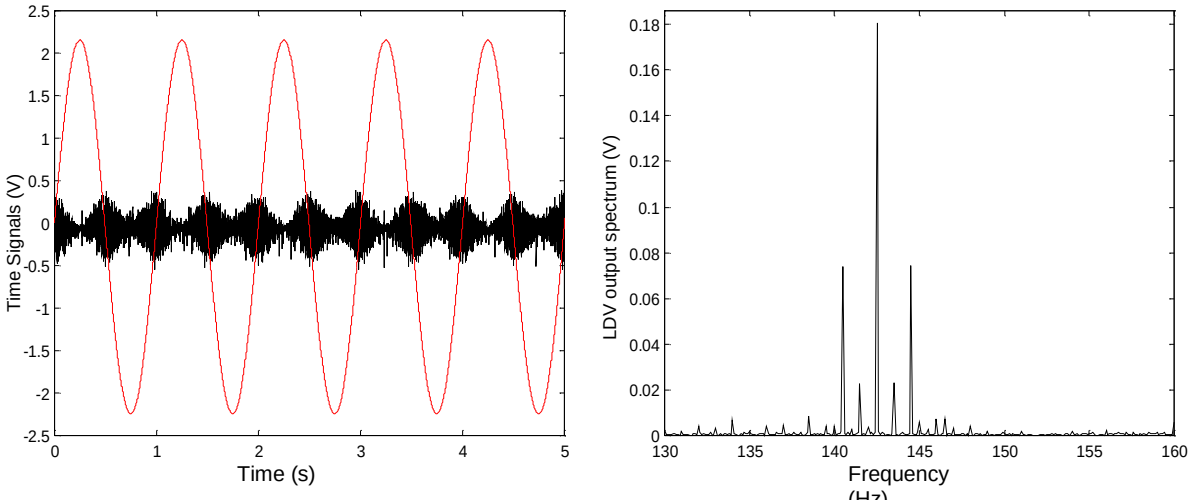


**Figure 7. 47** LDV time history (black) and mirror driver signal (red) in the left-hand plot and LDV output spectrum the right-hand plot.

Only 4 sidebands were needed in this case to measure ODS real and imaginary components.

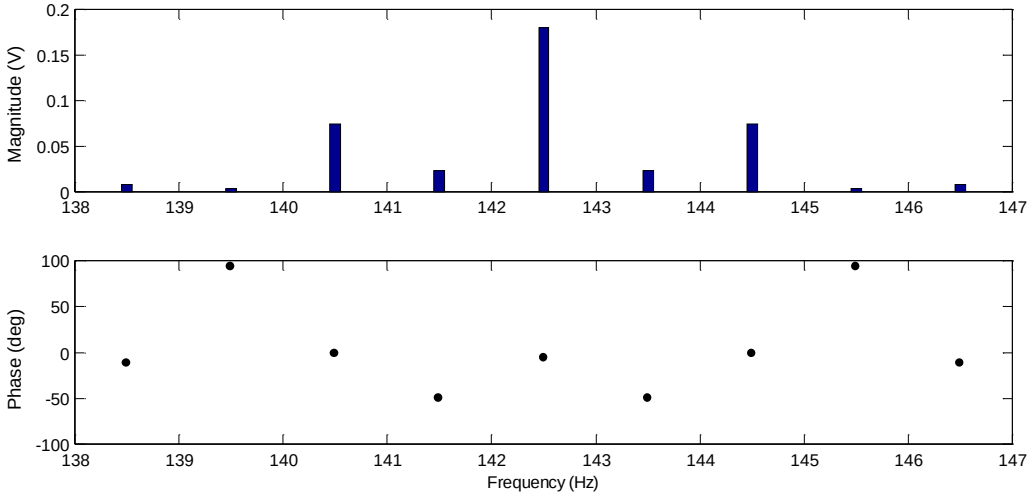


**Figure 7. 48** LDV spectrum magnitude and phase.

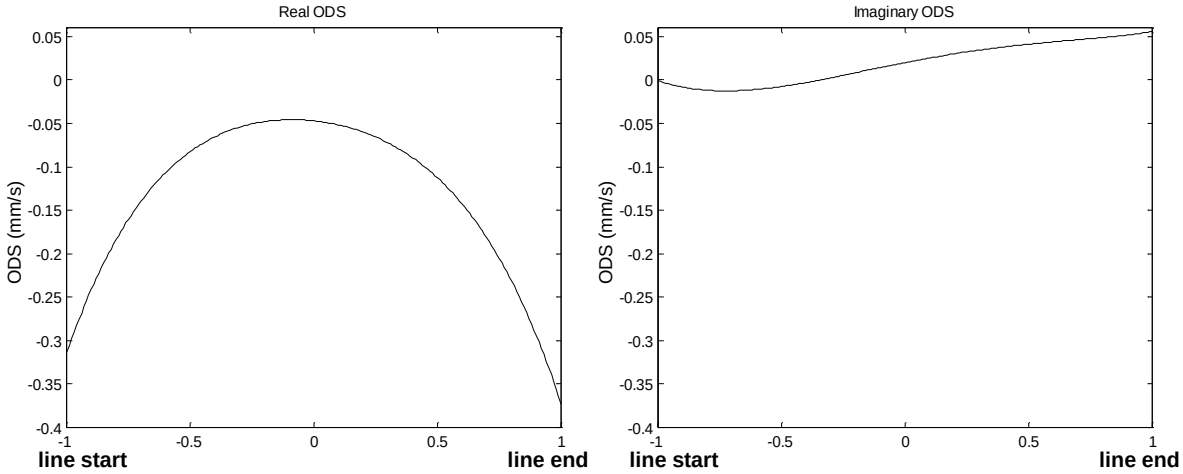


**Figure 7. 49** ODS Real and Imaginary components at the resonance of 142.5 Hz.

The real parts of each line-ODS are plotted together in Figure 7.50, to produce a 2-D ODS. Figure 7.51 shows the two-dimensional ODS, derived by the discrete scan technique described in subsection 7.3.1, is illustrated.

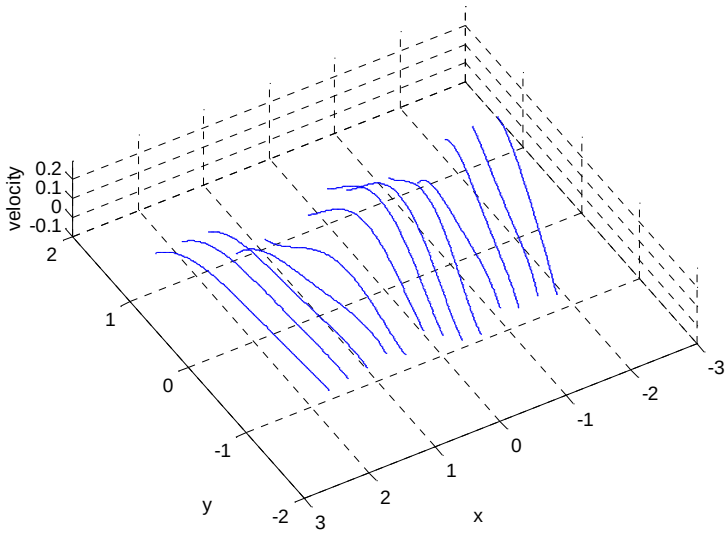


**Figure 7. 50** 2-D ODS at 142.5Hz recovered by raster continuous scanning technique.

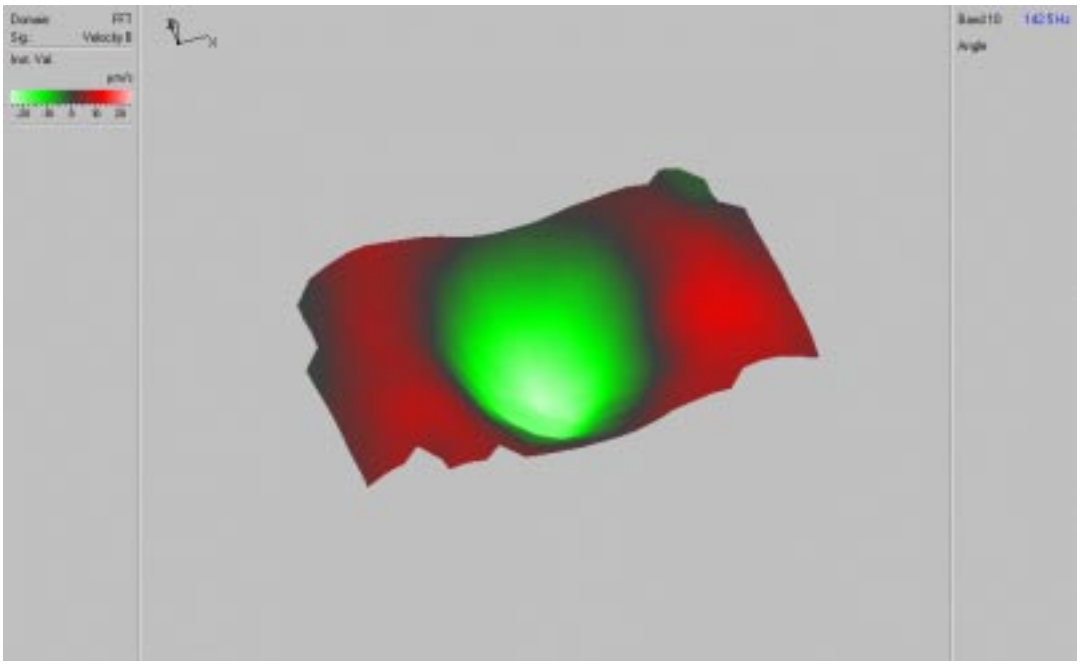

**Figure 7. 51** 2-D ODS at 142.5Hz recovered by single point-by-point scanning technique.

## *7.4. Two-Dimensional Long - Scan Technique Application to Practical Cases*

### *7.4.1 Introduction*

In order to prove the validity of the techniques described in Section 5.5 ( i.e. two dimensional scan methods) practical case studies are addressed:

- the structure employed for MDOF continuous scanning techniques in Section 7.2, sketched in Figure 7.1.
- the rear panel of the IVECO DAILY truck, already mentioned in Section 7.3, see Figure 7.23;

Two-dimensional area scans at uniform and sinusoidal rate were applied. In the first case study, i.e. the irregular plate, with a cut-away section and a hole, the demodulation technique were employed since the scanned surface and,

consequently, the ODS associated were not smooth. In the second example sinusoidal area scans were achieved.

### *7.4.2 Two-dimensional Uniform-Rate Scan*

The irregular plate was excited at one of its natural frequencies, specifically 242 Hz, and scanned by the laser beam driven by a triangular wave at 1.2 Hz in the *y*-direction and at 0.02 Hz in the *x*-direction. In practice, the acquisition was done in only 25 seconds, so that the x-axis was swept just once as if the *x*-scan would be a linear ramp function. The data sampling rate was then 1000 Samples/s so that the scanned lines were 60 along which 25000 data points were sampled. In order to cover the whole surface of the plate, the scan necessarily passed over the hole and, because of its shape, outside the top left part of the plate, see Figure 7.52.

A 100 Hz low-pass filter was used on the LDV output signal to limit speckle noise spike amplitudes.

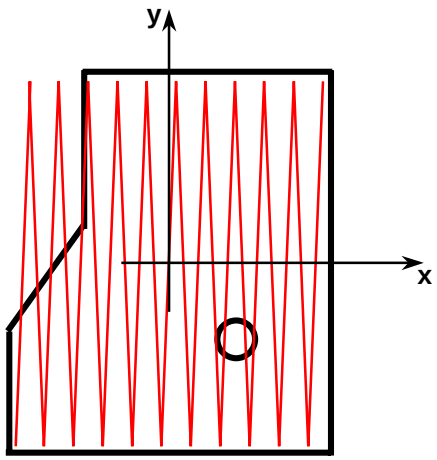


**Figure 7. 52** Scanned area over the plate surface.

Figure 7.53 shows the complete LDV output (top plot) and the zoomed time signal (bottom plot) depicted together with the mirrors driver signals in order to emphasise the modulation due to the laser beam motion.

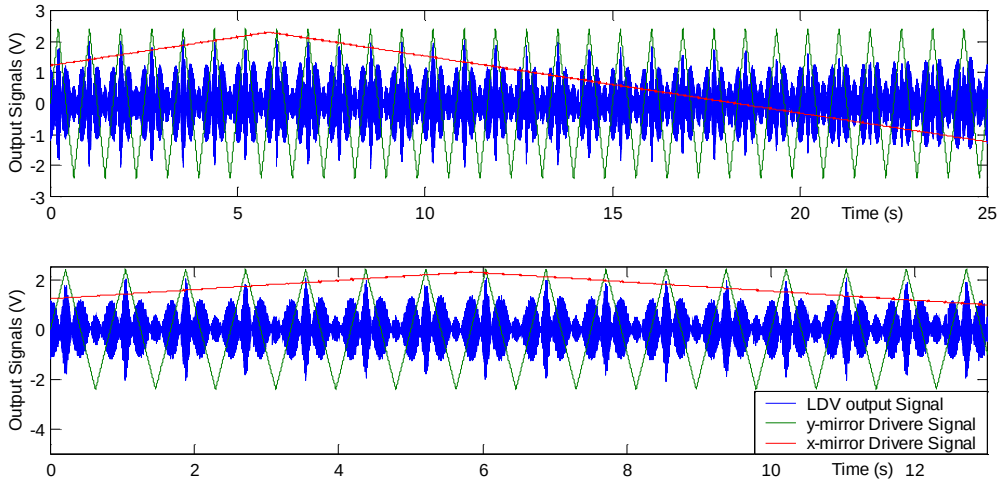


**Figure 7. 53** LDV output signal and mirrors driver signals within a complete acquisition (25 s) in the top plot, and zoomed signals in the bottom plot.

After the demodulation process, the 3-D presentation of the ODS is obtained by plotting the demodulated LDV signal against the *x*- and *y*-mirror driver signals in a 3-D picture, as shown in Figure 7.54. In-phase and out-of-phase components are deduced by the usual process which minimise the output, to give effectively zero imaginary part of the ODS.

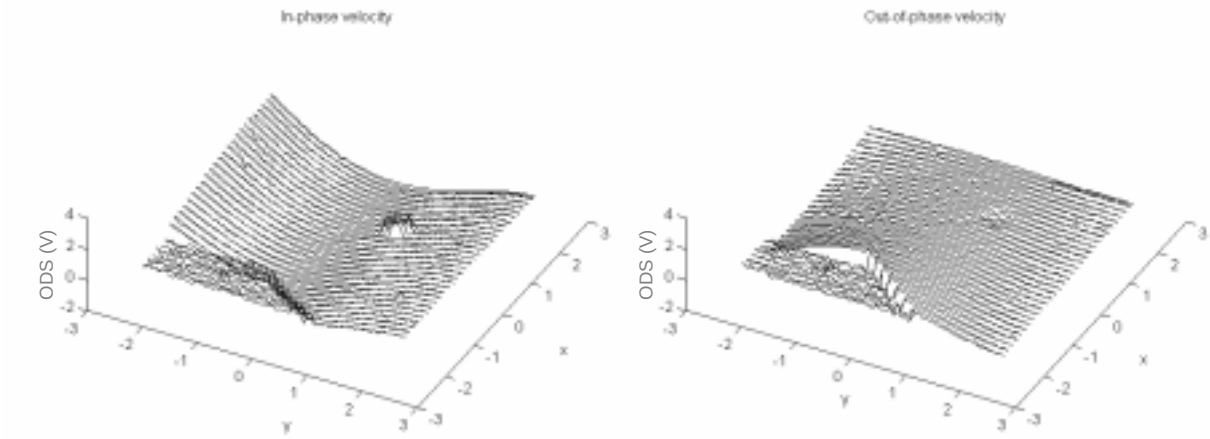


**Figure 7. 54** In-phase ( left ) and out-of-phase ( right ) components of the ODS at 242 Hz.

It is clear how the basic bending mode of the plate is interrupted by the hole and the plate edge, therefore it is immediate to deduce that a polynomial expression can not reasonably represent the ODS. In the demodulated ODS can be noticed the presence of the speckle noise as spikes occurring in the ODS representation, see Figure 7.54.

### *7.4.3 Sinusoidal Two-dimensional Scan on the Rear Panel of the IVECO Lorry Cab*

A sinusoidal area scan over part of the panel was performed by driving the LDV beam-directing mirrors with two sinewaves at different frequencies, 0.3 Hz along the *x-axis* and 5 Hz along the *y-axis*. An area of ± 0.6275 m times ± 0.435 m was covered, as shown in Figure 7.55. The position of the laser head and the excitation conditions were the same as described in subsection 7.3.2; but measurements were repeated at several natural frequencies found from a point-by-point scanning technique. The frequency set was 85 Hz, 112.5 Hz, 137.5 Hz, 146.5 Hz, 185 Hz, 191.3 Hz, 211.3 Hz, 230 Hz.

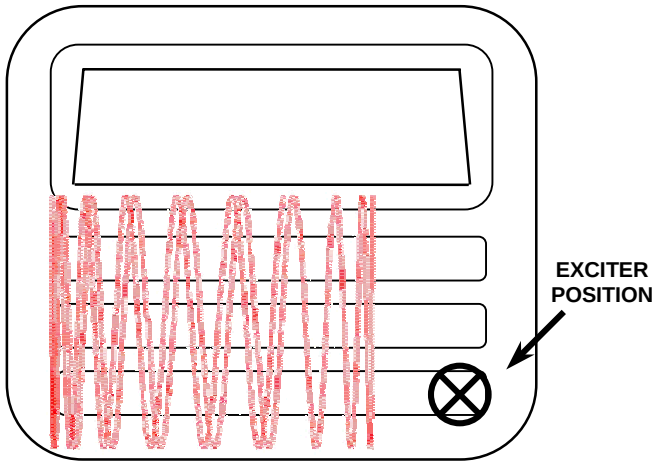


**Figure 7. 55** Measurement set-up sketch.

The LDV output was acquired together with the force reference signal and the mirror driver signals, one of which (*y*-mirror driver) was used to trigger the acquisition. The time histories measured when the structure was excited at its

first natural frequency (i.e. 85 Hz) are illustrated in Figure 7.55. Data acquisition took 40 secs at this frequency.

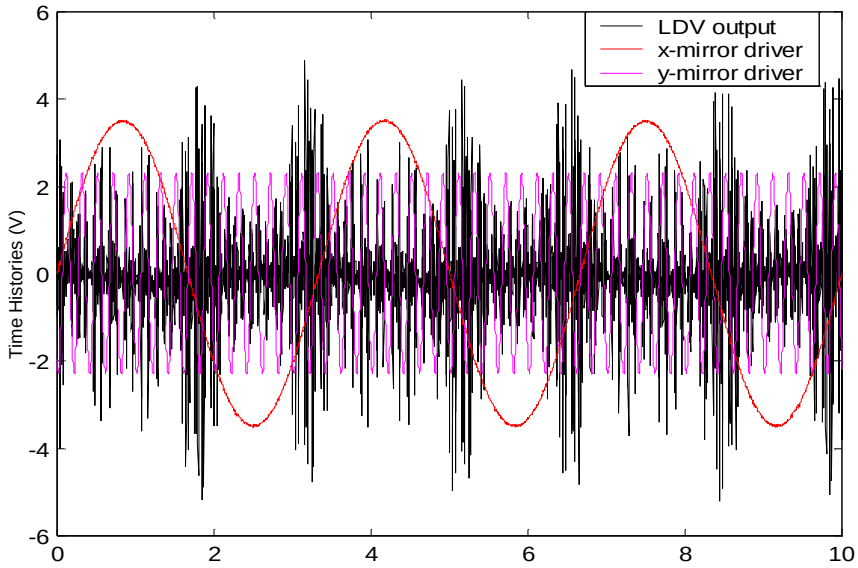


**Figure 7. 56** LDV output and mirrors driver signals.

The LDV output spectrum (Figure 7.56) clearly exhibits the double symmetry of the sideband structure (9 sidebands in x- and y-direction were found to be significant). Detailed examination showed that the ODS could be defined reliably using nine x- and y-sidebands.

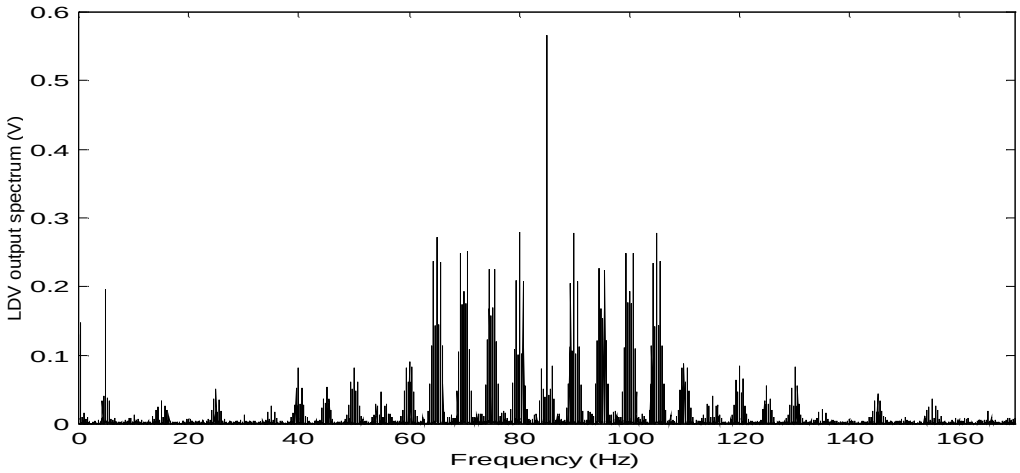


**Figure 7. 57** LDV spectrum.

Real and imaginary components of the ODS were recovered by post-processing of the LDV output, by using LabVIEW routines developed for the purpouse. In those programs, the mirror delay is also taken into consideration (in this case the needed phase shift was -3.67º for the *x*-mirror and -5.4º for the *y*-mirror).

After the sideband extraction at the known frequencies ($85 \pm n \times 5 \pm m \times 0.3$) Hz, assuming *n* and *m* integer values between 0 and the number of sidebands chosen, (i.e. 9) the amplitude and phase spectrum of the LDV output appears as the one in Figure 7.58.

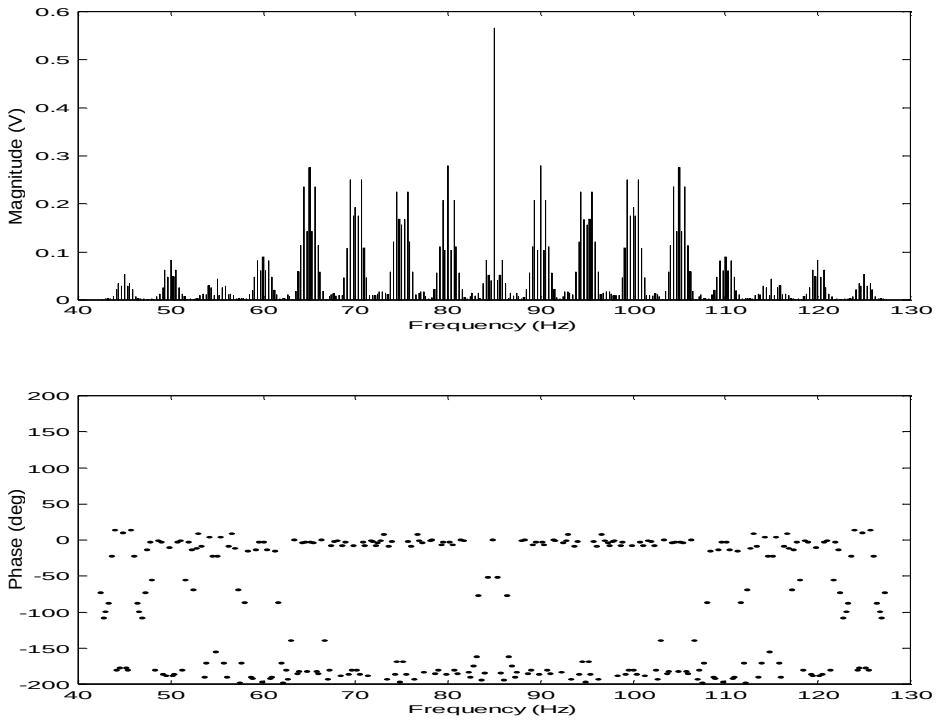


**Figure 7. 58** LDV spectrum amplitude (in V) and phase (in deg).

Real and imaginary ODSs recovered by transforming the sideband matrix derived from the LDV spectrum are shown in Figure 7.59. The same ODS, found via a discrete scan, is shown in Figure 7.60.

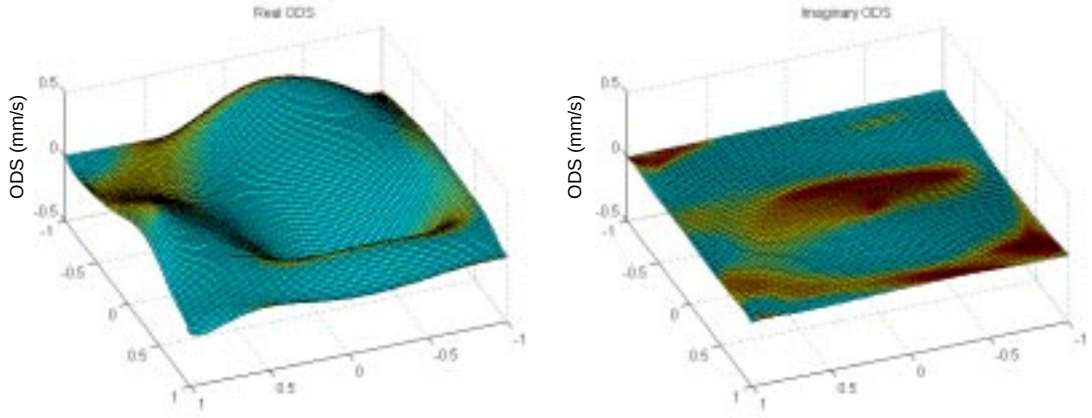


**Figure 7. 59** Real and Imaginary ODS at 85 Hz.

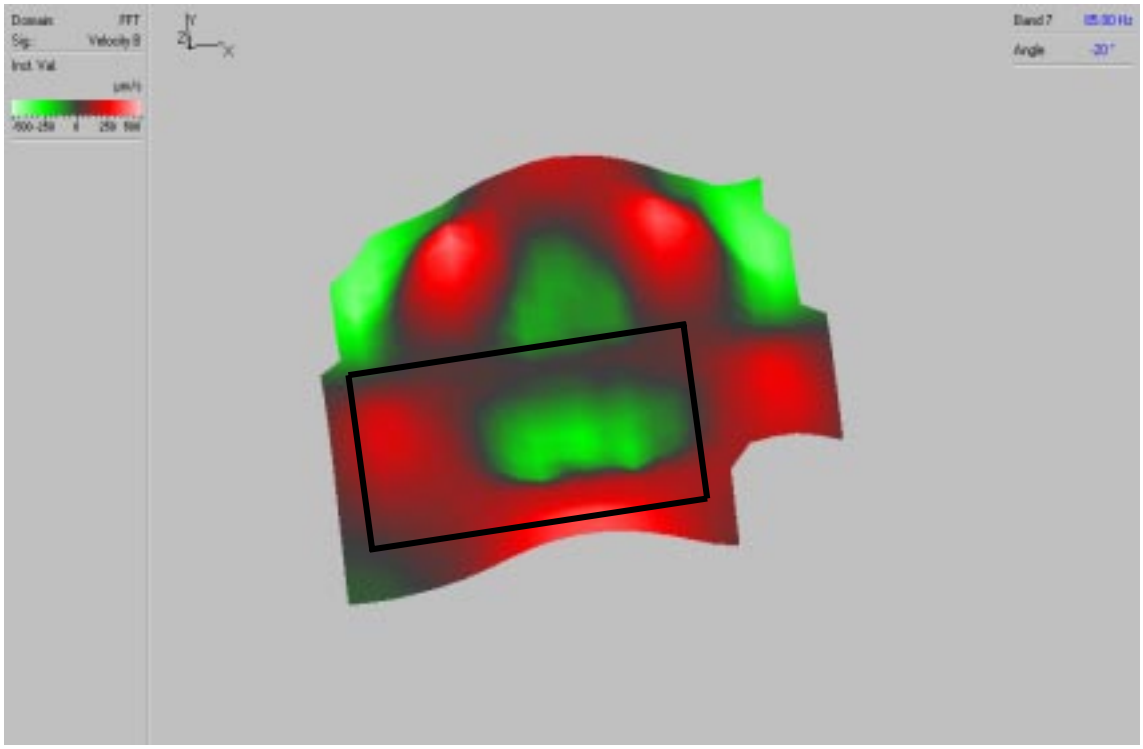

**Figure 7. 60** ODS derived by discrete scan, showing the area where the continuous scan was perormed.

ODS plots derived for each of the other natural frequencies in the set are included as Figures 7.61 to 7.67.

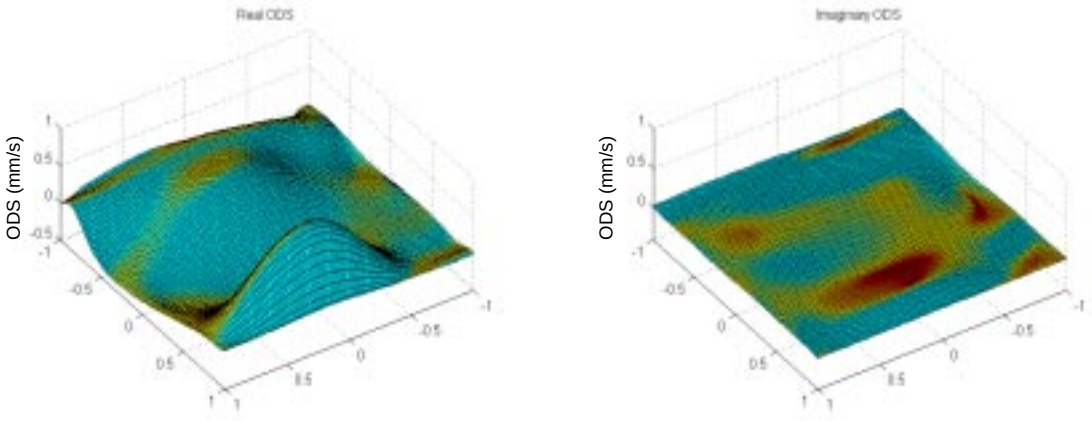


**Figure 7. 61** Real and Imaginary ODS at 112.5 Hz.

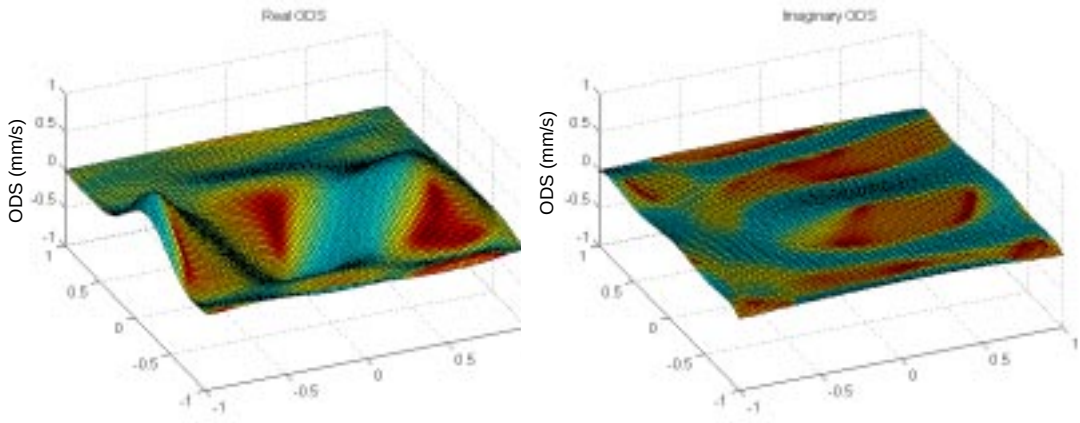


**Figure 7. 62** Real and Imaginary ODS at 137.5Hz**.**

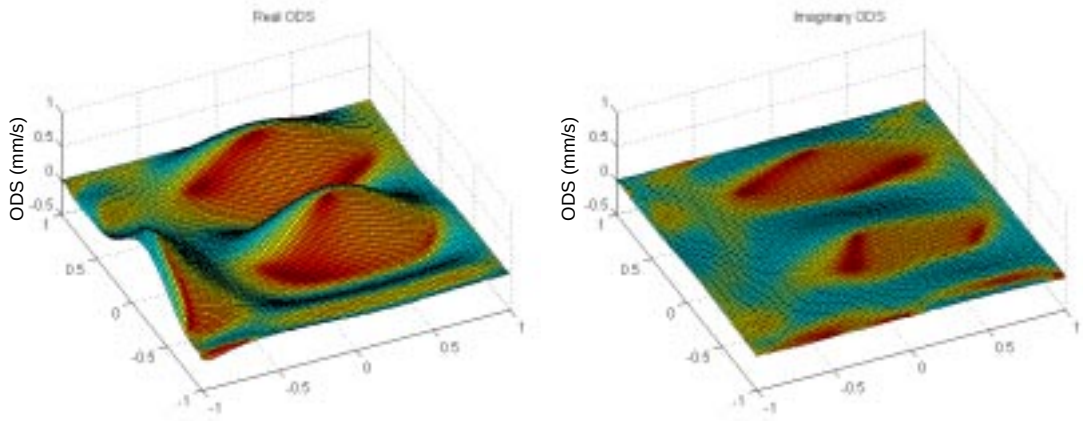


**Figure 7. 63** Real and Imaginary ODS at 146.5 Hz.

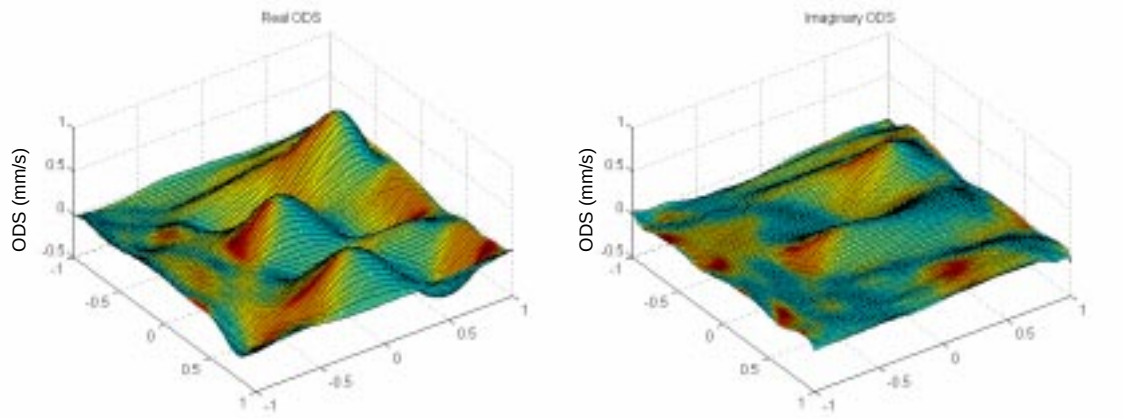


**Figure 7. 64** Real and Imaginary ODS at 185 Hz.

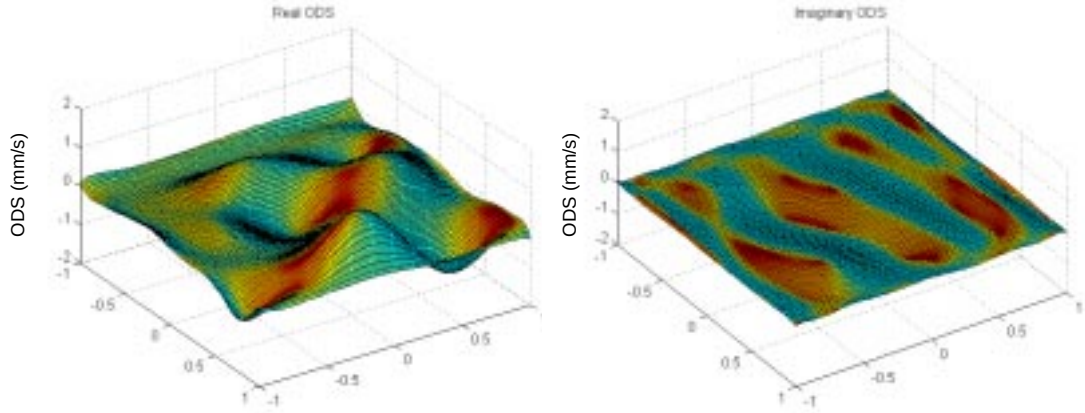


**Figure 7. 65** Real and Imaginary ODS at 191.3 Hz.

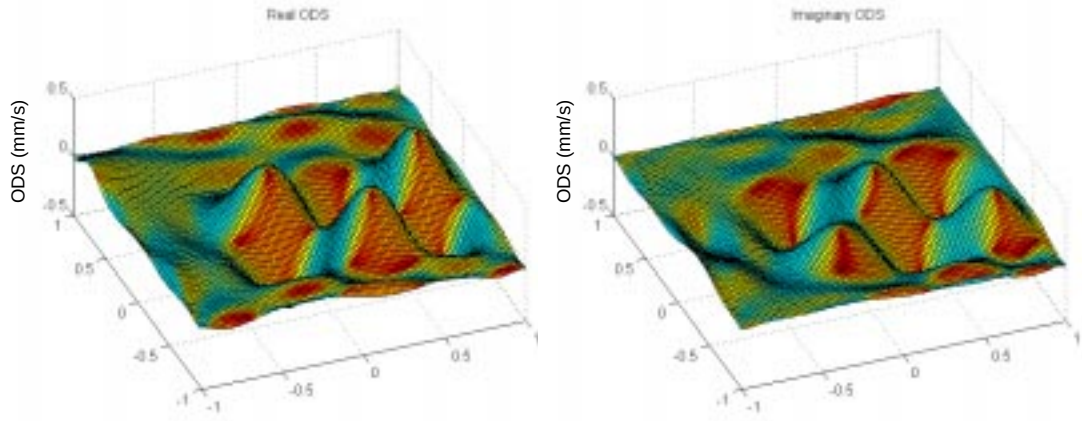


**Figure 7. 66** Real and Imaginary ODS at 211.3 Hz.

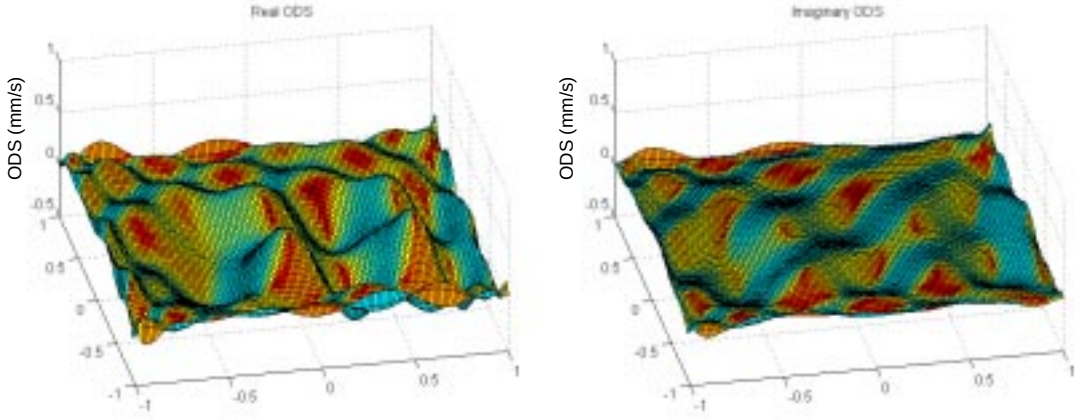


**Figure 7. 67** Real and Imaginary ODS at 230 Hz.

In the last two modes, the imaginary ODS component was relatively large. Its effect was very noticeable in an ODS animation, in which travelling wave components could be clearly seen.

## *7.5. Conclusions*

Several continuous scan LDV techniques, developed and analysed in Chapters 4 and 5, have been applied to practical case studies in this chapter. In some cases, together with the continuous methods, a conventional point-by-point survey has been performed in order to have a basis of comparison for the new techniques.

The most important advantage of the CSLDV was found to be the time-saving. In fact a point-by-point survey took about 30 mins, compared with a 2D-area survey in 40 secs. In reality the point-by-point technique employed a broad-band excitation giving responses at, effectively, 1600 different frequencies, whereas the area scan only provided data at the one test frequency. On the other hand, having obtained broadband spectrum data, response ODSs are, in practice, usually only required at a few natural frequencies. Moreover, the spatial resolution of the discrete scan methods is given by the number of points where the measurements took place (the maximum number of point is 512×512).

In contrast, on the continuous scanning technique two cases can be outlined: (i) continuous scans at uniform rate and (ii) continuous sinusoidal scans. In the first case the ODS spatial resolution depends on the laser scanning speed and the sample rate employed in the acquisition process, see subsection 7.3.2, i.e. it is limited by the acquisition system performance only. In the second case (continuous sinusoidal scanning technique) the ODS spatial resolution is completely arbitrarily. In fact, the ODS is derived as a polynomial whose coefficients are derived from the measured LDV output spectrum components at the vibration frequency and its sidebands. The resolution used for the representation of this polynomial can then be chosen in an arbitrary way completely independent from the acquisition parameters.

# Chapter 8 Conclusions and Suggestions for Further Work

## *8.1. Overall Conclusions*

The primary objective of the research described in this thesis was to explore continuous scanning laser Doppler vibrometry in all its facets by analysing the working principles and the experimental application of each different technique, i.e. short linear, small circular, conical and conical-scans (see Chapter 4) and long one-dimensional and two-dimensional scans (see Chapter 5). Modal analysis applied on FRF data measured by CSLDV techniques (specifically, sinusoidal area scans) by performing step-sine tests are addressed in Chapter 5, see Section 5.6.

One important specific topic in this thesis is the exploration of the laser techniques possibilities when used in the continuous scanning operation. This implies that a detailed investigation of the laser-related phenomenon of speckle noise (which is the main cause of pollution of measured data in LDV technology) has been undertaken. In Chapter 2 the phenomenon is introduced and illustrated while in Chapter 6 a model of speckle noise is outlined in order

to be able to include in the CSLDV test model the contribution of the noise as well. The investigation of the speckle noise phenomenon led to the following conclusions:

1) first, the frequency broadening of the LDV output spectrum has been explored (Section 2.5). Because of the speckle noise, the LDV signal presents an output spectrum with components not only at the vibration frequency but also at its harmonics. By performing a statistical analysis of the light intensity received by the photodetector collecting the light backscattered from the vibrating tested surface, it was found that the most important parameter governing the broadening of the LDV spectrum is the laser beam width at its intersection with the object surface, i.e. the focus of the laser spot. By carefully maintaining the laser beam focus on the vibrating object during the measurement, the frequency broadening can be reduced to the point where it is almost imperceptible;
2) secondly, the nature of the speckle noise when the measuring laser beam scans continuously over the surface of a vibrating surface can be explained. It was shown that the noise is concentrated at the scan frequency and its harmonics. Consequently, by arranging the scan speed in relation to the vibration frequency that needs to be measured, the frequency range of interest in the post-processing for the vibration response recovery (i.e. the vibration frequency and its sidebands) can be made to lie far apart from the scan frequency harmonics. The spectral components at the resonance frequency and its sidebands can then be almost free from speckle noise.

## *8.2. Summary of the Major Conclusions*

### *8.2.1 Development of the CLSDV Techniques for MDOF Vibration Response and ODS Measurements*

The first objective of the work described in this thesis was to develop continuous scanning methods by analysing their working principles. For

detailed discussion and remarks concerning the specific results obtained, the conclusions section of each chapter (Sections 2.11, 3.8, 4.7, 5.7, 6.7 and 7.5) can be consulted.

However, in summary, the following observations may be made in the analysis of the CSLDV technology applied to vibration measurement:

1) CSLDV technology has been shown to be reliable when applied to MDOF vibration response measurements. As demonstrated in Chapter 4, where experiments in a simple cube specimen were undertaken, and in Chapter 7 (Section 7.2), where practical structures were tested, the technique resulted to be a reliable new method for rotational degrees of freedom measurement.

2) As far as CSLDV application to ODS measurements is concerned, it is concluded that the main advantage is the high spatial resolution with which the ODS can be represented. In fact, with the ODS being expressed as a polynomial series derived from the spectral components of the LDV output at the vibration frequency and its sidebands, the resolution used for its representation is completely arbitrary. This is different to the results when a traditional point-by-point scanning technique is used, see Chapters 3, 5 and 7. It should be pointed out as a concluding remark on the CSLDV technology application that this method also provides a major reduction of the quantity of data to be stored (since only the polynomial coefficients or the spectral components of the LDV signal at the resonance frequency and its sidebands are required for the post-process) and a time saving on the actual test (since the time needed for the laser beam to scan the whole surface is only a few seconds). However, a direct comparison with the point-by-point (“standard”) technique is difficult to make, since the experimental conditions are different. The standard technique requires a long acquisition time but it measures over a large frequency range while the CSLDV technique can

be applied with mono-frequency excitations only. Consequently, the amount of data available in the frequency domain is larger for the standard technique than for the continuous scanning one. Against this, it must be noted that there is a generally redundancy in the data recorded with a broadband excitation since not all these data are required for ODS recovery, only the response at resonances being of interest. In conclusion, it can be stated that if only a small number of resonance frequencies are of interest (as is usually the case) we are not obliged to measure many hundred of spectral lines (a large number of which we do not need) as the point-by-point technique does. Alternatively, a continuously scanning step-sine test around the frequencies of interest will allows us to save time in both the phases of measurement and post-processing.

3) An important topic which has been explored within the objective of developing the CSLDV techniques is the modal analysis performed on FRF data obtained by using area scans in a step-sine test fashion. It has been concluded that a very small amount of data needs to be processed (a number of FRFs corresponding to the order of the polynomial representing the ODS) without any loss in the final spatial resolution of the mode shape representation. On the other hand, when a point-by-point scanning technique is used, a large number of points must be measured and analysed depending on the spatial resolution with which it is required to describe the mode shape.

### *8.2.2 Simulation of the CLSDV Techniques*

The second specific objective of this research was to perform numerical simulations of the CSLDV techniques in order to model experimental tests performed by the continuous scanning measurement technology.

Numerically-simulated LDV outputs for a laser beam scanning along a vibrating surface have been used to investigate the working principles of

CSLDV techniques when applied for ODS recovery. The simulation has been shown to be very useful to understand the detailed working of this new measurement method.

A numerical simulation of a complete experimental test carried out by using continuous scanning techniques has been done by means of the new approach known as “virtual testing”. The simulated or “virtual” test model, which includes also the simulation of the effect of the speckle noise, has been applied for the first time to LDV testing when the laser beam is scanned across the vibrating target structure. The description of the model and the results obtained from the “virtual test” performed by using the model itself were shown to work in Chapter 6 by comparing the results achieved with an actual CSLDV experiment.

### *8.2.3 Experimental Validation of the CLSDV Techniques*

In order to realise the objective of experimentally validating the CLSDV techniques, simple test pieces (such as beams, plates and solid cubes) were used. In Chapters 4 and 5, the CSLDV techniques have been tested in all their facets and it was shown that the experimental and simulated results agreed.

Moreover, the results obtained by applying CSLDV and point-by-point (traditional) techniques have been compared side by side. It can be concluded that the new short scanning technique is a reliable method for measuring rotational degrees of freedom. Indeed, this method was shown to be very accurate in comparison with the traditional way of deriving the rotational response of a vibrating structure by performing two translational single point measurements and determine their first derivative.

The accuracy of CSLDV techniques was also compared with the standard point-by-point technique when applied to the ODS recovery of vibrating structures. In both the cases of one and two-dimensional ODSs (i.e. linear and area scans)

the deflection shapes of the surface derived by the two different methods were compared with the analytical ODSs. MAC values were calculated as well (see Subsections 5.5.4.3.2 and 5.5.4.3.3) to validate the CSLDV technique experimental results and it was shown that this new technique works better than the conventional point-by-point one.

### *8.2.4 Application of the CLSDV Techniques to Industrial Case Studies*

Applications of the CSLDV techniques were made on several practical structures (see Chapter 7) in order to prove that the technology developed in this research works effectively in different kinds of experimental conditions (different test surfaces: irregular plates, vehicles body, ...).

The main conclusion that can be drawn from the experiments is that the big advantage of using CSLDV techniques by comparison with the point-by-point ones for ODS recovery, is the effective time saving in the acquisition phase and in the post-processing of measured data, as the applications described in this thesis clearly show.

Continuous short-scan methods for rotational degrees of freedom measurements have been shown to work well also on irregular structures and to be reliable in comparison with the translational single point measurements.

Finally, demodulation techniques have been applied on an irregular plate and it was demonstrated that the direct demodulation of the LDV output is a fast way of obtaining the ODS of the vibrating surface and it can be applied to many kinds of structure (i.e. with discontinuities in the measured surface). In the case presented in Chapter 7, the tested plate presented a hole which has been detected by the scanning laser and thus it appeared on the ODS recovered.

## *8.3. Suggestions for Further Work*

In the research work described in this thesis, CSLDV techniques have been explored and shown to have many advantages with respect to the standard point-by-point scanning techniques. However, in this work, the continuous scanning technology developed in this work has been confined to cases of mono-frequency vibration. The subsequent phase of research could, then, be directed towards the exploration of continuous scanning methods when a general multi-frequency excitation is applied to the measured structure.

There are further opportunities for investigation of exploitation of the CSLDV techniques to a wider range of applications, such as in the testing of machines running under operating conditions. The continuous scanning technique has been applied, also by the author, under conditions of self-excited excitation (i.e. to brake disc "squeal", see subsection 5.4.5 and reference [18]), but this excitation was still stable at one frequency only. Therefore, the LDV technology performance when used in cases where the excitation would not be necessarily mono-frequency should be studied in future projects. As already stated in Chapter 3, Section 3.1, the most important areas to be explored might be:

- CSLDV techniques applied in impact tests,
- CSLDV techniques used in case of narrow-band excitation, and
- CSLDV techniques applied in experimental configuration in which broad-band multi-sine excitation are applied.

In conclusion, further investigations could be performed within the topic of CSLDV measurements of structures subjected to general excitation.

# References


[1] Ewins, D. J., (2000). Modal testing. *Research studies press LTD*.

[2] Stanbridge, A. B., Ewins, D. J., Khan, A.Z., (1998). Fault identification in vibrating structures using a SLDV. In *Proceedings of the third International Conference on Vibration measurement by Laser Techniques,* Vol.2868, pp. 449-457, Ancona.

[3] Stanbridge A. B., Ewins D. J., (1996).Using a continuously-scanning LDV for modal testing. In *Proceedings of IMAC XIV,* Dearborn.

[4] Drain, L. E., (1980). The Laser Doppler Technique. *J. Wiley & Sons.*

[5] Dubbeldam, G. C., (1975). In *Proceedings of LDA Symposium*, pp. 588-92, Copenaghen.

[6] Bucher, I., Schmiechen, P., Robb, D. A., Ewins, D. J., (1994). A laser-based measurement system for measuring vibration on rotating discs. In *Proceedings of the first International Conference on Vibration Measurements by Laser Techniques*, Vol. 2358, pp. 398-408, Ancona.

[7] Stanbridge, A. B., Ewins, D. J., (1995). Modal Testing of Rotating Discs using a Scanning LDV. In *Proceedings of ASME*, Boston.

[8] Stanbridge, A. B., Ewins D. J., (1996). Measurement of translational and angular vibration using a scanning laser Doppler vibrometer. *Shock and Vibration*, Vol. 3, No. 2, pp. 141-152.

[9] Stanbridge A. B., Ewins D. J., (1996). Measurement of total vibration at a point using a conical-scanning LDV. In *Proceedings of the* s*econd International Conference on Vibration Measurements by Laser Techniques*, Vol. 2868, pp. 126-136, Ancona.

[10] Sriram, P., Hanagud, S., Craig, J., Komerath, N. M., (1990). Scanning laser Doppler technique for velocity profile sensing on a moving surface. In *Applied Optics*, Vol. 29, No. 16, pp. 2409-2417.

[11] Sriram, P., Craig, J., Hanagud, S., (1990). A scanning laser Doppler vibrometer for modal testing. In *International Journal of Analytical and Experimental Modal Analysis*, Vol. 5, No. 3, pp. 155-167.

[12] Sriram, P., Hanagud, S., Craig, J., (1992). Mode shape measurement using a scanning laser Doppler vibrometer. In *International Journal of Analytical and Experimental Modal Analysis*, Vol. 7, No. 3, pp. 168-178.

[13] BRITE/EURAM III project VALSE, (01/02/1998-31/05/2001). A new technology for vibration measurement of stationary and moving structures using scanning laser Doppler velocimetry. *Project reference* BRPR-CT97-0594.

[14] Stanbridge, A. B., Martarelli M., Ewins, D. J., (1999). The scanning laser Doppler vibrometer applied to impact modal testing. In *Proceedings of IMAC XVII*, Orlando.

[15] Stanbridge, A. B., Martarelli, M., Ewins, D. J., (1999). Measuring area mode shapes with a scanning laser Doppler vibrometer. In *Proceedings of IMAC XVII*, Orlando.

[16] Stanbridge, A. B., Martarelli, M., Ewins, D. J., (2000). Measuring strain response mode shapes with a continuous-scan LDV. In *Proceedings of the fourth International Conference on Vibration Measurements by Laser Techniques*, Vol. 4072, pp. 160-168, Ancona.

[17] Stanbridge, A. B., Martarelli, M., Ewins, D. J., (2000). Measuring area vibration mode shapes with a continuous-scan LDV. In *Proceedings of the*

*fourth International Conference on Vibration Measurements by Laser Techniques*, Vol. 4072, pp. 176-183, Ancona.

[18] Stanbridge, A. B., Martarelli, M., Ewins, D. J., (2001). Rotating disc vibration analysis with a circular-scanning LDV. In *Proceedings of IMAC XIX*, Kissimmee.

[19] Stanbridge, A. B., Martarelli, M., Ewins, D. J., (2001). Analysis of close mode shapes using a scanning LDV. In *Proceedings of IMAC XIX*, Kissimmee.

[20] Martarelli M., Stanbridge, A. B., (1999). Measurement of translational and rotational vibration at a point using a scanning laser Doppler vibrometer – A users guide. BRITE/EURAM project VALSE Technical report, V2.01.

[21] Stanbridge, A. B., Martarelli M., (1999). Measurement of vibration mode shape using a scanning LDV – A users guide. BRITE/EURAM project VALSE Technical report, V2.02.

[22] Martarelli M., Stanbridge, A. B., (2000). Measurement of Operating Deflection Shapes using an LDV – A users guide. BRITE/EURAM project VALSE Technical report, V2.05.

[23] Martarelli M., Stanbridge, A. B., (2000). Application to practical case studies - Measurement. BRITE/EURAM project VALSE Technical report, V4.01.

[24] Dainty, J. C. (1975). Laser speckle and related phenomena. *Edited by J. C. Dainty [et al.]*.

[25] Jackeman, E., McWhirter, J. G., (1976). Fluctuations in radiation scattered into the Fresnel region by a random-phase screen in uniform motion. *Journal of Physics*, Vol. 9, No. 5, pp. 785-797.

[26] Asakura, T., Takai, N., (1981). Dynamic laser speckles and their application to velocity measurements of the diffuse object. *Applied Physics*, Vol. 25, pp. 179-194.

[27] Churnside, J. H., (1982). Speckle from a rotating diffuse object. *Journal of Optical Society of America*, Vol. 72, No. 11, pp. 1464-1469.

[28] Mencuccini, C., Silvestrini, V., (1988). Physics II. *Liguori*.

[29] Strean, R. F., Mitchell, L. D., Barker, A. J., (1996). Global noise characteristics of a laser Doppler vibrometer part 1: theory. In *Proceedings of*

*the* s*econd International Conference on Vibration Measurements by Laser Techniques*, Vol. 2868, pp. 2-11, Ancona.

[30] Asakura, T., Takai, N., (1978). Dynamic statistical properties of vibrating laser speckle in the diffraction field. *Applied Optics*, Vol. 17, No. 23, pp. 3785-3793.

[31] Durst, F., Melling, A., Whitelaw, J. H., (1976). Principles and practice of laser-Doppler anemometry. *Academic Press.*

[32] Halliwell, N. A., (2000). Short course on laser vibrometry. *Fourth International Conference on Vibration Measurements by Laser Techniques,* Ancona.

[33] Stanbridge, A. B., Khan, A. Z., Ewins, D. J., (2000). Modal testing using impact excitation and a scanning LDV. *Shock and Vibration,* Vol. 7, pp. 91-100.

[34] Vanlanduit, S., Guillaume, P., Schoukens, J., (2001). Broadband vibration measurements using a continuously scanning laser vibrometer. In *Proceedings of IMAC XIX*, Kissimmee.

[35] Castellini, P., Cupido, E., Bendel, K., (2001). Vibration measurements on wind-screen wipers by tracking laser Doppler vibrometer**.** In *Proceedings of IMAC XIX*, Kissimmee.

[36] Martarelli, M., Revel, G. M., Santolini, C., (1998). Automated modal analysis by scanning laser vibrometry: problems and uncertainties associated with the scanning system calibration**.** In *Proceedings of IMAC XVI*, Santa Barbara.

[37] Tomasini, E. P., Paone, N., (1998). Specifications of required SLDV performance. BRITE / EURAM project VALSE Technical report, V1.01.

[38] Leissa, A. W., (1969). Vibration of Plates. *NASA SP-160.*

[39] Stanbridge A. B., Ewins D. J., (1999). Modal testing using a scanning laser Doppler vibrometer. *Mechanical System and Signal Processing*, Vol. 13, No. 2, pp. 255-270.

[40] Tomasini, E. P., Castellini, P., Paone, N., (1999). Tracking of rotational motions. BRITE / EURAM project VALSE Technical report, V3.02.

[41] Stanbridge A. B., Ewins D. J., (1998). Scanning laser Doppler vibrometer measurements for vibrating beam model updating. In *Proceedings of IMAC XVI*, Santa Barbara.

[42] Stanbridge A. B., Ewins D. J., (1998). Identification of dynamic properties of beams using a scanning LDV. In *Proceedings of IMAC XVI*, Santa Barbara.

[43] Timoshenko, S. P., Young, D. H., Weaver, W., jr., (1974). Vibration problems in engineering. *J. Wiley & Sons.*

[44] Korn, G. A., Korn, T. M., (1968). Mathematical Handbook for scientists and engineers. *McGraw-Hill.*

[45] Denman, M., Halliwell, N., Rothberg, S., (1996). Speckle noise reduction in Laser vibrometry: experimental and numerical optimisation. In *Proceedings of the second International Conference on Vibration Measurements by Laser Techniques*, Vol. 2868, pp. 12-21, Ancona.

[46] Gasparetti, M., Revel, G. M., Tomasini, E. P., (1998). Theoretical modeling and experimental evaluation of an in-plane laser Doppler vibrometer in different working conditions. In *Proceedings of the third International Conference on Vibration Measurements by Laser Techniques*, Vol. 3411, pp. 317-327, Ancona.

[47] BRITE/EURAM III project QUATTRO, (01/01/1998-30/09/2000). Quantitative treatement and testing of rotational degrees of freedom. *Project reference* BRPR-CT97-0540.

[48] Ziaei-Rad, S., Martarelli, M., Ewins, D. J., (2000). Measuring RDOFs using laser Doppler vibrometer. In *Proceedings of ISMA 25*, Leuven.

[49] Stanbridge, A. B. , Private Communication.

[50] Rothberg, S. J., Baker, J. R., Halliwell, N. A., (1989). Laser Vibrometry: Pseudo-Vibrations. *Journal of Sound and Vibration*, Vol. 135(3) pp. 516-522.

Bibliography:

Castellini, P., Revel, G.M., (1998). Damage Detection and Characterisation by Processing of Laser Vibrometer Measurement Results: Application on Composite Materials. In *Proceedings of the third International Conference of Vibration Measurement by Laser Techniques*, Vol.2868, pp. 458-468, Ancona.

Jones, R., Wykes, C., (1983). Holographic and speckle interferometry. *Cambridge university press.*

Beckmann, P., Spizzichino, A., (1963). The scattering of electromagnetic waves from rough surfaces. *Pergamon press.*

Yamaguchi, I. Theory and applications of speckle displacement and decorrelation. In *Speckle metrology*, edited by Sirohi, S.

Berne, J. B., Pecora, R., (1976). Dynamic light scattering : with applications to chemistry, biology and physics. *J. Wiley & Sons.*

Li, B., Liang, J. W., Yin, C. Y., (1995). Study on the measurement of in-plane displacement of solid surfaces by laser Doppler velocimetry. *Optics & Laser Technology*, Vol. 27, No. 2, pp. 89-93.

Strean, R. F., Mitchell, L. D., Barker, A. J., (1996). Global noise characteristics of a laser Doppler vibrometer part 2: experiments using beam dynamics. In *Proceedings of the* s*econd International Conference on Vibration Measurements by Laser Techniques*, Vol. 2868, pp. 97-105, Ancona.

Takai, N., Iwai, T., Asakura, T., (1981). An effect of curvature of rotating diffuse objects on the dynamics of speckles produced in the diffraction field. *Applied Physics*, Vol. B 26, pp. 185-192.

Churnside, J. H., Yura, H. T., (1981). Velocity measurement using laser speckle statistics. *Applied Optics.* Vol. 20, No. 20, pp.3539-3541.

Ohtsubo, J., (1980). Velocity measurement using the time-space cross-correlation of speckle pattern. *Optics Communications.* Vol. 340, No. 2, pp.147-152.

Stanbridge, A. B., Martarelli M., (1999). Measurement of rotating disc vibration using a non-synchronous circular-scanning LDV – A users guide. BRITE/EURAM project VALSE Technical report, V3.02.

Stanbridge, A. B., Martarelli M., (1999). Conical LDV scanning on a rotating disc. BRITE/EURAM project VALSE Technical report, V3.05.

# APPENDIX

## *A.1. LabVIEW Programs*

### *A.1.1 Shaker Control*

Figure A.1 shows the LabVIEW control panel of the sine excitation generator controlling an HP33120A arbitrary waveform generator which drives the shaker, as described in Subsection 5.3.2.2.

Parameter settings are:

(i) Waveform generator instrument descriptor, which is the address of the HP33120A driven via a GPIB board set in the measurement PC.

(ii) Waveform generator frequency shape (sinewave), frequency (in Hz) and amplitude (in Volts) as required for the vibration input. Zero offset is usually set.

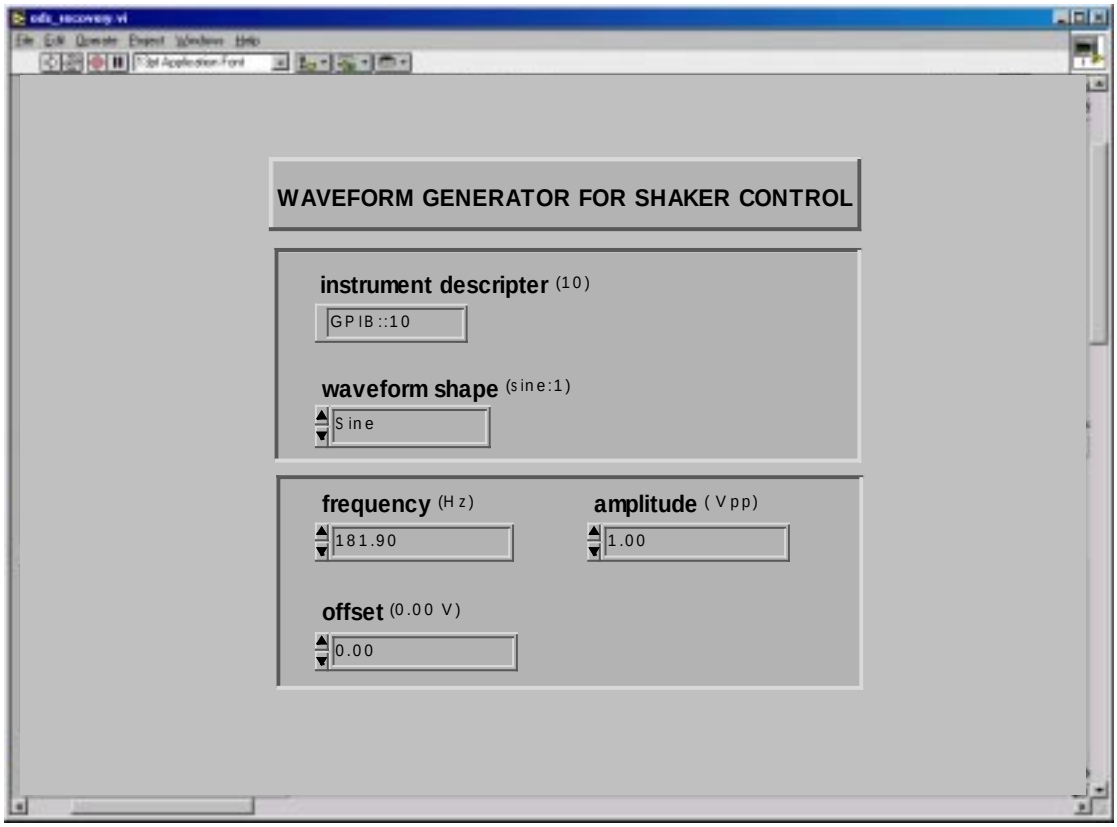


**Figure A. 1** Shaker control panel.

### *A.1.2 Mirror Driver Control – Case of Scans at Uniform Rate*

Figure A.2 depicts the LabVIEW control panel of the mirror driver producing triangular waves used to feed the scanning mirrors placed on the laser head in order to make the laser beam to scan at uniform rate (see Subsection 5.3.2.2).

Parameter settings are:

(i) Device number corresponding to the output card (in this case an I/O NI 4451 with two output channels) producing the waveforms used to feed the mirrors.

(ii) Output channels' number.

(iii) Buffer length and sample rate adjusted to give the required resolution for the mirror driver signals.

(iv) *X*- and *y*-waveform amplitudes (in Volts) and frequency (in Hz).

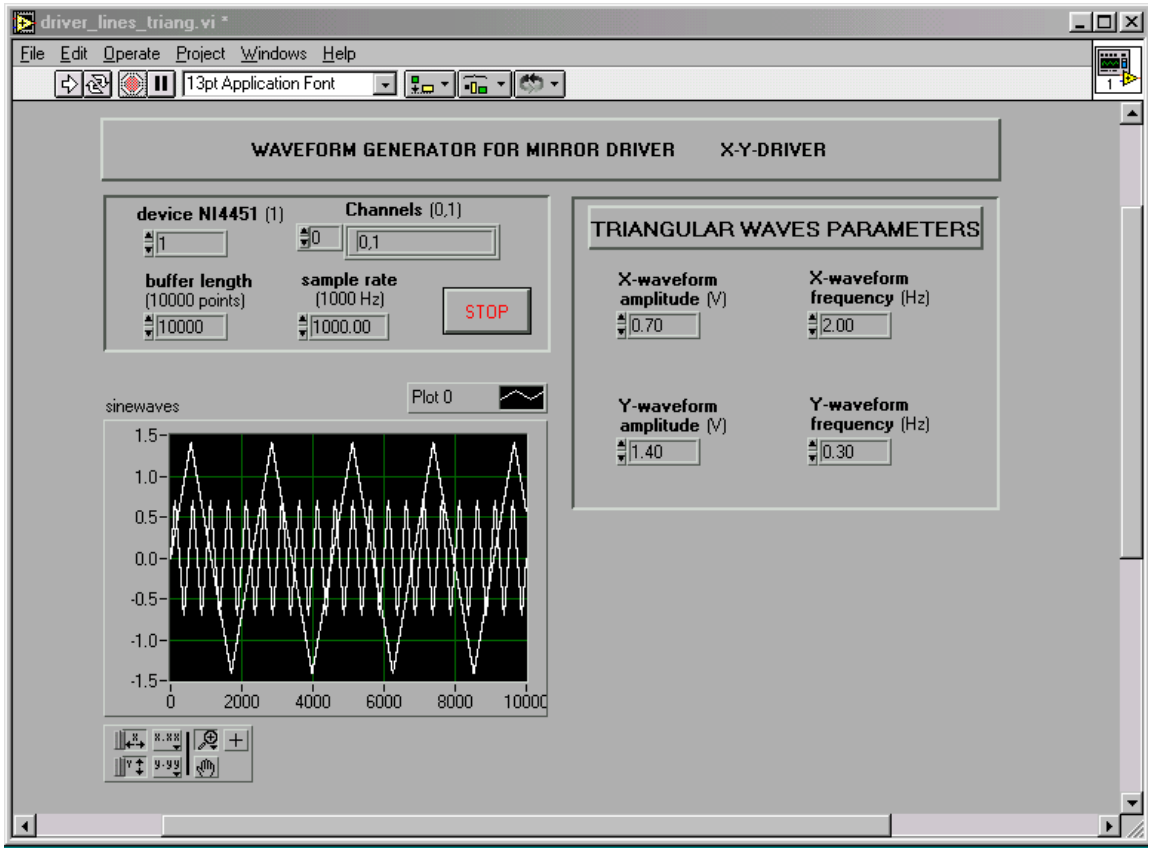


**Figure A. 2** Mirror driver control panel- case of triangular waves.

### *A.1.3 Acquisition Control*

Figure A.3 illustrates the LabVIEW control panel for the acquisition of time histories. It is possible to acquire up to four channels, usually the LDV output, the two mirror drivers (if a 2-dimensional scan is performed), and the reference force signal (see Subsections 5.3.2.2, 5.3.3.3, 5.5.4.3.1).

Parameter settings are:

(i) Device number corresponding to the input card (in this case an NI 4452 with four input channels).

(ii) Input channels' number.

(iii) Trigger channel number which, specifically, corresponds to one of the mirror driver signals.

(iv) Trigger slope and level, usually, rising and 0 V if the acquisition has to start when the sinewave goes through zero.

(v) Number of samples and sample rate (in Hz).

(vi) Time limit which must be longer than the sample time.

(vii) Name of the file where the acquired data would be stored.

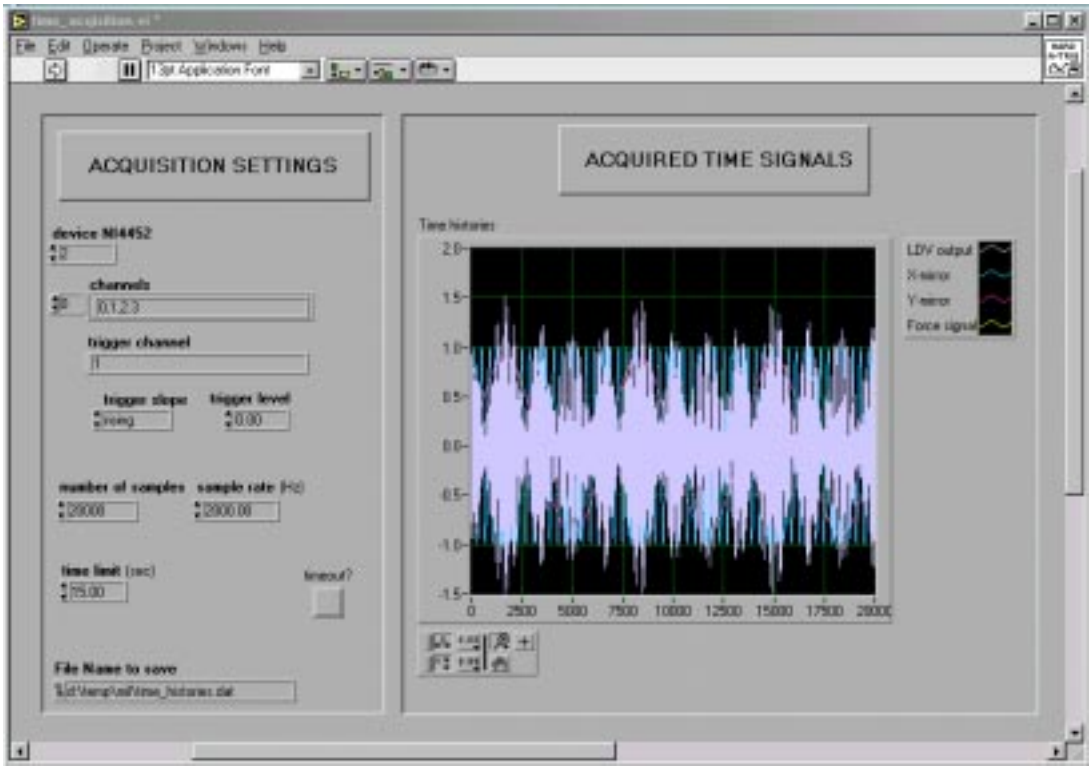


**Figure A. 3** Acquisition control panel.

### *A.1.4 Demodulation Program*

The LabVIEW control panel for the demodulation process is depicted in Figure A.4. The procedure applied consists of a multiplication of the LDV time signal by sine and cosine at the excitation frequency and a filtering out of the high frequency components (see Subsection 5.3.2.2). The in-phase and out-of-phase components of the ODS obtained are shown in the right-hand side of the panel.

Parameter settings are:

(i) Name of the file to open where the LDV output signal was recorded.

(ii) Excitation frequency.

(iii) Sample rate used during the acquisition.

(iv) Filter type, i.e. lowpass in case of demodulation processing.

(v) Cut-off frequency of the low-pass filter.

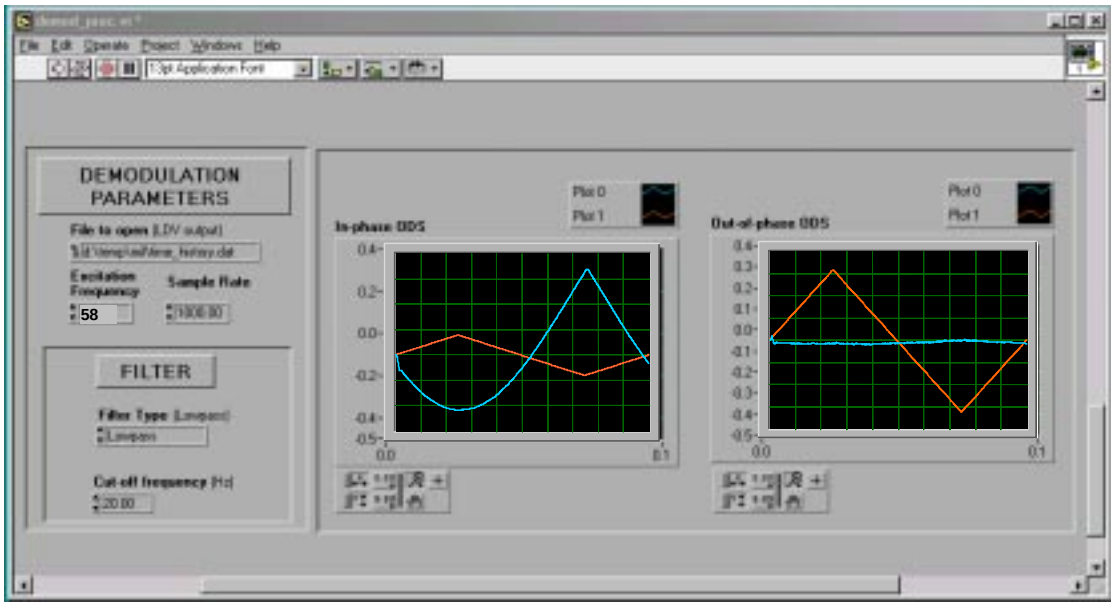


**Figure A. 4** Demodulation program control panel.

### *A.1.5 Mirror Driver Control – Case of Sinusoidal Scans*

Figure A.5 shows the LabVIEW control panel of the mirror driver producing sinewaves which drive the mirrors in order to make the laser beam to scan in one- or two-dimensional sinusoidal pattern (see Subsections 5.3.3.3 and 5.5.4.3.1).

Parameter settings are:

(i) Device number corresponding to the output card (in this case an I/O NI 4451 with two output channels) producing the waveforms used to feed the mirrors.

(ii) Output channels' number.

(iii) Buffer length and sample rate.

(iv) *X*- and *y*-waveform amplitudes (in Volts) and frequency (in Hz).

(v) *Y*-waveform phase which is usual 0° as the *x*-waveform phase. In the case of circular scans, only, this value is set at 90°.

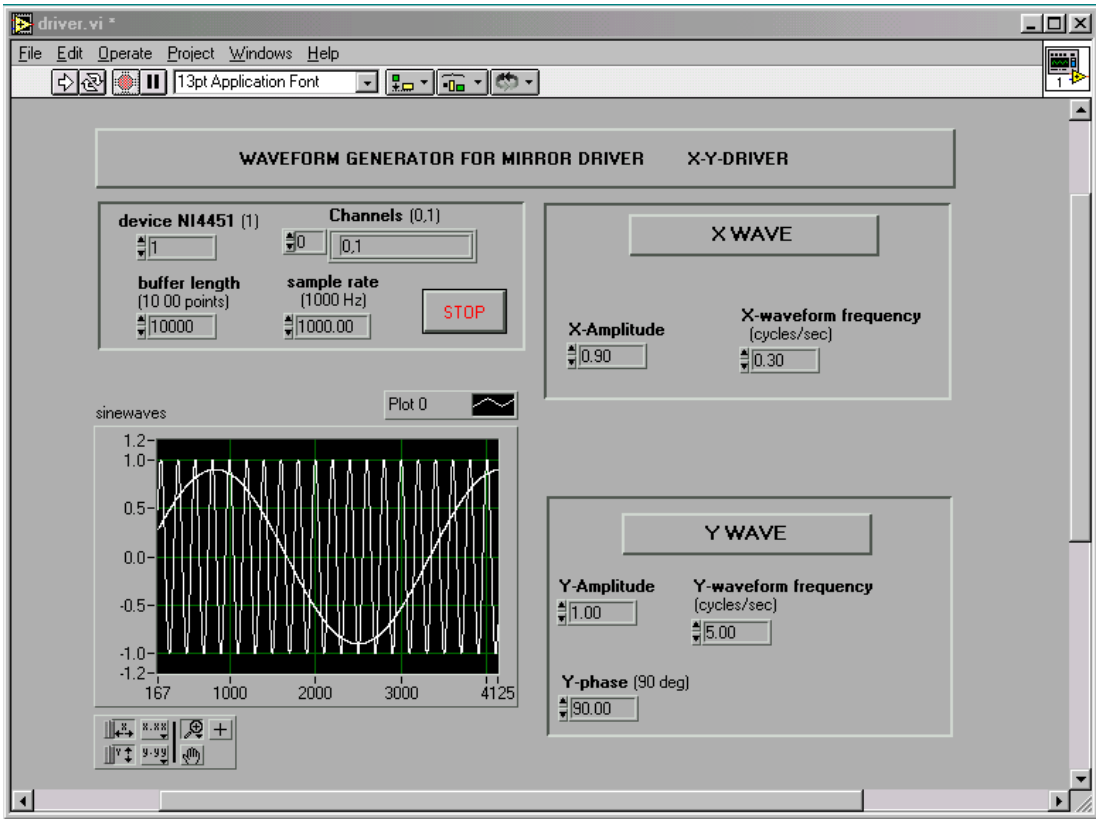


**Figure A. 5** Mirror driver control panel- case of sinewaves.

### *A.1.6 Spectrum Analyser Program*

This is a LabVIEW control program used to visualise the LDV output spectrum (as required in Subsection 5.5.4.3.1), see Figure A.6 for the control panel.

Parameter settings are:

(i) Device number corresponding to the input card (in this case an NI 4452).

(ii) Input channel's number.

(iii) Number of samples and sample rate (in Hz).

(iv) Window to be applied to the LDV time signal.

(v) Unit of the spectral components (in Volts or dB).

(vi) Axis scale, logarithmic or linear.

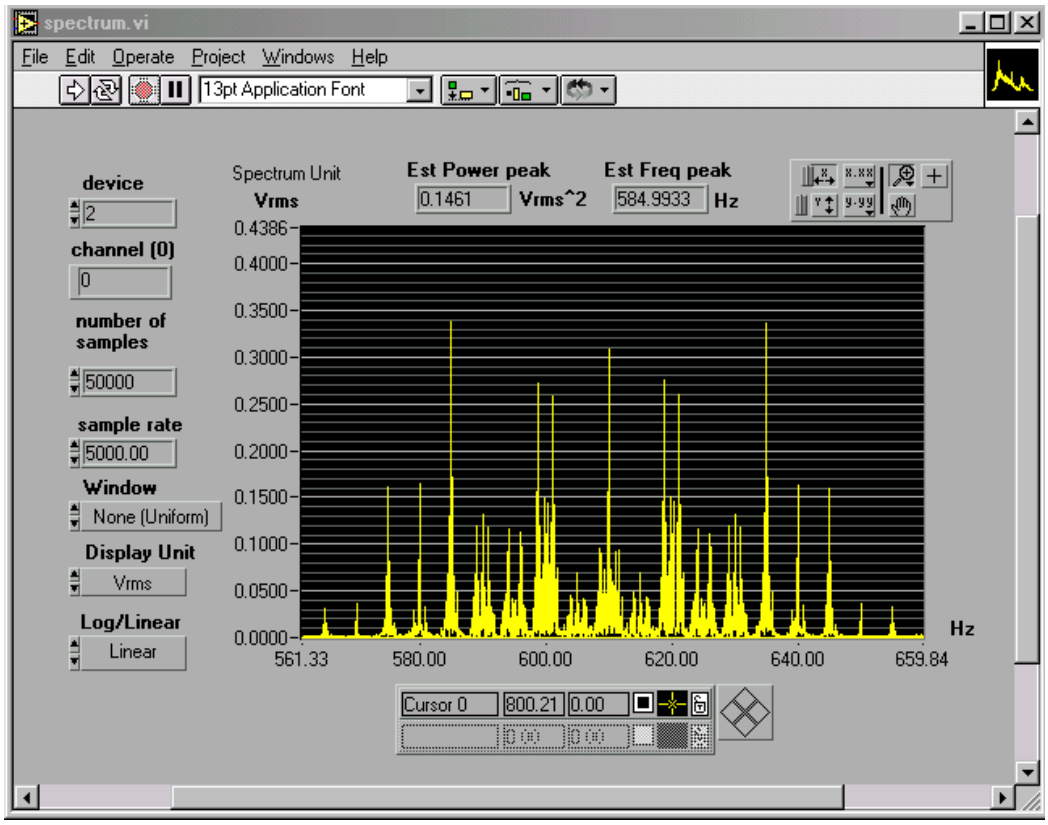


**Figure A. 6** Spectrum analyser control panel.

### *A.1.7 ODS Recovery Program*

This LabVIEW program performs the curve-fit of the LDV time signal and recovers the ODS of the measured surface from the spectral components of the LDV output at the excitation frequency and its sidebands (see Subsection 5.5.4.3.1). The control panel is split into two parts: Figure A.7 shows the part concerning the parameter settings and the visualisation of the spectral components of the LDV output at the frequencies of interest; Figure A.8 illustrates the final result, i.e. the real and imaginary components of the ODS.

Parameter settings are:

(i) Sample rate (in Hz) used in data acquisition.

(ii) Excitation frequency (in Hz).

(iii) Number of sidebands of interest in *x*- and *y*-direction.

(iv) Frequency (in Hz) of the waveforms driving the *x*- and *y*-mirror.

(v) Phase correction to be taken into account because the *x*- and *y*-mirror delay.

(vi) Name of the file to open where the LDV output time history is stored.

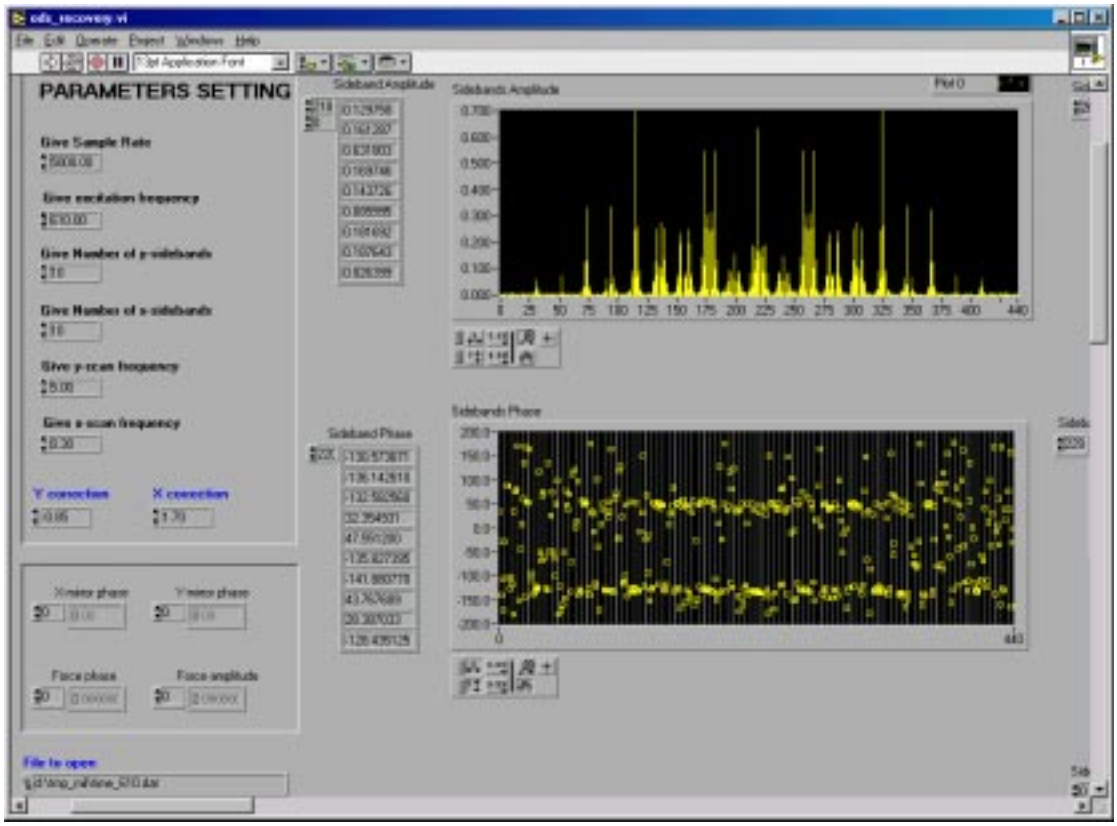


**Figure A. 7** ODS recovery control panel – parameter settings and spectral components visualisation.

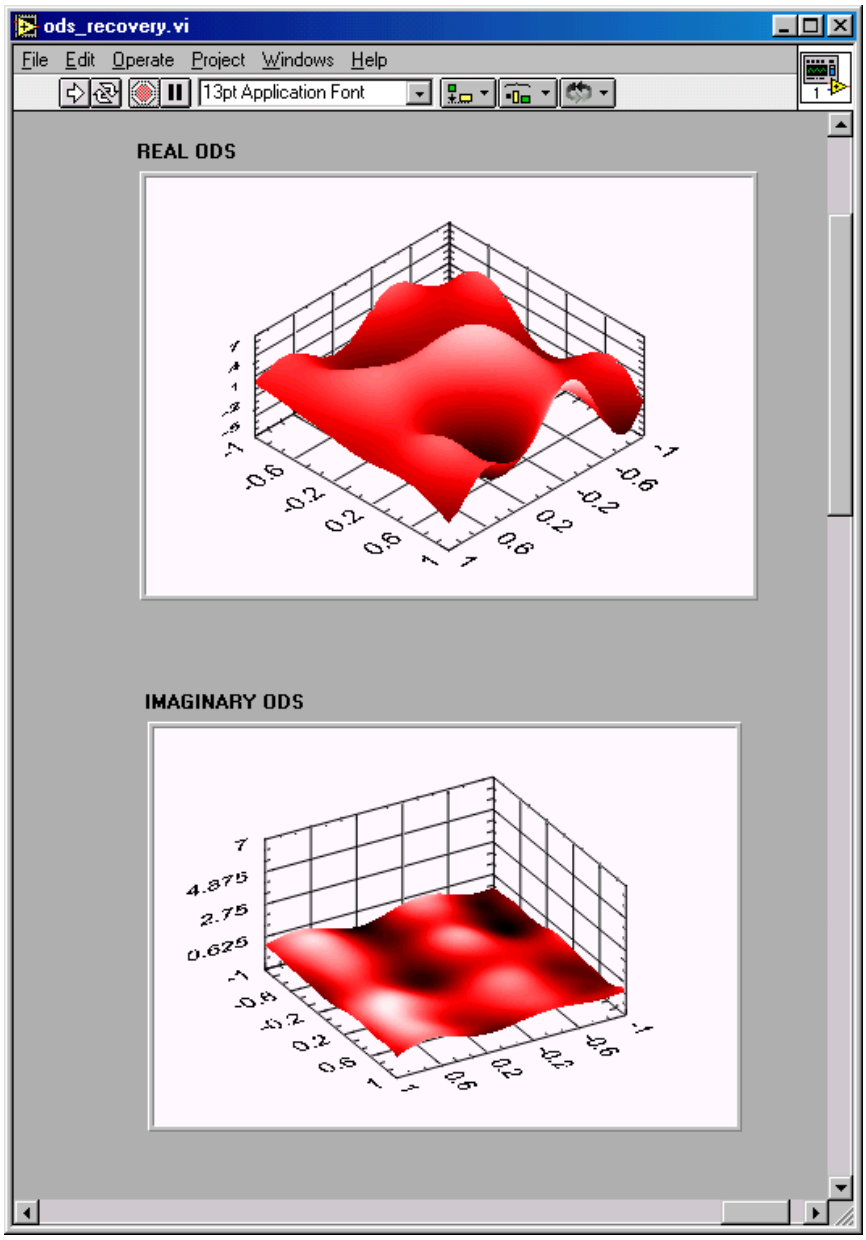


**Figure A.8** ODS recovery control panel – ODS real and imaginary components representation.

### *A.1.8 Automatic Shaker Control and Acquisition Control for Step-Sine Tests*

Figure A.9 shows the control panel of the LabVIEW program which controls the excitation force applied to the shaker and the acquisition in a step-sine test undertaken when a small circular or a short linear scan is performed on the tested surface, see Subsection 7.2.1 for the detailed description of the procedure.

Parameter settings are:

1) For the excitation control:

   (i) Waveform generator instrument descriptor.

   (ii) Waveform generator frequency shape (sinewave) and amplitude (in Volts) .

   (iii) Start excitation frequency, frequency step (in Hz) and number of steps to be done in the step-sine test.

2) For the scanning parameters:

   Scan rate (in Hz) and scan radius or scan length (in mm) if the CSLDV technique used is a circular or a linear scan, respectively.

3) For the acquisition parameters these are the same as already described in appendix A.1.3 for the acquisition control program.

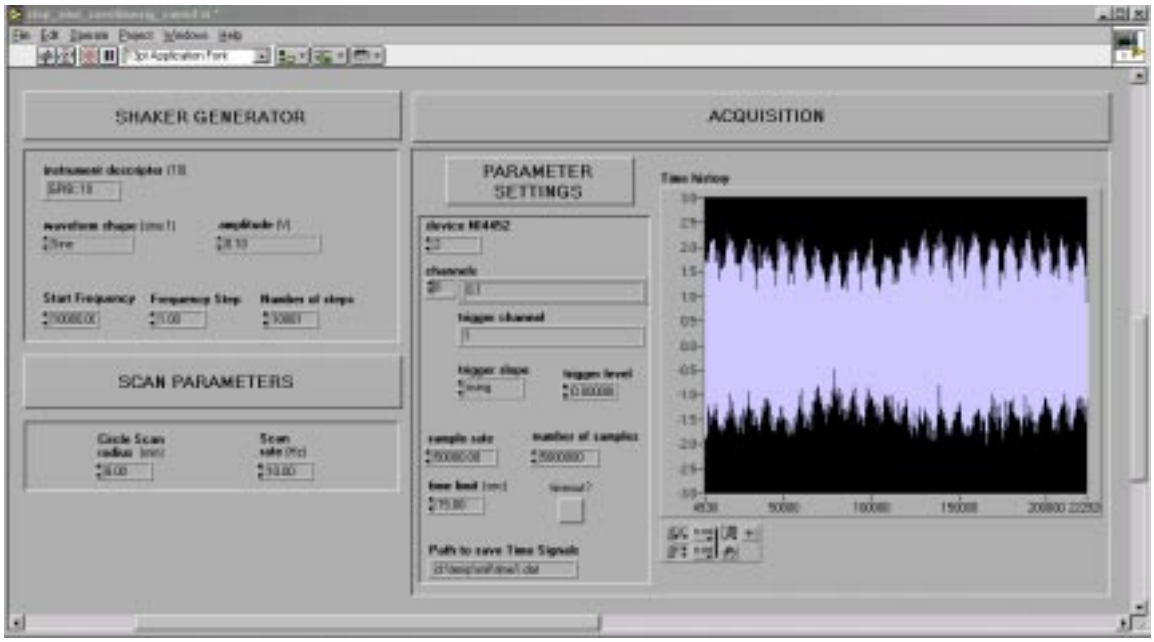


**Figure A. 9** Step-sine test control panel.

## *A.2. Measured FRF data from CSLDV Techniques*

Figures from A.10 to A.29 show the sideband FRFs at frequencies from 34 to 35.9 Hz measured by using area scans in the step-sine test performed on the GARTEUR structure as described in Subsection 5.6.2.

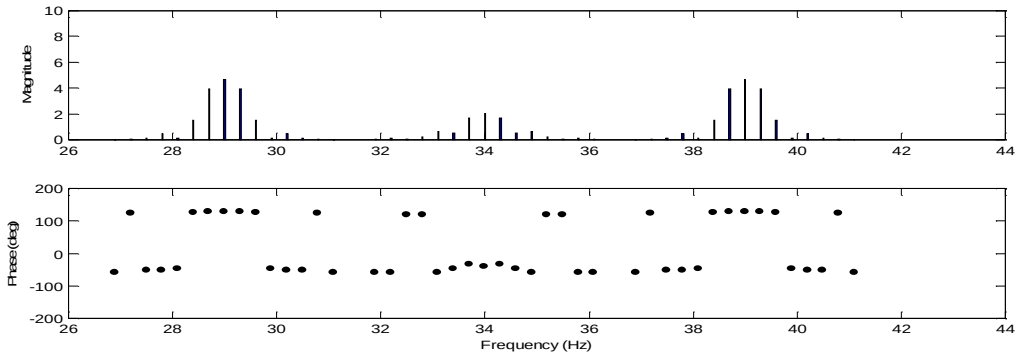


**Figure A. 10** Sideband FRF at the excitation frequency of 34 Hz.

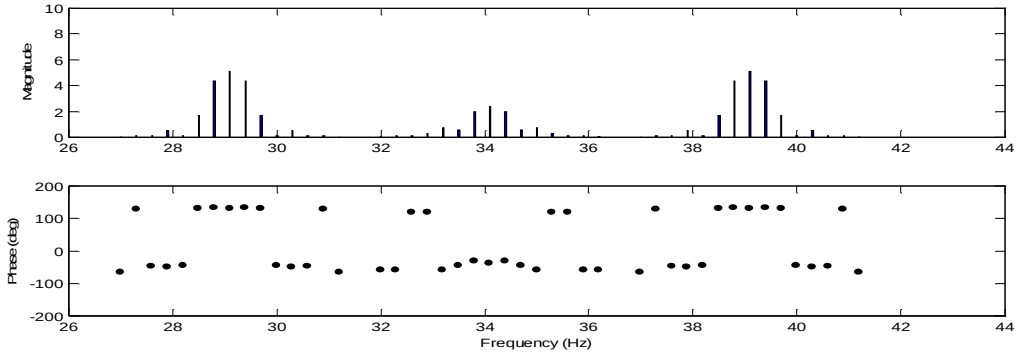


**Figure A. 11** Sideband FRF at the excitation frequency of 34.1 Hz.

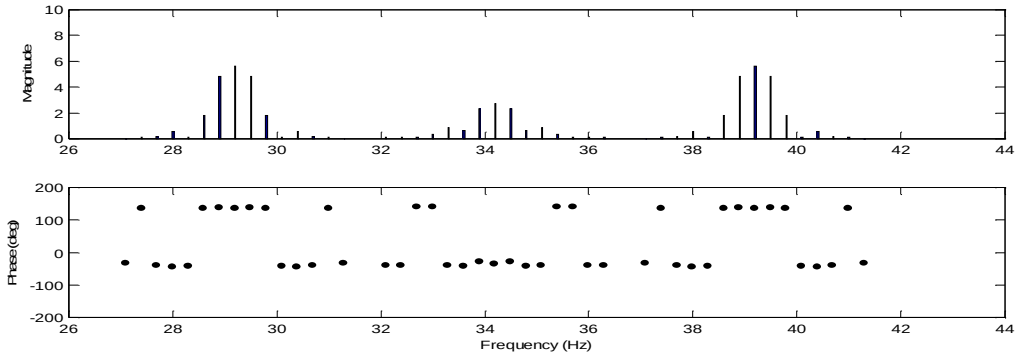


**Figure A. 12** Sideband FRF at the excitation frequency of 34.2 Hz.

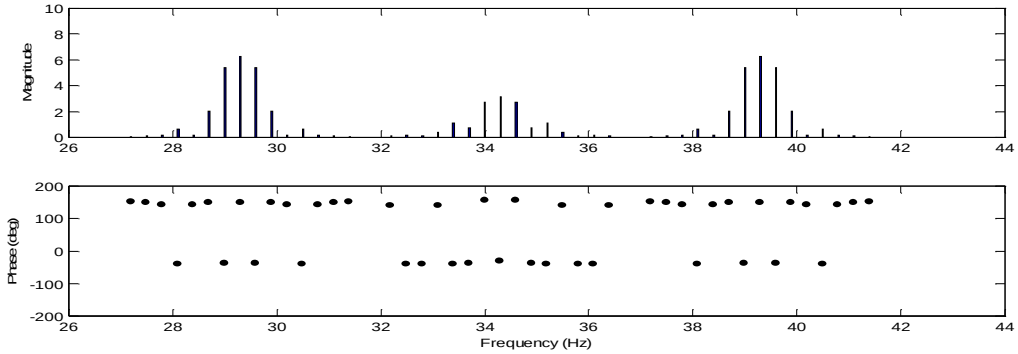


**Figure A. 13** Sideband FRF at the excitation frequency of 34.3 Hz.

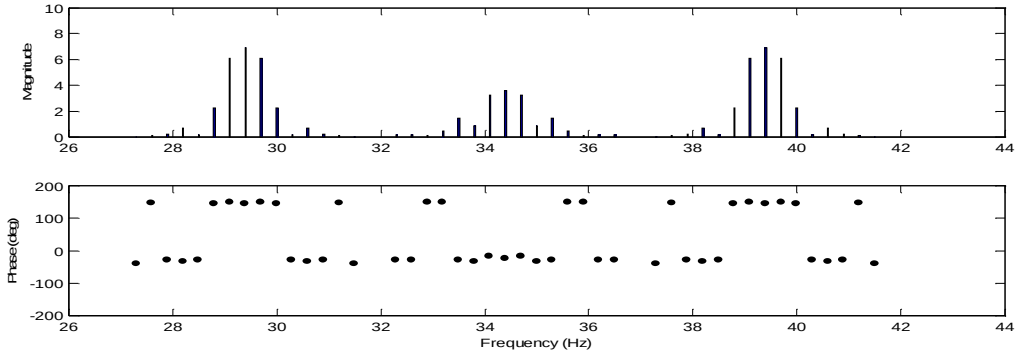


**Figure A. 14** Sideband FRF at the excitation frequency of 34.4 Hz.

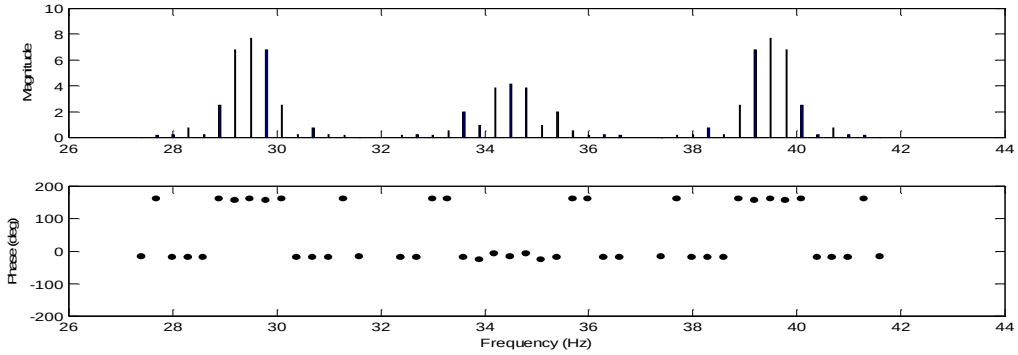


**Figure A. 15** Sideband FRF at the excitation frequency of 34.5 Hz.

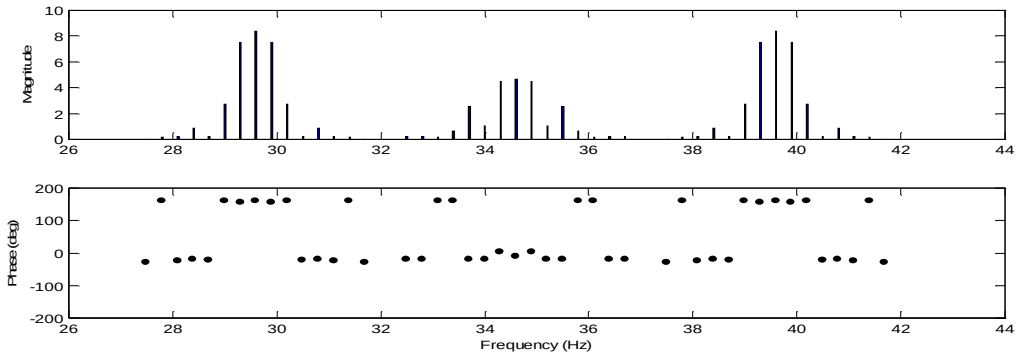


**Figure A. 16** Sideband FRF at the excitation frequency of 34.6 Hz.

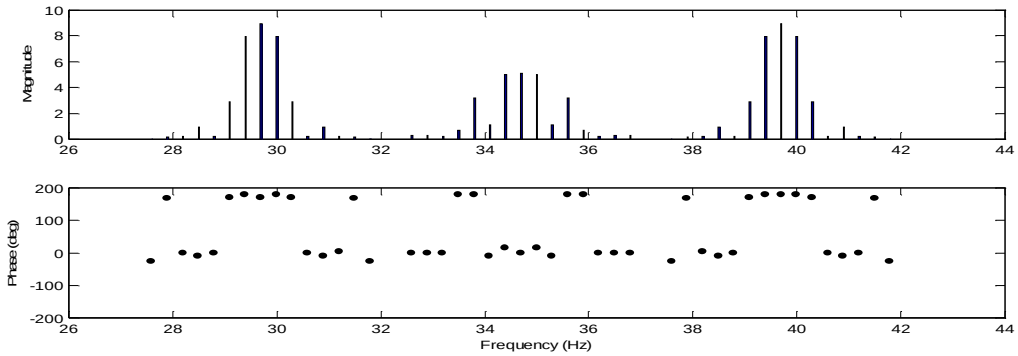


**Figure A. 17** Sideband FRF at the excitation frequency of 34.7 Hz.

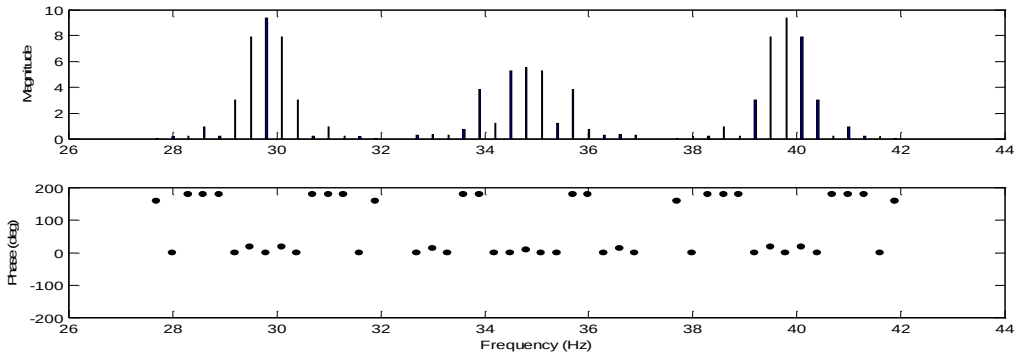


**Figure A. 18** Sideband FRF at the excitation frequency of 34.8 Hz.

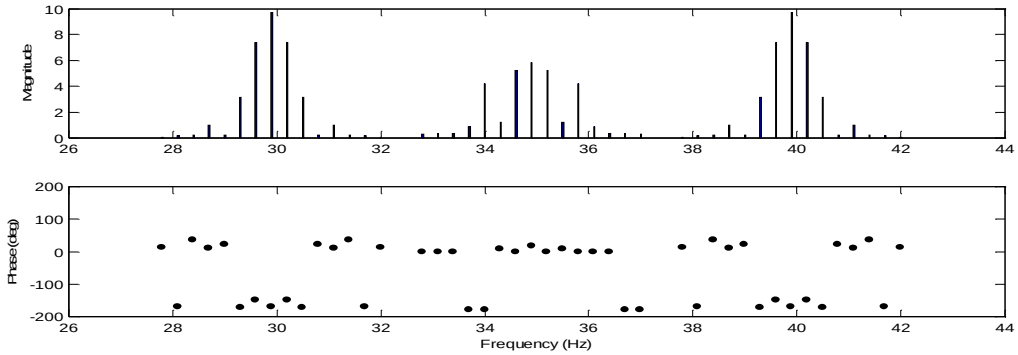


**Figure A. 19** Sideband FRF at the excitation frequency of 34.9 Hz.

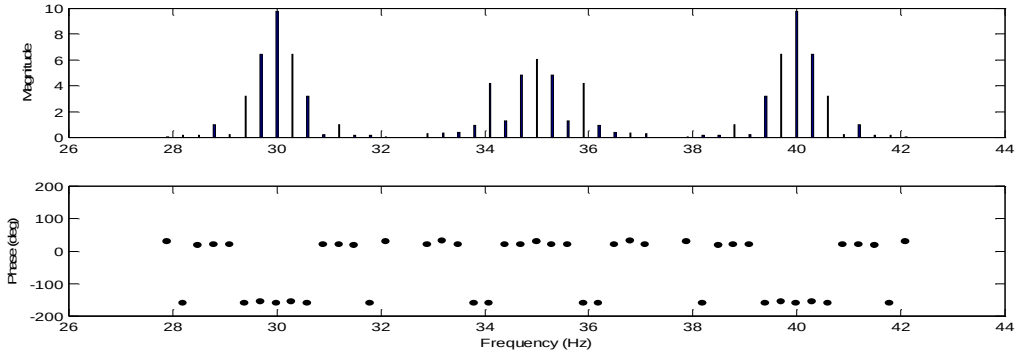


**Figure A. 20** Sideband FRF at the excitation frequency of 35 Hz.

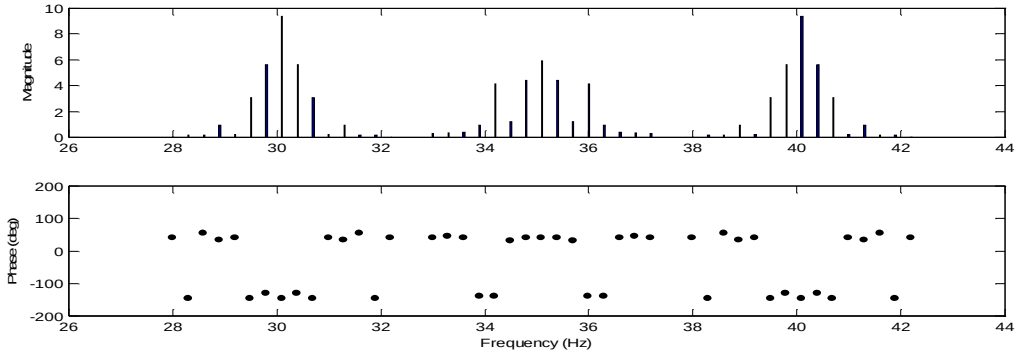


**Figure A. 21** Sideband FRF at the excitation frequency of 35.1 Hz.

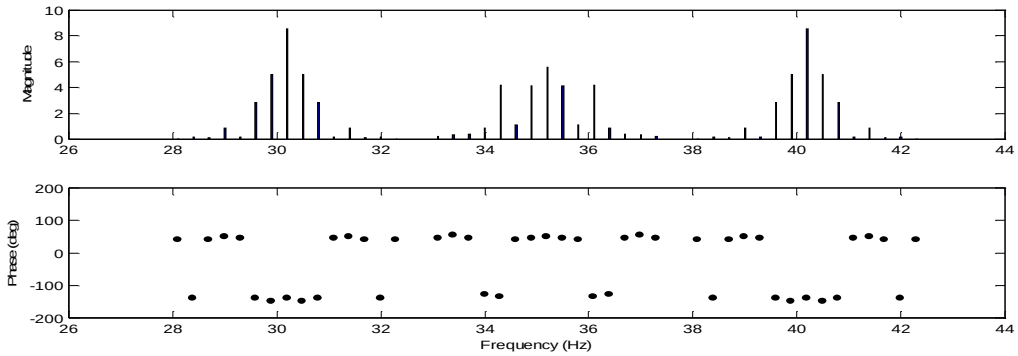


**Figure A. 22** Sideband FRF at the excitation frequency of 35.2 Hz.

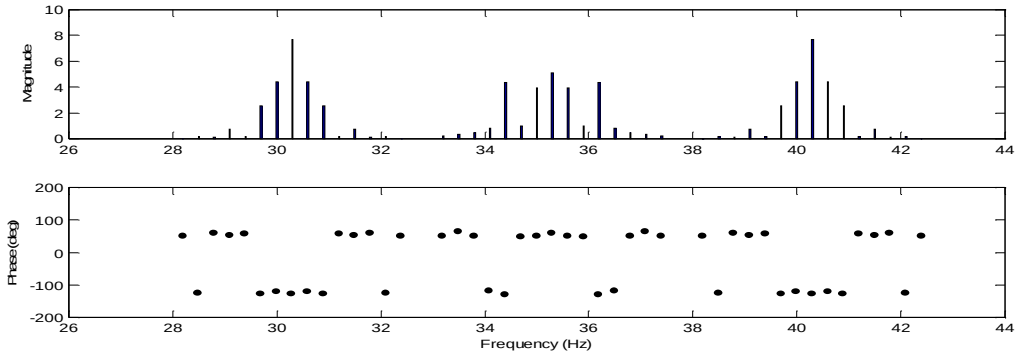


**Figure A. 23** Sideband FRF at the excitation frequency of 35.3 Hz.

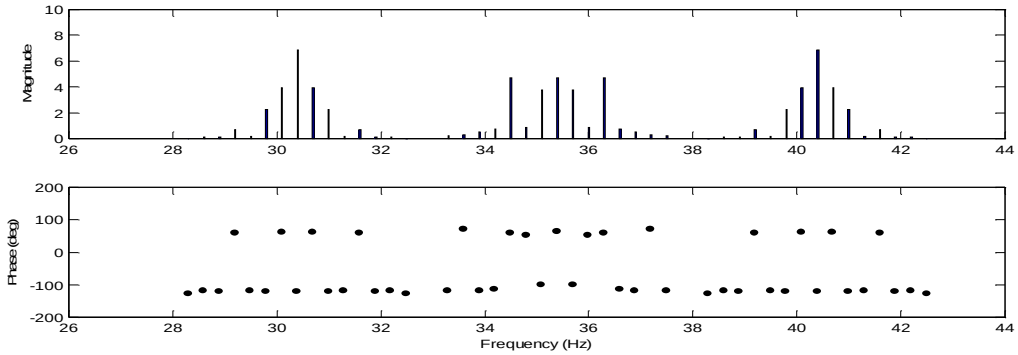


**Figure A. 24** Sideband FRF at the excitation frequency of 35.4 Hz.

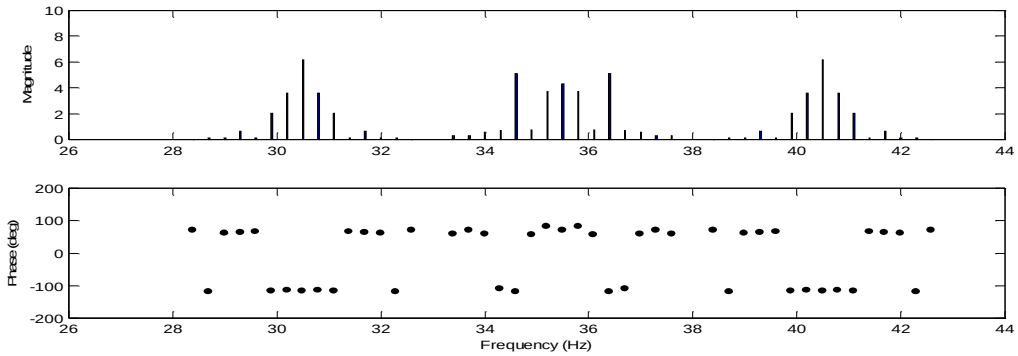


**Figure A. 25** Sideband FRF at the excitation frequency of 35.5 Hz.

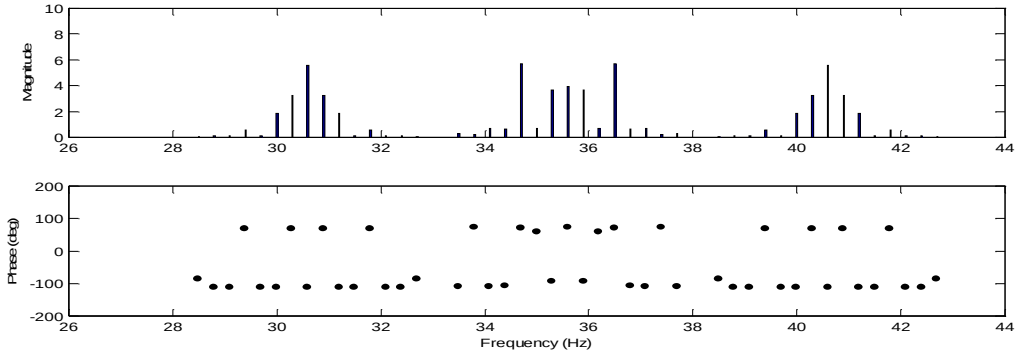


**Figure A. 26** Sideband FRF at the excitation frequency of 35.6 Hz.

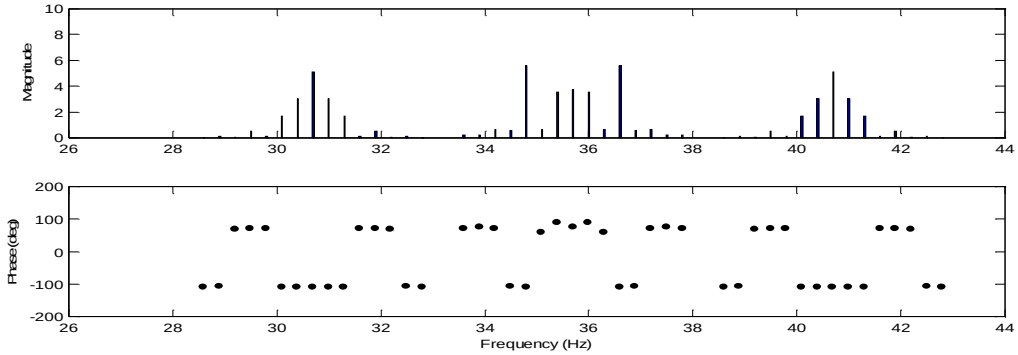


**Figure A. 27** Sideband FRF at the excitation frequency of 35.7 Hz.

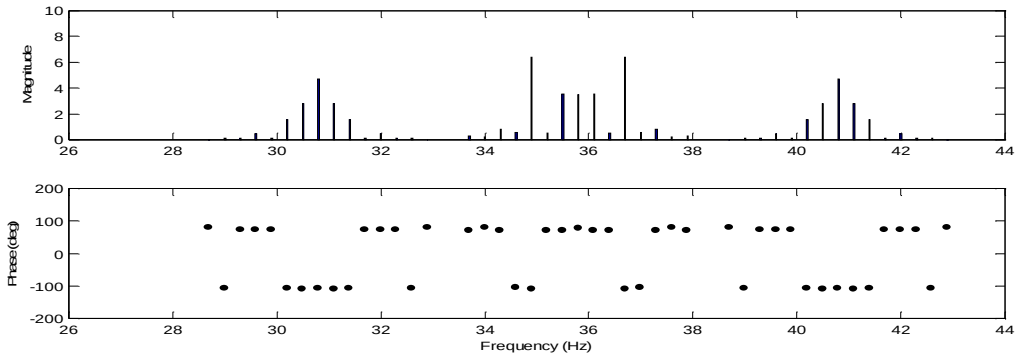


**Figure A. 28** Sideband FRF at the excitation frequency of 35.8 Hz.

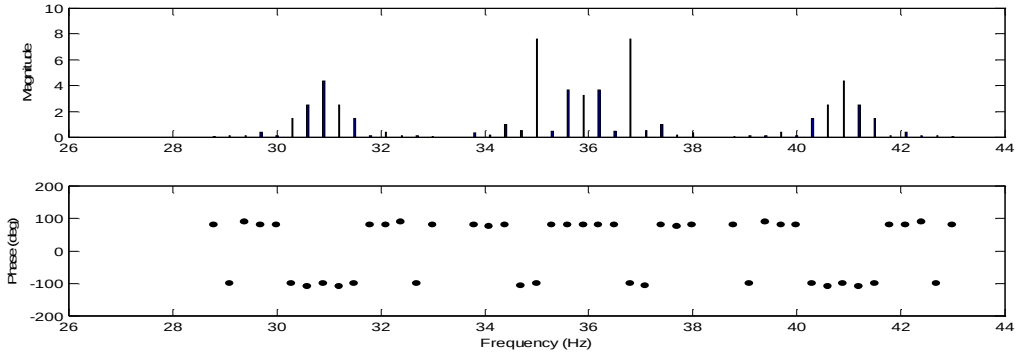


**Figure A. 29** Sideband FRF at the excitation frequency of 35.9 Hz.